Ting Guo

X-ray Nanochemistry

Concepts and Development

Nanostructure Science and Technology

Series editor

David J. Lockwood, FRSC
National Research Council of Canada
Ottawa, Ontario, Canada

Ting Guo

X-ray Nanochemistry

Concepts and Development

Springer

Ting Guo
Department of Chemistry
University of California
Davis, CA, USA

Dedicated to Rick Smalley and Kent Wilson, my mentors, for their kindness, inspiration, and willingness to teach.

Preface

More than a century after the discovery of X-rays, these energetic photons are being used widely to image objects in both real and reciprocal spaces. Real-space imaging includes dental X-rays and airport scanners. X-ray crystallography works in the reciprocal space, which helps us discover the structure of materials such as proteins and DNA molecules. Unlike these usages of X-rays, X-ray nanochemistry studies X-ray-driven chemical reactions in nanosystems, starting with X-ray ionization of atoms to create reactive chemical species such as electrons and reactive oxygen species. X-ray nanochemistry also studies the applications of these fundamental processes. Another way to define X-ray nanochemistry is that it creates, utilizes, and links atomic, molecular, and nanoscale events and studies how to use these events to transform X-ray energy into other forms of energy. There are a number of applications of X-ray nanochemistry, and one of which is cancer treatment. Unlike traditional radiotherapy, X-ray nanochemistry can help release a lethal dose of drugs from nanoscale machines with just the dose of dental X-rays at precise locations in the body, thus eliminating all side effects of radiotherapy and even chemotherapy. Future applications also include the creation of nanometer pixels for data storage that can be written or read with nanometer dimension X-ray beams. Invisible ink is another product that can be created through X-ray nanochemistry research. Other applications include fast-charging batteries with X-rays or imaging hidden dynamics with nanometer resolution in vivo.

The process of discovery is akin to walking in a dark universe before the Big Bang. The universe needs a long time to accumulate enough zero-point energy to set off the Big Bang. The discovery of X-ray nanochemistry experiences a similar process. Time, random thoughts, and all sorts of experiments are needed to lay the groundwork for the arrival of the main events. I was trained in nanoscience in the Smalley group at Rice University and then in X-ray spectroscopy in the Wilson group at the University of California at San Diego. The passing of Wilson and then Smalley played important catalytic roles in pushing me to create this new discipline. Their teachings and passing helped me realize that a combination of nanoscience and X-ray spectroscopy may help improve radiotherapy that could one day lead to better

cancer treatment or management. The original idea was to use 3 nm gold nanoparticles acting as a silver bullet to sensitize radiotherapy to destruct cancer, an idea described in proposals. I wrote and talks I gave around the country between 2001 and 2004. Around the same time, there were several other efforts – for example, Das and his colleagues reported using microspheres to enhance the effectiveness of X-ray irradiation in 2000; measurements were done using chemical assays as well as cells. From the 1990s to the 2010s, Meisel and LaVerne in the Radiation Laboratory at the University of Notre Dame studied the interactions of various nanoparticles with ionization radiation, mainly γ-rays. Another related area of research is that there existed five decades of work, spanning the 1960s through the 2010s, performed by Hofer, Karnas, Kasis, Fairchild, and many others in the area of Auger electron therapy using complexes such as iododeoxyuridine (IUdR) containing radioactive elements such as ^{129}I. Soon after my group reported our findings at the ACS annual meeting in August 2004, Hainfeld et al. reported results of their year-long experiments to determine dose-enhancement factors for the treatment of tumors in mice with 1.9 nm gold nanoparticles under X-ray irradiation. The gold nanoparticles were synthesized as contrast agents used in transmission electron microscopy, a line of work Hainfeld et al. had conducted for nearly two decades prior to their 2004 publication. Their 2004 work quickly helped others realize the potential of using nanomaterials to increase absorption of X-rays. Around the same time, my group published our first results on using 5 nm gold nanoparticles to enhance the breakage of DNA single and double strands under X-ray irradiation. Seven years after all these experiments, X-ray nanochemistry was formally coined by my group in one of our 2012 publications.

Today, X-ray nanochemistry has the potential to progress far beyond the early pictures painted or implied more than a decade ago. The main goal back then was to use simple gold nanoparticles to increase X-ray absorption and improve the efficacy of cancer treatment, although other goals such as making it easier to detect X-ray-driven chemical events were also envisioned. I recall a time when I talked to one of my graduate students, Fang Shan, in 2001 about why we should pursue work in the direction of combining X-ray spectroscopy with nanoscience while she was performing ultrafast X-ray measurements using the table-top ultrafast X-ray source in my lab at UC Davis. Although I explained the reason was to enhance the interaction cross-sections between X-rays and targeted chemical events so that our table-top ultrafast X-ray instrument could be used to study more reactions, deep down I was motivated by the passing of Wilson a few months prior, and Smalley, who had developed leukemia a couple of years prior. It is fair to say that without them I would not be able to create and work in this new field. I would like to dedicate this book to honor Smalley and Wilson for their kindness and inspiration.

X-ray nanochemistry, as described in this book, is still in its infancy. It is desirable to create the highest enhancement by systematically creating, isolating, and studying different categories and types of enhancement for the purpose of combining them to achieve a much greater total enhancement. It is likely that many of the mechanisms that support these enhancements have not been developed. For example, organometallic chemistry and biochemistry need to be explored to help realize high enhancements. As explained in this book, nature, based on our current

knowledge, has not yet developed systems to harvest X-ray radiation. This means that researchers working in this discipline will have to do everything from scratch.

A major application area of X-ray nanochemistry to date is cancer treatment. Working on applications is exciting and inspirational. Trained as a physical chemist, I am not easily satisfied with incremental changes. I hope that the science of X-ray nanochemistry can be more independently developed without "hindrance" from the demand for commercial developments. On the other hand, it is beneficial to know what applications there might be down the road. This is why the book contains two main parts, the fundamental science spanning Chaps. 2, 3, 4, 5, 6 and 7 and potential applications described in Chaps. 8, 9, 10 and 11.

It is difficult to write about a subject in its infancy. X-ray nanochemistry and its applications will continue to grow, probably at an accelerated pace in the next decade. Although the table of contents of this book remains the same as what I submitted to Springer five years ago, hundreds of publications have appeared in this time span and these results are incorporated to make the book fuller. As the discipline evolves, however, current thinking may be revised or even proven wrong. I expect that many new theories, nanomaterials, complex nanomachines, instruments, and measurements will become available soon and I am excited to be working in this discipline.

I would like to thank those who helped the writing of this book. All my students are coauthors, even though their names are not on the author list. They have helped me realize many experimental and theoretical dreams described in this book. I would like thank all my students, particularly Guangjun Cheng, Fang Shan, Josh Carter, Dan Masiel, Erica Foley (undergraduate student who published our first paper on X-ray nanochemistry), Rhiannon Porter, Yongquan Qu, Alex Sutherland (undergraduate student who published 11 papers in 4 years), Neal Cheng, Zane Starkewolf, Larissa Miyachi (undergraduate student), R. Andrew Davidson, Arjun Sharmah, Zi Yao (undergraduate student), Jennifer Lien, Ryan Taylor (undergraduate student), Joan Chang, Josh Alamillo, Kristin Peck, and Mengqi Su. I also thank the authors whose works are cited in this book. Thanks are also extended to my colleague Milburn, who kindly reviewed the book and provided invaluable suggestions. Lastly, I would like to thank my family, my parents, my sister Shu, and my brother Jie. I would not be able to do anything if it were not for their constant love, support, and encouragement. I would also like to acknowledge the support of the National Science Foundation, whose chemistry division and especially the program of Macromolecular, Supramolecular, and Nanochemistry (MSN) has supported the development of X-ray nanochemistry. This work would be also impossible without the support of the University of California. I taught a graduate class on X-ray nanochemistry at UC Davis, and the notes developed from that class have helped the writing to a degree as well, though this book is much more extensive than the content of the class.

Davis, CA, USA   Ting Guo
February 2018

Contents

Abbreviations

3-CCA	coumarin 3-carboxylic acid
4-POBN	α-(4-pyridyl-1-oxide)-N-tert-butylnitrone
7-OHCCA	7-hydroxycoumarin 3-carboxylic acid
Agu	silver-coated gold nanoparticles
APF	amino-phenyl-fluorescein
APS	advance photon sources
AuNPs	gold nanoparticles
BMPO	5-tert-butoxycarbonyl-5-methyl-1-pyrroline N-oxide
BODIPY	boron-dipyrromethene
BrdU	bromodeoxyuridine
CaP	calcium phosphate
CaPELs	calcium phosphate encapsulated liposomes
CCD	charge coupled devices
CCS	cell cycle synchronization
CEPA	2-carboxyethylphosphonic acid
CT	computed tomography
CTAB	cetyl trimethylammonium bromide
CTAC	cetyl trimethylammonium chloride
DBP	dibutyl phthalate
DBPMPO	5-(dibutoxy- phosphoryl)-5-methyl-1-pyrroline N-oxide
DCF	dichlorofluorescien
DEF	dose enhancement factor
DEPMPO	5-(diethoxyphosphoryl)-5-methyl-1-pyrroline N-oxide
DEU	dose enhancement units
DHE	di-hydro-ethidium
DLS	dynamic light scattering
DMSO	dimethyl sulfoxide
DMPO	5,5-dimethyl-1-pyrroline-N-oxide
DNA	deoxyribonucleic acid

DOTAGA	1,4,7,10-tetraazacyclododececane,1-(glutaric acid)-4,7,10-triacetic acid
DOX	doxorubicin
DPPH	2,2-diphenyl-1-picrylhydrazyl
DSBs	double strand breaks
DSP	c,c,t-(diamminedichlorodisuccinato)Pt(IV)
EDTA	ethylene diamine tetraacetic acid
EGSnrc	electron gamma shower national research council
EMPO	2-ethoxycarbonyl-2-methyl-3,4-dihydro-2H-pyrrole-1-oxide
EPR	electron paramagnetic resonance
EPR	epidermal permeation and retention
FRET	Förster resonance energy transfer
FTIR	Fourier transform infrared
GNP	gold nanoparticle
GQD	graphene oxide quantum dots
HU	Hounsfield units
IUdR	iododeoxyuridine
LEM	local effect model
LET	linear energy transfer
LLSG	lee-Lu-Sharmah-Guo
LMG	leucomalachite green
MCNP	Monte Carlo nanoparticle
MPA	mercaptoprionic acid
MTPM	4-methylthiophenylmethanol
NAC	N-acetyl cysteine
NLS	nuclear localization signal
NOREC	NIST Oak Ridge electron (transport) code
PAA	polyacrylic acid
PARTRAC	particle tracks
PDDA	polydiallyl-dimethyl ammonium chloride
PDMAT	pentakis(dimethylamido)tantalum
PEG	polyethylene glycol
PEI	polyethylenimine
PMMA	polymethylmethacrylate
PTE	2-phenylthioethanol
RBE	relative biological effectiveness
RGD	arginine-glycine-aspartic acid
ROS	reactive oxygen species
PVP	polyvinyl pyrrolidone
SAO	$SrAl_2O_4:Eu_2^+$
scDNA	supercoiled DNA
SEM	scanning electron microscope
SERS	surface enhanced Raman spectroscopy
SMCC	succinimidyl 4-(N-maleimidomethly)cyclohexane-1-carboxylate

SOD	superoxide dismutase
SOSG	singlet oxygen sensor green
SPR	surface plasmon resonance
SRB	sulforhodamine B
SSBs	single strand breaks
T1BE	type 1 biological enhancement
T1CE	type 1 chemical enhancement
T1PE	type 1 physical enhancement
T2CE	type 2 chemical enhancement
T2BE	type 2 biological enhancement
T2PE	type 2 physical enhancement
T3PE	type 3 physical enhancement
TAT	transactivator of transcription
TEM	transmission electron microscope
TEMPAMINE	4-amino-2,2,6,6-tetramethylpiperidine-1-oxyl
TEMPO	(2,2,6,6-tetramethylpiperidin-1-yl)oxyl
TEMPOL	4-hydroxy-2,2,6,6-tetramethylpiperidine-N-oxyl
TEMPONE	4-oxo-2,2,6,6-tetramethylpiperidine-1-oxyl
THPC	tetrakis-hydroxymethyl-phosphonium chloride
TMA	trimethylammonium
TOC	total organic carbon
TOPAS	tool for particle simulation
Tris	tris(hydroxymethyl) aminomethane
WP	weight percent
UCSP	up conversion silicon phthalocyanine/porphyrin
XANES	X-ray absorption near edge structure
XFCT	X-ray fluorescence computed tomography
XIET	X-ray induced energy transfer
XEOL	X-ray excited optical luminescence
XPS	X-ray photoelectron spectroscopy

Part I
Introduction

Chapter 1
X-Ray Nanochemistry: Background and Introduction

If you are flexible, you may not get what you want; If you are adamant, you may only get what you want.

1.1 Background and Introduction

1.1.1 Ionizing Radiation and Nature

Ionizing radiation research began with the discovery of X-rays in 1895 by Röentgen, who was awarded the first Nobel Prize in Physics in 1900. Other types of ionizing radiation were discovered soon after, with the discovery of γ-rays in 1900 by Villard. After a century of studying radiation biology, and as technologies improve and the level of exposure to man-made ionizing radiation decreases, there seems to be a lack of interest in studying radiation-related topics because large doses of ionizing radiation are generally perceived as harmful to humans. Exceptions to this are in the field of crystallography and medical imaging as well as cancer treatment, areas in which ionizing radiation is still being actively researched and used.

It turns out that ionizing radiation such as X-rays and γ-rays is ubiquitous in nature, as we are constantly being irradiated by them. For example, the annual background dose received by people living in Denver is equivalent to performing several head computed tomography (CT) per year. When ionizing radiation interacts with matter, whether it is air, water, tissues or nanomaterials, one of the most important events is ionization of core electrons in atoms in these materials, hence the name ionizing radiation. When X-ray photons interact with light elements such as oxygen, another absorption process known as Compton scattering occurs, which produces energetic electrons as well. As shown in Chap. 2, these electrons and positive ions left behind on the ionized species are capable of initiating or enabling chemical reactions. Knowing that ionizing radiation is omnipresent all the time on Earth, in our bodies, and around the world, and the interactions between the radiation and matter generate reactive electrons, radicals, and ions, the question to ask is whether nature has developed any kind of chemistry that specifically responds to ionizing radiation.

To answer this question, one may draw inspiration from a well-known process, photosynthesis. The dominating part of the electromagnetic spectrum from the sun is comprised of visible and ultraviolet photons, which interact strongly with some molecules and certain biological systems. It also can be said that nature created these molecules to respond or harvest sunlight energy delivered to Earth. Nature does this because certain biological systems need to draw energy from the sun, and this energy becomes the driving force for the growth of plants and other organisms on Earth. Biological systems such as human bodies, on the other hand, consume the organic matter but do not directly require solar energy to survive, with exceptions such as human skin absorbing UV light to produce vitamin D_3. If nature developed these molecules and photosystems to effectively respond to sunlight, can it also create any effective systems to respond to X-rays?

A possible mechanism developed in nature to respond ionizing radiation is DNA repair. Biological systems have to defend against reactive species such as hydroxyl radicals, which may be generated by UV light, ionizing radiation, or chemicals such as oxidized fats. X-rays produce these radicals when interacting with biological systems, which contain abundant water as well as other molecules that can produce radicals or react with radicals. The exact reason why biological systems developed these repair mechanisms is unknown because there are many means known to cause DNA damage. The outcome, nonetheless, is that chemicals in cells such as DNA repair proteins do exist and Lindahl, Modrich and Sancar won the Nobel Prize in Chemistry in 2015 for their work on this important topic.

Another clue that may help answer the question of whether nature created any systems to respond to ionizing radiation comes from the fact that all known natural living systems are made of light elements such as C, H, N, and O, and none of these systems contain large amounts of X-ray or γ-ray absorbing heavy elements. Based on the existing knowledge, although it is still too early to completely rule out the possibility that nature began to create proteins to repair nuclear DNA only after they were damaged by ionizing radiation billions of years ago, it is more likely that nature has not developed any specialized processes to respond to X-rays or other types of ionizing radiation. Given that ionizing radiation can generate a high local density of radicals and can directly ionize atoms in nuclear DNA molecules, it appears that nature is less prepared or that our current understanding is not advanced enough to claim that biological systems have evolved mechanisms or measures to specifically enhance or counter the effects of ionizing radiation. Even the most radioresistive bacteria such as *Deinococcus radiodurans,* which can survive 1000 Gy of irradiation, only have more efficient repair systems rather than sensitization mechanisms. In short, there is no existing enhancement mechanism in nature that harvests or thrives on ionizing radiation such as X-rays like photosystems do with sunlight.

If this reasoning is correct, much more work is needed to create artificial chemical or nanochemical systems to respond to X-rays. The upside of such a reality is this lack of natural systems may be a blessing in disguise. Rather than spending time figuring out what nature already offers, researchers can create and assemble materials that fulfill different functions. The hidden principles associated with these new materials will require investigation and creation, after which engineers can make

devices based on established principles. This is analogous to what we have done in the current digital world, beginning with the study of semiconductor materials and associated chemical and physical principles in the 1950s.

In summary, it looks certain that new materials will have to be created and principles be understood so that it is possible to use these new systems to build devices to respond to X-rays and other types of ionizing radiation. Those who are working in the discipline have to explore and create chemical and particularly nanochemical systems to do what we want them to do. Knowledge on at least two fronts will have to be advanced—creating new materials and developing novel physical and chemical principles. These new materials and systems and the principles will improve the enhancement as defined later in this book and beyond.

1.1.2 History of Nanochemistry

Nanochemistry is a scientific discipline that studies chemical processes made available by nanomaterials. The latter contain a vast number of materials, from simple nanoparticles or nanowires to hybrid, complex nanomaterials that support exotic functions such as sensing and catalysis. Like ionizing radiation, nanomaterials have existed for millennia. Many kinds of nanoparticles have probably existed in nature for billions of years. Simple, man-made, or engineered nanomaterials existed for thousands of years, dating back to ancient times when silver was used to stain glass. More recently, Faraday made gold and silver nanoparticles in the 1850s.

Nanochemistry is closely related to another field of work—nanotechnology, which is a more popular term. Nanotechnology is the applied form of nanochemistry, although the two are closely intertwined. The beginning of the nanotechnology era dated back to almost a century ago. There were several accounts in the 1920s where platinum nanoparticles were studied. Then, starting in the 1970s, platinum nanoparticle catalysts were further developed and widely used for automobiles and have continued to be used till now. The actual arrival of modern nanoscience, which is almost a synonym of nanochemistry, occurred in the late 1980s and early 1990s, when many new studies and nanomaterials emerged. For example, fullerenes were discovered by Smalley et al. [1]. Following this was the discovery of carbon nanotubes by Ijima [2]. Quantum dots were discovered by Bawendi et al. [3]. Studying these materials soon became popular in research laboratories around the world. Gold nanoparticles were synthesized by Brust et al. [4] with specialized sizes and coatings. In another effort, gold nanoparticles were used as a contrast agent in transmission electron microscopy by Hainfeld [5] and others in the late 1980s. Starting in the 1990s, almost every chemistry department in the United States has had some activities of nanoscale research. This created the basis for the nanotechnology boom in the 2000s when the United States began to invest heavily in infrastructures for nanotechnology. The establishment of the National

Nanotechnology Initiative (NNI) led by Roco and Tech [6] signaled the formal arrival of the true nanoscience era at the national level. Despite all these achievements, the era of nanotechnology probably has not yet arrived because there have been only a handful of real applications developed, such as using quantum dots in display devices.

1.1.3   Early Histories Related to X-Ray Nanochemistry

From what are shown above, simple nanoparticles and ionizing radiation may have existed for a long time. The study of catalysis using ionizing radiation and synthesis of nanomaterials using ionizing radiation has been ongoing since the 1920s. From very early times, the idea of using nanoparticles to catalytically improve the yield of relatively simple chemical reactions was examined. The radiation was usually γ-rays, and nanoparticles were either platinum black or oxide nanoparticles. In retrospect, these efforts were connected to the enhancement of the effectiveness of irradiation of ionizing radiation that is discussed in this book, which is formally defined as one of the main goals of X-ray nanochemistry research. The scope of the impact, however, has been significantly expanded from molecular hydrogen production in the early times to generation of reactive oxygen species, DNA damage, and polymerization at present. All of these research topics belong to X-ray nanochemistry research.

As stated earlier, research on interactions of ionizing radiation with nanomaterials began in the 1920s when interactions of electrons, γ-rays, α particles, and other types of ionizing radiation with catalysts and nanoparticles were used to investigate catalytic production of chemicals, such as hydrogen. More studies were undertaken after the invention of nuclear technologies capable of producing intense ionizing radiation and nuclear waste, the latter of which presents a storage problem. Motivations for work in this area are the same now as they were then. For example, it is important to understand if and how nanomaterials can be used to produce or stop the generation of hydrogen gas when irradiated with ionizing radiation.

These studies comprised part of the early history of systematic study of ionizing radiation nanochemistry. Most results obtained using other types of ionizing radiation can help X-ray nanochemistry, and, conversely, most of the principles developed in X-ray nanochemistry can be used to improve the outcome of these early works. Though the radiation types are interchangeable, the content contained in these early works encompassed only a small part of X-ray nanochemistry. As this book shows, the scope of X-ray nanochemistry extends far beyond those early studies involving γ-rays and nanoparticle catalysts.

A related area in early studies that does not fall into the current scope of X-ray nanochemistry research was the production of nanomaterials using ionizing radiation. X-ray synthesis of nanoparticles is different from X-ray nanochemistry because it only involves reduction of ions by X-ray-generated species in solutions to form nanoparticles and has not considered using nanomaterials under X-ray irradiation to

augment the effects of X-ray irradiation. If the synthesis of nanomaterials using ionizing radiation were proven to be dependent on nanomaterials under irradiation, then this process would belong to X-ray nanochemistry.

1.1.4   Early Works Outside UC Davis

Interactions of ionizing radiation with nanomaterials may not have led to the creation of X-ray nanochemistry so quickly if not for the immense medical application potential of X-ray nanochemistry, ranging from imaging to treatment. Development of nanomaterials, nanochemistry, nanoscience, and nanotechnologies has been accelerated by the desire to use these techniques in medical applications. Several experimental demonstrations that helped create or accelerated the creation of the discipline of X-ray nanochemistry are described here.

One specific work closely related to X-ray nanochemistry was the use of externally introduced materials, such as implants, in the human body. Castillo et al. [7] noticed increased damage near the implants. Another closely related study that helped with the conception of X-ray nanochemistry was the use of a radiosensitizer iododeoxyuridine (IUdR) for Auger electron therapy. IUdR and related compounds containing radioisotopes were delivered into the body, after which Auger electrons were released to destruct cells. IUdR research could be traced back to the 1960s, although Auger therapy, which was still being understood in the late 1990s, overlapped with some of the early studies in X-ray nanochemistry, which began in the early 2000s. Hunting et al. [8] studied bromodeoxyuridine (BrdU) in causing single-strand breaks in DNA. The idea of using these compounds to make cancer cells more sensitive to radiation, unfortunately, has not reached its promised potential in the early days as it is difficult to make these materials target tumors or to deliver large enough quantities to tumors in the body without causing serious side effects. It was around this time when Guo began his career in the Department of Chemistry at UC Davis. The nanomaterials proposed by Guo starting from 2001 were aimed to overcome these serious problems facing IUdR or BrdU.

The work performed by Das et al. [9] was also connected to the development of X-ray nanochemistry. The study, although employing gold microspheres and not nanomaterials, was the closest to using nanomaterials in cancer treatment at the time. It is evident that the results by Das et al. [9] were medical application oriented and many cellular and medical works presented within the realm of X-ray nanochemistry resembled the work by Das et al.

Studies carried out by Meisel and LaVerne at the University of Notre Dame Radiation Laboratory and other researchers around the world helped create X-ray nanochemistry as well. For example, radiation nanochemistry was studied in Meisel's lab in the 1990s and 2000s. Works by Meisel and Laverne were generally conducted using γ-rays, which were different from many works covered by X-ray nanochemistry even though there were similarities between how nanomaterials

interact with the two types of ionizing radiation. Differences between the two are explained in Sect. 1.1.8.

These developments were seeds sown by researchers that would later grow and ripen into the then little-known field of X-ray nanochemistry. Yet like many chemical reactions, there usually is a catalyst for a major event to occur, and this catalyst was the passing of Wilson in 2001.

1.1.5   Development of X-Ray Nanochemistry in the Guo Lab at UC Davis

The stories behind the development of X-ray nanochemistry are associated with many groups, but here, the events as they happened in the Guo laboratory at UC Davis are recounted. X-ray nanochemistry work in the Guo laboratory at UC Davis commenced in 1999, two years before Guo's postdoctoral adviser Wilson passed away from cancer in 2001. Wilson had a dream of using X-rays to visualize chemical reactions, a dream shared by 16 postdoctoral scholars he hired in the early 1990s. Guo studied the synthesis of nanotubes and transition metal clusters in Smalley's laboratory at Rice University and then ultrafast X-ray spectroscopy in Wilson's lab at the University of California, San Diego. At UC Davis, he studied chemical reactions using tabletop ultrafast X-ray pulses. Many problems arose, and one of them was that the number of ultrafast X-ray photons was not enough to allow measurements of dynamics in solutions of regular metal complexes, severely limiting the number of chemical systems the technique could study. Construction of the fourth-generation synchrotron sources, such as the Linac Coherent Light Source (LCLS) at the Stanford Radiation Laboratory, had begun, which made the tabletop ultrafast X-ray measurements less appealing. At that time, Wilson passed away, and his passing gave Guo both a reason and a clue. It also seemed natural to combine nanomaterials with X-rays to increase the interaction cross-sections so that ultrafast X-rays have a better chance to be used to interrogate important chemical reactions.

In late 2001, Guo submitted his first proposal on studying X-ray nanochemistry. The proposal was turned down. The proposed work was to use sub-3 nm diameter gold nanoparticles and X-rays to damage DNA molecules, and the work was carried out by students who also worked on several other projects including ultrafast X-ray spectroscopic investigations of dynamic structures of metal complexes in solutions, a project supported by the National Science Foundation. Supported by the University of California, Guo and his students were able to demonstrate that DNA molecules were damaged with enhancement using small gold nanoparticles. The results were published in 2005, and the lead author was an undergraduate student Foley [10].

Their work was helped by several other faculty members at UC. Their generosities accelerated the pace of research. Still, it took nearly 4 years before the results were published in 2005, which came out a few months after Hainfeld et al. published

their paper, showing that nanoparticles could be used to increase the survivability of cancer-bearing mice under X-ray irradiation.

Knowing all these happened in one laboratory, one can speculate how much more effort was needed in other laboratories around the world, including Hainfeld's, which had worked for nearly 20 years on using gold clusters as a contrast agent for electron microscopy prior to their animal work published in 2004. These are speculations by the author of this book (Guo) since the author does not have first-hand experience with other laboratories.

The nanochemistry component did not emerge until 2007, when the surface of nanoparticles was modified to accommodate targeting ligands. The term X-ray nanochemistry was first mentioned in a publication by Guo et al. [11]. Although one may debate about the influence of the timing of these events on the creation of X-ray nanochemistry, it was definitely in that time span when the theme of X-ray nanochemistry emerged. It may be unimportant to pinpoint the exact time when X-ray nanochemistry was established. Knowing the content of those proposals by Guo in 2001, which was to use sub-3 nm gold nanoparticles to replace IUdR or equivalents as a highly specialized method to destroy cancer or cancerous DNA, it is prudent to state that these two early efforts from Guo's laboratory and from Hainfeld's laboratory/company only revealed a glimpse of the essence and full scope of current day X-ray nanochemistry, which is still quickly growing.

1.1.6 Formal Introduction of X-Ray Nanochemistry

X-ray nanochemistry is a brand new discipline. As stated in the preface, X-ray nanochemistry studies X-ray-driven chemical reactions in nanosystems, starting with X-ray ionization of atoms to create reactive chemical species such as electrons and reactive oxygen species. X-ray nanochemistry also includes the creation of nanomaterials to enable these reactions as well as methods to characterize these reactions. In other words, X-ray nanochemistry creates, utilizes, and links atomic, molecular, and nanoscale events and studies how to use these events to transform X-ray energy into other forms of energy, a definition given earlier in this chapter. X-ray nanochemistry also contains current applications in biology, cancer treatment, catalysis, sensing, and environmental science. Future applications in other areas are also possible.

X-ray nanochemistry can be regarded as being introduced over a few years, depending on how it is viewed. For example, Guo et al. [12] and Guo et al. [13] both discussed relevant aspects of X-ray nanochemistry. In a few publications in 2011 and 2012, the concept of X-ray nanochemistry became clearer. Finally, in a publication in 2012, Guo et al. [11] performed the first experiment that was directly connected to X-ray nanochemistry. Regardless of the exact time when X-ray nanochemistry or X-ray nanotechnology began, three facts are clear.

Firstly, Hainfeld et al. [14] were the first to use nanoparticles to enhance the effectiveness of X-ray irradiation in radiotherapy, and Guo et al. [10] were the first to

report on using nanomaterials to enhance damage of DNA by X-rays. Secondly, X-ray nanochemistry was only formally introduced and described by Guo et al. [11]. These three publications mark the arrival of a scientific and technological era that was different from the past. There is a vast amount of literature describing many different aspects of using nanomaterials to improve all aspects of X-ray applications, and it is the aim of this book to discuss these aspects. Thirdly, while these early works in X-ray nanochemistry are the foundation of X-ray nanochemistry, the content described in these early publications does not fully represent the scope of X-ray nanochemistry. The number of nanochemical processes in these early works was limited, and other works have since greatly expanded the scope. As shown in this book, many areas have been simultaneously developed. The scope of the work performed to date in the area of X-ray nanochemistry is broad, ranging from imaging to treatment to catalysis and sensing. Theoretical work is also a major part of X-ray nanochemistry.

The application aspects of X-ray nanochemistry are often emphasized over the fundamental chemistry or nanochemistry. However, one must realize that the depth and future of X-ray nanochemistry rely on chemistry and especially nanochemistry. For example, improved understanding of the surface chemistry of nanomaterials has helped advance X-ray imaging through improved uptake and delivery. Therefore, it is critical to continue to develop these fundamental understandings. Formal introduction and creation of X-ray nanochemistry has helped emphasize the study of fundamental chemical processes that may eventually revolutionize many applications in X-ray nanochemistry. Although nanomaterials can increase the effectiveness of X-ray irradiation, it is now clear that merely using simple nanomaterials to replace existing or traditional materials does not significantly increase the effectiveness. This means that primitive nanomaterials are not the novel solution people have been looking for to solve many problems, as Guo, the author of this book, had naively imagined in the 2001 proposal. At that time, the full impact of nanomaterials was unclear. As this book shows, X-ray nanochemistry may eventually support novel applications desired by many researchers.

This book attempts to define the scope of X-ray nanochemistry, which is a discipline that continues to grow and expand. Fundamental science will be critical to the future development of X-ray nanochemistry. Although it is difficult to foresee the future, one thing is almost certain: new developments will largely rely on the development of theories and complex nanomaterials. The next edition of this book will be quite different. However, there will be strong overlap between this edition and the next because the most fundamental processes, such as physical and chemical enhancement, will be the same. Therefore, this book tries to find a balance between fundamental studies and applications as well as between simple, primitive studies and experiments using elaborate nanomaterials.

One motivation of writing this book is to include a more complete review and evaluation of the literature in the area of X-ray nanochemistry. The number of papers published per year in the discipline has increased significantly in recent years, as shown in Fig. 1.1. There are numerous reviews in each subfield of X-ray nanochemistry, but there is currently not a single document covering the whole
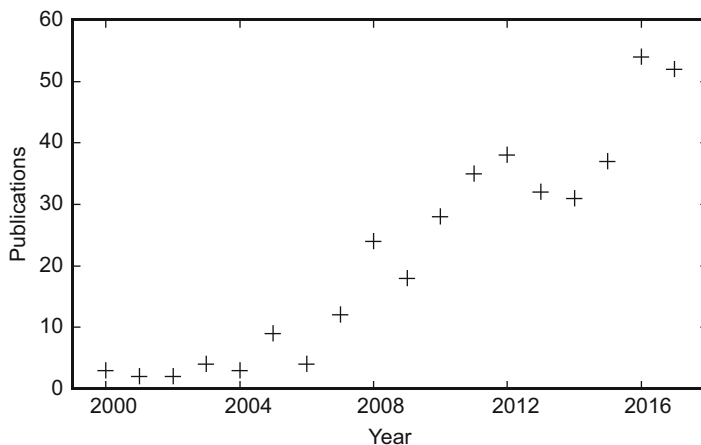
Fig. 1.1 Number of publications per year in the discipline of X-ray nanochemistry in the last 17 years, since 2000. The number of publications in 2017 is extrapolated based on the number of publications from 1/1/2017 through 6/30/2017

spectrum of work in X-ray nanochemistry. This situation is partially caused by the fast pace of the growth in the interest of cancer treatment within X-ray nanochemistry. There are many applications including imaging, treatment, catalysis, and biology that make researchers excited about the usage of nanomaterials. On the other hand, the recognition and establishment of X-ray nanochemistry, and a collection of the entire literature, as they are organized in this book, may help researchers connect with the larger community conducting X-ray nanochemistry research.

If the tradition of naming the applied side of nanoscience as nanotechnology is followed, then the applied side of X-ray nanochemistry can be called X-ray nanotechnology. As it is shown in this book, both are important, especially if the two are synergistically developed. It is important to develop the fundamental aspects of X-ray nanochemistry independent of the constraints and burdens from X-ray nanotechnology. Only then can the true potential of X-ray nanochemistry be unlocked, recognized, and reached.

1.1.7 Categories and Types of Enhancement and Enhancement Units

At the beginning of X-ray nanochemistry research, only one category of enhancement was known to researchers, and this enhancement was regarded as being caused by increased absorption of X-rays by nanomaterials. The enhancement is now categorized as physical enhancement. Other terms have been used, including dose enhancement factors or dose enhancement ratios.

Physical enhancement can be further divided into three types. The first type is the constant enhancement by electrons depositing energy in the whole sample volume. The second type is caused by electrons depositing energy near the surface of nanoparticles, and the enhancement is called nanoscale energy deposition or nanoscale enhancement. The third is caused by increased emission of UV-Vis light as the result of adding nanomaterials. All three types of physical enhancement require the added nanomaterials to strongly absorb X-rays. These concepts are described in Chap. 2.

Other categories of enhancement exist, one of which is chemical enhancement. A criterion for chemical enhancement to occur is that the enhancement has to be enabled by catalytic chemical reactions, which does not happen in physical enhancement. There are several types of chemical enhancement as well. The first is caused by catalysis enabled by reactive species generated in solution by X-rays. This type of chemical enhancement does not involve increased production of reactive oxygen species. The second type of chemical enhancement involves catalytic production or destruction of radicals. Both types are described in Chap. 3.

Another category of enhancement is biological enhancement, which is not yet well known but has been speculated in several reports. There are at least two types of biological enhancement identified in this book. The first type involves enhanced damage to biological samples such as cells without direct damage to any biological components in the cell by X-ray absorbing nanomaterials. The second type addresses responses of a biological system to direct damage of certain components in the cell, especially those next to the nanomaterials. A discussion of these types of biological enhancement is given in Chap. 4.

Accurate and conclusive proof of all these enhancement categories and types is by no means complete, and new mechanisms and nanomaterials will continuously be developed. As applications, nanomaterials, and methods used in X-ray nanochemistry continue to expand, more types and categories may be discovered.

In this book, the enhancement is gauged by dose enhancement units (DEU). Researchers have developed many ways to quantify the magnitude of enhancement, independent of the categories and types. Commonly used terms include dose enhancement factors (DEFs), dose enhancement ratios (DER), and nanoscale or microscopic dose enhancement factors (nDEFs or mDEFs). The units are times, fold, percentage, or simply unitless. DEU is introduced to mirror the Hounsfield units in X-ray imaging. All enhancement factors in X-ray nanochemistry use DEU. It is the ratio (hence can be unitless) of energy deposition with the added nanomaterials to that without the nanomaterials. This calculation of enhancement results in relative enhancement in reference to the effect of radiation without nanomaterials. As a result, 1.0 DEU relative enhancement means no enhancement. If the enhancement is calculated per weight percentage (WP) of gold in water of nanomaterials, for example, then absolute enhancement must be used, and the unit is DEU WP^{-1}. The absolute enhancement value is the relative enhancement value minus 1.0. Hence an absolute enhancement of 1.0 DEU per 1 WP of gold in water gives rise to 1.0 DEU WP^{-1}. One should not use relative enhancement values when calculating unit WP enhancement. For instance, if a relative enhancement is 1.5 DEU for 2 WP gold

in water, which means the absolute enhancement value is 0.5 DEU, then the corresponding unit WP enhancement is 0.75 DEU WP^{-1} if relative enhancement is used, or 0.25 DEU WP^{-1} if the absolute enhancement value is used. The first value would mean the absolute enhancement is -0.25 DEU for 1 WP of gold, which is wrong. The second value is correct, suggesting an enhancement of 0.25 DEU for 1 WP of gold in water. For this reason, absolute enhancement is used throughout this book unless otherwise noted.

1.1.8 Similarities and Differences Between X-Rays and Other Types of Ionizing Radiation

Meisel of Notre Dame once commented to the author of this book that there is little difference between X-rays and γ-rays. This statement is correct to a degree. X-rays and γ-rays are both low-linear energy transfer (LET) ionizing radiation, meaning that they are not highly absorbed by matter. Nonetheless, interaction cross-sections of X-rays with matter are quite different from that of γ-rays with matter. As shown in Chap. 2, the interaction cross-sections of the same element, such as gold, can change nearly four orders of magnitude within the X-ray energy range of 1–100 keV. Absorption cross-sections of different elements (e.g., gold and oxygen or water) may differ by 100-fold at the same X-ray energy. In contrast, absorption cross-sections for different elements for either electrons or γ-rays are much closer, often differing by as little as a few times. This makes it much more desirable to use X-rays over other types of radiation to interact with nanomaterials dissolved in media to obtain high enhancements. Many publications have shown the advantages of using X-rays over γ-rays for enhancement purpose. Nonetheless, materials and concepts developed within X-ray nanochemistry can be readily used for γ-rays, albeit with much smaller values of enhancement.

Many features can make X-rays more favorable than other types of ionizing radiation, and four of them are shown here. First, X-rays are much safer to handle than any other types of ionizing radiation. It is easy to shield X-rays used in X-ray nanochemistry, which are often below 200 keV or even less than 100 keV. X-rays are produced with X-ray tubes, which can be switched off when not in use. For low energy X-rays such as 20 keV, using them is almost as safe as a laser pointer if safety rules are strictly followed. γ-rays are difficult to contain or shield, even though they can also be produced with electricity. Radioactive elements in large quantities are the most dangerous, although a small amount of Am241 emitting α-particles is used in smoke detectors in almost every house in the United States. This proves that small amounts of ionizing radiation can be safely used if proper science and technologies are developed.

The second advantage of using X-rays with nanochemistry is that X-ray sources are far more inexpensive and accessible than sources emitting other types of ionizing radiation. For example, a microfocus X-ray source currently costs around $30,000,

and such a source can be conveniently interfaced with other instruments such as optical microscopes to perform necessary measurements required by X-ray nanochemistry research. Furthermore, miniature sources costing less than $10,000 are adequate for a majority of experiments when lesser doses of X-rays are needed to cause measurable enhancements with the advancement in X-ray nanochemistry. Monochromatic X-rays are also available at many synchrotron sources, which are conveniently accessible to researchers around world. These user-friendly facilities are well-managed and are constantly upgraded.

Thirdly, X-rays are distinctly favored over other types of ionizing radiation because of the large interaction cross-sections between X-rays and nanomaterials of heavy elements. When γ-rays are used, although the fundamental principles are similar, the interaction is much less effective. The favorable interactions between X-rays and nanomaterials make it easier to develop advanced theories, experiments, and nanosystems. Once new nanochemical mechanisms are developed that can provide high enhancement factors, these new mechanisms can be used for all types of ionizing radiation.

The fourth advantage of using X-rays is that heavy elements such as gold absorb X-rays intensely in the water window—an energy interval between 80 and 100 keV, within which water absorbs X-rays minimally. This is not true for other types of ionizing radiation such as electrons or γ-rays—all the elements have about the same absorption cross-sections, including water.

Table 1.1 summarizes the results of comparison of several important parameters associated with X-rays and γ-rays.

One may ask why X-ray nanochemistry does not belong to the traditional field of radiation chemistry. Radiation chemistry uses mainly pure liquids, metal ions, or organic compounds in solutions. The introduction of nanomaterials, catalysis, and enhancement processes completely changes the chemistry happening in these systems. Although nanomaterials such as oxides or metal nanoparticles may have existed in nature for a long time, radiation chemistry generally does not include these particles. Many new types of nanomaterials, ranging from hybrid nanoparticles to nanocapsules, are being incorporated into X-ray nanochemistry. It is thus foreseeable that in the future, X-ray nanochemistry will be more different from radiation chemistry than now.

γ-rays are generally used for their high penetrating power. When a large dose is needed deep in an object and the surface dose has to be kept manageable, then γ-ray is the only option. However, X-ray nanochemistry will usher in a new platform of

Table 1.1 Comparison of X-rays and γ-rays

Properties	γ-rays	X-rays
Photon energy	>1.2 MeV	0.1–100 keV (up to 300 keV)
Penetration depth (water, 1/e)	>15 cm	Over 5 cm
Common sources	Linear accelerators	Tubes
Mass attenuation coefficients by gold	$0.05 \text{ cm}^2/\text{g}$	$5.1 \text{ cm}^2/\text{g}$
Access to water window (80–100 keV)	No	Yes (heavy elements)

nanomaterials, which can respond to and function with very low doses of X-rays. Under this circumstance, there is no need to use γ-rays as X-rays can deliver enough dose to activate the function of the nanomaterials anywhere in the body or elsewhere without causing side effects. Until then, there is still a place for γ-rays even though they do have many more unwanted properties than X-rays.

1.1.9 Difference Between X-Ray Nanochemistry and X-Ray Synthesis of Nanomaterials

Much work has been done in the area of using ionizing radiation to synthesize nanomaterials, especially metallic nanoparticles such as gold or silver nanoparticles. Early work in this area was demonstrated by Henglein and Meisel [15]. Belloni and Mostafavi [16] summarized works in this area more than a decade ago. A more recent example was given by Divan et al. [17] who reported the results of their study of using X-rays to deposit gold nanoparticles formed from a gold salt onto bulk SiO_2 and GaAs surfaces. Work by Hwu et al. [18] showed gold nanoparticle formation under intense X-ray irradiation. The works in this area are summarized in a recent review by Abedini et al. [19] although more reports continue to appear in the literature. All of these works are not considered as part of X-ray nanochemistry because the active role of nanomaterials is missing. Unless the synthesis of nanomaterials by ionizing radiation is influenced by nanomaterials, either pre-made or made in situ, the studies are not included in X-ray nanochemistry. However, the division between these two fields may not be final since one may find suitable nanomaterials that indeed interact with X-rays during their growth. Until then, we will distinctly call this a method of nanomaterial synthesis rather than a research component of X-ray nanochemistry.

1.1.10 X-Ray Nanotechnology and X-Ray Nanobiology

X-ray nanotechnology can be considered as applied X-ray nanochemistry. To date, the most advanced applications of X-ray nanochemistry are in X-ray imaging of nanomaterials and cancer treatment using nanoparticles, as discussed in Chap. 9. This book also describes other applications, including sensing and catalysis, which can be regarded as part of X-ray nanotechnology as well. Future work in the area of X-ray nanotechnology may include X-ray-charged batteries, X-ray writing/reading memory devices, and security materials or technologies.

One may wonder about the possibility of creating a new field called X-ray nanobiology, which is to develop nanobiological systems to maximize the effectiveness of X-ray irradiation. Such a need may exist because X-ray nanochemistry, in its current form, may not be able to create the highest magnitude of enhancement. Biochemical and especially biological systems may be used to augment physical and chemical enhancement to further increase the total enhancement.

1.1.11 The Developing Trend and Impact of X-Ray Nanochemistry

The number of research groups working in the area of X-ray nanochemistry increased from the Guo lab in 2001, to several in 2004, to more than 50 across the world in 2012. Now, the number of groups that have published in X-ray nanochemistry as defined in this book is over 200. Figure 1.2 shows a world map highlighting the groups that have conducted work in the research area of X-ray nanochemistry. The work includes theoretical, imaging, chemical, physical, and medical research, as well as clinical trials and medical treatment of patients. Between 2004 and July 2017, these groups published more than 390 papers in the area of using nanomaterials to increase the effectiveness of X-ray radiation. The annual trend of these publications is shown in Fig. 1.1, and most of these papers are cited in this book.

It is clear that X-ray nanochemistry is still in its infancy and there are many ongoing developments, as evidenced in recent publications and this book. Impacts of X-ray nanochemistry to date are still limited, with the most visible impact being in the area of cancer treatment. As shown in Chap. 9, there are many potentially powerful cancer imaging and treatment approaches derived from X-ray absorbing nanomaterials and X-ray nanochemistry. Several cases of clinical trials using rare earth oxide nanoparticles are reported.

There have been almost no publications on IUdR or similar compounds since the start of X-ray nanochemistry more than a decade ago. Nanomaterials present superior properties and seem to have completely replaced those compounds. On the other

Fig. 1.2 Groups currently conducting research in X-ray nanochemistry. The dots represent groups that work in the area and published papers cited in the book. The size of the dots is proportional to the number of publications at that location. The largest dots represent 10–20 publications per location, medium dots represent 3–9 publications per location, and small dots represent 1–3 publications at that location

hand, the Auger electron therapy that was studied prior to the development of X-ray nanochemistry may be enhanced by X-ray nanochemistry. A recent study reported the advantage of combining Auger therapy with physical enhancement by nanomaterials by Ye et al. [20]. X-ray-activated prodrugs are still being researched, but X-ray nanochemical research has also outpaced that field. In the future, it may be possible to combine both prodrugs and Auger therapy with X-ray nanochemistry to further improve the effectiveness of X-ray irradiation with nanomaterials.

As Chaps. 2, 3, 4, and 5 show, fundamental properties and principles have been discovered or developed in X-ray nanochemistry. X-ray nanochemistry has enabled chemists to investigate a completely new area of research at the interface of many disciplines. This new interdisciplinary research field will allow advanced principles and mechanisms to be developed and discovered. These research activities expand far beyond those defined by radiation chemistry using compounds. If it is possible to discover all the individual enhancements, maximize them, and constructively combine them, then it is possible to create a total enhancement that is much higher than currently measured values. If that happens, then it is possible to find a method to treat cancer without side effects of lateral damage by radiotherapy or systemic toxicity with chemotherapy. This new method can release a lethal dose of drugs from an otherwise nontoxic drug carrier with pinpoint accuracy in the body after exposing to a radiation dose that causes no side effects. In this sense, X-ray nanochemistry is bringing the dream of finding that magic bullet to destruct cancer closer to reality.

Nanomaterials in biological systems may have greater functionalities than those predicted based on their physical properties when dissolved in aqueous solutions. These nanomaterials may be excellent catalysts and may have farther-reaching functions than mere X-ray absorbers in complex environments, such as cells under ionizing radiation. As nanomaterials become more intricate and advanced in design, our understanding about biology will advance. This is another impact X-ray nanochemistry can make.

It is likely that when X-ray nanochemistry will have reached its full potential, a revolutionary change or paradigm shift will occur. Increasingly more complex nanomaterials are being developed, and improvements, although often incremental, are gradually revolutionizing applications such as radiotherapy. Currently a 30% or even 100% improvement to radiotherapy may be realized using large amounts of nanomaterials. However, many obstacles such as high costs and severe side effects exist. As shown in this book, it is possible to achieve much higher enhancement values. If enhancements can reach 100 DEU, then less than 0.1 Gy of radiation can be used to cause various, 10-Gy equivalent responses in controlled nanochemical environments such as nanoreactors. The responses include chemical, mechanical, electrical, magnetic, optical, and beyond. Other possible responses include triggering secondary processes such as drug release and sensing activities.

High local enhancements may also enable X-ray sensing and security products, although it is still too early to predict how successful these potential applications can be. In addition, several imaging methods using nanomaterials under X-ray irradiation are being developed, which may be commercialized in the future. These applications are discussed in Part IV of this book.

1.2 Other Reading Materials Related to X-Ray Nanochemistry

There are no existing reviews or books on X-ray nanochemistry prior to the publication of this book. However, there are many reviews on nanomaterial synthesis, enhanced radiotherapy using nanoparticles, and X-ray imaging assisted by nanoparticles. Many of these reviews are mentioned in various places throughout the book. For example, summaries of theoretical works are given in Chap. 2. In Chap. 6, reviews and books on nanomaterial syntheses are presented. In Chap. 9, reviews in medical applications are shown. A few reviews briefly mentioned relevant topics covered in this book. In one of these review articles, for example, Allen et al. [21] briefly mentioned the terms of physical, chemical, and biological enhancement, but the authors did not separate the types within each category as described in this book. Other reviews, including that by Chithrani et al. [22], reviewed the field of using gold nanoparticles for therapy. The content in these reviews does not fully cover X-ray nanochemistry because their emphasis is placed on cancer therapy. In several reviews on nanomaterials and their applications such as those by El-Sayed and Murphy et al. [23], the authors mentioned the idea of using nanomaterials for enhancing the performance of radiotherapy of photodynamic therapy. These discussions are informative and connected to X-ray nanochemistry although still different from X-ray nanochemistry.

1.3 Outline of the Book

This book consists of five parts. An introduction and discussion of background is described in Chap. 1, which is Part I. Part II of the book includes fundamental concepts and principles, which contain categories and types of enhancement. Part II includes Chaps. 2, 3, 4, and 5. Part III of the book covers nanomaterials and their syntheses in Chap. 6 and methods used in X-ray nanochemistry in Chap. 7. These two chapters show how enhancement in X-ray nanochemistry is measured with chemical reactions and probed with various methods. Part IV of the book, including Chaps. 8, 9, 10, and 11, discusses applications and principles related to applications. Biological, medical, radiolytic, catalytic, environmental, and sensing applications are among those discussed. In addition to these four parts, Part V, which includes Chap. 12, briefly concludes and describes future possibilities that may be investigated in X-ray nanochemistry.

Discussion of the literature is arranged chronologically in each chapter by corresponding authors; if multiple papers exist from each corresponding author, then the publications are grouped together for that author.

References

1. Kroto, H. W., Heath, J. R., O'Brien, S. C., Curl, R. F., & Smalley, R. E. (1985). C60: Buckminsterfullerene. *Nature, 318*, 162–163.
2. Iijima, S. (1991). Helical microtubules of graphitic carbon. *Nature, 354*, 56–58.
3. Bawendi, M. G., Steigerwald, M. L., & Brus, L. E. (1990). The quantum-mechanics of larger semiconductor clusters (quantum dots). *Annual Review of Physical Chemistry, 41*, 477–496.
4. Brust, M., Walker, M., Bethell, D., Schiffrin, D. J., & Whyman, R. (1994). Synthesis of Thiol-Derivatised gold nanoparticles in a 2-phase liquid-liquid system. *J Chem Soc Chem Comm*, 801–802.
5. Hainfeld, J. F. (1987). A small gold-conjugated antibody label - improved resolution for electron microscopy. *Science, 236*, 450–453.
6. Roco, M. C., & Tech, N. S. E. (2004). Nanoscale science and engineering: Unifying and transforming tools. *AICHE Journal, 50*, 890–897.
7. Castillo, M. H., Button, T. M., Doerr, R., Homs, M. I., Pruett, C. W., & Pearce, J. I. (1988). Effects of radiotherapy on mandibular reconstruction plates. *American Journal of Surgery, 156*, 261–263.
8. Cecchini, S., Girouard, S., Huels, M. A., Sanche, L., & Hunting, D. J. (2004). Single-strand-specific radiosensitization of DNA by bromodeoxyuridine. *Radiation Research, 162*, 604–615.
9. Herold, D. M., Das, I. J., Stobbe, C. C., Iyer, R. V., & Chapman, J. D. (2000). Gold microspheres: A selective technique for producing biologically effective dose enhancement. *International Journal of Radiation Biology, 76*, 1357–1364.
10. Foley, E., Carter, J., Shan, F., & Guo, T. (2005). Enhanced relaxation of nanoparticle-bound supercoiled DNA in X-ray radiation. *Chemical Communications*, 3192–3194.
11. Davidson, R. A., & Guo, T. (2012). An example of X-ray Nanochemistry: SERS investigation of polymerization enhanced by nanostructures under X-ray irradiation. *Journal of Physical Chemistry Letters, 3*, 3271–3275.
12. Carter, J. D., Cheng, N. N., Qu, Y. Q., Suarez, G. D., & Guo, T. (2007). Nanoscale energy deposition by x-ray absorbing nanostructures. *The Journal of Physical Chemistry. B, 111*, 11622–11625.
13. Cheng, N. N., Starkewolf, Z., Davidson, A. R., Sharmah, A., Lee, C., Lien, J., & Guo, T. (1950). Chemical enhancement by Nanomaterials under X-ray irradiation. *J. Am. Chem. Soc. Commun., 2012*(134), 1950–1953.
14. Hainfeld, J. F., Slatkin, D. N., & Smilowitz, H. M. (2004). The use of gold nanoparticles to enhance radiotherapy in mice. *Physics in Medicine and Biology, 49*, N309–N315.
15. Henglein, A., & Meisel, D. (1998). Radiolytic control of the size of colloidal gold nanoparticles. *Langmuir, 14*, 7392–7396.
16. Belloni, J., & Mostafavi, M. (2001). Radiation chemistry of nanocolloids and clusters. In C. D. Jonah & B. S. M. Rao (Eds.), *Radiation chemistry: Present status and future trends* (Vol. 87, 1st ed., pp. 411–452). Elsevier Science. Amsterdam, The Netherlands.
17. Divan, R., Ma, Q., Mancini, D. C., & Keane, D. T. (2008). Controlled X-ray induced gold nanoparticles deposition. *Rom J Inf Sci Tech, 11*, 71–84.
18. Wang, C. H., Hua, T. E., Chien, C. C., Yu, Y. L., Yang, T. Y., Liu, C. J., Leng, W. H., Hwu, Y., Yang, Y. C., Kim, C. C., et al. (2007). Aqueous gold nanosols stabilized by electrostatic protection generated by X-ray irradiation assisted radical reduction. *Materials Chemistry and Physics, 106*, 323–329.
19. Abedini, A., Daud, A. R., Hamid, M. A. A., Othman, N. K., & Saion, E. (2013). A review on radiation-induced nucleation and growth of colloidal metallic nanoparticles. *Nanoscale Research Letters, 8*, 474.
20. Sung, W., Jung, S., & Ye, S. J. (2016). Evaluation of the microscopic dose enhancement for nanoparticle-enhanced auger therapy. *Physics in Medicine and Biology, 61*, 7522–7535.

21. Her, S., Jaffray, D. A., & Allen, C. (2017). Gold nanoparticles for applications in cancer radiotherapy: Mechanisms and recent advancements. *Advanced Drug Delivery Reviews, 109*, 84–101.
22. Jelveh, S., & Chithrani, D. B. (2011). Gold nanostructures as a platform for combinational therapy in future cancer therapeutics. *Cancer, 3*, 1081–1110.
23. Dreaden, E. C., Alkilany, A. M., Huang, X. H., Murphy, C. J., & El-Sayed, M. A. (2012). The golden age: Gold nanoparticles for biomedicine. *Chemical Society Reviews, 41*, 2740–2779.

Part II
Concepts

Chapter 2
Physical Enhancement of the Effectiveness of X-Ray Irradiation

Check for updates

Fast growing trees provide shade early on, but these trees develop fewer deep roots

2.1 Introduction

X-ray nanochemistry is a new discipline that studies how nanomaterials improve the effectiveness of X-ray irradiation from both fundamental and applied perspectives. The categories and types of enhancement in X-ray nanochemistry are briefly summarized in Sect. 1.1.7. In this chapter, the most frequently intended enhancement, physical enhancement, is studied. The chapter also covers basic physical principles important to understanding physical enhancement, as well as three types of physical enhancement. Each type is described in detail, comprehending theoretical simulations and experimental investigations.

This section begins with an introduction of physical enhancement and motivations to study physical enhancement, followed by a brief account of early studies of physical enhancement.

2.1.1 Physical Enhancement: Introduction

The most straightforward benefit of adding nanomaterials into a medium under X-ray irradiation is the increase of absorption of X-rays by such a mixture. The increased absorption becomes detectable when adequate amounts of nanomaterials of heavy elements are introduced into a medium of low-Z elements. As shown in Chaps. 3, 4, and 5 of this book, other benefits also exist, which include significant increases in the yield of chemical reactions involving X-ray-generated species such as reactive oxygen species even if X-ray absorption caused by the added nanomaterials is below the detection limit. All these benefits are referred to the increased effectiveness of X-ray irradiation or simply enhancement in this book.

Increased absorption of X-rays by nanomaterials generally leads to increased energy deposition in the medium when the mixture is irradiated with X-rays. The enhancement caused by the increased X-ray absorption by nanomaterials is called physical enhancement because X-ray absorption and energy deposition in a medium are physical processes. According to this definition, the initial idea conceived by Guo in 2001 of using nanomaterials to improve the effectiveness of X-ray irradiation or other types of ionizing radiation is categorized into physical enhancement because the proposed idea relied solely on increased absorption of X-rays by the gold nanomaterials added into DNA aqueous solutions, which alone were less X-ray absorbing. As shown in this chapter, however, only a fraction of the published reports actually measured physical enhancement, whereas enhancement measured in many other reports was heavily influenced by nonphysical processes such as catalysis. A more practical definition of physical enhancement is that it should be *a direct and linear response from increased X-ray absorption caused by the added nanomaterials*. If the increased amount of absorption is negligible, such as 10^{-4}, then the direct response should also be negligible even if a linearly responding enhancement is detected. The response in those cases must be caused by nonphysical processes and therefore cannot be called physical enhancement.

Physical enhancement exhibits in many forms, including increased or decreased fluorescence from molecules, single- or double-strand breaks of DNA molecules, degree or amount of polymerization, cell death, protein damage, hydrogen production, or tumor destruction. All of these can be affected directly and linearly by the increased absorption of X-rays. The directness and linearity mentioned above require physical enhancement be free from any chemical, biological, or other influences that are discussed later in this chapter as well as in Chaps. 3, 4, and 5. Such absence in return guarantees that the measured properties are linearly dependent on and solely caused by the increased X-ray absorption from the added nanomaterials. Physical enhancement is the focus of discussion of this chapter, and the mechanisms behind the definition given above will be fully explained.

2.1.2   Physical Enhancement: Motivations

There are at least four main motivations behind studying physical enhancement. First, majority of published results cited increased absorption of X-rays by nanomaterials as the origin of their measured enhancement, and hence all those reports intended to study physical enhancement. As physical enhancement is important to many ongoing research efforts, it is critical to understand the impact and limitations of physical enhancement, a phenomenon that will be defined again later in this chapter.

The second motivation is that studying physical enhancement has a distinct advantage of being able to verify measured enhancement values with theory because the enhancement is a physical process of increased energy deposition in the medium in which the nanomaterials are embedded. Many groups have theoretically modeled

the dose enhancement factor, a term commonly used in the literature and equivalent to physical enhancement defined in this chapter. Theoretical studies of enhancement have the advantage of automatically eliminating any factors other than physical enhancement. Therefore, experimentally measured enhancement values can be predicted and verified with existing theories.

The same luxury cannot be extended to studying other enhancement mechanisms such as chemical or biological enhancement, two processes investigated in Chaps. 3 and 4, respectively. As shown in Chap. 1 and throughout this book, those other enhancements can also increase the effectiveness of X-ray irradiation when suitable nanomaterials are added to the samples. There are no well-developed theories to date, however, that can be used to predict chemical or biological enhancement, as defined in this book, because physical enhancement manifested in chemical or biological settings does not always follow the same theories as in simpler settings of water. Such understanding and the establishment of theoretical tools to study chemical or biological understanding are only possible after catalysis and biological pathways are incorporated into theoretical models. As a result, although each category and type of enhancement demands scrutiny, so far only physical enhancement can be satisfactorily studied with both theory and experiment.

The third motivation to study physical enhancement is to acquire the ability to create, isolate, and maximize it. Although physical enhancement sounds simple or simpler than other categories of enhancement, it is still difficult to experimentally create and probe only physical enhancement due to interferences from many other effects such as chemical or biological enhancement discussed in Chaps. 3 and 4. Nanomaterials are often catalytically active, and a complete removal of this property requires sophisticated synthetic treatments of the surface of nanomaterials. In addition to designing and synthesizing nanomaterials to enable physical enhancement, proper chemical reactions have to be selected to measure the enhancement so that the probing reactions are not affected by nanomaterials. Studying physical enhancement, therefore, provides the benefit of isolating physical enhancement from other enhancements and identifying several types of physical enhancement.

The fourth motivation is that if one can isolate and optimize chemical, physical, and biological enhancement, then it is possible to combine these optimized enhancements to create a much higher total enhancement. Algorithms governing how different types of physical enhancement or different categories of enhancement combine are discussed in Chap. 5.

2.1.3   Physical Enhancement: Early History

Prior to the publication of the majority of the reports of using nanomaterials to increase the effectiveness of X-ray irradiation through physical enhancement, one of the earliest accounts related to the process was the increased radiation dose around metal implants observed by Castilo et al. [1]. It was noted in that study that the dose around metal implants irradiated with 6 MV photons was 17–23% higher than

without metal implants. This led researchers to speculate that metal implants may be used to enhance the absorption of X-rays and destruct cells or tumors nearby. However, metal implants are bulky, and the idea was noted but not pursued further.

In a related work, Regulla et al. [2] and Regulla et al. [3] used metallic gold irradiated with 40–100 kV X-rays to generate secondary electrons to treat malignant tissue. The authors observed a sharp drop in the cell surviving fraction when 150-µm-thick bulk gold films were used. An enhancement of more than 100 DEU was measured in the surrounding tissue-equivalent polymethylmethacrylate (PMMA), and an over 50 DEU enhancement was detected through C3H 10 T1/2 cell inactivation. The next event closely related to measuring physical enhancement was reported by Das et al. [4]. The authors employed micron-sized gold particles and X-rays to treat a chemical system and three cell lines. The authors observed enhancements whose values were close to the predicted values based on increased absorption of X-rays by the added micromaterials. However, it is difficult to rule out contributions from other factors because the study used cell assays to measure enhancements, which are intrinsically complicated processes that may be subjected to biological modification. Nonetheless, the observed results should be largely physical enhancement because micron-sized gold particles or larger-sized metals possessed much smaller surface areas and had less mobility in cells than nanoparticles, making chemical or biological enhancement less likely.

As mentioned in Chap. 1, compounds of heavy elements have been used with ionizing radiation to increase localized absorption of radiation. One example was given by Karnas et al. [5]. However, adding large amounts of these compounds was challenging, and the results generated limited impacts. Another limitation of using compounds rather than nanoparticles was the severe cytotoxicity associated with large quantities of these compounds. In contrast, nanoparticles such as gold nanoparticles pose little cytotoxicity while significantly increasing X-ray absorption. Using nanomaterials of heavy elements to enhance the effectiveness of X-ray irradiation through increasing absorption of X-rays was also the original motivation behind works by Hainfeld et al. [6] and Guo et al. [7].

The idea of using nanomaterials to replace compounds such as radiolabeled iododeoxyuridine (IUdR) was first proposed by Guo [8]. In retrospect, the reasoning in the original proposal relied on pure physical enhancement, i.e., to use nanomaterials to increase absorption of X-rays. Guo presented preliminary results at many chemistry seminars around the country between 2001 and 2004 and presented the results also at the 2004 American Chemical Society annual meeting in August 2004 in Philadelphia [9]. Physical enhancement was cited as the cause for the observed enhancement.

Soon after publications by Hainfeld et al. in 2004 and Guo et al. in 2005, many reports on the topic of using nanomaterials to enhance the effectiveness of X-ray irradiation appeared in the literature. The trend of the number of publications per year is shown in Fig. 1.1. It may be said that these two papers initiated the study of physical enhancement. In light of many other possible roles of nanomaterials, the discussion in this chapter is restricted to reports whose enhancements arise predominantly from a physical origin. On the other hand, if physical enhancement

is predicted to play only a minor role while other categories of enhancement pose greater contributions to the total enhancement, then discussion will be given in the chapters concerning those other categories of enhancement. For example, if it is apparent that chemical enhancement dominates, then the publication will be discussed in Chap. 3. Similarly, if work uses cell viability for detection, then the reported enhancement will be discussed in Chap. 8 or 9 unless measured enhancement values are very close to theoretically predicted physical enhancement values. Although matching the measured and theoretically predicted enhancement values is not the necessary and sufficient condition to assign physical enhancement to account for a specific experimental enhancement result, reports are discussed here based on this agreement without a complete understanding of enhancement mechanisms. Due to this method of selection, only a limited number of publications are included in this chapter. Many other publications are discussed in other chapters.

2.2   Basic Physical Principles Behind Physical Enhancement

As stated earlier, physical enhancement is caused by the absorption and scattering of X-rays by electrons in atoms of nanomaterials. The cross-section of interactions between X-rays and electrons in atoms depends on parameters such as the number and type of electrons in atoms, i.e., whether they are core or valence electrons. In general, an atom with more electrons and a material of a higher density interact more strongly with X-rays. The former gives rise to the atomic number (Z) dependency of X-ray absorption cross-section. As a result, adding heavy elements such as gold into light element background media such as water increases the overall absorption of X-rays by the aqueous solution. If enhancement originates from physical processes, then we call the outcome of these processes physical enhancement regardless of the species detected, which can be radicals or visible fluorescence. It is important to notice that physical enhancement is the direct and linear response of X-ray absorption increase caused by nanomaterials. One form of the linear responses is the increased yield of electrons emitted from nanoparticles. In contrast, if there is a significant enhancement with little or no increased absorption of X-rays by nanomaterials, then other enhancement mechanisms rather than physical enhancement should dominate. When γ-rays are used, interactions of nanomaterials with secondary charged particles such as Compton electrons generated from γ-rays interacting with water may be more important than direct absorption of γ-rays by nanomaterials.

In order to fully understand physical enhancement, basic principles governing how X-rays interact with matter including nanomaterials are described. The description includes X-ray interactions with atoms, electron emission and X-ray fluorescence upon X-ray absorption by atoms, and electron interactions with atoms.

2.2.1 *X-Ray Interactions with Atoms and Compounds*

2.2.1.1   **Attenuation of X-Rays by Atoms and Compounds**

Physical enhancement in a sample derives from increased absorption of X-rays by nanomaterials added to the sample. The most efficient way to increase X-ray absorption by a low-Z medium is to add nanoparticles made of heavy elements into the medium. This is because equal volumes of materials made of heavy elements can absorb X-rays much more strongly than light elements. Here, we start with atoms and proceed to addressing bulk materials and nanomaterials. X-ray absorption by atoms may be considered as X-rays absorbed by atomic gases without any collective processes such as interatomic excitation or de-excitation, an assumption that may need corrections when nanomaterials or bulk materials are studied.

X-ray absorption by atoms of an element depends on the atomic number of the element and X-ray energy. At the same X-ray energy, elements of higher Z absorb more X-rays. Figure 2.1 (left panel) shows typical X-ray mass attenuation coefficients (blue line) and mass energy absorption coefficients (red line) as a function of X-ray energy for gold atoms. Attenuation is caused by X-rays not detected by a detector after X-rays pass through the sample. Absorption, on the other hand, is the amount of X-ray energy absorbed by the sample. Therefore, absorption is a fraction of attenuation, depending on the X-ray energy and material. Attenuation is governed by Beer's law via measuring transmission of X-rays through a sample. The expression and units of mass attenuation coefficients are μ/ρ and cm^2/g, respectively. μ is the attenuation
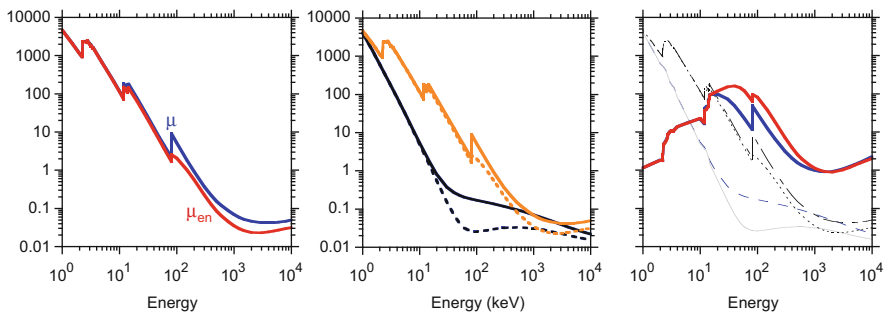
Fig. 2.1 Interactions of X-rays with matter. The left panel shows typical mass attenuation (blue line) and mass energy absorption coefficients (red line) of gold atoms interacting with X-rays of different energies. Contributions from photoelectric, scattering, and pair production are included. For heavy elements such as gold, scattering contributes much less than either photoelectric, which dominates below the K absorption edge at 80.7 keV for gold, or pair production, which dominates at energies above 1 MeV. For comparison, the middle panel shows the two coefficients for gold and water. The difference between mass attenuation coefficients (solid lines) and mass energy absorption coefficients (dashed lines) is more significant for water than gold. The largest differences among these coefficients occur around 100 keV. (Adopted from the National Institute of Standards and Technology website). The right panel shows the ratios of the two coefficients for gold and water: the blue line is the ratio of the mass attenuation coefficients for the two elements, and the red line is the ratio of mass energy absorption coefficients for the two elements

coefficient, and ρ is density. One can calculate attenuation coefficients by multiplying mass attenuation coefficients with density ρ of the material, at a specific X-ray energy. The mass energy absorption coefficient, or μ_{en}/ρ, is different. This parameter is shown for gold in Fig. 2.1 (left panel, red line). The main difference between mass attenuation coefficient μ/ρ and mass energy absorption coefficient μ_{en}/ρ (cm^2/g) is that the former includes all the X-ray photons that do not enter the detector after transmission, whereas the latter represents only the X-ray photons whose energy is deposited in the sample. The more visible difference between these two parameters for gold occurs only at X-ray energies greater than the K edge of gold (80.73 keV). Figure 2.1 (middle panel) shows the two coefficients for gold (orange lines) and water (black lines). The dashed lines are mass energy absorption coefficients, and solid lines are mass attenuation coefficients for gold and water. Attenuation may be caused by the photoelectric effect, scattering, or pair production, depending on the element and the energy of X-rays. If a sample is infinitesimally thin, then attenuation can be quite different from absorption at certain X-ray energies because a significant amount of the attenuated energy may escape from the samples in the form of X-ray fluorescence and even secondary electrons. For thick samples, the two are closer because the escaped energy from one part of the sample is reabsorbed by other parts of the sample.

The ratios of mass attenuation coefficients and mass energy absorption coefficients for gold and water are shown in Fig. 2.1 (right panel). The mass attenuation coefficient ratios (blue line) have the highest values at 20 keV and have a local maximum at 81 keV. This means X-ray imaging of gold in water has the highest contrast at these energies. The ratio of mass energy absorption coefficients for gold to water (red line) is the highest at approximately 50 keV. This means irradiation of gold in water gives rise to the highest physical enhancement at this energy. Several works have shown similar plots. For example, the ratio of mass energy absorption coefficients is confirmed by Künzel et al. [10] using only 0.05 WP gold in water. The theoretically predicted contrast is 5%. Although gold is shown here, other heavy element candidates such as tungsten, lanthanides, bismuth, and even uranium can produce similar effects. Nahar et al. [11] discussed the possibility of using uranium to produce an enhancement.

2.2.1.2   Emission of Electrons After X-Ray Absorption

Electrons are emitted from X-ray absorbing atoms through several processes. For heavy elements and X-ray energies in the keV range, the highest probability event is emission of photoelectrons, which occurs when ionization of bound electrons in atoms leads to the production of free electrons, also known as photoelectrons. For X-ray energies below 150 keV, photoelectric processes dominate when there is a match between the ionization potential and X-ray energy. The primary photoionization process is the ionization of the first electron. Afterward a hole is created in the atomic orbitals, and other processes, such as the emission of Auger electrons, may ensue. Auger electrons may be produced if a hole is filled without the emission of fluorescent X-rays. The Auger process can be understood as if a virtual photon is
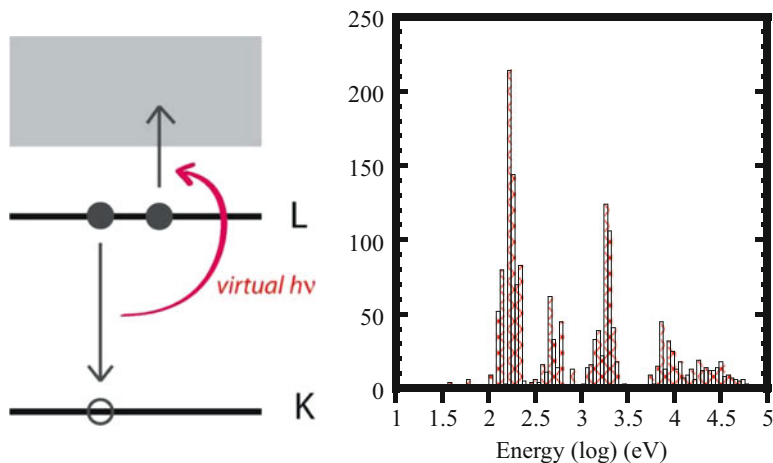
Fig. 2.2 Electron emission from atoms after X-ray absorption. The left panel interprets Auger processes in which a K hole is filled by an L shell electron, leading to the ejection of another L shell electron or electrons in other shells with lower binding energies or ionization potential. A virtual photon may be invoked to help understand the process. The right panel shows an electron energy spectrum emitted from gold atoms interacting with 70 keV X-rays. Electrons at 200 eV, 1 keV, and 10 keV are most abundant. (Reprinted with permission from Guo et al. [12]. Copyright (2007) American Chemical Society.)

emitted when the first hole is filled—the photon gets absorbed by the atom to ionize another bound electron before this photon escapes from the atom, as shown in Fig. 2.2 (left panel). Therefore, totally two electrons are emitted: one photoelectron and one Auger electron. This process can propagate to lower ionization energy levels such as M, N, and outer shells. For gold atoms, a K hole on average produces nearly five electrons. The first electron released from the atom is the primary photoelectron, and the rest are Auger electrons, which are also called secondary electrons. A spectrum of electrons emitted from gold atoms interacting with 70 keV X-rays is shown in Fig. 2.2 (right panel), which was calculated using a homemade package developed by Guo et al. [12]. The theoretical package is similar to a later version created by Guo et al. [13] and Sharmah et al. [14], which is named LLSG in this book and is described in the Appendices.

A similar work was performed recently by Casta et al. [15]. Their results on electrons emitted from gold atoms upon X-ray absorption are shown in Fig. 2.3, which are in good agreement with results shown in Fig. 2.2 (right panel).

More recently, Incerti et al. [16] employed the latest version of Geant4 (10.2) and simulated Auger electron emission from gold nanoparticles. The newest version of Geant4 allows one to study full (or fuller) Auger cascading processes. One noticeable difference between the results obtained in this study and other investigations was a five- to sevenfold increase of low-energy electrons below 200 eV.

Another aspect of electron emission from atoms or nanoparticles upon X-ray absorption concerns the anisotropic angular distribution of these electrons.
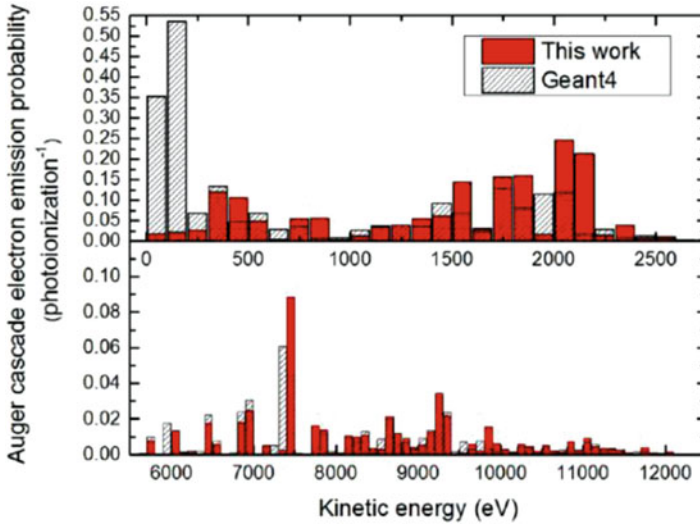
Fig. 2.3 Electron emission from gold atoms by Casta et al. [15] which generally agree with results by Carter et al. [12] shown in Fig. 2.2 (right panel). The outcomes from two codes, one of them being Geant4, are compared. The main difference between the two is the high yield of electrons below 200 eV predicted using Geant4. (Casta et al. [15]. With permission from Springer.)

Sajo et al. [17] reported their findings, which addressed emission of electrons from nanoparticles irradiated with X-rays. Decades earlier, Kabachnik et al. [18] studied anisotropy of Auger electrons emitted from atoms. Although Auger electron anisotropy is theoretically interesting, its practical impact may be limited unless subnanometer probes are used to detect electrons emitted from nanoparticles near their surface.

X-rays can also be attenuated in a sample through scattering of X-rays by electrons in atoms, either elastically by Thomson scattering process or inelastically through Compton scattering. Energetic X-rays interacting with weakly bound or free electrons generally belong to this category. Elastic collisions change the direction of X-rays, and inelastic collisions change both the direction and energy of X-rays. After inelastic scattering, the scattered X-rays lose small amounts of energy that are transferred to Compton electrons. Figure 2.4 shows a calculated Compton electron spectrum obtained from water irradiated with 70 keV X-rays. A large portion of electrons have a kinetic energy around 2 keV (first vertical dash line). A second peak of the emission probability profile appears at 25 keV (second vertical dash line), although its peak intensity is 20% of that at 2 keV. Compton scattering of X-rays by gold is much weaker and can be neglected for incoming X-rays in the 20–150 keV range because the photoelectric effect dominates in this energy range.

The third dominating process is pair production. An absorbed γ-ray photon near a nucleus produces a positron and an electron, each at 511 keV when the photon energy is greater than 1.022 MeV. These energetic particles then interact with and deposit energy in the surrounding media. The penetration depth of these particles in

Fig. 2.4 A typical electron energy spectrum for water irradiated with 70 keV X-rays. Electrons are generated mainly from Compton scattering. The peak energies are visible at ca. 2 keV and 25 keV. (Reprinted with permission from Guo et al. [12]. Copyright (2007) American Chemical Society.)
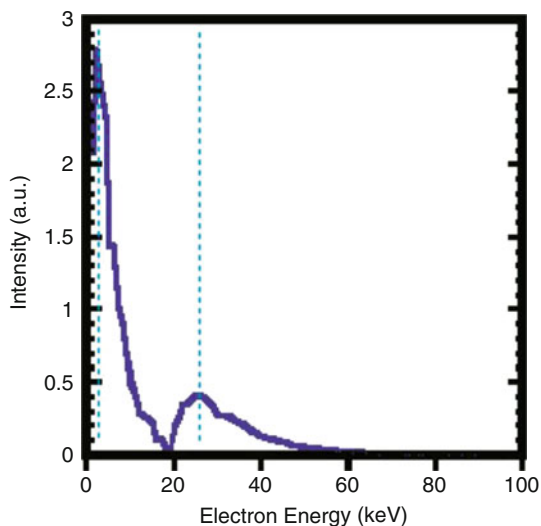
water is approximately 5 mm. Many elements have similar mass attenuation coefficients for pair production. For example, gold and oxygen atoms have almost the same mass attenuation coefficients (and mass energy absorption coefficients) due to pair production at approximately 1 MeV, as shown in Fig. 2.1.

2.2.1.3   Emission of Secondary X-Rays or X-Ray Fluorescence After X-Ray Absorption

The spectrum of secondary X-rays or fluorescent X-rays after absorption of primary or incoming X-rays by gold or other elements can also be computed with existing packages such as Geant4. A typical secondary X-ray spectrum is shown in Fig. 2.5, obtained by Casta et al. [15]. The incoming X-rays were at much higher energies (60 keV) than the secondary X-rays, which were at fixed energies. The role of these secondary fluorescent X-rays was speculated by Misawa et al. [19] to be important for causing type 2 chemical enhancement, a process discussed in Sect. 3.4.2.

2.2.1.4   Summary of X-Ray Attenuation

X-ray attenuation is described by the total attenuation coefficients when all three types of interactions (photoelectric, Compton scattering, and pair production) are included, which are the results presented in Fig. 2.1 showing mass attenuation coefficients for gold and water from 1 keV to 10 MeV.

Mass attenuation coefficients differ by element. Figure 2.1 (middle panel) shows two species that are most frequently used in this book: gold and water. In thin samples, there is little or no reabsorption of secondary X-ray photons, and all the
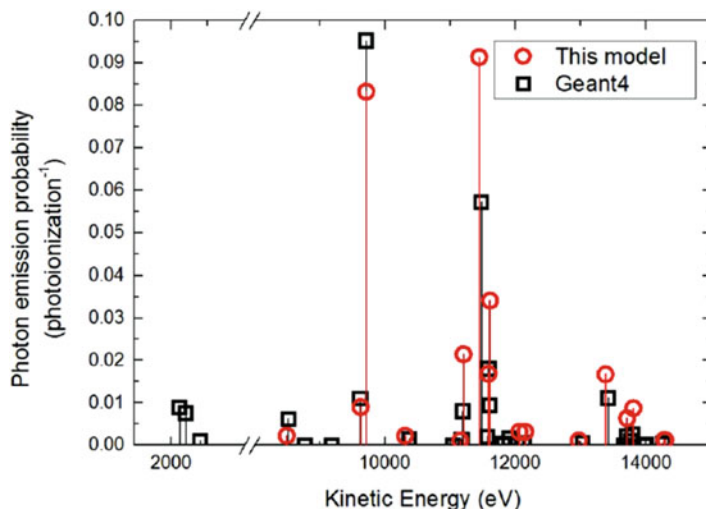
Fig. 2.5 Secondary X-ray photon emission from gold upon irradiation by 60 keV X-rays. (Casta et al. [15]. With Permission from Springer.)

secondary X-rays are considered as having escaped. It is seen in Fig. 2.1 that attenuation is strongly dependent on X-ray energy. For H_2O or O, mass energy absorption (not attenuation) coefficients decrease to a minimum around 100 keV, above which the coefficients are relatively constant till the photon energy reaches 10 MeV. On the other hand, mass attenuation coefficients for water decrease at a slower rate when the photon energy is greater than 40 keV but continue to decrease at the same rate till the photon energy reaches 10 MeV. The mass attenuation coefficients or mass energy absorption coefficients for the oxygen and gold are almost the same at X-ray energies between 1 MeV and 10 MeV. These characteristics are the basis of many applications discussed in this book and the main reasons for using X-rays rather than γ-rays to irradiate nanomaterials even though the latter have much higher penetration powers. Absorption of γ-rays by different elements is almost the same, leaving the total absorption mainly determined by the density of the material.

Compounds interacting with X-rays follow an addition algorithm for each atom in the compounds. Subtle changes imposed by valence electrons in compounds can generally be neglected when X-ray absorption by the compounds is considered because the X-ray energy is much higher than the binding energy of valence electrons. However, those weak interactions do exist, and there are many publications in the literature devoted to studying them.

2.2.1.5   Energy Deposition During Electron Interactions with Matter

The above discussion explains how X-rays are attenuated by atoms or compounds and how electrons are generated. Interactions of X-rays with matter include another

part, which is energy deposition by these electrons in X-ray absorbing atoms and their surroundings. In most cases, not all of the attenuated energy is absorbed by X-ray absorbing atoms and their surrounding because some energy escapes from the sample of interest in the form of high-energy secondary fluorescent X-ray photons. Although secondary X-ray fluorescence can also deposit energy in the medium, especially in thick samples, the amount of deposition made by these secondary photons accounts for only a fraction of the total energy deposition, as shown by Byrne et al. [20]. This means that the general trend of energy deposition does not change when secondary X-ray photons are included, even in thick samples. As a result, few reports have explored the role of secondary X-ray photons.

There are at least three ways to simulate how electrons deposit energy. The first is to use a formula-based approach such as the well-known Bethe formula to model electron energy loss in matter, which leads to the commonly used term *stopping power* [21]. This approach ignores the production of additional electrons in the matter during the energy deposition process. In many cases, this assumption is adequate to predict energy deposition. The second approach is to model deposition using collision-based methods such as Geant4 developed by Allison et al. [22]. In this case, all collisions between energetic electrons and electrons in atoms are studied, and new electrons produced from these collisions are tracked, and their interactions with atoms in the matter are simulated. It is foreseeable that this collision-based approach is more accurate in terms of predicting electrons released from X-ray absorbing atoms. Most calculations shown in publications, however, use the stopping power approach to simulate energy loss processes in X-ray absorbing materials even though doing so underestimates the number of low (<200 eV)-energy electrons emitted from the X-ray absorbing materials. The third method is what was event-based such as that adopted by NOREC, a code that calculates energy deposition in water. The NOREC package is reviewed in Sect. 2.3.3.

It is possible to estimate the significance of contribution by the collision process mentioned above. Even though the absolute cross-sections of electrons interacting with atoms are much higher than that of X-rays interacting with atoms, the difference between cross-sections of X-rays interacting with different elements is usually much greater than the difference between cross-sections of electrons interacting with different elements. Figure 2.6 shows differences of cross-sections between boron $(Z = 5)$ and indium $(Z = 49)$ interacting with electrons between 100 eV and 10 keV. The results suggest that the ratio of the cross-sections of electrons interacting with indium to boron is only a factor of 3, which is much lower than the ratio of 100 fold for 30 keV X-rays interacting with these two elements. The materials are atomic species. This shows that the ratio of cross-sections of electron interactions with indium to those with boron is 3% of that of X-rays. This low percentage suggests that absorption of X-rays by 1 WP indium in boron is the same as that of boron, but it takes 30 WP of indium in boron to double the absorption of electrons by the mixture. Therefore, energy loss for electrons in media of light elements cannot be dominated by a small amount of heavy elements. The same estimation applies to gold and water. If it were not for this fact, nanomaterials would not only increase the absorption of X-rays but also absorb much more energy possessed by the electrons

Fig. 2.6 Relative electron interaction cross-sections for boron and indium with electron energies between 100 eV and 100 keV. (Derived from the National Institute of Standards and Technology website.)
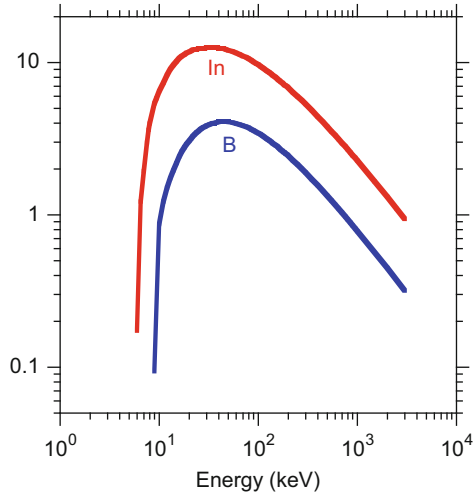
released from nanomaterials or water after X-ray absorption. Similar conclusions have been reached by others. For example, Pattison et al. [23] observed similar results in their theoretical comparison between electrons and X-rays interacting with uranium particles in the body. Their analysis suggested that it was not necessary to consider collisions of electrons in nanomaterials for generating more electrons.

2.2.2 X-Ray Interactions with Thin and Thick Bulk Solid Samples

In the last section, X-ray attenuation, electron emission, and energy deposition are considered for thin samples. Gas phase samples can be regarded as thin to X-rays, and interactions between secondary photons and materials are not likely. When the density of materials is high such as in solids or liquids, however, not all secondary X-rays can escape if the sample is thick.

For many heavy elements though, μ/ρ is similar to μ_{en}/ρ below the K edge, as shown in Fig. 2.1. For light elements, the two can be drastically different in certain energy regions. Figure 2.7 shows the two coefficients for water between 10 keV and 10 MeV. At 100 keV, the two differ by an order of magnitude. For thin samples, mass energy absorption coefficients μ_{en}/ρ have to be used to predict energy deposition. When X-rays interact with thick samples, reabsorption of fluorescent or secondary X-rays needs to be considered. For thick samples of heavy elements and X-rays below the K edge or for water below 20 keV, the two coefficients are almost identical, meaning all secondary X-rays are absorbed within the sample volume.

The difference between the two is caused by whether or not scattered photons or secondary X-ray fluorescence may be captured by the sample. For thin samples of
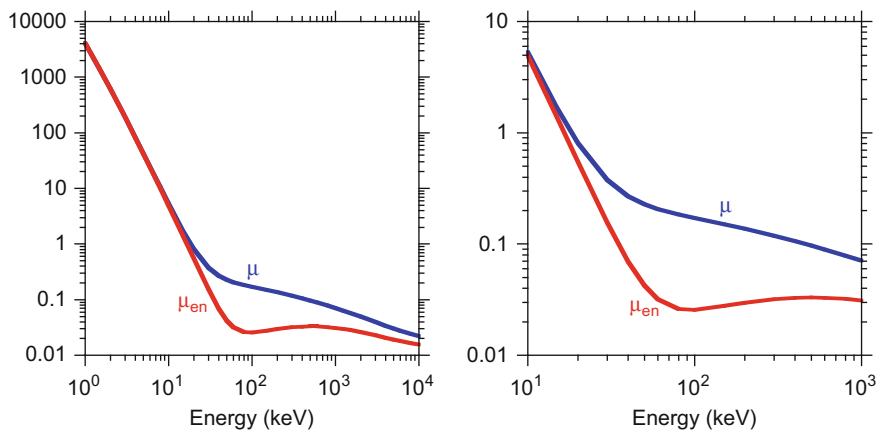
Fig. 2.7 Mass attenuation coefficients and mass energy absorption coefficients for water. The right panel shows data between 10 keV and 1 MeV, with the biggest difference occurring from 80 keV to 100 keV, between which the energy transfer from X-rays to water is minimal. (Data adapted from the National Institute of Standards and Technology website.)

light elements, we normally consider secondary photons to have escaped from the samples for X-ray energies commonly used in X-ray nanochemistry, i.e., between 20 keV and 150 keV. Therefore, deposition is normally represented by μ_{en}/ρ, which is mass energy absorption coefficient. For thick samples and especially thick samples of heavy elements interacting with X-ray energies below the K edge, one may directly use mass attenuation coefficient μ/ρ because all the photons, regardless of primary or secondary, are absorbed in the same volume of the sample irradiated by primary X-rays and the total incoming X-ray energy is transferred to the deposited energy.

Sample thickness may affect enhancement to a certain degree. Since water is often used as the background medium in the cases discussed in this book, energy deposition in water or other media is used in the denominator to calculate enhancement. An example is shown in Fig. 2.8 in which X-rays passing through a thin and a thick sample are illustrated. For the thin sample (left panel), secondary photons escape. For the thick sample (right panel), secondary photons remain and deposit energy in the sample, albeit in a larger volume than the beam path of the primary X-rays. The purple halo around the original X-ray beam path in the right panel shows the escape depth of secondary photons (for illustration only). Figure 2.8 (right panel) also illustrates how X-rays pass through a thin section of the thick sample. The escape depth of secondary X-ray photons may be comparable to or lower than that of primary X-rays in media of low-Z elements. Therefore, both primary and secondary photons need to be considered in the thick sample case, as studied by Byrne et al. [20]. The unit WP enhancement was found to be 1.9 DEU WP^{-1} for 70 keV X-rays, which was about 35% higher than the thin sample configurations. In most cases discussed in this book, the thin sample configuration is used, i.e., secondary photons are not considered. It is important to note that the strictest way to treat X-ray
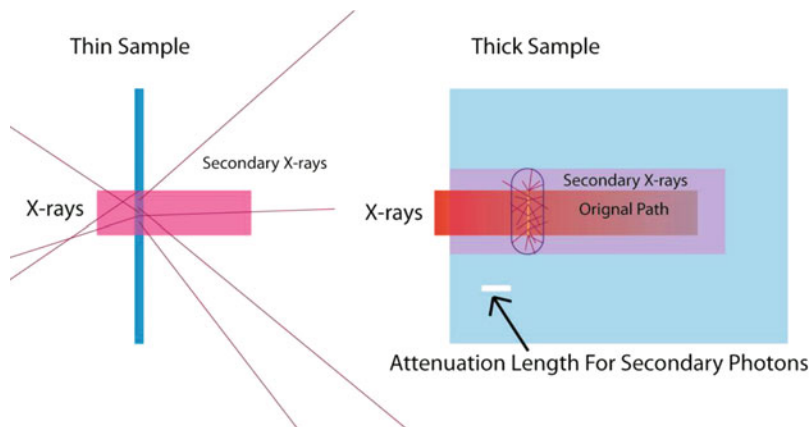
Fig. 2.8 Difference between thin and thick samples irradiated with X-rays. For the thin sample, secondary photons escape from the sample. For the thick sample, all the energy carried by X-rays is absorbed. The volume of deposition in the thick sample case is greater than that defined by the original X-ray beam passage

absorption and subsequent energy deposition is to treat the interactions in thin samples and then integrate over the whole sample while considering fluorescence as shown in the right panel of Fig. 2.8. However, it is generally adequate to use the thin sample approximation for enhancements encountered in this book.

2.2.3 X-Ray Interactions with Nanomaterials

2.2.3.1 Electron Emission and Energy Deposition

X-ray interactions with nanomaterials, especially small nanoparticles such as clusters or nanoparticles of less than a few nanometers in diameter, are similar to that of atoms and compounds. For large (>100 nm) gold nanoparticles, however, electrons produced in nanoparticles may be significantly attenuated during their transport in the nanoparticles because electrons have to traverse through long paths of solid materials made of heavy elements. In this case, energy deposition in the media outside of nanomaterials may deviate from and is less than the sum of deposition made by all the atoms in nanoparticles. Similarly, for other materials such as core-shell nanostructures, electrons emitted from the core may be attenuated by the shell, with its magnitude of attenuation depending on the materials and dimensions of the nanostructures. As a result of attenuation of electrons in nanoparticles, the amount of energy deposited in the media is reduced or increased, depending on the location of interest. If the number of low-energy electrons is increased, then local energy deposition near the surface of nanomaterials is increased. However, such attenuation always reduces the total enhancement, which include both local and remote
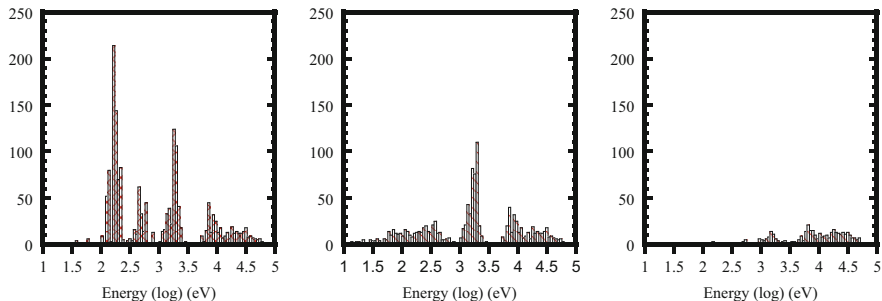
Fig. 2.9 Number of electrons (*y*-axis) as a function of gold nanoparticle size and their energies (*x*-axis). Electrons emitted from gold atoms, 3 nm gold nanoparticles, and 5-nm thick gold nanotubes are shown in the left, middle, and right panels, respectively. Low-energy electrons below 100 eV are heavily attenuated by 3 nm gold nanoparticles, whereas high-energy electrons (>10 keV) remain about the same in these three cases. The calculations are for 1000 electrons emitted from atoms in each material. (Reprinted with permission from Guo et al. [12]. Copyright (2007) American Chemical Society.)

enhancement. The latter always decreases due to attenuation of the total electron energy carried by electrons escaped from nanoparticles. Results obtained from a simulation performed by Guo et al. [12] are given in Fig. 2.9. The calculated results are designed to demonstrate attenuation of electrons by nanomaterials, so the simulations are performed with a fixed number of 1000 electrons produced through X-ray absorption by gold atoms (left panel), 3 nm diameter gold nanoparticles (middle panel), and 50-nm-thick gold nanotubes (right panel). The results show fewer electrons are emitted from larger nanoparticles for a fixed number of electrons generated within a nanoparticle because of attenuation of electrons by larger nanomaterials.

Another method to simulate electron emission from nanoparticles irradiated with X-rays is by fixing the probability of absorption of X-rays by nanoparticles instead of the total number of absorption events or electrons emitted per nanoparticle. As a result, more electrons are emitted from larger particles because they contain more atoms per nanoparticle and can therefore absorb more X-rays under the same dose of irradiation. Unlike results shown in Fig. 2.9, the absolute number of low-energy electrons increases, causing an increase in nanoscale energy deposition near the surface of nanoparticles. Figure 2.10 shows results obtained by Casta el al. [15]. This does not contradict what is shown in Fig. 2.9 because of the two different settings of simulation. It is interesting to notice that the electron spectra in Fig. 2.10 do not show the apparent "hardening" characteristics as seen for X-rays traversing through samples, which is the increase of relative number of high-energy X-rays. Instead, more low-energy electrons are emitted from larger nanoparticles due to energy attenuation of electrons by gold nanoparticles. This can be called "softening" of electron emission from large nanoparticles. Collisions between electrons and atoms in nanoparticles are not included in these simulations. Instead, stopping power is used in both publications and in most published simulation works. The results only show electrons in the intermediate energy range between 3 and 13 keV.
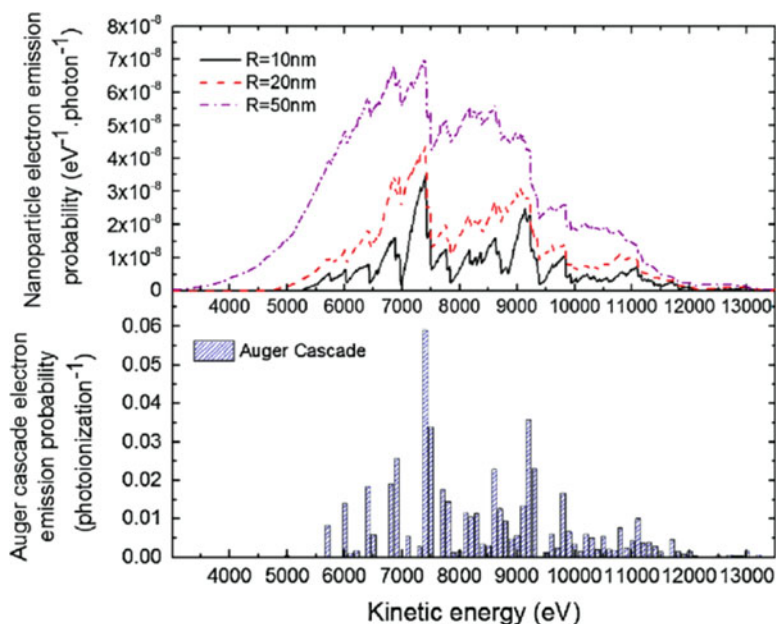
Fig. 2.10 Electron emission from 10, 20, and 50 nm radius gold nanoparticles under 60 keV X-ray irradiation. Higher numbers of low-energy electrons are emitted from larger gold nanoparticles despite greater attenuation of electrons by greater numbers of gold atoms in larger gold nanoparticles. (Casta et al. [15]. With Permission from Springer.)

Casta et al. [24] experimentally measured the emission of electrons from plane metal samples and nanoparticles in vacuum. The excitation X-ray energy was 1253 eV, and gold nanoparticles employed were 6 nm in diameter. The ratio of the measured electron emission from gold nanoparticles to plane metallic gold displayed a prominent peak at low energies below 100 eV; the ratio was 5.1 for electrons below 10 eV.

Another method to treat electron transport in materials is to consider individual collisions using a Monte Carlo method, which is expensive but more accurate for predicting low-energy electrons emitted from nanoparticles. The benefits of using the collision-based approach are still being evaluated. Results shown in Fig. 2.10 by Casta et al. [15] employed an improved code over the Geant4 program to calculate physical enhancement. The authors observed increased number of electrons emitted from larger gold nanoparticles. However, they did not invoke discrete electron transport processes in nanomaterials.

In an attempt to more accurately evaluate electrons released from nanoparticles, Kim et al. [25] indicated that they experimentally studied the intra-nanoparticle (or interatomic as the authors called it) relaxation process for electrons in gold nanoparticles. Figure 2.11 shows the process described by Kim et al. However, no theoretical calculations were performed. The method the authors used to
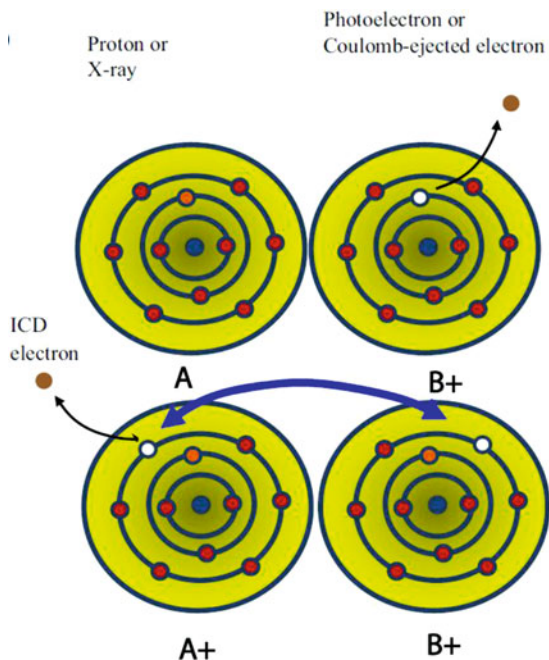
Fig. 2.11 Proposed intra-nanoparticle (or interatomic) electron excitation mechanism by Kim et al. In this case, an electron emitted from an atom in the nanoparticles may ionize another atom in the same nanoparticle. The overall effect may be identical to stopping power as far as the total energy is concerned. However, the exact electron energy distribution of electrons emitted from the nanoparticle with intra-nanoparticle excitation may differ from that without considering such a process. (Adapted from Kim et al. [25]. With Permission from Springer.)

experimentally measure the enhancement of electron emission might not detect the intra-nanoparticle electron interactions including the electron relaxation and collision attenuation processes. In the experimental work, Kim et al. used rhodamine to detect enhanced radical production. Their measured enhancement derived from reduced rhodamine fluorescence from X-ray irradiated solutions containing gadolinium ionic compounds compared to those containing gadolinium nanoparticles. Measured enhancement was 0.8 DEU according to the authors, which was equivalent to an 80% increase in radicals produced by nanoparticles compared to ions. Although the concept seemed correct, the results could be strongly affected by scavenging properties of gadolinium ions versus gadolinium nanoparticles in solutions. If this scavenging hypothesis was true, then the results obtained by the authors were not the effect of intra-nanoparticle atomic events. Despite this concern, the authors raised an interesting question with respect to the role of collision-based electron transport in nanoparticles.

More recently Ueda et al. [26] experimentally studied electron relaxation or the charge transfer processes of filling vacancies generated through photoionization of atoms of interest by electrons from neighboring atoms in a cluster. The authors used a Ne-Kr cluster system in the gas phase, but the process should also happen to an

ionized atom in nanoparticles by a hard X-ray photon. This is another example of intra-nanoparticle electron relaxation processes. These processes have not been considered in many theoretical simulations, and their impact on electron emission from nanoparticles upon X-ray ionization will need to be evaluated.

These low-energy electrons have many utilities in X-ray nanochemistry. For example, indirect evidence was provided by Sanche et al. [27] to show how low-energy electrons damage DNA molecules. The authors measured G values of strand breaks of plasmid DNA by low-energy (0.52, 0.96 and 1.5 keV) electrons created from 1.5 keV X-rays interacting with the DNA films and found that G values increased as a function of the DNA film and saturated when the film thickness was greater than 30 nm and remained constant till 160 nm. The authors claimed that low-energy electrons produced from X-ray absorbing DNA thin films could escape the thin films when the film thickness was less than 30 nm, but the amount of escaping began to decrease when the thickness was greater than 30 nm, which was why the G values were lower when the thickness was less than 30 nm.

Another interesting phenomenon was studied by Sajo et al. [17], which was angular anisotropy around gold nanoparticles under X-ray irradiation. Auger electron emission anisotropy was discussed by Viefhaus et al. [28], although theoretical simulations of dose enhancement generally do not consider this factor. This omission is acceptable because the anisotropy only exists within a short distance of the surface of small nanoparticles after direct X-ray absorption. Therefore, unless probes are located only near the surface, anisotropy would not be observed or measured experimentally. Nonetheless, it will be interesting to design nanoscale probes to detect this anisotropy in the future.

When γ-rays (MeV X-rays) interact with nanomaterials and their surrounding media, energy deposition is dominated by secondary electrons and positrons (similar to electrons except for carrying a position charge) interacting with the media and nanomaterials because absorption cross-sections of γ-rays for indium and boron (or gold and oxygen) are almost the same, leaving absorption by the two mainly differentiated by their densities. The ratio of cross-sections for electrons interacting with indium to boron is approximately three times. This means for 1 WP of indium in boron, enhancement of γ-ray absorption is only 0.01 DEU, and enhancement caused by secondary electrons/positrons is 0.03 DEU. Similar values exist for gold in water. Enhancement values for γ-rays are therefore much lower than those for X-rays between 20 and 150 keV, which are on the order of 1.0 DEU for 1 WP of gold in water, as shown in this chapter.

2.2.3.2 Scintillation and Photon Emission

Another mechanism of physical enhancement to the effectiveness of X-ray irradiation is through X-ray scintillation or X-ray-induced scintillation in nanomaterials, either with or without doping. Scintillation has been extensively studied, and X-ray-induced scintillation has also been investigated for decades. Adding suitable nanomaterials into a sample can create or increase UV-Vis emission under X-ray
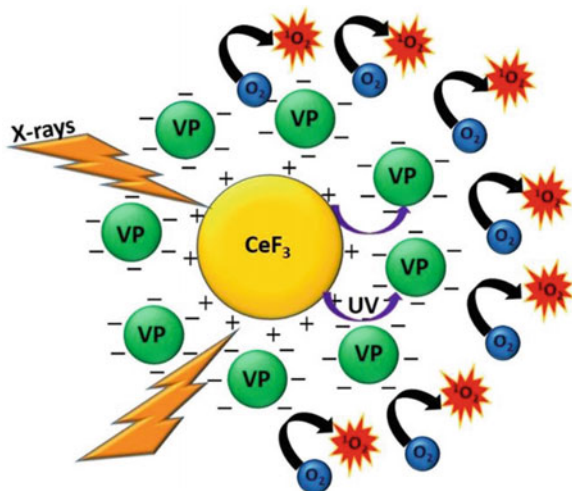
Fig. 2.12 Nanoparticle scintillation via X-ray excitation as illustrated by Goldys et al. [29]. In this illustration, X-rays were absorbed by CeF$_3$ rare earth nanoparticle. Subsequent optical fluorescence, i.e., scintillation, from the nanoparticle was absorbed by porphyrin (VP) molecules, which then helped convert O$_2$ to singlet oxygen. (Adapted with permission from [29] under CC BY 4.0.)

irradiation, thereby creating enhancements. A typical mechanism is illustrated in Fig. 2.12, which was described in the work by Goldys et al. [29]. In this study, X-rays were absorbed by rare earth nanoparticles. The emitted UV light was absorbed by molecules that were used to generate other chemicals such as singlet oxygen. Other illustrations of X-ray-induced scintillation in nanomaterials are available in the literature. Similar energy diagrams for X-ray scintillation and subsequent energy transfer processes are presented in several review articles including that by Cui et al. [30].

Scintillation can derive from either direct absorption of X-rays by nanoscintillators or excitation by electrons generated from X-ray interactions with water. In the first scenario, nanoscintillators dissolved in water increase X-ray absorption similar to gold in water irradiated with hard X-rays if the nanoscintillators are more X-ray absorbing than water. This increased absorption produces electrons that deposit energy in the nanomaterials as well as in the medium or water. In the case where nanomaterials do not strongly absorb X-rays, excitation of scintillation can come from Compton electrons produced in water under X-ray irradiation. Energy deposited within the nanomaterials is not normally calculated because enhancements refer to increased energy deposition in the medium due to nanomaterials. This, however, is not the case for X-ray scintillation. UV-Vis light or scintillation is the gauge of physical enhancement as the result of X-ray or electron excitation. Once excited, the scintillation property dominates, as water does not emit much UV-Vis light when irradiated with X-rays. Therefore, it is often inconvenient to use the ratio of UV-Vis light intensity measured with nanoscintillators to without

them to gauge this type of physical enhancement. Instead, scintillation quantum yield or its equivalent is often used to gauge X-ray scintillation enhancement. Another way to quantify this enhancement is to compare a nanoscintillator to a standard scintillating material. Unfortunately, such a standard has not been established.

2.3   Physical Enhancement by Nanomaterials: General Discussion

The previous section defines how X-rays are absorbed, how electrons are released, and how these electrons interact with atoms in both nanomaterials and their surroundings. These three steps are all physical processes. It is now possible to discuss energy deposition processes that create physical enhancement, a term so called because the creation of physical enhancement does not require assistance from chemical or biological processes or reactions of other origins. However, this does not mean chemical or biological processes are not involved in the detection of physical enhancement. The whole process from generation to detection of physical enhancement is displayed in Fig. 2.13, which includes at least four steps. The first three steps are absorption of X-rays, emission of electrons, and energy deposition by these electrons. The fourth step is detection and a necessary step for the measurement of physical enhancement. This step often involves using chemical or biological reactions to indirectly measure physical enhancement, which render these physical enhancement measurements subject to the influence of chemical or biological processes.

As can be seen in Chaps. 3, 4, and 5 and 8, 9, 10, and 11, numerous methods can be used to detect physical enhancement, and the choice of method in the detection step shown in Fig. 2.13 can directly influence the magnitude of the measured enhancement. In this chapter, emphasis is placed on physical enhancement that is not severely influenced by detection methods.
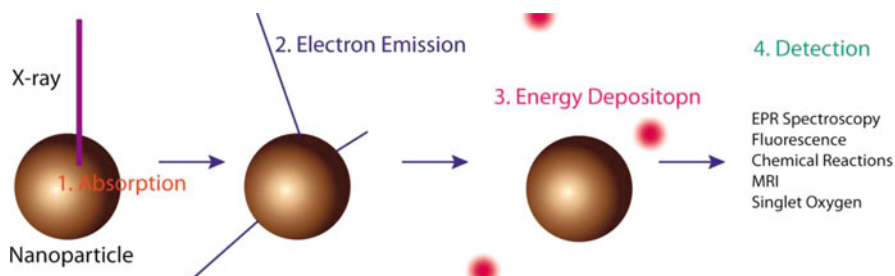
Fig. 2.13 Flowchart showing the process of X-ray absorption by nanomaterials in a medium, electron release from the nanomaterial, energy deposition by electrons in the medium, and subsequent detection of enhancement. Only a few detection methods are listed

In theory, X-ray photoelectron spectroscopy (XPS) and X-ray imaging seem to be more suitable methods for directly measuring physical enhancement when compared with chemical or biological reactions. However, these two approaches are not used in physical enhancement measurements for the following reasons. XPS measurements are usually performed in vacuum, which means that XPS cannot directly measure the theoretically defined physical enhancement due to the missing medium surrounding the nanoparticles. Once there is a surrounding medium such as water, it is difficult to deploy XPS. This dilemma must be properly addressed before XPS or other similar high-vacuum-based technologies can be used to accurately determine physical enhancement.

Another way to measure physical enhancement is through attenuation measurements, which may be obtained through X-ray imaging. Many researchers have investigated nanomaterials as X-ray imaging contrast agents. For example, Hainfeld et al. [31] used gold nanoparticles as an X-ray contrast agent. These gold nanoclusters increased contrast similarly to uranyl acetate. In a similar example, Tu and Lo et al. [32] investigated using gold nanoparticles as contrast media. However, as shown in Fig. 2.1 (right panel), attenuation or contrast increase is not the same as energy deposition enhancement because of the difference between mass attenuation coefficients and mass energy absorption coefficients. Furthermore, some of the absorbed energy may be retained by the nanomaterials. As a result of these two constraints, one may infer energy deposition enhancement or the enhancement of the effectiveness of X-ray irradiation by gold nanomaterials through imaging of 1–100 nm nanomaterials uniformly distributed in background media with X-rays lower than 20 keV or higher than 80 keV. The ratios of coefficients for heavy to light elements are almost identical in these two energy regions. This, however, rules out the possibility of using imaging to accurately measure physical enhancement in most cases because enhancements are usually obtained between 20 keV and 200 keV. Nonetheless, imaging can still be used as a general guidance.

In the following, definition of physical enhancement and results of theoretical simulations and experimental measurements of physical enhancement are presented and discussed.

2.3.1 Definition of Physical Enhancement

2.3.1.1 Definition of Physical Enhancement

The simplest and most straightforward definition of physical enhancement is the enhancement that is caused by increased absorption of X-rays by the added nanomaterials. Physical enhancement can be calculated as the ratio of energy deposited in the targeted volume with nanomaterials to that without nanomaterials. Figure 2.14 illustrates this definition and calculation of physical enhancement. From this definition, it can be seen that the enhancement only exists when there is a medium into which electrons can deposit energy. Moreover, physical enhancement
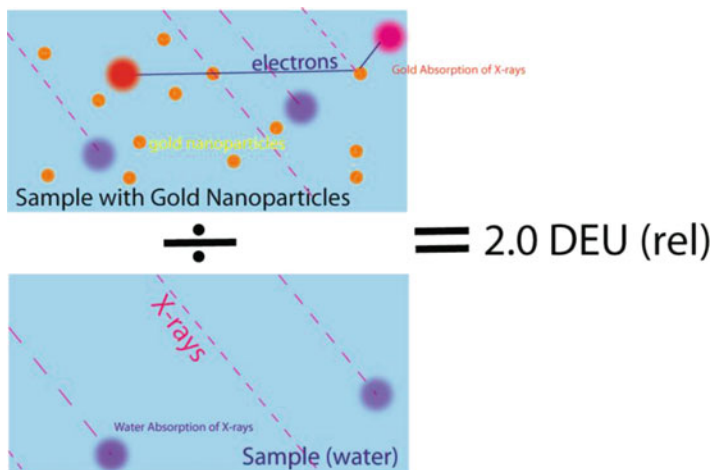
Fig. 2.14 Illustration of how physical enhancement is calculated by taking the ratio of energy deposition in the sample with nanoparticles to energy deposition in the sample without nanoparticles. Physical enhancement is also called dose enhancement factors or dose enhancement ratios in other studies. The whole sample is uniformly irradiated. Two events of absorption (dark-purple-colored balls) through Compton scattering are shown in the bottom panel or denominator for the case without nanoparticles. An additional absorption event happens in the top panel or numerator in which an X-ray photon is absorbed by a gold nanoparticle (orange-colored dots), producing two electrons that lead to two additional energy deposition events (red-colored balls). The low-energy electron deposits energy near the X-ray absorbing gold nanoparticle at the upper right corner in the top panel, and the high-energy electron deposits energy along the track as well as at the end of the track. The numerical value of 2.0 DEU (rel) is obtained and is for illustrative purposes only. As explained in Chap. 1, this value is for relative enhancement. Absolute enhancement is 1.0 DEU

is a pure physical process. Equation 2.1 shows how physical enhancement is calculated.

Figure 2.14 can also be expressed mathematically. Equation 2.1 shows how to calculate enhancement if the amount of energy deposited in the volume of interest with nanomaterials and that without nanomaterials are known. In this case, the enhancement is simply the ratio of the two, as shown in Eq. 2.1.

$$\text{Enh} = \frac{\text{Energy deposition with nanomaterials}}{\text{Energy deposition without nanomaterials}} (\text{DEU}) \qquad (2.1)$$

The units are DEU, as stated in Sect. 1.1.7.

One way to conveniently calculate theoretical physical enhancement was devised by Guo et al. [13]. The method involved first calculating the X-ray flux needed to deposit 1 Gy in water and then using that same flux to calculate energy deposited in the same volume of water in the presence of nanomaterials. The numerical value, in the unit of Gy, of the amount of energy deposited in water is the predicted physical enhancement. In other words, enhancement is the numerical value of the dose

deposited in water by electrons emitted from nanomaterials using the X-ray flux that deposits 1 Gy of dose in water. Enhancement units are DEU rather than Gy. For example, if a 2 Gy dose is deposited in water in the presence of gold nanoparticles using a flux of X-rays that deposit 1 Gy in water, then the enhancement is 1.0 DEU, which is absolute enhancement as defined in this book. An absolute enhancement of 1.0 DEU means doubling the energy deposited in the volume of interest by X-rays interacting with nanomaterials.

Not only does enhancement calculation need a medium, it is also imperative to irradiate a large volume of sample. The dimensions of the volume of the medium should exceed the upper limit of the distance traveled by energetic electrons in media such as water, which can be as long as tens of microns. Theoretical calculations using X-ray beams comparable to the nanoparticle size may yield exceedingly high enhancement factors. This is because the probability of X-rays hitting a nanoparticle increases significantly if the X-ray beam size is the same as the nanoparticle diameter. Another way to understand this is from the perspective of how the enhancement is calculated. Reduction of X-ray beam size increases the enhancement because the denominator in Eq. 2.1 is reduced while the numerator is kept the same by not directly irradiating the surrounding water with X-rays. Although the theoretical results obtained with small X-ray beam sizes cannot be directly compared with experimental values because the entire sample is generally irradiated by X-rays in practical cases, the simulation results can still be useful. If nanometer diameter X-ray beams are available in the future to irradiate only one nanoparticle at a time, these simulation results may be directly compared with experimental results.

2.3.1.2 Units of Physical Enhancement and Absolute and Relative Physical Enhancement

As discussed in Sect. 1.1.7, units of the enhancement are dose enhancement units (DEU), which are introduced in this book. Commonly used units in the literature are dose enhancement factors (DEF), dose enhancement ratios (DER), or unitless. Once units are set, the enhancement can be defined as either relative or absolute enhancement, two definitions also discussed in Sect. 1.1.7. Absolute enhancement is used as the default method of enhancement expression throughout this book unless otherwise noted. When ambiguous, "abs" or "rel" notation is used to clarify the nature of enhancement.

2.3.1.3 Other Considerations

Before we thoroughly examine physical enhancement, several general conditions require further explanation. Firstly, most theoretical studies model only thin samples. This means that secondary fluorescence does not need to be considered and mass energy absorption and not mass attenuation coefficients are used. For gold in calcium or implants in bones, the difference between the two coefficients for the

same element is moderate. For water, the difference is significant, and the two coefficients differ by more than tenfold for X-rays between 30 and 120 keV. For thick samples, secondary X-ray fluorescence may need to be included. However, the absorbed energy from these secondary X-rays is a fraction of the primary X-rays. Byrne et al. [20] theoretically estimated enhancement by irradiating a 3 cm cubic phantom embedded with gold, which was a thick sample, and the outcome was different from other simulations. As a result of using thick samples, an additional enhancement was found in this work. Nonetheless, the difference was only a fraction of the enhancement obtained without considering secondary fluorescence, suggesting only small errors are introduced when treating thick samples thin. Such thick sample effect was not considered in most studies described in this book, however, because the dimensions of nanomaterial-embedded samples in these reports were generally small compared to the penetrating depth of X-rays.

Secondly, it is important to point out that physical enhancement by definition is caused by enhanced absorption of X-rays by added nanomaterials. This is different from other categories of enhancement caused by the introduction of nanomaterials *without* causing a detectable increase in absorption of X-rays. For instance, when 10 ppm gold is added into water, X-ray absorption increase is only 0.1% due to the addition of gold. Such a small increase is below the detection limit of almost all techniques. If a significant enhancement is observed experimentally in this case, and if the probing species are uniformly distributed in the whole sample, then the cause cannot be physical, and other categories of enhancement such as chemical or biological enhancement would need to be invoked to explain the observed enhancement.

2.3.2   Early Works on Physical Enhancement from Nanomaterials

Physical enhancement has only recently begun to be more widely recognized in the literature. Prior to the introduction of the term, the most commonly used name equivalent to physical enhancement was dose enhancement factors (DEF). However, DEFs can be used on any category or type of enhancement and are closely related to the medical use of ionizing radiation. With the advancement of X-ray nanochemistry, however, radiotherapy will be fundamentally changed—it is possible to use small doses of ionizing radiation to trigger the release of drugs to destruct tumors. It is therefore more appropriate to use physical or chemical enhancement to specify enhancements occurring in confined and often nanoscale spaces. Here, published works in the early days using nanomaterials to increase the effectiveness of X-ray irradiation without clear reference to physical enhancement are briefly reviewed. Enhancements are used if the nanomaterial loading is unknown and unit WP enhancements are used when the loading is known. The former have the unit of DEU and the latter use the unit of DEU WP^{-1}.

The most relevant early work was done by Das et al. [4] who employed micron-sized metal beads and cells as the testing platforms to measure the enhancement. An enhancement of 0.42 DEU was observed with 1 WP gold particles in a chemical system (Fricke dosimeter) using 100, 140, 200, and 240 kVp X-rays. Measured enhancements were close to theoretically predicted physical enhancement values. In addition, Das et al. used three cell lines to determine the enhancement, and similar enhancement values were obtained.

The first study reported in the literature using nanomaterials was performed by Hainfeld et al. [6] using 1.9 nm gold nanoparticles. This work will be reviewed in more detail later in this section. The detection was based on the mouse model. Therefore, it is possible that the detected enhancement was not the theoretically predicted physical enhancement due to possible entanglement with biological effects. Another investigation of physical enhancement was carried out by Guo et al. [7]. DNA single-strand breaks (SSBs) were used to detect enhancement. Although these two works intended to measure physical enhancement, their measured enhancements may not completely originate from increased X-ray absorption by nanomaterials because biochemical or biological reactions were used to probe enhancement.

Almost immediately after these experimental works, theories were used to predict physical enhancement. Cho [33] was the first to theoretically evaluate the enhancement observed by Hainfeld et al. The findings were that with 0.7 WP of gold in tumor, the dose enhancement factor, or physical enhancement, was approximately 1.0 DEU for 140 kVp X-rays or 1.4 DEU WP^{-1} for the total physical enhancement. Since this was a theoretical study of energy deposition enhancement, chemical or biological enhancement was automatically eliminated. High enhancement factors were limited to the tumor region loaded with significant amounts of gold. For 6 MeV γ-rays, the enhancement was predicted to be a few percent for 3 WP of gold in tissue. As will be shown later in this chapter, these predictions were generally correct. Figure 2.15 shows results obtained by Cho, which suggested the existence of constant or uniform enhancement as well as a microscale or even nanoscale enhancement.

2.3.3   Theoretical Modeling of Physical Enhancement

2.3.3.1   Theoretical Simulation of Physical Enhancement

To date physical enhancement is the only enhancement that can be predicted theoretically with a high level of confidence. However, physical enhancement is difficult to be directly and experimentally verified because the most direct way to measure physical enhancement should be directly measuring electrons emitted from nanomaterials in water or other media. All the experimentally obtained values have been indirectly measured using chemical or biological reactions. Many theoretical calculation programs and packages can calculate physical enhancement with a varying degree of success and accuracy. Some of the published reports on physical
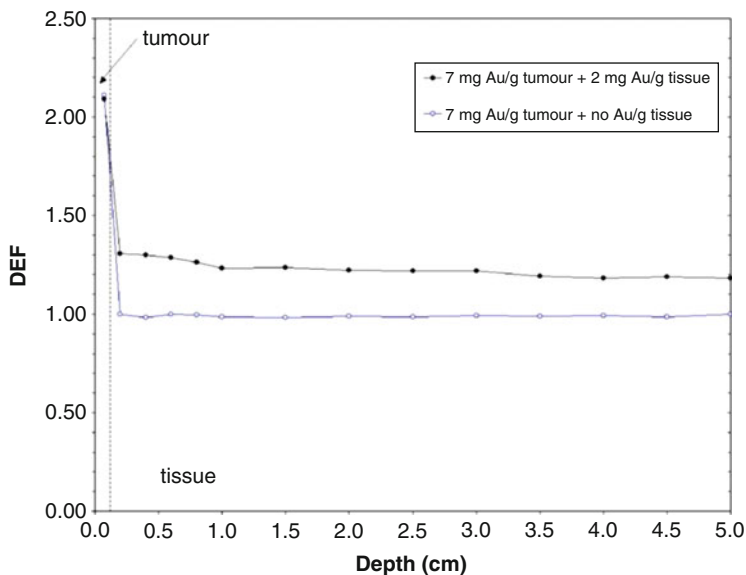
Fig. 2.15 Calculated energy deposition or enhancement for gold in tumor phantoms. Energy deposition is shown as being unitless but can be in DEU (Cho (Cho, 2005) [33] DOI: https://doi.org/10.1088/0031-9155/50/15/N01. © Institute of Physics and Engineering in Medicine. Reproduced with permission from IOP Publishing. All rights reserved.)

enhancement are listed in Table 2.1, using one of the corresponding authors. Some of these programs are briefly discussed in this section. Theoretical studies on specific types of physical enhancement reported in the literature are listed in Tables 2.4 and 2.5. Theoretical packages listed in Table 2.1 are discussed in Sect. 2.3.3.2. In many studies, more than one package was used, and in those cases, the first two packages are given in Table 2.1.

The basic principle of calculation is as follows: X-rays interact with and absorbed by nanomaterials and surrounding media. Electrons are emitted from nanomaterials after X-ray absorption and the media through Compton scattering. Water is the most commonly used medium through which electrons traverse and deposit energy. The energy deposition events by these electrons are tracked and calculated. Secondary X-ray fluorescence and Compton X-rays generated from nanomaterials are generally not included in the calculations due to their minimal contributions in the thin sample configuration. The ratio of energy deposition by electrons released from nanomaterials in water to that by electrons generated in water alone is calculated as the value of enhancement. As shown in Table 2.1, the enhancement values are generally around 1 DEU WP^{-1}, with two exceptions, due to the unique X-ray irradiation configuration.

Table 2.1 Summary of the results of theoretically predicted physical enhancement. The reports are listed chromatically using (one of) the corresponding author. Enhancement values are chosen for 1 WP nanomaterials in media, when such data is available

Element	Energy	Package (1)	Package (2)	Enhancement (DEU)	References
Al/Ni/Mo/W/Pb	1.3 MeV	EGSnrc	PEGS4	0.48–5.5	Yoshida et al. [34]
Pb, steel, Al	1.3 MeV	EGSnrc		1.27	Yoshida et al. [35]
Au	140 kVp, 4 and 6 MV	BEAMnrc	EGS4	1.57	Cho [33]
Au	50 kVp, ^{125}I, ^{169}Yb	MCNP5	EGSnrc	1.14	Cho et al. [36]
Au	50 kVp, 6 MV	MCNP	NOREC	988[b]	Jones et al. [37]
Mn, Co, Zr, Au	27–1333 kVp	EGS4		0.2–0.7	Roeske et al. [38]
Au	150 kVp, 15 MV	Geant4		1.0	McMahon et al. [39]
Au(LXXI–LXXVII)	68 and 82 keV, 2 MeV	Geant4		10.4	Nahar et al. [40]
Au	44, 66, 88 keV and 60–140 kVp	EGS5		Absorption	Yusa et al. [41]
Au	Ir-192	Geant4		0.67	Zhang [42]
Porous silica	50 keV electrons	MC		Various	Gervais [43]
Au (0.7 WP)	30–600 keV	MCNPX		0.4–1.54	Gokeri [44]
Au	10–200 keV	MCNPX		1.33	Van den Heuvel et al. [45]
Au	6 and 15 MV	Geant4	LEM	0.43 (4.5 Gy)	McMahon et al. [46]
Au (0.05 WP)	20–150 keV	Mc (LEM)		0.1–0.4	McMahon et al. [47]
Au	20, 300 keV, 6 MeV	MCNP-5	PENELOPE		Pignol et al. [48]
Au	150 kVp	Geant4		0.36–1.6	Amato et al. [49]
Au (0.7 WP)	50–120 keV, 1.33 MeV, 6 and 18 MV	MCNPX		0.4–1.1	Mesbahi et al. [50]
Au	81–100 keV	MCNP5		Fluorescence	Cho et al. [51]
Au	250 kVp	Geant4	CLHEP	Electron emission	Jeynes et al. [52]
Pt/TiO$_2$	546 keV (electrons)	MC		Absorption	Kwon et al. [53]
Au (single NP)	60–150 keV	Geant4	EGSnrc	1000	Li et al. [54]
Gd, Au	Ir-192, 6 MV	BEAMnrc	PEGS	0.23	Zhang et al. [55]
Au	200 MeV	Geant4	Gate	0.7	Martínez-Rovira

Pt (0.7 WP)	160 kVp, 6 MV	Geant4		0.4–1.1	Pradhan et al. [56]
Au, Pt, Ag, Gd	1 MeV (protons)	Quantum ESPRESSO		57 (electrons, <25 eV)	Verkhovtsev et al. [57]
Au	10–500 keV	EGSnrc	Geant4		Chang et al. [58]
None (IMRT)	2–10 mv	EGS4/BEAM		–	Deng et al. [59]
Au	100 keV	LLSG	Geant4	1.0	Guo et al. [14]
Au	10, 100 keV	Geant4		Electron emission	Incerti et al. [16]
Au (1.5 WP)	20 keV, 6 MV, 100, 200, 300 kVp	PENELOPE		<2.0 (50 keV)	Koger et al. [60]
Au	150 eV–2 MeV	PENELOPE		Relative	Koger et al. [61]
Au (single NP)	85 keV	Geant4-GATE		–	Retif et al. [62]
Fe, Au	6 mv	Geant4-GATE	CLHEP	FeNPs>AuNs	Retif et al. [63]
Au	160 keV, 6 and 15 MV	Geant4	LEM	–	Attilli et al. [64]
Au	73 and 139.5 keV	Geant4		0.90	Byrne et al. [20]
Au (2 WP)	20 keV–1 MeV	EGSnrc	HetMS	3.1 (20 keV)	Martinov et al. [65]
Au (single NP)	80, 120 kVp	SCEPTEr		Electron emission	Sajo et al. [17]
Au (2 WP)a	51 keV, 150 kVp, 6 MV	TOPAS-nBio		0.2a	Schuemann et al. [66]
None	20–370 keV	EGSnrc		–	Thomson et al. [67]

a AuNPs are distributed in the extracellular media
b brachytherapy irradiation configuration with the source at the nanoparticle

2.3.3.2 Theoretical Packages for Physical Enhancement Calculations

Many groups employed standard packages, and only a few groups developed their own to theoretically predict physical enhancement. These packages are listed in Table 2.2, and they have been used either in whole or in part for physical enhancement calculations. Among them, GEANT4, PENELOPE, EGS4, ERGnrc, NONRC, and LLSG are frequently used by researchers. Lee-Lu-Sharmah-Guo (LLSG) is a combination of a homemade Mathematica code with Geant4 and NOREC and is reviewed in the Appendices.

Based on Table 2.2, at least ten packages have been developed to date to simulate physical enhancement. Almost all the packages are based on a Monte Carlo (MC) algorithm. Here, the original work related to these packages is briefly described.

The Canadian National Research Council (NRC) has presented an electron gamma shower (EGS) software toolkit, hence called EGSnrc, that can model coupled electron-photon transport in materials. EGSnrc is a Monte Carlo-based method, and it utilizes other software such as BEAMnrc that can model a beam of radiation transporting through multiple materials. The latter also uses other packages such as DOSXYZnrc to evaluate radiation dose in a voxel (3D pixel). EGSnrc was built based on EGS4 code developed by NRC and Stanford Linear Accelerator Center (SLAC).

Geant4 is an open-source code that has been developed by an international team of scientists for more than a decade. Three major references are Agostinelli et al. [22], Allison et al. [70], and Allison et al. [71]. Geant4 is a toolkit that can be used to simulate the passage of particles including X-rays and electrons through matter such as gold. It is a Monte Carlo method and currently has many projects, one of which is Geant4-DNA or G4DNA that simulates radiolytic events after the absorption of ionizing radiation. Geant4 package also interfaces or includes other important models such as PENELOPE. For example, Geant4-PENELOPE code has been developed specifically to address how low-energy electrons interact with matter. Many other libraries are used to build the C++ program executable in Geant4.

McMahon et al. [47] studied energy deposition by nanoparticles irradiated with X-rays using the local effect model (LEM) developed by Scholz and Elsässer et al. [73]. LEM assumes that biological responses are linearly dependent of the local dose. Recent revisions to the approach have been made to take into consideration factors such as radical diffusion and track structures developed by Elsässer et al. [73].

Lee, Lu, Sharmah, and Guo have built a package that utilizes Geant4, NOREC, and a homemade Mathematica code to simulate physical enhancement of variously shaped nanostructures including spheres, shells, donuts, aggregates of spherical nanoparticles, and nanoparticle-nanoshell dimers. The program takes advantages of Geant4 and NOREC, with the added benefit of being able to simulate nanostructures of many shapes. Users can also add new shapes to the existing code.

Martinov et al. [65] described a heterogeneous multiscale (HetMS) model derived from EGSnrc package. Their new package can cover X-ray energies between 20 keV

Table 2.2 Summary of theoretical packages used to simulate physical enhancement of X-ray effects. The packages are arranged alphabetically

Package/program	Referencs and organizations	Algorithm
EGS4/EGSnrc/BEAMnrc/ DOSXYZnrc	Rogers et al. [68, 69]. INMS NRC/SLAC	Monte Carlo; coupled electron-photon transport
Geant4	Allison et al. [22, 70, 71]. International Consortium	Monte Carlo; absorption, emission, and transport of particles as well as interactions with targets
HetMS	Martinov and Thomson [65]. Carleton Univ.	Multiscale Monte Carlo; extended EGSnrc
LEM	[46, 72, 73].	Local biological effect
LLSG (Lee-Lu-Sharmah-Guo)	Guo et al. [12], Lee et al. [13], Sharmah et al. [14]. UC Davis	Mathematica, Geant4/NOREC
MCNP/MCNP6/MCNPX	Armstrong et al. [74] Los Alamos National Security, LLC	Monte Carlo; continuous energy radiation transport
NOREC	Borak et al. [75]. NCRP, CSU	Event-based Monte Carlo; particle transport in liquid water
PARTRAC	Friedland et al. [76, 77]. IRP	Biophysical Monte Carlo; transport of particles in water and water radiolysis
PENELOPE	Salvat et al. [78, 79]. IEC	Electron and positron transport in matter, analytic methods
TOPAS-nBio	McNamara et al. [80]. MGH	Radiolytic events in cells; based on Geant4-DNA

and 1 MeV. The authors consider the main advantage of HetMS being able to estimate the enhancement over large, macroscopic volumes, of the order of 1 cm^3. Little enhancement was found with 1 MeV X-rays for 2 WP gold in a phantom.

MCNP or Monte Carlo N-Particle code is a proprietary package developed by Los Alamos National Security, LLC. It has many functions that simulate particle transport processes similarly to Geant4. MCNP has an extended version called MCNPX, and its latest version is MCNPX2.7. Other variations of the MCNP code include MCNP5 and MCNP6.

NOREC is a Monte Carlo code that simulates electron tracks in liquid water. It is an event-by-event code, which was originally developed at the Oak Ridge National Laboratory and then expanded to include data from the National Institute of Standards and Technology (NIST). Borak et al. [75] revised and reviewed the code, which now tracks electrons, energy deposition events, and secondary electrons in liquid water. NOREC can perform event-by-event calculations in water, whereas the condensed history codes EGSnrc or MCNP cannot. Hence, NOREC simulations can reach nanometer spatial resolution in energy deposition.

PARTRAC is a Monte Carlo-based code that simulates radiation track structures in media such as water and especially how these structures can cause DNA damage or other biological responses. PARTRAC was developed by Friedland et al. [77], and modifications to the PARTRAC code have since been developed. PARTRAC has been compared with NOREC, and the results suggest the two are similar concerning the stopping power and other parameters.

PENELOPE is a Monte Carlo code used to simulate coupled electron-photon transport similar to other packages discussed here. The program was first developed in 2003, and most recent improvements were made in 2011. The latest version can simulate inelastic events with nanometer resolution and calculate ionization cross-sections as well as mass energy deposition coefficients. PENELOPE can be combined with Geant4 to simulate low-energy electron inelastic collision events with the added capability of calculating sophisticated geometries of materials.

The Tool for Particle Simulation (TOPAS) and TOPAS-nBio were developed by McNamara et al. [80] for radiobiology studies. TOPAS-nBIO has been developed to address microscale and nanoscale interactions between particles and cellular components. The simulation can track electrons with 2 eV kinetic energy and incorporates DNA geometries and strand breaks.

2.3.3.3 Results of Theoretical Simulations of Physical Enhancement

As stated in Chap. 1, discussion in this book is arranged chronically according to the corresponding authors. If there is more than one paper from the same author, then publications are grouped together for this corresponding author. When there are multiple similar papers from the same group, one or several publications are discussed in depth, whereas the remaining receive brief mention.

Readers may ask why certain papers are discussed in this section while others in other sections. The papers discussed in this section contain at least physical

enhancement as a whole, whereas papers discussed in subsequent sections isolate at least a specific type of physical enhancement. If a paper discusses both physical enhancement and a particular type of physical enhancement, then this paper is shown in both sections.

Cho [33] reported the first theoretical simulation study of enhancement. His findings were that (1) enhancement from gold nanoparticles under MeV X-rays, commonly known as medical X-rays, was minimal (<7%) with nearly 1 WP of gold in tissue and (2) 1 WP of gold produced an enhancement greater than 1.0 DEU using 140 keV X-rays. These results suggested that if clinical conditions are similar to those used in the simulation, then gold nanoparticles are not useful in improving radiotherapy when MeV medical X-rays are used. Cho et al. [36] and Jones et al. [37] expanded the calculation to include microdosimetry around nanoparticles. The authors used a concept called microscopic dose enhancement factors (mDEFs), which were enhancement around individual gold atoms calculated using the NOREC code with 100 nm resolution. The enhancement was computed as the ratio of energy deposition with gold atoms in a water particle to the pure water particle. For individual particles, the dose was shown to decrease to 10^{-6} at 10 μm away from the nanoparticle for 50 keV X-rays. The relative dose decreased to 10^{-4} at the same distance for 6 MeV X-rays interacting with the same particle. As shown by Guo et al. [12], the dose deposited in background water by X-rays alone was much higher than these values (see Fig. 2.34).

Guo et al. [12] created a homemade program based on a Monte Carlo method to simulate physical enhancement. The concept of nanoscale energy deposition was introduced for the first time in this publication. Their program was used to simulate the entire process of X-ray absorption, including core-hole relaxation and transport of electrons in nanoparticles as well as in water. PENELOPE method was employed to calculate all atomic events such as photoelectron and secondary electron production including Auger electron production that is currently included in Geant4. Energy deposition in water by electrons was also calculated using this homemade code. Energy loss was modeled using Bethe formula to calculate the stopping power [81]. 3 nm diameter gold nanoparticles were employed in the study, and DNA strand breaks were used as the endpoint to measure enhancement of energy deposition. DNA strand break reactions were also simplistically modeled. Theoretically, the enhancement was found to be highest at the surface of nanoparticles. Experimentally, up to 2.0 DEU enhancement was measured. However, theoretically predicted physical enhancement averaged over the whole sample was only 0.4 DEU. The remaining 80% of the enhancement measured experimentally was not assigned and may be attributed to chemical enhancement discussed in Chap. 3, although at the time of study, chemical enhancement was not discovered. The code used in this work was the first version of their program, which was modified in a subsequent publication by Guo et al. [13].

A new version of the code was created by Guo et al. [13], which was different from the 2007 version in many ways. In this new package, electronic events were modeled by Geant4, and energy deposition in water was modeled using NOREC. A homemade Mathematica program was created to generate shapes of nanostructures
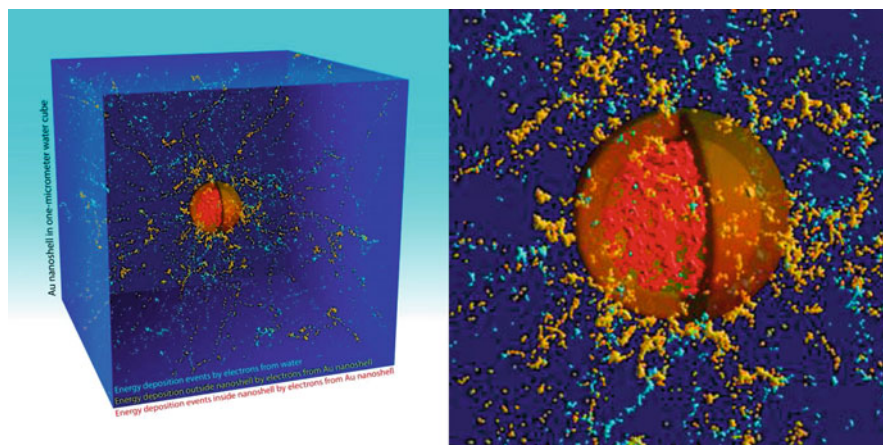
Fig. 2.16 Calculated enhancement for different geometries of gold nanostructures, with an example of a gold shell shown here. The enhancement is 60 DEU at the center of a 200 nm outer diameter, 20-nm-thick gold shell. The left panel shows the shell in the middle of a water cube. Energy deposition events are shown in both panels. Red-colored dots represent energy deposition events inside the shell by electrons produced from the gold shell, yellow-colored dots are events outside the shell by electrons emitted from the gold shell, and cyan-colored dots are events by electrons produced in water through the Compton scattering process. (Reprinted with permission from Guo et al. [13]. Copyright (2012) American Chemical Society.)

for estimation of energy deposition enhancement, which included nanoscale energy deposition enhancement. The work focused on creating nanostructures that may generate the highest nanoscale energy deposition densities around the nanostructures. Figure 2.16 shows the enhancement from a 200 nm outer diameter gold nanoshell of 20 nm thickness, producing a 60-DEU enhancement at the center of the gold nanoshell.

The program was further developed by Guo et al. [14] in which the authors added several materials into the code. In this publication, the authors introduced the concept of X-ray-induced energy transfer (XIET) between donors and acceptors. Donors in this work were 100 nm diameter gold nanoparticles (AuNPs), and acceptors were water nanoparticles trapped in calcium phosphate-enclosed liposomes (CaPELs). It was found that when the two nanomaterials were in contact with each other in aqueous solutions, gold nanoparticle donors absorb X-rays to generate electrons that enter liposomes and deposit energy in or donate energy to the water nanoparticles in CaPELs. XIET efficiency was expressed as enhancement in units of DEU. For a single 100 nm AuNP contacting a single 100 nm CaPEL, the enhancement was 2.0 DEU. As the AuNP moved away from the trapped water nanoparticle, enhancement decreased. Enhancement was seen to increase when more than one AuNP donor surround the acceptor. Figure 2.17 (left panel) shows the magnitude of energy deposition in terms of enhancement in the water nanoparticle inside the acceptor as a function of distance between the donor and acceptor as defined by Guo et al. [14]. In these calculations, the sample was uniformly irradiated
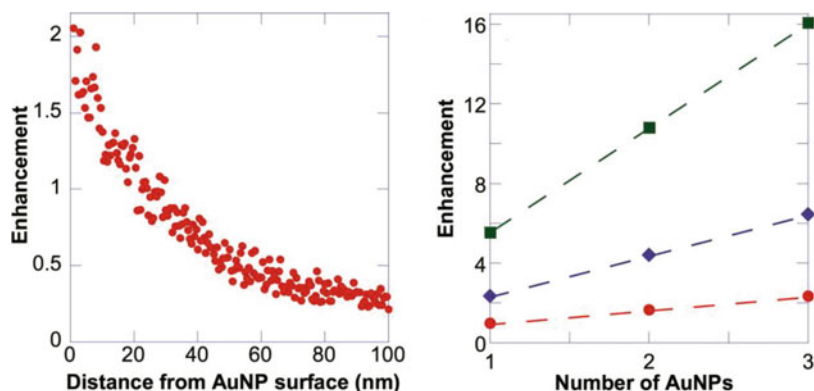
Fig. 2.17 XIET efficiency in terms of enhancement simulated by Guo et al. [14]. Enhancement is the ratio of energy deposition in the nanoscale acceptor with gold nanoparticles (AuNPs) to that without gold nanoparticles. Exponential decay as a function of separation distance between the AuNP and the acceptor is shown in the left panel. Enhancement increases linearly as a function of number of AuNP donors in contact with the acceptor (right panel). (Reprinted with permission from Guo et al. [14]. Copyright (2016) American Chemical Society.)

by X-rays, and a pair of donor-acceptor was considered. The dependency of XIET efficiency as a function of number of donors (AuNP) per acceptor is shown in the right panel. Three sizes of AuNPs were used, and the energy transfer efficiency was found to increase linearly with the number of donors.

Yusa et al. [82] used a Monte Carlo method to estimate the contrast increase in X-ray imaging by gold nanoparticles. For 0.6 WP gold in water and X-ray energies at 44, 66, and 88 keV, the authors observed a contrast increase equivalent to 70%. At 44 keV, contrast increase should be the same as energy deposition because mass attenuation coefficients and mass energy absorption coefficients are nearly the same for these elements at this energy. At 66 and 88 keV, contrast increase deviates from the physical enhancement.

McMahon et al. [39] explored gold nanoparticles as a contrast agent for therapeutic use. They used the Geant4 code to calculate energy deposition in a tumor with 1 WP gold buried 5 cm deep in healthy tissues. Both healthy and tumor tissues were simulated using a four-element tissue approximation. The authors proposed the use of a parameter called figure of merit. An enhancement of 0.7–1.0 DEU was predicted, resulting in a 0.7–1.0 DEU WP^{-1} unit WP enhancement. McMahon et al. [47] theoretically studied energy deposition by electrons emitted from gold nanoparticles under X-ray irradiation and confirmed that over 99% of the 20 nm gold nanoparticles did not directly absorb 100 keV X-rays when exposed to a 1 Gy of X-rays. This is similar to what was predicted by Guo et al. [12] in which 10^{-6}, or one in one million (ppm), of the 3 nm gold nanoparticles was found directly absorbing X-rays after exposed to a 1 Gy of X-rays. It is important to point out that these gold nanoparticles can still be ionized by Compton electrons generated in water. This latter type of ionization would only depend on the dose and not on the type of

ionizing radiation, regardless of whether it is X-ray or γ-ray. The results obtained by McMahon et al. [47] showed a steep decay of enhancement or relative biological effectiveness (RBE) as a function of distance, decreasing to the background or uniform enhancement at approximately 50 nm away from the surface, which is similar to results obtained by several groups including those observed by Guo et al. [12] and Guo et al. [83]. The authors called the nonuniform enhancement local effect model (LEM), which is similar to nanoscale energy deposition described by Guo et al. McMahon et al. [84] investigated the elemental effect on local enhancement based on LEM, and the results presented a complex picture of the dependency of enhancement on the element.

Zhang et al. [42] used a modified Geant4 code to calculate enhancement from gold nanoparticles in a water phantom. They found an enhancement of 0.6 DEU at 380 keV with a gold loading of 9.6 WP in water. The X-ray energy was outside the optimal absorption energy range for gold. The results were equivalent to 0.06 DEU WP^{-1}, which is much lower than 1 DEU WP^{-1} unit WP enhancement at the optimal X-ray energy of 50 keV.

Pradhan et al. [85] developed a code to calculate resonant X-ray absorption by nanoparticles consisting of highly ionized ions such as Au^{76+}. The suggested scenario is extremely difficult to realize experimentally because nearly all the electrons in gold atoms have to be removed. Nahar and Pradhan et al. [40] calculated enhancement by gold nanoparticles embedded in tumor tissue phantoms. They specifically studied the resonant excitation configuration mentioned above. Their calculated DEFs were greater than 10 DEU for 10 WP of gold in water or tissue, a result that was numerically similar to the results obtained by other enhancement calculations. In a subsequent publication, Lim et al. [86] confirmed that X-rays below 100 keV can interact strongly with nanoparticles, whereas MeV photons do not. Although the authors used platinum atoms instead of nanoparticles, the results should be similar to those using nanoparticles.

Several calculations using metal foils under MeV photon irradiation have been presented in the literature. One of such works was done by Watanabe et al. [87]. Although bulk metals rather than metal nanoparticles were used, the results shed some light on how metals absorbed X-rays and released either electrons or low-energy X-rays to destruct tumor cells near the metal surface.

Van den Heuvel et al. [45] studied X-ray energy dependency of dose enhancement. They used an MCNPX code and found that continuum X-rays emitted from X-ray tubes were as good as monochromatic X-rays for generating enhancement. The results can be explained by the energy dependency of enhancement, which derives from the Auger electrons released from gold irradiated by X-rays of different energies. Pattison et al. [23] used an EGSnrc code to estimate dose enhancement factors by depleted uranium particles under background γ-ray irradiation. They found that the enhancement was between 1 and 10 DEU for pure uranium particles ranging from 1 to 10 microns in diameter. The predicted enhancement was much lower than the 500 to 1000 DEU enhancement hypothesized by Busby et al. [88].

Berbeco et al. [89] calculated enhancement by endothelial cell-targeting gold nanoparticles. Their work described a local dose enhancement factor for 100 nm

diameter gold nanoparticles surrounding a model blood vessel. The X-ray energies were 100 keV and 6 MeV, and the authors found that 100 keV X-rays were optimal for creating the highest enhancement. For 100 keV and 3 WP of gold in tissues, the enhancement was calculated to be 0.55 DEU, which is equivalent to a unit WP enhancement of 0.18 DEU WP^{-1}. This relatively low enhancement was caused by the large average distance between gold nanoparticles lining the exterior walls of the nuclei of endothelial cells and the target as well as the single cell setting used in the calculation. The latter would generate little uniform physical enhancement.

Chow et al. [90] used the Geant4 code and calculated dose enhancement by gold nanoparticles in media under X-ray irradiation. X-ray energies used in their calculations were 50 kVp, 250 kVp, and 6 MeV. The authors employed an irradiation configuration in which the X-ray beam size was identical to the nanoparticle diameter. Using this configuration, rather than uniform irradiation of the whole sample, they obtained enhancement of 10–2000 DEU, mainly because of small amounts of energy deposited in the unirradiated water around gold nanoparticles. Figure 2.18 shows the irradiation configuration (left panel) and results (right panel). Based on the enhancement results shown in the right panel, the attenuation of electron energy by 100 nm gold nanoparticles is approximately 25%. This value is similar to those obtained in other studies shown in this section.

The uncharacteristically high enhancement obtained by Chow et al. shown above can be explained as follows. The comparison is illustrated in Fig. 2.19. When a 10 nm X-ray beam irradiates a single 10 nm gold nanoparticle and not the surrounding water, as shown in the right panel of Fig. 2.19, energy deposition in the whole water volume of interest without the gold nanoparticle is lower than when the surrounding volume of water is uniformly irradiated with X-rays (left panel). Consequently, energy deposition contributing to the denominator of Eq. 2.1 used to calculate the enhancement is much less when the surrounding volume of water is

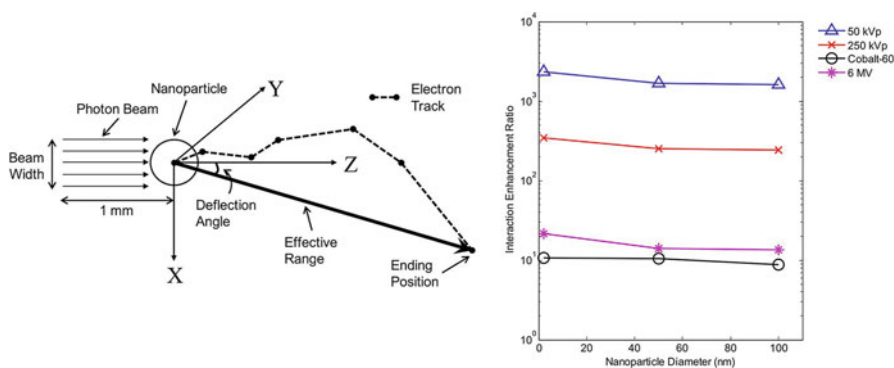**Fig. 2.18** Enhancement calculation by Chow et al. [90]. The enhancement was calculated using an X-ray beam size identical to the diameter of the nanoparticle under investigation (left panel). The results are shown in the right panel. Enhancements of nearly 2000 were obtained for 50 keV X-rays (blue line or triangles). (Reprinted with permission from Chow et al. [90]. Copyright (2011) by American Association of Physicists in Medicine.)
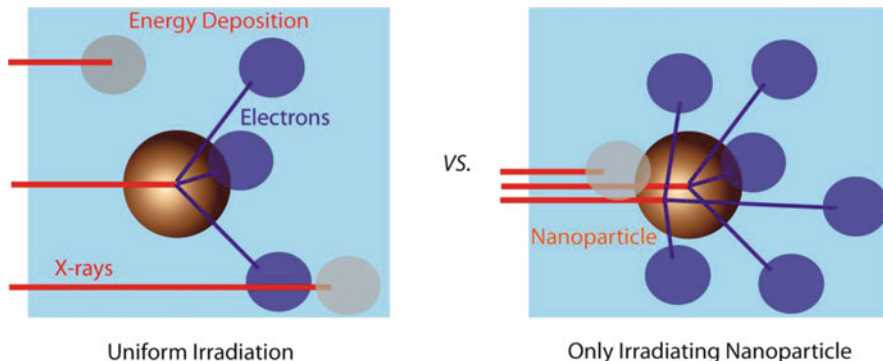
Fig. 2.19 Explanation of high enhancements when irradiating only nanoparticles and not the volume of their media using nanometer-wide X-ray beams. The left panel shows a uniform irradiation case in which X-rays cause energy deposition events everywhere. In this case, the ratio of energy deposition by electrons emitted from the X-ray absorbing gold nanoparticle (blue balls) to that from water through Compton scattering (gray balls) is 3/2 or 1.5 DEU, assuming each electron depositing the same amount of energy. In the right panel, X-rays only irradiate the nanoparticle. Although X-rays can still interact with water along the beam path, more X-rays are absorbed by the nanoparticle due to its stronger absorption of X-rays, and hence more energy is deposited by electrons emitted from the nanoparticle, leading to a greater enhancement. The enhancement is now 6/1 or 6.0 DEU, which is four times the enhancement obtained with uniform irradiation shown in the left panel. The theoretical narrow beam irradiation configuration can also be considered as in the case of brachytherapy

not irradiated by X-rays (right panel), leading to much higher enhancements. Although most practical cases employed the irradiation configuration shown in the left panel of Fig. 2.19, the results obtained using the narrow beam irradiation configuration shown in the right panel in Fig. 2.19 can still be useful for comparison purposes.

Pignol et al. [48] simulated energy deposition by gold nanoparticles under X-ray and γ-ray irradiation. The authors used 1.9, 5, 30, and 100 nm diameter gold nanoparticles and five different X-ray energies as well as 6 MV γ-rays. Electron emission spectra from these gold nanoparticles were investigated. The simulation employed MCNP-5 and PENELOPE codes, and the latter tracked electrons whose kinetic energy was as low as 50 eV. The authors found the dose doubled (1.0 DEU) when 0.5–0.6 WP of gold was irradiated with 20 keV X-rays. Hence, the unit WP enhancement was as high as 2.0 DEU WP^{-1}. They also found that for 20 keV X-rays, 100 nm gold nanoparticles retained ~25% of the energy carried by electrons emitted from gold atoms, similar to the value obtained by Chow et al. shown above. The enhancement was reduced to 0.005 DEU WP^{-1} for 6 MV X-rays.

Ngwa et al. [91] studied the enhancement by gold nanoparticles next to a model cell. Their enhancement was achieved with ^{103}Pd emitting X-rays at 21 keV, an X-ray source commonly used in brachytherapy. As noted earlier in this chapter, the enhancement is the highest for gold nanoparticles under irradiation of X-rays at this energy. The authors called the enhancement nuclear dose enhancement factor, or
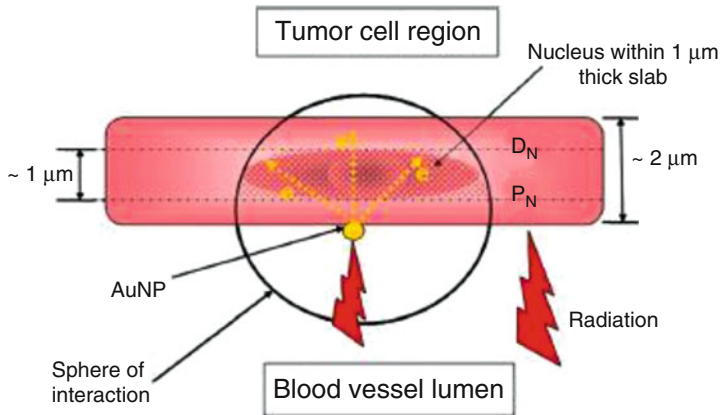
Fig. 2.20 Illustration of how enhancement of energy deposition in the nucleus surrounded by gold nanoparticles calculated by Ngwa et al. The average enhancement in the central 5% and 10% volume fraction of the cell was calculated. The predicted enhancement was 80 DEU with 14 WP of gold around the cell. (Ngwa et al. [91] DOI: https://doi.org/10.1088/0031-9155/57/20/6371. © Institute of Physics and Engineering in Medicine. Reproduced with permission from IOP Publishing. All rights reserved.)

nDEF, and found that the nDEF reached up to 80 DEU for nanoparticles positioned outside the cells with a 14 WP gold loading. This magnitude of enhancement was close to that obtained with the 20-nm-thick gold shell and 200 nm outer diameter shown in Fig. 2.16. The enhancement was equivalent to 4.5 DEU WP^{-1}. Figure 2.20 shows their calculation arrangement.

Zygmanski et al. [92] employed Geant4 (version 4.9.4) together with a PENELOPE-based code and calculated the enhancement from gold shells. They found an enhancement of 160 DEU at the center of a 100-nm-thick, 2 cm radius gold shell irradiated with 40 keV X-rays. The enhancement was represented by dose enhancement ratios (DER), and DER of various geometries were predicted. The results were also calibrated using a CEPXS/ONEDANT code. They also used microbeam configurations to emulate clinical situations and simulated four cases of different configurations. Both single and multiple gold nanoparticles were used in the simulation.

Mesbahi et al. [50] used a MCNP code to predict physical enhancement with gold nanoparticles in phantoms. The simulated enhancement profiles followed the profiles of the loading of the nanoparticles. They also observed a strong energy dependency, showing an enhancement of 1.1 DEU for 90 keV X-rays and a 0.7 WP loading. The enhancement at 120 keV was only 0.2 DEU at the same loading.

Zhang et al. [55] used a BEAMnrc code to simulate enhancement of radiotherapy using MeV photons and gadolinium nanoparticles. They found that a 2 WP loading of gadolinium in tissue (or 20 mg/mL) produced an enhancement of less than 0.03 DEU. Enhancement from the same amount of gold was around 0.05 DEU. These values agreed with the results obtained by others shown in this chapter.

Li et al. [54] compared PENELOPE2011, Geant4, and ESGnrc packages with regard to their ability of predicting enhancement using gold nanoparticles of 2 to 100 nm in diameter. They observed a 10–1000 DEU enhancement, which was significantly greater than the expected values of physical enhancement. The high enhancements were mainly caused by the X-ray beam size being the same as the diameter of nanoparticles, therefore underestimating the amount of energy deposited in the surrounding water. This configuration is similar to what Chow et al. [90] employed, which is shown in Fig. 2.18. The unusually high enhancements are also explained in Fig. 2.19. The authors found that enhancement quickly decreased to near zero as the spot of interest moved away from the surface of nanoparticles, a result similar to those found by others.

Casta et al. [15] used a homemade code to simulate the electrons emitted from nanoparticles after X-ray irradiation. The functions of their code were similar to Geant4 and the code developed by Guo et al. [12], although the authors employed what they call a probabilistic approach. Electron and photon emission from 10 to 100 nm diameter gold nanoparticles were calculated. The code used energy attenuation of electrons in gold, similar to the use of Bethe formula, to predict the energy of electrons emitted from gold nanoparticles. The authors presented detailed electron and photon emission data. The results suggested that approximately 80% of the absorbed X-ray energy from 60 keV X-rays was carried by energetic electrons, a value similar to those obtained by Guo et al. [12] who estimated the value to be 85% for the same energy range of X-rays. Casta et al. also estimated the amount of energy carried by secondary X-ray fluorescence and Auger electrons, both of which were approximately 6% of the total energy released from the nanoparticles after X-ray absorption. They also found a small amount of energy (~4%) was lost to the nanoparticles. Similar to other methods, the predicted electron spectrum may underestimate the significance of low-energy electrons (<200 eV) because the code does not include collisions or interactions of electrons with atoms in nanoparticles when simulating transport of electrons in nanoparticles.

It is important to notice that enhancements exist only when nanomaterials are dissolved or embedded in a medium—standalone nanomaterials in space do not create physical enhancement due to a lack of medium into which electrons can deposit energy. Nevertheless, once the absolute yield of electrons emitted from nanoparticles is experimentally measured or theoretically modeled, enhancement can be predicted for nanoparticles in a medium.

As can be seen in the following sections and the rest of the book, most of the reports did not break down physical enhancement into different types, which was reasonable at the beginning of X-ray nanochemistry research when such division was not needed. However, as it is shown in several publications, such separation is beneficial to the advancement of the field of X-ray nanochemistry, including the goal of achieving the maximum total enhancement.

2.3.4   Experimental Investigations of Physical Enhancement

There have been many reports in the literature that at least intended to measure physical enhancement. However, specific types of physical enhancement were measured in only a small number of reports. Although the rest claimed to study physical enhancement or its equivalent, their results could not be conclusively attributed to a specific type of physical enhancement or to physical enhancement at all due to a lack of control over experimental conditions. In this section, only those experimental studies considered to have strong connections to physical enhancement measurements are discussed. In Sect. 2.4, only those studies whose results can be conclusively categorized into specific types of physical enhancement are presented and discussed. The criteria for selecting those works are given below. Other reports will be covered in Chaps. 3, 4, and 5 and Chaps. 8, 9, 10, and 11.

In order to assess the origin of enhancement, the amount of gold in a sample has to be known. This is equivalent to stating that the uptake information is needed when quantitative understanding is sought about the origin of enhancement in in vitro or in vivo experiments. Once the amount of gold is known, physical enhancement can be theoretically estimated, assuming that gold nanoparticles are uniformly distributed, which is not always true. If experimental conditions are suitable for physical enhancement measurements, and if the measured enhancement values are close to those predicted theoretically, then the measured enhancement is at least theoretically claimed to be caused by physical enhancement. In this section, the origin of enhancement is at least partially assigned to physical enhancement as long as the measured enhancement value is within an order of magnitude of the theoretically predicted physical enhancement. In the next section, the two values need to be within 50% or a factor of two of each other for the measured enhancement to be called a specific type of physical enhancement. However, unless experimental conditions support only physical enhancement, neither criterion is a neccesary and sufficient condition of physical enhancement being the main and only cause for the measured enhancement. A small number of reports in the literature describing strict physical enhancement are discussed in this and the next section.

The reports discussed here have their measured enhancement values within an order of magnitude of the theoretically predicted physical enhancement values. Results from experiments with unknown loadings will not be reviewed here, and discussion about these reports will be given in the corresponding chapters later in this book based on their application areas. For example, an enhancement studied with mice without biodistribution data will be described only in Chap. 9. Using this guideline, many publications can appear in several chapters because the observed enhancements in these publications have multiple origins such as physical, chemical, or biological enhancement. Future work will be needed to conclusively assign the origin(s) of enhancement.

Many enhancements originated from physical enhancement. Further, the process of physical enhancement measurements can introduce other categories of enhancement. For example, it is common to use chemical reactions to detect chemical species generated in water via energy deposition of electrons emitted from nanomaterials. These chemical species include reactive oxygen species, and the reactions include those species reacting with spin traps to form spin adducts.

These measurement processes can introduce other enhancements when the probing reactions are catalyzed by nanoparticles. As we will show in Chap. 3, there are cases where enhancement is detected in the absence of conditions that would give rise to physical enhancement. In those cases, it is important to recognize that the measured enhancement is not caused by physical enhancement.

The categorization of the reports is based on the measured enhancement values being close to those predicted for physical enhancement. However, this does not mean the assignment is conclusive, as coincidences may exist when multiple pathways are available. All pathways must be studied before physical enhancement can be sufficiently and necessarily proven as the sole source of enhancement. Only after this is done can one claim that the measured enhancement is caused by the predicted enhancement. Unfortunately, most of the results shown in this book, with a few exceptions, do not fit into this precise categorization.

As it will become clear toward the end of this chapter that some of the results discussed here belong to specific types of physical enhancement or their combinations. The publications that clearly and exclusively study one of these three specific types of physical enhancement will be reviewed in Sect. 2.4. Benefits of this categorization will be demonstrated in Chap. 5 when higher total enhancements are achieved through the work of isolation, optimization, and recombination of individual enhancements using desired nanomaterials. Table 2.3 lists several groups that have experimentally studied physical enhancement and their results.

Table 2.3 Experimental results of physical enhancement measurements

Platform/ reactions	Nanomaterials/ loading (WP)	X-ray energy (kVp)	Enhancement (DEU)	References
Mouse tumor model	1.9 nm AuNPs/ 0.7–1.8	250 kVp	0.4–5.5	Hainfeld et al. [6]
DNA SSBs	5 nm AuNPs/ 0.01–0.1	100 kVp	0.1–2	Guo et al. [7, 12]
DNA SSBs	Gold nanotubes/ 100	100 kVp	2–15	Guo et al. [93]
Prostate cell line	AuNPs/0.07	200 kVp	0.1–0.5	Roa and Xing et al. [94]
DNA	Cisplatin	Electrons (1 eV–60 keV)	0–4.5	Sanche et al. [95–97]
DNA SSBs/ electrophoresis	38 nm AuNPs/ 0.3	<70 keV	0.48	Sicard-Roselli et al. [98]
Radiographic films	Pd foil	18 MV	0.43	Watanabe et al. [87]
In vitro and in vivo	5 nm AuNPs	150 kVp		Hebert et al. [99]
	Depleted uranium particles	Background radiation	1–10	Pattison et al. [23]
Clonogenic assay	AuNPs/30	300 kVp	0.1–1.1	Latimer [100]
Cell/DNA (unspecified)	AuNPs	40 KV	~1.0	Su et al. [101]

AuNPs: gold nanoparticles

The first publication trying to prove the existence of physical enhancement using nanomaterials was carried out by Hainfeld et al. [6] using 1.9 nm gold nanoparticles on a mouse tumor model. Hainfeld et al. had worked in the field of using gold clusters and nanoparticles to enhance the contrast of TEM imaging for two decades prior to their 2004 publication, an experience that allowed the authors to make these nanoparticles highly soluble and stable in water. The surface of gold nanoparticles was unknown. Up to 18 mg/mL gold nanoparticle aqueous solution, or 1.8 WP gold in water, was intravenously injected into mouse tail veins, and accumulation was found near the tumor and other organs such as the liver. The tumor volumes were recorded, and it was found that tumor sizes decreased to nearly zero after 30 days when the cancer-bearing mice were treated with the gold nanoparticle and 250 kVp X-rays. The authors cited the high-Z factor of gold nanoparticles as the cause for the observed enhancement, implying the cause of enhancement to be physical. Based on the tumor size data shown in their publication, which is also shown here in Fig. 2.21, the enhancement was calculated to be 0.58 DEU by the author of this book using the method described in Sect. 7.2.1. In the calculation, relative tumor sizes of no treatment at 3 days (5.20 mm^3), at 3 days after irradiation (1.60 mm^3), and at 3 days after treatment of gold + irradiation (0.80 mm^3) were used. However, it is clear from Fig. 2.21 that the tumor sizes do not follow the exponential growth model described in Sect. 7.2.1. Instead of this relatively low enhancement, the authors predicted an enhancement of 5.5 DEU for a 1.8 WP loading of gold in blood using an EGS4 code, which seemed to agree with the ratio of tumor size for "gold only" to
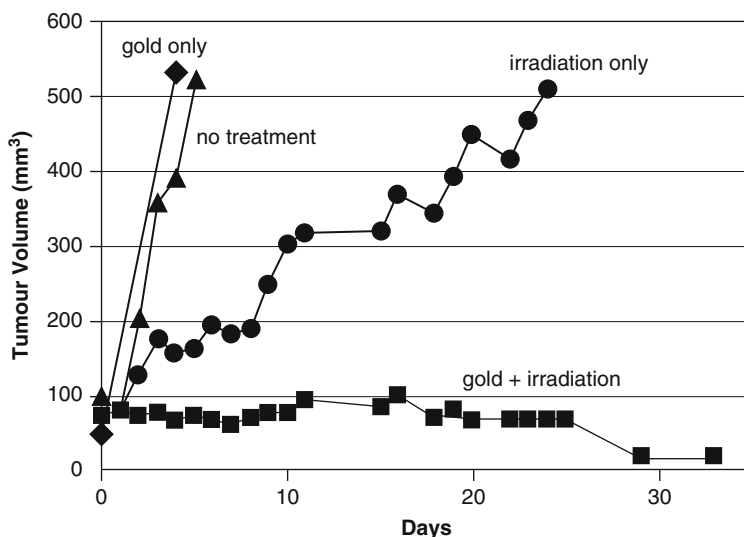

Fig. 2.21 Enhanced tumor suppression reported by Hainfeld et al. The enhancement of irradiated gold-loaded mice is 0.25 DEU based on the gold loading in tumor. An enhancement of 5.5 DEU was cited by the authors. (Hainfeld et al. [6] DOI: https://doi.org/10.1088/0031-9155/49/18/N03. © Institute of Physics and Engineering in Medicine. Reproduced with permission from IOP Publishing. All rights reserved.)

"gold + irradiation" at day 3 as shown in Fig. 2.21. The estimated physical enhancement (based on the average value shown in this chapter) would be approximately 0.25 DEU for a loading of 0.23 WP of gold in the tumor irradiated with 250 kVp X-rays, which is much lower than the enhancement factor cited by the authors but is close to the value calculated using the method shown in Sect. 7.2.1. If a loading of 1.8 WP in the blood is used, the predicted enhancement would be approximately 2.0 DEU, close to what was predicted by the authors. Consequently, the results are shown here even though the enhancement was measured using a complicated mouse model. These results reveal the drawbacks of using the magnitude of enhancement in complex systems to gauge the origin of enhancement, as a number of endpoints can be used to estimate the enhancement, each reaching a different enhancement value.

Guo et al. [7] reported the finding of enhancement measurements using 5 nm gold nanoparticles to damage or cause single-strand breaks (SSBs) to plasmid DNA molecules under 100 kVp X-ray irradiation. In their work, gold nanoparticles were mixed with DNA and irradiated with X-rays. An enhancement of up to 1.0 DEU was measured after 2–4 Gy of radiation. The amount of gold in water was approximately 0.07 WP, which can support approximately 0.1 DEU of physical enhancement and was within an order of magnitude of the measured enhancement value. It is not possible to rule out chemical or other types of enhancement because the size of gold nanoparticles was small and the quantity was large. Guo et al. [12] conjugated each of 5600 base pairs of plasmid DNA with approximately ten 3 nm gold nanoparticles and investigated enhanced strand breaks under X-ray irradiation. Conjugation was through intercalation of ethidium ligands tethered to the surface of gold nanoparticles, and ethidium ligands were sandwiched between base pairs to establish conjugation. The enhancement was nearly 1.0 DEU when scavengers such as tris (hydroxymethyl)aminomethane/ethylenediaminetetraacetic acid (Tris/EDTA) were added to reduce the background water contribution. Theoretical predictions using a Monte Carlo method developed by the authors suggested that only 20% or an enhancement of 0.4 DEU was caused by the nanoparticles. This implies that the remaining 80% of the measured enhancement was caused by other enhancements such as chemical enhancement discussed in Chap. 4.

Not all the cases of adding gold nanomaterials resulted in enhancement. Guo et al. [93] noted that enhancement was severely reduced when adding bare gold nanotubes into aqueous solutions. Since detection was through DNA strand breaks by hydroxyl radicals which were scavenged by the surface of metallic gold, gold nanotubes in the solution both generated an enhancement via increasing X-ray absorption and reduced the enhancement through scavenging. The amount of gold nanotubes, which was nearly 100 WP gold in water, should generate an enhancement of 100 DEU. However, only a 2.0 DEU enhancement was measured. Adding hydroxyl radical scavengers improved the enhancement to 15 DEU, which was 15% of the predicted physical enhancement, making the measured enhancement within an order of magnitude of the predicted physical enhancement. A schematic shown in Fig. 2.22 (left panel) describes the process as well as the results (right panel).
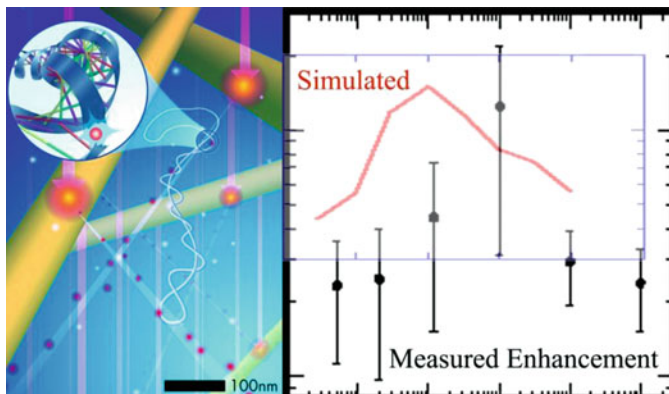
Fig. 2.22 Gold nanotube enhancement of DNA strand breaks in plasmid DNA by X-rays. The left panel illustrates the mechanisms, showing hydroxyl radicals (red dots) generated by electrons traversing in water (white lines). Both experimental studies (data points with error bars in the right panel) and theoretical simulations (red line in the right panel) were performed. The work was done by Guo et al. (Reprinted from Guo et al. [93]. Copyright (2012) with permission from Elsevier.)

Metal nanoparticles or bulk materials under X-ray irradiation have been used to increase the yield of chemical reactions, which should be at least partially caused by physical enhancement. For example, Yoshida et al. [35] used bulk metals to enhance the effectiveness of radiation on decomposition of CO_2 to CO. The authors attributed the enhancement to electrons released from the metals, suggesting that the enhancement was most likely of physical origin. Their work used γ-rays, although X-rays are expected to produce similar results. The measured enhancement was as high as 5.8 DEU for stainless steel meshes.

Roa and Xing et al. [94] studied gold nanoparticles for their radiation enhancement properties using a prostate cancer cell line. The uptake results showed 7×10^4 gold nanoparticles per cell, which was equivalent to 0.07 WP gold loading in the cell (using cell weight of 1 ng), which should produce an enhancement of 0.1 DEU. The experimental enhancement measured with the inhibition rate was between 0.1 and 0.5 DEU, agreeing with the theoretically predicted values of physical enhancement.

Sanche et al. performed a number of measurements to study low-energy electron damage to DNA molecules under various conditions in the past decade and a half. Resonance interactions were found between these low-energy electrons and DNA molecules in vacuum. Two examples are shown here, which were described by Sanche et al. [96] and Sanche et al. [97]. Electron-DNA resonance interactions observed by Sanche et al. may affect damage of DNA in water because X-rays can interact with water and nanomaterials to produce electrons and reactive oxygen species that then interact with DNA molecules. Hence, for this reason, works by Sanche et al. are briefly mentioned here to alert readers of the possibility of electrons emitted from nanomaterials directly interacting with molecules such as DNA. The results obtained by Sanche et al. [95] who investigated the mechanisms of DNA
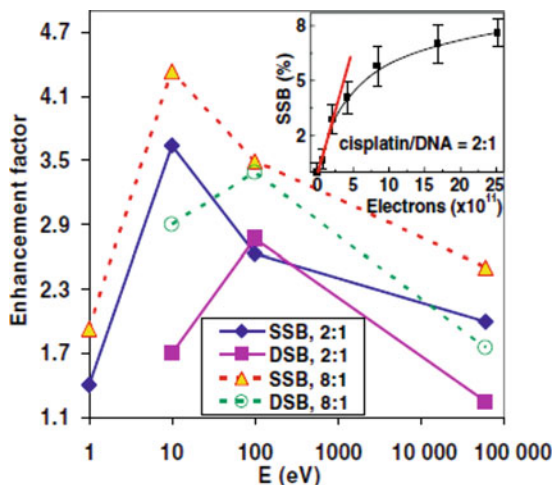
Fig. 2.23 Results of DNA strand break enhancement measurements when the cisplatin-bound dry DNA molecules were irradiated by electrons in vacuum. The results were obtained using gel electrophoresis and indicated that although pure DNA strand breaks did not favor low-energy electrons (not shown here), cisplatin-bound DNA molecules had experienced a maximum amount of SSBs for 10 eV electrons. The publication is one of a long series of studies conducted by Sanche et al. (Reprinted (Fig. 1) with permission from Sanche et al. [95]. Copyright (2008) by the American Physical Society.)

damage by (1–60,000 eV) electrons are shown in Fig. 2.23. Many (up to eight) cisplatin molecules were conjugated to each DNA molecule and single-strand breaks (SSBs) and double-strand breaks (DSBs) were measured after irradiation of the cisplatin-DNA adducts. The enhancement was obtained by comparing the results with cisplatin to without cisplatin. The highest enhancement of 3.1 DEU to the yield of SSBs occurred to cisplatin-bound DNA molecules irradiated with 10 eV electrons. The results did not completely rule out a role of catalysis by metal complexes such as cisplatin.

Sicard-Roselli et al. [98] studied how gold nanoparticles of different sizes affected damage to DNA under X-ray irradiation. Gold nanoparticles spanning 8–92 nm in diameter were explored. DNA damage was studied with X-ray energies between 17 and 70 keV using various X-ray filters. The dose was 1.6 Gy, close to what was used by Guo et al. [7] to treat DNA. Gel electrophoresis was used to determine DNA strand breaks. Supercoiled plasmid DNA molecules were used in the study which became circular after single-strand breaks (SSBs). The authors observed a strong X-ray energy dependency. For a loading equivalent of 0.3 WP gold in water, the enhancement was measured to be 0.48 DEU, giving rise to a unit mass enhancement of 1.2 DEU WP^{-1}, which matched the theoretically predicted total physical enhancement.

Watanabe et al. [87] reported results of an enhancement study that showed increased energy deposition at or near added high-Z element materials. The material
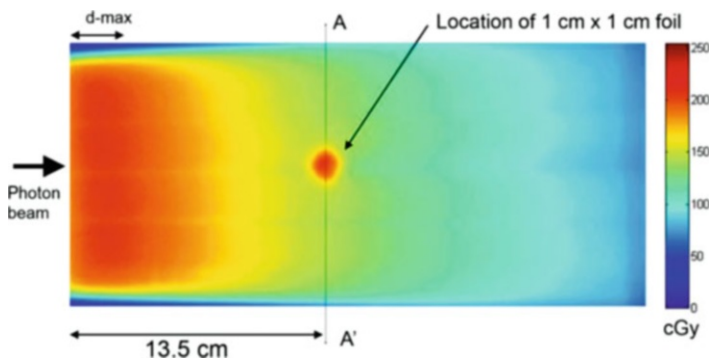
Fig. 2.24 Enhancement of energy deposition by lead in a phantom irradiated with 18 MV X-rays. The enhancer was made of 1-mm-thick, 1×1 cm^2 lead plates separated by 4 mm. (Reprinted with permission from Watanabe et al. [87]. Copyright (2009) by American Association of Physicists in Medicine.)

can be nanomaterials, although the material used in their study was lead embedded in a phantom. An 18 MV X-ray photon beam from a linear accelerator was used. A radiographic film placed between two lead foils separated by 4 mm was used for measurements of energy deposition. The results are shown in Fig. 2.24. The measured dose shown in Fig. 2.24 was 140 cGy without the lead foils and 210 cGy with them, representing an enhancement of 0.43 DEU. Enhanced energy deposition was visible in the radiographic film shown in Fig. 2.24. This was one of the most direct ways to visualize energy deposition enhancement. This and the next two reports are shown here because they have potential to measure predominantly physical enhancement since the methods do not support other enhancements.

Hebert et al. [99] performed a radiosensitization study using gold nanoparticles. They measured the loading of gold using MRI and determined the enhancement using in vitro and in vivo mouse models. The X-ray energy was 150 kVp and dose was 10 Gy. The dominating gold nanoparticle size was 5 nm in diameter. Although no direct loading of gold or enhancement values were given, this method seemed to allow nondestructive retrieval of both enhancement and loading information.

Ma and Su et al. [101] used gold nanoparticles to damage nuclear DNA and observed an enhancement of nearly 1.0 DEU with an unspecified amount of nanoparticles in the cell. The authors observed increased uptake for positively charged polyelectrolyte surfactants. This result and other works are also presented in Chap. 8 or 9 because they belong to biological or medical applications. Similarly, Latimer [100] found that cell-penetrating peptides (CPPs) can improve uptake. With such improvement, the author investigated a number of scenarios in which gold nanoparticles were found to help increase the effectiveness of X-ray irradiation such as reactive oxygen species generation. Both reports invoked physical enhancement to explain the majority of their observed enhancements.

There is at least one complexity associated with these measurements, which is that detection used indirect methods such as chemical reactions, which make the

detection subject to chemical enhancement by gold nanoparticles specified in Sect. 1.1.7. There is no guarantee that these detection methods can fiducially measure physical enhancement. Calibrations using well-synthesized and purified nanomaterials are necessary in the future to validate these methods.

In the following, reports on enhancement dominated by each specific type of physical enhancement are discussed. The results presented here have less ambiguity in measuring a specific type of physical enhancement through the work of eliminating other categories or types of enhancement.

2.4 Three Types of Physical Enhancement

Results shown in Sect. 2.3 indicate that physical enhancement exists in many studies, and the magnitude of the experimentally measured enhancements is often not too different from the theoretically predicted values. Here, only those experimental results closely agreeing with the theoretically predicted ones are presented even though this criterion alone cannot guarantee physical enhancement is the only enhancement in these studies. Furthermore, based on the results shown so far, it is evident that there are several types of physical enhancement. Three types of physical enhancement, which are briefly introduced in Sect. 1.1.7, are formally introduced and discussed in this section. These types exist because each of them is derived from a set of unique physical processes that are different from the others. Such division makes it possible to isolate a type, maximize it, and then recombine it with other types of physical enhancement or even other categories of enhancement such as chemical or biological enhancement for a maximum overall enhancement. The main difference between works presented in this section and those in Sect. 2.3 is that all the results presented in this section can be more closely matched to a type of physical enhancement. Several reports mentioned in this section are also discussed in Sect. 2.3.

2.4.1 Definition of Three Types of Physical Enhancement

Physical enhancement can be further divided into at least two different types because there are low- and high-energy electrons emitted from nanoparticles made of high-Z elements under X-ray irradiation. Low-energy electrons can create so-called nanoscale energy deposition or type 2 physical enhancement, and high-energy electrons can cause constant or uniform energy deposition or type 1 physical enhancement. For example, energetic Auger electrons and photoelectrons traveling microns in water can generate type 1 physical enhancement. Low-energy electrons, on the other hand, only deposit energy near the surface of nanoparticles. These electrons therefore generate type 2 physical enhancement.

A majority of the published reports to date have measured the sum of types 1 and 2 physical enhancement because probes used to detect enhancements are uniformly distributed in the whole sample volume, meaning that the probes detect the accumulated types 1 and 2 physical enhancement over the whole volume. Under such a condition, the magnitude of the accumulated type 2 physical enhancement is a fraction of type 1 physical enhancement for gold nanoparticles 500 nm in diameter or less, and together the two types constitute the commonly known dose enhancement factor. If probes are uniformly distributed in the whole volume of the sample and there is little scavenging by the surface of nanomaterials, then the total enhancement is dominated by type 1 physical enhancement. The percentage of the accumulated type 2 physical enhancement in the total physical enhancement is dictated by the percentage of energy carried by low-energy electrons escaping from the nanoparticles. This fraction is 15% or less for 100 nm diameter or smaller gold nanoparticles. Normally, type 2 physical enhancement cannot be easily measured unless probes are preferentially positioned near X-ray absorbing nanoparticles. Nonetheless, theoretical calculations can always isolate type 2 physical enhancement from the total physical enhancement. To date, Guo et al. [14] published the only results of experimentally measured type 2 physical enhancement.

For a given experimental condition, there is usually a fixed value of type 1 physical enhancement per weight percentage (WP) of the element in the background medium. The value of type 1 physical enhancement is nearly constant over the sample volume. For example, it is shown in this chapter that approximately 1.56 DEU type 1 physical enhancement is generated from 1 WP of gold (atoms) in aqueous solution irradiated by 33 keV X-rays. The magnitude of type 1 physical enhancement is 0.7 DEU for 1WP of 500 nm diameter gold nanoparticles due to attenuation of electrons in these large nanoparticles. This means under such an experimental condition, the effective dose of X-rays or the effectiveness of X-ray irradiation approximately doubles due to the addition of the gold. This rule of thumb can help researchers quickly assess whether their observed enhancement is caused by type 1 physical enhancement. For instance, with 400 nm diameter gold nanoparticles at a concentration of 10 pM, which is equivalent to 1 WP of gold in water, peak type 2 physical enhancement can be as high as 28 DEU (near or within 1 nm of the surface), although the accumulated type 2 physical enhancement over the sample volume is approximately 0.48 DEU. When the two types are added, the total physical enhancement is 1.33 DEU for X-rays at 33 keV, of which 0.85 DEU is from type 1 physical enhancement and 0.48 DEU is from average type 2 physical enhancement. Both quantities are only true to a 1 WP gold loading in water. They can also be expressed by 0.85 DEU WP^{-1} and 1.33 DEU WP^{-1}. On the other hand, peak type 2 physical enhancement, which is 28 DEU, cannot be expressed in DEU WP^{-1} because it is originated from a single nanostructure.

It is important to point out types 1 and 2 physical enhancement coexist almost all the time, and normally it is difficult to separate them if the probes are uniformly distributed throughout the whole sample instead of being positioned only near the surface of nanomaterials. For high concentrations of small, sub-10 nm nanoparticles, for example, the total volume fraction of type 2 physical enhancement is larger, but

the magnitude of type 2 physical enhancement is smaller. In addition, these small nanoparticles can also introduce other categories of enhancement such as chemical enhancement because they are often catalytically active and have large surface area per unit mass. Large nanoparticles create higher type 2 physical enhancement near the surface. However, the volume fraction of type 2 physical enhancement region is smaller for these larger nanoparticles compared to the smaller nanoparticles. Therefore, the total enhancement in both cases is still dominated by type 1 physical enhancement if probes are uniformly distributed. Type 2 physical enhancement may dominate only if probes are tethered to or located near the surface of nanoparticles. This has been recently demonstrated experimentally by Guo et al. [14].

As stated in Sects. 1.1.7 and 2.2.3.2, the third type of physical enhancement is enhancement or creation of fluorescent light from the added nanomaterials in samples irradiated with X-rays. This enhancement is based on the traditional scintillation produced by electrons generated as a result of X-ray ionization of atoms in nanomaterials or by Compton scattering of X-rays by low-Z element media such as water. These electrons interact with scintillators to produce electron-hole pairs in semiconductor nanomaterials or excited states in rare earth nanoparticles or other nanomaterials. Recombination of electron-hole pairs or relaxation of excited electronic states results in the emission of UV-Vis photons. Since fluorescence may traverse far in the sample, there is no need to confine probes to the surface of nanoparticles unless resonance energy transfer such as FRET is the mechanism for transferring energy from scintillation photons to other species coated on the surface of scintillators. Results of experiments studying type 3 physical enhancement have been reported in the literature but under other designations such as X-ray excited optical luminescence (XEOL) or scintillation. Here, this class of enhancement is formally named type 3 physical enhancement.

Another way to define type 3 physical enhancement is to use absolute quantum yield of X-ray scintillators because fluorescent light produced in water is usually minimal and difficult to detect, which makes it difficult to use Eq. 2.1 to numerically calculate the magnitude of this type enhancement. Besides measuring light emission, yet another way to gauge type 3 physical enhancement is to trap and measure chemical species such as singlet oxygen generated in water by scintillation light. An enhancement value can be obtained by comparing the amount of singlet oxygen produced with nanomaterials to that produced without nanomaterials.

Figure 2.25 illustrates the mechanisms of and differences among the three types of physical enhancements. Type 1 physical enhancement is stochastic and can be detected in the whole sample volume. It is shown in Fig. 2.25 by two long lines representing the tracks of energetic electrons traveling in water. An additional short line represents the low-energy electron depositing energy near the nanoparticles. The rate of energy loss, as defined by linear energy transfer rate, is much higher for this low-energy electron than the two other high-energy electrons traversing through the type 2 physical enhancement region. As a result, type 2 physical enhancement is largely caused by the low-energy electrons. Type 2 physical enhancement is also stochastic but only exists near the surface. Type 3 physical enhancement is exhibited by UV-Vis light emission from the added nanomaterials, as it is induced by electrons
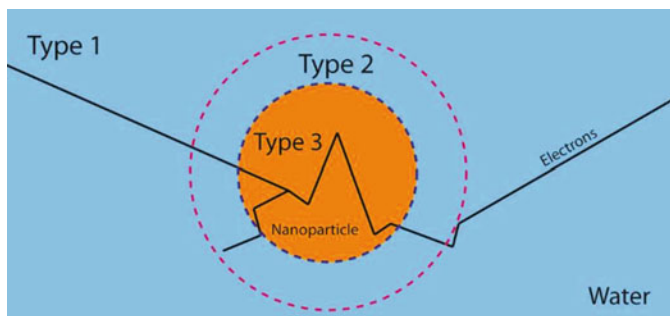
Fig. 2.25 Three types of physical enhancement: type 1 physical enhancement is uniform through-out the whole sample volume; type 2 physical enhancement exists only near the surface, and type 3 physical enhancement is the increased light emission from the nanoparticle and fills the whole sample volume as well

interacting with nanomaterials. These electrons can be produced by the X-rays absorbing nanomaterials or Compton electrons via scattering of X-rays by water. Type 3 physical enhancement can both occupy the whole sample because it is carried by visible photons, which is in the wave form, or be confined to a region near the surface if the photon energy is reabsorbed by chromophores near the surface through FRET.

Merits of separating physical enhancement into these types are manyfold. Firstly, these types of enhancement exist in different locations in the sample. Type 2 physical enhancement, at least the highest peak enhancement, is near the surface of nanomaterials, while types 1 and 3 physical enhancements are the same everywhere in the sample, including in the type 2 physical enhancement region. However, energies responsible for causing type 1 physical enhancement cannot be absorbed at one place because the electrons are spread over the whole volume. Type 3 enhancement is everywhere as well, but because UV-Vis photons are the medium through which enhancement is created and photons can be absorbed at a single location, it is possible to concentrate type 3 physical enhancement to specific locations through FRET. Therefore, type 1 physical enhancement is a bulk prop-erty, type 2 physical enhancement or its peak portion is a nanoscale property, and type 3 physical enhancement can be either a bulk or nanoscale or even molecular property. Secondly, separation of these types foretells the magnitude of these enhancement types so that researchers do not have unrealistic expectations for one type or the other. For example, the theoretically predicted magnitude of type 1 physical enhancement is on the order of 1 DEU WP^{-1} for gold in water for 33 keV X-rays. This enhancement extends to the whole sample volume. In contrast, type 2 physical enhancement can be as high as 40 DEU for a single 600 nm radius gold nanosphere, albeit existing in only a small fraction of the sample volume. If an enhancement of 20 DEU is needed, then type 2 physical enhancement has to be used unless 20 WP gold can be delivered to the target region, which is nearly impossible. Thirdly, the separation or categorization makes it easier for other new

types of enhancements to be discovered. In addition, separation also allows for combinations of any of the three enhancements or even other categories of enhancement. For example, it is possible to use type 2 physical enhancement to increase fluorescence, i.e., type 3 physical enhancement. Mixing X-ray absorbing gold nanoparticles with fluorophores that normally absorb X-rays weakly may increase the fluorescence yield.

Most works published to date did not identify or differentiate these types, and in most cases, only the total physical enhancement was mentioned or measured. As a result, only a small number of publications are discussed here because they have explicitly described these enhancement types in their reports. In a few papers, anti-enhancement or chemical enhancement is discussed in addition to the types of physical enhancement, and these works are mentioned here. It is also important to point out that physical enhancement is different from absorption enhancement or increased imaging contrast, so those papers discussing imaging contrast enhancement are not covered here either. The latter is based on attenuation and not energy transfer or deposition and is discussed in Chap. 9. In the next three subsections, results on each of the three types of physical enhancement are discussed.

2.4.2   Type 1 Physical Enhancement

Type 1 physical enhancement (T1PE) remains almost constant in the whole sample volume and influences probes uniformly distributed in the whole volume of the sample. To generate type 1 physical enhancement, nanomaterials are also uniformly embedded in the sample, which is irradiated with X-rays to generate type 1 physical enhancement that is measured with probes. Theoretically, type 1 physical enhancement can be accurately estimated. Experimentally, although it is the unintended or default enhancement in most cases, type 1 physical enhancement may not be significant if nanoparticles are small or when other enhancements such as chemical or biological enhancement are strong. Chemical enhancement will not be discussed here but will be presented in Chap. 3. The most deliberate efforts of isolating and measuring type 1 physical enhancement are presented in this subsection. In most cases, the total physical enhancement is measured and is the linear sum of types 1 and 2 physical enhancements with equal weights. A shorthand T1PE is only used when the full term becomes redundant.

2.4.2.1   Definition of Type 1 Physical Enhancement

Type 1 physical enhancement is the near constant enhancement in the whole volume. If energy deposition density by the electrons emitted as a result of X-ray irradiation is defined as EDD, then EDD_{T1PE} is the EDD created by type 1 physical enhancement and EDD_{T2PE} is that by type 2 physical enhancement. It is important to point out that

EDD_{T1PE} or type 1 physical enhancement is almost a constant throughout the whole sample, whereas EDD_{T2PE} or type 2 physical enhancement changes drastically as a function of location: it is the greatest at the surface of nanoparticles and is almost zero even just tens of nanometers away from the surface for small nanoparticles. Similarly, if V_{Total} is assigned as the total volume, then V_{T1PE} and V_{T2PE} are the volumes for the two types of physical enhancement. $V_{T1PE} = V_{Total}$ because type 1 physical enhancement exists everywhere. The volume of the nanomaterials is considered negligible here. Then we have

$$Enh_{Total} = V_{T1PE} \times EDD_{T1PE} + V_{T2PE} \times EDD_{T2PE} \qquad (2.2)$$

Because V_{Total} or $V_{T1PE} \gg V_{T2PE}$, especially for large nanoparticles at low concentrations, the following approximation is true:

$$Enh_{Total} \approx V_{Total} \times EDD_{T1PE} = Enh_{T1PE} \qquad (2.3)$$

In theory, there is a fixed relationship between the magnitudes of type 1 physical enhancement and average type 2 physical enhancement, and this relationship is determined by the energy carried by high- and low-energy electrons. The relationship is also dependent of the size of the nanoparticles. The amounts of energy carried by these two groups of electrons depend on the elements in the nanomaterials, X-ray energy, and size of nanomaterials. For gold, the ratio of energies carried by low- to high-energy electrons is around 17.5% for 3 nm nanoparticles under 33 keV X-ray irradiation but changes depending on the X-ray energy and size of nanoparticles. This means that for gold nanomaterials, the magnitude of type 1 physical enhancement is at least six times greater than that of type 2 physical enhancement (0.85/0.15 = 5.7). Therefore, for simplicity, it is possible to equate type 1 physical enhancement to the total physical enhancement. When probes are nonuniformly distributed in the sample, this assumption is no longer valid.

The spatial profile of type 1 or 2 physical enhancement becomes apparent when energy deposition is theoretically modeled, and the results are shown in Sect. 2.4.3.2. Figure 2.26 illustrates physical enhancement from silica-coated gold nanoparticles in water that includes types 1 and 2 physical enhancement. For the silica thickness illustrated here, type 2 physical enhancement, represented by the red dashed line, is largely buried in the 15-nm-thick silica layer. As a result, the enhancement is almost exclusively type 1 physical enhancement, which is caused by all the gold nanoparticles in the sample volume. Figure 2.26 shows a high type 1 physical enhancement, represented by the green dotted line in the whole sample, caused by a high concentration of large gold nanoparticles. If the concentration is low or the nanoparticles are small, or both, then type 1 physical enhancement is negligible. In such cases, the measured enhancement is dominated by type 2 physical enhancement, as shown by the red dashed line in Fig. 2.26. Without the silica layer, the total physical enhancement is the sum of both types of enhancement.
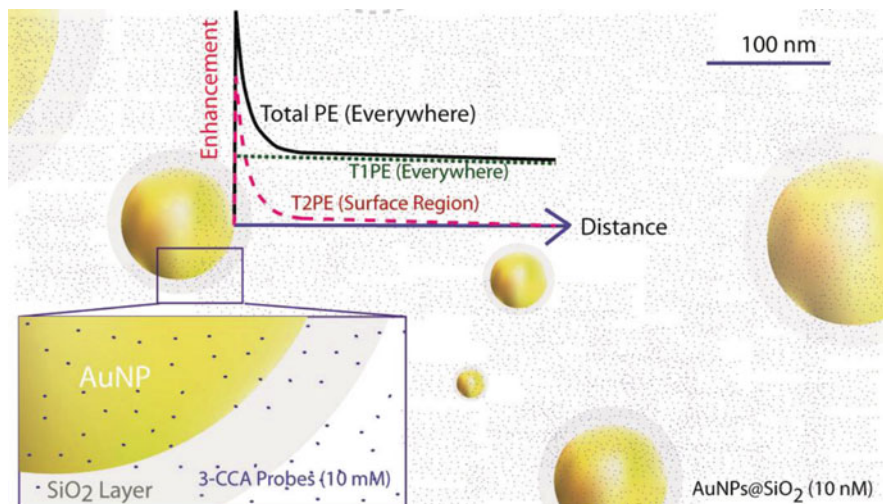
Fig. 2.26 Illustration of type 1 physical enhancement. Several gold nanoparticles are shown, each covered with a layer of silica. Type 2 physical enhancement is shown near the surface of the nanoparticles. Average type 2 physical enhancement is only a small fraction of the total physical enhancement, depending on the concentration and size of the gold nanoparticles

2.4.2.2   Results of Theoretical Calculations of Type 1 Physical Enhancement

The results reviewed here contain dominating (>50%) type 1 physical enhancement based on the comparison between the experimentally measured enhancement and the theoretically predicted type 1 physical enhancement. Theoretical modeling of physical enhancement can best illustrate differences between types 1 and 2 physical enhancement. Most of the theoretical reports shown in Sect. 2.3 can potentially make such differentiation, but these reports generally did not separate the two, and to date there are no calculations on T3PE (scintillation) due to a lack of theoretical approaches to simulate the scintillation processes in materials under consideration. Even though these calculations can differentiate type 1 from type 2 physical enhancement, the enhancement is generally dominated by type 1 physical enhancement. Hence, in most cases, there is no need to separate the two unless the probes are not uniformly distributed throughout the sample. Here, only a few exemplary calculations are presented.

Cho [33] estimated the enhancement in types 1 and 2 physical enhancement regions (see Fig. 2.15). This was the first theoretical study of types 1 and 2 physical enhancement, as defined in this chapter. Several other reports have presented similar results, and Table 2.4 shows a summary of these calculations. The results are exclusively due to physical enhancement and do not account for any other origins such as chemical or biological enhancement because these are theoretical predictions. Based on the enhancement mechanisms for physical enhancement, only large

Table 2.4 Summary of results of theoretical type 1 physical enhancement studies, many of which did not separate type 1 physical enhancement from type 2 physical enhancement

Element	Size (nm)	Energy	Enhancement (DEU)	UWPEnh[a] (DEU WP^{-1})	References
Au, U, UO$_2$			5000		Busby [88]
Au	Atomic	140 kVp	5.06	0.7	Cho [104]
Au	Atomic	50 kVp, ^{125}I, ^{169}Yb, Ir-192	2.7	3	Cho et al. [36]
U	1000	200 keV	Up to 16.7[b]	–	Pattison et al. [23]
Au		497 keV	2.17	0.72	Yoon et al. [105]
Au	2, 50, 100	50 kVp, 250 kVp, 60Co, 6 MV	10–2000[c]	–	Chow et al. [90]
Au	2–50	20–150 keV	0.06[d]/1.1[e]	1.2	McMahon et al. [106]
Au	88	100 kVp	Up to 7.0	1.0	Guo et al. [103]
Au	70	100 kVp	0.7	0.7	Guo et al. [107]
Au	30, 50	1170 keV, 6 MV	0.5–2.95[f]	–	Gh et al. [108]
Au, Pt	100,000	380 keV	0.15–0.3[g]		Parsai et al. [109]
Au	Atomic	100 kVp, 150 kVp	0.69–1.91	0.98–1.06	Sharma et al. [110]
Z = 14–80 (0.05 WP)	20	1 keV–10 MeV	<0.3	6.0[g]	McMahon et al. [84]

[a]UWPEnh is unit weight percentage enhancement
[b]Single microparticle configuration
[c]Single nanoparticle irradiation configuration
[d]Physical enhancement
[e]Type 2 physical enhancement
[f]Wire configuration
[g]Both types of physical enhancement

amounts of X-ray absorbing nanomaterials may generate measurable type 1 physical enhancement. The results of average dose enhancement factor are given in Table 2.4. As explained earlier, dose enhancement factors are presented in units of DEU or DEU WP^{-1} in this book. Only those calculations showing the enhancement factors are listed here.

Many theoretical approaches have also been used to predict effects similar to type 1 physical enhancement. Watanabe et al. [87] simulated the increase from adding materials that strongly absorb ionizing radiation, and their results were similar to type 1 physical enhancement. However, their study did not employ nanomaterials. Berbeco et al. [102] studied a cell slab embedded with 100 nm gold nanoparticles. They developed a Monte Carlo code and calculated energy deposition. For gold loadings between 0.7 WP and 14 WP in the cell, their theoretical prediction of enhancement ranged from 0.2 DEU to 3.4 DEU. These enhancement values contained both types 1 and 2 physical enhancement.

McMahon et al. [47] calculated the dose enhancement factor for 20 nm gold nanoparticles. Macroscopic enhancement, as the authors called it, was equivalent to the sum of types 1 and 2 physical enhancement, and its value was 0.07 DEU for a 0.05 WP gold loading. This translated to a unit weight percentage enhancement of 1.4 DEU WP^{-1}, identical to the value presented in this chapter. The authors obtained this value using the predicted relative biological effectiveness (RBE) of irradiation of the MDA-MB-231 cell line.

Guo et al. [103] simulated type 1 physical enhancement. The nanomaterials were silica-coated gold nanoparticles. The simulation was performed using LLSG package that includes Geant4 and NOREC codes. The results showed 1 DEU WP^{-1} unit WP enhancement. This enhancement value did not contain type 2 physical enhancement, as it was reduced by the 10–15 nm thick silica layer.

Table 2.4 collects several theoretical works that investigated type 1 physical enhancement. It is important to point out that many of the works presented in the table did not separate type 1 from 2 physical enhancement. As a result, in most cases, both types were included. Based on Table 2.4, the total enhancement is energy dependent, and at 33 keV X-rays, which is the average energy from a 100 kVp X-ray source, the enhancement is 1.4 DEU WP^{-1}. If type 2 physical enhancement is excluded, then type 1 physical enhancement is 1.0 DEU WP^{-1}. These values can be used as general benchmark values for estimating type 1 physical enhancement and total physical enhancement. If the measured values are too different from these values, then other types or categories of enhancement may be responsible.

There are a few reports that showed enhancements exceeding 2000 DEU. As explained in Sect. 2.3.3.3, these results are not in contradiction with the conclusions drawn here. The extraordinarily high enhancements are due to the irradiation configuration those studies used to calculate their enhancement factors, which is defined as the ratio of energy deposition in the volume of interest with gold nanoparticles to that without gold nanoparticles when these sample volumes are irradiated by an X-ray beam. From this definition, enhancement changes as a function of the beam diameter. With smaller X-ray beam diameters, the denominator in the formula of enhancement calculation is significantly reduced, resulting in

higher enhancements. In reality, the X-ray beams are much wider than the diameters of nanoparticles, so these calculated enhancements cannot be directly compared with experimentally measured enhancement values. Nonetheless, these calculations can be used to estimate relative enhancements from different elements or morphologies, even though they are not suitable for predicting the absolute physical enhancement by nanomaterials.

Another noticeable outcome is the significant difference between type 1 physical enhancement for X-rays of 100 kVp and 1 MeV. For 100 kVp X-rays, which have an average X-ray energy of 33 keV, the enhancement is close to 1.4 DEU WP^{-1} for gold in water (including both types of physical enhancement). At 1 MeV, the enhancement decreases to 0.05 DEU WP^{-1} of gold in water. This is the incentive to use 100 kVp X-rays if nanomaterials are used to generate physical enhancement. If experimentally measured enhancement values at these two energies are both high, then the enhancement could not be caused by type 1 physical enhancement regardless of uptake amounts. This criterion can be used to identify chemical and biological enhancements discussed in Chaps. 3 and 4.

2.4.2.3   Results of Experimental Investigations of Type 1 Physical Enhancement

Nearly all the experimental works reported in the literature begin their investigations with the intent to measure the total physical enhancement. Since type 2 physical enhancement is a small fraction of type 1 physical enhancement in most cases without any specially designed nanomaterials and probes, and if there are no interferences from enhancements such as type 3 physical enhancement, chemical enhancement, biological enhancement, or anti-enhancement, then physical enhancement is dominated by type 1 physical enhancement. However, this is seldom the case, as demonstrated in Chaps. 3 and 4. The works discussed here contain results with approximately the same theoretically predicted total physical enhancement and experimentally measured enhancement. Other works are discussed either in Sect. 2.3 or in other chapters of the book according to the dominating enhancement mechanisms such as chemical or biological enhancement.

The first work of detecting type 1 physical enhancement was performed by Das et al. [4] who used gold particles to enhance damage to cells and observed an enhancement of 1.0 DEU from a loading of 0.5 WP gold under 100 keV X-ray irradiation. The calculated type 1 physical enhancement was 0.5 DEU, close to the measured value. Therefore, even though the authors did not use nanoparticles, their work is mentioned here.

The cleanest type 1 physical enhancement measurement was conducted by Guo et al. [103] using large gold nanoparticles coated with a layer of silica. The average nanoparticle size including the 10-nm-thick silica coating was 108 nm. X-rays from a 100 kVp microfocus X-ray source were used without filters or with Al and several other filters to modify the X-ray energies. Through this study, an enhancement of 1.0 DEU was measured with 1 WP of gold in water using Al foil-filtered X-rays,
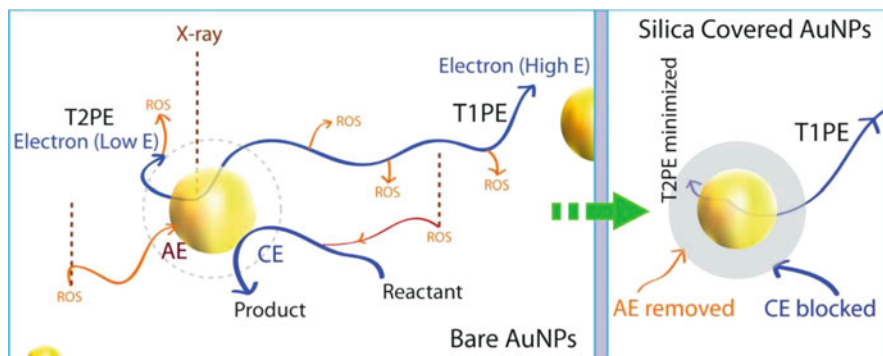
Fig. 2.27 Illustration of type 1 physical enhancement (T1PE) from silica-coated gold nanoparticles (AuNPs@SiO$_2$). In order to exclusively measure T1PE, chemical enhancement (CE) including anti-enhancement (AE) must be eliminated, as shown here. Type 2 physical enhancement (T2PE) is buried in the silica layer. Measurement results along with simulated enhancements were reported by Guo et al. [103]. (Reprinted with permission from Guo et al. [103]. Copyright (2014) American Chemical Society.)

removing X-rays below 15 keV. The maximum enhancement was 5.0 DEU for a 7 WP gold loading in water, at which point the sample was a thick paste. The lowering of enhancement at such high nanoparticle concentrations could be caused by electrons losing a significant fraction of energy within the nanoparticles. Figure 2.27 illustrates how type 1 physical enhancement was measured by Guo et al. and how other enhancements were blocked or minimized. In their case, neither chemical enhancement (CE) nor anti-enhancement (AE) could occur because the gold surface was covered with silica. Type 2 physical enhancement (T2PE) was buried within the silica layer, and as a result, type 1 physical enhancement (T1PE) dominated. The conclusion was that the physical enhancement or type 1 physical enhancement was indeed of the order of 1 DEU WP^{-1} of gold in water, which agreed with the theoretically predicted value.

Another experimentally demonstrated type 1 physical enhancement was obtained with a very high loading of gold nanotubes by Guo et al. [93]. In that work, gold nanotubes with silica nanowire cores were synthesized and used. The nanotubes were used in the form of a matrix in water, and nearly 100 WP of gold was immersed in water. DNA molecules were dissolved in water as well. The synthesis of nanotubes is described in Chap. 6. Theoretically, 100 WP of gold in water should generate 100 DEU type 1 physical enhancement or 140 DEU total physical enhancement. However, the results shown in Fig. 2.22 indicate that only a 2 DEU enhancement was measured when these nanotubes were mixed with the probing DNA molecules. The process was analyzed, and it is now understood that the low enhancement was caused by the scavenging property of the bare gold surface of gold nanotubes that significantly reduced the enhancement. As a result, gold nanotubes scavenged most hydroxyl radicals produced by electrons released from the nanotubes despite the predicted 100-fold increase in X-ray absorption by 100 WP

gold nanotubes in water, as shown in Fig. 5.8 (right panel) of Chap. 5. This work showed that scavenging of hydroxyl radicals by the bare gold surface was severe. Once scavengers such as DMSO or Tris were added into the solution to reduce scavenging by the gold surface, enhancement was partially restored to 15 DEU.

More recently Guo et al. [107] studied total physical enhancement by large PEG-coated gold nanoparticles using electron paramagnetic resonance (EPR) spectroscopy. Spin trap 5-tert-butoxycarbonyl-5-methyl-1-pyrroline N-oxide (BMPO) was used to react with reactive oxygen species generated under X-ray irradiation with assistance from gold nanoparticles. The spin trap reactions were apparently not influenced by these large, 70 nm diameter gold nanoparticles because the enhancement was linearly dependent on the concentration of gold nanoparticles within a large concentration range. The measured WP mass type 1 physical enhancement was 0.7 DEU WP^{-1}, about half of the predicted physical enhancement. Figure 2.32 shows the results. The reduction of enhancement was considered to be caused by scavenging of PEG-coated gold nanoparticles or possibly other factors.

Another work of measuring type 1 physical enhancement was performed by Guo et al. [14]. The probes were water nanoparticles in calcium phosphate-enclosed liposomes (CaPELs), which were loaded with sulforhodamine B (SRB) dye molecules dissolved in the aqueous solution nanoparticles taking shape inside CaPELs. Type 1 physical enhancement was created by 100 nm diameter gold nanoparticles. Physical enhancement was determined by the reduction of fluorescence from SRB. The slope of enhancement was 1 DEU WP^{-1} as the gold concentration was increased from 0.05 WP to nearly 1 WP. The results are shown in Fig. 2.40. The slope was in good agreement with the theoretically predicted type 1 physical enhancement.

2.4.2.4 Other Works of Detecting Type 1 Physical Enhancement with Nanomaterials

Xu and Zhang et al. [111] and Yang and Xu et al. [112] investigated diselenide polymer particles under γ-ray irradiation. They constructed a polymer aggregate nanostructure made of diselenide block copolymer micelles. Upon irradiation with γ-rays, the micelles disintegrated and released doxorubicin trapped in the micelles. The authors used HepG2 cells (human liver cancer cells) for detection of radiation-induced cleavage of the diselenide bond. Figure 2.28 shows the working mechanism of their constructs and enhancement.

Ma and Su et al. [113] created a new nanosystem based on lithography of nanoparticles and used the system to study cell damage under X-ray irradiation. In their work, microdiscs consisting of layers of gold nanoparticles were constructed. The number of nanoparticle layers was varied and cell death monitored. Figure 2.29 (left panel) shows the nanostructures created and the results (right panel) of their cellular study. The enhancement was more than 2 DEU according to the authors. This system has potential to provide a clean environment for the study of pure physical enhancement, although type 2 physical enhancement also plays a major role.
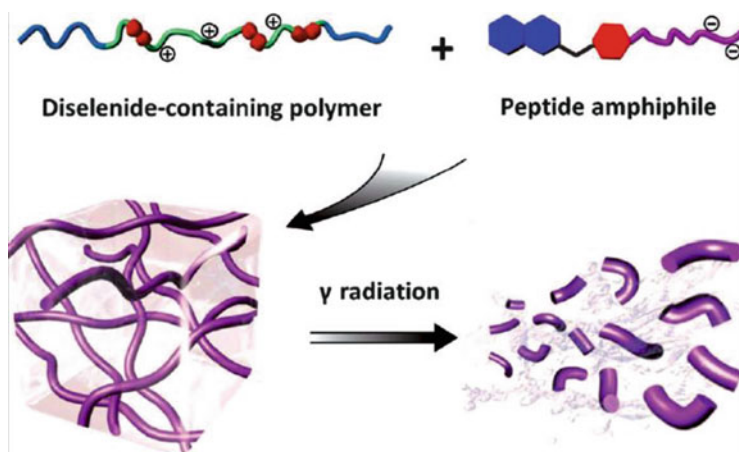
Fig. 2.28 Illustration of ionizing radiation-induced bond cleavage and drug release, which shows micelles made of diselenide disintegrating upon irradiation. (Reprinted with permission from Xu and Zhang et al. [111]. Copyright (2011) by John Wiley and Sons.)
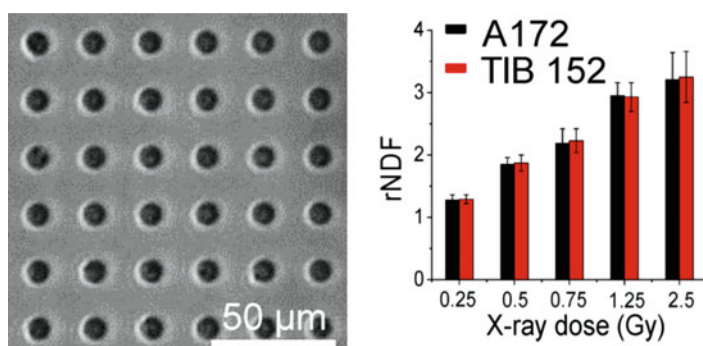

Fig. 2.29 Enhancement to cell damage by microdiscs made of layers of gold nanoparticles. The left panel shows a phase contrast image of the gold microdiscs on PVA-coated glass, and the right panel shows the relative nuclear diffusion factor (rNDF), a method to quantify DNA damage, as a function of X-ray dose. (Adapted with permission from Ma and Su et al. [113]. Copyright (2015) American Chemical Society.)

2.4.2.5 Benchmarking Type 1 Physical Enhancement

There are several physical methods in conjunction with the choice of nanomaterials that can be used to isolate and measure type 1 physical enhancement. Besides isolation from type 2 physical enhancement, one must always confirm the absence of chemical or biological enhancement when studying type 1 physical enhancement. Several methods of measuring dominant type 1 physical enhancement are discussed in the following.

Silica-Covered Large Gold Nanoparticles for Measuring Type 1 Physical
Enhancement

As stated before, the cleanest way to generate type 1 physical enhancement is to
remove other types such as types 2 or 3 physical enhancement and other categories
of enhancement such as chemical enhancement while keeping type 1 physical
enhancement as intact as possible. One of such experiments was performed by
Guo et al. [103] using thin silica-coated large gold nanoparticles mentioned earlier.
The 8–10-nm-thick silica layer removed chemical enhancement and prevented anti-
enhancement because both enhancements require the surface of gold nanoparticles to
function. Type 2 physical enhancement was buried by the silica layer because the
highest type 2 physical enhancement occurs within 10 nm of the surface of 88 nm
gold nanoparticles. Lastly, this thin layer of silica only attenuated type 1 physical
enhancement by less than 5% because the enhancement was mainly caused by
energetic electrons, which can easily penetrate through the silica layer. Figure 2.30
(left panel) shows the results. The more accurate data is in the low gold loading
region (less than 1.0 WP) where little saturation occurred in the measurement. Based
on the slope of enhancement as a function of WP in this region, the total enhance-
ment or type 1 physical enhancement was 1 DEU WP^{-1}. Adding dimethyl sulfoxide
(DMSO), a hydroxyl radical scavenger, did not affect the results (middle panel),
further confirming that the results were due to physical enhancement. The right panel
shows that type 1 physical enhancement depended on X-ray energy. When unfiltered
X-rays were used, the measured enhancement was only 10% of the enhancement
obtained with filtered X-rays.

The results showed an enhancement of 1.0 DEU for 1 WP of gold in water
irradiated with 100 kVp X-rays, with filtering to remove low-energy X-rays below
15 keV. This is a benchmark enhancement value for type 1 physical enhancement
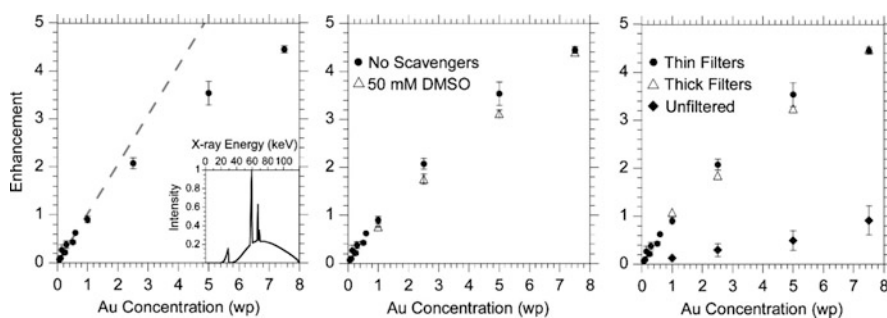using gold in water under the specified conditions because no other enhancements

Fig. 2.30 Exclusive type 1 physical enhancement from silica-coated gold nanoparticles. The slope
shown in the left panel was 1.0 DEU WP^{-1} for gold in water. Adding DMSO as a hydroxyl radical
scavenger did not change the slope, as shown in the middle panel. The enhancement was energy
dependent and was lower when low-energy X-rays (unfiltered) were used, as shown in the right
panel. (Reprinted with permission from Guo et al. [103]. Copyright (2014) American Chemical
Society.)

were enabled under the given experimental conditions. Changing the X-ray energies changed the magnitude of type 1 physical enhancement, as shown in Fig. 2.1 (right panel).

One may argue that since type 1 physical enhancement is close to total physical enhancement in most cases, it is not important to separate type 1 physical enhancement from the total physical enhancement. Such an argument has some merit. Nonetheless, one of the benefits of the separation is that types 1 and 2 physical enhancement can be independently discussed. Furthermore, the results in most published works are subjected to chemical or other enhancements if the surface is catalytically active. Use of nanomaterials possessing only type 1 physical enhancement can help remove other categories and types of enhancement and hence can be used to better assess the origin of enhancement in complex environments such as cells and animals.

EPR Spectroscopy

Electron paramagnetic resonance (EPR) spectroscopy is a powerful method for investigating radicals, which are often produced when ionizing radiation interacts with water. The method itself is briefly described in Chap. 7, and readers who are interested in learning the technique can review Sect. 7.2.7. Here, results of works using EPR spectroscopy to determine type 1 physical enhancement are described and discussed.

Guidelli et al. [114] reported results of their EPR study of 5 nm diameter gold nanoparticles mixed with alanine, which showed 70% and 160% increases in the EPR signal amplitude at loadings of 1 and 3 WP gold in the samples, respectively. These values corresponded to enhancements of 0.7 and 1.6 DEU. The results are shown in the left panel of Fig. 2.31. In a similar study, Guidelli et al. [115] showed a
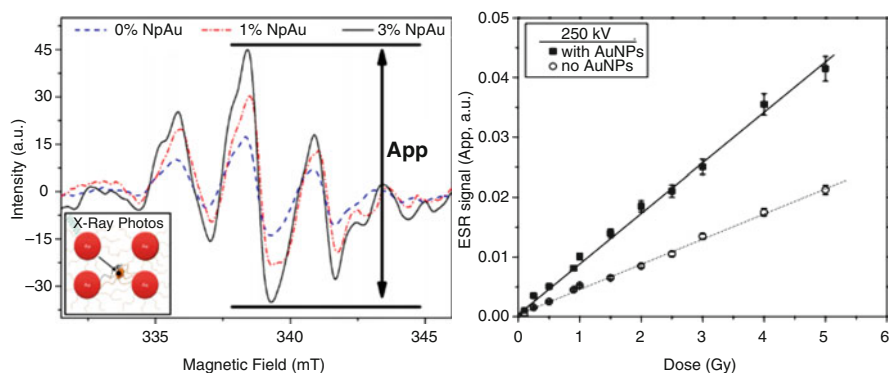
Fig. 2.31 EPR measurements of enhancement from gold nanoparticles under X-ray irradiation. The left panel shows the results obtained by Guidelli et al. and the right panel shows those by Wolfe et al. (Reprinted (adapted) with permission from Guidelli et al. [114]. Copyright (2012) American Chemical Society and ©Institute of Physics and Engineering in Medicine. Reproduced with permission from IOP Publishing and Wolfe et al. [116]. All rights reserved.)

much greater slope of response of the EPR signal at low loadings of below 0.05 WP gold in water than at high loadings (>0.1 WP). Those results are given in Chap. 3 (Fig. 3.1), which indicate the existence of chemical enhancement.

Wolfe et al. [116] investigated dose enhancement of radiation therapy using gold nanoparticles and EPR dosimetry. The authors mixed alanine in its powder form with gold nanoparticles and measured EPR response after the mixtures were irradiated with 250 kVP and 6 MeV X-rays. The loading of gold was only 0.1 WP, and the authors observed an enhancement of nearly 1 DEU. This value is nearly 10 times higher than what simulated type 1 physical enhancement would support. No enhancement data as a function of gold loading was available. Enhancement at 6 MeV was about 0.25 DEU, which was also higher than the predicted type 1 physical enhancement for the loading and X-rays at this energy. The right panel of Fig. 2.31 shows their results obtained under 250 kVp X-ray irradiation.

Geso et al. [117] used alanine-gold nanoparticle pellets as an EPR dosimeter to determine enhancement by gold nanoparticles. Gold nanoparticles of 8.2 nm average diameter were used. Among other results presented in their report, the authors showed a 70–100% increase in EPR signal intensity with 3 WP gold in alanine irradiated with X-rays from an 80 kVp source with a 2.2 mm thick Al foil filter. Dose dependency was linear up to 22 Gy. In contrast, a signal increase of less than 10% was recorded when MV X-rays were used. More recently, Geso et al. [118] reported similar findings. 5 nm diameter gold nanoparticles were used, which were irradiated with protons, kV and MV X-rays. Again, kV X-rays generated the highest enhancement, followed by MV X-rays. Protons did not yield any enhancement. These results were in partial agreement with the theoretical predictions shown in this book.

Guo et al. [107] examined the enhancement caused by 70 nm PEG-coated gold nanoparticles. They employed BMPO spin trap reagent to react with hydroxyl or superoxide radicals or both to form much more stable radical spin adducts for study with EPR spectroscopy. The spin trap reactions are shown in Fig. 2.32, and four conformers are shown. Also shown are the EPR profiles of the conformers. The measured EPR profiles were decomposed to obtain the composition of the radicals and their conformers. The results showed that spin adducts contained 80% hydroxyl radical BMPO-adduct conformer I and 20% hydroxyl radical BMPO-adduct conformer II. The EPR results are shown in the right panel of Fig. 2.32. The study found an enhancement of 0.7 DEU for a 1-WP gold loading. The EPR response was linear in the span of low to high concentrations of gold nanoparticles, suggesting physical enhancement was responsible for the increased production of radicals. If chemical or anti-enhancement dominates, then such linearity would not exhibit over such a large concentration range. For X-ray energies and gold nanoparticle concentrations used in the work, the measured enhancement was approximately 70% of the theoretically predicted type 1 physical enhancement measurement or 50% of the total physical enhancement. The reduction can be attributed to several factors, including scavenging of hydroxyl radials and catalytic spin trap interconversion by gold nanoparticles. Future work is needed to fully identify these factors.

In summary, EPR spectroscopy can be a convenient and useful method to investigate enhancement mechanisms. Spin trapping reactions are generally simpler
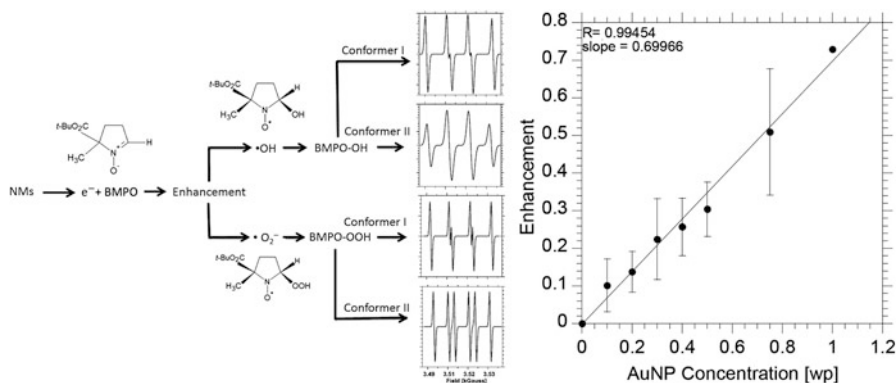
Fig. 2.32 EPR measurements of type 1 physical enhancement from 70 nm gold nanoparticles under X-ray irradiation. The EPR spin trap reaction is shown in the left panel. Also shown are the conformers and EPR profiles of these conformers. The right panel shows a linear relationship between measured signal intensities and gold concentrations. (Adapted with permission from Guo et al. [107]. Copyright (2016) American Chemical Society.)

than many of the currently used fluorescence dosimetric reactions, and the detection of radicals using EPR spectroscopy can be more directly related to the concentration of radicals. However, interconversion between hydroxyl and superoxide radicals or their spin trap adducts may be both interesting and complex. Furthermore, care must be taken to examine whether gold nanoparticles can catalyze the conversion reactions between radical adducts, even without X-ray irradiation. Such interconversion was observed by Guo et al. [107]. Similar interconversion processes have been observed in other settings. For example, interconversion between superoxide and hydroxyl radical adducts was also observed by Wang et al. [119] who studied the generation of singlet oxygen, hydroxyl, and superoxide radicals by a boron-dipyrromethene (BODIPY) dye under 532 nm light irradiation.

Dosimetric UV-Vis for Measuring Type 1 Physical Enhancement

Geso et al. [120] developed a unique matrix of polymer reactions to respond to hydroxyl radicals produced by X-ray irradiation. UV-Vis spectroscopy was then used to measure X-ray dose. The materials in the matrix included polyurethane and leucomalachite green. Such a method might be used to measure type 1 physical enhancement, although no such attempt has been made. One possible drawback of this method is that these polymerization reactions may be subjected to chemical enhancement. Future work is needed to either help isolate polymerization reactions from the surface of nanoparticles that generate type 1 physical enhancement or use non catalytic nanomaterials for type 1 physical enhancement.

2.4.3 *Type 2 Physical Enhancement*

Type 1 physical enhancement is nearly constant across the whole sample volume and is only significant when large amounts of nanomaterials, for example, greater than 0.1 WP, are present. In contrast, type 2 physical enhancement is the strongest near the surface of nanomaterials and rapidly decreases as the point of interest moves away from the surface. These characteristics are most prominent when the size of nanoparticles is less than 100 nm. When the size is greater than 100 nm in diameter, the tail end of type 2 physical enhancement can extend to 100 nm away from the surface.

It is important to point out that in order to easily detect type 2 physical enhancement, large amounts of nanomaterials are also needed if no measures are taken to reduce the signal from the medium interacting with X-rays. One such measure is to deliberately position the probes only near the surface of nanomaterials, which would possibly allow type 2 physical enhancement to be measurable even for small amounts of large individual or aggregate nanostructures.

Unlike type 1 physical enhancement, which is uniform throughout the sample volume, the magnitude of type 2 physical enhancement is position sensitive. Theoretical volume of interest used in calculating type 2 physical enhancement is often chosen for conveniently setting up the calculation. For spherical nanoparticles, this volume usually consists of spherical shells of a finite thickness off the surface of the spheres. More recently, other shapes have been studied, and a special case of X-ray-induced energy transfer (XIET) is discussed in this section. For practical measurements, the volume of interest depends on the shape of the distribution profiles of probes or acceptors. If the probes or acceptors are small, positioned directly off the surface of nanomaterials, and can discriminately detect local enhancement, then the maximal type 2 physical enhancement can be measured. If a probe detects a finite volume, then type 2 physical enhancement averaged within this volume is measured, which can be significantly lower than the peak type 2 physical enhancement at the surface of the sphere if the volume is large. This point will be further clarified in Sect. 2.4.3.4, which discusses XIET between large gold nanoparticle energy donors and water nanoparticle acceptors.

Here, type 2 physical enhancement is defined first, followed by a discussion of results obtained through theoretical investigations. Results of experimental works studying type 2 physical enhancement are subsequently described. Lastly, XIET is discussed as a special case of type 2 physical enhancement.

2.4.3.1 Definition of Type 2 Physical Enhancement

Type 2 physical enhancement is the position-sensitive energy deposition created by low-energy electrons emitted from X-ray absorbing nanomaterials added into a low-Z element matrix. It has also been called nanoscale energy deposition, nanoscale dose enhancement factors, or local effect. Type 2 physical enhancement is still a

physical enhancement, meaning the origin of this enhancement is still caused by X-ray absorption by the nanomaterials, a physical process. It is different from type 1 physical enhancement, which is uniform over the whole sample volume. In contrast, type 2 physical enhancement is the highest at the surface of nanomaterials, and its magnitude decreases rapidly as the point of interest moves away from the surface.

Many theoretical works have shown the existence of nonuniform enhancement profiles. For example, Cho [33] showed the dose enhancement factor around a tumor phantom filled with gold. The results are discussed in Sect. 2.3.2 and shown in Fig. 2.15. In another work, Jones et al. [37] studied what they called microscopic dose enhancement around gold nanoparticles of unspecified sizes. The authors observed decreasing energy deposition as the point of examination moved away from the nanoparticles surface. Similar to but slightly different from several other calculations, this work employed the source of radiation in the form of brachytherapy, i.e., placing a point source at the center of a phantom together with the gold and calculating the radial enhancement factor. As a result, the enhancement calculated was exceedingly high. Further discussion is given in Sect. 2.4.3.2 and Fig. 2.36.

The concept of nanoscale enhancement, which is also referred to as type 2 physical enhancement near the surface of nanomaterials, was formally established by Guo et al. in [12] and again in [13]. Some of their calculated enhancements can be verified experimentally. Figure 2.33 illustrates the spatial profile of type 2 physical enhancement by displaying energy deposition events around a gold nanoshell in water under X-ray irradiation. The color-coded energy deposition events reveal a high density of deposition events near the gold nanoshell by electrons emitted from the gold nanoshell (blue) versus those from water (gray). The latter are evenly dispersed throughout the solution.
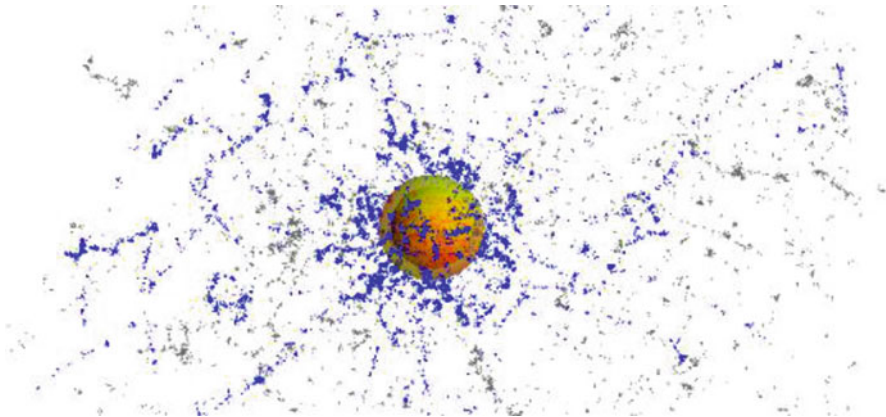
Fig. 2.33 Illustration of type 2 physical enhancement using a gold nanoshell in water under X-ray irradiation. The blue dots are the energy deposition events made by electrons emitted from the gold shell, which are in a higher density near the surface of the shell. The gray spots are the energy deposition events made by Compton electrons generated from interactions of X-rays with water

2.4.3.2 Theoretical Modeling and Calculations of Type 2 Physical Enhancement

A number of studies have been conducted to theoretically simulate type 2 physical enhancement. Their works are listed in Table 2.5, which only lists the works of studying type 2 physical enhancement.

The magnitude of type 2 physical enhancement near the surface of individual nanoparticles can be significantly greater than type 1 physical enhancement. Nevertheless, it is more difficult to experimentally measure type 2 physical enhancement than total physical enhancement because probing nanoscale enhancement requires that probes be placed exclusively near the surface of nanoparticles. This is partially caused by the high peak type 2 physical enhancement that exists only in a very small volume fraction. On the other hand, type 2 physical enhancement can be conveniently theoretically simulated. Guo et al. [12] reported theoretical and experimental studies of type 2 physical enhancement from individual 3 nm gold nanoparticles. Experimental type 2 physical enhancement measurements in this work were made possible by conjugating DNA molecules to the surface of 3 nm gold nanoparticles. The authors found that the energy deposition profile by electrons emitted from 3 nm gold nanoparticles decayed exponentially as a function of distance from the surface of nanoparticles. The absolute enhancement on the surface of these 3 nm gold nanoparticles was nearly 6 DEU at 1 nm off the surface. However, the thickness of the shell in which type 2 physical enhancement was significant was thin, of the order of less than 2 nm for a single 3 nm diameter gold nanoparticle, beyond which the enhancement decreased to less than 1.5 DEU. The results are shown in Fig. 2.34. Interactions between gold nanoparticles and electrons produced in water through Compton scattering are also evaluated, and energy deposition by these interactions produced an enhancement that was less than 10% of that by X-rays interacting with gold nanoparticles. The theoretical results are shown in Fig. 2.34, and experimental data is shown in Fig. 3.12.

In a subsequent publication, Guo et al. [13] calculated type 2 physical enhancement of many different nanostructures and nanoparticle aggregates. The enhancement, defined here using average energy deposition density in a 2-nm-thick spherical shell-like region immediately beyond the surface of spherical nanoparticles, was up to 39 DEU near the surface of a single 600 nm radius (1.2 μm diameter) gold nanoparticle. For a 150 nm (300 nm diameter) radius gold nanoparticle, the surface type 2 physical enhancement was 19 DEU. Figure 2.35 shows the enhancement from a single gold nanoparticle depositing energy at the surface of the nanoparticle (green solid line). The enhancement generated by the nanoparticle increases as a function of size. This shows two direct benefits of using type 2 physical enhancements. Firstly, significant enhancements can be achieved with a single gold or heavy element nanoparticle. Secondly, closely spaced nanoparticles can deposit much more energy locally than isolated single nanoparticles of the same mass. For example, two closely spaced 150 nm radius gold nanoparticles can generate an enhancement of 38 DEU in the narrow space between them. Also shown in Fig. 2.35 is an enhancement of 3.0

Table 2.5 Groups that preformed theoretical simulation of type 2 physical enhancement

Element	Size (nm)	Energy	Enhancement (DEU)	References
Au	3	100 kVp	0.4	Guo et al. [12]
Au	Nanoshell	33 keV	60	Guo et al. [13]
Au	100 nm diameter nanotubes	100 kVp	15	Guo et al. [93]
Au	90	100 kVp	2.0	Guo et al. [14]
Au	–	50 kVp, 6MV, ^{125}I, 103Pd, ^{169}Yb, Ir-192	350–500	Jones et al. [37]
Au	2–3	250 kV		Marques et al. [121]
Au	2, 50, 100	50, 250 kVp, ^{60}Co, 6 MV	10–2000[a]	Chow et al. [90]
Au	2–50	20–150 keV	1.1	McMahon et al. [106]
Au	40	50, 100 keV	2–3	McMahon et al. [122]
Au	20	1 keV–10 MeV	6.0 or higher	McMahon et al. [84]
Au	1.9	80–120 kVp	1.5	Ngwa et al. [123]
Au	1.9	100 kVp	9	Ngwa et al. [91]
Au, Pt, Bi	1.9	50 kVp	8	Su et al. [124]
Au	400	80 kVp, 6 MV	1.23–14.5	Douglass et al. [125]
Au	50	6 mv	0.2–3.4	Berbeco et al. [102]
Au	100 nm slab	20 keV	110	Zygmansk et al. [92]
Au	10, 20, 50	60 keV	0.07	Casta et al. [15]
Au	250, 230, etc.	2.7–43.5		Wardlow et al. [126]
Au		35–95 keV	17.5	Moshirian et al. [127]

[a]Single particle irradiation configuration
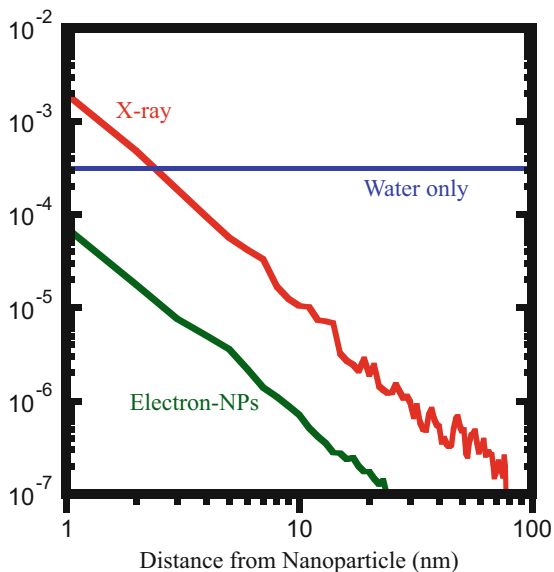
Fig. 2.34 Illustration of type 2 physical enhancement surrounding a 3 nm gold nanoparticle immersed in water irradiated with X-rays. Energy deposition by electrons emitted from nanoparticles as a result of X-rays interacting with the nanoparticle is shown (red line). Contribution from Compton electrons interacting with the nanoparticles is also given (green line). The Compton electrons are generated from X-rays interacting with water. Also displayed is energy deposition from X-rays interacting with water (blue line). (Reprinted with permission from Guo et al. [12]. Copyright (2007) American Chemical Society.)

DEU from 2 WP gold atoms in water (blue dotted line). The atoms were distributed over the whole sample, and the calculated enhancement included both types of physical enhancement. The total physical enhancement from 2 WP gold nanoparticles (red dashed line) of different sizes decreased as a function of size due to attenuation of electron energy in large gold nanoparticles. For large gold nanoparticles such as the 600 nm radius particles, type 2 physical enhancement from a single nanoparticle can be greater than ten times the sum of types 1 and 2 physical enhancement from 2 WP gold atoms in water. The slightly lower enhancements at the surface of small nanoparticles shown in Fig. 2.35 than the sum of two types of physical enhancement for 2 WP gold in water were caused by the former simulation being performed for a single nanoparticle whereas the latter being done with atoms or particles uniformly distributed in the sample.

Jones et al. [37] theoretically studied what they called microscopic dose enhancement factor (mDEF) around gold nanoparticles using the EGSnrc code as well as the NOREC code. The authors employed several X-ray sources, including broad-spectrum sources such as X-ray tubes (50 kVp), accelerators (6 MV), and brachytherapy sources such as ^{103}Pd (21 keV X-rays). No gold nanoparticles were used. Instead, 0.7 WP gold atoms in water were treated as the gold nanoparticle-loaded tumor
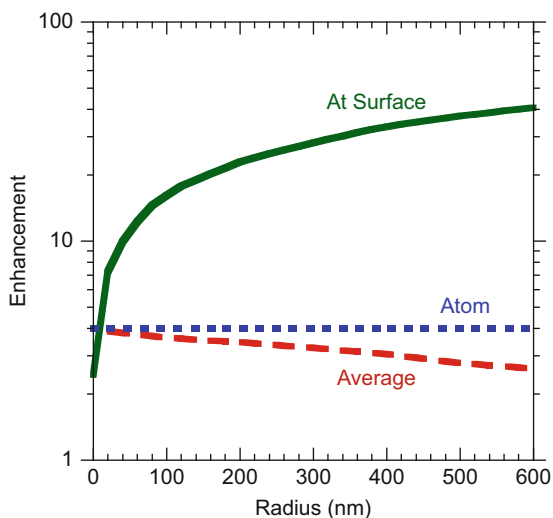
Fig. 2.35 Type 2 physical enhancements at the surface of spherical nanoparticles and sum of both types of physical enhancement due to gold atoms. For a 600 nm radius gold nanoparticle, enhancement near surface was 39 DEU (green solid line). In contrast, the average enhancement from 2 WP of these nanoparticles uniformly distributed in the whole sample was 1.5 DEU (dashed red line). 2 WP gold atoms uniformly distributed throughout a water volume gave an average enhancement of 3.0 DEU (blue dashed line). These results were calculated using 40 keV X-rays. (Reprinted with permission from Guo et al. [13]. Copyright (2012) American Chemical Society.)

phantom. The size of the tumor was large, $3 \times 3 \times 3$ cm^3. Dose enhancement in the phantom was the summed contribution from all the atoms. X-rays irradiated samples in the brachytherapy mode, meaning that X-rays emitted radially and isotropically from the center (a single point) of the sample. Under these conditions, enhancements were calculated and results are shown in Fig. 2.36. The enhancement was the ratio of energy deposition in water with gold to without gold. The enhancement values were high because of the way the enhancement was computed—the gold nanoparticle (GNP) at the center received irradiation of most X-rays.

McMahon et al. [47] performed a theoretical study of nanoscale energy deposition around nanoparticles under X-ray irradiation. The authors calculated type 1 physical enhancement, which they called macroscopic enhancement, and type 2 physical enhancement, an enhancement defined by a local effect model (LEM) in their work. Figure 2.37 shows their results from 20 nm gold nanoparticles at a loading of 0.05 WP under 40 keV X-rays. The authors used a term called relative biological effectiveness (RBE) for their theoretically predicted results. They found that 2, 20, and 50 nm diameter gold nanoparticles had similar nanoscale energy deposition profiles. The macroscopic enhancement defined in their work was 0.075 DEU, which was reasonable for their gold loading of 0.05 WP. Type 2 physical enhancement, which was called the local effect in their work, was as high as 1.05 DEU at 2 nm away from the gold-filled region.
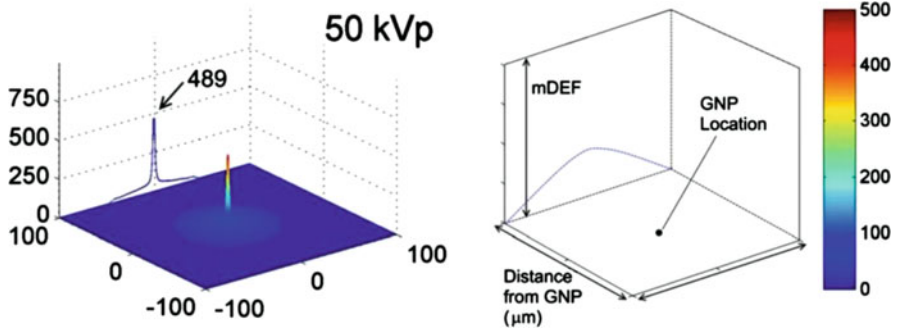
Fig. 2.36 Calculated enhancement of an X-ray irradiated gold-loaded water phantom in brachytherapy configuration—the source of radiation was placed at the center together with the gold-loaded water. A graphical representation is shown based on the calculated enhancement around a gold-loaded region, shown here as GNP, under irradiation of 50 kVp X-rays. The maximum microscopic dose enhancement factor (mDEF) was 489 at the center (i.e., location of the X-ray source). mDEF is the dose enhancement factor that arises from replacing a hypothetical water nanoparticle with a gold nanoparticle or gold-loaded water nanoparticle. (Reprinted with permission from Jones et al. [37]. Copyright (2010) by American Association of Physicists in Medicine.)
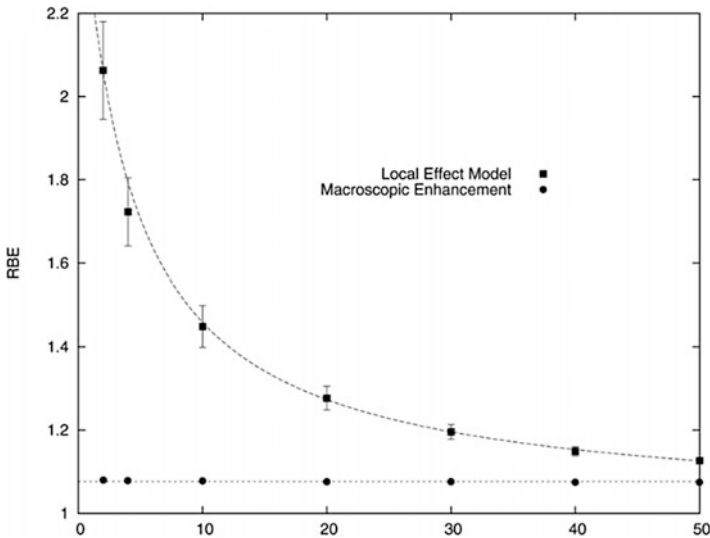
Fig. 2.37 Local effect model (LEM) investigated by McMahon et al. [47], which is similar to type 2 physical enhancement near the surface of a nanoparticle defined in this section (squares). Average dose effect, or type 1 physical enhancement, due to addition of gold nanoparticles is also shown (circles). (Reprinted with permission from Springer Nature Scientific Reports [47] Copyright (2011).)

McMahon et al. [122] theoretically modeled the enhancement of energy deposition by gold nanoparticles decorating mitochondria in the cell under X-ray irradiation. The authors employed the Geant4-DNA package to perform the simulation. Although the authors stated that simulation was performed on an event-by-event basis, this is different from the collision-based approach defined in this chapter. Therefore, no intra-nanoparticle processes were considered. Each mitochondrion was surrounded by 50 40 nm diameter gold nanoparticles. The dimensions of the mitochondrion were 1.8 μm × 1 μm × 0.6 μm. Localized electron emission was shown near the mitochondria. The results suggested that type 1 physical enhancement was minimal; an enhancement of 2–3 DEU was found at several spots within the cell, which was equivalent to type 2 physical enhancement of the same value.

Ngwa et al. [123] defined a nucleus dose enhancement factor (nDEF) and calculated energy deposition in cells with gold nanoparticles under 100 kVp X-ray irradiation. The gold nanoparticles were positioned around cell nucleus, as shown in Fig. 2.20. Simulated enhancement was found to decrease from 9 DEU to 3.5 DEU as the point of energy deposition moves from the surface to 200 nm away from the surface of the gold nanoparticles. The authors attributed the cause of enhancement to Auger electrons emitted from gold nanoparticles, which can explain the spatial profile of the observed enhancement.

Kim et al. [25] proposed a possible intra-nanoparticle collision mechanism that may affect type 2 physical enhancement. However, no theoretical investigations were conducted. A simple estimation of the impact of this mechanism using the cross-sections of electrons interacting with gold and water shown in Fig. 2.7 suggests an upper limit of 3% increase to the amount of energy possessed by low-energy electrons responsible for type 2 physical enhancement. This does not mean the impact of this 3% increase on type 2 physical enhancement is 3% because this amount of energy change is distributed in a very small volume of the type 2 physical enhancement region. Since the amount of energy carried by the low-energy electrons is approximately 15% of the total energy released from gold nanoparticles without considering the collision-induced production of low-energy electrons, a simple estimation suggests that the increase of type 2 physical enhancement is 20% based on the 3% increase to the existing 15% energy carried by low-energy electrons without considering the intra-nanoparticle processes. Further study will be needed to theoretically and experimentally determine this factor.

Several other calculations have shown the location dependency of physical enhancement, which is considered as type 2 physical enhancement. For example, Su et al. [124] showed the calculated enhancement by platinum, gold, and bismuth elements in cellular configurations. They found enhancement contours followed the metal loading profiles closely, with a 100–200 nm resolution, as shown in Fig. 2.38 (left panel). They also found that bismuth generated an enhancement more than twice the enhancement by gold or platinum of the same WP when only Auger electrons were considered. When only photoelectrons were considered, the increase from gold to bismuth was only 28%.

Douglass et al. [125] predicted similar outcomes of 3D energy deposition profiles for gold irradiated with kV or MV photons. Their results are shown in Fig. 2.38 as
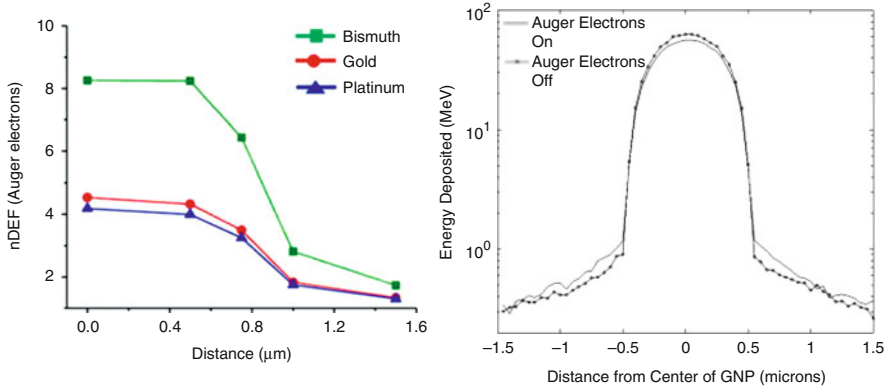
Fig. 2.38 The left panel shows the nucleus dose enhancement factor (nDEF) as a function of distance between the nanoparticles and nucleus due to Auger electrons for nanoparticles of 1.9 nm diameter at a loading of 7 mg/g or 0.7 WP under 50 kVp X-ray irradiation. The nucleus occupies 10 percent of the cell volume in their calculations. (Adopted with permission from Su et al. [124]. Copyright (2012) American Chemical Society.) The right panel displays the results of an energy deposition profile calculated by Douglass et al., showing the absorbed dose due to Auger electrons at many locations. (Reprinted with permission from Douglass et al. [125]. Copyright (2013) by American Association of Physicists in Medicine.)

well (right panel). The vertical axis uses a log scale, and the Auger contribution was relatively large, with more than a 10% increase when Auger electrons were counted. The result was in agreement with several other studies.

Verkhovtsev et al. [57] recently proposed an interesting idea of using fast ions to excite the surface plasmon of gold nanoparticles. The outcome was an increased release of low-energy (1–10 eV) electrons from these gold nanoparticles. Although no experimental data is available, the proposed mechanisms may have impact on type 2 physical enhancement.

Ye and Schuemann et al. [66] reported results of their theoretical study of physical enhancement in a cell coated with gold nanoparticles. They assumed both circular and elliptical two-dimensional cell shapes. The authors also introduced several new definitions such as sensitivity enhancement ratios (SERs) and mean dose enhancement factors (MDEFs) to quantity the enhancement. 150 kVP and 50 keV X-rays and 2, 15, 20, and 50 nm gold nanoparticles at 2 WP were employed in the simulation. It is found that enhancement could be achieved without cellular uptake of nanoparticles, although no direct comparison to nanoparticles in the nuclei was made.

2.4.3.3 Experimental Investigations of Type 2 Physical Enhancement

The first experimental work of measuring type 2 physical enhancement was performed by Guo et al. [12]. They showed that when small, 3 nm gold nanoparticles were conjugated to plasmid DNA through intercalation, the damage was much
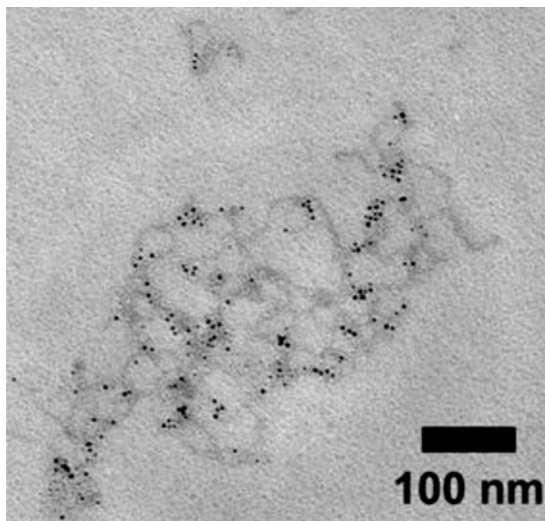
Fig. 2.39 Transmission electron microscopy (TEM) image showing conjugation of 3 nm gold nanoparticles to supercoiled DNA (scDNA). Theoretically predicted type 2 physical enhancement at the surface of the nanoparticles accounted for only 20% of the measured damage of single-strand breaks (SSBs). The origin of enhancement for the other 80% was unidentified. (Reprinted with permission from Guo et al. [12]. Copyright (2007) American Chemical Society.)

higher than without conjugation. Figure 2.39 shows the evidence of gold nanoparticle conjugation to DNA. The TEM image revealed that gold nanoparticles were all adjacent to the DNA strands. The results, which are given in Fig. 3.12, showed that enhancements were as high as 2.0 DEU, which were measured in the presence of tris (hydroxymethyl)aminomethane (Tris) scavengers to reduce the contribution from water which appears in the denominator of enhancement calculation. Enhancement was 0.4 DEU without Tris. Theoretical estimations predicted a type 2 physical enhancement of 0.4 DEU with Tris, which was only 20% of the measured value. It is possible that chemical enhancement such as those discussed in Chap. 3 also existed as the surface of gold nanoparticles could facilitate the migration of radicals from the damaged bases to phosphodiester bond sites and cause bond breaking, i.e., DNA backbone cleavage.

Currell et al. [128] reported results of their study of energy-dependent damage of nuclear DNA in MDA-MB-231 cells. 1.5 Gy of monochromatic X-rays from synchrotron radiation were used. Uptake imaging measurements showed that 1.9 nm gold nanoparticles used in the study mainly localized near the nuclear membranes. The measured enhancement was between 0.1 and 1.0 DEU and was energy dependent. The authors attributed the measured enhancement to the local effect model (LEM), which was similar to type 2 physical enhancement. The authors also discussed differences between types 1 and 2 physical enhancement and suggested that magnitudes of their equivalent type 2 physical enhancement, or the biophysical model as the authors called it, were much closer to the measured
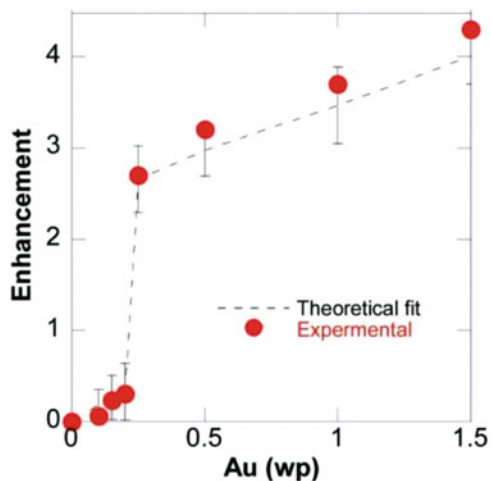
Fig. 2.40 Experimental results of total enhancement (red dots) as a function of concentration of gold nanoparticles. The enhancement units are DEU. Except for the jump around 0.25 WP, enhancement increased at a slope of 1 DEU WP^{-1}, which was caused by type 1 physical enhancement. The jump at 0.25 WP was believed to be caused by type 2 physical enhancement. (Adapted with permission from Guo et al. [14]. Copyright (2016) American Chemical Society.)

enhancement values at different X-ray energies. These results suggested that LEM or type 2 physical enhancement was the cause for the measured nuclear DNA damage.

To date, exclusive type 2 physical enhancement was only measured by Guo et al. [14]. The authors created a nanoscale acceptor that they claimed could dynamically bind to 100 nm diameter PEGylated gold nanoparticles. Each calcium phosphate liposome nanoscale acceptor was filled with water to form water nanoparticles, which were considered as energy acceptors. They are called acceptors because they can receive energy deposited by electrons emitted from nearby gold nanoparticles under X-ray irradiation. Some of the deposited energy in acceptors produced hydroxyl radicals, which reacted with probe molecules, sulforhodamine B (SRB), stored in the nanoscale acceptors. These reactions damaged SRB and reduced fluorescence from SRB. The acceptor is shown in Fig. 6.9. Figure 2.40 shows their experimental results. The enhancement of damage to SRB followed a slope of 1 DEU WP^{-1} of gold in water, which is close to the calculated type 1 physical enhancement as shown above. The total enhancement experienced a sudden jump at around a loading of 0.2 WP gold in water. The magnitude of the jump was slightly greater than 2.0 DEU. This jump was attributed to energy deposited in the acceptor by electrons emitted from a single gold nanoparticle donor next to the acceptor. The whole process can also be considered as energy transfer from X-ray absorbing gold nanoparticle donors to acceptors, a process described in the following section as X-ray-induced energy transfer (XIET).

2.4.3.4   XIET and Other Concepts

As noted above, large gold nanoparticles can generate significant type 2 physical enhancement immediately beyond their surface. The enhancement can be readily measured if the probe molecules or nanostructure acceptors are placed near or on the surface of nanoparticles. Under X-ray irradiation, absorbed X-ray energy by gold nanoparticles is transferred to the molecules or acceptors. We call the X-ray absorbing gold nanoparticles donors because they emit electrons that eventually deposit energy elsewhere, as if they donate energy. Nanostructures that detect the energy deposited by electrons emitted from donors are therefore called acceptors.

Type 2 physical enhancement dictates that the energy transfer from donors to acceptors should decay rapidly as the distance between the two increases. This was observed by Guo et al. [14]. The process was called X-ray-induced energy transfer (XIET, pronounced "excite") between donors and acceptors. Because the process is particle (i.e., electron) based, the absolute transfer efficiency is low. In the optical wavelength region, a similar process, Förster resonance energy transfer (FRET), exists, and its efficiency can be as high as 100%. Figure 2.41 illustrates the XIET process. Figure 2.17 shows the distance dependency results, and for the configuration shown in Fig. 2.41, the energy transfer efficiency decreases exponentially as a function of distance between the donor and acceptor.

The acceptors used by Guo et al. [14] were calcium phosphate-enclosed liposomes (CaPELs) filled with aqueous solutions of sulforhodamine B (SRB) dye molecules. As electrons emitted from gold nanoparticle donors traversed into
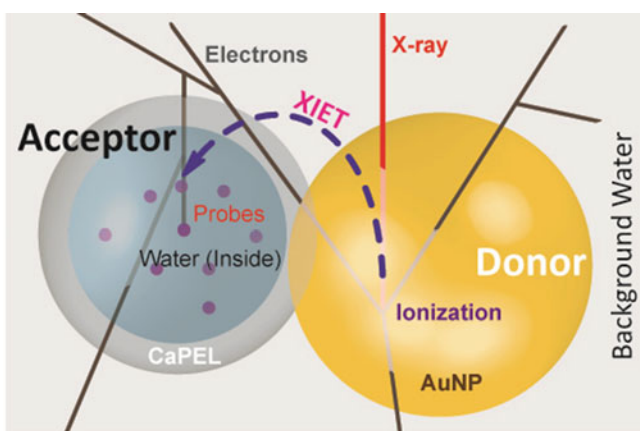
Fig. 2.41 Illustration of the XIET process. Electrons emitted from a gold nanoparticle (shown here) as well as from X-rays interacting with water (not shown) deposited energy in a nanoscale acceptor made of calcium phosphate-enclosed liposome (CaPEL) which contained probing fluorescent molecules dissolved in water. The fluorescent molecules react with hydroxyl radicals produced in water inside CaPEL, resulting in reduction of fluorescence. XIET efficiency was then determined by the amount of fluorescence reduction. (Reprinted with permission from Guo et al. [14]. Copyright (2016) American Chemical Society.)

CaPELs and deposited energy in the enclosed water, hydroxyl radicals were produced, which reacted with SRB and rendered them less fluorescent. The magnitude of fluorescence decrease was used to determine the enhancement by the gold nanoparticle donors. The enhancement was then used to gauge XIET efficiency. The experimental results were close to those predicted by theory, despite the fact that Bethe formula was used to predict the efficiency of XIET. Therefore, intra-nanoparticle collisions may not play an important role in this work. However, this does not necessarily hold true for all cases. When smaller acceptors are directly placed on the surface of nanoparticles, the electron transport effect within donor nanoparticles may be more important.

The main difference between type 2 physical enhancement and XIET is the choice of the shape of the targeted volume. As explained by Guo et al. [14], type 2 physical enhancement uses a generic volume of interest such as a thin spherical shell directly surrounding spherical nanoparticle donors. On the other hand, the shape of the volume of interest in XIET is that of the acceptor next to the donor.

Many parameters can affect the efficiency of XIET, with one such parameter being distance. Figure 2.17 shows XIET as a function of distance. The exponential decay distance constant was 20 nm. Detailed mechanisms were explained by Guo et al. [83]. XIET efficiency is dependent on the energy of X-rays as well, and there should be two peaks in the efficiency profile between 10 and 100 keV, at around 15 keV and 85 keV, because type 2 physical enhancement depends on relatively low-energy electrons emitted from nanoparticles under X-ray irradiation. When the X-ray energy is just a few keV above the K or L edges, the enhancement is strong.

2.4.4 Type 3 Physical Enhancement

As shown in Sect. 2.3, the addition of high-Z nanomaterials into a sample can increase X-ray absorption by the sample, leading to increased energy deposition by X-rays and production of reactive oxygen species in the sample. X-rays can also be converted into UV-Vis photons if scintillation nanomaterials are present. If pure water is used as the base of enhancement, then the magnitude of enhancement can be extraordinarily high because little UV-Vis light is produced when pure water is irradiated with X-rays. This form of enhancement has not been formally described in the enhancement mechanisms given in this chapter, or in the literature of X-ray nanochemistry, despite the discussion of X-ray scintillation in numerous reports.

We call X-ray-induced scintillation type 3 physical enhancement for two reasons. The first is that the production of UV-Vis photons is a physical process. The second reason can be best understood from three perspectives. Firstly, excitation of scintillators or fluorophores in the added nanomaterials is created by electrons produced from either X-ray absorption by the nanomaterials before these electrons escape from the nanomaterials or Compton scattering of X-rays by the medium such as water. This is different from types 1 and 2 physical enhancement, which relies on electrons released from the nanomaterials. Figure 2.25 illustrates the differences

among three types of enhancement from this perspective. Secondly, the enhanced species in type 3 physical enhancement are photons, not electrons as in the other two types. These photons generate a constant enhancement similar to type 1 physical enhancement unless processes such as FRET are used to localize the enhancement. Thirdly, the enhancement values could be significantly different from the other two types because little scintillation is produced from X-ray absorption by pure water. Therefore, new ways are needed to represent this new type of physical enhancement.

The third type is formally named and described in this chapter for the first time, although work in this area has been conducted by many groups under the term scintillation or X-ray excited optical luminescence (XOEL). Identification of this third type of enhancement may lead to the development of other types or processes of enhancement that can be used to further increase the overall enhancement.

It is worth pointing out that an enhancement mechanism may only be called type 3 physical enhancement if there is enhanced generation of UV-Vis photons from the X-ray or electron-absorbing nanomaterials. If nanomaterials are non-fluorescent, but there is enhancement from increased production of UV-Vis photons emitted from fluorophores conjugated to or near X-ray or electron-absorbing nanomaterials, then the enhancement belongs to type 1 or type 2 physical enhancement. For example, Du and Wang et al. [129] showed a gold nanoparticle-enhanced photodynamic system in which enhanced generation of singlet oxygen was detected. This work should belong to type 1 or 2 physical enhancement because gold nanoparticles do not emit UV-Vis photons under X-ray irradiation. However, if small, fluorescent gold nanoparticles are used, then the enhancement detected may be called type 3 physical enhancement.

2.4.4.1 Two Ways to Measure and Calculate Type 3 Physical Enhancement

Type 3 physical enhancement is clearly dependent on the scintillating properties of nanomaterials. For instance, rare earth nanoparticles can effectively absorb X-rays and emit UV-Vis photons and are a suitable nanomaterial for generating type 3 physical enhancement. Some nanomaterials only weakly absorb X-rays but instead can interact with Compton electrons or other charged particles produced in water under X-ray irradiation to generate UV-Vis light and therefore can also effectively generate type 3 physical enhancement. In many cases, UV-Vis photons emitted from nanomaterials can generate singlet oxygen or other reactive oxygen species in aqueous solutions. If singlet oxygen probes are used to detect singlet oxygen, then type 3 physical enhancement can also be detected. UV-Vis photons and singlet oxygen are hence at least the two species with which type 3 physical enhancement can be determined.

The method of detecting UV-Vis light emitted from nanomaterials under X-ray irradiation to determine type 3 physical enhancement seems straightforward. The enhancement obtained using the ratio of the amount of UV-Vis light generated with nanomaterials to that without nanomaterials, however, could be inconveniently high

because there is little UV-Vis light produced in pure water without the nanomaterials. Therefore, instead of comparing to the light produced from pure water under X-ray irradiation, it is more convenient to assess enhancement by measuring the absolute X-ray to UV photon conversion efficiency. There is no need to compare the amount of light to that emitted from pure water under X-ray irradiation because the latter is zero or nearly zero. This eliminates the need to measure UV-Vis light without nanomaterials. The absolute quantum efficiency measurements were shown by Guo et al. [130]. In this work, X-ray to UV-Vis light energy conversion efficiency was used to gauge the enhancement. This method is not subjected to interference from other enhancements.

The other way to quantify type 3 physical enhancement is to measure the enhancement of production of reactive oxygen species such as singlet oxygen. When this method is used, the denominator of the enhancement calculation equation is the amount of reactive oxygen species generated in pure water, which is not zero. Precautions have to be taken because the reactions used for the production of singlet oxygen may be subjected to chemical enhancement or scavenging by nanomaterials. To date, most scintillators have not been known to be effective catalysts for producing or destroying singlet oxygen. However, chemical reactions used to probe singlet oxygen such as singlet oxygen sensor green (SOSG) may interact with gold nanoparticles to generate unpredicted results.

2.4.4.2 Experimental Measurements of Type 3 Physical Enhancement

Many experiments have been devoted to studying X-ray-induced scintillation or type 3 physical enhancement as it is called in this book, although elsewhere they are often under the designation of photodynamic therapy, scintillation, or X-ray excited optical luminescence (XEOL). For instance, Chen et al. [131] described a method of using X-rays to drive photodynamic therapy for cancer treatment. They called the X-ray-absorbing, light-emitting nanoparticles coated with photodynamic therapy conjugates "self-lighting photodynamic therapy." The authors did not perform in vitro or in vivo work, although they considered the nanoparticles selected in their work "in vivo luminescent nanoparticles." Another nanomaterial the authors employed was 15 nm diameter $LaF_3:Ce^{3+}$ nanoparticles, and the luminescence spectrum had a peak at 350 nm. 20 nm diameter $BaFBr:Eu^{2+}/Mn^{2+}$ nanoparticles were another material that supported type 3 physical enhancement. The material exhibited persistent luminescence up to a few minutes after X-ray irradiation. Although no direct enhancement results were obtained, the concept and important experimental components were demonstrated in this report. This type of enhancement is related to XEOL, which can be studied with time-resolved techniques. For example, Föhlisch et al. [132] demonstrated an optical X-ray cross-correlator with femtosecond resolution that can be used to study XEOL processes.

Chen et al. [133] reported their finding of using $LaF_3:Tb^{3+}$ conjugated with meso-tetra(4-carboxyphenyl)porphine to produce luminescence and singlet oxygen under X-ray irradiation. The authors observed enhanced singlet oxygen generation with

both components, suggesting that nanoparticles or conjugates may transfer energy to each other to enhance singlet oxygen generation. In the future, these techniques may be used to interrogate X-ray excited fluorescence in nanomaterials.

Capala et al. [134] estimated the yield of singlet oxygen as a result of irradiating LuI_3 and LaF_3 scintillators with X-rays. The authors adopted a daily fractionation dose of 2 Gy for a total dose of 50–70 Gy. They used a conversion formula to calculate the yield of singlet oxygen under irradiation of 20, 200, and 2000 keV X-rays from brachytherapy sources. The authors concluded that the X-ray energy should not exceed 300 keV for efficient and clinically relevant production of singlet oxygen for use in cancer treatment. The mechanisms of singlet oxygen production were believed to be mediated by UV-Vis photons emitted from rare earth nanoparticles and not from electrons emitted from nanoparticles interacting with water or other species.

Withers et al. [135] showed an enhancement of 0.55 DEU with a 0.012 WP loading of cerium-doped lanthanum fluoride nanocrystals in water. The nanocrystals were 10–12 nm in diameter and 4–6 nm in thickness. The photons were γ-rays from ^{137}CS, and Fricke dosimetry was used as the measurement platform. The authors suggested that the enhancement was caused by hydroxyl and hydroperoxyl radicals detected by the Fenton dosimeter. The radicals were generated by UV light emitted from the nanocrystrals, according to the authors. These values gave rise to a unit WP enhancement of 4.6 DEU WP^{-1}. If it is type 1 physical enhancement from 0.1 WP $Ce:LaF_3$ at 662 keV, then enhancement should be below 0.01 DEU. Therefore, the observed enhancement should be caused by type 3 physical enhancement, i.e., by the increased fluorescence of the nanocrystals under X-ray irradiation.

Barnett et al. [136] detected light emitted from quantum dots made of CdTe and ZnO upon absorption of keV X-rays to quantify the energy transferred from X-rays to light. They considered these quantum dots as X-ray sensors. Their results showed the response of CdTe quantum dots had better linearity than ZnO with respect to the X-ray photon energy, hence providing guidance to using these nanomaterials for generating type 3 physical enhancement.

Vo-Dinh et al. [137] studied cell killing by nanoscintillators under X-ray irradiation. They used yttrium oxide nanoscintillators for X-ray absorption and subsequent scintillation near 370–400 nm, which was used to excite psoralen molecules for singlet oxygen generation. Spectral overlap between the scintillation and psoralen absorption below 375 nm was not extensive. In addition, the authors conjugated TAT ligands onto the surface of Y_2O_3 nanoscintillators. Figure 2.42 shows the overall synthetic approach (left panel) as well as the enhancement results (right panel) using cell number density measurements. The gray diamonds represent the results with X-rays and the black squares without X-rays. Nearly 20% additional cell destruction was measured at 100 ppm incubation concentration under X-ray irradiation. Uptake data was unavailable.

Rare earth nanoparticles such hafnium oxide nanoscale crystallites have been used by *Nanobiotix Inc.* to augment radiotherapeutic treatment of cancer cells and tumors. The hafnium oxide nanoparticles developed by *Nanobiotix Inc.* were called NBTXR3. *Nanobiotix Inc.* conducted clinical trials in the United States, and their
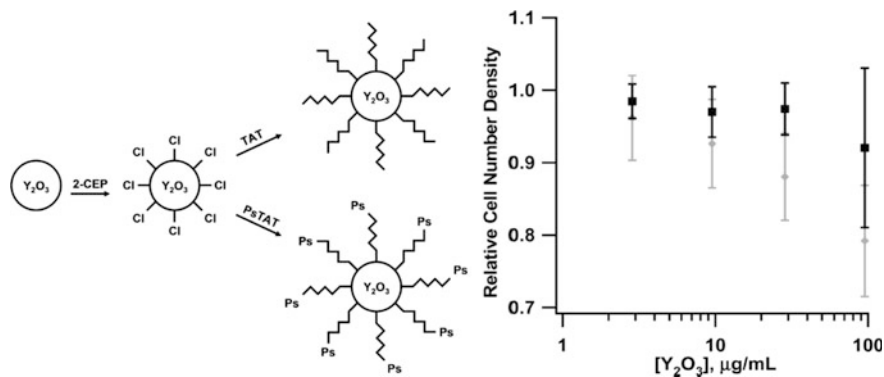
Fig. 2.42 Results by Vo-Dinh et al. using a nanoscintillator-based singlet oxygen generator for cell destruction. The left panel shows the molecular construction of the complex used in the study, and the right panel shows the results of the density of cells survived after treated with TAT-Y_2O_3 or PsTAT-Y_2O_3 nanoparticle composites with X-rays (gray diamonds) and without X-rays (black squares). (Reprinted with permission from Vo Dinh et al. [137]. Copyright (2011) American Chemical Society.)

results were encouraging. The latest results published in 2016 showed that 71% of the 22 patients treated with NBTXR3 experienced tumor shrinkage, while 22% of the patients experienced tumor size increase. The clinical results are discussed in Chap. 9. However, it is unclear whether the enhancement was caused by electrons or scintillation light emitted from hafnium nanoparticles. In publications by Maggiorella et al. [138] and Marill et al. [139], it was found that hafnium nanoparticles were localized at the surface of endosomes in high-concentrations, a configuration that should support a strong type 2 physical enhancement. However, the possibility of scintillation cannot be ruled out, even though hafnium oxide is not known for its superior scintillation properties among rare earth oxide nanoparticles.

Yang et al. [140] demonstrated a method of using lanthanide nanoparticles as scintillators for X-ray photodynamic therapy. The nanoparticle size was approximately 40 nm in diameter and was covered with a layer of silica. Rose bengal was coated onto the surface of the silica layer. Upon X-ray excitation, LaF_3:Tb nanoparticles emitted 543 nm light that was absorbed by rose bengal through FRET, as claimed by the authors. Emission at 585 nm by rose bengal generated singlet oxygen, which was considered as the active species to destruct cancer cells. Figure 2.43 shows the results, with the arrows in the figure indicating the decrease of emission from the scintillator and increase of subsequent emission from rose bengal through FRET.

Guo et al. [130] measured the absolute quantum conversion efficiency from X-rays to UV-Vis photons using inexpensive, compact, and flexible thin-film photovoltaic devices. Such measurements helped determine the performance of nanoscintillators without interference from other chemical reactions that could be catalytically modified. The nanomaterials were europium-doped gadolinium oxide

Fig. 2.43 X-ray- and light-induced photoluminescence in Tb-doped LaF$_3$ nanoparticle-rose bengal (RB) composites. RB was excited for singlet oxygen generation. The top panel shows fluorescence spectra with different amounts of RB in the conjugates. Emission at 543 nm from Tb was reduced as emission at 585 nm from RB increased. The lower panel shows the absorption spectrum of RB (black line, right axis) and the photoluminescence spectra from UV (red line, left axis) and X-ray (blue line, left axis) excitation. (Adapted in part from Yang et al. [140] with permission from the Royal Society of Chemistry.)
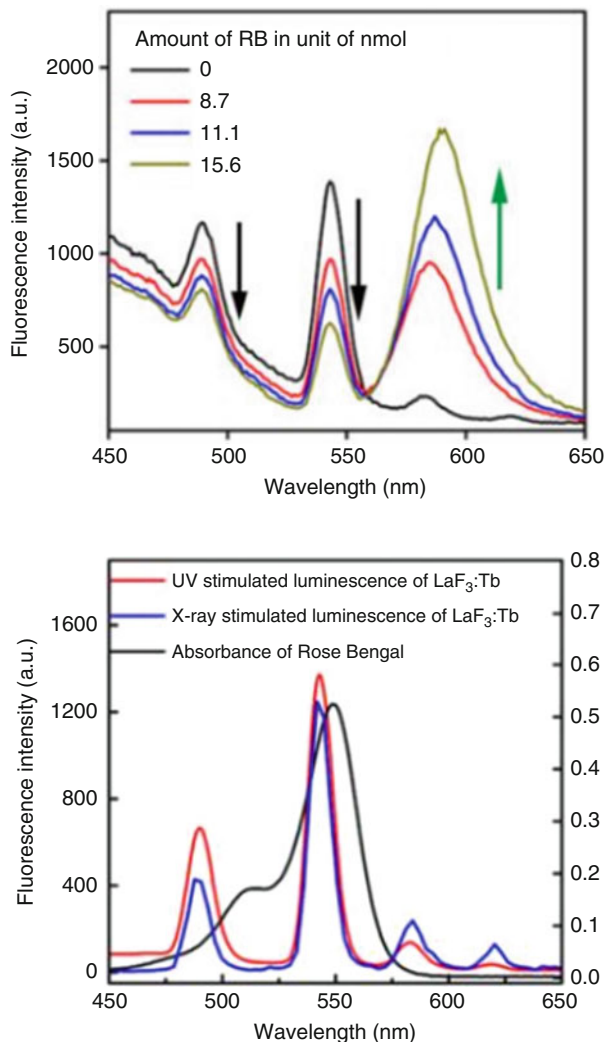
(Eu^{3+}:Gd$_2$O$_3$) nanoparticles. Figure 2.44 (left panel) shows their experimental setup. Using this homemade apparatus, the authors determined the absolute quantum yield of the X-ray nanoscintillator, which was 6% for the nanoscintillator (right panel).

Réfrégiers et al. [141] studied lanthanide micelles to produce singlet oxygen for X-ray-induced radiophotodynamic therapy, which the authors called RPDT. The lanthanide in the form of ions was chelated to C12 ligands to form micelles. The authors then measured production of singlet oxygen. Their results suggested a tenfold increase in the production of singlet oxygen compared to unirradiated rare earth micelles at a loading of 20 μM rare earth micelles.
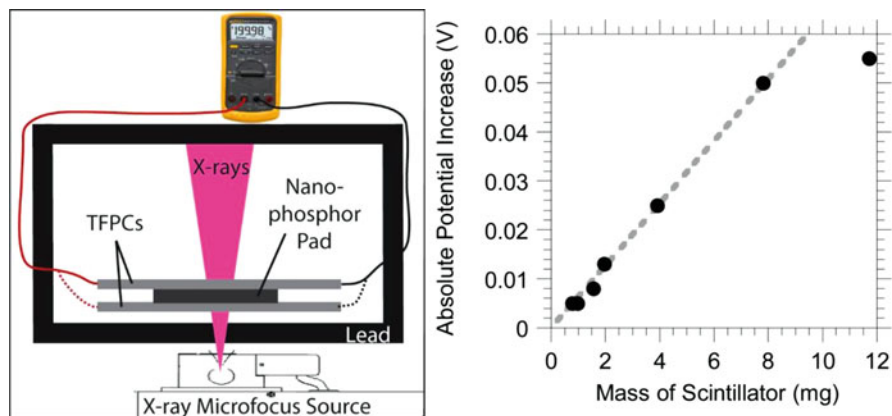
Fig. 2.44   X-ray-induced fluorescence in Eu^{3+}-doped Gd_2O_3 nanoparticles measured with thin-film photovoltaic cells (TFPCs). The left panel shows the apparatus in which a microfocus X-ray device was used to excite the nanoscintillator sandwiched between two TFPCs. A multimeter was used to measure the voltage generated from light emitted from the scintillators and absorption by TFPCs. The right panel shows the voltage response. (Adapted with permission from Guo et al. [130]. Copyright (2014) American Chemical Society.)

Kirakci and Lang et al. [142] reported a new molybdenum cluster-based nanoscintillator suitable for X-ray excitation. The emission from the molybdenum clusters in aqueous solutions was at 690 nm, which was quenched when singlet oxygen was generated. The authors also embedded the clusters in polystyrene films, which acted as an energy transfer matrix for converting X-rays into radioluminescence.

Cai et al. [30] reviewed recent developments in several areas including enhanced photodynamic therapy using scintillation processes. Sixteen scintillators were mentioned for cancer therapy. To date, the optimal scintillation processes are still not well-defined, and the overall mechanisms become even more complicated with the addition of energy transfer from scintillator to photodynamic agents. Moreover, scintillation after X-ray irradiation also occurs, as demonstrated by Chen et al. [143] in their work on ZnS:Cu,Co nanoparticles, to which photosensitizers tetrabromorhodamine-123 molecules were attached.

2.4.5   Combination of Three Types of Physical Enhancement

It is foreseeable that both types 1 and 2 physical enhancement can be combined with type 3 physical enhancement. The process is similar to those discussed in Chap. 5 in which different enhancements are combined. Likewise, XIET can also be used with type 3 physical enhancement. These possibilities make it more attractive to separate physical enhancement into types so that they can be optimized separately and then combined for maximal total effects.

Type 3 physical enhancement offers a unique way to convert X-ray energy into UV-Vis photon energy because photons behave differently than electrons. This connects X-ray nanochemistry to photocatalysis, photodynamic therapy, and photochemistry. It is important to point out that only the production of UV-Vis photons is emphasized in this type of enhancement. The production of singlet oxygen or other species is often used to detect type 3 physical enhancement. However, as stated above, those reactions may be modified by chemical processes such as catalysis. Detection of UV-Vis photons are not subjected to such potential interference.

2.4.6   Exceptions

Several principles different from the ones described here were developed. These new principles did not rely on deriving enhancements from creating electrons in X-ray absorbing nanomaterials. For example, results presented by Xu and Zhang et al. [111] seemed to rely on radicals produced in solutions rather than by the added selenium compounds. In their study, the diselenium bond could be broken by radicals produced in solutions. Subsequent disintegration of the polymer nanoparticles connected together by diselenium bonds resulted in the release of drugs upon X-ray irradiation. This enhancement of drug release efficiency is different from what has been discussed in this chapter. Another work that is different from what has been discussed in this chapter was presented by Pradhan et al. [85] in which highly ionized gold atoms were used. Such ionization is difficult to achieve using any currently available ionization methods. If indeed such ionic state could be achieved, then the solution itself would have been so severely modified that it would be nearly impossible to measure the enhancement. Tseng et al. [144] presented an interesting case of using gold nanoparticles to increase hydrogel polymerization induced by X-ray irradiation. X-rays were successfully used to induce hydrogel formation with gold nanoparticles, and when 20 mM of bare gold nanoparticles 15–20 nm in diameter was used, the time needed for complete polymerization was reduced by 66%, thereby creating a threefold increase or 2.0 DEU enhancement. However, the exact mechanisms responsible for the observed enhancement were unclear because both type 1 and 2 physical enhancements and possibly chemical enhancement described in Chap. 3 could cause the observed enhancement. Future work is needed to study these processes.

2.5   Conclusions and Future Work

Three types of physical enhancement are described in the chapter. The first two rely on the electrons released from nanomaterials upon absorption of X-rays, and the third is dependent on the UV-Vis photons emitted from nanomaterials. Physical principles behind these enhancements are briefly discussed, and theoretical and

experimental works for each type are presented. It is shown that a majority of the works reported in the literature detects the sum of accumulated types 1 and 2 physical enhancement, and its magnitude is approximately 1.0 DEU WP^{-1} for gold nanomaterials in water. In contrast, type 2 physical enhancement can produce higher magnitudes of enhancement from a single nanostructure. The peak values of the enhancement ranges from 9 to 39 DEU from a single 40 nm to 600 nm radius gold nanoparticle. Type 3 physical enhancement, which depends on the emission of UV-Vis light from nanomaterials, can be measured in at least two ways. The first is through X-ray to UV-Vis conversion efficiency, and the second is by measuring the yield of singlet oxygen or other reactive oxygen species.

Physical enhancement is the best understood process among all enhancement mechanisms. This understanding and the division into three types make it possible to use nanomaterials and analytical methods to isolate these enhancement types and then use the optimized nanomaterials and experimental conditions to support the combination of these isolated enhancements to generate the highest total enhancement. Chapter 5 highlights three ways to combine these types and categories of enhancement. Another interesting area in the near future is the combination of several processes to maximize singlet oxygen generation. Currently it is possible to use types 1 and 2 physical enhancement to further increase type 3 physical enhancement. It is also possible to include other enhancements such as chemical enhancement so that UV-Vis scintillation photons and electrons can better excite the photosensitizers through photocatalysis or photochemistry.

There are still unsettled issues amidst these exciting developments. For example, researchers have studied physical enhancement using biological systems such as cells and animals. There are many ways to increase damage to biological targets by X-ray irradiation, and physical enhancement is only one of them. Even though almost all the publications have cited physical enhancement as the main cause for their observed enhancements, this assumption is to a large extent inaccurate. Readers can refer to Chaps. 3 and 9 to review possible explanations for the measured enhancements. These explanations should include at least chemical and biological enhancement.

The motivations behind trying to find true origins of the measured enhancements under various conditions are to discover intrinsic natural processes that occur only in the synthetic and assembled nanomaterial world and to achieve the highest total enhancement. Unless each step and its mechanism are understood, the full potential of using nanomaterials to increase the effectiveness of X-ray irradiation will be difficult to reach. To accomplish these goals, the most critical task is to improve nanochemistry and synthesize the best nanomaterials to create the highest total enhancement. It is also important to design proper analytical methods to measure enhancement. Chapters 6 and 7 list the information currently available on nanomaterials and their synthesis as well as the methods and instruments currently used to study enhancement. In the future, time-resolved X-ray measurements will be of great assistance to shed light on the transient nature of the enhancement mechanisms.

A specific physical tool to measure enhancement is X-ray photoelectron spectroscopy, which is the most direct measurement to assess the yield of electrons released from nanomaterials under X-ray irradiation. Results from such work can help benchmark theoretical simulations. DNA in vacuum could also be an ideal target to measure enhancement, and more advanced and yet simpler methods in these directions are being pursued. As shown in Chap. 10, catalytic reactions may also be used to probe enhancement.

Theory is urgently needed to help understand and differentiate different categories or types of enhancement. Theoretical understanding may also help expand the number of types of physical enhancement or even categories of enhancement. To date, only electrons released from nanomaterials are utilized in theoretical study of physical enhancement. Future theories may include chemical catalysis and even biological pathways. These understandings will be needed before all these enhancement mechanisms can be understood.

In summary, many aspects of physical enhancement have been discovered and studied, and many more need to be explored and investigated. In the next 5–10 years, we may see the maturity of this area of research. Once the highest physical enhancement is reached with desired nanomaterials following newly established principles, future work will focus on how to integrate the optimized physical enhancement with other categories of enhancement.

References

1. Castillo, M. H., Button, T. M., Doerr, R., Homs, M. I., Pruett, C. W., & Pearce, J. I. (1988). Effects of radiotherapy on mandibular reconstruction plates. *American Journal of Surgery, 156*, 261–263.
2. Regulla, D. F., Hieber, L. B., & Seidenbusch, M. (1998). Physical and biological interface dose effects in tissue due to X-ray-induced release of secondary radiation from metallic gold surfaces. *Radiation Research, 150*, 92–100.
3. Regulla, D., Schmid, E., Friedland, W., Panzer, W., Heinzmann, U., & Harder, D. (2002). Enhanced values of the RBE and H ratio for cytogenetic effects induced by secondary electrons from an X-irradiated gold surface. *Radiation Research, 158*, 505–515.
4. Herold, D. M., Das, I. J., Stobbe, C. C., Iyer, R. V., & Chapman, J. D. (2000). Gold microspheres: A selective technique for producing biologically effective dose enhancement. *International Journal of Radiation Biology, 76*, 1357–1364.
5. Karnas, S. J., Moiseenko, V. V., Yu, E., Truong, P., & Battista, J. J. (2001). Monte Carlo simulations and measurement of DNA damage from x-ray-triggered Auger cascades in iododeoxyuridine (IUdR). *Radiation and Environmental Biophysics, 40*, 199–206.
6. Hainfeld, J. F., Slatkin, D. N., & Smilowitz, H. M. (2004). The use of gold nanoparticles to enhance radiotherapy in mice. *Physics in Medicine and Biology, 49*, N309–N315.
7. Foley, E., Carter, J., Shan, F., & Guo, T. (2005). Enhanced relaxation of nanoparticle-bound supercoiled DNA in X-ray radiation. *Chemical Communications*, 3192–3194.
8. Guo, T. (2002). Gold metal nanoparticles as high affinity anti-cancer agent for photon activation therapy, Submitted to Cancer Research Coordinating Committee, Jan 2002: UC Davis.
9. Guo, T. (2004). Nanoparticle enhanced X-ray therapy. In *ACS annual meeting*. Philadelphia.

10. Kunzel, R., Okuno, E., Levenhagen, R. S., & Umisedo, N. K. (2013). Evaluation of the X-ray absorption by gold nanoparticles solutions. *Nanotechnology, 203*(5), 865283.

11. Nahar, S. N., Pradhan, A. K., & Lim, S. (2011). K-alpha transition probabilities for platinum and uranium ions for possible X-ray biomedical applications. *Canadian Journal of Physics, 89*, 483–494.

12. Carter, J. D., Cheng, N. N., Qu, Y. Q., Suarez, G. D., & Guo, T. (2007). Nanoscale energy deposition by x-ray absorbing nanostructures. *The Journal of Physical Chemistry. B, 111*, 11622–11625.

13. Lee, C., Cheng, N. N., Davidson, R. A., & Guo, T. (2012). Geometry enhancement of nanoscale energy deposition by x-rays. *Journal of Physical Chemistry C, 116*, 11292–11297.

14. Sharmah, A., Yao, Z., Lu, L., & Guo, T. (2016). X-ray-induced energy transfer between nanomaterials under X-ray irradiation. *Journal of Physical Chemistry C, 120*, 3054–3060.

15. Casta, R., Champeaux, J. P., Moretto-Capelle, P., Sence, M., & Cafarelli, P. (2015). Electron and photon emissions from gold nanoparticles irradiated by X-ray photons. *Journal of Nanoparticle Research, 17*, 3.

16. Incerti, S., Suerfu, B., Xu, J., Ivantchenko, V., Mantero, A., Brown, J. M. C., Bernal, M. A., Francis, Z., Karamitros, M., & Tran, H. N. (2016). Simulation of Auger electron emission from nanometer-size gold targets using the Geant4 Monte Carlo simulation toolkit. *Nuclear Instruments and Methods in Physics Research Section B: Beam Interactions with Materials and Atoms, 372*, 91–101.

17. Gadoue, S. M., Toomeh, D., Zygmanski, P., & Sajo, E. (2017). Angular dose anisotropy around gold nanoparticles exposed to X-rays. *Nanomedicine: Nanotechnology, Biology and Medicine, 13*, 1653–1661.

18. Kabachnik, N. M., & Sazhina, I. P. (1996). Non-dipolar effects in angular distributions of photoinduced Auger electrons. *Journal of Physics B: Atomic, Molecular and Optical Physics, 29*, L515–L519.

19. Misawa, M., & Takahashi, J. (2011). Generation of reactive oxygen species induced by gold nanoparticles under x-ray and UV irradiations. *Nanomedicine: Nanotechnology, Biology and Medicine, 7*, 604–614.

20. Byrne, H. L., Gholami, Y., & Kuncic, Z. (2017). Impact of fluorescence emission from gold atoms on surrounding biological tissue-implications for nanoparticle radio-enhancement. *Physics in Medicine and Biology, 62*, 3097–3110.

21. Joy, D., & Luo, S. (1989). An empirical stopping power relationship for low-energy electrons. *Scanning, 11*, 176–180.

22. Agostinelli, S., Allison, J., Amako, K., Apostolakis, J., Araujo, H., Arce, P., Asai, M., Axen, D., Banerjee, S., Barrand, G., et al. (2003). GEANT4-a simulation toolkit. *Nuclear Instruments and Methods in Physics Research Section A, 506*, 250–303.

23. Pattison, J. E., Hugtenburg, R. P., & Green, S. (2010). Enhancement of natural background gamma-radiation dose around uranium microparticles in the human body. *Journal of the Royal Society Interface, 7*, 603–611.

24. Champeaux, R. C. J. P., Sence, M., Moretto-Capelle, P., & Cafarelli, P. (2015). Comparison between gold nanoparticle and gold plane electron emissions: A way to identify secondary electron emission. *Physics in Medicine and Biology, 60*, 9095–9105.

25. Seo, S. J., Han, S. M., Cho, J. H., Hyodo, K., Zaboronok, A., You, H., Peach, K., Hill, M. A., & Kim, J. K. (2015). Enhanced production of reactive oxygen species by gadolinium oxide nanoparticles under core-inner-shell excitation by proton or monochromatic X-ray irradiation: Implication of the contribution from the interatomic de-excitation-mediated nanoradiator effect to dose enhancement. *Radiation and Environmental Biophysics, 54*, 423–431.

26. You, D., Fukuzawa, H., Sakakibara, Y., Takanashi, T., Ito, Y., Maliyar, G. G., Motomura, K., Nagaya, K., Nishiyama, T., Asa, K., et al. (2017). Charge transfer to ground-state ions produces free electrons. *Nature Communications, 8*, 14277.

27. Alizadeh, E., & Sanche, L. (2012). Absolute measurements of radiation damage in nanometer-thick films. *Radiation Protection Dosimetry, 151*, 591–599.

28. Viefhaus, J., Cvejanovic, S., Langer, B., Lischke, T., Prumper, G., Rolles, D., Golovin, A. V., Grum-Grzhimailo, A. N., Kabachnik, N. M., & Becker, U. (2004). Energy and angular distributions of electrons emitted by direct double Auger decay. *Physical Review Letters, 92*, 083001.

29. Clement, S., Deng, W., Camilleri, E., Wilson, B. C., & Goldys, E. M. (2016). X-ray induced singlet oxygen generation by nanoparticle-photosensitizer conjugates for photodynamic therapy: Determination of singlet oxygen quantum yield. *Scientific Report-UK, 6*, 19954

30. Kamkaew, A., Chen, F., Zhan, Y. H., Majewski, R. L., & Cai, W. B. (2016). Scintillating nanoparticles as energy mediators for enhanced photodynamic therapy. *ACS Nano, 10*, 3918–3935.

31. Hainfeld, J. F., Slatkin, D. N., Focella, T. M., & Smilowitz, H. M. (2006). Gold nanoparticles: A new X-ray contrast agent. *The British Journal of Radiology, 79*, 248–253.

32. Tu, S. J., Yang, P. Y., Hong, J. H., & Lo, C. J. (2013). Quantitative dosimetric assessment for effect of gold nanoparticles as contrast media on radiotherapy planning. *Radiation Physics and Chemistry, 88*, 14–20.

33. Cho, S. H. (2005). Estimation of tumour dose enhancement due to gold nanoparticles during typical radiation treatments: A preliminary Monte Carlo study. *Physics in Medicine and Biology, 50*, N163–N173.

34. Yoshida, T., Tanabe, T., Chen, A., Miyashita, Y., Yoshida, H., Hattori, T., & Sawasaki, T. (2003). Method for the degradation of dibutyl phthalate in water by gamma-ray irradiation. *Journal of Radioanalytical and Nuclear Chemistry, 255*, 265–269.

35. Yoshida, T., Tanabe, T., Okabe, Y., Sawasaki, T., & Chen, A. (2005). Decomposition of carbon dioxide by metals during gamma irradiation. *Radiation Research, 164*, 332–335.

36. Cho, S. H., Jones, B. L., & Krishnan, S. (2009). The dosimetric feasibility of gold nanoparticle-aided radiation therapy (GNRT) via brachytherapy using low-energy gamma−/x-ray sources. *Physics in Medicine and Biology, 54*, 4889–4905.

37. Jones, B. L., Krishnan, S., & Cho, S. H. (2010). Estimation of microscopic dose enhancement factor around gold nanoparticles by Monte Carlo calculations. *Medical Physics, 37*, 3809–3816.

38. Roeske, J. C., Nunez, L., Hoggarth, M., Labay, E., & Weichselbaum, R. R. (2007). Characterization of the theorectical radiation dose enhancement from nanoparticles. *Technology in Cancer Research & Treatment, 6*, 395–401.

39. McMahon, S. J., Mendenhall, M. H., Jain, S., & Currell, F. (2008). Radiotherapy in the presence of contrast agents: A general figure of merit and its application to gold nanoparticles. *Physics in Medicine and Biology, 53*, 5635–5651.

40. Montenegro, M., Nahar, S. N., Pradhan, A. K., Huang, K., & Yu, Y. (2009). Monte Carlo simulations and atomic calculations for Auger processes in biomedical nanotheranostics. *The Journal of Physical Chemistry. A, 113*, 12364–12369.

41. Yusa, N., Jiang, M., Mizuno, K., & Uesaka, M. (2009). Numerical evaluation of the effectiveness of colloidal gold as a contrast agent. *Radiological Physics and Technology, 2*, 33–39.

42. Zhang, S. X., Gao, J. F., Buchholz, T. A., Wang, Z. L., Salehpour, M. R., Drezek, R. A., & Yu, T. K. (2009). Quantifying tumor-selective radiation dose enhancements using gold nanoparticles: A Monte Carlo simulation study. *Biomedical Microdevices, 11*, 925–933.

43. Ouerdane, H., Gervais, B., Zhou, H., Beuve, M., & Renault, J. P. (2010). Radiolysis of water confined in porous silica: A simulation study of the physicochemical yields. *Journal of Physical Chemistry C, 114*, 12667–12674.

44. Gokeri, G., Kocar, C., & Tombakoglu, M. (2010). Monte Carlo simulation of microbeam radiation therapy with an interlaced irradiation geometry and an au contrast agent in a realistic head phantom. *Physics in Medicine and Biology, 55*, 7469–7487.

45. Van den Heuvel, F., Locquet, J. P., & Nuyts, S. (2010). Beam energy considerations for gold nano-particle enhanced radiation treatment. *Physics in Medicine and Biology, 55*, 4509–4520.

46. McMahon, S. J., Hyland, W. B., Muir, M. F., Coulter, J. A., Jain, S., Butterworth, K. T., Schettino, G., Dickson, G. R., Hounsell, A. R., O'Sullivan, J. M., et al. (2011). Nanodosimetric effects of gold nanoparticles in megavoltage radiation therapy. *Radiotherapy and Oncology, 100*, 412–416.

47. McMahon, S. J., Hyland, W. B., Muir, M. F., Coulter, J. A., Jain, S., Butterworth, K. T., Schettino, G., Dickson, G. R., Hounsell, A. R., O'Sullivan, J. M., et al. (2011). Biological consequences of nanoscale energy deposition near irradiated heavy atom nanoparticles. *Scientific Reports-UK, 1*. https://doi.org/10.1038/srep00018.

48. Lechtman, E., Chattopadhyay, N., Cai, Z., Mashouf, S., Reilly, R., & Pignol, J. P. (2011). Implications on clinical scenario of gold nanoparticle radiosensitization in regards to photon energy, nanoparticle size, concentration and location. *Physics in Medicine and Biology, 56*, 4631–4647.

49. Amato, E., Italiano, A., Leotta, S., Pergolizzi, S., & Torrisi, L. (2013). Monte Carlo study of the dose enhancement effect of gold nanoparticles during X-ray therapies and evaluation of the anti-angiogenic effect on tumour capillary vessels. *Journal of X-ray Science and Technology, 21*, 237–247.

50. Mesbahi, A., Jamali, F., & Gharehaghaji, N. (2013). Effect of photon beam energy, gold nanoparticle size and concentration on the dose enhancement in radiation therapy. *BioImpacts: BI, 29-35*(29), 3.

51. Manohar, N., Jones, B. L., & Cho, S. H. (2014). Improving x-ray fluorescence signal for benchtop polychromatic cone-beam x-ray fluorescence computed tomography by incident x-ray spectrum optimization: A Monte Carlo study. *Medical Physics, 41*, 101906

52. Jeynes, J. C. G., Merchant, M. J., Spindler, A., Wera, A. C., & Kirkby, K. J. (2014). Investigation of gold nanoparticle radiosensitization mechanisms using a free radical scavenger and protons of different energies. *Physics in Medicine and Biology, 59*, 6431–6443.

53. Kim, B. H., & Kwon, J. W. (2014). Plasmon-assisted radiolytic energy conversion in aqueous solutions. *Scientific Reports-UK, 4*, 5249.

54. Li, W. B., Müllner, M., Greiter, M. B., Bissardon, C., Xie, W. Z., Schlattl, H., Oeh, U., Li, J. L., & Hoeschen, C. (2014). Monte Carlo simulations of dose enhancement around gold nanoparticles used as X-ray imaging contrast agents and radiosensitizers. In *Medical imaging 2014: Physics of medical imaging; Proc. of SPIE* (Vol. 9033, p. 90331K). California, United States: San Diego.

55. Zhang, D. G., Feygelman, V., Moros, E. G., Latifi, K., & Zhang, G. G. (2014). Monte Carlo study of radiation dose enhancement by gadolinium in megavoltage and high dose rate radiotherapy. *PLoS One, 9*, e109389.

56. Lim, S. N., Pradhan, A. K., Barth, R. F., Nahar, S. N., Nakkula, R. J., Yang, W. L., Palmer, A. M., Turro, C., Weldon, M., Bell, E. H., et al. (2015). Tumoricidal activity of low-energy 160-KV versus 6-MV X-rays against platinum-sensitized F98 glioma cells. *Journal of Radiation Research (Tokyo), 56*, 77–89.

57. Verkhovtsev, A. V., Korol, A. V., & Solov'yov, A. V. (2015). Revealing the mechanism of the low-energy electron yield enhancement from sensitizing nanoparticles. *Physical Review Letters, 114*, 063401.

58. Dou, Y., Guo, Y. Y., Li, X. D., Li, X., Wang, S., Wang, L., Lv, G. X., Zhang, X. N., Wang, H. J., Gong, X. Q., et al. (2016). Size-tuning ionization to optimize gold nanoparticles for simultaneous enhanced ct imaging and radiotherapy. *ACS Nano, 10*, 2536–2548.

59. Zhang, Y., Feng, Y. M., Ming, X., & Deng, J. (2016). Energy modulated photon radiotherapy: A Monte Carlo feasibility study. *BioMed Research International, 2016*, 1–16.

60. Koger, B., & Kirkby, C. (2016). Optimization of photon beam energies in gold nanoparticle enhanced arc radiation therapy using Monte Carlo methods. *Physics in Medicine and Biology, 61*, 8839–8853.

61. Koger, B., & Kirkby, C. (2016). A method for converting dose-to-medium to dose-to-tissue in Monte Carlo studies of gold nanoparticle-enhanced radiotherapy. *Physics in Medicine and Biology, 61*, 2014–2024.

62. Retif, P., Bastogne, T., & Barberi-Heyob, M. (2016). Robustness analysis of a Geant4-GATE simulator for nanoradiosensitizers characterization. *IEEE Transactions on Nanobioscience, 15*, 209–217.

63. Retif, P., Reinhard, A., Paquot, H., Jouan-Hureaux, V., Chateau, A., Sancey, L., Barberi-Heyob, M., Pinel, S., & Bastogne, T. (2016). Monte Carlo simulations guided by imaging to

predict the in vitro ranking of radiosensitizing nanoparticles. *International Journal of Nanomedicine, 11*, 6169–6179.

64. Ferrero, V., Visona, G., Dalmasso, F., Gobbato, A., Cerello, P., Strigari, L., Visentin, S., & Attili, A. (2017). Targeted dose enhancement in radiotherapy for breast cancer using gold nanoparticles, part 1: A radiobiological model study. *Medical Physics, 44*, 1983–1992.

65. Martinov, M. P., & Thomson, R. M. (2017). Heterogeneous multiscale Monte Carlo simulations for gold nanoparticle radiosensitization. *Medical Physics, 44*, 644–653.

66. Sung, W. M., Ye, S. J., McNamara, A. L., McMahon, S. J., Hainfeld, J., Shin, J., Smilowitz, H. M., Paganetti, H., & Schuemann, J. (2017). Dependence of gold nanoparticle radiosensitization on cell geometry. *Nanoscale, 9*, 5843–5853.

67. Oliver, P. A. K., & Thomson, R. M. (2017). A Monte Carlo study of macroscopic and microscopic dose descriptors for kilovoltage cellular dosimetry. *Physics in Medicine and Biology, 62*, 1417–1437.

68. Rogers, D. W. O., Faddegon, B. A., Ding, G. X., Ma, C. M., We, J., & Mackie, T. R. (1995). Beam – A Monte-Carlo code to simulate radiotherapy treatment units. *Medical Physics, 22*, 503–524.

69. Kawrakow, I. (2000). Accurate condensed history Monte Carlo simulation of electron transport. I. EGSnrc, the new EGS4 version. *Medical Physics, 27*, 485–498.

70. Allison, J., Amako, K., Apostolakis, J., Araujo, H., Dubois, P. A., Asai, M., Barrand, G., Capra, R., Chauvie, S., Chytracek, R., et al. (2006). Geant4 developments and applications. *IEEE Transactions on Nuclear Science, 53*, 270–278.

71. Allison, J., Amako, K., Apostolakis, J., Arce, P., Asai, M., Aso, T., Bagli, E., Bagulya, A., Banerjee, S., Barrand, G., et al. (2016). Recent developments in GEANT4. *Nuclear Instruments and Methods in Physics Research Section A, 835*, 186–225.

72. Scholz, M., & Kraft, G. (1996). Track structure and the calculation of biological effects of heavy charged-particles. *Advances in Space Research-Series, 18*, 5–14.

73. Elsässer, T., & Scholz, M. (2007). Cluster effects within the local effect model. *Radiation Research, 167*, 319–329.

74. Armstrong, J., Brown, F. B., Bull, J. S., Casswell, L., Cox, L. J., Dixon, D., Forster, R. A., Goorley, J. T., Hughes, H. G., & Favorite, J. (2017). In C. J. Werner (Ed.), *MNCP user's manual. Code version 6.2; LA-UR-17-29981*. Los Alamos: Los Alamos National Security, LLC.

75. Semenenko, V. A., Turner, J. E., & Borak, T. B. (2003). NOREC, a Monte Carlo code for simulating electron tracks in liquid water. *Radiation and Environmental Biophysics, 42*, 213–217.

76. Paretzke, H. G., Turner, J. E., Hamm, R. N., Ritchie, R. H., & Wright, H. A. (1991). Spatial distributions of inelastic events produced by electrons in gaseous and liquid water. *Radiation Research, 127*, 121–129.

77. Friedland, W., Dingfelder, M., Kundrat, P., & Jacob, P. (2011). Track structures, DNA targets and radiation effects in the biophysical Monte Carlo simulation code PARTRAC. *Mutation Research/Fundamental and Molecular Mechanisms of Mutagenesis, 711*, 28–40.

78. Baro, J., Sempau, J., Fernandezvarea, J. M., & Salvat, F. (1995). Penelope – An algorithm for Monte-Carlo simulation of the penetration and energy-loss of electrons and positrons in matter. *Nuclear Instruments and Methods in Physics Research Section B, 100*, 31–46.

79. Salvat, F., Fernandez-Varea, J. M., & Sempau, J. (2011). *PENELOPE-2011: A code system for Monte Carlo simulation of electron and photon transport*. Nuclear Energy Agency: Barcelona.

80. McNamara, A., Geng, C., Turner, R., Mendez, J. R., Perl, J., Held, K., Faddegon, B., Paganetti, H., & Schuemann, J. (2017). Validation of the radiobiology toolkit TOPAS-nBio in simple DNA geometries. *Physica Medica, 33*, 207–215.

81. Bethe, H., & Ashkin, J. (1953). In E. Segre (Ed.), *Experimental nuclear physics*. New York: Wiley.

82. Ysua, N., Jiang, M., Mizuno, K., & Usesaka, M. (2009). Numerical evaluation of the effectiveness of colloidal gold as a contrast agent. *Radiological Physics and Technology, 2 (1)*, 33–39.

83. Sharmah, A., Mukherjee, S., Yao, Z., Lu, L., & Guo, T. (2016). Concentration-dependent association between weakly attractive nanoparticles in aqueous solutions. *Journal of Physical Chemistry C, 120*, 19830–19836.

84. McMahon, S. J., Paganetti, H., & Prise, K. M. (2016). Optimising element choice for nanoparticle radiosensitisers. *Nanoscale, 8*, 581–589.

85. Pradhan, A. K., Nahar, S. N., Montenegro, M., Yu, Y., Zhang, H. L., Sur, C., Mrozik, M., & Pitzer, R. M. (2009). Resonant X-ray enhancement of the Auger effect in high-Z atoms, molecules, and nanoparticles: Potential biomedical applications. *The Journal of Physical Chemistry. A, 113*, 12356–12363.

86. Lim, S., Montenegro, M., Pradhan, A. K., Nahar, S. N., Chowdhury, E., & Yu, Y. (2013). Broadband and monochromatic X-ray irradiation of platinum: Monte Carlo simulations for dose enhancement factors and resonant theranostics. In M. Long (Ed.), *World congress on medical physics and biomedical engineering* (Vol. 39, pp. 2248–2251). Berlin Heidelberg: Springerlink. Springer-Verlag.

87. Alkhatib, A., Watanabe, Y., & Broadhurst, J. H. (2009). The local enhancement of radiation dose from photons of MeV energies obtained by introducing materials of high atomic number into the treatment region. *Medical Physics, 36*, 3543–3548.

88. Busby, C. (2005). Depleted uranium weapons, metal particles, and radiation dose. *European Journal of Biology Bioelectromagnet, 1*, 82–93.

89. Berbeco, R. I., Ngwa, W., & Makrigiorgos, G. M. (2011). Localized dose enhancement to tumor blood vessel endothelial cells via megavoltage X-rays and targeted gold nanoparticles: New potential for external beam radiotherapy. *International Journal of Radiation Oncology, Biology, Physics, 81*, 270–276.

90. Leung, M. K. K., Chow, J. C. L., Chithrani, B. D., Lee, M. J. G., Oms, B., & Jaffray, D. A. (2011). Irradiation of gold nanoparticles by x-rays: Monte Carlo simulation of dose enhancements and the spatial properties of the secondary electrons production. *Medical Physics, 38*, 624–631.

91. Ngwa, W., Makrigiorgos, G. M., & Berbeco, R. I. (2012). Gold nanoparticle enhancement of stereotactic radiosurgery for neovascular age-related macular degeneration. *Physics in Medicine and Biology, 57*, 6371–6380.

92. Zygmanski, P., Liu, B., Tsiamas, P., Cifter, F., Petersheim, M., Hesser, J., & Sajo, E. (2013). Dependence of Monte Carlo microdosimetric computations on the simulation geometry of gold nanoparticles. *Physics in Medicine and Biology, 58*, 7961–7977.

93. Carter, J. D., Cheng, N. N., Qu, Y. Q., Suarez, G. D., & Guo, T. (2012). Enhanced single strand breaks of supercoiled DNA in a matrix of gold nanotubes under X-ray irradiation. *Journal of Colloid and Interface Science, 378*, 70–76.

94. Zhang, X. J., Xing, J. Z., Chen, J., Ko, L., Amanie, J., Gulavita, S., Pervez, N., Yee, D., Moore, R., & Roa, W. (2008). Enhanced radiation sensitivity in prostate cancer by gold-nanoparticles. *Clinical and Investigative Medicine, 31*, E160–E167.

95. Zheng, Y., Hunting, D. J., Ayotte, P., & Sanche, L. (2008). Role of secondary low-energy electrons in the concomitant chemoradiation therapy of cancer. *Physical Review Letters, 100*, 198101.

96. Zheng, Y., Cloutier, P., Hunting, D. J., & Sanche, L. (2008). Radiosensitization by gold nanoparticles: Comparison of DNA damage induced by low and high-energy electrons. *Journal of Biomedical Nanotechnology, 4*, 469–473.

97. Alizadeh, E., & Sanche, L. (2012). Precursors of solvated electrons in radiobiological physics and chemistry. *Chemical Reviews, 112*, 5578–5602.

98. Brun, E., Sanche, L., & Sicard-Roselli, C. (2009). Parameters governing gold nanoparticle X-ray radiosensitization of DNA in solution. *Colloids and Surfaces B: Biointerfaces, 72*, 128–134.

99. Hebert, E. M., Debouttiere, P. J., Lepage, M., Sanche, L., & Hunting, D. J. (2010). Preferential tumour accumulation of gold nanoparticles, visualised by magnetic resonance imaging: Radiosensitisation studies in vivo and in vitro. *International Journal of Radiation Biology, 86*, 692–700.

100. Latimer, C. L. (2013). *Octaarginine labelled 30 nm gold nanoparticles as agents for enhanced radiotherapy* (Vol. Master of Science). Department of Medical Biophysics; University of Toronto, Toronto, p 81.
101. Zhang, P. P., Qiao, Y., Wang, C. M., Ma, L. Y., & Su, M. (2014). Enhanced radiation therapy with internalized polyelectrolyte modified nanoparticles. *Nanoscale, 6*, 10095–10099.
102. Detappe, A., Tsiamas, P., Ngwa, W., Zygmanski, P., Makrigiorgos, M., & Berbeco, R. (2013). The effect of flattening filter free delivery on endothelial dose enhancement with gold nanoparticles. *Medical Physics, 40*, 031706.
103. Davidson, R. A., & Guo, T. (2014). Average physical enhancement by nanomaterials under X-ray irradiation. *Journal of Physical Chemistry C, 118*, 30221–30228.
104. Cho, S. H. (2005). Estimation of tumor dose enhancement due to gold nanoparticles during typical radiation treatments: A preliminary Monte Carlo study. *Medical Physics, 32*, 2162–2162.
105. Cho, S., Jeong, J. H., Kim, C. H., & Yoon, M. (2010). Monte Carlo simulation study on dose enhancement by gold nanoparticles in brachytherapy. *Journal of the Korean Physical Society, 56*, 1754–1758.
106. McMahon, S. J., Hyland, W. B., Brun, E., Butterworth, K. T., Coulter, J. A., Douki, T., Hirst, D. G., Jain, S., Kavanagh, A. P., Krpetic, Z., et al. (2011). Energy dependence of gold nanoparticle radiosensitization in plasmid DNA. *Journal of Physical Chemistry C, 115*, 20160–20167.
107. Chang, J., Taylor, R. D., Davidson, R. A., Sharmah, A., & Guo, T. (2016). Electron paramagnetic resonance spectroscopy investigation of radical production by gold nanoparticles in aqueous solutions under X-ray irradiation. *The Journal of Physical Chemistry. A, 120*, 2815–2823.
108. Abolfazi, M. K., Mahdavi, S. R., Mahdavi, M., & Gh, A. (2015). Studying effects of gold nanoparticle on dose enhancement in megavoltage radiation. *Journal of Biomedical Physics and Engineering, 5*(4), 185–190.
109. Paudel, N., Shvydka, D., & Parsai, E. I. (2015). Comparative study of experimental enhancement in free radical generation against Monte Carlo modeled enhancement in radiation dose position due to the presence of high Z materials during irradiation of aqueous media. *International Journal of Medical Physics, Clinical Engineering and Radiation Oncology, 4*, 300–307. 300.
110. Kakade, N. R., & Sharma, S. D. (2015). Dose enhancement in gold nanoparticle-aided radiotherapy for the therapeutic photon beams using Monte Carlo technique. *Journal of Cancer Research and Therapeutics, 11*, 94–97.
111. Ma, N., Xu, H. P., An, L. P., Li, J., Sun, Z. W., & Zhang, X. (2011). Radiation-sensitive diselenide block co-polymer micellar aggregates: Toward the combination of radiotherapy and chemotherapy. *Langmuir, 27*, 5874–5878.
112. Cao, W., Zhang, X. L., Miao, X. M., Yang, Z. M., & Xu, H. P. (2013). Gamma-ray-responsive supramolecular hydrogel based on a diselenide-containing polymer and a peptide. *Angewandte Chemie International Edition, 52*, 6233–6237.
113. Zhang, P. P., Qiao, Y., Xia, J. F., Guan, J. J., Ma, L. Y., & Su, M. (2015). Enhanced radiation therapy with multilayer microdisks containing radiosensitizing gold nanoparticles. *ACS Applied Materials & Interfaces, 7*, 4518–4524.
114. Guidelli, E. J., Ramos, A. P., Zaniquelli, M. E. D., Nicolucci, P., & Baffa, O. (2012). Synthesis and characterization of gold/alanine nanocomposites with potential properties for medical application as radiation sensors. *ACS Applied Materials & Interfaces, 4*, 5844–5851.
115. Guidelli, E. J., & Baffa, O. (2014). Influence of photon beam energy on the dose enhancement factor caused by gold and silver nanoparticles: An experimental approach. *Medical Physics, 41* (032101), 1–8.
116. Wolfe, T., Guidelli, E. J., Gomez, J. A., Baffa, O., & Nicolucci, P. (2015). Experimental assessment of gold nanoparticle-mediated dose enhancement in radiation therapy beams using electron spin resonance dosimetry. *Physics in Medicine and Biology, 60*, 4465–4480.

117. Smith, C. L., Ackerly, T., Best, S. P., Gagliardi, F., Kie, K., Little, P. J., McCorkell, G., Sale, C. A., Tsunei, Y., Tominaga, T., et al. (2015). Determination of dose enhancement caused by gold-nanoparticles irradiated with proton, X-rays (kV and MV) and electron beams, using alanine/EPR dosimeters. *Radiation Measurements, 82*, 122–128.

118. Smith, C. L., Best, S. P., Gagliardi, F., Tominaga, T., & Geso, M. (2017). The effects of gold nanoparticles concentrations and beam quality/LET on dose enhancement when irradiated with X-rays and protons using alanine/EPR dosimetry. *Radiation Measurements, 106*, 352–356.

119. Wang, J. G., Hou, Y. J., Lei, W. H., Zhou, Q. X., Li, C., Zhang, B. W., & Wang, X. S. (2012). DNA photocleavage by a cationic BODIPY dye through both singlet oxygen and hydroxyl radical: New insight into the photodynamic mechanism of BODIPYs. *Chemphyschem, 13*, 2739–2747.

120. Youkhana, E., Gagliardi, F., & Geso, M. (2016). Two-dimensional scanning of PRESAGE® dosimetry using UV/VIS spectrophotometry and its potential application in radiotherapy. *Biomedical Physics and Engineering Express, 2*, 045009.

121. Marques, T., Schwarcke, M., Garrido, C., Zucolotto, V., Baffa, O., & Nicolucci, P. (2010). Gel dosimetry analysis of gold nanoparticle application in kilovoltage radiation therapy. *Journal of Physics: Conference Series, 250*, 012084.

122. McMahon, S. J., McNamara, A. L., Schuemann, J., Prise, K. M., & Paganetti, H. (2016). Mitochondria as target for radiosensitization by gold nanoparticles. *Journal of Physics Conference Series, 777*, 012008.

123. Ngwa, W., Makrigiorgos, G. M., & Berbeco, R. I. (2012). Gold nanoparticle-aided brachytherapy with vascular dose painting: Estimation of dose enhancement to the tumor endothelial cell nucleus. *Medical Physics, 39*, 392–398.

124. Hossain, M., & Su, M. (2012). Nanoparticle location and material-dependent dose enhancement in X-ray radiation therapy. *Journal of Physical Chemistry C, 116*, 23047–23052.

125. Douglass, M., Bezak, E., & Penfold, S. (2013). Monte Carlo investigation of the increased radiation deposition due to gold nanoparticles using kilovoltage and megavoltage photons in a 3D randomized cell model. *Medical Physics, 40*(071710), 1–9.

126. Wardlow, N., Polin, C., Villagomez-Bernabe, B., & Currell, F. (2015). A simple model to quantify radiolytic production following electron emission from heavy-atom nanoparticles irradiated in liquid suspensions. *Radiation Research, 184*, 518–532.

127. Zabihzadeh, M., Moshirian, T., Ghorbani, M., Knaup, C., & Behrooz, M. A. (2018). A Monte Carlo study on dose enhancement by homogenous and inhomogeneous distributions of gold nanoparticles in radiotherapy with low energy X-rays. *Journal of Biomedical Physics and Engineering*, *8*(1), I–XVI.

128. McQuaid, H. N., Muir, M. F., Taggart, L. E., McMahon, S. J., Coulter, J. A., Hyland, W. B., Jain, S., Butterworth, K. T., Schettino, G., Prise, K. M., et al. (2016). Imaging and radiation effects of gold nanoparticles in tumour cells. *Scientific Reports-UK, 6*, 19442.

129. Oo, M. K. K., Yang, Y. M., Hu, Y., Gomez, M., Du, H., & Wang, H. J. (2012). Gold nanoparticle-enhanced and size-dependent generation of reactive oxygen species from protoporphyrin IX. *ACS Nano, 6*, 1939–1947.

130. Davidson, R. A., Sugiyama, C., & Guo, T. (2014). Determination of absolute quantum efficiency of X-ray nano phosphors by thin film photovoltaic cells. *Analytical Chemistry, 86*, 10492–10496.

131. Chen, W., & Zhang, J. (2006). Using nanoparticles to enable simultaneous radiation and photodynamic therapies for cancer treatment. *Journal of Nanoscience and Nanotechnology, 6*, 1159–1166.

132. Gahl, C., Azima, A., Beye, M., Deppe, M., Dobrich, K., Hasslinger, U., Hennies, F., Melnikov, A., Nagasono, M., Pietzsch, A., et al. (2008). A femtosecond X-ray/optical cross-correlator. *Nature Photonics, 2*, 165–169.

133. Liu, Y. F., Chen, W., Wang, S. P., & Joly, A. G. (2008). Investigation of water-soluble x-ray luminescence nanoparticles for photodynamic activation. *Applied Physics Letters, 92*, 043901.

134. Morgan, N. Y., Kramer-Marek, G., Smith, P. D., Camphausen, K., & Capala, J. (2009). Nanoscintillator conjugates as photodynamic therapy-based radiosensitizers: Calculation of required physical parameters. *Radiation Research, 171*, 236–244.

135. Withers, N. J., Rivera, A. C., Plumley, J. B., Smolyakov, G. A., Triño, N. D., Sankar, K., Timmins, G. S., Akins, B. A., & Osiński, M. (2009). Scintillating-nanoparticle-induced enhancement of absorbed radiation dose. In T. M. J. M. Osinski & K. Yamanoto (Eds.), *Proceedings of SPIE(Vol. 7189, p. 718917)*. San Jose: SPIE.

136. Gao, X., Kang, Q. S., Yeow, J. T. W., & Barnett, R. (2010). Design and evaluation of quantum dot sensors for making superficial x-ray energy radiation measurements. *Nanotechnology, 21*, 285502.

137. Scaffidi, J. P., Gregas, M. K., Lauly, B., Zhang, Y., & Vo-Dinh, T. (2011). Activity of psoralen-functionalized nanoscintillators against cancer cells upon X-ray excitation. *ACS Nano, 5*, 4679–4687.

138. Maggiorella, L., Barouch, G., Devaux, C., Pottier, A., Deutsch, E., Bourhis, J., Borghi, E., & Levy, L. (2012). Nanoscale radiotherapy with hafnium oxide nanoparticles. *Future Oncology, 8*, 1167–1181.

139. Marill, J., Anesary, N. M., Zhang, P., Vivet, S., Borghi, E., Levy, L., & Pottier, A. (2014). Hafnium oxide nanoparticles: Toward an in vitro predictive biological effect? *Radiation Oncology, 9*, 150.

140. Elmenoufy, A. H., Tang, Y. A., Hu, J., Xu, H. B., & Yang, X. L. (2015). A novel deep photodynamic therapy modality combined with CT imaging established via X-ray stimulated silica-modified lanthanide scintillating nanoparticles. *Chemical Communications, 51*, 12247–12250.

141. Kraščākovā, S., Giuliani, A., Lacerda, S., Pallier, A., Mercere, P., Toth, E., & Refregiers, M. (2015). X-ray-induced radiophotodynamic therapy (RPDT) using lanthanide micelles: Beyond depth limitations. *Nano Research, 8*, 2373–2379.

142. Kirakci, K., Kubat, P., Fejfarova, K., Martincik, J., Nikl, M., & Lang, K. (2016). X-ray inducible luminescence and singlet oxygen sensitization by an octahedral molybdenum cluster compound: A new class of nanoscintillators. *Inorganic Chemistry, 55*, 803–809.

143. Ma, L., Zou, X. J., Bui, B., Chen, W., Song, K. H., & Solberg, T. (2014). X-ray excited ZnS: Cu,co afterglow nanoparticles for photodynamic activation. *Applied Physics Letters, 105*, 013702.

144. Tseng, S.-J., Chien, C.-C., Liao, Z.-X., Chen, H.-H., Kang, Y.-D., Wang, C.-L., Hwu, Y., & Margaritondo, G. (2012). Controlled hydrogel photopolymerization inside live systems by X-ray irradiation. *Soft Matter, 8*(5), 1420–1427.

Chapter 3
Chemical Enhancement

> *Getting a degree and being educated are totally two different things—the first is a transaction and the second a transformation.*

3.1 Introduction

Enhancement of the effectiveness of X-ray irradiation by nanomaterials may come directly from increased absorption of X-rays by nanomaterials. The enhancement can be extended to ionization of atoms, production reactive oxygen species, yield of reactions, destruction cells and tumors, reading/writing with X-rays, emission of light, and charge of batteries. The absorption of X-rays by nanomaterials and subsequent events enable physical enhancement described in Chap. 2. There are at least three types of physical enhancement. As noted in Chap. 2, however, physical enhancement is generally measured with chemical reactions because these reactions are, in many cases, the only way to measure the enhancement in aqueous solutions or in other matrices or media. These probing chemical reactions include, for example, polymerization reactions or hydroxylation reactions that lead to DNA strand breaks. It is conceivable that the probing reactions are influenced by nanomaterials because many nanomaterials are catalysts as well. If indeed these probing or dosimetric reactions are catalyzed, then they cannot fiducially be used to determine the enhancement. When this happens, an increased yield of overall reactions in the presence of nanomaterials does not mean that more electrons or reactive oxygen species are generated; instead, it can also mean one or more steps in the overall reactions are catalyzed by the nanomaterials. In such cases, increased yields of reactions are considered as the result of chemical enhancement of the effectiveness of X-ray irradiation.

3.1.1   Clues of the Existence of Chemical Enhancement

The first clue of the existence of chemical enhancement emerged in 2007 when Guo et al. [1] studied DNA damage by 10–100 ppm loadings of 3 nm gold nanoparticles. In this study, DNA strand break reactions were used to probe the enhancement, and a Monte Carlo method was used to theoretically model the enhancement. As shown in Chap. 2, type 1 physical enhancement should be negligible at such low gold loadings, but peak type 2 physical enhancement was possible because DNA molecules were next to the gold nanoparticles. The simulated type 2 physical enhancement by the authors was 0.4 DEU, which was only 20% of the measured total enhancement of 2.0 DEU (see Fig. 3.12). Taking the concentration of gold nanoparticles in units of weight percent (WP) into consideration, the unit weight percent (WP) enhancement was 800 DEU WP^{-1}, clearly out of reach for type 1 physical enhancement. Further, type 2 physical enhancement could not explain the measured enhancement. In this case, a nonphysical, i.e., chemical, enhancement would be able to account for the 1.6 DEU enhancement if there were no other enhancements than type 2 physical enhancement and chemical enhancement. This type of enhancement is termed type 1 chemical enhancement because we consider this the most frequently occurring chemical enhancement. Additional details on the work are given in Sect. 3.4.1. In another published work, McMahon et al. [2] observed a similar result using monochromatic X-rays irradiating gold nanoparticle-DNA aqueous solutions. Their experimental results, which showed equivalent to an enhancement of 0.3 DEU and a unit WP enhancement of 200 DEU WP^{-1}, could not be explained by physical enhancement either. In both cases, physical (including types 1 and 2) enhancement was low because there were only small amounts of small gold nanoparticles in solutions at the ppm level.

Both reports mentioned above indicated the existence of nonphysical processes that contributed to the measured overall enhancement. Neither reports cited increased production of hydroxyl radicals as the possible explanation, which was claimed by Misawa et al. [3] who measured enhancement with amino-phenyl-fluorescein (APF) and di-hydro-ethidium (DHE) molecules. Based on their measurements, the authors suggested that the enhancement was caused by increased production of reactive oxygen species and particularly superoxide radicals, possibly catalyzed by the surface of gold nanoparticles. They attributed the increased reactivity of gold nanoparticles to physical changes such as increased emission of secondary photons and Auger electrons. If their findings are true, it is possible to invoke a second type of chemical enhancement, which can be called type 2 chemical enhancement. This part is discussed in Sect. 3.4.2.

3.1.2   Introduction of the Concept of Chemical Enhancement

The concept of chemical enhancement was formally introduced for the first time in 2012 by Guo et al. [4] in which a significant increase was noticed in the yield of 7-hydroxycourmarin 3-carboxylic acid (7-OHCCA) formation as a result of hydroxylation of coumarin 3-carboxylic acid (3-CCA) in the presence of small amounts (~10 ppm) of 3–30 nm diameter gold nanoparticles in aqueous solutions under X-ray irradiation. This reaction was developed as a dosimetric reaction by Makrigiorgos et al. [5] and Pin et al. [6]. The amounts of gold used in this work were too small to produce any measurable type 1 physical enhancement, and type 2 physical enhancement was also negligible due to lack of conjugation of 3-CCA on the gold nanoparticles. In addition, the enhancement was dose-rate dependent, which could not be possible if only physical enhancement was present, as physical enhancement should depend on the total dose rather than dose rate. In addition, the measured enhancement required the gold surface and superoxide radicals. Enhancement disappeared completely when the surface of gold nanoparticles was covered with more inert materials such as silica or when superoxide radical was scavenged by chemicals such as superoxide dismutase (SOD). All these results pointed to a nonphysical enhancement process. The study is an example of type 1 chemical enhancement because the suggested mechanism did not involve enhanced production of reactive oxygen species.

Recently the results presented by Guo et al. [4] were confirmed by Sicard-Roselli et al. [7], who detected increased production of 7-OH coumarin and studied how surfactants affected the properties of gold nanoparticles [8]. However, the explanation given by Sicard-Roselli et al. was that the enhancement was caused by increased production of reactive oxygen species, similar to that proposed by Misawa et al. [3]. As increased production of hydroxyl radicals was cited as the cause for enhancement, the results would be considered as type 2 chemical enhancement. These discussions show that it is important to investigate mechanisms to obtain a more conclusive determination of the cause for the observed enhancement.

Another report of chemical enhancement was presented by Guo et al. [9] in which a polymerization reaction was used to probe the enhancement. In this work, aniline monomers coated on the surface of nanoparticles were catalytically converted to polyaniline by the gold surface activated by hydroxyl radicals produced in water under X-ray irradiation. The driving force of this enhancement was experimentally determined to be hydroxyl radicals reacting with gold-core, silver-shell structures. The core-shell structure was necessary to minimize spontaneous polymerization by the nanomaterials, which may be caused by incompletely reduced metals or residual metal ions in the nanoparticles. The results shown in this work marked the highest chemical enhancement factor reported to date, which was over 30 DEU. This type of enhancement also belongs to type 1 chemical enhancement in which nanomaterials are believed to be activated by hydroxyl radicals, and this radical-driven catalytic activity is responsible for the measured enhancement. No increased production of hydroxyl radicals was detected.

3.1.3   Other Supporting Evidence for Chemical Enhancement

There are other reports that also suggest the existence of chemical enhancement. For example, Alqathami and Geso et al. [10] studied gold nanoparticle-enhanced X-ray absorption by 50 nm gold nanoparticles in a tissue-equivalent mixture containing polyurethane resin precursors mixed with initiators and leucomalachite green (LMG) dye molecules. The mixture was used to measure dose enhancement using 100 kV and 6 MV X-rays. The authors defined the enhancement as the ratio of slopes of optical density change as a function of X-ray dosage with gold nanoparticles to without gold nanoparticles. In their mixtures, the loading of gold was 0.5 mM or 0.01 WP (0.098 g/1000 g). According to Chap. 2, type 1 physical enhancement from this mass of gold should only be 0.01 DEU, which was far below the measured enhancements 0.77 DEU and 0.1 DEU for 100 kVp and 6 MV X-rays, respectively. Figure 3.1 shows their results. Type 2 physical enhancement should be negligible because the detecting molecules are uniformly distributed in the samples and away from the surface of the gold nanoparticles.

Other evidence of chemical enhancement exists. For instance, methyl radicals were produced when alanine was irradiated with X-rays. Guidelli et al. [11, 12] reported the results of using electron paramagnetic resonance (EPR) spectroscopy to investigate the enhancement. The authors did not employ spin-trapping agents but instead utilized the stable, EPR-active alanine radicals generated by X-rays in the presence of 3 WP of 5 nm gold nanoparticles. Their results showed a complicated response of enhancement as a function of gold nanoparticle concentrations, a response that bore the signature of chemical enhancement, i.e., a fast rise of enhancement at low concentrations and then reaching a plateau at high concentrations. This may be caused by complex reactions involving carbon radicals produced in the presence of small gold nanoparticles. Although it is impossible to rule out physical enhancement at high loadings, the measured enhancements at low loadings (below 0.05 WP) should not be caused by physical enhancement because the WP
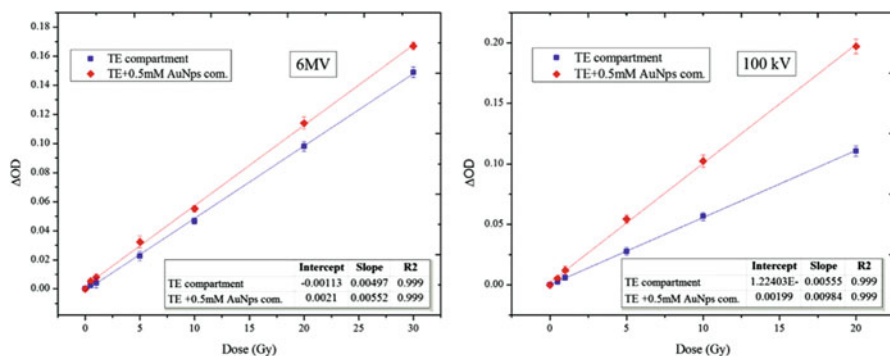
Fig. 3.1 Enhancement of the effectiveness of X-ray irradiation by 50 nm gold nanoparticles irradiated with 6 MV (left panel) and 100 kVp (right panel) X-rays. (Reprinted from Alqathami and Geso et al. [10]. Copyright (2012) with permission from Elsevier.)
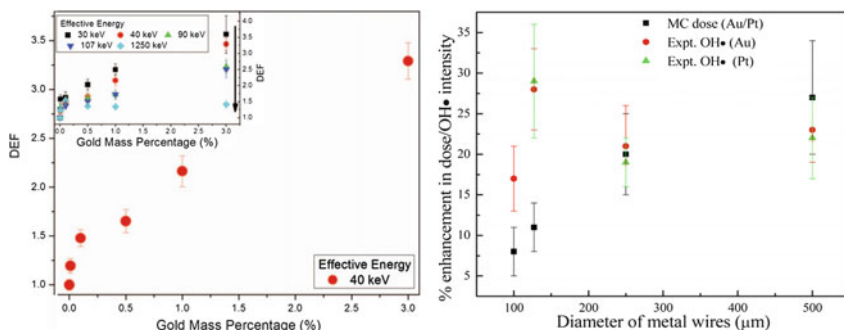
Fig. 3.2 EPR measurements of enhancement. The left panel shows the results obtained with 5 nm gold nanoparticles, whereas the results shown in the right panel were obtained with 125 and 250 nm in dia. wires. Two dashed lines are drawn for guiding purpose in the left panel. (Left panel: reprinted (Fig. 3) with permission from Guidelli et al. [12]. Copyright (2014) by the American Physical Society. Right panel: Paudel et al. [13]. Copyright © by authors and Scientific Research Publishing Inc. CC BY 4.0.)

was too low and probes were uniformly distributed so that types 1 and 2 physical enhancement were both low. Figure 3.2 (left panel) shows their results. Dashed lines are drawn to show two significantly slopes at low and high gold concentrations. The steep slope at low gold concentrations is 29 times the gentle one.

In a similar study, Paudel et al. [13] measured hydroxyl radical generation around a Pt or Au metal wire. EPR spectroscopy and spin trap 5,5-dimethyl-1-pyrroline *N*-oxide (DMPO) were used to detect the hydroxyl radical. A Monte Carlo method was used to simulate the enhancement. The experimental results showed a 25% increase of hydroxyl radical production using 125 μm Au or Pt wires, whereas Monte Carlo calculations predicted an increase around 10%. For 250 μm wires, the two results agreed. These results suggest that the enhancement observed for a 125 μm wire was possibly caused by chemical enhancement. Figure 3.2 (right panel) shows their results. If these explanations are true, then the slopes for chemical enhancement are generally much higher than physical enhancement for the same gold nanoparticles.

3.1.4 A Special Kind of Chemical Enhancement: Anti-Enhancement

Another kind of chemical enhancement is anti-enhancement, which as defined, is the reduction of the effectiveness of X-ray irradiation when nanomaterials are added. Many nanomaterials cause anti-enhancement. For example, gold nanoparticles coated with various ligands were known to be anti-oxidants through the work of Esumi et al. [14] and Liu et al. [15]. Anti-enhancement is considered as a kind of type 2 chemical enhancement because it affects the production of reactive

oxygen species. The enhancement by certain nanomaterials could be higher if it is not for the negative influence from anti-enhancement associated with these nanoparticles. This further demonstrates the need for isolation of every category and type of enhancement because when anti-enhancement is unidentified and embedded in the commonly reported enhancements, elimination of it could further increase the total enhancement. Several reports on anti-enhancement are discussed in Sect. 3.4.

All these reports point to the existence of chemical enhancement, which differs from physical enhancement in the sense that chemical enhancement does not need enhanced absorption of X-rays by nanomaterials. Since physical enhancement is commonly measured with chemical reactions, chemical enhancement can potentially exist in all physical enhancement measurements. This also creates a problem, which is that the measured enhancement cannot be easily assigned to physical or chemical enhancement due to the presence of both enhancements. For instance, it is perceivable that chemical enhancement is stronger in more complex reactions because each step in a complex reaction can be catalyzed. In contrast, simpler reactions are more likely governed by only physical enhancement. For example, EPR measurements using simpler spin trap reactions may not be subjected to chemical enhancement unless complex radical generation or interconversion reactions are used. The latter can happen when no spin traps are used, and an example was the response detected by Guidelli et al. who showed a nonlinear response with respect to gold nanoparticle concentration (Fig. 3.2). When trapping agents are used, reaction pathways may be significantly simplified, which can be used to detect physical enhancement. An example was shown by Guo et al. [16] who measured type 1 physical enhancement using 5-tert-butoxycarbonyl-5-methyl-1-pyrroline N-oxide (BMPO) spin traps and 70 nm gold nanoparticles to avoid chemical enhancement. Chemical enhancement may still exists, however, when small gold nanoparticles with large surface areas are used.

Applications of chemical enhancement reported in the literature to date are limited. As shown in Chap. 4, biological enhancement may be connected to chemical enhancement. In Chaps. 8 and 9, it can be seen that many results cannot be explained by physical enhancement. Therefore, even though chemical enhancement is not explicitly mentioned in many of the reports shown in this book, it could have already played an important role in the overall enhancement in those works. Much more effort is needed to conclusively determine the origin and working mechanisms of chemical enhancement. These future studies can help bring chemical enhancement to the forefront of research and applications of X-ray nanochemistry.

In the following, chemical enhancement is defined first. A brief account of principles behind chemical enhancement using catalytic reactions is then given, followed by a full account of chemical enhancement, including discussion of related publications. Chemical enhancement naturally depends on nanomaterials and reactions. Therefore, there can potentially be many types of chemical enhancement even though only a few examples have been demonstrated in the literature and given here. Catalysis is also mentioned in Part IV, Chap. 10 of this book, which discusses applications of X-ray nanochemistry in catalysis. The major difference between

chemical enhancement discussed in this chapter and those in Chap. 10 is that, here, catalysis is discussed to understand fundamental aspects of X-ray nanochemistry and, in Chap. 10, catalysis is discussed as an application of X-ray nanochemistry. Nevertheless, catalytic principles for these two chapters are the same.

3.2   Definition of Chemical Enhancement

3.2.1   Definition of Chemical Enhancement

Chemical enhancement is defined as the enhancement of the effectiveness of X-ray irradiation by catalytic nanomaterials dissolved or embedded in media. Similar to physical enhancement, chemical enhancement can be quantified by the ratio of signal with nanomaterials to without nanomaterials when there are little or no physical or other enhancements. The detected signals are considered equivalent to the amount of chemicals of interest. For instance, fluorescence is the signal if fluorescent molecules are the product of interest. When DNA strand breaks are the product, the detected signal is the amount of fluorescence emitted from dye-stained bands in gel electrophoresis. Many other detection methods exist, and as such, the results of measurements do not recognize or differentiate the mechanisms of enhancement but are only used to calculate the ratio of two signals, with nanomaterials to without nanomaterials. Therefore, unless the goal is to understand the mechanisms, there is little incentive for researchers to isolate any of these enhancements. However, as shown in Chap. 2 and later, categorizing and isolating enhancements may significantly improve our mechanistic understanding of the enhancement and, more importantly, allow a much higher total enhancement to be obtained if different types and categories of enhancement are properly combined.

There are at least two types of chemical enhancement. If the amount of reactive oxygen species remains the same while the signal representing the quantity of the product increases as the result of adding nanomaterials, the enhancement is called type 1 chemical enhancement. This is claimed to be the case of the study conducted by Guo et al. [4] and is equivalent to stating that enhancement occurs at a different reaction stage or step than the production of reactive oxygen species. Enhancement is classified as type 2 chemical enhancement, if reactive oxygen species are produced in greater or less quantities due to the presence of nanoparticles. Type 2 chemical enhancement is claimed to be observed by several groups, including Misawa et al. [3]. However, mechanisms of catalytic production of reactive oxygen species still require scrutiny. The reduction of reactive oxygen species through anti-enhancement, a specific case of type 2 chemical enhancement, has also been observed by many groups.

Another way to differentiate types of chemical enhancement is to identify when enhancement occurs during the measurement. If enhancement occurs after X-ray irradiation, i.e., only using X-ray-generated species but not X-rays themselves, then it is type 1 chemical enhancement. For example, the enhancement is called type

1 chemical enhancement if there is an enhancement when gold nanoparticles are mixed X-ray irradiated water. In this case, radicals produced by X-rays react with probes to form radical intermediates, whose conversion to the product is catalzed by gold nanoparticles in the mixing stage. The enhancement should be type 2 chemical enhancement, if there is no enhancement when the irradiation-then-mixing experiment is performed, and the enhancement only exhibits when the mixture of gold nanoparticles and probes is irradiated.

3.2.2   Differences Between Physical and Chemical Enhancement

In order to properly measure chemical enhancement, it is important to separate chemical enhancement from physical enhancement. There are several ways to differentiate the two enhancements. The first characteristics of chemical enhancement is that it is dependent on X-ray dose rate, especially at low dose rates as demonstrated by Guo et al. [4]. In contrast, physical enhancement does not depend on dose rate. Another characteristic is the dependency of chemical enhancement on X-ray energy. For example, type 1 chemical enhancement needs reactive oxygen species produced in water to drive catalytic reactions occurring at the surface nanomaterials. As a result, type 1 chemical enhancement favors low-energy X-rays because low-energy X-rays can effectively generate more reactive oxygen species in water. On the other hand, physical enhancement relies on the contrast of absorption between nanomaterials and water as shown in Fig. 2.1 (right panel), and its dependency on X-ray energy should follow a different profile than chemical enhancement. A more complete discussion is given in Sect. 3.6.

The magnitude of unit WP enhancement is the third parameter with which one can use to differentiate chemical from physical enhancement. Dose enhancement units (DEU) are the derived units used in this book for measurement of enhancement, as shown in Sect. 1.1.7. For chemical enhancement, it is possible to express enhancement in terms of unit WP enhancement with units of DEU WP^{-1}. The unit WP enhancement for chemical enhancement is often much higher than type 1 physical enhancement because chemical enhancement takes advantage of absorption of X-rays by the surrounding medium, such as water when the WP of nanomaterials is low such as those below 100 ppm and absorption by water dominates. In typical chemical enhancement measurements, the mass of water far exceeds the mass of nanomaterials, and consequently the contribution from X-ray absorption by water is stronger than the contribution of X-ray absorption by nanomaterials. For these reasons, the magnitude of unit WP enhancement is the third parameter with which one can use to differentiate chemical from physical enhancement. An example is shown in Fig. 3.2 (left panel) in which the steeper slope at low gold nanoparticle concentrations would correspond to chemical enhancement and the gentle slope at much higher gold nanoparticle concentrations would correspond to physical enhancement.

Type 2 physical enhancement and chemical enhancement can also be differentiated through nanochemical modifications, such as covering nanoparticles with a thin (<5 nm) layer of inert materials such as oxides, which completely removes chemical enhancement but leaves type 2 physical enhancement largely intact. This is still synthetically challenging due to the demand for very small thicknesses of the oxide layer. An alternative is to embed probes for detecting type 2 physical enhancement inside inert shells and place the shells next to X-ray-absorbing nanoparticles such as gold nanoparticles so that the embedded probes will not be exposed to the gold surface but are still able to accept energy deposition from electrons emitted from gold nanoparticles, as demonstrated by Guo et al. [17]. No chemical enhancement exists inside the shells because the probes are completely isolated from contacting the gold surface.

3.3   Catalysis Behind Chemical Enhancement

Catalytic reactions are critical to X-ray nanochemistry and especially chemical enhancement. For this reason, several types of popular catalytic reactions are briefly reviewed here. The most obvious connection between chemical enhancement and catalysis is heterogeneous catalytic reactions, which are the original driving force behind developing nanomaterials more than half a century ago. Homogeneous catalytic reactions involving coordination chemistry and metalloenzymatic reactions are connected to chemical enhancement as well, but only heterogeneous catalysis is reviewed here. Catalytic reactions involving reactive oxygen species produced in water are discussed as well since many reactive oxygen species are generated in water irradiated with X-rays.

3.3.1   Heterogeneous Catalysis of Nanomaterials Activated by X-Ray-Generated Species

Heterogeneous catalysis using nanomaterials can be traced back to the early twentieth century, and the applied side of heterogeneous catalysis is reviewed in Chap. 10. Only the most relevant fundamental knowledge intimately connected to chemical enhancement is reviewed here. Both intrinsically catalytically active nanomaterials and nanomaterials activated by other species are discussed, both of which require the surface of nanoparticles be catalytically active. Work reviewed here only includes those that have been published in areas closely related to chemical enhancement, as the field of heterogeneous catalysis itself is too broad to review here.

Nanoparticles can be effective catalysts for many reasons, and five of them are mentioned here. First, these nanoparticles have large surface areas per unit mass,

○ Absorbant/Reactant

Gold Atom and Nanoparticles

1   13   55   147
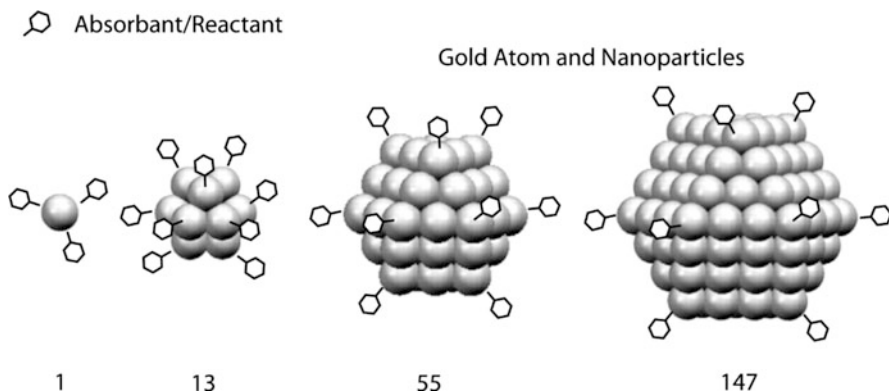
Fig. 3.3 Illustration of the advantage of nanoparticle catalysts. For a homogeneous catalyst of one atom, it has the highest reactant coverage per unit mass, with three phenyl ligands shown here conjugated to the atom. Each atom in homogeneous catalysis is a potentially a catalyst. For the smallest nanoparticles (13 atoms), the percentage of potentially catalytic atoms is still high, with 12 out of 13 atoms capable of hosting reactants to perform catalysis. This ratio decreases drastically as the size of nanoparticles increases, falling below 50% when the nanoparticles are larger than 2–3 nm in diameter. (Nanoparticles are adopted from dx.di.org. (http://sustainable-nano.com/2014/06/10/two-ways-to-make-nanoparticles/))

making catalytic sites easily accessible by reactants and reaction intermediates. Secondly, their surface atoms are less than fully coordinated. The surface atoms of nanoparticles are similar to the central atoms in homogeneous catalysts—both can be highly active by being nucleophilic. Consequently, these surface atoms can potentially interact with reactants and stabilize reaction intermediates, a process that lowers reaction energy barriers. Figure 3.3 illustrates small nanoparticles having a large number of atoms with unsaturated coordination per unit mass. The percentage of surface atoms decreases precipitately as the size increases. Thirdly, alloy nanoparticle catalysts can be used to support a variety of reactions. Yang et al. [18] reviewed this topic. The fourth feature is the possibility of combining the substrate effect with the intrinsic properties of nanoparticles. Bond et al. [19] discussed this feature in detail in their book. The fifth property is the existence of an interface between substrates and nanoparticles. The interface effect unites contributions from two or more types of materials, such as a metal and an oxide. These five catalytic properties can exist separately or in combination, making catalysis an interesting but complex and challenging process.

Table 3.1 shows the five features of catalysis discussed above. To date, only the first two of the five properties mentioned above have been explored within the context of chemical enhancement in X-ray nanochemistry.

One of the earliest catalysts was platinum nanoparticles, a close cousin of gold nanoparticles, which was used to convert CO to CO_2. Results in this area was summarized by Bond et al. [19] in their recent book. Other properties, such as radiolysis of water to produce H_2, were also studied, and the results are reviewed in Chap. 10.

Table 3.1 Five properties of nanomaterial catalysts and their impact on catalysis

Properties	Impact
Surface area per unit mass	Number of catalytic sites per unit mass
Coordination number of surface atoms	Activity of surface atoms
Alloy effect	Multiple elements (electronic structures)
Substrate effect	Electronic structures
Interface effect	Multiple surfaces
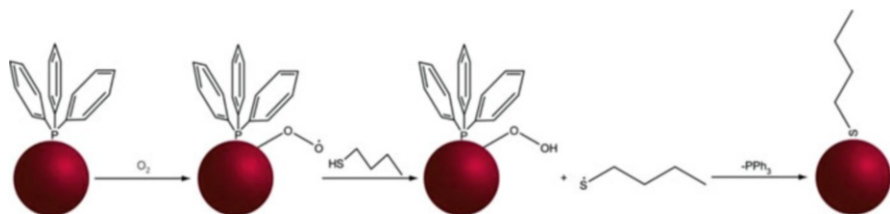
Fig. 3.4 Proposed radical production process on the gold surface by Chechik et al. An oxygen molecule was hypothesized to be adsorbed on the surface of the gold nanoparticle. The adsorbed oxygen then became a superoxide radical that abstracts hydrogen from the thiol in solutions. The unprotected thiol ligand replaced the existing ligand on the gold nanoparticles. (Adapted and redrawn based on the original drawing [20].)

Many of the nanomaterials used in X-ray nanochemistry are catalytically active. For example, gold nanoparticles are known to be catalysts for water oxidation of CO, as shown in Chap. 10. The nanomaterials can also be excited by other species to make them catalytically active. For example, Chechik et al. [20] showed an interesting mechanism through which O_2 can help replace ligands on the surface of gold nanoparticles. The proposed mechanism is shown in Fig. 3.4. In their work, EPR measurements provided experimental evidence for the existence of superoxide radicals, which were detected indirectly using spin trap 5,5-dimethyl-1-pyrroline N-oxide (DMPO). This suggested superoxide radicals could be produced using only molecular oxygen and gold nanoparticles, without X-rays. It is worth pointing out that the superoxide radical shown here is attached to gold nanoparticles. Evidence for their proposed mechanisms came from EPR detection of the butanethiol radical $C_4H_9S\bullet$, suggesting the adducts could not be quenched by gold nanoparticles. The authors did not observe the DMPO adduct of the superoxide radical. In addition, spin adducts of DMPO with tert-BuOO• were detected when *tert*-butyl hydroperoxide was mixed with phosphine protected gold nanoparticles. No radicals were detected without gold nanoparticles or molecules oxygen. DMPO superoxide spin adducts were not detected, which may be caused by other species reacting with superoxide radicals on the gold surface before DMPO could react the radicals and form adducts. No work to date has shown that hydroxyl radicals can be similarly produced without X-rays. Their results might partially explain the increased superoxide radical

production observed by Misawa et al. [3], who also did not observe increased catalytic production of hydroxyl radicals.

In two publications, Cui et al. [21] and Cui et al. [22] showed that gold nanoparticles interacted with H_2O_2 or O_2 to enhance chemiluminescence. Gold nanoparticles of different sizes were used. The authors attributed the enhancement to catalytic properties of relatively large, >25 nm, gold nanoparticles. Figure 3.5 shows their proposed mechanisms in one of their studies, which involved addition of gold-mediated molecular oxygen to luminol to form an intermediate. In another study, H_2O_2 instead of O_2 was used. Both works have implication on chemical enhancement because gold nanoparticle aqueous solutions irradiated with X-rays should be able to catalyze chemiluminescence similar to H_2O_2-mediated chemical reactions because H_2O_2 can be produced by X-ray irradiation of water.

Other studies of catalysis in the presence of gold nanoparticles and molecular oxygen, although lacking use of X-rays, can shed light on reaction mechanisms and provide useful information on catalysis involving X-rays. Lambert et al. [23] investigated catalysis involving molecular oxygen and gold nanoparticles of only 55 atoms. Their results suggested that only gold nanoparticles smaller than 2 nm were catalytically active toward certain reactions. Substrates were involved in the work by Lambert et al., and the exact catalytic mechanisms were complex. Nonetheless, the results showed the impact of size of gold nanoparticles on their catalytic properties (Fig. 3.6).

Ito et al. [24] discussed catalytic production of hydroxyl radicals involving gold nanoparticles. DMSO was used to trap hydroxyl radicals. The authors used chemical methods instead of X-rays to generate reactive oxygen species and claimed that the

Fig. 3.5 Reaction pathway proposed by Cui et al. (Adapted from Cui et al. [22].) The process involved molecular oxygen reacting with luminol in the presence of gold nanoparticles as the catalyst
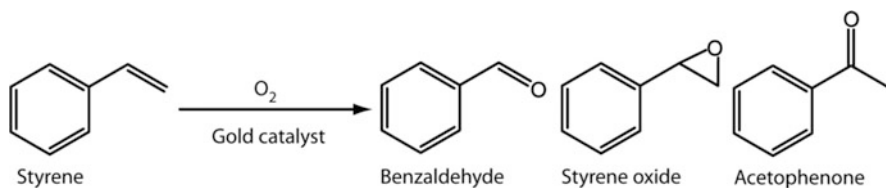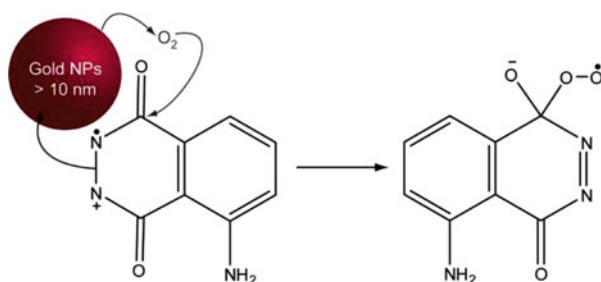
Fig. 3.6 Reaction pathways from styrene to three different products using 55-atom gold nanoparticles and molecular oxygen. (Adapted from http://nanotechweb.org/cws/article/tech/35551)
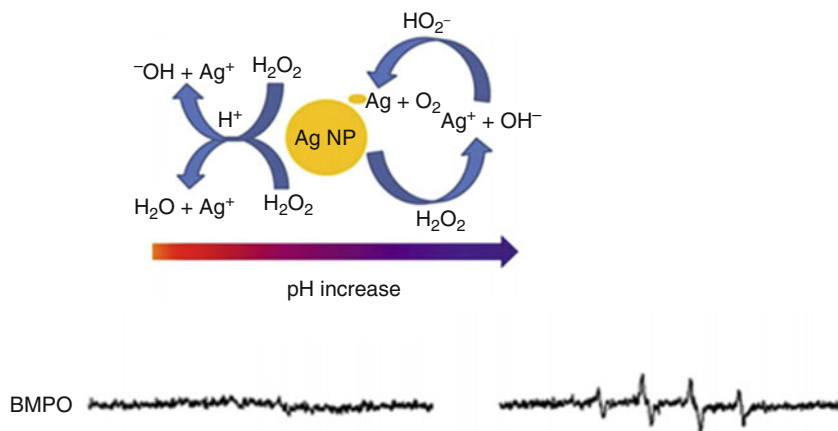
Fig. 3.7 Proposed radical production on the surface of silver nanoparticles (top panel). The bottom panel shows EPR spectra from spin trap BMPO (lower left) alone and the spin adduct (lower right). (Reprinted and adapted from Yin et al. [26]. Copyright (2015) with permission from Elsevier.)

production was enhanced by gold nanoparticles. Cao et al. [25] studied a gold nanoparticle catalytic system in which dismutation of superoxide radicals by nearby copper(II) was enhanced by gold nanoparticles, which was a demonstration of a complex, surface-catalyzed homogeneous-like catalytic reaction. In this example, Cu(II) was the catalytic center, which interacted with O_2. When the copper center was tethered to the surface of gold nanoparticles, which was functionalized with amine to trap O_2 molecules, the authors claimed that the negatively charged gold surface helped improve dismutation through catalysis.

Metallic surfaces can also function as metal ions in homogeneous catalytic reactions such as the Fenton reaction. For example, Yin et al. [26] reported the result of their studies on generation of hydroxyl radicals and hydrogen peroxide in the presence of silver and gold nanoparticles using EPR spectroscopy. Figure 3.7 (top panel) shows the proposed mechanism in which silver was oxidized by H_2O_2 and reduced by OH^-. The plot on the lower right panel shows the EPR profile of the spin adduct BMPO, which indicated the adduct was a hydroxyl radical spin adduct. However, dynamic measurements have to be performed to explain the mechanisms because the superoxide radical adduct may convert to the hydroxyl radical adduct. It is possible that hydroxyl radicals observed elsewhere can also be produced through this pathway since X-ray irradiation of water also produces hydrogen peroxide. Yin and Wu et al. [27] studied catalytic properties of Pd nanostructures using EPR spectroscopy, and similar processes of conversion from H_2O_2 to hydroxyl radicals were proposed based on experimental results.

Oxide nanoparticles under X-ray irradiation can also catalytically produce reactive oxygen species. For example, Kotler and Gonzalez et al. [28] showed that superoxide and hydroxyl radicals were produced when silicon nanoparticles were irradiated with X-rays in cells. In this case, X-rays were supposed to be absorbed by

nanoparticles to produce energetic electrons. It is also possible that silicon nanoparticles were mainly irradiated by Compton electrons produced in water due to silicon's low-Z status. Both X-ray-produced electrons in silicon and Compton electrons could excite the nanoparticles to create electron-hole pairs, which could migrate to the surface of nanoparticles to oxidize water molecules to form hydroxyl radicals and reduce oxygen molecules to create superoxide radicals. These reactions catalyzed by the surface of oxide nanoparticles can therefore support chemical enhancement. Another work performed by Kim et al. [29] invoked a similar reaction pathway through which reactive oxygen species were produced by gadolinium oxide nanoparticles. However, it is unclear whether the production of reactive oxygen species was through catalysis.

The reactants and products presented in the reactions discussed here are similar to those produced in X-ray-irradiated aqueous solutions even though most of the catalytic reactions described here do not directly involve X-ray irradiation. Studying these reactions can therefore help understand chemical enhancement to the effectiveness of X-ray irradiation, which is essentially chemical reactions catalyzed by nanomaterials in solutions or media irradiated with X-rays.

3.3.2 Parameters of Nanomaterials Influencing Heterogeneous Catalysis

Many factors can affect catalysis by nanomaterials. Several of them, including size, shape, composition, and surfactant of nanoparticles, are discussed here.

3.3.2.1 Size and Shape Effect

The size of nanoparticles is the most critical factor for two reasons. First, the size determines the curvature of the surface, which in turn controls the coordination number of surface atoms that give rise to catalytic properties of nanomaterials. The simplest case is bare nanoparticles, and Fig. 3.3 illustrates the importance of size of bare nanoparticles. Another factor derived from size is the surface area per unit mass. More surface atoms per unit mass means higher catalytic activities because it is the surface atoms that perform catalysis. In this regard, homogeneous catalysts have the highest surface area per unit mass. However, heterogeneous catalysis may provide unique advantages such as high densities of sites and multiple, closely positioned sites with unique electronic structures required for certain catalysis.

The shape of nanoparticles can also influence activity, and this influence can be understood as an extension of the size effect. Moreover, differently shaped nanomaterials can support unique reaction pathways and complex local structures at the extremities of these particles. Although the unit mass surface area may be smaller for these shapely nanostructures, their unique structures may support prolonged activity of highly active catalytic sites.

Fig. 3.8 Ligand effects on chemical enhancement. Three ligands are shown here, which may cause the surface of a gold nanoparticle to be negatively or positively charged or to remain charge neutral
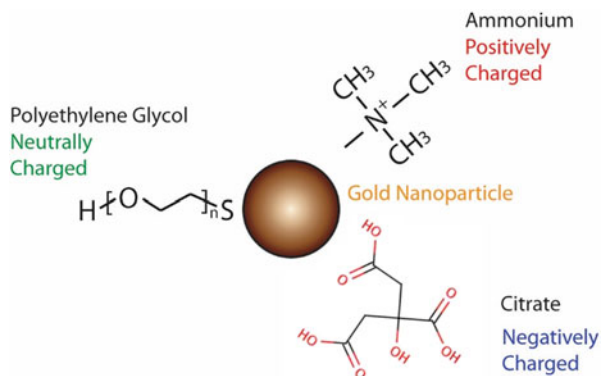
3.3.2.2 Surfactant Effect

Many properties are influenced by surfactants on nanomaterials. For example, surfactants can affect the particle surface charge density, improve solubility of nanoparticles in media, increase cellular uptake of nanomaterials, or enable these nanoparticles to target tumor cells. Surfactants may also impact chemical enhancement because they can scavenge or help produce more reactive oxygen species. As a result, surfactants on nanoparticles exert great influences on catalytic properties, ranging from substantially enhancing, to neither enhancing nor anti-enhancing, to severely anti-enhancing the effectiveness of X-ray irradiation. Figure 3.8 illustrates how surface charge may be changed using three different ligands or surfactants.

3.3.3 X-Ray Radiation-Induced Catalytic Reactions by Metal Nanoparticles

When X-rays irradiate nanomaterials in a medium such as water, reactions may be catalytically promoted because of the involvement of reactive oxygen species (ROS) and nanomaterials. Five commonly encountered ROS exist in large quantities under X-ray irradiation of water: hydroxyl radicals; superoxide radicals; solvated electrons; hydrogen atoms, which are also radicals; and hydrogen peroxide. Hydrogen atoms and solvated electrons are included even though they do not contain oxygen. In addition, singlet oxygen is often considered a powerful ROS. Quantities of ROS vary as a function of time in pulsed radiolysis of water due to different ROS lifetimes. For continuous X-ray irradiation, concentrations of these ROS are constant. Table 11.1 shows the lifetimes and yields of these ROS in units of G values, which are the number of species generated per 100 eV of absorbed energy. If trapping reagents are used, then the integrated or accumulated yields are obtained. For example, hydroxyl radicals have a lifetime between ns and μs, depending on the environment. To probe it, in one method, minimally fluorescent 3-CCA molecules

react with hydroxyl radicals to form highly fluorescent molecules 7-OHCCA, whose fluorescence intensity is measured to reveal the total or accumulated yield of hydroxyl radicals. When a high-enough concentration of 3-CCA is present without any other chemicals including gold nanoparticles, the total amount of hydroxyl radicals can be measured with a high accuracy. A proposed reaction mechanism involving reaction of 3-CCA with hydroxyl radicals to form fluorescent 7-OHCCA is shown in Fig. 3.9. Note that without catalytic nanoparticles, the proposed reactions are not catalytic reactions but involving oxygen. Therefore, this reaction can fiducially measure the dose of X-rays when only 3-CCA is dissolved in water and irradiated with X-rays. In the presence of gold nanoparticles, however, hydroxyl radical production and each step of the proposed reaction shown in Fig. 3.9 or other new pathways can be catalyzed, making it difficult to assign the exact step that is catalyzed. Addition of catalysts such as small gold nanoparticles makes the reaction of 3-CCA to 7-OHCCA conversion unreliable as a dosimetric reaction to quantify the yield of hydroxyl radicals or dose of ionizing radiation.

Many metal nanoparticles are intrinsically catalytically active. Moreover, due to high chemical potentials of ROS produced in water under X-ray irradiation, many nanomaterials and especially metallic nanoparticles can become catalytically or more active toward one or more steps in multiple-step reactions.

Each step of a complex reaction can be catalyzed, so the total product yield may be greater even if quantities of reactants are the same or lower due to scavenging of
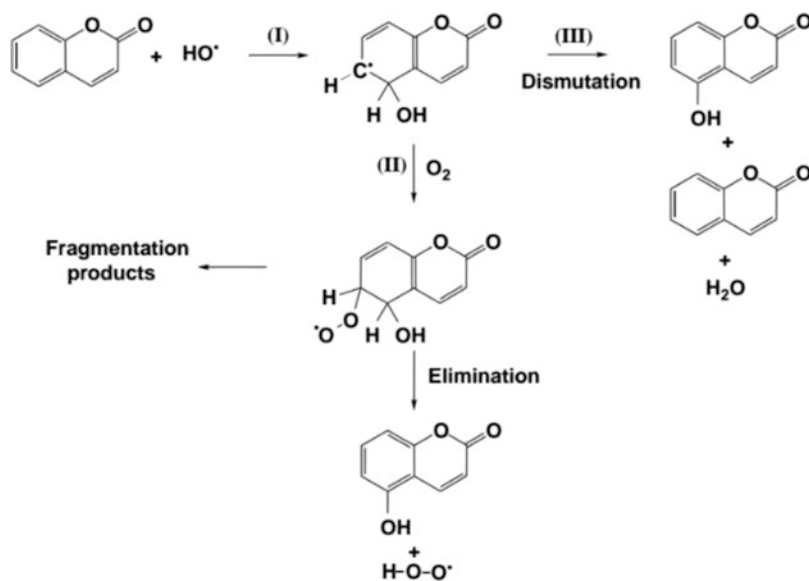
Fig. 3.9 Proposed reaction pathways from 3-CCA to 7-OHCCA involving at least two intermediate reaction steps. Any of these steps can be catalyzed or scavenged by the gold surface, which can be activated by superoxide radicals or other ROS. (Reprinted from Pin et al. [6]. Copyright (2005) with permission from Elsevier.)
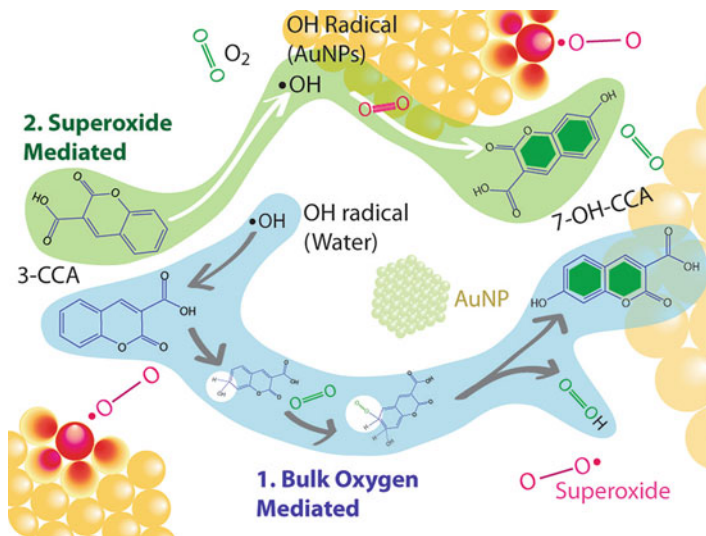
Fig. 3.10 Proposed pathways of chemical enhancement or catalytic reactions on the surface of gold nanoparticles enabled by superoxide radicals. Two possible mechanisms are shown here. The gray arrows show one of them and the white arrows show the other. (Reprinted with permission from Guo et al. [4]. Copyright (2012) American Chemical Society.)

nanoparticles. One such example is illustrated in Fig. 3.10 in which the probe reaction shown in Fig. 3.9 is catalyzed by gold nanoparticles. Guo et al. [4] showed that the second and/or third intermediate step of the multiple-step reaction shown in Fig. 3.9 can be catalyzed by gold nanoparticles and superoxide radicals. Figure 3.10 describes the proposed catalytic mechanism with catalysis occurring at the second step and/or third step of 3-CCA to 7-OHCCA conversion after the initial hydroxylation reaction.

These results indicate that many reactions, including many dosimetric reactions, can be catalyzed by metal nanoparticles, and the catalytic pathways make studying these reactions and properties of gold or other nanoparticle catalysts both challenging and interesting.

3.3.4 Other Factors Important to X-Ray-Driven Heterogeneous Catalysis

In addition to the properties of nanomaterials, X-ray energy and dose rate are the two other parameters that can affect X-ray nanochemical catalysis and hence chemical enhancement.

3.3.4.1   X-Ray Energy Dependency

It is known that absorption of X-rays by nanomaterials and media is highly dependent on X-ray energy. If the medium is water, then for practical concentrations such as less than 1 WP of gold in water, X-rays at low (<20 keV) and high energies (>100 keV) are absorbed more strongly by water than nanomaterials such as gold. This can be derived from data shown in Fig. 2.1 (middle panel). Type 1 chemical enhancement is driven by reactive oxygen species generated in water through Compton scattering of X-rays by water and is not through direct absorption of X-ray by nanomaterials; as a result, X-ray energies outside the optimal nanoparticle absorption region are preferred.

   This means that a complete energy spectrum of X-rays from 10 to 150 keV is ideal for generating both chemical and physical enhancements, with 30–100 keV X-rays absorbed by nanomaterials to generate high physical enhancement and 10–15 keV/100–150 keV X-rays absorbed by water to generate high chemical enhancement. The whole-energy spectrum can generate a maximum total enhancement because the combination of chemical and physical enhancements follows a multiplication algorithm, as demonstrated in Chap. 5.

3.3.4.2   X-Ray Dose-Rate Dependency

Physical enhancement does not depend on dose rate because dose rate does not affect how X-rays are absorbed by nanomaterials, at least using any of the currently available X-ray sources. On the other hand, dose rate affects chemical enhancement as the rates at which ROS are generated may affect how chemical reactions are catalyzed. For instance, if superoxide radicals are involved in a catalytic reaction that can be expressed in the following chemical reaction equations, then enhancement may be dose-rate dependent because three X-ray-generated species, e_{aq}^-, $\bullet O_2^-$, and $\bullet OH$, are now participating in the reactions, rather than just one when no catalysis is involved (i.e., in the absence of nanomaterials).

   Without catalysis, the reactions are

$$RH \text{ (reactant)} + \bullet OH \rightarrow \bullet RH\text{-}OH \text{ (intermediate)} \qquad (3.1)$$

$$\bullet RH\text{-}OH \text{ (intermediate)} + O_2 \rightarrow R\text{-}OH \text{ (product)} + O_2H^- \qquad (3.2)$$
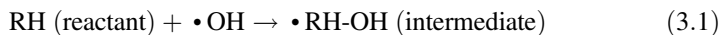
   With catalysis, reactions are more complex. One possible pathway is that •OH production is catalytically increased, as shown in Eq. 3.3.

$$\text{Water} \xrightarrow{Cat, X-ray} \bullet OH + \text{other ROS} \qquad (3.3)$$

   If this is true, then together with Eqs. 3.1 and 3.2, more products are generated. However, there should be no apparent dependency on dose rate under this circumstance.

Yet another pathway is possible, as shown in Eqs. 3.4, 3.5, 3.6, and 3.7. In this case, there is no need to invoke the catalytic hydroxyl radicals (•OH) production pathway shown in Eq. 3.3. The alternative pathway includes the following reaction steps:

$$RH \text{ (reactant)} + \bullet OH \rightarrow \bullet RH\text{-}OH \text{ (intermediate)} \tag{3.4}$$

$$e_{aq}^{-} + O_2 \rightarrow \bullet O_2^{-} \tag{3.5}$$

$$Cat \text{ (nanomaterial)} + \bullet O_2^{-} \rightarrow Cat^{*} \text{(catalytically active nanomaterial)} \tag{3.6}$$

$$\bullet RH\text{-}OH \text{ (intermediate)} + O_2 \overset{Cat*}{\rightarrow} R\text{-}OH \text{ (product)} + O_2H^{-} \tag{3.7}$$
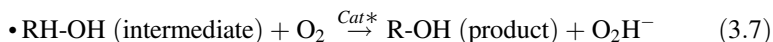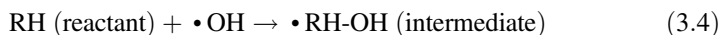
If Eqs. 3.4, 3.5, 3.6, and 3.7 are true, then the overall yield can be higher in the presence of gold nanoparticles even when the amount of hydroxyl radicals is lower due to scavenging of hydroxyl radicals by gold nanoparticles. The increase in the yield is caused by catalysis described by Eqs. 3.4, 3.5, 3.6, and 3.7: As the amount of catalysts (Cat*) depends on the concentration of superoxide radicals ($\bullet O_2^{-}$), which relies on the dose-rate-dependent concentration of solvated electrons, the outcome depends on dose rate. This differs from the scenario without catalysis, which depends only on dose because •OH is only species involved. Reactions 3.4, 3.5, 3.6, and 3.7 represent a specific pathway of reactions, and other pathways are possible. It is important to point out that the dose-rate dependency may weaken or disappear completely at high dose rates as saturation takes place.

In summary, nanoparticles such as gold nanoparticles can catalyze reactions involving X-ray-generated species and radicals. As shown in this chapter, nanoparticles often catalyze far more than the production of reactive oxygen species.

3.4   Types of Chemical Enhancement

As discussed in Chap. 2, enhancement encountered in X-ray nanochemistry is usually measured with chemical reactions in aqueous solutions, and these reactions are strongly influenced by reactive oxygen species and nanomaterials. A few examples are given here. Although only two types of chemical enhancement are considered in this chapter, other types may exist. Chemical enhancement is identified as a fundamental process, which also serves the purpose of simplifying enhancement mechanisms as well as facilitating isolation and optimization of each category and type of enhancement so that these individual enhancements can be combined to produce a much higher total enhancement, as shown in Chap. 5.

Type 1 chemical enhancement catalytically increases reaction yields without interfering with the production of reactive oxygen species, as defined by Eqs. 3.4, 3.5, 3.6, and 3.7. The catalytic property of the nanomaterials may be intrinsic or

activated by reactive oxygen species. In one example, as discovered by Guo et al. [4], gold nanoparticles were activated by superoxide radicals to convert 3-OHCCA radical intermediates into the product of 7-OHCCA. This type of chemical enhancement does not require nanoparticles to absorb X-rays; it only needs nanomaterials to possess catalytic properties to convert intermediates into products, thus resulting in increased reaction yields. This type can be understood as indirect enhancement because it only relies on X-ray-generated and often long-lived intermediates and not nanoparticles directly absorbing X-rays.

Type 2 chemical enhancement can either catalytically increase or scavenge the reactive oxygen species by nanomaterials irradiated with X-rays, as defined by Eq. 3.3. Increased production was observed by Misawa et al. [3] of superoxide radicals and by Sicard-Roselli et al. [7] of hydroxyl radicals. However, the measurements led the authors in these two works to conclude that there were increased production of ROS were similar to those performed by Guo et al., which are mentioned above. Scavenging results were obtained by many groups and can be explained by the scavenging property associated with nanomaterials.

3.4.1   Type 1 Chemical Enhancement

As mentioned above, type 1 chemical enhancement addresses catalytic reactions which do not lead to increased production or scavenging of reactive oxygen species. Chemical reactions usually contain multiple steps, and one or more of these steps may be catalyzed by the surface of nanoparticles that are either intrinsically active or activated by reactive oxygen species produced in water under X-ray irradiation. Nanoparticles in type 1 chemical enhancement do not need to absorb X-rays, especially in the case where added nanoparticles comprise much less than 1 WP of the water medium.

Several reactions supporting type 1 chemical enhancement are described in the following.

3.4.1.1   Hydroxylation Reactions

Hydroxylation reactions have been widely studied. One example is hydroxylation of 3-CCA molecules to form fluorescent 7-OHCCA molecules. This reaction is not a single-step reaction and involves at least two intermediate steps and multiple products, one of which is 7-OHCCA. Another example of hydroxylation reactions is DNA strand breaks, which are complex reactions involving base damage followed by radical migration to the sugar moiety, eventually causing phosphodiester bond breakage or strand breaks.

Hydroxylation Reactions Leading to DNA Strand Breaks

One of the well-studied hydroxylation reactions is DNA strand breakage. Two examples briefly appeared in Chap. 2 are discussed here. One commonly recognized pathway of strand breakage starts at the addition of •OH to the base, such as thymine and cytosine, to form a radical. This pathway is reviewed by Wagner et al. [30]. The beginning of another pathway for DNA strand breaks given in the literature is shown in Fig. 3.11 where an •OH reacts with the base to abstract H from thymine, cytosine, or 5-methylcytosine. The radical initially residing on the base can migrate to the sugar group and eventually move to the phosphodiester linkage to cause the cleavage of one or more P-O bonds and strand breaks. These two pathways share similar subsequent steps of reactions after initial radical reactions.

In the presence of gold nanoparticles, each of the reaction steps described in Fig. 3.11 may be catalyzed. Although not yet investigated in the literature, several possibilities are speculated here. First, the base may be more easily damaged in the presence of gold nanoparticles. Next, transfer from the base radical to the sugar moiety and backbone may be easier in the presence of the gold surface. Lastly, low-energy electrons may enhance backbone cleavage as Sanche et al. suggested, which are shown in Sect. 8.2.2. Though possible, none of these pathways have been experimentally or theoretically observed or studied.

Experimentally, the first evidence of the existence of type 1 chemical enhancement was shown by Guo et al. [1], who measured single-strand break yields of plasmid DNA conjugated to gold nanoparticles caused by X-ray irradiation. The results showed an unexplainable amount of enhancement or strand breaks beyond that supported by physical enhancement. In this study, enhancement only occurred
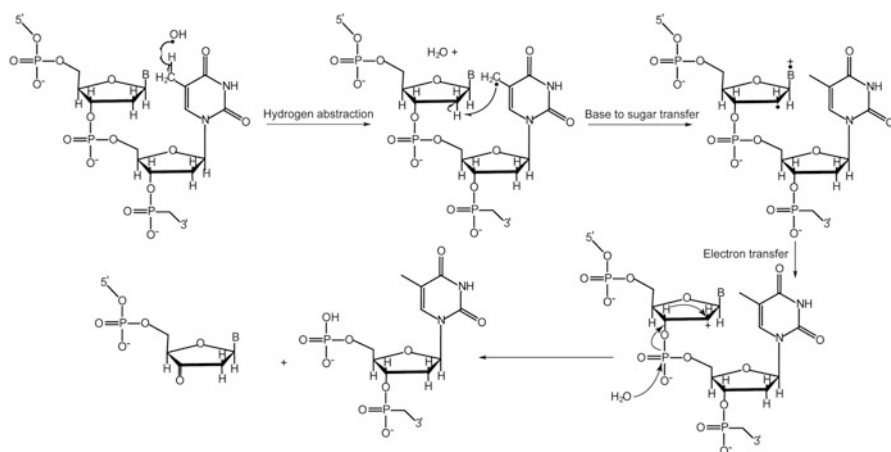
Fig. 3.11 A DNA strand break pathway. Abstraction of hydrogen is initiated through reaction with a hydroxyl radical, followed by migration of the radical to the sugar base and then to the phosphodiester bond, which leads to strand breaks. The proposed DNA strand break pathway is partially based on Fig. 12 in Burrows and Muller [31]
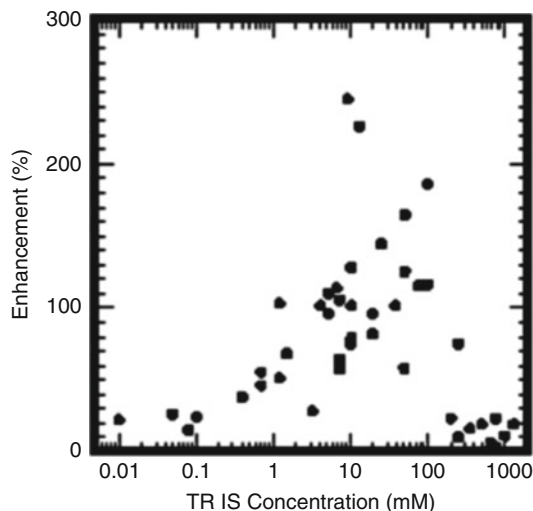
Fig. 3.12 DNA damage in the form of single-strand breaks by gold nanoparticles under X-ray irradiation measured with gel electrophoresis. Enhancement was measured as a function of the concentration of •OH scavenger Tris. Highest enhancement of 2.0 DEU was obtained at 10 mM Tris. (Reprinted with permission from Guo et al. [1]. Copyright (2007) American Chemical Society.)

when gold nanoparticles were conjugated to the plasmid DNA and an approximately 2.0 DEU total enhancement was observed using approximately 10 ppm gold and 10 mM tris(hydroxymethyl)aminomethane (Tris) in water. Figure 3.12 shows the results. Type 1 physical enhancement was negligible because the amount of gold nanoparticles was insignificant. Type 2 physical enhancement was much higher than type 1 physical enhancement due to conjugation of gold nanoparticles to DNA molecules. The measured enhancement was 0.2 DEU without Tris, as shown in Fig. 3.12. The estimated type 2 physical enhancement was only 10% for the 100 nm diffusion distance of hydroxyl radicals in pure water. Enhancement increased as more Tris was added to the samples. At 10 mM Tris, diffusion distances of radicals such as hydroxyl radicals in water were less than 10 nm. According to Fig. 2.34, theoretically predicted type 2 physical enhancement was less than 0.4 DEU at this short diffusion distance, thereby accounting for only 20% of the measured enhancement. Recent evidence provided by work conducted in the Guo lab suggests that similarly small gold nanoparticles mildly scavenged hydroxyl radicals. In the framework of chemical enhancement, this new enhancement belongs to type 1 chemical enhancement.

Figure 3.13 illustrates possible explanations for the experimentally observed Tris-dependent enhancement results shown in Fig. 3.12. Four possible combinations are shown, i.e., with and without Tris and with and without gold nanoparticles. The left two panels are used to calculate enhancement without Tris, and the right two panels are used to calculate enhancement with Tris, showing how the addition of Tris
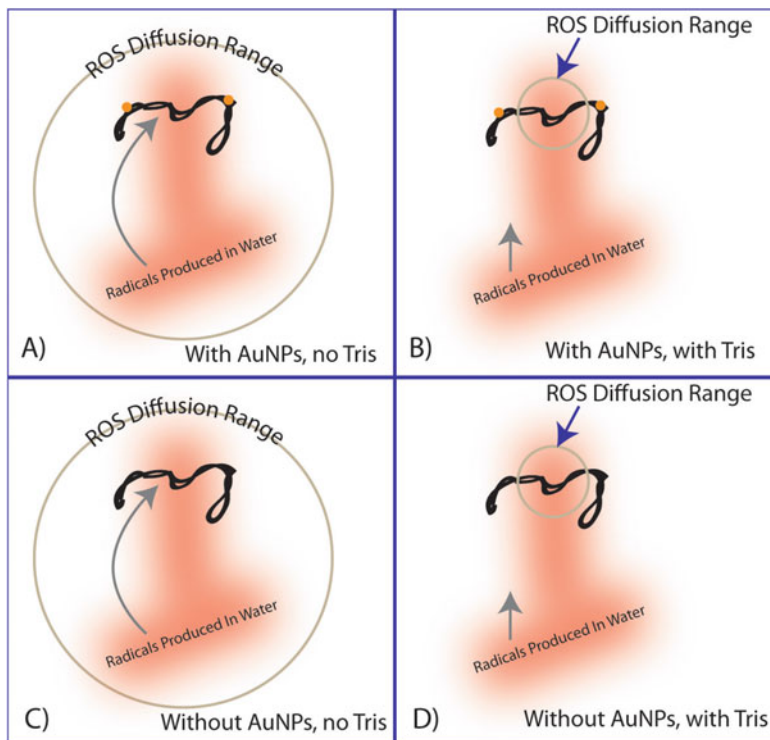
Fig. 3.13 Illustration of how scavengers improve type 1 chemical enhancement. Reactive oxygen species (ROS, as shown by brown-colored streaks) diffusion distance is assumed to be 100 nm (the large circles of the gray line) when there is no Tris (panels A and C) so that ROS produced within a 100 nm radius of the supercoiled DNA (scDNA) can react with and cleavage DNA (black lines). Consequently, the damage of DNA by the amount of water absorbing X-rays is large, so is the denominator in the enhancement calculation equation. As a result, the enhancement is low without Tris. When Tris is added, the diffusion range is reduced to less than 10 nm (the small gray line circles in panels B and D), which reduces the effective volume of water responsible for absorbing X-rays and producing ROS to cleave DNA. Based on this figure, the enhancement without Tris is A/C, which has a large denominator; the enhancement with Tris is B/D, whose denominator is much smaller and the effect of gold nanoparticles (golden dots) is much more prominent

increases the enhancement. Contributions from radicals with gold nanoparticles are shown in panels A and B, and contributions from radicals without gold nanoparticles are shown in panels C and D. The lower enhancement occurs when gold nanoparticles (golden colored dots) are used without Tris, i.e., A versus C. Due to the large diffusion distance of radicals (shown by the gray circles in A and C) in water without Tris, a large, overwhelming amount of radicals produced in water by Compton electrons can react with and cleave DNA strands (black lines). This Compton electron contribution enters the enhancement calculation in the denominator, therefore making the enhancement under this condition low. The contribution of radicals from the gold nanoparticles, which are conjugated to the DNA, is small

compared to the contribution from water because of the use of small gold nanoparticles. Higher enhancement occurs when both Tris and gold nanoparticles are present. This is shown in the right two panels B and D in Fig. 3.13. Most of the radicals produced in water by Compton electrons (brown-colored streaks) cannot reach DNA due to short diffusion distances (10 nm) of radicals in the presence of Tris, as shown by the small gray circles in panels B and D. In this case, Tris reduces the denominator in the enhancement calculation, giving rise to a higher enhancement. Based on these arguments, enhancement should occur near the surface of gold nanoparticles if the measured enhancement becomes higher when Tris is added. Otherwise enhancement should remain the same when Tris is added.

One may argue that it is also possible for small gold nanoparticles to catalyze the production of •OH. Although this is possible, the pathway proposed by Misawa et al. [3] required small gold nanoparticles to absorb X-rays and emit X-ray fluorescence. This is not likely because the probability of these small gold nanoparticles directly absorbing X-rays is only 10^{-4} after irradiation with X-rays of a few Gy. If we assume that every absorption event leads to a strand break, then only 10^{-3} of the supercoiled DNA would be damaged with an average ten gold nanoparticles per supercoiled DNA, which is still far less than the 10–20% of damage observed in the experiments.

McMahon et al. [2] investigated enhancement of damage to plasmid DNA molecules irradiated with monochromatic X-rays using gold nanoparticles. The X-ray energy spanned 11.8–80 keV with an up to 50 Gy total dose. Citrate-coated, 11.9–37.5 nm in diameter gold nanoparticles were used. In their experiments, the loading of gold ranged from one gold nanoparticle per 640 bp to 21,600 bp, corresponding to a gold loading of 0.032 WP to 0.16 WP. For physical enhancement without targeting, the corresponding enhancement would be 0.03–0.16 DEU. Their experimental results, however, showed an enhancement of 0.6–1.4 DEU, equivalent to unit WP enhancement of 20–47 DEU WP^{-1}, and 0.05–0.3 DEU for 0.16 WP loading, corresponding to 0.2–2 DEU WP^{-1}, respectively. Figure 3.14 shows the results. Since gold nanoparticles were not conjugated to DNA, type 2 physical enhancement was not likely the cause of enhancement. The measured enhancement values clearly surpass the enhancement value of 1.4 DEU WP^{-1} predicted for physical enhancement.

It is reasonable to assume that the results obtained by McMahon et al. [2] were similar to what was shown by Guo et al. [1]. If gold nanoparticles under X-ray irradiation did not catalytically produce •OH, then the observed enhancements in both experiments were type 1 chemical enhancement. There was no biological enhancement because no cells were involved, though one may argue that DNA cleavage might partially belong to biochemical (not biological) enhancement. Since there was no conjugation between DNA and gold nanoparticles in McMahon's report, type 2 physical enhancement from their gold nanoparticles should not cause the observed enhancement. Ultimately, it is necessary to directly determine the yield of reactive oxygen species using a method free from chemical enhancement before a specific mechanism can be conclusively attributed to a specific type or category of enhancement.
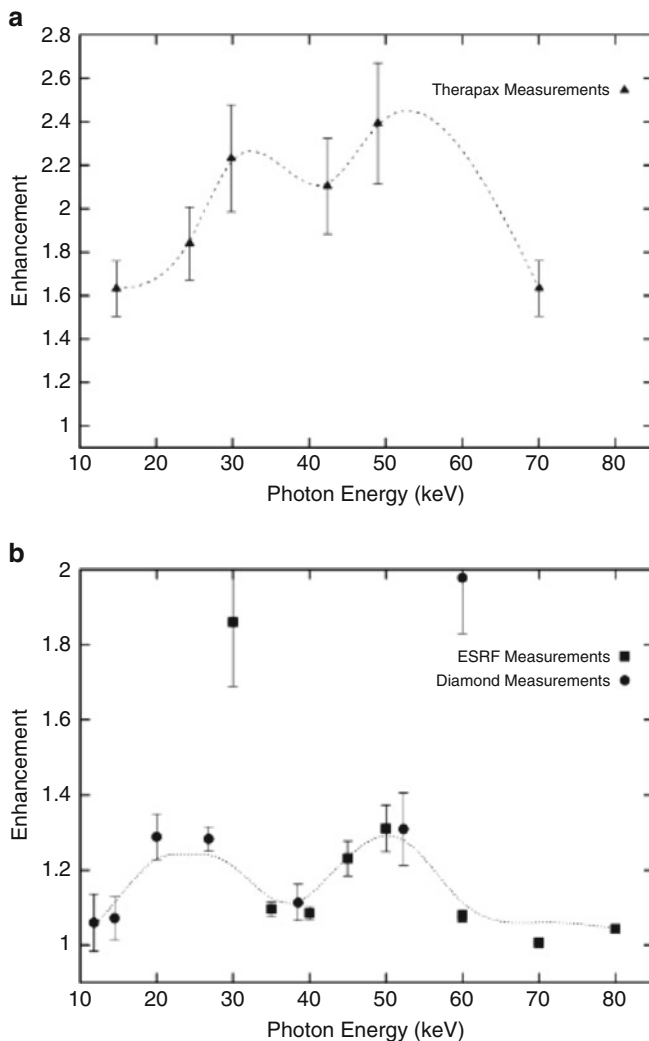
Fig. 3.14 DNA damage by gold nanoparticles with monochromatic X-rays from a synchrotron source. Energy-dependent enhancement was observed in both cases (top and lower panels). (Reprinted with permission from McMahon et al. [2]. Copyright (2011) American Chemical Society.)

Hydroxylation Reactions of Small Molecules

Guo et al. [4] studied enhancement of a dosimetric reaction influenced by gold nanoparticles under X-ray irradiation. PEGylated gold nanoparticles of five different sizes were synthesized, purified, and used to enhance the yield of a dosimetric reaction, 3-CCA to 7-OHCCA conversion shown in Fig. 3.9. The results showed

an enhancement of 2–4 DEU using 0.1–0.5 WP 7 nm PEG gold nanoparticles at 20 Gy/min dose-rate irradiation and 0.5 DEU using 1–100 ppm 3–7 nm gold nanoparticles at 3 Gy/min dose rate. The observed enhancement was nearly 10,000 times higher than the predicted type 1 physical enhancement. Since the probe molecules have no affinity toward gold nanoparticles, type 2 physical enhancement should be only a fraction of type 1 physical enhancement as indicated in Chap. 2. Further, as mentioned above, the measured enhancements were dose-rate dependent, which means the enhancement could not be physical. The enhancement also depended on the surface of gold nanoparticles. When the surface of gold nanoparticles was covered with a layer of silica, no enhancement was detected. Enhancement also depended on superoxide radicals. Table 3.2 shows the results of using nine different scavengers, among which superoxide dismutase (SOD) completely stopped the enhancement.

Taken together, these results suggest that enhancement cannot be physical. Figure 3.15 shows the proposed enhancement mechanism. Since 3-CCA probe molecules are uniformly distributed over the whole volume, longer-lived 3-•OHCCA radical intermediates have enough time to diffuse to the surface of gold nanoparticles to be converted to 7-OHCCA, as shown in the pathway illustrated in Fig. 3.10. For these reasons, it is speculated that the enhancement belongs to type 1 chemical enhancement, meaning the enhancement does not rely on the increased production of •OH but derives from catalytic conversion of the 3-•OHCCA intermediate to the 7-OHCCA final product.

Misawa et al. [3] employed amino-phenyl fluorescein (APF) and dihydroethidium (DHE) to probe hydroxyl and superoxide radicals separately. The authors did find increased catalytic production of superoxide radicals. Consequently, their results are categorized as type 2 physical enhancement even though the results are similar to what is shown by Guo et al. described in this section.

Table 3.2 Testing the scavenger effect on enhancement of 3-CCA to 7-OHCCA conversion. Totally nine chemicals were used to test the role of reactive oxygen species. SOD completely eliminated enhancement

Scavenger tests					
Chemical	Concentration	Function	Original (%)	W/AuNPs (%)	Rel. Enh. (%)
Ascorbic acid	Up to 0.5 mM	OH, O_2^-, O_2^*	100	100	0
SOD	Up to 0.5 mg/mL	O_2^-	100	100	0
DMSO	0–5 mM	•OH	16.6	16.6–24.9	0–50
O_2 removed	<10%	O_2	50	60–70	20–40
$NaNO_3$	Up to 100 mM	Solvated e^-	100	110–150	10–50
Sodium azide	Up to 1 mM	O_2^* (singlet)	100	110–150	10–50
Fe^{2+}	Up to 50 μM	H_2O_2	100	100	0
Fe^{3+}	Up to 50 μM	*ibid*	100	110–150	10–50
H_2O_2	Up to 50 μM	*ibid*	100	110–150	10–50
Nothing	—	Control	100	110–150	10–50
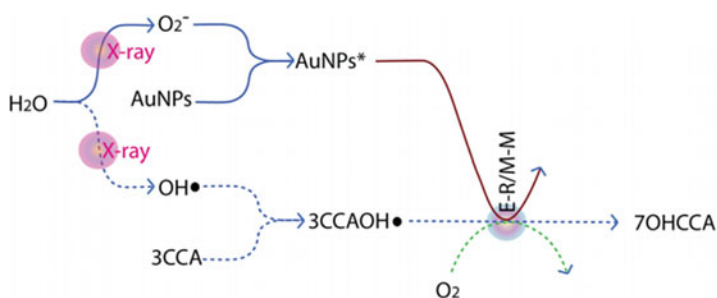
Fig. 3.15 Proposed mechanisms for type 1 chemical enhancement enabled by superoxide radicals to convert 3-CCA to 7-OHCCA. (Reprinted with permission from Guo et al. [4]. Copyright (2012) American Chemical Society.)

3.4.1.2   Superoxide-Enabled Catalytic Reactions

As shown above, reactive oxygen species such as superoxide radicals and solvated electrons may help drive catalytic reactions in the presence of nanoparticles such as gold nanoparticles. Results shown by Guo et al. [4] as mentioned above were considered as catalysis by gold nanoparticles enabled by superoxide radicals. Future time-resolved experiments are needed to directly confirm the reaction pathways and types of chemical enhancement.

3.4.1.3   Polymerization Reactions

Guo et al. [9] reported the first case of studying polymerization reactions within the framework of X-ray nanochemistry. It was also the first time the term "X-ray nanochemistry" was used. Although first coined in this publication, the field of X-ray nanochemistry covers topics dating back to the early twentieth century, and results published between 2004 and 2012 using carefully synthesized nanoparticles to enhance the effectiveness of X-ray irradiation had helped solidify the field of X-ray nanochemistry.

The probe reaction in the work published by Guo et al. was polymerization of the aniline monomer, i.e., oxidation of aniline to form polyaniline, as shown in Fig. 3.16. There are many enantiomers of polyaniline, and only the fluorescent one was detected through surface-enhanced Raman spectroscopy (SERS). The experiment used gold shell-silver core nanostructures in which silver in the core was believed to remove residual positive charge left on gold in the shell due to the lower redox potential of silver; otherwise residual charges left on gold could spontaneously oxidize the aniline monomer.

The polymerization was believed to be catalyzed by the gold surface enabled by hydroxyl radicals, which were produced in water irradiated with X-rays. Physical enhancement was low since the concentration of the core-shell structure was low, but this low concentration did not exclude type 2 physical enhancement. The clue for the
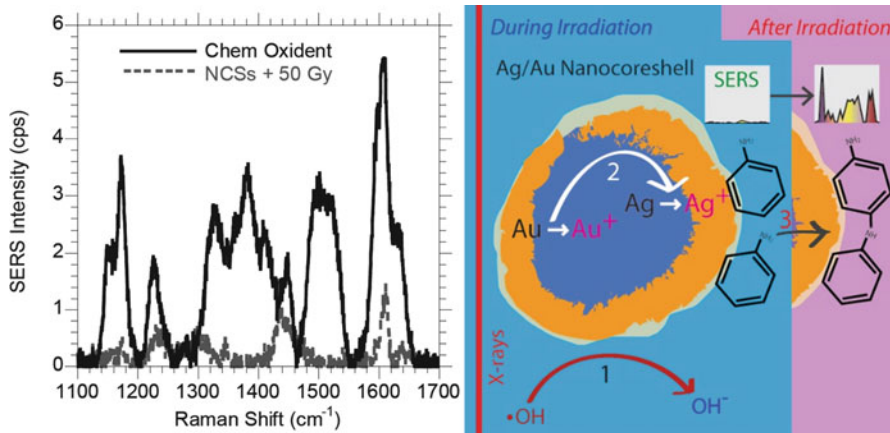
Fig. 3.16 Polymerization catalyzed by type 1 chemical enhancement enabled by hydroxyl radical activating gold-coated silver nanostructures. SERS was used to measure the enhancement. The enhancement results are shown in the left panel. The right panel shows the proposed mechanisms. (Adapted with permission from Guo et al. [9]. Copyright (2012) American Chemical Society.)

cause of enhancement was further deciphered when DMSO, an •OH scavenger, was added into the solution, which eliminated enhancement. This result suggested that enhancement could not come from type 1 or 2 physical enhancement. If type 1 physical enhancement dominates, then adding scavengers should not affect the enhancement. If enhancement was caused by type 2 physical enhancement, then adding DMSO would even increase the enhancement. Adding DMSO here had the same effect as adding SOD in the 3-CCA dosimetric experiment shown above. In that experiment, the superoxide radical was proven to be critical: When SOD was added, superoxide radicals were scavenged and enhancement was eliminated. Here, adding DMSO eliminated •OH and enhancement disappeared, proving that •OH was the driving force of the enhancement. All arguments considered, the observed enhancement was thought to be caused by catalytic reactions. As in the 3-CCA chemical enhancement case, •OH was unlikely to be catalytically produced by gold nanoparticles, because if it were, then enhancement would increase upon DMSO addition. Therefore, the observed enhancement was believed to be caused by catalytic reactions driven by •OH produced in water under X-ray irradiation. Activated catalytic reactions helped polymerize aniline monomers into polyaniline on the surface of nanostructures.

It was found by Maenosono et al. [32] that gold and silver in Au/Ag alloy nanostructures such as core-shell structures could redistribute charges. The authors employed X-ray absorption near-edge structure (XANES) spectroscopy to measure the charge state of Ag and Au in alloy nanostructures. In Au@Ag core-shell structures, gold was found to donate electrons to surface Ag, which was the reason surface Ag was less likely to be oxidized. The authors did not measure Ag@Au core-shell structures as shown in the work published by Guo et al. [9]. The charge transfer from Au ($5d$) to Ag in Au@Ag was intriguing, and future work should be performed on Ag@Au.

3.4.2   Type 2 Chemical Enhancement

Type 1 chemical enhancement relies on catalytic reactions that do not involve the production of reactive oxygen species (ROS) or X-ray absorption by nanomaterials. When ROS production is catalytically modified by nanomaterials, or if nanomaterials are thought to become catalytically active upon absorption of X-rays, the enhancement so created is called type 2 chemical enhancement, which is different from type 2 physical enhancement. Type 2 physical enhancement does not require the availability of the surface of nanomaterials; the enhancement exists even when the surface is covered by a very thin, chemically inert layer. In contrast, such a thin layer would eliminate type 2 chemical enhancement. Direct evidence is still being sought for proving the existence of type 2 chemical enhancement except for the reduction or scavenging of ROS. Type 2 chemical enhancement can be further divided into ROS increasing or scavenging processes or reactions.

3.4.2.1   Reactive Oxygen Species (ROS) Increasing Reactions

Nanomaterials may catalyze the production of ROS. In an example that did not involve normal ROS, Ionita et al. [33] found that gold nanoparticles influenced the production of radicals. In this example, the authors used spin traps to show that gold nanoparticles helped generate radicals from aniline or iodobenzene molecules or scavenge spin labels such as 4-aminotempo. The size of gold nanoparticles ranged from a few to tens of nanometers. The spin trap employed was DMPO. However, the authors confirmed no diphenylamine was produced, a result that could be explained by several reasons. For example, the locations of benzyl radicals and aniline radicals could be too far apart. Although their work did not involve ROS or X-rays, the authors did find that molecular oxygen seemed to be necessary for catalytic reactions involving gold nanoparticles.

Misawa et al. [3] reported on the findings of increased production of at least one kind of ROS, superoxide radicals, due to catalytic reactions enabled by the gold surface. In their experiment, two fluorescent probes, APF and DHE, reacted with hydroxyl and superoxide radicals, respectively, to form fluorescent molecules. These reactions are similar to the 3-CCA reaction with hydroxyl radicals discussed in Sect. 3.4.1. Five different sizes of citrate-covered gold nanoparticles, ranging from 5 nm to 250 nm, purchased from the British BioCell International Co. Ltd., were used without purification. Normally citrate ligands scavenge ROS such hydroxyl radicals, which is why PEGylated gold nanoparticles are more frequently used in enhancement measurements. Nonetheless, Misawa et al. observed enhancement using all five sizes of gold nanoparticles, at least for the production of superoxide radicals, and the measured enhancements were found to be dependent on the surface area or radius of the nanomaterials. The amounts of nanoparticles employed were on the order of 10–1000 ppm, which were too low to cause type 1 physical enhancement, and the molecules detected did not have affinity toward the gold nanoparticle
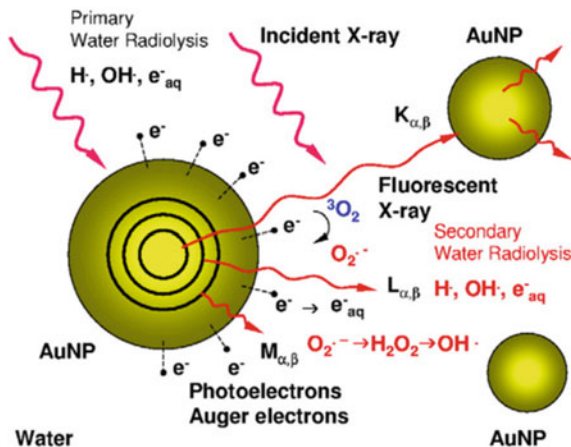
Fig. 3.17 Proposed enhancement mechanisms for gold nanoparticles under X-ray irradiation by Misawa et al. [3]. Catalytic production of superoxide radicals was proposed, which was attributed to secondary X-ray fluorescence interacting with gold nanoparticles. (Reprinted from Misawa et al. [3]. Copyright (2011) with permission from Elsevier.)

surface, making contribution from type 2 physical enhancement insignificant as well. Therefore, physical enhancement could not account for the reported enhancement. Figure 3.17 shows their suggested enhancement mechanisms. The authors attributed the observed enhancement to secondary X-ray fluorescence, which suggested the enhancement was of a physical origin. However, the impact of secondary X-ray fluorescence should be far weaker than that of primary X-rays for 10–1000 ppm of gold in water and broadband X-rays. Therefore, although it is more likely the enhancement observed by the authors was caused by chemical enhancement, the exact mechanisms were unclear. This enhancement is temporarily categorized as type 2 chemical enhancement because the authors suggested that enhancement was caused by increased production of ROS by gold nanoparticle catalysts.

As mentioned in the introduction, Chechik et al. [20] found superoxide radicals may be produced with gold nanoparticles dissolved in aerated water. If this happened in Misawa's study, then it might explain the results. However, it is unclear whether the measurements performed by Misawa et al. removed the background production of superoxide radicals. Future work is needed to clarify these points.

Gonzalez and Kotler et al. [28] showed that silicon nanoparticles in aqueous solutions enhanced the production of ROS when irradiated with 4 MV X-rays. The loading of 1–5 nm diameter silicon nanoparticles was 6.4 μM, and the enhancement was 10 DEU. Although it was claimed by Guo et al. [4] that the silica surface was relatively inert toward ROS, the amount of silica used in the Guo et al. experiment was three to five orders of magnitude less than that by Gonzalez and Kotler et al. If silica nanoparticles could enhance the production of ROS at the rate detected by Gonzalez and Kotler et al., then the enhancement should be less than 0.01 DEU at the concentrations used by Guo et al.
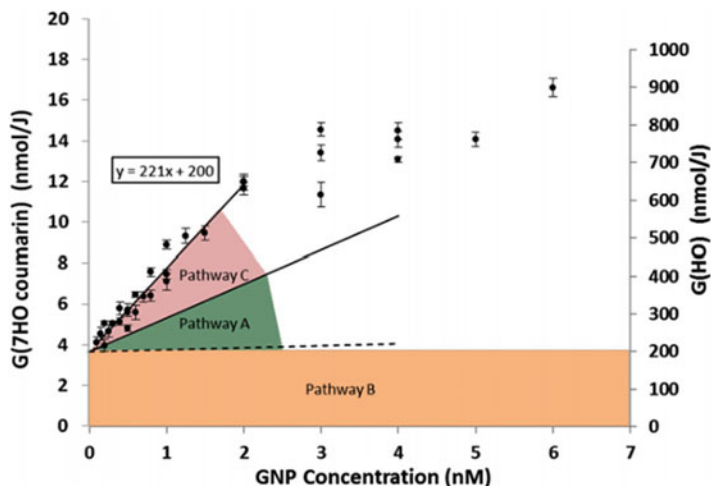
Fig. 3.18 Results of study of catalytic production of 7-OH coumarin obtained by Currell et al. Increased 7-OH coumarin yield was attributed to enhanced hydroxyl radical production. (Adapted from [7]. CC BY.)

Currell et al. [7] examined interactions of X-rays with gold nanoparticles using coumarin dosimetric reaction. The authors concluded that there was enhanced production of 7-OH coumarin based on their measurement of the 7-OH coumarin yield, and they attributed the observed enhancement to increased production of hydroxyl radicals by addition of gold nanoparticles. The results obtained by Currell et al. are shown in Fig. 3.18 and resemble those observed by Guo et al. [4], which also showed the increased production of 7-OH coumarin significantly surpassed that predicted for physical enhancement. Similar to the findings made by Guo et al. [4], Currell et al. also observed a dose-rate dependency, albeit a monotonic decay was observed by Currell et al. It is important to note that dose rates used by Currell et al. were between 65 Gy/min and 900 Gy/min, much higher than those used by Guo et al. between 3 Gy/min and 40 Gy/min. Based on Guo et al., saturation already occurred when the dose rate exceeded 3 Gy/min and complete saturation was reached above 20 Gy/min. Drastically different dose rates may contribute to the different dose-rate dependencies in these two studies. Their work is listed here under type 2 chemical enhancement because Currell et al. suggested that hydroxyl radical production was enhanced. However, mechanisms for increased production of ROS are difficult to explain. For example, since chemical enhancement requires large surface areas per unit mass of nanoparticles, smaller nanoparticles are preferred. However, only a very small fraction of these nanoparticles is directly ionized. For 1–2 nm gold nanoparticles, the percentage is below 0.01%. Definition of this type of enhancement may be revised when more accurate experimental data is available.

3.4.2.2 ROS Decreasing Processes or Anti-enhancement

Nanomaterials, when properly made and used, can help increase production of ROS or catalytically convert radicals to other forms of radicals or products. Nanomaterials with large surface areas, however, can also effectively scavenge ROS because the metal surface may be oxidized or reduced by ROS or bound to ROS. Oxidation or reduction of nanomaterials by radicals is well documented. Gold nanoparticles, for example, have been studied for their antioxidant properties. Esumi et al. [14] investigated gold-chitosan nanocomposites for their antioxidant potential. The average size of gold nanoparticle ranged from 5.7 to 13.4 nm. In their work, the hydroxyl radical was produced via the Fenton reaction using ferric sulfate and hydrogen peroxide. The authors did not find gold nanoparticles interfering with the Fenton reaction as observed in other studies and employed electron spin resonance (ESR) to determine the yield of hydroxyl radicals using spin trap DMPO. Reduction of ESR signal upon addition of gold-chitosan nanocomposites was observed. The authors did not discuss the possibility of gold nanoparticles interfering with the Fenton reaction and suggested that hydroxyl radicals were scavenged by gold-chitosan nanocomposites, which could still be true even if hydroxyl radicals were indeed produced and then scavenged.

Meisel and Levanon et al. [34] used interactions between stable radicals and small gold nanoparticles to study scavenging of radicals by gold nanoparticles. The authors added radical spin label (2,2,6,6-tetramethylpiperidin-1-yl)oxyl (TEMPO), 4-Oxo-2,2,6,6-tetramethylpiperidine-1-oxyl or 4-Oxo-TEMPO (TEMPONE), and 4-amino-2,2,6,6-tetramethylpiperidine-1-oxyl or 4-amino-TEMPO (tempamine) to gold nanoparticle aqueous solutions and studied products with electron paramagnetic resonance (EPR) spectroscopy. They found that radicals were adsorbed on the surface of nanoparticles because EPR signals were reduced. They attributed the reduction to electron exchange between electrons in the conduction band of gold nanoparticles and unpaired electrons in the stable radical spin labels. The authors also discovered a catalytic reaction when O_2 was involved with tempamine absorbed on the surface of gold nanoparticles. Moreover, the authors also detected some change to tempamine over time and suggested that the change was caused by conversion of tempamine to TEMPONE.

Liu et al. [15] discussed a case where 4.5 nm gold nanoparticles were functionalized with Trolox, an analog of antioxidant α-tocopherol, and 2,2-diphenyl-1-picrylhydrazyl (DPPH). The nanocomplex with both ligands on the gold surface was found to be eight times as scavenging as Trolox-coated gold nanoparticles.

Ionita et al. [33] described how gold nanoparticles interacted with free radicals. The authors found that EPR signals were quenched for radicals conjugated to the surface of gold nanoparticles. This quenching was different from scavenging defined in other publications in which radicals were destroyed. Instead, the authors considered conjugation of radicals to the surface of gold nanoparticles. Figure 3.19 shows the results of their proposed scavenging process.
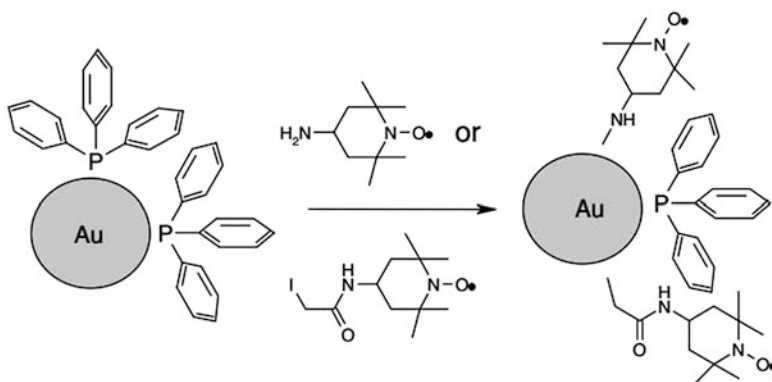
Fig. 3.19 An anti-enhancement scheme proposed by Ionita et al. The proposed mechanisms required specific ligands with functional groups other than the radical that have affinity toward the nanoparticles, as shown in the figure. (Adapted from Ionita et al. [33]. With permission from Springer.)

As discussed earlier in this chapter, small gold nanoparticles can also generate superoxide radicals from molecular oxygen absorbed on the metal surface. Further investigations are needed to fully understand these processes. Shirahata et al. [35] discussed interactions such as scavenging of superoxide and hydroxyl radicals by platinum nanoparticles. The authors used hypoxanthine-xanthine and Fenton reactions to produce these radicals and found that platinum nanoparticles did not scavenge hydroxyl radicals. Although this may be true, another possibility is that platinum nanoparticles indeed scavenged hydroxyl radicals, but because platinum nanoparticles also catalyzed other reaction step(s) in the probing reaction, the overall product yield remained the same or even higher despite scavenging or reduction of hydroxyl radicals. The authors found these platinum nanoparticles might scavenge superoxide radicals generated in HeLa cells by UVA light. Similarly sized platinum nanoparticles were found to catalytically convert 3-CCA to 7-OHCCA, which was claimed to be mediated by superoxide radicals by Guo et al. [4].

Watanabe et al. [36] investigated polyacrylic acid protected 2.0 nm platinum nanoparticles. They used EPR spectroscopy to detect peroxyl radicals chemically generated from azobis aminopropane dihydrochloride in the presence of oxygen and found that platinum nanoparticles reduced the amount of oxygen consumed during radical production. Figure 3.20 shows the results of DPPH radical production as a function of the concentration of platinum nanoparticles. The authors attempted to determine if these platinum nanoparticles scavenge hydroxyl radicals but encountered a problem of not being able to properly produce hydroxyl radicals using chemical methods such as Fenton reactions with Fe^{2+} or NaOH in the presence of platinum nanoparticles, a problem encountered by Guo et al. as well. The problem could either caused by platinum nanoparticles interfering with hydroxyl radical generation (Fe^{2+}) or the pH being too high for radical production. The authors did not use X-rays to produce radicals.

Fig. 3.20 Platinum nanoparticle scavenging or anti-enhancement results. Radical DPPH production was reduced by the platinum nanoparticles. (Watanabe et al. [36] DOI: https://doi.org/10.1088/0957-4484/20/45/455105. © Institute of Physics and Engineering in Medicine. Reproduced with permission from IOP Publishing. All rights reserved.)

(a)
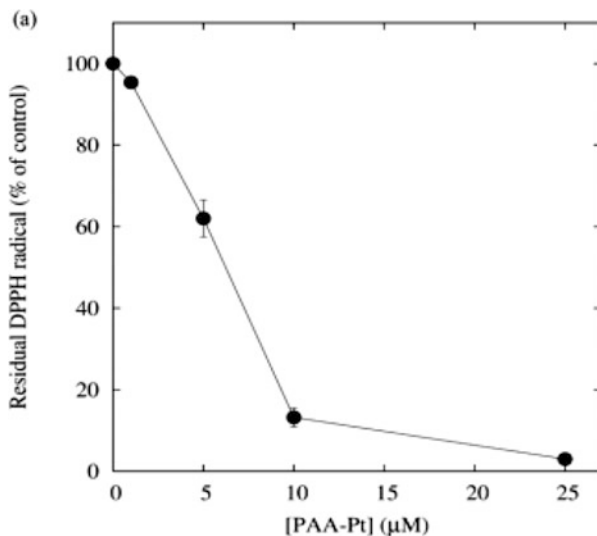
Guo et al. observed anti-enhancement caused by various ligands on nanoparticles. For instance, trimethylammonium (TMA) ligand-covered gold nanoparticles were highly water soluble, but the nanoparticles also caused strong anti-enhancement. In contrast, the same gold nanoparticles covered with PEG ligands could generate both chemical and physical enhancement, depending on the size of gold nanoparticles. It was concluded that although PEG scavenged ROS, anti-enhancement due to scavenging by PEG was weaker than the TMA ligand. Nanoparticle size is also salient in determining whether enhancement of a physical or chemical nature will prevail. For small (<10 nm in diameter) PEGylated gold nanoparticles, chemical enhancement dominates. For large (>80 nm in diameter) PEGylated gold nanoparticles, physical enhancement is strong. Carboxylated gold nanoparticles exhibited moderate anti-enhancement properties.

Another example of anti-enhancement is the gold nanotube case described in Chap. 2 (Fig. 2.22). In this study, the weight percentage of gold in water was 100 WP, meaning there were equal weights of gold and water in the solution/suspension. An enhancement of 100-DEU was expected from type 1 physical enhancement alone. The measured enhancement, however, was only 2 DEU. Analysis showed that 98% of hydroxyl radicals were scavenged by the gold surface, leaving only 2% of the hydroxyl radicals to generating type 1 physical enhancement.

Many experimental parameters can influence anti-enhancement. Anti-enhancement is particularly strong when nanoparticle concentrations are high, and total surface areas of the gold nanoparticles are large. Surfactants (or lack of them as in "naked" gold nanoparticles), X-ray energy, nanoparticle size, amount, and catalytic properties of nanoparticles can all affect anti-enhancement. If nanoparticles are fully covered with surfactants, then the surfactant properties are critical. If the surface is sparsely covered by weakly scavenging surfactants, then the nanoparticle surface

plays a more active role. Based on these works, anti-enhancement coexists with physical and chemical enhancement.

Anti-enhancement property can also be desirable. For example, nanomaterials giving rise to strong anti-enhancement may be used to protect healthy cells around tumors under radiotherapy. Such practice may be important after enhancement of destruction of tumors is optimized to reach the highest values. Nanoparticles with anti-enhancement can then be placed in the surrounding healthy tissues to protect them, giving rise to the highest differential between the fate of the two tissues. Therefore, studying anti-enhancement may have potential scientific as well as commercial impacts.

Considering all these possibilities, it is important to minimize or maximize individual enhancements and combine them properly to obtain the maximum total enhancement.

3.5 Other Possible Types of Chemical Enhancement

Chemical enhancement may be caused by low-energy electrons or solvated electrons. Sanche et al. (e.g., in Sanche et al. [37]) explored how electrons emitted from gold nanoparticles under X-ray irradiation interacted with DNA molecules in vacuum. Resonance absorption or enhanced DNA strand breaks were observed. Even though these works were performed in gas and solid phases, the observed pathways in these two phases may influence reactions in the liquid phase such as water. No speculation will be made here about reactions in solutions, but instead, a brief account of the results of gas and solid phase reactions is presented. This additional enhancement caused by low-energy electrons in the presence of the gold surface could belong to chemical enhancement. Figure 3.21 shows the evidence of resonant interactions between low-energy electrons and DNA (top panel) and an illustration of the suggested mechanisms (bottom panel).

Ionita et al. [33], using EPR spectroscopy, found that gold nanoparticles could help produce radicals other than reactive oxygen species. Their gold nanoparticles were protected with phosphine ligands. The authors found that aniline and iodobenzene could convert into benzyl and aniline radicals. Figure 3.22 shows their proposed reaction mechanism. Similar processes were suggested by Guo et al. [9] in which gold nanoparticles were found to spontaneously polymerize aniline into polyaniline. It is difficult to conclusively assign the results obtained by Ionita et al. to a specific type of chemical enhancement because it seemed that ROS did not participate in the reactions.

As noted in the introduction, Guidelli et al. [12] recorded a nonlinear response in the EPR signal for alanine radicals as a function of gold nanoparticle concentration. The signal response given in Fig. 3.2 (left panel) shows a steep rise at low gold nanoparticle concentrations. It is unclear whether catalysis was involved in the process. The nonlinear responses suggested the involvement of chemical processes.
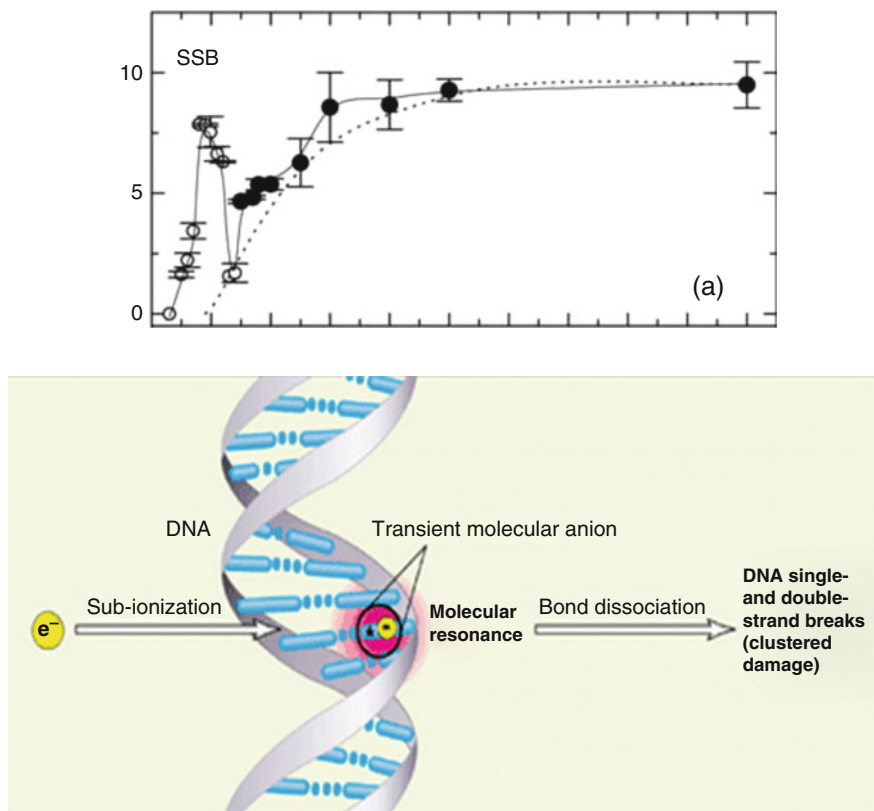
Fig. 3.21 DNA single strand breaks (SSB) by low-energy electrons. Other molecules may undergo the same process as well. The results, shown in the top panel, exhibit strong energy dependency at low-electron energy region. An illustration of the proposed mechanisms is shown in the bottom panel. (Top panel: adapted with permission from Sanche et al. [37]. Copyright (2015) by the American Physical Society. Bottom panel: adapted from website [38].)
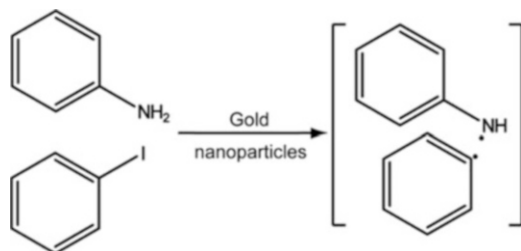
Fig. 3.22 Proposed pathway through catalysis of radical generation by gold nanoparticles. Other molecules may undergo the same process. (Graph adopted and redrawn based on Ionita et al. [33].)

3.6   Separating Physical from Chemical Enhancement

As discussed in Sect. 3.2.2, chemical and physical enhancements are different but share some similarities. It is important to distinguish between the two, especially between type 2 physical enhancement and type 2 chemical enhancement. Based on published results and discussions in this chapter and Chap. 2, there are several ways to differentiate type 2 physical enhancement from type 2 chemical enhancement.

First, measurements using different dose rates may help differentiate chemical from physical enhancement. Chemical enhancement depends on how radicals react with the surface of nanomaterials; as radicals have finite lifetimes, dose rate can change the magnitude of chemical enhancement. Other factors may also influence chemical enhancement. Although there is no guarantee that higher dose rates generate higher enhancements, it is certain dose rate changes chemical enhancement at low dose rates, e.g., below 3 Gy/min. This is shown by Guo et al. [4] and Currell et al. [7] in which varying dose rates produced different enhancements. In contrast, dose rate should not affect type 2 physical enhancement.

The second parameter is the diameter of nanoparticles. When nanoparticle diameter is changed, surface area per unit mass and degree of coordination saturation of the surface atoms are changed. Although type 2 physical enhancement may change as a function of the size of the nanoparticles, the change should be mild compared to chemical enhancement. The latter can change significantly when the diameter is changed, e.g., from 3 nm to 100 nm. Both Misawa et al. [3] and Guo et al. [4] experimentally demonstrated this effect.

Scavenging may affect chemical enhancement differently than it does to physical enhancement. If enhancement changes when scavengers are added, then it is possible that there is a chemical enhancement component in the total enhancement. This applies to probes uniformly distributed in the sample. When probes are localized at the surface of nanoparticles and type 2 physical enhancement is significant, adding scavengers can increase type 2 physical enhancement as well. In this case, it is more difficult to differentiate the two enhancements.

Another parameter that can be used to separate the two enhancements is X-ray energy. For chemical enhancement, low- or high-energy X-rays are preferred because these photons can more effectively produce more hydroxyl radicals in water than from enhanced absorption of these X-rays by nanomaterials, and high yields of hydroxyl radical production may favor chemical enhancement. This dependency of chemical enhancement on X-ray energy was shown in a recent publication by Guo et al. [39].

Lastly, it is possible to develop thin, inert surface layer covering nanoparticles to differentiate these two categories of enhancement. Type 2 physical enhancement should not change when such a thin layer is coated on the surface of nanoparticles. In contrast, type 2 chemical enhancement should completely disappear with this layer. These five factors, together with the unit WP enhancement values as discussed in Sect. 3.2.2, can be used to differentiate physical from chemical enhancement.

3.7   Conclusions and Future Work

Two types of chemical enhancement of X-ray effects are shown in this chapter. The first type emphasizes catalytic radical conversion reactions by gold nanoparticles without directly producing or scavenging reactive oxygen species. 3-CCA to 7-OHCCA dosimetric reaction is one such reaction that can be enhanced through type 1 chemical enhancement. DNA strand breaks are another reaction that can be catalyzed in this way. Type 2 chemical enhancement, which also includes anti-enhancement, involves direct catalytic production or destruction of reactive oxygen species by nanomaterials under X-ray irradiation. However, the exact mechanisms of this type of enhancement still require full elucidation.

Although equivalent processes of type 1 or 2 chemical enhancement have been suggested in the literature, these types still require more direct and conclusive experimental confirmation. For example, results from recent ongoing EPR measurements in the Guo lab suggest that type 1 chemical enhancement is indeed a valid hypothesis; enhancement exists without the need for increased production of ROS due to the added nanomaterials. There is yet no direct and conclusive experimental data to confirm the existence of radical increasing type 2 chemical enhancement except for anti-enhancement. Type 2 chemical enhancement is claimed based on almost the same experimental observations as type 1 chemical enhancement, except for the mechanisms were speculated differently. In situ measurements of ROS will be necessary in the future to conclusively confirm the existence of type 2 chemical enhancement.

Direct proof of type 1 and 2 chemical enhancement is important, and requires physical methods that can fiducially measure the amount of radicals and other chemicals as well as the state of the metal surface during catalysis. Future studies using methods such as EPR spectroscopy or time-resolved measurements are needed. Ultrafast X-ray spectroscopy may be used to interrogate reactive oxygen species responsible for the enhancement and catalysis by nanoparticles. Ultrafast extended X-ray absorption fine structure (EXAFS) may be used to study surface atoms to reveal if they are oxidized or reduced during enhancement reactions.

Chemical enhancement, as defined here, has just begun to be recognized. The need for such recognition is for the purpose of understanding enhancement mechanisms and optimizing the total enhancement, as explained in this chapter and in Chap. 5 where algorithms governing the combination of different categories and types of enhancements are presented. For example, it is known now that X-ray energy as well as sizes and concentrations of nanoparticles need to be optimized to generate strong physical and chemical enhancement. Furthermore, the environment has to be controlled and optimized. If the nanoparticle environment is exposed or open as in most applications discussed in Chaps. 8 and 9, then the total enhancement as predicted by theory or observed in more controlled chemical environments may be seriously compromised. Further work will be needed to study how to achieve high enhancements in different, more controlled environments. If the environment is controlled, such as that within non-permeable micelles, liposomes, or other isolated

volumes, then it is possible to accomplish high total enhancements or individual enhancements, an important step to considerably reduce the X-ray dosage needed to perform any function, including cancer treatment or reading/writing with X-rays.

Chemical enhancement may be significantly expanded in the future because there are a large number of chemical and biochemical reactions that can be catalyzed by a large number of nanomaterial catalysts under a large number of unique reactive environments created by irradiation of X-rays of medium such as water. As it is shown in this chapter, chemical enhancement including anti-enhancement often overwhelms physical enhancement when small nanoparticles with large surface areas are used. This means these nanoparticles will be used in future applications to influence or catalyze reactions, and many past applications using these small nanoparticle catalysts will have to be reevaluated if chemical enhancement was not properly determined and optimized. Further studies of these reactions will no doubt lead to the discovery of other types of chemical enhancement.

References

1. Carter, J. D., Cheng, N. N., Qu, Y. Q., Suarez, G. D., & Guo, T. (2007). Nanoscale energy deposition by x-ray absorbing nanostructures. *The Journal of Physical Chemistry. B, 111*, 11622–11625.
2. McMahon, S. J., Hyland, W. B., Brun, E., Butterworth, K. T., Coulter, J. A., Douki, T., Hirst, D. G., Jain, S., Kavanagh, A. P., Krpetic, Z., Mendenhall, M. H., Muir, M. F., Prise, K. M., Requardt, H., Sanche, L., Schettino, G., Currell, F. J., & Sicard-Roselli, C. (2011). Energy dependence of gold nanoparticle radiosensitization in plasmid DNA. *Journal of Physical Chemistry C, 115*, 20160–20167.
3. Misawa, M., & Takahashi, J. (2011). Generation of reactive oxygen species induced by gold nanoparticles under x-ray and UV irradiations. *Nanomedicine: Nanotechnology, 7*, 604–614.
4. Cheng, N. N., Starkewolf, Z., Davidson, A. R., Sharmah, A., Lee, C., Lien, J., & Guo, T. (1950). Chemical enhancement by nanomaterials under X-ray irradiation. *Journal of the American Chemical Society, 2012*(134), 1950–1953.
5. Makrigiorgos, G. M., Baranowskakortylewicz, J., Bump, E., Sahu, S. K., Berman, R. M., & Kassis, A. I. (1993). A method for detection of hydroxyl radicals in the vicinity of biomolecules using radiation-induced fluorescence of coumarin. *International Journal of Radiation Biology, 63*, 445–458.
6. Louit, G., Foley, S., Cabillic, J., Coffigny, H., Taran, F., Valleix, A., Renault, J. P., & Pin, S. (2005). The reaction of coumarin with the OH radical revisited: Hydroxylation product analysis determined by fluorescence and chromatography. *Radiation Physics and Chemistry, 72*, 119–124.
7. Sicard-Roselli, C., Brun, E., Gilles, M., Baldacchino, G., Kelsey, C., McQuaid, H., Polin, C., Wardlow, N., & Currell, F. (2014). A new mechanism for hydroxyl radical production in irradiated nanoparticle solutions. *Small, 10*, 3338–3346.
8. Gilles, M., Brun, E., & Sicard-Roselli, C. (2014). Gold nanoparticles functionalization notably decreases radiosensitization through hydroxyl radical production under ionizing radiation. *Colloids and Surfaces B: Biointerfaces, 123*, 770–777.
9. Davidson, R. A., & Guo, T. (2012). An example of X-ray nanochemistry: SERS investigation of polymerization enhanced by nanostructures under X-ray irradiation. *Journal of Physical Chemistry Letters, 3*, 3271–3275.

10. Alqathami, M., Blencowe, A., Yeo, U. J., Doran, S. J., Qiao, G., & Geso, M. (2012). Novel multicompartment 3-dimensional radiochromic radiation dosimeters for nanoparticle-enhanced radiation therapy dosimetry. *International Journal of Radiation Oncology Biology Physics, 84*, E549–E555.

11. Guidelli, E. J., Ramos, A. P., Zaniquelli, M. E. D., Nicolucci, P., & Baffa, O. (2012). Synthesis and characterization of gold/alanine nanocomposites with potential properties for medical application as radiation sensors. *ACS Applied Materials & Interfaces, 4*, 5844–5851.

12. Guidelli, E. J., & Baffa, O. (2014). Influence of photon beam energy on the dose enhancement factor caused by gold and silver nanoparticles: An experimental approach. *Medical Physics, 41* (032101), 1–8.

13. Paudel, N., Shvydka, D., & Parsai, E. I. (2015). Comparative study of experimental enhancement in free radical generation against Monte Carlo modeled enhancement in radiation dose position due to the presence of high Z materials during irradiation of aqueous media. *International Journal of Medical Physics, Clinical Engineering and Radiation Oncology, 4*, 300–307. 300.

14. Esumi, K., Takei, N., & Yoshimura, T. (2003). Antioxidant-potentiality of gold-chitosan nanocomposites. *Colloids and Surfaces B: Biointerfaces, 32*, 117–123.

15. Nie, Z., Liu, K. J., Zhong, C. J., Wang, L. F., Yang, Y., Tian, Q., & Liu, Y. (2007). Enhanced radical scavenging activity by antioxidant-functionalized gold nanoparticles: A novel inspiration for development of new artificial antioxidants. *Free Radical Biology & Medicine, 43*, 1243–1254.

16. Chang, J., Taylor, R. D., Davidson, R. A., Sharmah, A., & Guo, T. (2016). Electron paramagnetic resonance spectroscopy investigation of radical production by gold nanoparticles in aqueous solutions under X-ray irradiation. *Journal of Physical Chemistry A, 120*, 2815–2823.

17. Sharmah, A., Mukherjee, S., Yao, Z., Lu, L., & Guo, T. (2016). Concentration-dependent association between weakly attractive nanoparticles in aqueous solutions. *Journal of Physical Chemistry C, 120*, 19830–19836.

18. You, H. J., Yang, S. C., Ding, B. J., & Yang, H. (2013). Synthesis of colloidal metal and metal alloy nanoparticles for electrochemical energy applications. *Chemical Society Reviews, 42*, 2880–2904.

19. Bond, G. C., Louis, C., & Thompson, D. T. (2006). *Catalysis by gold, G. J. Hutchings* (p. 366). Catalytic Science Series, Vol. 6. London: Imperial College Press.

20. Ionita, P., Gilbert, B. C., & Chechik, V. (2005). Radical mechanism of a place-exchange reaction of an nanoparticles. *Angewandte Chemie, International Edition, 44*, 3720–3722.

21. Zhang, Z. F., Cui, H., Lai, C. Z., & Liu, L. J. (2005). Gold nanoparticle-catalyzed luminol chemiluminescence and its analytical applications. *Analytical Chemistry, 77*, 3324–3329.

22. Duan, C. F., Cui, H., Zhang, Z. F., Liu, B., Guo, J. Z., & Wang, W. (2007). Size-dependent inhibition and enhancement by gold nanoparticles of luminol-ferricyanide chemiluminescence. *Journal of Physical Chemistry C, 111*, 4561–4566.

23. Lambert, R. M., Turner, M., Golovko, V. B., Vaughan, O. P. H., Abdulkin, P., Berenguer-Murcia, A., Tikhov, M. S., & Johnson, B. F. G. (2008). Selective oxidation with dioxygen by gold nanoparticle catalysts derived from 55-atom clusters. *Nature, 454*, 981–U931.

24. Ito, S., Miyoshi, N., Degraff, W. G., Nagashima, K., Kirschenbaum, L. J., & Riesz, P. (2009). Enhancement of 5-Aminolevulinic acid-induced oxidative stress on two cancer cell lines by gold nanoparticles. *Free Radical Research, 43*, 1214–1224.

25. Cao, R., Cao, R., Villalonga, R., Diaz-Garcia, A. M., Rojo, T., & Rodriguez-Arguelles, M. C. (2011). Gold nanoparticles enhancing dismutation of superoxide radical by its bis (dithiocarbamato) copper(II) shell. *Inorganic Chemistry, 50*, 4705–4712.

26. He, W. W., Zhou, Y. T., Warner, W. G., Hu, X. N., Wu, X. C., Zheng, Z., Boudreau, M. D., & Yin, J. J. (2013). Intrinsic catalytic activity of au nanoparticles with respect to hydrogen peroxide decomposition and superoxide scavenging. *Biomaterials, 34*, 765–773.

27. Wen, T., He, W. W., Chong, Y., Liu, Y., Yin, J. J., & Wu, X. C. (2015). Exploring environment-dependent effects of Pd nanostructures on reactive oxygen species (ROS) using electron spin resonance (ESR) technique: Implications for biomedical applications. *Physical Chemistry Chemical Physics, 17*, 24937–24943.

28. Gara, P. M. D., Garabano, N. I., Portoles, M. J. L., Moreno, M. S., Dodat, D., Casas, O. R., Gonzalez, M. C., & Kotler, M. L. (2012). ROS enhancement by silicon nanoparticles in X-ray irradiated aqueous suspensions and in glioma C6 cells. *Journal of Nanoparticle Research, 14*, 741.

29. Seo, S. J., Han, S. M., Cho, J. H., Hyodo, K., Zaboronok, A., You, H., Peach, K., Hill, M. A., & Kim, J. K. (2015). Enhanced production of reactive oxygen species by gadolinium oxide nanoparticles under core-inner-shell excitation by proton or monochromatic X-ray irradiation: Implication of the contribution from the interatomic de-excitation-mediated nanoradiator effect to dose enhancement. *Radiation and Environmental Biophysics, 54*, 423–431.

30. Cadet, J., & Wagner, J. R. (2016). Radiation-induced damage to cellular DNA: Chemical nature and mechanisms of lesion formation. *Radiation Physics and Chemistry, 128*, 54–59.

31. Burrows, C. J., & Muller, J. G. (1998). Oxidative nucleobase modifications leading to strand scission. *Chemical Reviews, 98*, 1109–1151.

32. Nishimura, S., Anh, T. N. D., Mott, D., Ebitani, K., & Maenosono, S. (2012). X-ray absorption near-edge structure and X-ray photoelectron spectroscopy studies of interfacial charge transfer in gold-silver-gold double-shell nanoparticles. *Journal of Physical Chemistry C, 116*, 4511–4516.

33. Ionita, P., Spafiu, F., & Ghica, C. (2008). Dual behavior of gold nanoparticles, as generators and scavengers for free radicals. *Journal of Materials Science, 43*, 6571–6574.

34. Zhang, Z. Y., Berg, A., Levanon, H., Fessenden, R. W., & Meisel, D. (2003). On the interactions of free radicals with gold nanoparticles. *Journal of the American Chemical Society, 125*, 7959–7963.

35. Hamasaki, T., Kashiwagi, T., Imada, T., Nakamichi, N., Aramaki, S., Toh, K., Morisawa, S., Shimakoshi, H., Hisaeda, Y., & Shirahata, S. (2008). Kinetic analysis of superoxide anion radical-scavenging and hydroxyl radical-scavenging activities of platinum nanoparticles. *Langmuir, 24*, 7354–7364.

36. Watanabe, A., Kajita, M., Kim, J., Kanayama, A., Takahashi, K., Mashino, T., & Miyamoto, Y. (2009). In vitro free radical scavenging activity of platinum nanoparticles. *Nanotechnology, 20*, 455105.

37. Sahbani, S. K., Cloutier, P., Bass, A. D., Hunting, D. J., & Sanche, L. (2015). Electron resonance decay into a biological function: Decrease in viability of E-coli transformed by plasmid DNA irradiated with 0.5-18 eV electrons. *Journal of Physical Chemistry Letters, 6*, 3911–3914.

38. Radiation damage: A new understanding. In *Current research on molecular processing.* http://www.isa.au.dk/networks/eipam/radam-research.html

39. Davidson, R. A., & Guo, T. (2015). Multiplication algorithm for combined physical and chemical enhancement of X-ray effect by nanomaterials. *Journal of Physical Chemistry, 119*, 19513–19519.

Chapter 4
Biological Enhancement of X-Ray Effects

One needs to delocalize in order to build bonds with others

4.1 Introduction

Physical enhancement, in the form of the sum of linear combination of types 1 and 2 physical enhancement discussed in Chap. 2, is the enhancement to which most researchers attribute when using nanomaterials to enhance the effectiveness of X-ray irradiation. The use of chemical reactions to probe physical enhancement led to the discovery of chemical enhancement, as demonstrated in Chap. 3. Beyond these fundamental processes, the most popular application area researchers have envisaged for X-ray nanochemistry is cancer treatment, which can be accomplished through X-ray irradiation of nanoparticle-embedded, or targeted, cancer cells or tumors. Given the complex nature of biological systems, however, it would be extremely unlikely if nanomaterials in a biological setting exhibit the same enhancement as physical or chemical or both as in rather clean aqueous solutions. For example, it would be unlikely for a chemically inert nanomaterial to generate only type 1 or 2 physical enhancement when the nanomaterial is placed in cells or animals. Examples shown in this chapter indicated that most published works have obtained a narrow range of enhancement values between 0.1 and 1.0 DEU in biological systems even though the predicted physical enhancement values vary from below 0.01 to above 100 DEU. There are several cases where agreement was reached between theoretically predicted physical enhancement and experimentally measured enhancement values, but these agreements could be just coincidence rather than provide the proof that the assignment of physical or chemical or both to be solely responsible for the measured enhancement fulfills the necessary and sufficient conditions. These results seem to imply that there are biological responses that work outside the principles of the known physical and chemical enhancement, and these responses can be considered as biological enhancement factors or biological enhancement. A more complete definition of biological enhancement is *any*

enhanced destruction of biological systems by nanomaterials under X-ray irradiation that is beyond simple addition of the known effects of X-ray irradiation, physical or chemical or both, and cytotoxicity of nanoparticles.

Examples given in Chaps. 2 and 3 demonstrate how difficult it is to interpret experimental results of enhancement measurements, even in well controlled and relatively simple environments. For example, it is difficult to fully understand the outcome of enhancement measurements in pure and isolated systems, such as irradiating aqueous solutions of 3-CCA mixed with gold nanoparticles. Nonetheless, it is now possible to gain an increasing degree of control over nanomaterials and experimental conditions to produce predictable chemical and especially physical enhancement, as shown in Chaps. 2 and 3. This is not yet the case for biological enhancement, as it is defined in this chapter, although some progress has been made. The reality is that even if we know a few pathways such as DNA repairs by proteins that are important to biological enhancement, these pathways may not be exclusively investigated in the enhancement measurements due to the overwhelmingly large number of processes in cells and animals. Another factor is that X-ray nanochemistry is in its infancy, and most published works employed commercially available or easily synthesized nanomaterials in their enhancement measurements while following largely different experimental procedures, which make measurements difficult to control or compare. These problems are compounded by that fact that theories to date can only predict physical enhancement in cells; no quantum chemistry theories are currently available to model chemical or biological enhancement in the cell. These constraints make studying biological enhancement difficult. Though the original intention of using nanomaterials in these measurements was to take advantage of physical enhancement offered by these nanomaterials, the true causes for the observed enhancement in biological systems were complex and often are not physical but biological; the damage or death of cells was often not caused by increased absorption of X-rays by nanomaterials but by many other biological factors such as blocking the function of DNA repair proteins or somehow creating oxidative stress to mitochondria. It is quite possible that these nonphysical factors are the true and dominating causes for the measured enhancements. In this sense, although conducting animal research is considered by many researchers to be the fastest route to examine whether nanomaterials can enhance destruction of biological targets, a positive outcome alone cannot always validate the original intention. This chapter shows a few biological pathways or biological enhancement through which the measured enhancement can be explained.

Evidence supporting the existence of biological enhancement is summarized here, which shows that nanomaterials may cause more than just physical enhancement, chemical enhancement, or anti-enhancement. All of the publications cited seem to exhibit biological enhancement as defined above, but differentiation between chemical and biological enhancement may be subtle as biological enhancement may rely on chemical properties of nanomaterials. The main difference is that biological enhancement may not necessarily require existence of chemical enhancement, just as chemical enhancement exists without physical enhancement. If biological enhancement truly exists, then it can stand alone without the need for

physical or chemical enhancement. Assignment of these enhancements in a quantitative manner in biological settings requires much more work as one would have to exclusively prove the existence of biological enhancement when there are negligible physical and chemical enhancement, which is not an easy task. At least in the works cited in this chapter, the enhancement is unlikely to be caused by physical enhancement alone. Although nanomaterials in some of the works may cause chemical enhancement, as the systems tested are biological, we choose to assign the enhancement to biological enhancement unless chemical enhancement is clearly identified. This practical generalization may be oversimplified or even flawed. Future work will be needed to address this issue.

Similar to isolation of physical and chemical enhancement, the benefits of exploring biological enhancement are manifold. Firstly, it helps to understand how to improve radiotherapy. If only physical or chemical enhancement is considered, then researchers may miss key elements and fail to use biological enhancement to further increase the total enhancement; even worse, nanomaterials and other conditions may be optimized for wrong reasons. Secondly, nanomaterials that cause biological enhancement may be different from those that cause physical or chemical enhancement. Therefore, these nanomaterials alone may not cause any physical or chemical enhancement and yet can still cause biological enhancement. Thirdly, the magnitude of each of the enhancements can only be determined after all of them are identified, isolated, and studied separately. Finally, the field of biology may be advanced when biological enhancement is understood. For example, it is possible to use biological enhancement to modify specific biological pathways, such as ATP production by mitochondria in a cell, to understand how to regulate cellular functions using X-rays.

In this chapter, results from publications are presented to lend support to the identification of biological enhancement. Other results showing measurements of enhancement in biological systems are given in Chaps. 8 and 9, which list the papers published as applications of X-ray nanochemistry in biology and medicine. Whenever possible, publications will be used to exhibit the measured and predicted enhancement values, with the intention of identifying the existence of biological enhancement. Publications without uptake data will not be discussed here because they cannot be used to determine whether the enhancement is physical.

Biological enhancement similar to what is discussed here has been mentioned in the literature. For example, Butterworth et al. [1] speculated that biological mechanisms might play a role in radiosensitization. The authors compared these biological mechanisms with physical enhancement and explicitly pointed out the discrepancies between the predicted physical enhancement values and enhancement values obtained using biological systems. Sicard-Roselli et al. [2] reviewed the literature on using biological systems to evaluate the enhancement and noticed that in many cases the observed enhancement values were much higher than the predicted physical enhancement. The authors pointed out several possible pathways that were supposed to create the proposed biological effects. More recently Geso et al. [3] and Rosa et al. [4] reviewed the work in the area of radiosensitization. The authors discussed three possible enhancement pathways that gave rise to physical, chemical,

and biological enhancement, similar to what are discussed in this book. Discussions in these review articles demonstrate that these categories and types of enhancement are gaining recognition.

4.2 Two Types of Biological Enhancement

Even though its existence has not been conclusively demonstrated in the literature, biological enhancement has been mentioned in multiple reports. Biological enhancement makes sense; if catalysis can enable chemical enhancement as shown in Chap. 3, then complicated biological systems should be able to create much greater enhancements than chemical systems. For example, one possible pathway of biological enhancement is when small nanoparticles bind to and hinder the function of DNA repair proteins in cellular nuclei. Under X-ray irradiation, nuclear DNA molecules in the cell incur more damage when invaded by small gold nanoparticles than without gold nanoparticles because these nanoparticles interfere with the repair of the damaged DNA sites by X-rays, thus causing more cells to be damaged than theoretically predicted physical enhancement.

Similar to chemical enhancement, the work of biological enhancement may or may not require increased absorption of X-rays by nanomaterials. Much more complex than chemical enhancement, biological enhancement can manifest in complex cellular systems through many pathways. Many of the reports shown in this book referred to only physical enhancement and did not mention biological enhancement, despite the possibility of the true cause of the measured enhancement being biological enhancement. To assess whether a measured enhancement is caused by biological enhancement in this chapter, physical enhancement is predicted based on the uptake data. Chemical enhancement including anti-enhancement is not estimated because of lack of formal theories to evaluate the magnitude of chemical enhancement. If the measured enhancement values are significantly different from the predicted physical enhancement, then the enhancement is attributed to biological enhancement if the measurement is performed in a biological system. Chemical enhancement is not considered even If it could exist alongside biological enhancement.

Biological enhancement can be divided into two types, similar to the conventions of types 1 and 2 chemical enhancement or types 1, 2, and 3 physical enhancement. Type 1 biological enhancement does not cause any direct modification to biological targets by nanomaterials, so it can be viewed as indirect modification or damage mechanisms. Type 2 biological enhancement causes direct modifications or damage to biological targets.

4.2.1   Type 1 Biological Enhancement

Type 1 biological enhancement is an indirect enhancement because no damage is directly generated to any biological targets by nanomaterials and X-rays acting together. In other words, the nanoparticles under X-ray irradiation do not cause any direct damage to biological systems. This means that nanoparticles do not generate physical or chemical enhancement. An example of type 1 biological enhancement is nanomaterials blocking DNA repair pathways by binding to or hindering the function of repair proteins. Figure 4.1 (left panel) shows such a pathway, which can explain the observed enhancement of cellular damage or tumor treatment when small gold nanoparticles are used in combination with X-rays; the combined effect of X-rays and nanomaterials is higher than the sum of using nanomaterials or X-rays separately. Without X-rays and nanomaterials, there is no enhancement because there is nothing to repair. After X-ray irradiation, nanomaterial-bound repair proteins may not be able to perform their repairing functions, and therefore damaged nuclear DNA cannot be properly repaired, reducing cellular reproduction or increasing other damages. This creates an equivalent effect of nanomaterials causing more damage to nuclear DNA or cell death even though nanoparticles themselves do not generate any direct damage to the DNA molecules.

Type 1 biological enhancement requires nanomaterials only to hinder certain biological functions, such as DNA repair by proteins. In this example, a gold nanoparticle shown in Fig. 4.1 (left panel) blocks the active site of the repair protein, which may be located next to the target DNA molecule. The nanoparticle does not need to absorb X-rays or cause damage to create DNA strand breaks. The damage to DNA is done by radicals generated in water irradiated with X-Rays. Although biological samples contain high concentrations of scavengers, these scavengers do
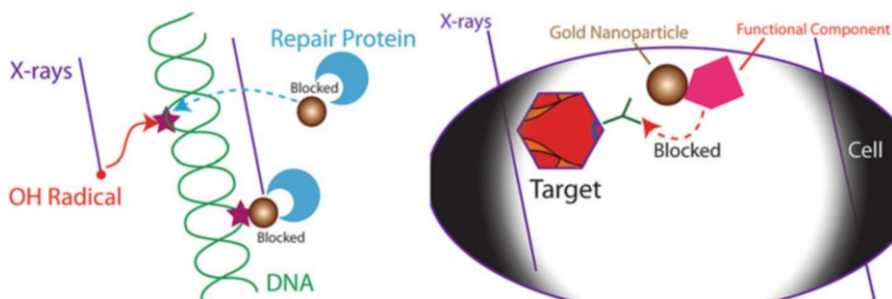
Fig. 4.1 Illustration of type 1 biological enhancement. The left panel shows an example of gold nanoparticles blocking the function of DNA repair proteins to achieve biological enhancement. Two nanoparticles at two positions are shown. The right panel shows a more general type 1 biological enhancement, in which the gold nanoparticle interferes with the function of another cellular component from distance

not interfere with the function of the nanomaterials because nanomaterials in type 1 biological enhancement do not cause any direct damage and is not subjected to scavenging interference. Figure 4.1 (right panel) shows a more generic pathway to damage a cellular component by a gold nanoparticle through type 1 biological enhancement. In this case, biological components that participate in the enhancement may not be located near the target.

In order to create type 1 biological enhancement, the nanomaterials have to meet several requirements. For example, if nuclear DNA damage is required, the size of nanoparticles has to be small enough so that the nanoparticles can easily enter the nuclei of human cells that have an average nuclear pore size of 5.2 nm (see Görlich et al. [5]). In addition, the nanoparticles should have affinity toward repair proteins or other biological targets. Besides nuclear DNA damage, other targets are available. For example, Taggart et al. [6] showed that 1.9 nm gold nanoparticles interacted with cellular enzyme protein disulfide isomerase (PDI) to cause disruption of thiol balance in the cell, eventually leading to cell death. Researchers currently have only begun to understand this type of enhancement, and consequently there is little optimization effort to create the optimal kind of nanoparticles for achieving the highest type 1 biological enhancement.

For this type of enhancement to work, there must not be any damage to the target by the nanoparticles under X-ray irradiation. For example, it is unnecessary for the repair proteins to be damaged by nanoparticles under X-ray irradiation—the gold nanoparticles just need to be bound to the protein to reduce or nullify the repair functionality. Once enough DNA sites are damaged, the cell dies or loses its reproductive ability, and various assays can be used to probe the responses.

4.2.2 Type 2 Biological Enhancement

Type 2 biological enhancement is biological amplification of direct damage of biological targets caused by nanomaterials located near the targets under X-ray irradiation. Nanomaterials bind to biological targets to cause enhanced damage under X-ray irradiation, and the damage can be further amplified biologically downstream. For instance, mitochondria or nuclear DNA can be directly damaged by electrons emitted from nanomaterials under X-ray irradiation or by reactive oxygen species the nanomaterials help generate when irradiated with X-rays. This mechanism is particularly plausible, given the fact that nanoparticles often aggregate once entering the cell, potentially causing type 2 physical enhancement or type 1 chemical enhancement or both. The effect of these damages can then be amplified to lead to significant cell damage or death due to the presence of both nanomaterials and X-rays.

Type 2 biological enhancement is not affected by high concentrations of scavengers in biological systems either because nanomaterials are close to biological targets or can emit electrons that deposit energy in the target region and cause damage. The damage may be caused by type 2 physical enhancement, although type 1 physical
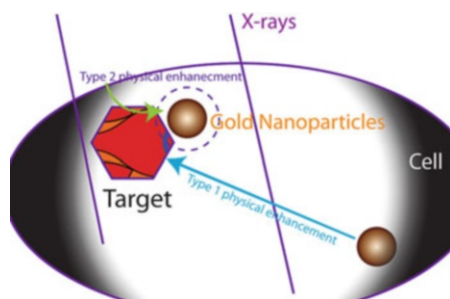
Fig. 4.2 Illustration of type 2 biological enhancement. The target to be damaged in the cell is shown together with two nanoparticles under X-ray irradiation through either type 2 physical enhancement/chemical enhancement by the nanoparticle next to the target, or type 1 physical enhancement by the nanoparticle afar from the target, or both. The damaged target then affects the survival of the cell, which can be detected using various assays

enhancement and chemical enhancement can also cause direct damage to biological components. Type 2 biological enhancement is illustrated in Fig. 4.2, which includes two gold nanoparticles: one next to the target and the other farther away from the target. The gold nanoparticle next to the target can provide type 2 physical enhancement or chemical enhancement. Once the target is damaged, the biological system will amplify the effect. Although the direct damage may be small, the final enhancement can be high due to biological amplification. Also shown in Fig. 4.2 is type 1 physical enhancement from the nanoparticle afar; large quantities of nanomaterials are required to cause damage to targets at a distance through type 1 physical enhancement.

Another pathway to destroy cells is by damaging DNA or RNA in bacteria. Unlike eukaryotic cells, there are no nuclear envelopes in prokaryotic cells, and the nuclear DNA can be damaged even with large nanomaterials that exert strong type 2 physical enhancement as shown in Fig. 2.35. However, the size or mass of DNA in bacteria is 1000 times smaller than nuclear DNA in eukaryotic cells; therefore, it takes greater doses (on the order of 1000 times) of X-rays to damage prokaryotic DNA in isolated cells. Due to this limitation, damaging prokaryotic cellular DNA in isolated cells is much more difficult than eukaryotic cellular DNA in isolated cells through the assistance of nanoparticles even if nanoparticles can cause high biological enhancement in bacterial DNA damage. For example, Su et al. [7] demonstrated a 37 DEU enhancement with bismuth nanoparticles. In this work, the authors considered the enhancement to be caused by only physical enhancement. Although physical enhancement should exist, biological enhancement should not be excluded. When the cells are not isolated as in organisms, bacteria can be damaged more efficiently by reactive oxygen species generated in the vicinity of the cells by ionizing radiation. Under this circumstance, the process of damaging prokaryotic cells using X-ray nanochemistry, together with proper targeting, can possibly help destruct harmful bacteria in humans.

4.3   Examples of Possible Biological Enhancement

Here, the existence of biological enhancement is demonstrated by the results of the measured enhancement values being significantly different from those predicted based on the uptake data. Other publications showing enhancement when using nanomaterials in biological systems are given in Chaps. 8 and 9. Even though the results suggest biological enhancement, none of the reports shown here actually cited biological enhancement as the origin of enhancement. Direct references to biological enhancement in the literature were given in the reviews by Rosa et al. [4] and Geso et al. [3].

4.3.1   Evidence for Biological Enhancement in Eukaryotic Cells

There have been many enhancement measurements taken place using biological systems. This section reviews evidence in these publications that suggests the existence of biological enhancement. Only the reports whose enhancement results did not match the predicted physical enhancement are mentioned here to support the existence of biological enhancement. It is impossible at this time to clearly assign enhancement mechanisms. The authors in these works may or may not state the cause for the enhancement, although most of the reports implied that the experimentally observed enhancement was caused by physical enhancement. In the future, it will be critical that biological enhancement is clearly isolated and measured. Although it is still impossible to rule out chemical enhancement, because the publications shown here all used biological systems such as cells or animals, biological instead of chemical enhancement is credited.

Hainfeld et al. [8] reported the first animal study of gold nanoparticle enhancement of radiotherapy. They observed an encouraging 86% increase in survival rate compared to 20% with X-rays alone. In a follow-up study, Hainfeld et al. [9] reported the biodistribution of 1.9 nm gold nanoparticles in mice. In these studies, gold loadings were high. Figure 4.3 shows the calculated loadings. For example, the concentration of gold in the blood was 15.9 mg/g or 1.59 WP 5 min after injection of 13.5 WP gold in water (135 mg/cc) into the mice. Gold loading in the tumor was only 0.23 WP. For 250 kVp, the predicted physical enhancement using the tumor loading was approximately 0.2 DEU. The time spent under irradiation was 5 min. If the survival fraction numbers were used in enhancement calculations, then the measured enhancement would be nearly 0.58 DEU. This value is higher than the predicted physical enhancement based on the biodistribution data, showing possible biological enhancement, even though the differences between the two is mild. The authors reported an enhancement of 5.5 DEU.

Roa and Xing et al. [10] used gold nanoparticles to treat prostate cancer to demonstrate the utility of gold nanoparticles in cancer therapy. The size of their
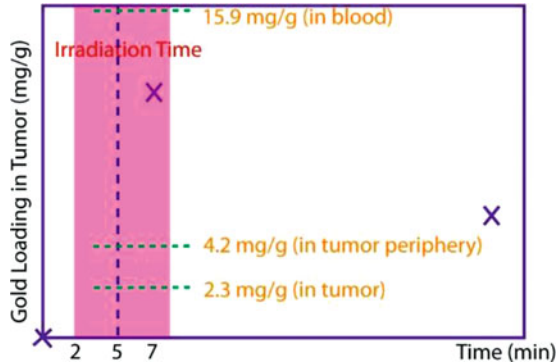
Fig. 4.3 Gold loading in mice as a function of time. The data was obtained by Hainfeld et al. [9]. The irradiation time was 5 min, during which the loading of gold was 0.23 WP in the tumor. If this value was used to predict physical enhancement, then the theoretically predicted enhancement was less than half of the measured value

nanoparticles was ca. 7 nm in diameter, and gold nanoparticles were coated with thiol glucose. The authors used DU-145 prostate cancer cell line. The radiation was 200 kVp X-rays, and dose was 2 Gy. The uptake was 67,000 nanoparticles per cell, corresponding to a 0.05 WP gold loading. This would give rise to a 0.05 DEU physical enhancement. The experimental enhancement measured with the inhibition rate was as high as 1 DEU, much higher than the predicted physical enhancement. The authors did note that the destruction of tumors did not completely correlate with the uptake concentrations of nanoparticles. Roa and Xing et al. [11] again investigated enhanced damage to human prostate cancer cells with the assistance of gold nanoparticles under X-ray irradiation. Based on their uptake data, the loading of 7×10^4 10 nm diameter gold in cells was 0.07 WP. Physical enhancement should be less than 0.07 DEU for 1.76 MeV X-rays from ^{137}Cs. The measured enhancement was between 0.5 DEU and 1.0 DEU, again suggesting strong biological enhancement.

Chithrani et al. [12] compared enhancement by gold nanoparticles under 105 kVp and 6 MeV X-ray irradiation. The gold size ranged from 14 to 74 nm, and the optimal size for maximum uptake was found to be 50 nm. Enhancements from 50 nm gold nanoparticles were 0.66 DEU and 0.15 DEU at these two X-ray energies, respectively. Due to the large sizes of the particles, the probability of the particles entering the nuclei was low, which almost eliminated the chance of biological enhancement through hindering the repair protein pathway. The loading of gold in cells was calculated to be around 1 WP based on the weight of gold in cells. This loading should produce approximately a 1 DEU enhancement in cell damage, which was higher than the measured 0.66 DEU enhancement for 105 kVp. For 6 MeV, the enhancement should be a few percent at most, which was lower than the measured enhancement of 0.15 DEU. This study showed a weak biological enhancement, which is expected due to the use of large gold nanoparticles.

Kong et al. [13] reported using 90 keV or 6 MeV X-rays to irradiate thioglucose-bound gold nanoparticles incubated with human ovarian cancer cell SK-OV-3 and found 0.3 DEU and 0.27 DEU enhancements in inhibition of cancer cell growth at these two energies, respectively. Using the uptake data provided in the report, the weight percentage of gold in the cell was only 0.024 WP, which should give rise to 0.03 DEU physical enhancement, much lower than the measured enhancement. In addition, the results were abnormal because the two enhancements should be quite different at two energies. These results again suggested the existence of biological enhancement although chemical enhancement was also possible.

Chen et al. [14] performed a study that revealed possible biological enhancement by gold nanoparticles (AuNPs). In their work, 2.0–2.5 nm gold nanoparticles conjugated with ubiquitin-like modifier ligands were used. These nanoparticles were designed to bind to DNA repair proteins with high affinity, partially due to the large number of ligands per nanoparticle. These nanoparticles themselves were not toxic and did not cause enhanced damage to the proteins under X-ray irradiation. However, under X-ray radiation the nanoparticles caused damage to the cell by blocking the repair function of the proteins. Figure 4.4 shows the formula of the
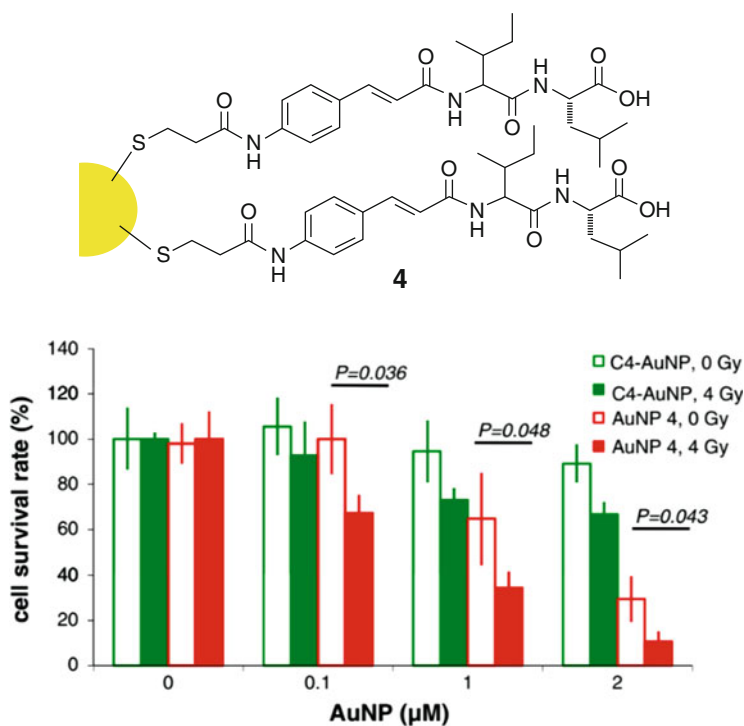
Fig. 4.4 An example of biological enhancement in which 2 nm gold nanoparticles were used to bind to DNA repair proteins in cells to increase cell death upon irradiation with X-rays. The top panel shows the ligand, and the bottom panel shows the results. (Reprinted from Chen et al. [14]. "Copyright (2012) National Academy of Sciences".)

ligand-conjugated gold nanoparticles (top panel) as well as the cell survival rate data (bottom panel). It is worth pointing out that at 0.1 μM incubation concentration, the only gold nanoparticles affecting the survival rate was AuNP **4**, which was the conjugated nanoparticles; controls or other kinds of gold nanoparticles did not show much damage. Physical enhancement was difficult to assess because the magnitude of uptake was unknown. The percentage of these small nanoparticles ionized by X-rays was small. For 4 Gy of irradiation, direct ionization percentage was less than 1 ppm. Due to this, physical enhancement should not play any significant role. Although chemical enhancement was possible, to date it is not known that proteins can be easily damaged with 4 Gy of X-rays, even with assistance of chemical enhancement. Therefore, it is more likely that this was a case of biological enhancement.

Rahman and Geso et al. [15] observed a 2.47 DEU enhancement using only a 0.02 WP gold nanoparticle loading in bovine aortic endothelial cells. The results are shown in Sect. 8.3.1. The authors employed monochromatic X-rays emitted from a synchrotron source and 1.9 nm gold nanoparticles. The X-ray energies ranged from 30 keV to 100 keV in 10 keV steps. The calculated enhancements by the authors ranged from 0.005 to 0.04 DEU, which were significantly lower than the experimentally measured enhancement values. Although the absolute values of the calculated and experimentally measured data were different, the trends were close to each other. The experimentally measured enhancements were 50–100 times higher than the theoretically predicted physical enhancement values. The drastic increase in the experimentally observed enhancement could come from biological enhancement. It was unclear as to which type of biological enhancement attributed to the observed damage.

Recently Guo and Xie et al. [16] studied radiotherapy using gold clusters containing only 29–43 gold atoms covered with reduced glutathione ligands. The loading of gold in the tumor was a few micrograms per g of tissue or 10^{-3} WP. Physical enhancement for such a small loading of gold would only be a fraction of 1%. Instead, the authors observed almost no growth of tumor volume after 28 days with gold nanoparticles, whereas tumors in mice without gold nanoparticles and radiation grew fivefold over 28 days. Figure 4.5 shows the results. As shown in the right panel, there is a clear advantage in using these small nanoparticles even though the uptake (shown in the left panel) was at the ppm level, which was extremely low. The results suggested that there must be a nonphysical enhancement that suppressed tumor growth. Although chemical enhancement cannot be ruled out, this was another case where biological enhancement was strongly indicated.

Geso et al. [3] used TiO_2 nanoparticles as radiosensitizers and performed both dosimetric and in vitro studies. The results are shown in Chap. 9, which indicated that in vitro enhancements were higher than dosimetrically obtained values. No theoretical studies were performed. The authors suggested the existence of both chemical and biological effects.
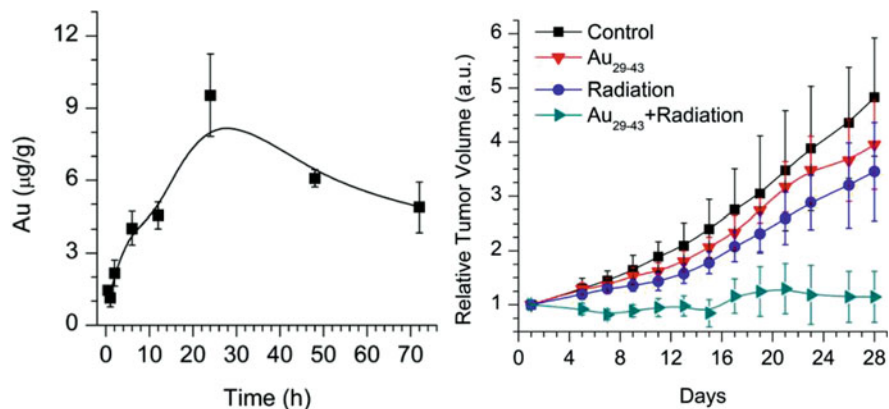
Fig. 4.5 Ultrasmall gold nanoparticles (Au_{29-43}) for radiotherapy. The left panel shows the uptake or loading measurements, and the right panel shows the tumor growth rate data. (Adapted from Guo and Xie et al. [16] CC BY 4.0.)

4.3.2 Biological Enhancement in Bacteria

Bacteria alone are generally thousands of times more radioresistive than isolated human cells. For example, LD_{50} for many human cell lines is around 4–5 Gy, as shown in Chaps. 8 or 9. For isolated bacteria such as *E. Coli* or *Pseudomonas aeruginosa*, LD_{50} are around 3000–4000 Gy, depending on the strains. One example given by Li et al. [17] showed an LD_{50} of 3600 Gy. This significant decrease in radiosensitivity or increase in radioresistance for bacteria compared to human DNA is largely caused by the chromosomal DNA size difference between the two: an average human nuclear DNA contains about 3000 mega base pairs (Mbp), whereas an average bacterial nuclear DNA contains about a Mbp. Chromosomal DNA of *E. Coli*, for example, is about 4.6 Mbp. This means that it is impossible to kill isolated bacteria in humans using enhancement mechanisms provided by current X-ray nanochemistry principles because commonly measured dose enhancement factors are less than 100 DEU. However, this is not the case for bacteria living in organisms such as human guts because X-rays can generate unfavorable conditions to bacteria. In these cases, bacteria are quite sensitive to ionizing radiation such as X-rays.

Bacteria can be killed with increased effectiveness using X-ray nanochemistry approaches. Adding nanoparticles made of heavy elements, and specially functionalized with targeting moieties such as antibodies, can enhance the radiosensitivity of bacterial cells under X-ray irradiation. In one report, Su et al. [18] theoretically calculated the damage to *E. Coli* by adding platinum, gold, and bismuth nanoparticles irradiated with diagnostic X-rays at three voltages of 50, 110, and 300 kVp. The results showed that damage by bismuth nanoparticles was greater than gold and platinum nanoparticles of a similar loading. The results are shown in Fig. 2.38 (left panel) for 0.7 WP bismuth in the cell irradiated with 50 kVp

X-rays. The theoretically predicted enhancement was only 0.03 DEU when photo-electrons were considered and became nearly 4.0 DEU when Auger electrons were included. The authors attributed the higher enhancement by bismuth to greater absorption cross-sections of X-rays by bismuth. In a related work, Su et al. [7] conducted an experimental work using *P. aeruginosa* as the target. In their work, they employed bismuth nanoparticles covered with antibodies and observed significant enhancement of cell damage for nanoparticles with antibodies. X-rays were from 40 kVp X-ray sources operated at 100 µA on an Ag target. 0.25 mm thick Al and 25 µm thick Ag filter were used to reduce low-energy (0–15 keV) X-rays. The dose rate was 400 mGy/20 min or 0.02 Gy/min, and irradiation time was 10 min, giving a total dose of 0.2 Gy, which was four orders of magnitude less than the 3600 Gy LD_{50} for isolated *P. aeruginosa* shown by Li et al. [17]. Due to the low operating voltage, low-energy X-rays used in this case may cause strong chemical enhancement or generate large quantities of reactive oxygen species that could etch or reduce nanoparticles, which can activate different enhancement pathways. The results showed a significant reduction in the ability of cell reproduction after X-ray irradiation of 0.2-Gy. The authors also conducted cytotoxicity measurements using HeLa cells as a control and found that unmodified bismuth could damage 21% of HeLa cells with a 0.02 WP incubation concentration, though no update data was available. Bismuth nanoparticles themselves did not cause additional toxicity to bacteria at a loading of up to 5 WP. The authors obtained a 37-fold enhancement based on their data, which is one of the highest enhancements measured to date. An enhancement of 11 DEU is obtained using the data shown in Fig. 4.6, which is close to the theoretically predicted enhancement value. It seems difficult to use type 1 or 2 physical enhancements or type 1 or 2 chemical enhancement to explain the results, as bismuth is generally not catalytically active. One possibility is that it may be caused by biological enhancement within *P. aeruginosa*. The exact mechanisms are unclear.

Fig. 4.6 Results of enhanced damage to bacterial cells using bismuth nanoparticles irradiated with X-rays. Enhancement obtained here was 37 DEU according to the authors. (Adapted in part from Su et al. [7] with permission of the Royal Society of Chemistry.)
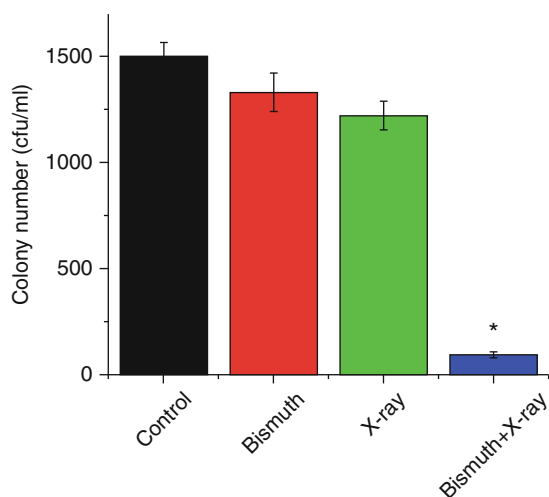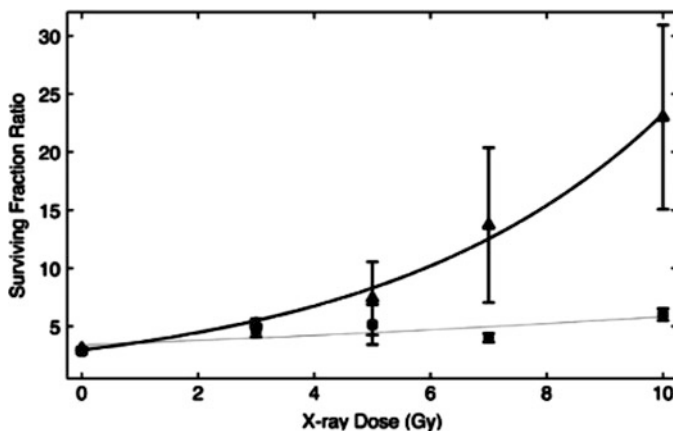
Fig. 4.7 Cell survival fraction measurements of brain tumor cells loaded with a platinum complex irradiated with 160 kVp (solid triangles) and 6 MV (solid squares) X-rays. Significant enhancement was measured for 160 kVp X-rays with 7 ppm loading of gold in the cell. Little enhancement was detected for 6 MV X-rays. (Reprinted from Barth et al. [19] CC BY.)

Another study was performed by Barth et al. [19] who used brain tumor cells in rats to measure the enhancement by terpyridine-coordinated platinum ions. The authors observed a measurable enhancement using 160 kVp X-rays and a platinum compound loading of below 7 ppm, an enhancement clearly surpassed the theoretically predicted enhancement for only type 1 or 2 physical enhancement based on increased X-ray absorption by nanomaterials. Figure 4.7 shows their experimental results. The authors stressed that future studies are needed to explain the observed enhancement. It is interesting to point out that 6 MV irradiation did not generate a similar enhancement to 160 kVp X-rays, suggesting that the enhancement should not arise from chemical enhancement. Since physical enhancement was too low, the observed enhancement was one of the most definitive result of biological enhancement.

4.3.3   Other Discussions of Biological Enhancement

In work performed by Allen et al. [20], the authors commented on the biological, chemical, and physical enhancement. Their results showed limited enhancement using gold nanoparticles and pentamidine under X-ray irradiation. The authors also pointed out two possible biological pathways: first, through affecting cell cycle synchronization (CCS) and second, through inhibition of radiation-induced DNA repair. The former can be type 1, type 2, or both biological enhancement, and the latter is considered as type 1 biological enhancement in this chapter. Cell cycle synchronization should require different experimental conditions from inhibition of DNA repair.

The impact of cell division cycle on uptake of nanomaterials has been reported and discussed, which is unique to biological systems and was reviewed by Sicard-Roselli et al. [2]. This cellular characteristic demonstrated the need for standard experimental procedures so that experimental results from different groups can be compared. Physical enhancement can be estimated when the uptake data is available, which may facilitate the determination of the magnitude of biological enhancement.

Another way to generate biological enhancement is accomplished through dose hypofractionation. The working of such methods relies on the intrinsic differences between damage to tumor and healthy cells by X-rays. It is possible that the addition of nanomaterials can expand the benefits of this approach, as mentioned by Jain et al. [21] in their review.

4.3.4   Differences Between Biological Enhancement and Other Enhancements

As shown in Chap. 2, physical enhancement may be predicted theoretically and then measured with carefully designed nanomaterials and experiments. There is no existing theory to predict chemical enhancement. However, chemical enhancement can be measured in well-controlled environments as demonstrated in Chap. 3 if nanomaterials can be properly prepared and physical enhancement can be adequately isolated or managed. It is much more difficult to isolate, measure, or theoretically predict biological enhancement. One necessary step is to isolate or remove physical and chemical enhancement before biological enhancement is measured. This is neither an easy nor impossible task. Based on the discussion in this chapter, biological enhancement may or may not require physical or chemical enhancement. For example, type 1 biological enhancement does not require either enhancement. In contrast, type 2 biological enhancement does need either or both enhancements. These relationships will help define and determine biological enhancement.

4.4   Conclusions and Future Work

Evidence shown in this chapter suggests the existence of biological enhancement caused by nanomaterials in biological systems irradiated with X-rays. Several works indicate that unless biological enhancement exists, it is difficult to explain the results based on only physical enhancement. Results showns in this chapter suggest that even chemical enhancement could not explain the results. Ideally, experiments should be done with nanomaterials that possess neither physical nor chemical enhancement to prove conclusively the existence of biological enhancement. Unfortunately, there has been no detailed theoretical study of biological enhancement

other than predicting DNA damage by radiation in presence of nanomaterials [22] using the code PARTRAC, as reviewed by Friedland et al. [23]. Bridging this theoretical gap is possibly more important than experiments themselves as the theory will guide the design and execution of experiments as well as explain the results.

In this chapter two types of biological enhancements are described. The experimental results shown here do not conclusively support one or the other, although several reports come close to achieving this goal. These reports are cited here because the results cannot easily be explained with physical and chemical enhancement defined in Chaps. 2 and 3. Confirmation of the existence of biological enhancement in the forms described in this chapter will have to wait until well-designed experiments are performed. A full understanding of biological enhancement would require biological studies at the cellular and animal levels. Studying nanomaterial-adding biological systems, however, has a much higher degree of difficulty than studying chemical or physical enhancement in aqueous solutions. Working with nanomaterials without careful characterization or purification methods may produce results that are heavily influenced by chemicals in the nanomaterials but not the nanomaterials themselves. Future work must be performed with high purity nanomaterials, although purification could alter nanomaterials.

It is an exciting time for X-ray nanochemistry because many new experiments and theoretical works will be performed in the area of biological enhancement. Future work will most likely be developed on several fronts simultaneously, including nanobiology or nanochemical biology and their X-ray derivatives, such as X-ray nanobiology, X-ray chemical biology, or X-ray nanochemical biology. Biological enhancement may have to be achieved through clever nanomaterial-assistant biological experiments because biology seems to suppress radicals generated by X-rays. Nanobiology may have to be used to overcome this barrier; it is possible to use biology to help realize the goals of X-ray nanochemistry that would otherwise be difficult to reach with simple chemical or nanochemical systems. Another particular area of work that can potentially benefit the study of biological enhancement is theoretical modeling. Currently, it is too difficult to theoretically model the whole cell, although modeling certain pathways is within reach. Creating biological enhancement using X-ray nanochemistry in biological systems may help improve theoretical understanding of these systems. Simulations may be developed to model important biological pathways in combination with nanobiology and chemical biology to understand biological enhancement.

References

1. Butterworth, K. T., McMahon, S. J., Currell, F. J., & Prise, K. M. (2012). Physical basis and biological mechanisms of gold nanoparticle radiosensitization. *Nanoscale, 4*, 4830–4838.
2. Brun, E., & Sicard-Roselli, C. (2016). Actual questions raised by nanoparticle radiosensitization. *Radiation Physics and Chemistry, 128*, 134–142.

3. Youkhana, E., Feltis, B., Blencowe, A., & Geso, M. (2017). Titanium dioxide nanoparticles as radiosensitisers: An in vitro and phantom-based study. *International Journal of Medical Sciences, 14*, 602–614.

4. Rosa, S., Connolly, C., Schettino, G., Butterworth, K. T., & Prise, K. (2017). Biological mechanisms of gold nanoparticle radiosensitization. *Cancer Nanotechnology, 8*(1), 2.

5. Mohr, D., Frey, S., Fischer, T., Guttler, T., & Gorlich, D. (2009). Characterisation of the passive permeability barrier of nuclear pore complexes. *The EMBO Journal, 28*, 2541–2553.

6. Taggart, L. E., McMahon, S. J., Butterworth, K. T., Currell, F. J., Schettino, G., & Prise, K. M. (2016). Protein disulphide isomerase as a target for nanoparticle-mediated sensitisation of cancer cells to radiation. *Nanotechnology, 27*, 215101.

7. Luo, Y., Hossain, M., Wang, C. M., Qiao, Y., An, J. C., Ma, L. Y., & Su, M. (2013). Targeted nanoparticles for enhanced X-ray radiation killing of multidrug-resistant bacteria. *Nanoscale, 5*, 687–694.

8. Hainfeld, J. F., Slatkin, D. N., & Smilowitz, H. M. (2004). The use of gold nanoparticles to enhance radiotherapy in mice. *Physics in Medicine and Biology, 49*, N309–N315.

9. Hainfeld, J. F., Slatkin, D. N., Focella, T. M., & Smilowitz, H. M. (2006). Gold nanoparticles: A new X-ray contrast agent. *The British Journal of Radiology, 79*, 248–253.

10. Zhang, X. J., Xing, J. Z., Chen, J., Ko, L., Amanie, J., Gulavita, S., Pervez, N., Yee, D., Moore, R., & Roa, W. (2008). Enhanced radiation sensitivity in prostate cancer by gold-nanoparticles. *Clinical and Investigative Medicine, 31*, E160–E167.

11. Roa, W., Zhang, X. J., Guo, L. H., Shaw, A., Hu, X. Y., Xiong, Y. P., Gulavita, S., Patel, S., Sun, X. J., Chen, J., Moore, R., & Xing, J. Z. (2009). Gold nanoparticle sensitize radiothrapy of prostate cancer cells by regulation of the cell cycle. *Nanotechnology, 20*(375101), 1–9.

12. Chithrani, D. B., Jelveh, S., Jalali, F., van Prooijen, M., Allen, C., Bristow, R. G., Hill, R. P., & Jaffray, D. A. (2010). Gold nanoparticles as radiation sensitizers in cancer therapy. *Radiation Research, 173*, 719–728.

13. Geng, F., Song, K., Xing, J. Z., Yuan, C. Z., Yan, S., Yang, Q. F., Chen, J., & Kong, B. H. (2011). Thio-glucose bound gold nanoparticles enhance radio-cytotoxic targeting of ovarian cancer. *Nanotechnology, 22*(285101), 1–8.

14. Li, Y. J., Perkins, A. L., Su, Y., Ma, Y. L., Colson, L., Horne, D. A., & Chen, Y. (2012). Gold nanoparticles as a platform for creating a multivalent poly-SUMO chain inhibitor that also augments ionizing radiation. *Proceedings of the National Academy of Sciences of the United States of America, 109*, 4092–4097.

15. Rahman, W. N., Corde, S., Yagi, N., Aziz, S. A. A., Annabell, N., & Geso, M. (2014). Optimal energy for cell radiosensitivity enhancement by gold nanoparticles using synchrotron-based monoenergetic photon beams. *International Journal of Nanomedicine, 9*, 2459–2467.

16. Zhang, X. D., Luo, Z. T., Chen, J., Song, S. S., Yuan, X., Shen, X., Wang, H., Sun, Y. M., Gao, K., Zhang, L. F., Fan, S. J., Leong, D. T., Guo, M. L., & Xie, J. P. (2015). Ultrasmall glutathione-protected gold nanoclusters as next generation radiotherapy sensitizers with high tumor uptake and high renal clearance. *Scientific Reports UK, 5*, 8669.

17. Li, Y. Y., Wang, Z. L., Liu, X. X., Tang, J. Y., Peng, B., & Wei, Y. Q. (2016). X-ray irradiated vaccine confers protection against pneumonia caused by pseudomonas aeruginosa. *Scientific Reports UK, 6*, 18823.

18. Hossain, M., & Su, M. (2012). Nanoparticle location and material-dependent dose enhancement in X-ray radiation therapy. *Journal of Physical Chemistry C, 116*, 23047–23052.

19. Lim, S. N., Pradhan, A. K., Barth, R. F., Nahar, S. N., Nakkula, R. J., Yang, W. L., Palmer, A. M., Turro, C., Weldon, M., Bell, E. H., & Mo, X. (2015). Tumoricidal activity of low-energy 160-KV versus 6-MV X-rays against platinum-sensitized F98 glioma cells. *Journal of Radiation Research (Tokyo), 56*, 77–89.

20. Her, S., Cui, L., Bristow, R. G., & Allen, C. (2016). Dual action enhancement of gold nanoparticle Radiosensitization by Pentamidine in triple negative breast cancer. *Radiation Research, 185*, 549–562.

21. Coulter, J. A., Butterworth, K. T., & Jain, S. (2015). Prostate cancer radiotherapy: Potential applications of metal nanoparticles for imaging and therapy. *The British Journal of Radiology, 88*, 20150256.
22. Xie, W. Z., Friedland, W., Li, W. B., Li, C. Y., Oeh, U., Qiu, R., Li, J. L., & Hoeschen, C. (2015). Simulation on the molecular radiosensitization effect of gold nanoparticles in cells irradiated by x-rays. *Physics in Medicine and Biology, 60*, 6195–6212.
23. Friedland, W., Dingfelder, M., Kundrat, P., & Jacob, P. (2011). Track structures, DNA targets and radiation effects in the biophysical Monte Carlo simulation code PARTRAC. *Mutation Research Fundamental and Molecular Mechanisms of Mutagenesis, 711*, 28–40.

Chapter 5
Isolation, Optimization, and Combination of Individual Enhancements

It would be nice if we had scientific politics. Instead we have political science.

5.1 Introduction

As shown in Chaps. 2, 3, and 4, there are at least three categories of enhancement, and each category can be further divided into several types. More than one category or type of enhancement usually exists in a specific study. If these individual enhancements can be combined constructively, then the total enhancement may be significantly greater than any individual enhancements. On the other hand, if these enhancements are randomly combined, then the total enhancement may be even lower than the highest individual enhancements. This chapter analyzes several scenarios and algorithms reported in the literature that have successfully demonstrated the benefits of such constructive combinations.

The ultimate goal of researching the algorithms governing the combination of individual enhancements is to achieve a maximum total enhancement. To reach this goal, at least four areas of research need scrutiny. The first area is to design nanomaterials for the highest individual enhancements so that these enhancements can be combined. This is equivalent to isolating and maximizing individual enhancements. Often, although not always, different enhancements need different nanomaterials. For instance, large gold nanoparticles are needed to generate strong type 1 physical enhancement, whereas small gold nanoparticles are needed to enable high chemical enhancement. Figure 5.1 illustrates several individual enhancements that can be generated from a nanoparticle. Enhancement units are DEU. The second area of interest is related to finding the necessary nanomaterials and experimental conditions for the highest total enhancement when the nanomaterials are combined because often this requires the use of many different kinds of nanomaterials, and conditions have to be adjusted away from those used to achieve optimal individual enhancements. If conditions are not properly prepared, many individual enhancements interfere destructively with each other. An example is that type 2 chemical enhancement such as anti-enhancement reduces physical enhancement, as shown in
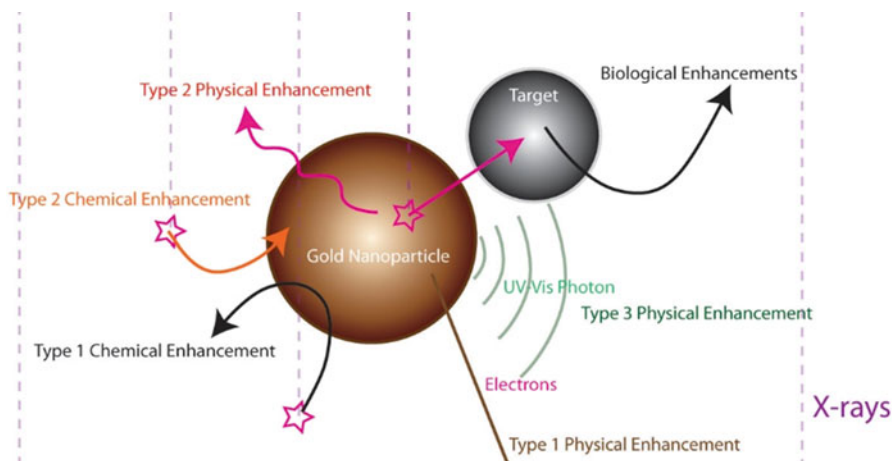
Fig. 5.1 Categories and types of enhancement by nanomaterials under X-ray irradiation. A gold nanoparticle is depicted here. Upon irradiation, electrons and light emit from the gold nanoparticle and interact with either a target or medium around the nanoparticle. Type 1 physical enhancement derives from energetic electrons, type 2 physical enhancement originates from low-energy electrons, and type 3 physical enhancement is represented by the UV-Vis photon shown here. Also shown is type 1 chemical enhancement from reactions catalyzed by the surface of the gold nanoparticle and type 2 chemical enhancement from scavenging of radicals by the surface. Type 2 biological enhancement is described here (as indicated by "Biological Enhancement")

Sect. 3.4.2.2. It is also possible that when chemical enhancement is combined with physical enhancement, not only small nanoparticles with large surface areas per unit mass are needed to work with large nanoparticles with inert surface to produce the highest total enhancement, but also the X-ray energies need to be adjusted so that the total enhancement is the highest even though individual enhancements at this energy are not. This is because the optimal energies for physical and chemical enhancement are different, with low (<20 keV)- or very high (>100 keV)-energy X-rays favoring chemical enhancement and moderate (50–60 keV)-energy X-rays being ideal to generate physical enhancement. As a result, X-ray energies need to be correctly selected if a maximum total enhancement is desired. The third area is the design or selection of probe reactions to take advantage of the available enhancements because suitable probing reactions need to be chosen to fiducially measure the total enhancement. This is true especially because chemical enhancement is dependent on probing reactions and these probing reactions can be influenced by chemical enhancement. The last area is the discovery of algorithms controlling how the total enhancement depends on individual enhancements. The search for algorithms can provide the guidance for studying the other three areas mentioned above.

In summary, individual enhancements have to be isolated, optimized, and eventually combined using a suitable selection of carefully prepared nanomaterials, experimental conditions, as well as reactions to help uncover the algorithms for the combined individual enhancements. Three examples of combining individual enhancements are given in this chapter.

5.2   Isolation and Optimization of Individual Enhancements

Combination of enhancements begins with isolation and optimization of each enhancement. According to Chaps. 2, 3, and 4, there are many categories of enhancement, and each category contains several types. For example, there are three types of physical enhancement. Type 1 physical enhancement is associated with relative constant enhancement over the whole sample volume, and type 2 physical enhancement refers to local or nanoscale enhancement near the surface of nanomaterials. Type 3 physical enhancement relates to increased UV-Vis photon emission from nanomaterials upon irradiation with X-rays. There exist at least two types of chemical enhancement, and each type has many variations, depending on the probing or target reactions, whether it is hydroxylation or polymerization or other kinds of reactions. There is also biological enhancement, which could potentially contain different types of enhancement as well. These enhancements can coexist or interfere with each other constructively or destructively. For instance, almost all nanomaterials can cause physical enhancement, and large nanoparticles can generate strong type 2 physical enhancement near the surface. High concentrations of large nanoparticles can also generate type 1 physical enhancement. Small nanomaterials can generate chemical enhancement, anti-enhancement, or both, depending on the nanoparticles and chemical reactions. So what are the algorithms governing the total enhancement when these individual enhancements are combined?

This section describes how to isolate and optimize individual enhancements, and discussion is limited to the individual enhancements appeared in the literature. In the following, isolation of types 1 and 2 physical enhancement is briefly reviewed, followed by discussion of type 1 chemical enhancement and anti-enhancement as a special case of type 2 chemical enhancement. It is important to consider anti-enhancement because it should be minimized if the highest enhancement is to be obtained. These discussions are brief because the detailed methods to isolate these enhancements are already given in Chaps. 2 and 3. No discussion is given to biological enhancement as there are no publications on isolation and optimization of biological enhancement or combinations of this enhancement with other enhancements. However, it is foreseeable that biological enhancement will play an important role in future work to help achieve a higher total enhancement.

5.2.1   Isolation and Optimization of Type 1 Physical Enhancement

As shown in Chap. 2, integrated types 1 and 2 physical enhancement was the original enhancement researchers initially intended to create. In order to detect pure type 1 physical enhancement, other enhancement processes are removed. A discussion on how to achieve type 1 physical enhancement is given in Sect. 2.4.2. To date, only a limited number of reports are dedicated to studying exclusive type 1 physical
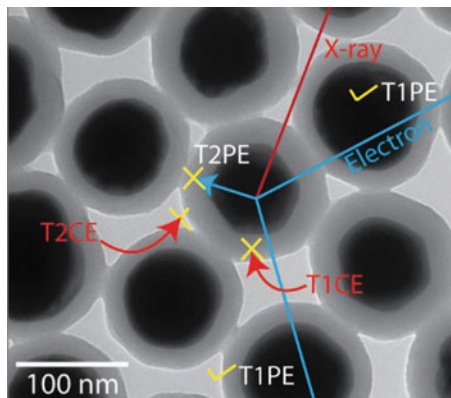
Fig. 5.2 Illustration of types 1 and 2 physical enhancements (T1PE and T2PE) and types 1 and 2 chemical enhancements (T1CE and T2CE). In this case, all enhancements except for T1PE are eliminated because the surface of gold nanoparticles is covered with a layer of silica. (Adapted with permission from Guo et al. [1]. Copyright (2014) American Chemical Society.)

enhancement. To do so, for example, it is necessary to have minimal or no anti-enhancement or chemical enhancement, which requires the nanomaterials to have an inert surface while allowing electrons to easily escape. Another requirement is that the nanomaterials should have insignificant type 2 physical enhancement.

One such material was a gold nanoparticle covered with a silica layer as demonstrated by Guo et al. [1]. This example is discussed in detail in Sect. 2.4.2, and only a brief recount is given here. Silica is inert, or at most mildly reactive, in many environments. The silica layer on the surface of gold can be quite thin, as Chap. 6 shows. These large gold nanoparticles covered with thin silica coatings are ideal for increasing absorption of X-rays, transferring as much of the absorbed energy as possible to the surrounding, while minimally scavenging nearby radicals. Figure 5.2 shows a TEM image of this nanomaterial and its associated properties. Low-energy electrons responsible for creating type 2 physical enhancement (T2PE) are stopped and buried in the silica layer outside the gold core. No chemical enhancement exists because the silica layer completely covers the gold surface. A schematic is shown in Chap. 2 (Fig. 2.26). The outcome is that there is only type 1 physical enhancement (T1PE). As type 1 physical enhancement requires large quantities of gold nanoparticles, high concentrations of silica-covered gold nanoparticles are needed. Fortunately, solubility of these silica-covered gold nanoparticles can be made greater than 15 WP of gold in water.

No other attempts have been made to isolate or maximize type 1 physical enhancement. Nonetheless, many publications shown in this book have reported detection of the total enhancement whose magnitude is close to the theoretically predicted type 1 physical enhancement. These reports are given in Chaps. 2, 3, 4, 8, and 9.

5.2.2   *Isolation and Optimization of Type 2 Physical Enhancement*

Type 2 physical enhancement is more difficult to isolate. As shown in Sect. 2.4.3, specially made nanomaterials are needed to probe type 2 physical enhancement. This is because the probes have to be placed near the surface of X-ray-absorbing, energy-donating nanomaterials. Otherwise, type 1 physical enhancement dominates. In addition, chemical enhancement will have to be eliminated. These requirements make it difficult to isolate type 2 physical enhancement. The only experimental example available in the literature to date was demonstrated by Guo et al. [2] using aqueous solutions of sulforhodamine B (SRB) molecules contained in calcium phosphate-enclosing liposomes (CaPELs). The enhancement was caused by electrons released from energy-donating gold nanoparticles—these electrons deposited energy in the water body contained in CaPELs. The water in CaPELs was the actual acceptor, although CaPELs could be called acceptors as well since they contained water. As a result, gold nanoparticles are called donors, and CaPELs are termed acceptors. The deposited energy was used to produce reactive oxygen species that reacted with SRB molecules trapped in CaPELs to render SRB less fluorescent. Enhancement was calculated based on the magnitude of reduced fluorescence of SRB. The mechanism is shown again in Fig. 5.3. In this case, type 1 physical enhancement (T1PE) also existed but was isolated from type 2 physical enhancement (T2PE) through changing the concentration of gold nanoparticle donors—type 2 physical enhancement exhibited a jump as the concentration crossed 0.25 WP of
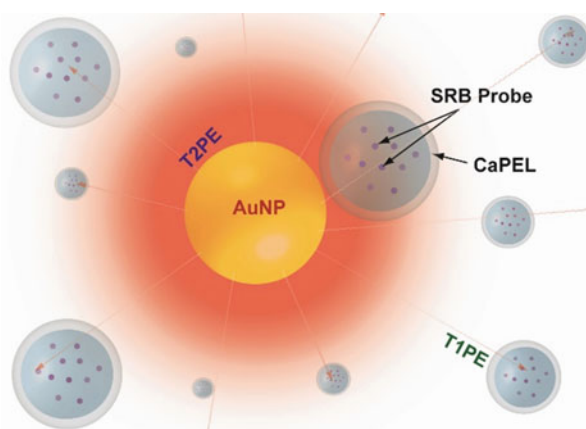
Fig. 5.3 An example of experimental determination of type 2 physical enhancement (T2PE) using CaPEL nanoscale probes. T2PE was caused by gold nanoparticles (AuNPs), and strong T2PE only existed near the surface of AuNPs. Type 1 physical enhancement (T1PE) also existed, but it was uniformly distributed over the whole volume. Therefore, only the CaPEL near the AuNP experienced T2PE; the rest of CaPELs could only detect T1PE. There was no chemical enhancement because the probe reactions were not exposed to the nanoparticles. (Adapted with permission from Guo et al. [2]). Copyright (2016) American Chemical Society.)

gold loading, whereas type 1 physical enhancement was shown as a continuous background at a slope of 1 DEU WP^{-1}. The results are shown in Fig. 2.40 in Sect. 2.4.4.3.

5.2.3   Isolation and Optimization of Type 1 Chemical Enhancement

Chemical enhancement relies on the catalytic surface of nanomaterials. To date, all the examples demonstrating type 1 chemical enhancement employed gold nanoparticles or gold-silver core-shell structures. In the aniline polymerization case shown in Sect. 3.4.1.3, probing reactions were localized on the surface of nanomaterials. In other examples, molecules participating in probe reactions were not bound to the surface but migrated to the surface of nanomaterials during X-ray irradiation. For example, it is suggested that 3-CCA-•OH intermediate diffused to the catalytically active gold surface where they were converted to the product 7-OHCCA. The surface was activated by superoxide radicals. All of these examples are discussed in Chap. 3 and are briefly summarized in Fig. 5.4. The figure presents a rather abstract type 1 chemical enhancement process in which the nanoparticle in the middle (dark colored sphere) is either catalytically active itself or activated by reactive oxygen species such as superoxide radicals. The targeted reaction is then catalyzed by the gold surface. Nonactivated nanomaterials, such as other
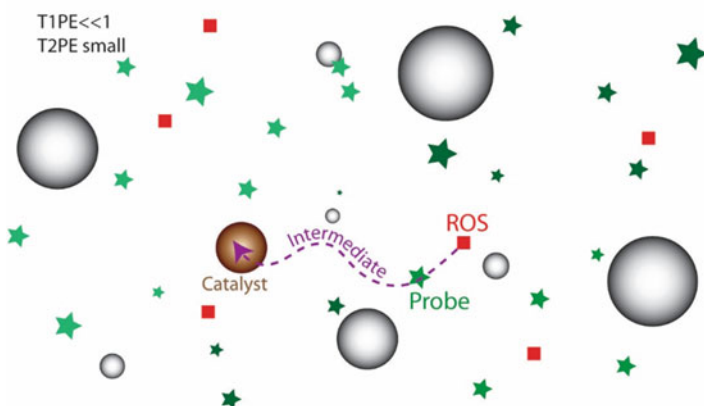
Fig. 5.4   Isolation of type 1 chemical enhancement, which is shown here catalyzed by the surface of the gold nanoparticle (spheres) in the middle (brown colored sphere) of the graph to convert a radical intermediate to the product. Reaction yield depends on catalytic properties of the activated nanoparticle. Other enhancements should be kept low. One way to accomplish this condition is to use small gold nanoparticles (< 10 nm) at low weight percentages (ppm), which can keep T2PE small and T1PE << 1.0 DEU. The use of high concentrations of probes (green stars) can help minimize the role of anti-enhancement from nanoparticles. Reactive oxygen species (ROS) are produced by X-rays

nanoparticles (gray colored) shown in Fig. 5.4, do not participate in any reactions due to lack of catalytic activity. This type of chemical enhancement does not require change to the production of reactive oxygen species and is fundamentally different from type 2 chemical enhancement, which is reserved for those cases where reactive oxygen species are produced at higher or lower yields, possibly caused by catalytic or scavenging properties of nanomaterials.

5.2.4   Isolation and Optimization of Type 2 Chemical Enhancement: Anti-Enhancement

Type 2 chemical enhancement deals with either catalytically increased or decreased production of reactive oxygen species. The latter is also called anti-enhancement, so anti-enhancement is a special case of type 2 chemical enhancement. Several groups have attributed their increased reaction yields to type 2 chemical enhancement, though their explanations are not conclusively validated because type 1 chemical enhancement may also be present and could have rendered the same results. More complete isolation of these two types of enhancement is needed to conclusively validate them in the future.

As a special case of type 2 chemical enhancement, anti-enhancement has been studied independently by several groups, as shown in Chap. 3. For example, Esumi et al. 2003 [3] found that gold-chitosan nanocomposites behaved as antioxidants. Anti-enhancement was also detected when studying enhancement of X-ray effects by nanoparticles under X-ray irradiation. Miyamoto et al. [4] found platinum nanoparticles inhibited the propagation of linoleate peroxidation. Guo et al. [5] learned about anti-enhancement in the study of type 1 chemical enhancement of gold and other nanoparticles. Guo et al. (Carter et al., unpublished) observed scavenging properties of gold nanoparticles with different surfactants, which are discussed in Chap. 3.

Liu et al. [6] reported the results of optimization or maximization of scavenging properties of nanomaterials under X-ray irradiation. Their effort may lead to a novel antidote for ionizing radiation. It is understood that scavenging properties depend on several aspects of nanomaterials, including size, surface, composition, and surfactants. It is possible to utilize the scavenging ability of the nanomaterials to convert the scavenged chemical energy to other forms of chemical energy, such as catalytic potential.

5.2.5   Biological Enhancement and Other Possible Enhancements

Isolation of biological enhancement is both interesting and challenging. As discussed in Chap. 4, there may be several types of biological enhancement.

Biological enhancement should be independent of other enhancements; biological enhancement does not need chemical or physical enhancement just as chemical enhancement does not need physical enhancement to exist. The proof of its existence requires more stringent designs of nanomaterials including their size, shape, surface, surfactants, and targeting moieties. It also requires careful selection of X-ray energy, dose, dose rate, and the energy spectrum. Further, carefully selected characterization methods and assays are needed to report and confirm the enhancement.

No other categories or types of enhancement have been mentioned in the literature. However, it is impossible to rule out the possibility of their existence.

5.3 Combination of Optimized Individual Enhancements and Algorithms

To date, there are three examples of combination of individual enhancements. One of them is the combination of types 1 and 2 physical enhancement by Guo et al. [2]. Another addresses the combination of type 1 physical enhancement and type 1 chemical enhancement by Guo et al. [1]. The final example is pertinent to the incorporation or avoidance of anti-enhancement, which has been investigated by several groups. All three cases are discussed here. Experimental results are given first, followed by derivations of algorithms. In all three cases, the combined total enhancements are found to follow simple algebraic algorithms with respect to individual enhancements. Specifically, it is found that types 1 and 2 physical enhancement follow an addition algorithm when combined. Type 1 physical enhancement and type 1 chemical enhancement follow a multiplication algorithm. Anti-enhancement follows a subtraction algorithm.

5.3.1 Addition Algorithm for Types 1 and 2 Physical Enhancement

5.3.1.1 General Description

The total physical enhancement should be the sum of these two enhancements as far as energy deposition is concerned because of the intrinsic enhancement mechanisms that give rise to types 1 and 2 physical enhancement. By definition, both types of enhancement originate from electrons released from nanomaterials as a result of X-ray absorption. Type 1 physical enhancement is caused by energetic electrons that traverse microns in distance in the sample and therefore is an almost constant enhancement as long as the interparticle distance is shorter than the average distance traveled by an electron. This physical picture has been painted in several figures in this chapter. Under this condition, which is satisfied when nanoparticle concentrations are greater than 1 nM, type 1 physical enhancement is uniform or constant

throughout the whole sample. Type 2 physical enhancement is a local or nanoscale enhancement, is caused by low-energy electrons, and is the strongest near nanomaterials. The amount of energy carried by low-energy electrons emitted from nanoparticles responsible for type 2 physical enhancement is a fraction (10–20%) of the total energy deposited by the electrons released from nanoparticles irradiated with X-rays from an X-ray tube or microfocus X-ray tube. This means the integrated type 2 physical enhancement is about 10–20% of the total enhancement, while type 1 physical enhancement accounts for the remaining 80–90%. For example, the energy deposited into the type 2 physical enhancement region around 100 nm gold nanoparticles is 12% of the total energy deposited in the sample irradiated with monochromatic X-rays at 33 keV or X-rays emitted from a 100 kVp X-ray source. If the amount of reactive oxygen species is proportional to the amount of energy deposited by the electrons and if detection is over the whole volume, then types 1 and 2 physical enhancements should produce proportional amounts of reactive oxygen species.

Another way to look at the total enhancement is from the perspective of volume fraction. The volume fraction of type 2 physical enhancement is small compared with type 1 physical enhancement, as shown in Eq. 2.3. For 100 nm diameter gold nanoparticles, type 2 physical enhancement volume covers only a 30 nm (1/e) thick shell from the surface of these nanoparticles. For large, over 100 nm gold nanoparticles, concentrations are usually less than nM, corresponding to an interparticle distance of 1 μm. In these cases, the volume fraction of type 2 physical enhancement is less than 0.1% of type 1 physical enhancement. If the nanoparticle size is smaller (i.e., less than 10 nm in diameter), then peak values of type 2 physical enhancement from these nanoparticles is lower, but the volume fraction is greater, resulting in a similar type 1 to 2 physical enhancement ratio. As a result, if the probes are uniformly distributed over the whole sample, then the measured enhancement is the sum of integrated types 1 and 2 physical enhancement.

One can derive the total physical enhancement based on theoretically predicted energy deposition at different locations in a sample. The location of probes becomes an important factor if probes are not uniformly distributed in samples. The measured total enhancement, therefore, may deviate from the theoretically predicted total enhancement depending on the choice and location of chemical probes. Figure 5.5 illustrates this relationship. Typically, the integrated type 1 physical enhancement dominates the measured enhancement if the probing chemical species are uniformly distributed in the whole volume of the sample. In this case, integrated type 2 physical enhancement only accounts for approximately 1/6th of the total enhancement. Type 1 physical enhancement is too weak to be detected when compared with type 2 physical enhancement if the following three conditions are all met: (1) the magnitude of type 2 physical enhancement is significantly greater than 1.0 DEU (2) nanoparticle concentrations are low, and (3) probes are placed only in the type 2 physical enhancement region as shown in Fig. 5.5. If all three conditions are met, then type 2 physical enhancement dominates. For high concentrations of large nanoparticles, both type 1 and type 2 enhancements are detectable near the surface of nanoparticles, and the algorithm is the sum of two individual enhancements.
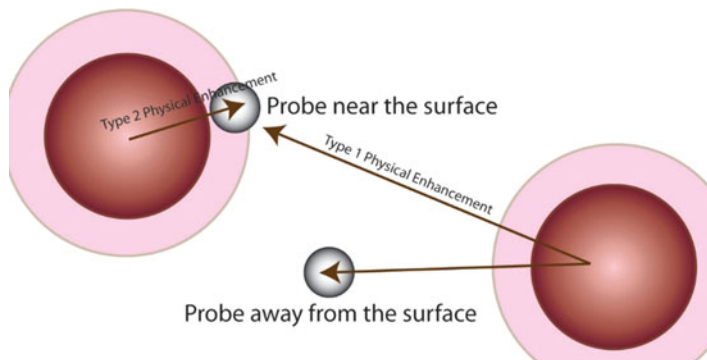
Fig. 5.5 Illustration of a combination of types 1 and 2 physical enhancement. Type 2 physical enhancement exists near the surface of the nanoparticles (pink regions). Type 1 physical enhancement exists as a constant everywhere in the sample. Two nanoscale probes are shown; the one near the surface can detect both types, whereas the one away from the surface can detect mainly type 1 physical enhancement

These scenarios show that the total physical enhancement is the linear addition of the integrated types 1 and 2 physical enhancements, and the coefficients depend on the size and concentration of the nanoparticles and location of the probes.

5.3.1.2   Experimental Results of the Addition of Types 1 and 2 Physical Enhancement

Experimentally, Guo et al. [2] showed that it was possible to extract the algorithm controlling the combination of types 1 and 2 physical enhancement using nanoscale probes. The authors constructed a nanoscale probe, which they called an energy acceptor, to receive energy donated by electrons released from nearby gold nanoparticles upon X-ray irradiation. They called the X-ray-absorbing gold nanoparticles energy donors. Direct X-ray absorption by the acceptors was much weaker than that by gold nanoparticle donors. The system is described in Sect. 2.4.3.4. The whole process was called X-ray-induced energy transfer (XIET). In this work, the nanoscale probe was calcium phosphate-enclosed liposomes (CaPELs) with an aqueous solution of sulforhodamine B (SRB) molecules trapped inside. The outer diameter of the probe was 100 nm, which was the same as the gold nanoparticles (AuNPs). The X-rays were from a microfocus X-ray source operated at 100 kVp. The acceptors were mixed with AuNPs and irradiated with X-rays. Based on the results, it was believed that AuNPs and CaPELs formed transient heterodimers when the AuNP concentration was greater than 0.2 nM, and every CaPEL was in contact with one AuNP above this AuNP concentration. This process was theoretically modeled and discussed in another publication by Guo et al. [7]. When AuNPs were in contact with CaPELs, the nanoscale probes experienced a strong enhancement that was caused by type 2 physical enhancement. In the
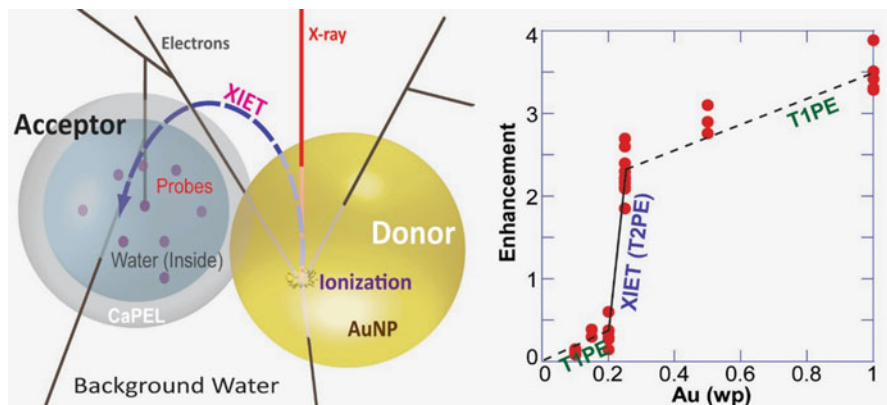
Fig. 5.6 Illustration (left panel) and experimental results (dots, right panel) of an addition algorithm of type 1 physical enhancement (T1PE) and type 2 physical enhancement (T2PE). Also shown in the right panel are lines drawn for the guidance of the trends. The gentle slope represents magnitude of T1PE and the steep one represents that of T2PE. (Adapted with permission from Guo et al. [2]). Copyright (2016) American Chemical Society.)

concentration range employed by the authors, type 1 physical enhancement was also detected.

The results are shown in Fig. 5.6. The total enhancement, integrated enhancement over the whole sample volume, is shown in the right panel as a function of AuNP concentration. In the presence of large enough quantities of AuNPs, there was always type 1 physical enhancement, which increased as AuNP concentration increased and became measurable when the concentration was greater than 0.1 WP. Type 1 physical enhancement, as defined, was nearly constant throughout the sample and was independent of type 2 physical enhancement. The gentler slope shown in the right panel of Fig. 5.6 was on the order of 1 DEU WP^{-1} and was caused by type 1 physical enhancement. A sudden increase in enhancement at 0.25 WP was believed to be caused by type 2 physical enhancement. The total enhancement was therefore the addition of types 1 and 2 physical enhancement, or it can be said that the two followed an addition algorithm when both were present. It was possible to have multiple gold nanoparticles attached to a single acceptor. If there was no attraction between the donors and acceptors at high concentrations of gold nanoparticle donors, then there was no type 2 physical enhancement, i.e., the jump of enhancement at 0.25 WP.

5.3.1.3   Derivation of the Addition Algorithm Between Types 1 and 2 Physical Enhancement

When both type 1 physical enhancement (T1PE) and type 2 physical enhancement (T2PE) are strong, such as at the locations near the surface of large gold nanoparticles irradiated by X-rays, and if both can be detected without interference

from other processes, then we can derive an algorithm for the combination of the two. The theoretical derivation is shown as follows. Absolute or abs superscript is omitted for absolute enhancement in this book because it is the default enhancement. If relative enhancement is used, then the enhancement is labeled rel in superscript.

If only T1PE exists with an absolute enhancement factor ε_{T1PE} (DEU), then the absolute signal gain with this T1PE is

$$\Delta I_{T1PE} = I_{original} \times \varepsilon_{T1PE} \tag{5.1}$$

$I_{original}$ is the original signal intensity measured without any enhancement. The intensity can local or integrated. The signal can be fluorescence signal measured with fluorimetry or gel electrophoresis. Similarly, if there is only T2PE with an enhancement factor ε_{T2PE} (DEU), then the absolute signal increase with only T2PE is

$$\Delta I_{T2PE} = I_{original} \times \varepsilon_{T2PE} \tag{5.2}$$

The total signal is the sum of two signals if both T1PE and T2PE are present because the two enhancements are caused by electrons depositing energy into a medium such as water, and such deposition bears no interference on each other. As a result, the following is true:

$$\Delta I_{Total} = \Delta I_{T1PE} + \Delta I_{T2PE} = I_{original}(\varepsilon_{T1PE} + \varepsilon_{T2PE}) = I_{original} \times \varepsilon_{Total} \tag{5.3}$$

or

$$\varepsilon_{Total} = \varepsilon_{T1PE} + \varepsilon_{T2PE} \tag{5.3a}$$

Therefore, the two types of physical enhancement should be additive, and this is correct only for the absolute enhancement.

Depending on the expression of the enhancement, relative total enhancement is

$$I_{Total}^{rel} = \Delta I_{T1PE} + \Delta I_{T2PE} + I_{original} = I_{original} \times (\varepsilon_{T1PE} + \varepsilon_{T2PE} + 1) \tag{5.4}$$

It is possible to use relative enhancement factors ε^{rel}, which are the common enhancement values defined in the literature. The relative and absolute enhancements follow the simple relationship of $\varepsilon^{rel} = \varepsilon + 1$, which has been shown in Chaps. 1 and 2. Although relative enhancement is commonly used in the literature, in this book absolute enhancement is the choice of use because of the convenience of using absolute enhancement in the expression of unit WP enhancement. Equation 5.4 can also be written as

$$I_{Total}^{rel} = \Delta I_{T1PE} + \Delta I_{T2PE} + I_{original} = I_{original} \times \left(\varepsilon_{T1PE}^{rel} + \varepsilon_{T1PE}^{rel} - 1\right) \tag{5.5}$$

or:

$$I_{Total}^{rel} = I_{original} \times \left(\varepsilon_{T1PE}^{rel} + \varepsilon_{T1PE}^{rel} - 1\right) = I_{original} \times \varepsilon_{Total}^{rel} \tag{5.6}$$

and

$$\varepsilon_{\text{T1PE}}^{\text{rel}} + \varepsilon_{\text{T1PE}}^{\text{rel}} - 1 = \varepsilon_{\text{Total}}^{\text{rel}} \tag{5.6a}$$

Using the example shown in Fig. 5.6, $\varepsilon_{\text{T1PE}} = 0.3$ DEU and $\varepsilon_{\text{T2PE}} = 2.0$ DEU at 0.25 WP of gold in water, noticing both are absolute enhancement, consistent with the conventions used in the rest of book. Specifically, $\varepsilon_{\text{Total}} = 2.3$ DEU and $\varepsilon_{\text{Total}}^{\text{rel}}$ = 3.3 DEU at 0.25 WP.

5.3.2   Multiplicity Algorithm for Types 1 Physical and Chemical Enhancement

5.3.2.1   Experimental Results

Physical enhancement measured for a nanomaterial-containing sample under X-ray irradiation of a specific dose rate should be equivalent to irradiating the same sample without the nanomaterials using X-rays of a higher dose rate for the same duration of irradiation. The ratio of the two dose rates, the theoretically calculated dose based on the enhancement to the one actually used in the experiment, is the magnitude of enhancement. This is equivalent to stating that adding nanomaterials is the same as increasing the dose rate of X-rays received by the sample alone, without nanomaterials, by increasing the X-ray dose rate from the X-ray source. Physical enhancement itself, however, is not dependent on the dose rate. If it were, the algorithms would be more complicated than those shown in Eqs. 5.1, 5.2, 5.3, 5.4, 5.5, and 5.6. On the other hand, chemical enhancement is dependent on the dose rate as shown by Guo et al. [5]. Chemical enhancement using the same nanomaterials changes as a function of dose rate, increasing linearly as a function of dose rate at low dose rates and reaching saturation above a threshold dose rate. These two different dependencies on dose rate govern the algorithm relating the total enhancement to physical and chemical enhancement. If two kinds of nanoparticles can be used so that one particle facilitates physical enhancement with little chemical enhancement and the other enables chemical enhancement without causing physical enhancement, then it is possible to extract the total enhancement algorithm when both nanoparticles are present. This was what Guo et al. [1] demonstrated.

In their work, 90 nm silica-coated gold nanoparticles were used to mainly drive type 1 physical enhancement (T1PE), and 3 nm gold nanoparticles were employed to provide dominant (type 1) chemical enhancement (CE). The total enhancement was analyzed in relation to individual enhancements at different concentrations of silica-coated gold nanoparticles, and the algorithm was deduced. This use of two kinds of gold nanoparticles was better than using a single sized or single kind of gold nanoparticles because physical and chemical enhancement were both strong when the two kinds of nanoparticles were used, which resulted in a high total enhancement. Figure 5.7 illustrates the mechanisms and experimental results. The left panel describes how type 1 physical enhancement and type 1 chemical enhancement
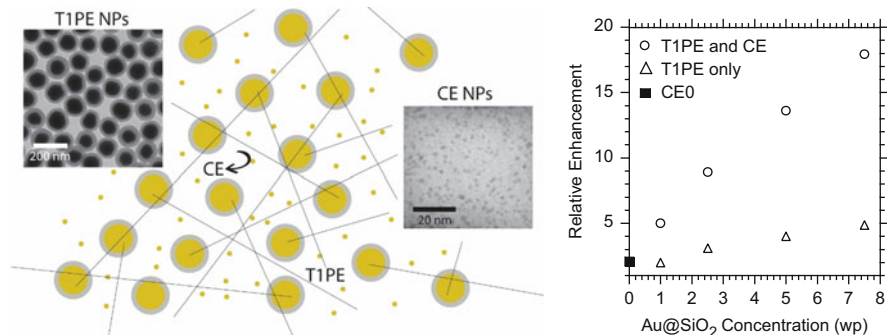
Fig. 5.7 Illustration (left panel) of combined physical and chemical enhancement, and display of experimental results (right panel) for the combination of type 1 physical enhancement (T1PE) and type 1 chemical enhancement (T1CE). T1CE (or CE as shown in the left panel) can exist (■) without Au@SiO₂. (Adapted with permission from Guo et al. [1]. Copyright (2015) American Chemical Society.)

generate their enhancements. The right panel shows the experimental results. Type 1 physical enhancement is shown (empty triangles, Δ) as a function of the concentration of silica-covered gold nanoparticles. The slope at low concentrations of gold nanoparticles was approximately $1.0\ \mathrm{DEU\ WP^{-1}}$, agreeing with the generic unit WP type 1 physical enhancement shown in Chap. 2. The X-rays were from a tungsten microfocus X-ray source operated at 100 kVp with filters. Type 1 chemical enhancement alone was 2.0 DEU with 3 nm tetrakis-hydroxymethyl-phosphonium chloride (THPC)-coated gold nanoparticles. The loading of this gold nanoparticle was only 0.01 WP, giving rise to negligible type 1 physical enhancement of 0.01 DEU. Therefore, the enhancement observed with adding the 3 nm THPC-coated gold nanoparticles was type 1 chemical enhancement (solid squares, ■). When the two nanoparticles were mixed, the total enhancement was higher (empty circles, □). The slope was $4.0\ \mathrm{DEU\ WP^{-1}}$ at low loadings of silica-coated gold nanoparticles, which was a three-fold increase over the silica-coated nanoparticles alone, demonstrating the benefit of using the combined enhancements. As shown below, this outcome can be explained by a multiplication algorithm for the two individual enhancements.

In addition to the experimental data shown above, it is possible to derive an algorithm from their definitions as shown in Chaps. 2 and 3 when both physical and chemical enhancement are present. The total enhancement is derived theoretically as follows.

5.3.2.2 Derivation of the Multiplication Algorithm for Type 1 Physical Enhancement and Type 1 Chemical Enhancement

According to Eq. 5.1, if there is type 1 physical enhancement alone, then the actual signal with only type 1 physical enhancement is

$$I_{\text{T1PE}}^{\text{rel}} = \Delta I_{\text{T1PE}} + I_{\text{original}} = I_{\text{original}} \times \varepsilon_{\text{T1PE}} + I_{\text{original}} = I_{\text{original}} \times \varepsilon_{\text{T1PE}}^{\text{rel}} \qquad (5.7)$$

Again $\varepsilon_{\text{T1PE}}^{\text{rel}}$ is the relative T1PE enhancement factor, and $\varepsilon_{\text{T1PE}}^{\text{rel}} = \varepsilon_{\text{T1PE}}^{\text{abs}} + 1$. Usually the superscript for absolute enhancement is omitted as stated above.

Equation 5.7 can be simplified as follows:

$$I_{\text{T1PE}}^{\text{rel}} = I_{\text{original}} \times \varepsilon_{\text{T1PE}}^{0,\text{rel}} \qquad (5.8)$$

in which $\varepsilon_{\text{T1PE}}^{0,\text{rel}}$ is noted here to emphasize the relative enhancement factor is for T1PE only, without any other enhancements. Equation 5.8 is essentially the same as Eqs. 5.1 and 5.2 except that relative signal and enhancement are used here.

If there is type 1 chemical enhancement alone, then

$$I_{\text{T1CE}}^{\text{rel}} = I_{\text{original}} \times \varepsilon_{\text{T1CE}}^{0,\text{rel}} \qquad (5.9)$$

The enhancement factor in this equation is also relative enhancement, and 0 is noted because T1CE is the only enhancement.

Type 1 chemical enhancement is dependent on dose rate of X-rays and is assumed to be linearly dependent on the dose rate according to Guo et al. [5]. The latter should be valid at least at low dose rates. When both T1PE and T1CE are present, and if Eq. 5.9 is used as the base to derive the algorithm, then I_{original} and $\varepsilon_{\text{T1CE}}^{0,\text{rel}}$ in Eq. 5.9 are different when T1PE is present.

With T1PE in place, the signal that T1CE acts upon is no longer I_{original}. It is

$$I_{\text{Original}}^{\text{with T1PE,rel}} = I_{\text{original}} \times \varepsilon_{\text{T1PE}}^{0,\text{rel}} \qquad (5.10)$$

Notice that I_{original} in Eqs. 5.7, 5.8, 5.9, and 5.10 is the original signal without any gold nanoparticles. With T1PE, the dose rate is also increased. If the original dose rate is D_0, then the dose rate in the presence of T1PE is

$$D_{\text{T1PE}} = D_0 \times \varepsilon_{\text{T1PE}}^{0,\text{rel}} \qquad (5.11)$$

If an enhancement is not dependent on dose rate such as T1PE, then dose rate does not enter into the enhancement equation. However, T1CE is dependent on dose rate. T1CE at this new, higher dose rate is

$$\varepsilon_{\text{T1CE}}^{\text{with T1PE}} = \varepsilon_{\text{T1CE}}^0 \times \frac{D_{\text{T1PE}}}{D_0} = \left(\varepsilon_{\text{T1CE}}^{0,\text{rel}} - 1\right) \times \frac{D_{\text{T1PE}}}{D_0} \qquad (5.12)$$

In this case, absolute enhancement $\varepsilon_{\text{T1CE}}^0$ *has to* be used because only chemical enhancement is dose rate dependent. For example, when there is no chemical enhancement, Eq. 5.12 correctly predicts the absolute chemical enhancement is zero even if T1PE is not zero. The term $\left(\varepsilon_{\text{T1CE}}^{0,\text{rel}} - 1\right)$ is used because $\varepsilon_{\text{T1CE}}^{0,\text{rel}}$ includes the unenhanced part of the signal, which should not be subjected to any further enhancement. Converting the absolute to relative T1CE:

$$\varepsilon_{\text{T1CE}}^{\text{with T1PE, rel}} = 1 + \left(\varepsilon_{\text{T1CE}}^{0,\text{rel}} - 1\right) \times \frac{D_{\text{T1PE}}}{D_0} \tag{5.13}$$

Consequently, when both T1PE and T1CE are present, we can insert Eqs. 5.10 and 5.13 into Eq. 5.9

$$I_{\text{Total}}^{\text{rel}} = I_{\text{Original}}^{\text{with T1PE, rel}} \times \varepsilon_{\text{T1CE}}^{\text{with T1PE, rel}} = I_{\text{original}} \times \varepsilon_{\text{T1PE}}^{0,\text{rel}} \times \varepsilon_{\text{T1CE}}^{\text{with T1PE, rel}} \tag{5.14}$$

This is equivalent to

$$\varepsilon_{\text{Total}}^{\text{rel}} = \frac{I_{\text{Total}}^{\text{rel}}}{I_{\text{original}}} = \varepsilon_{\text{T1PE}}^{0,\text{rel}} \times \varepsilon_{\text{T1CE}}^{\text{with T1PE, rel}} \tag{5.15}$$

The total signal used here is the actual signal (relative), which includes the enhancement. Therefore, when physical and chemical enhancement are combined, the total enhancement should be the product of the two, although the actual chemical enhancement factor is the one in the presence of physical enhancement or T1PE, not the original chemical enhancement at the lower dose rate without T1PE.

If the original chemical enhancement $\varepsilon_{\text{T1CE}}^{0,\text{rel}}$ is used, then we can insert Eq. 5.13 into Eq. 5.14:

$$I_{\text{Total}}^{\text{rel}} = I_{\text{original}} \times \varepsilon_{\text{T1PE}}^{0,\text{rel}} \times \left(1 + \left(\varepsilon_{\text{T1CE}}^{0,\text{rel}} - 1\right) \times \frac{D_{\text{T1PE}}}{D_0}\right) \tag{5.16}$$

Inserting Eq. 5.11 in to Eq. 5.16, we have

$$I_{\text{Total}}^{\text{rel}} = I_{\text{original}} \times \varepsilon_{\text{T1PE}}^{0,\text{rel}} \times \left(1 + \left(\varepsilon_{\text{T1CE}}^{0,\text{rel}} - 1\right) \times \varepsilon_{\text{T1PE}}^{0,\text{rel}}\right) \tag{5.17}$$

And the total enhancement is

$$\varepsilon_{\text{Total}}^{\text{rel}} = \frac{I_{\text{Total}}^{\text{rel}}}{I_{\text{original}}} = \varepsilon_{\text{T1PE}}^{0,\text{rel}} \times \left(1 + \left(\varepsilon_{\text{T1CE}}^{0,\text{rel}} - 1\right) \times \varepsilon_{\text{T1PE}}^{0,\text{rel}}\right) \tag{5.18}$$

If both chemical enhancement and physical enhancement are strong, such as the case in which $\varepsilon_{\text{T1CE}}^{0,\text{rel}}$ is 4.0 DEU and $\varepsilon_{\text{T1PE}}^{0,\text{rel}}$ is 7.0 DEU, then the second term in the parenthesis in Eq. 5.18 is much greater than 1.0. Under this condition, Eq. 5.18 can also be approximated to

$$\varepsilon_{\text{Total}}^{\text{rel}} = \varepsilon_{\text{T1PE}}^{0,\text{rel}} \times \varepsilon_{\text{T1PE}}^{0,\text{rel}} \times \left(\varepsilon_{\text{T1CE}}^{0,\text{rel}} - 1\right) = \varepsilon_{\text{T1PE}}^{0,\text{rel}}2 \times \varepsilon_{\text{T1CE}}^{0} \tag{5.19}$$

This means that the final total enhancement is quadratically dependent on $\varepsilon_{\text{T1PE}}^{0,\text{rel}}$ and linearly proportional to $\varepsilon_{\text{T1CE}}^{0}$. It is important to point out that derivation of Eqs. 5.18 or 5.19 does not take dose rate saturation for T1CE into consideration. When saturation is reached, the total enhancement is lower.

The results shown in Sect. 5.3.2.1 can be examined here to see if they agree with Eq. 5.18 or 5.19. For 1 WP large gold nanoparticles, $\varepsilon_{\text{T1PE}}^{0,\text{rel}} = 2.1$ DEU. For chemical enhancement, $\varepsilon_{\text{T1CE}}^{0,\text{rel}} = 2.3$ DEU for 0.01 WP THPC gold nanoparticles. The total

enhancement (rel) should be $\varepsilon_{\text{T1PE}}^{0,\text{rel}} \times \left(1 + \left(\varepsilon_{\text{T1CE}}^{0,\text{rel}} - 1\right) \times \varepsilon_{\text{T1PE}}^{0,\text{rel}}\right) = 2.1 \times (1 + 1.3 \times 2.1) = 7.8$, which is higher than the experimental value of 5.0. This overestimation may be caused by saturation of chemical enhancement at the experimental dose rate. It is expected that when lower dose rates are used in these experiments, a better agreement between the experimental data and those predicted by Eq. 5.18 may be reached. It is expected that at low dose rates, Eq. 5.19 can be used to accurately predict the total enhancement because T1PE and T1CE are strong and there is no saturation.

5.3.3   Algorithms Involving Anti-Enhancement

5.3.3.1   Experimental Results

In early times, producing physical enhancement was the purpose of using nanomaterials. Now, the use of nanomaterials has spread to chemical enhancement and possibly biological enhancement. Most of the published enhancement studies do not mention anti-enhancement, which is a special kind of type 2 chemical enhancement defined in this book, even though most of the time anti-enhancement coexists with other enhancements. In several cases, anti-enhancement even dominates.

Guo et al. (Carter et al., unpublished) studied the effect of surfactants on enhancement. The results are discussed in Sect. 3.4.2.2. For example, PEG ligands were found to mildly scavenge hydroxyl radicals. Trimethylammonium (TMA) ligands severely scavenged hydroxyl radicals. The probe reaction used to study scavenging by gold nanoparticles was hydroxylation of 3-CCA. The scavenging ability of these ligands was inferred from the yield of conversion from 3-CCA to 7-OHCCA because hydroxyl radical yield was not directly measured.

Metallic surfaces scavenge hydroxyl radicals because hydroxyl radical has a higher redox potential than many metal atoms. This is shown in the example of gold nanotubes given in Chap. 2. It is shown that the theoretically predicted type 1 physical enhancement was 100 DEU, whereas only 2 DEU was detected experimentally through measuring single-strand breaks of supercoiled DNA. Therefore, there was a 98% scavenging or enhancement reduction or anti-enhancement. This was not caused by the surfactants, but by the gold surface itself because gold nanotubes did not have any surfactants. Figure 5.8 shows the results obtained by Guo et al. [8]. The left panel shows a TEM image of gold nanotubes. The right panel shows the results of theoretically simulated fractions of hydroxyl radicals reacting with the gold surface, indicating more than 95% of hydroxyl radicals were scavenged by the gold surface even with DNA in solution. Consequently, the measured enhancement was approximately 2.0 DEU due to the presence of highly scavenging gold surfaces. When other scavengers, such as Tris, were added into the solution, the extent of scavenging by the gold surface was reduced. This result is shown in Fig. 5.8 (right panel) in which scavenging was theoretically simulated. As noted, scavenging by gold nanotubes at 100 mM Tris is restricted to within 5 nm of the nanotube surface.
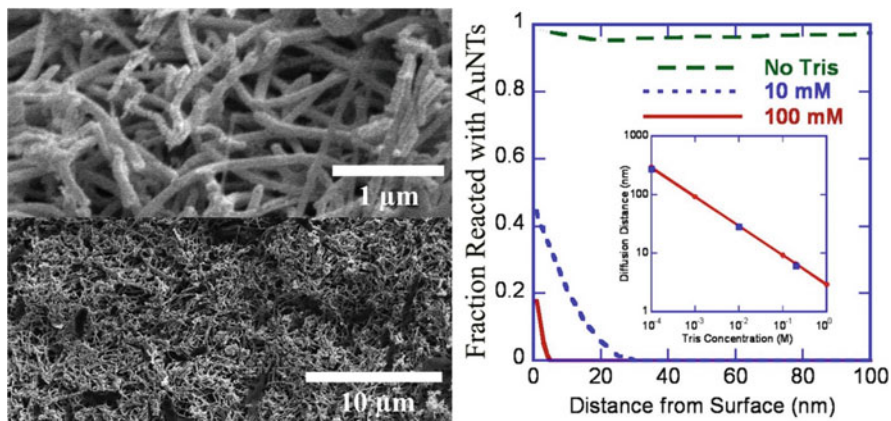
Fig. 5.8 Gold nanotubes (left panel) and theoretically predicted anti-enhancement (right panel) caused by them. Theoretical results showed that without scavengers such as Tris, nearly all (98%) of hydroxyl radicals were scavenged by the surface of gold nanotubes with 100 WP gold nanotubes in water. When 100 mM Tris was added, only a small fraction of hydroxyl radicals reacted with gold nanotubes. (Adapted from Guo et al. [8]. Copyright (2012) with permission from Elsevier.)
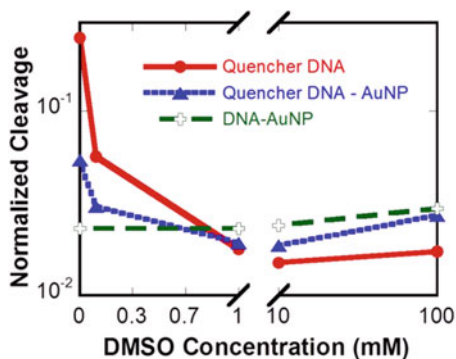
Fig. 5.9 Hydroxyl radical cleavage of DNA strands anchored on the surface of gold nanoparticles. The DNA strand break yield decreased from 25% per 100 Gy for free DNA in solution (red solid line) to 2.5% per 100 Gy for DNA strands conjugated on the surface of gold nanoparticles (green dashed line). One explanation was the scavenging of the gold surface. The other possibility was the lowered reactivity when DNA molecules were anchored to the surface. (Adapted with permission from Guo et al. [9]). Copyright (2013) of the Royal Society of Chemistry.)

Another example of surface scavenging was demonstrated using cleavage of DNA strands next to the gold nanoparticle surface. The work was done by Guo et al. [9]. The overall results showed X-ray triggered release of drug molecules in breast cancer cells. The reaction yield, i.e., single-strand breaks (SSB) of DNA strands (12-mer) linked to the surface of 15-nm diameter gold nanoparticles was ten times lower than the DNA in solution. Figure 5.9 shows the results. Free DNA in solution (dashed line) showed 25% SSB yield per 100 Gy versus the yield of 2.5%

SSB per 100 Gy for the same DNA conjugated to the surface of gold nanoparticles. This reduction might be partially caused by the scavenging of the gold surface toward hydroxyl radicals, which were needed to cleave DNA backbones. Other possible explanations included lowered reactivity between radicals and DNA anchored to the surface of nanoparticles.

The utility of anti-enhancement has not been fully demonstrated. In one case, gold nanoparticles were found to be antioxidants by Liu et al. 2007 [6]. For complex applications such as cancer therapy, it may be beneficial to combine anti-enhancement with enhancement so that anti-enhancement can be used to protect healthy cells in the X-ray beam path from radiation damage. El-Sayed et al. 2017 [10] studied this effect.

5.3.3.2 Derivation of Subtraction Algorithm for Anti-enhancement and Other Enhancements

When anti-enhancement dominates, the value of $\varepsilon_{\text{T2CE}}^{\text{rel}}$ is below 1.0, meaning the absolute enhancement value $\varepsilon_{\text{T2CE}}$ is negative. In this case, the measured signal $I_{\text{T2CE(anti)}}^{\text{rel}}$ is below I_{original}, and the absolute signal is negative. According to Sect. 5.3.2.2, chemical enhancement is dose rate dependent and physical enhancement influences the outcome as if the dose rate were changed. However, it is not clear whether anti-enhancement is dose rate dependent. Since scavenging does not require activation by another radical or reactive species, it is reasonable to assume scavenging is not dose rate dependent. If this is the case, then Eq. 5.14 will be different for anti-enhancement, which should be revised to

$$I_{\text{Total}}^{\text{rel}} = I_{\text{Original}}^{\text{with T1PE, rel}} \times \varepsilon_{\text{T2CE, anti}}^{\text{rel}} = I_{\text{original}} \times \varepsilon_{\text{T1PE}}^{0,\text{rel}} \times \varepsilon_{\text{T2CE, anti}}^{\text{rel}} \qquad (5.20)$$

This gives rise to a relative enhancement connected to both type 1 physical enhancement and anti-enhancement.

Using Eq. 5.20 and the results shown in Fig. 5.9, it is possible to calculate enhancement for the gold nanotubes. $\varepsilon_{\text{T2CE, anti}}^{\text{rel}}$ is only 0.03 because the scavenging is nearly 97%. The absolute enhancement factor in Eq. 5.20 becomes $\varepsilon_{\text{T2CE}}^{\text{rel}} \times \varepsilon_{\text{T1PE}}^{\text{rel}}$ $-1 = 0.03 \times 100-1 = 2.0$ DEU (abs). For 100 WP, the unit WP enhancement is hence only 0.02 DEU WP^{-1}. Such a low unit WP enhancement was caused by scavenging of the gold surface of the bare gold nanotubes.

One particular case of anti-enhancement is to use the scavenging property to enable enhancement. As shown in Chap. 3, there is a special chemical enhancement example in which the gold surface of silver-gold core-shell nanostructures scavenged hydroxyl radicals to oxidize aniline monomers deposited on the surface. The results were published by Guo et al. [11] and is shown in Sect. 3.4.1.3. The mechanism was determined indirectly, so it would be prudent to explore the dynamics with more direct physical measurements, such as time-resolved spectroscopy, in the future. In this example, scavenging was converted into enhancement.

5.4   Other Combinations

Chapter 4 discusses biological enhancement. Here, there is no discussion of biological enhancement. This omission does not mean that biological enhancement cannot be combined with other enhancements or that biological enhancement is not important. On the contrary, it is expected that biological enhancement can help amplify physical and chemical enhancements by large margins because of the nature of biological processes. The main problem associated with using biological enhancement lies in the fact that biological enhancement, to date, is still not well-understood from a theoretical perspective. Due to this lack of understanding, it is difficult to predict the algorithm governing the combined total enhancement when biological enhancement is involved. On the one hand, it is possible that biological enhancement may dominate, and the total enhancement is the same as biological enhancement. On the other hand, physical or chemical enhancement may be exponentially amplified. Future work will be needed to clarify these uncertainties.

Other possible cases include combining chemical enhancement using γ-rays with biological enhancement. γ-rays may produce minimal physical enhancement due to low interaction cross-sections in that energy range. However, γ-rays can produce chemical enhancement because its relatively large interaction cross-sections with water is as high as that with heavy elements. If nanomaterials are properly made and if biological enhancement is constructively combined, then it is possible to use γ-rays and nanomaterials to achieve high biological enhancement as well as a total enhancement.

It is also possible to combine more than two individual enhancements to obtain a much higher total enhancement, although such a process has not been demonstrated.

5.5   Conclusions and Future Work

This chapter explains the benefits of isolation, optimization, and combination of individual enhancements. Three examples are given: the combinations of types 1 and 2 physical enhancement, types 1 physical and chemical enhancement, and the involvement of anti-enhancement. Types 1 and 2 physical enhancement follow an addition algorithm. Types 1 physical and chemical enhancement follow a multiplication algorithm with respect to physical enhancement and the modified chemical enhancement, i.e., the new chemical enhancement after taking into account the dose rate increase caused by physical enhancement. A subtraction algorithm applies to anti-enhancement.

Algorithms controlling the combined individual enhancements are critical to generating the highest total enhancement using multiple nanomaterials and multiple individual enhancement mechanisms. Depending on the type and magnitude of individual enhancements, the combined enhancements can be higher or much

higher. Understandably, multiple nanomaterials are often needed to accomplish the highest combined total enhancement.

Biological enhancement is not included here as it is still unclear exactly how biological enhancement works, even though the existence of biological enhancement seems certain. Once the nanomaterials and experiments designed to isolate biological enhancements can be made, and after the mechanisms are determined, then it will be possible to combine biological enhancement with other enhancements to obtain high total enhancement values.

Based on the magnitude of individual enhancements discussed in Chaps. 2, 3, and 4, it may be most beneficial to combine type 2 physical enhancement, type 1 chemical enhancement, and biological enhancement. It will be interesting to study and uncover the algorithm governing the total enhancement after combining all these enhancements. The algorithm may be dependent on the nanomaterials and processes with which the total enhancement is measured. Among all the studies in X-ray nanochemistry, this area can be the most exciting because of the potential to obtain high total enhancements. However, the work is also possibly the most difficult due to the requirements for nanomaterials and measurement platforms. For example, if biological enhancement is involved, then the mechanisms of enhancement need to be understood before this category of enhancement can be combined with other enhancements.

References

1. Davidson, R. A., & Guo, T. (2015). Multiplication algorithm for combined physical and chemical enhancement of X-ray effect by nanomaterials. *Journal of Physical Chemistry C, 119*, 19513–19519.
2. Sharmah, A., Yao, Z., Lu, L., & Guo, T. (2016). X-ray-induced energy transfer between nanomaterials under X-ray irradiation. *Journal of Physical Chemistry C, 120*, 3054–3060.
3. Esumi, K., Takei, N., & Yoshimura, T. (2003). Antioxidant-potentiality of gold-chitosan nanocomposites. *Colloid Surface B, 32*, 117–123.
4. Watanabe, A., Kajita, M., Kim, J., Kanayama, A., Takahashi, K., Mashino, T., & Miyamoto, Y. (2009). In vitro free radical scavenging activity of platinum nanoparticles. *Nanotechnology, 20*, 455105.
5. Cheng, N. N., Starkewolf, Z., Davidson, A. R., Sharmah, A., Lee, C., Lien, J., & Guo, T. (1950). Chemical enhancement by nanomaterials under X-ray irradiation. *Journal of the American Chemical Society Communication, 2012*(134), 1950–1953.
6. Nie, Z., Liu, K. J., Zhong, C. J., Wang, L. F., Yang, Y., Tian, Q., & Liu, Y. (2007). Enhanced radical scavenging activity by antioxidant-functionalized gold nanoparticles: A novel inspiration for development of new artificial antioxidants. *Free Radical Biology & Medicine, 43*, 1243–1254.
7. Sharmah, A., Mukherjee, S., Yao, Z., Lu, L., & Guo, T. (2016). Concentration-dependent association between weakly attractive nanoparticles in aqueous solutions. *Journal of Physical Chemistry C, 120*, 19830–19836.
8. Carter, J. D., Cheng, N. N., Qu, Y. Q., Suarez, G. D., & Guo, T. (2012). Enhanced single strand breaks of supercoiled DNA in a matrix of gold nanotubes under X-ray irradiation. *Journal of Colloid and Interface Science, 378*, 70–76.

9. Starkewolf, Z. B., Miyachi, L., Wong, J., & Guo, T. (2013). X-ray triggered release of doxorubicin from nanoparticle drug carriers for cancer therapy. *Chemical Communications, 49*, 2545–2547.
10. Aioub, M., Panikkanvalappi, S. R., & El-Sayed, M. A. (2017). Platinum-coated gold nanorods: Efficient reactive oxygen scavengers that prevent oxidative damage toward healthy, untreated cells during plasmonic photothermal therapy. *ACS Nano, 11*, 579–586.
11. Davidson, R. A., & Guo, T. (2012). An example of X-ray Nanochemistry: SERS investigation of polymerization enhanced by nanostructures under X-ray irradiation. *Journal of Physical Chemistry Letters, 3*, 3271–3275.

Part III
Nanomaterials and Methods

Chapter 6
Nanomaterials for X-Ray Nanochemistry

It takes strength to speak one's mind. It takes skill to communicate.

6.1 Introduction

The nanomaterials used in the initial experiments of X-ray nanochemistry were small gold nanoparticles. Guo stated in his 2001 proposal that less than 3 nm gold nanoparticles were ideal because the originally perceived enhancement was derived only from electrons released from nanoparticles upon X-ray absorption by these nanoparticles. Without performing numerical simulations, it was estimated that the smaller the nanoparticles, the more electrons, including Auger and secondary electrons, could escape from the nanoparticles and deposit energy into the surrounding medium such as water or tissues. Therefore, in their first publication, Guo et al. [1] used 5 nm gold nanoparticles synthesized based on a method developed by Brust et al. [2]. Similarly, Hainfeld et al. [3] chose 1.9 nm gold nanoparticles in their first work. The company formed by Hainfeld et al. (Nanoprobe Inc.) manufactured and sold 1.9 nm gold nanoparticles to many groups, which used these 1.9 nm nanoparticles to measure enhancement.

Based on the results presented in Chaps. 2, 3, 4, and 5, it is clear that the size of gold nanoparticles affects the number and energy spectrum of electrons escaping from gold nanoparticles. Large nanoparticles (up to 100 nm dia.) may retain a significant fraction (up to 25%) of energy due to electron energy loss in these nanoparticles. Small nanoparticles, especially less than 5 nm metal nanoparticles, have negligible electron retention. However, contrary to the original expectations, these small gold nanoparticles may not exhibit meaningful physical enhancement unless at high concentrations, at which the surface area of these nanoparticles is so large that other properties, such as scavenging or catalytic functions, overwhelm physical enhancement. Further, these small nanoparticles may interact strongly with many probe molecules, such as DNA molecules, repair proteins, or coumarin-3-carboxylic acid (3-CCA) and its intermediates. The size of nanoparticles also controls cellular uptake as these small sizes may not be ideal for maximum cellular

uptake as demonstrated by many reports including Chithrani et al. [4]. In a more recent publication, Hainfeld et al. [5] used 11 nm gold nanoparticles instead of 1.9 nm gold nanoparticles. On the other hand, large nanoparticles may have solubility problems, especially in applications that require long circulation times. For several reasons, such as maximum uptake by cells or minimal chemical enhancement, the ideal particle size for creating strong physical enhancement is 50 nm. On the other hand, the ideal size for chemical enhancement is less than 10 nm, possibly below 5 nm. These results demonstrate the importance of selecting the right size of nanomaterials for applications in X-ray nanochemistry. For this reason, nanomaterials used in X-ray nanochemistry and their synthesis are reviewed here based on their sizes.

In addition to the particle size that can affect the percentage and energy spectrum of escaping electrons, other parameters such as surface area, surfactants, composition, and shape of the nanomaterials can also affect the magnitude of enhancement, especially chemical and possibly biological enhancement. For type 3 physical enhancement, there is no ideal size, at least not yet being claimed, although crystallinity can be an important factor. These properties as well as how surfactants are chemically attached to the surface of nanoparticles are briefly reviewed in this chapter.

Many types of nanomaterials have been used to generate the enhancement in the context of X-ray nanochemistry, and this chapter summarizes these nanomaterials, which are a very small subset of the nanomaterials that have been synthesized since the beginning of the era of nanotechnology and nanoscience. Several books and reviews, such as those by Ozin and Arsenault [6] and El-Sayed et al. [7], are available, which discuss synthesis, properties, and applications of these nanomaterials. In this chapter, the emphasis is placed on discussion of the nanomaterials that have been used in measuring enhancements defined in X-ray nanochemistry. Alternative nanomaterials are mentioned whenever appropriate.

Methods used for characterization of these nanomaterials are briefly mentioned as well. The characterization parameters are similarly chosen to reflect their prominence in controlling the enhancement. However, such a choice is based on current published results, therefore having its limitations and may change in the future. Special characterization methods may be invented in the future for the purpose of uncovering the origins of enhancement.

6.2   Nanomaterial Properties

It is desirable to use a set of parameters to define the structure of a nanomaterial. Once these parameters are found, they can be conveniently used to infer the properties of the nanomaterial because the structure of a nanomaterial usually determines its properties. From X-ray nanochemistry perspective, these parameters, either in part or whole, can influence the enhancement by the nanomaterial. In addition to defining nanomaterials, these parameters may also be used to refine the control of interactions between nanomaterials and their surroundings, such as

Table 6.1 Parameters used to define the nanomaterials that have been used in the enhancement measurement in X-ray nanochemistry

Parameters	Range	Properties
Radius	0.1–1000 nm	Surface-to-volume atoms, surface area, X-ray absorption, cellular uptake, solubility, surface plasmon response
Shape	Aspect ratio (rods), thickness/length (prisms)	Surface plasmon response
Composition	Elemental, oxide, polymer	Mobility in solution
Surface	Metal and oxide	Catalytic
Surfactants	Metal, functional groups, and oxide	Solubility, mobility, scavenging
Alloy	2–4 elements	Catalytic, surface plasmon response
Core-shell	Number and thicknesses	Protection of surface (oxide), surface plasmon response
Aggregates	2–1000	Nanoparticles mass, surface plasmon response, other nanostructures

proteins, DNA, other molecules, or nanomaterials. However, not all the parameters are yet known to researchers. For example, the structural parameters critical to influencing chemical enhancement are only speculated but not well defined. Another example of difficult-to-define parameters is that some properties are a continuous function of the structural parameters, thereby creating a situation where nearly an infinite number of parameters are needed to define a nanomaterial. In these cases, currently available parameters may be insufficient to define the nanomaterial, or the parameters are insufficiently defined.

Seven generic parameters used to define a nanomaterial are given in Table 6.1, which include the radius/dimension, shape (including aspect ratio, thickness, etc., depending on the shape and structures), composition, surface coverage of surfactants, alloy, core-shell, and aggregates. Table 6.1 also lists the connections between the properties and parameters, although the properties shown in the list are not exhaustive. There may be other parameters derived from the ones listed in the table that can be used to better define the nanomaterials. Among the parameters listed in Table 6.1, surface-to-volume ratio and total surface area per unit mass are commonly used in X-ray nanochemistry. Though useful, other parameters are difficult to define. For example, crystallinity is one such parameter that can affect the type 3 physical enhancement or magnetic response of nanomaterials. Other parameters, such as the profile of UV-Vis or SERS spectra, may also be important but are not listed in Table 6.1. Another parameter or even a set of parameters is that defines the carrier(s) of nanomaterials, whether it is pure water or aqueous solutions. Unfortunately, this parameter is usually not specified clearly enough to enable researchers to consider its impact on enhancement. In the future, a set of parameters may be attached or associated to each nanomaterial so that a specific nanomaterial can be readily defined based on these parameters in a necessary and sufficient way.

In the following, four major categories of nanomaterials and their syntheses are briefly discussed.

6.3   Nanomaterials and Syntheses

Four major categories of nanomaterials discussed in this section have been used in enhancement measurements reported in the literature. They are (1) spherical nanoparticles, (2) nonspherical nanoparticles, (3) aggregates of the same nanoparticles, and (4) assembly of different nanomaterials. The majority of nanomaterials are spherical, including alloy and core-shell- and liposome- or micelle-based nanomaterials.

6.3.1   Spherical Nanoparticles

The most popular nanomaterials are spherical nanoparticles, which include quantum dots, metal and semiconductor nanoparticles, core-shell structures, liposomes and micelles, and polymer-based nanoparticles. Nanomaterials discussed here have been used in enhancement measurements in the context of X-ray nanochemistry. The intended enhancements include types 1, 2, and 3 physical enhancement and types 1 and 2 chemical enhancement. To date, there are only several intended uses of these nanoparticles for biological enhancement as discussed in Chap. 4 (e.g., see Figs. 4.4 and 4.5). The spherical nanoparticles are reviewed according to their composition.

6.3.1.1   Gold Nanoparticles

The discussion here is arranged according to the size of gold nanoparticles, from the smallest to the largest. The nanoparticles developed or used by a particular group are discussed in tandem. This is similar to the style used throughout this book.

Gold nanoparticles are the most popular spherical nanoparticles used in X-ray nanochemistry as reported in the literature. Several reviews are available. Brust el al. [8] summarized the literature on the synthesis and self-assembly of these nanoparticles. A review of applications of gold nanoparticles was given by Forbes et al. [9]. Another review was written by El-Sayed and Murphy et al. [7], which covered almost all gold nanoscale species. The methods of synthesis were generally not invented by the researchers working in the field of X-ray nanochemistry. There were a few exceptions, however, in which nanomaterials were either made for the first time for the use in X-ray nanochemistry or were refined to become more suitable for enhancement measurements. In addition, nanoparticles made according to the methods reported in the literature often require further modifications to suit for applications in X-ray nanochemistry. However, there

are no full-scale reviews on gold nanoparticle synthesis for X-ray nanochemistry. Here, a brief summary of gold nanoparticle synthesis is given specifically for measuring X-ray nanochemical enhancement.

There are many sizes and coatings of spherical gold nanoparticles, ranging from a few scores of atoms to 1.9 nm in diameter, to more than 300 nm in diameter. The smallest gold nanoparticles only had 29–43 gold atoms. They were synthesized by Xie et al. [10] using a method of adding chloroauric acid into glutathione (GSH) aqueous solutions at 25 °C followed by reaction at 70 °C for 24 h. Au_{29-43} nanoclusters coated with GS ligands were obtained.

Other small gold nanoparticles have been made. Small gold nanoparticles were synthesized by Nanoprobes, Inc. The most recent name for this nanoparticle is AuroVist™ and is marketed mainly as a contrast agent for transmission electron microscopy and microCT. These small nanoparticles were highly soluble (>15 WP) in blood as well as in water, which made them suitable for imaging. For X-ray nanochemistry, these small nanoparticles may be more prone to cause chemical and biological enhancement than physical enhancement as discussed in Chaps. 2, 3, 4, and 5. The synthetic procedure was not reported, but Brust et al. [2] reported synthesis of 1–3 nm gold nanoparticles. The synthesis reported by Brust et al. was performed in a two-phase, organic and aqueous, solvent system. The results are shown in Fig. 6.1.

Hainfeld et al. [5] used 11 nm gold nanoparticles for enhancement of radiotherapy to treat brain tumors in mice. Nanomaterial synthesis was not disclosed, but as shown before and here in this section, gold nanoparticles whose size ranged from 3 to 300 nm were made and used in various enhancement measurements. Even though the nanoparticles used in many studies were purchased, to date there is no direct evidence to suggest that these purchased gold nanoparticles are substantially different from those synthesized using the disclosed methods.

In a series of publications, Guo et al. synthesized gold nanoparticles ranging from 3 to 150 nm in diameter and used them in studies of X-ray nanochemistry. Guo et al. [1] developed a method that was the combination of the approaches developed by Whitesides et al. [11], Brust et al. [2], and Rotello et al. [12]. The method allowed Guo et al. [1] to make 5.6 nm trimethylammonium (TMA) dodecanethiol-covered

Fig. 6.1 1–3 nm gold nanoparticles synthesized by Brust et al. [2]. A TEM image of the nanoparticles is shown here. (Adapted from Brust et al. [2] with permission of the Royal Society of Chemistry.)

5 nm
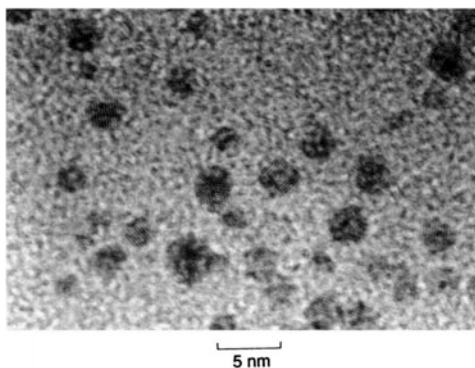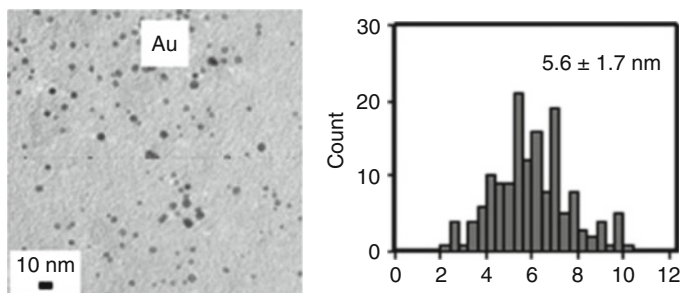
Fig. 6.2 5.6 nm gold nanoparticles synthesized by Guo et al. [1]. A TEM image is shown in the left panel and size distribution is shown in the right panel. (Adapted from Guo et al. [1] with permission of the Royal Society of Chemistry.)

gold nanoparticles. The key step of the synthesis was the attachment of thiol ligands to gold nanoparticles as the zero-valent gold nanoparticles were formed. Gold ions were reduced by sodium borohydride, and the nanoparticles were readily covered with tetraoctylammonium ligands. Once covered, the nanoparticles were transferred automatically to an organic solvent phase. These nanoparticles can be coated with other ligands using ligand exchange reactions as explained later in this section. The nanoparticles were used in enhanced DNA strand break measurements under X-ray irradiation. These nanoparticles are shown in Fig. 6.2.

Guo et al. [13] adopted methods to synthesize 3, 7, and 30 nm gold nanoparticles. The 3 nm gold nanoparticles were synthesized by adopting a method developed by Baiker et al. [14, 15] using sodium hydroxide as the reducing agent and tetrakis-hydroxymethyl-phosphonium chloride (THPC) as the protection ligand. The authors also synthesized 7 nm gold nanoparticles by first reducing gold ions with sodium citrate and then sodium borohydride. Polyethylene glycol (PEG) or mercaptopropionic acid (MPA) ligands were used to protect the surface of the gold nanoparticles. For larger gold nanoparticles, such as 30 nm gold nanoparticles, modified Turkevich method from the original Turkevich method [16] was used. In another work, 16 nm gold nanoparticles were synthesized for conjugation of DNA molecules to the surface of gold nanoparticles, and results were published by Guo et al. [17]. The nanoparticles are shown in the left panel of Fig. 6.3. Larger 88 nm gold nanoparticles were synthesized based on a seed growth method developed by Perrault and Chan [18], and the approach was used to prepare large gold nanoparticles by Guo et al. [19]. Figure 6.3 (right panel) shows the gold nanoparticles made by Chan et al. The seed growth method was particularly effective in producing uniformly sized 88 nm gold nanoparticles. The 88-nm diameter gold nanoparticles are shown in Fig. 6.10 and are covered with a silica layer.

Hwu et al. in Wang et al. [20] and Liu et al. [21] as well as in Liu et al. [22] showed the results of synthesis of PEGylated gold nanoparticles under synchrotron X-ray irradiation and then used the nanoparticles for enhancement measurements. The synthesis was similar to reduction of gold salts in aqueous solutions, except that
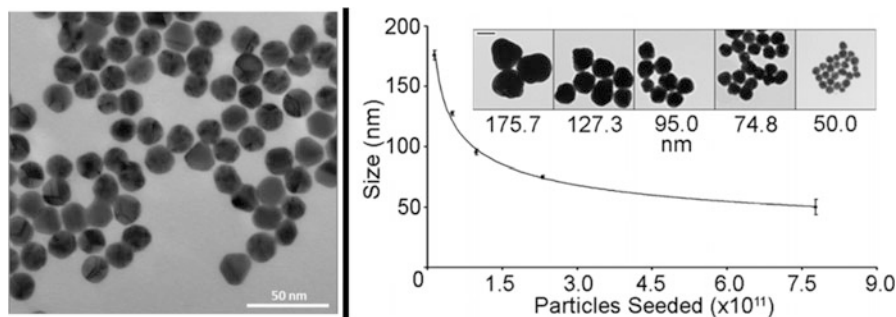
Fig. 6.3 16 nm gold nanoparticles synthesized by Guo et al. [17], and 50–200 nm gold nanoparticles by Perrault and Chan [18]. (Left panel: Adapted from Guo et al. [17] with permission of the Royal Society of Chemistry. Right panel: Adapted with permission from Perrault and Chan [18]. Copyright (2009) American Chemical Society.)

the reducing agent were the chemicals produced in water under X-ray radiation. The size of gold nanoparticles ranged from 15 to 18 nm. The gold nanoparticles were used to obtain enhancement of X-ray radiation effect on damaging cells. Kumar et al. [23] discussed what the authors called third-generation gold nanoparticles optimized for radiation therapy. The authors first obtained THPC-covered small gold nanoparticles. The second step of PEGylation was used to cover the surface of nanoparticles with PEG ligands to increase solubility. The size of these gold nanoparticles was small, between 1 and 3 nm, far below the optimal size of gold nanoparticles for maximum uptake by cells as found by Chithrani et al. [4]. Their optimization was conducted according to three parameters: (1) surfactants, (2) nanoparticle size, and (3) magnitude of enhancement.

"Naked" gold nanoparticles were made by Hwu et al. [24] and Meisel et al. [25]. The latter followed a method developed by Evanoff and Chumanov for making silver nanoparticles [26]. The method involved reaction of Au_2O_3 with H_2 for 10 min. The authors reported the formation of 20–100 nm gold nanoparticles. A size distribution is shown in Fig. 6.4.

Several groups have developed methods to synthesize large gold nanoparticles that can be used in physical enhancement measurements. For example, Eychmuller and Ziegler [27] reported the synthesis of gold nanoparticles ranging from 15 to 300 nm. The authors adopted the seed growth method in which gold nanoparticle seeds were made using the citrate reduction method. Subsequent growth to form larger gold nanoparticles was accomplished using trisodium citrate and ascorbic acid to reduce gold ions. Figure 6.5 shows several different sizes of gold nanoparticles. Any of these nanoparticles may be used for enhancement measurements, though none of them has been used. Their methods can be compared to Puntes et al. [28], who also discussed synthesis of up to 200 nm gold nanoparticles. Puntes et al. employed only sodium citrate but adopted a more elaborate gold salt addition and temperature control scheme. Another example was given by Wang et al. [29] who also demonstrated a method with which they synthesized gold nanoparticles using a

Fig. 6.4 20–100 nm
"naked" gold nanoparticles
synthesized by Meisel et al.
[25]. (Adapted with
permission from Meisel
et al. [25]. Copyright (2010)
American Chemical
Society.)
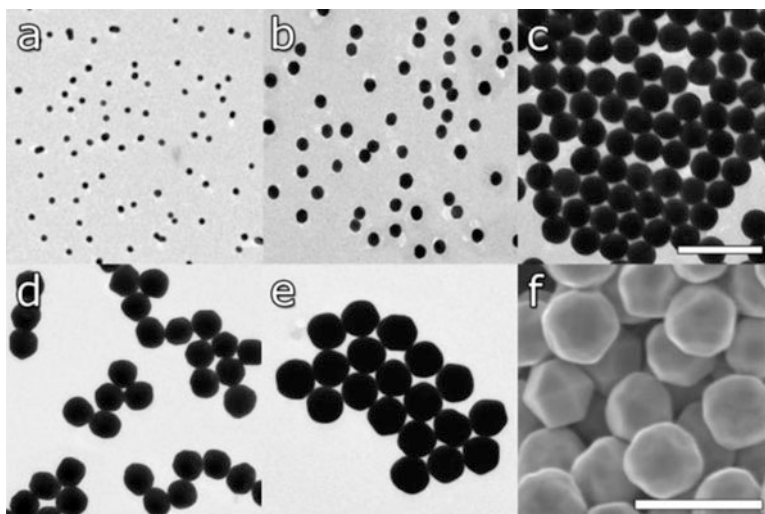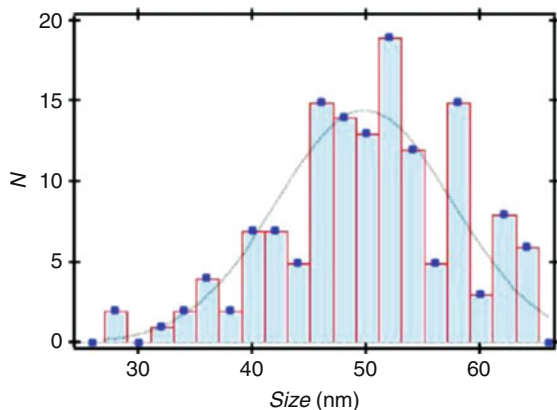
Fig. 6.5 15–300 nm gold nanoparticles synthesized by Eychmuller and Ziegler. The figure shows TEM images of 15, 31, 69, 121, and 151 nm and SEM image of 294 nm gold nanoparticles. The scale bars are 200 nm for (**a–c**) and 500 nm for (**d–f**). (Adapted with permission from Eychmuller and Ziegler [27]. Copyright (2011) American Chemical Society.)

seed growth method from 12 nm diameter citrate-covered gold nanoparticles. The final size ranged from 30 to 220 nm in diameter. The seeded growth was carried out using H_2O_2 as the reducing agent. In addition to gold salt and H_2O_2, citrate was also added. The shape was quasi-spherical.

Fig. 6.6 5 nm Pt
nanoparticles used in the
work published by Guo et al.
[13]. The scale bar is 20 nm
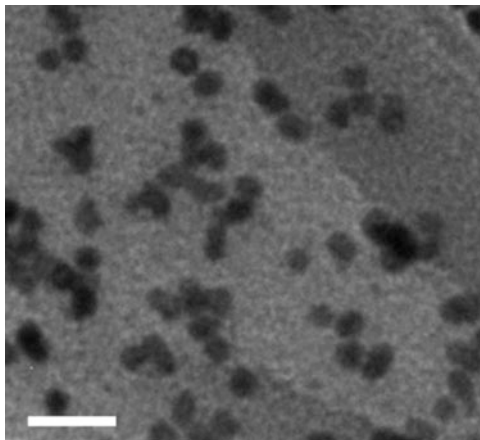
6.3.1.2   Platinum Nanoparticles

Platinum nanoparticles resemble gold nanoparticles in many ways. However, its popularity has not yet reached a comparable status to gold nanoparticles because platinum nanoparticles of different sizes and surface coverage are more difficult to prepare. In the enhancement measurement work presented by Guo et al. [13], the author adopted a method developed by Somorjai et al. [30]. Platinum salt was reduced by sodium hydroxide in ethylene glycol solution. Approximately 1–5 nm diameter platinum nanoparticles were made, depending on the synthetic condition. The nanoparticles were then protected by polyvinylpyrrolidone (PVP, MW 29,000) in HCl ethanol solution. Figure 6.6 shows a TEM image of the nanoparticles. The average size was 5 nm.

6.3.1.3   Silver Nanoparticles

Silver nanoparticles were used in enhancement measurements using synchrotron X-rays by Guo et al. [13]. The nanoparticles were the same as those used in surface-enhanced Raman spectroscopy (SERS) measurements performed by Guo et al. [31]. Synthetic methods were essentially the same as the methods used to synthesize gold nanoparticles, which were made from citrate reduction of gold salt in aqueous solutions, a method adopted from an approach reported by Scherer et al. [32]. These silver nanoparticles were protected by citrate ligands. Guo et al. (unpublished) also synthesized bare silver nanoparticles using sodium borohydride as the reducing agent. The synthesis was performed in silver salt solutions in an ice-water chilled bath, a method first reported by Solomon et al. [33]. These silver nanoparticles were large, 30 ± 6 nm, as shown in Fig. 6.7.

Fig. 6.7 Silver nanoparticle
synthesized by Guo et al.
and used in the work
published by Guo et al.
[13]. The average size is
30 nm and the scale bar is
100 nm

100 nm
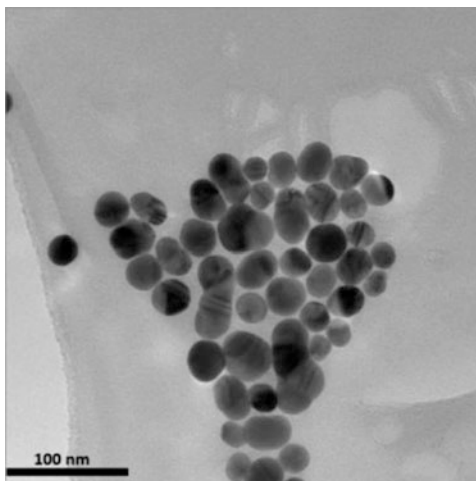
6.3.1.4   Bismuth Nanoparticles

Bismuth nanoparticles were used in enhancement measurements. For example, Li
et al. [34] made 3–4 nm bismuth nanoparticles for targeted delivery and in vitro and
in vivo studies. The nanoparticles were synthesized at 260 °C in oleylamine solu-
tions, a method commonly used in transition metal nanoparticle syntheses.

6.3.1.5   Silver-Core-Gold-Shell Nanoparticles

Metallic nanoparticles commonly have residual electric charges left on them after
reduction of ions. Although this is not a problem in most applications, oxidation of
the aniline monomers on the surface of nanoparticles by reactive oxygen species
such as hydroxyl radicals was sensitive to such residual charges, which was dem-
onstrated by Guo et al. [35]. For this reason, a silver core was added to gold
nanoparticles to take away excessive positive charges from gold because silver has
a slightly lower reduction potential.

   The synthesis of core-shell structure is as follows. First, silver nanoparticles
(AgNPs) were made. Gold salt was then added and reduced in the presence of
AgNPs to form gold nanoshells (AuNSs). It is speculated that charges on
AgNP@AuNSs reside on Ag, which can be represented as AgNP$^+$@AuNSs. The
silver-core-gold-shell nanostructures are different from gold core, silver shell
nanostructures (AuNP@AgNSs), which were prepared by Shankar et al.
[38]. According to the authors, charges possessed by the latter seem to reside on
the gold core rather than the silver shell, which should be represented as AuNP$^+$
@AgNSs. It is unknown if neither, either, or both are correct, and confirmation
requires direct experimental measurements in the future. Figure 6.8 shows silver-
core, gold-shell spherical nanoparticles synthesized by Guo et al. [35]. These

Fig. 6.8 Gold-shell-silver-core spherical nanoparticles used to demonstrate type 1 chemical enhancement of polymerization of the aniline monomers, which was detected by SERS. (Adapted with permission from Guo et al. [35]. Copyright (2012) American Chemical Society.)
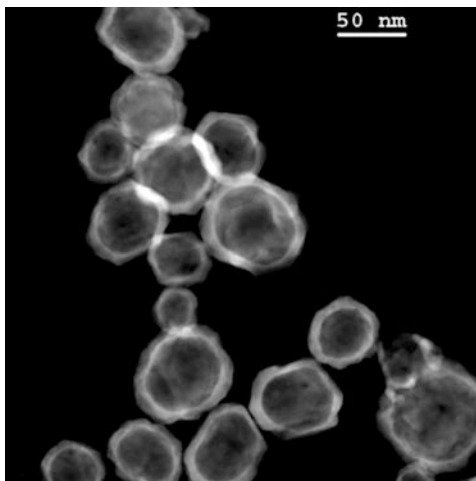
nanostructures also supported strong surface-enhanced Raman spectroscopy (SERS) processes, especially when they aggregated. SERS was used to probe the product of polymerization reaction of the aniline monomer.

6.3.1.6 Liposomes and Calcium Phosphate Enclose Liposomes

Calcium phosphate-enclosed liposomes (CaPELs) have been made as nanoscale probes to detect or measure type 2 physical enhancement by Guo et al. [36]. Sulforhodamine B (SRB) aqueous solution was first entrapped in liposomes formed from phospholipids in aqueous solutions. After extrusion, uniformly sized liposomes were formed, as shown in Fig. 6.9 (panel A or left panel). Then calcium chloride and phosphoric acid were added to the solution at pH 10 to grow a layer of calcium phosphate (CaP) on the exterior of the liposomes, facilitated by the phosphate end group of the lipids. Once the desired CaP thickness was reached, 2-carboxyethylphosphonic acid (CEPA) was added. Figure 6.9 (panel B or right panel) shows the final product. CaP shell safely protects the inner aqueous solution of SRB from chemical enhancement. As a result, this nanoscale probe is ideal to study type 1 or 2 physical enhancement.

6.3.1.7 Silica-Covered Gold Nanoparticles

In order to measure type 1 physical enhancement, nanomaterials with inert surfaces are needed. However, even PEGlyated gold nanoparticles may generate type 2 physical enhancement as well as chemical enhancement. To isolate type 1 physical enhancement from other enhancements, one option is to coat an inert oxide layer
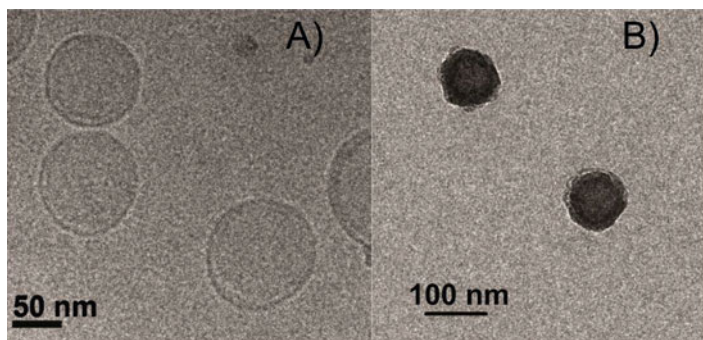
Fig. 6.9 Liposomes (A or left panel) and calcium phosphate-covered liposomes (B or right panel). The calcium phosphate-enclosed liposomes (CaPELs) were used to probe nanoscale energy deposition by nanomaterials. The results of enhancement measurements using these nanoscale probes are shown in Figs. 2.40 and 2.41. (Adapted with permission from Guo et al. [36]. Copyright (2016) American Chemical Society.)

Fig. 6.10 Silica-covered gold nanoparticles by Guo et al. [19]. The gold nanoparticles were made using a seed growth method developed by Perrault and Chan [18]. Silica coating was then conducted. (Adapted with permission from Guo et al. [19]. Copyright (2014) American Chemical Society.)
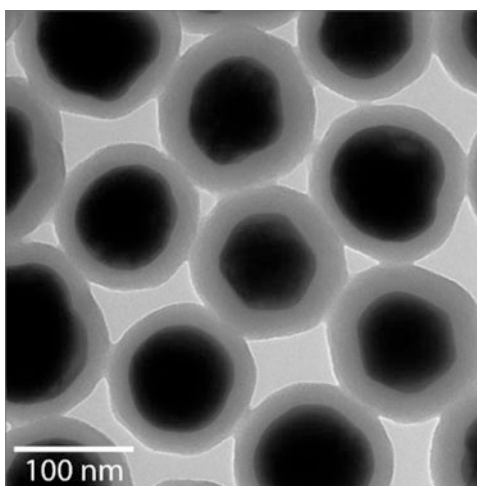
onto large gold nanoparticles. Silica is a viable candidate for such coverage. Figure 6.10 shows the results of silica-covered gold nanoparticles synthesized by Guo et al. [19]. The large gold nanoparticles were made from the seed growth method mentioned earlier. Two methods of silica layer growth were used. One related to using ammonium to reduce TEOS to form relatively thick silica layers, and the other was to use arginine to reduce TEOS to form thin layers of silica as reported by Kraus et al. [37]. The latter can coat a thin layer (<4 nm) silica onto gold nanoparticles.
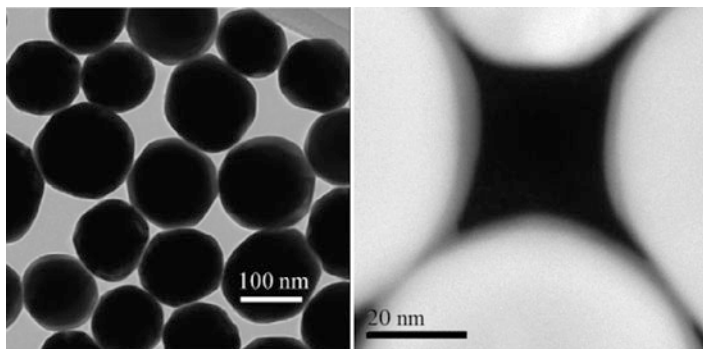
Fig. 6.11 Silver-covered gold spherical nanoparticles (Agu). The gold nanoparticles were made using a seed growth method developed by Perrault and Chan [18]. Silver coating was then conducted. (Reprinted from Guo et al. [39]. Copyright (2016) with permission from Elsevier.)

6.3.1.8 Silver-Coated Gold Nanoparticles (Agu)

Silver-coated gold nanoparticles have been synthesized by several groups. For example, as mentioned above, Shankar et al. [38] found that silver on gold nanoparticles was more resistive to chemical oxidation. Guo et al. [39] synthesized a special nanostructure called Agu that had a thin layer (<2 nm) of silver covering large (>50 nm diameter) spherical gold nanoparticles. When the thickness was between 0.5 and 2 nm for 100 nm diameter gold nanoparticles, change of surface plasmon resonance peak position followed a sigmoidal profile as a function of Ag thickness on Au. The nanomaterials were used to detect etching of silver by X-ray irradiation, as shown in Sect. 11.4. In the synthesis, gold nanoparticles were first synthesized, followed by adding Ag salt into a reducing environment of ascorbic acid. The concentration of gold nanoparticles was high so that reduced Ag ions were immediately coated onto gold nanoparticles rather than forming small silver nanoparticles en masse. Figure 6.11 shows the results. The light gray color in both left and right panels indicates the silver layer.

6.3.1.9 Palladium-Coated Hollow Gold Nanoparticles

Hao, Sun, and Mao et al. [40] synthesized hollow gold nanoparticles using reduction of gold salt in the presence of hydrogen nanobubbles. The method was first established by the authors in 2009 (see Huang et al. [41]). Hao and Sun et al. [42] used a similar method to prepare palladium-coated hollow gold nanoparticles for treating tumors. The authors first prepared the hollow gold shells. The gold shells were 25 nm thick with a 50 nm inner diameter. Then copper was coated onto the surface of hollow gold nanoparticles, followed by galvanic replacement of Cu with ^{103}Pd, which emits 21 keV X-rays with a 16-day half-life.

6.3.1.10 Oxide Nanoparticles

These are nonmetal oxide nanoparticles. For example, silica nanoparticles are available from many manufacturers. Aldrich produces SM-30, HS-40, and TM-50, which were used by Meisel et al. [43] in their radiolysis measurements. These nonmetal oxide nanoparticles were only occasionally used in enhancement measurements described in Chaps. 2, 3, 4, and 5, and most of these nanoparticles were considered inert or non-catalytic in terms of generating the enhancement as defined in X-ray nanochemistry. Therefore, the discussion is limited to the applications of radiolysis.

6.3.1.11 Transition Metal Oxide Nanoparticles

Many transition metals can potentially be used to generate the enhancement defined in this book. In a recent work, Sasaki et al. [44] utilized a unique transition metal nanomaterial, titanium peroxide (TiO_x) nanoparticles, to create enhancement to the effectiveness of X-ray irradiation. The nanoparticles were modified from anatase titanium oxide TiO_2 nanoparticles by first costing TiO_2 nanoparticles with polyacrylic acid (PAA) and then treating the nanoparticles with peroxide H_2O_2. As shown in Fig. 6.12, the nanoparticles are highly porous or gel-like. The average size measured using dynamic light scattering (DLS) was 50 nm, as shown in the right panel of Fig. 6.12. Enhancement of radiotherapy was measured using tumor cells and tumors in mice.

Chen et al. [45] synthesized mesoporous tantalum oxide nanoparticles ($m-Ta_2O_5$) and used them to improve the effectiveness of chemoradiotherapy. The authors coated the surface of the 60-nm diameter nanoparticles with PEG ligands ($m-Ta_2O_5$-PEG) followed by loading doxorubicin (DOX) into the nanoparticles ($m-Ta_2O_5$-PEG/DOX). The final size was close to 90 nm in diameter. The drug
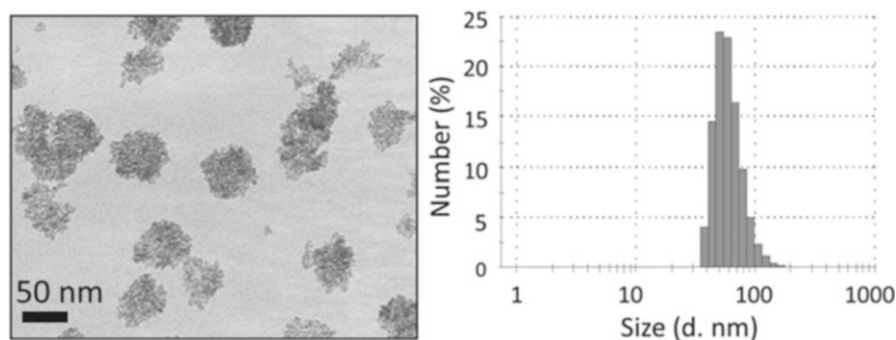
Fig. 6.12 Titanium peroxide nanoparticles produced from anatase titanium oxide (TiO_2) nanoparticles. A TEM image is shown in the left panel. The average size was 50 nm based on DLS measurements, as shown in the right panel. (Adapted with permission from Sasaki et al. [44]. Open Access under CC BY 4.0 International License.)

was completely released within 5 min when pH was lowered from 7.4 to 5.0. No toxicity was observed with the m-Ta_2O_5-PEG. Best results were obtained with m-Ta_2O_5-PEG/DOX under X-ray irradiation, which based on the data was equivalent to the addition of DOX and m-Ta_2O_5-PEG under X-ray irradiation.

6.3.1.12   Rare Earth Oxide Nanoparticles

A large number of rare earth nanoparticles have been synthesized. These nanoparticles can strongly absorb X-rays and subsequently emit UV light, which is responsible for type 3 physical enhancement described in Chap. 2. The light emission mechanisms associated with rare earth nanoparticles are associated with different quantum dots. Generally speaking, rare earth nanoparticles emit line emissions of atomic natural linewidths, whereas quantum dot emission is a narrow band of a few nanometers in bandwidth. Among these rare earth nanoparticles, several of them have been used in enhancement studies.

Cao et al. [46] discussed the preparation of Gd_2O_2S:Tb nanoparticles. Tb^{3+} ions were doped to improve luminescence. The nanoparticles were more homogeneous because of the presence of sulfur. The nanoparticles were directly used to generate type 3 physical enhancement. In another study, rare earth-doped semiconductor nanoparticles were made by Townley et al. [47]. The nanoparticles were used to augment radiotherapy in vivo. Specifically, the authors used Gd-doped TiO_2 nanoparticles as an enhancer for type 3 physical enhancement. The nanoparticles were aggregates. Synthesis was achieved by mixing various rare earth nitrate salts (hydrate) with titanium isopropoxide and isopropanol. The precipitate was then washed and treated to obtain nanoparticles, which were then covered with a silica layer or fluorescent molecules. These nanoparticles were then tested in vitro for their enhancement properties in reducing cell viability under X-ray irradiation. Yang et al. [48] developed a LaF_3:Tb@SiO_2/dye nanoparticle system to enhance X-ray-induced photodynamic therapy efficacy. Figure 6.13 shows the TEM images of nanoparticles.

Fig. 6.13 Lanthanide-doped fluorides nanoparticles (**a**) and silica coated such nanoparticles (**b**). (Adapted from Yang et al. [48] with permission of the Royal Society of Chemistry.)
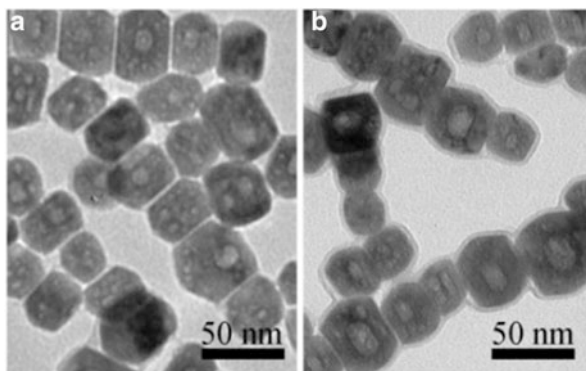
Along the same line, Hu and Yang et al. [49] showed that it was possible to use X-rays to excite LaF$_3$:Tb scintillating nanoparticles for therapeutic purpose. FRET process was detected in this work.

More recently, Cai et al. [50] reviewed the work of using scintillating nanoparticles for photodynamic therapy. The authors summarized recent publications in this research area, and many rare earth nanoparticles were discussed in their review.

6.3.1.13 Quantum Dots

Quantum dots have been used in X-ray scintillation and imaging. The synthesis and applications of quantum dots have been described in the literature, as recently reviewed by Medintz et al. [51]. Quantum dot nanomaterials are now widely available from many companies. Quantum dots to date are mainly used for generating type 3 physical enhancement. Briefly, quantum dots are made by reducing two or more salts in the presence of high affinity ligands toward the elements in the quantum dots. In a typical synthesis, NaHTe and Cd(ClO$_4$)$_2$ solutions are reduced by mercaptopropionic acid (MPA) in water. If the surfactants are organic, further chemical modification is needed to make quantum dots soluble in water. Ligand exchange reactions can be used to replace the ligands. In one example, Kang et al. [52] developed a CdTe quantum dot of different sizes. The central wavelength of emission shifted as the size of quantum dots change. The authors also embedded the quantum dots in polymers to form composites.

Beaulieu et al. [53] described the results of coating the surface of CdSe quantum dots with ZnS, CdZnS, and CdS to preserve the fluorescence of CdSe quantum dots under X-ray irradiation. The diameter of these quantum dots with multiple protective layers was 6–8 nm. The radioluminescence decayed mildly under 120 keV X-ray irradiation, dropping only 4% over 2 kGy irradiation, which was three times better than that of uncoated CdSe quantum dots; the latter decreased by 12% after the same dose of irradiation, which was already much better than the behavior of CdSe or CdSe/ZnS quantum dots shown in reports in the literature that showed a 50% drop in radioluminescence after only 100 Gy irradiation. For example, Stodilka et al. [54] reported the behavior of CdSe quantum dots coated with ZnS. Radioluminescence decreased to 20% after irradiation of 100 Gy of 1–2 MV γ-rays. In a similar work, Withers et al. [90] revealed the poor luminescence stability of CdSe/ZnS quantum dots under 662 keV γ-rays. Radioluminescence dropped to 1/e after 200 Gy irradiation.

6.3.1.14 Silicon and Germanium Semiconductor Nanoparticles

Silicon nanoparticles were made in top-down methods by Gonzalez et al. [55] and were used in X-ray nanochemistry by Gonzalez and Kotler et al. [56]. The method of synthesis was electrochemical etching, which was different from the more
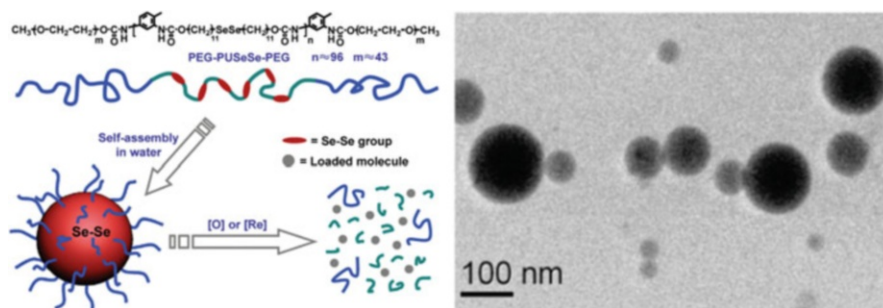
Fig. 6.14 Spherical polymer nanoparticles made of diselenide complexes for X-ray triggered release of payloads. (Adapted with permission from Xu and Zhang et al. [58]. Copyright (2010) American Chemical Society.)

conventional, bottom-up methods developed by Kauzlarich et al. [57]. Electrochemical etching was simpler, though the size control was less precise than the bottom-up method. After sonication to obtain silicon nanoparticles, their surface was functionalized with several ligands including amine and enoate. The size distribution was broad, covering the range of 1–8 nm.

6.3.1.15   Other Spherical Nanoparticles

Several selenium nanomaterials have been made and used to enhance the effectiveness of X-ray irradiation. For example, selenium-selenium polymer nanoparticles were prepared by Xu and Zhang et al. [58]. The nanomaterial was used in several experiments to measure the radiation triggered release of payloads. Figure 6.14 shows the protocol to make the nanoparticles as well as a TEM image of the nanomaterial. In addition, other selenium nanoparticles were used for X-ray enhancement, and the results are shown in Sect. 9.8.

6.3.1.16   Clusters

In addition to nanoparticles, various clusters have been synthesized to improve the efficacy of conversion of X-rays to other forms of energy. For example, Kirakci and Lang et al. [59] synthesized octahedral molybdenum clusters to function as X-ray nanoscintillators. The compound can increase the production of singlet oxygen by absorbing X-rays and emitting 690 nm photons, therefore making it possible to generate X-ray-induced luminescence and singlet oxygen. These properties remained the same when the compound or cluster was embedded in polystyrene films, which further increased the yield of singlet oxygen generation and luminescence through energy transfer from polystyrene to the cluster. Figure 6.15 shows the structure (left panel) of the cluster and an application scheme (right panel).
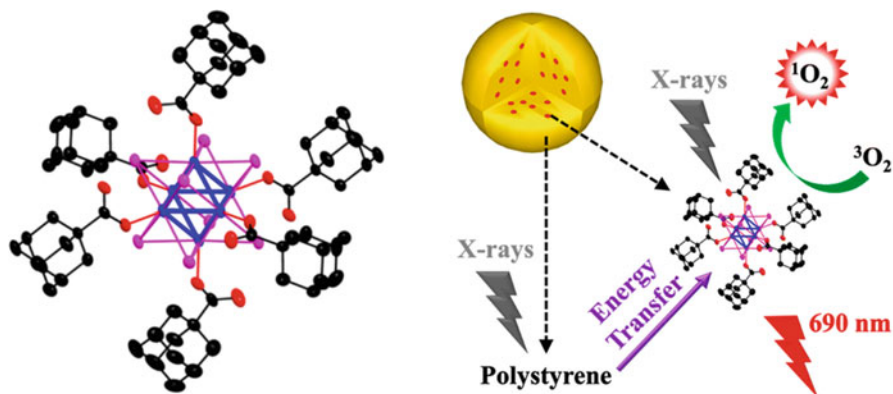
Fig. 6.15 Inorganic clusters made of molybdenum (left panel). The right panel shows how X-rays are used to excite the clusters to produce singlet oxygen. The clusters under X-ray irradiation emit 690 nm light. (Adapted with permission from Kirakci and Lang et al. [59]). Copyright (2016) American Chemical Society.)

6.3.2 Nonspherical Nanoparticles

Besides spherical nanoparticles, other forms of nanomaterials can also enable enhancement to the effectiveness of X-ray irradiation. These nanomaterials are nanotubes, nanorods, nanowires, nanoprisms, and nanodisks. This book does not enumerate all the currently available nanomaterials and only covers those nanomaterials that have been used in X-ray enhancement measurements reported in the literature or those that have been used in the syntheses of nanomaterials for enhancement measurements. For example, Tian and Pan et al. [60] studied PEGylated Au@Pt nanodendrites for CT imaging and radiotherapy. The synthesis began with the synthesis of 8 nm gold nanoparticles. Pt was then incorporated onto the gold nanoparticles by adding $Pt(acac)_2$ and oleylamine. PEG ligands were then conjugated to the surface. The overall diameter of the nanomaterial was 30 nm. The nanomaterial was mildly toxic to cells, with cell viability dropping to 85% at 0.1 mg/mL incubation concentrations.

The most massive nanomaterials used in X-ray enhancement measurements were gold nanowires or nanotubes. They were 100–200 nm in diameter and microns long. These nanotubes packed in solution or space like haystacks and had space voids between the nanotubes for analytes or targets. This nanomaterial created the highest weight percentage (WP) of gold in water, which could potentially produce the highest physical enhancement. However, as it is shown in Chaps. 2 and 5, this was not the case as the surface of bare gold nanomaterials scavenged radicals and reduced the amount of reaction oxygen species.

The synthesis of gold nanotubes employed silica nanowire cores. First, silica nanowires were grown from catalytic reactions using cobalt or other nanoparticles as catalysts based on a method developed by Guo et al. [61]. Two nanometer cobalt

Fig. 6.16 Gold nanotubes made from silica nanowires. The figure shows the silica nanowire (SiNW) core and the gold nanotube coating. (Reprinted from Guo et al. [62]. Copyright (2006), with permission from Elsevier.)

nanoparticle catalysts were deposited on the surface of silicon wafers, which were then placed in a high-temperature furnace. Silane gas was flown through the high-temperature region, and silica nanowires (SiNW) were produced. The wires were collected using a razor blade to peel the silica nanowire film off the wafer. The nanowires were dispersed in water, into which small THPC-covered gold nanoparticle seeds were added and silica nanowires were covered with THPC-covered gold nanoparticles. An aged gold salt aqueous solution and weak reducing agents were added into the gold nanoparticle-coated silica nanowire solution, and gold nanotubes were formed. The synthesis was done at room temperature or in a high-temperature microwave oven autoclave device. The nanotubes grown in the microwave device had a smoother surface. Figure 6.16 shows a typical gold nanotube, exposing a section of SiNW.

The synthesized nanotubes can be directly used for enhancement measurement. However, because microwave synthesis was a surfactant ligand-free method, gold was exposed to the solution and could directly react with reactive oxygen species, which resulted in the destruction of hydroxyl radicals because gold has a lower reduction potential than the hydroxyl radical. Future work will be needed to modify the surface of gold nanotubes so that it does not scavenge reactive oxygen species.

Krishnan et al. [63] synthesized gold nanotriangles and used them in in vitro and in vivo work. Seeded growth methods developed by Murphy et al. [64] were adapted in the nanoprisms or nanotriangle synthesis which used seed gold nanoparticles and cetyltrimethylammonium chloride (CTAC) ligands in multiple growth steps. The nanotriangles were nearly equilateral triangles with an edge length of 61 nm. In vivo results showed mild enhancement; biodistribution results showed a clear accumulation of 5 ppm of the nanomaterials in the tumor. Based on the magnitude of physical enhancement caused by gold nanomaterials shown in Chap. 2, it is clear that the amount of enhancement observed in the work cannot be caused by physical enhancement by the nanomaterials even for only a mild enhancement.

6.3.3   Aggregated Nanoparticles

Aggregation of nanomaterials is not preferred in many applications of nanotechnology and nanoscience. Nonetheless, dimers and aggregates can enhance X-ray effects similar to a shell of gold shown in Chap. 2. There are several reports of how to make nanoparticle dimers. The actual syntheses, however, were rather difficult, so more work needs to be done to make nanoparticle dimer synthesis more readily available. Here, several methods are briefly discussed. Nann et al. [65] showed that 10 nm gold nanoparticles were attached to 100 nm silica nanoparticles. Lithography was another approach to make these structures. El-Sayed et al. [66] demonstrated that dimer distance between gold nanoparticles influenced SPR response. It should be pointed out that these aggregates were not used in X-ray nanochemistry measurements.

Tsourkas et al. [67] used oil-water emulsions to trap 1.9 nm gold nanoparticles in small micelles of nanometer sizes. The micelle emulsion was stabilized with amphiphilic diblock copolymer polyethylene oxide (4 k Dalton)-polycaprolactone (3 k Dalton). Both 1.9 nm gold nanoparticles and the polymers were dissolved in toluene, which was then mixed with water. The mixture was emulsified in an ultrasonic bath. Centrifuge separation was used to extract the desired size fraction; small particles were removed via filtration. The final product is shown in Fig. 6.17.

Su et al. [68] used aggregates of gold nanoparticles to fabricate microdisks. A polydimethylsiloxane stamp with the footprint of microdisks was immersed in a polyelectrolyte solution to form a layer of several electrolytes, to which a layer of gold nanoparticles was attached. The diameter of the disks was approximately 5 μm. The height of each electrolyte/gold assembly was approximately 22 nm. Multiple layers of gold and electrolytes were formed. Up to five layers were made in a single disk in the example shown in the report. These disks were then mixed with cells to form cell/disk heterodimers for X-ray enhancement measurements. Figure 6.18 illustrates how the microdisks are made.

Fig. 6.17 Formation of aggregated gold nanoparticles in micelles. 1.9 nm gold nanoparticles were trapped in micelles. (Adapted with permission from Tsourkas et al. [67]. Copyright (2014) American Chemical Society.)

● 1.9 nm AuNP

PEG(4k)   PCL(3k)
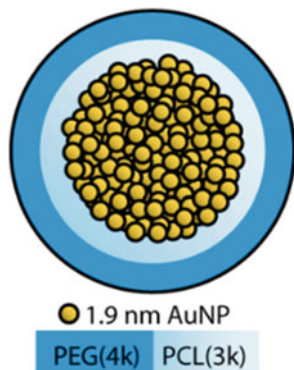
Fig. 6.18 Multilayered
gold nanoparticle micro
disks for enhancement of the
effectiveness of X-ray
irradiation. (Adapted with
permission from Su et al.
[68]. Copyright (2015)
American Chemical
Society.)
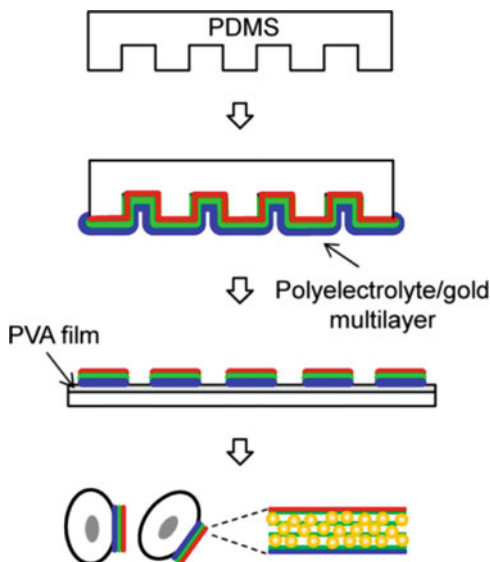
6.3.4   Complex Nanomaterials

These nanomaterials are more than just aggregates of one kind of nanoparticle—the
final nanomaterials are assembled from several different kinds of nanomaterials or
chemicals. Currently, there are several examples, and much more work can be done
in this area. One example showing a glimpse of the potential of these nanomaterials
was given by Fologea et al. [69], who assembled several molecular components into
a nanoassembly. Figure 9.43 shows the targeted assembly. The authors envisioned a
unique application for this nanoassembly. Another complex spherical nanomaterial
was synthesized by Xie et al. [70], who assembled a few components to form a
nanostructure the authors called SAO that promotes the formation of singlet oxygen
while under X-ray irradiation. The nanostructure is shown in Fig. 6.19, which
describes a structure of SAO and how it helps production of singlet oxygen.

Bu and Shi et al. [71] synthesized a complex nanomaterial that had a rare earth
core and a silica shell covered with photodynamic therapy reagents such as porphy-
rin IX and targeting ligands such as TAT peptide (GRKKRRQRRRPQ). Porphyrin
IX molecules were embedded in silica, and the nanoparticles were also covered with
PEG ligands. The overall size of the nanomaterial was approximately 50 nm. The
authors named the nanomaterial UCSPs-PEG/TAT, which was responsive to both
X-ray and near-infrared irradiation to produce reactive oxygen species. Bu and Shi
et al. [72] also reported the synthesis and application of a similar nanomaterial,
PEG-USMSs-SNO, that had nitric oxide (NO) donors within the nanoparticles.

Another example was given by Guo et al. [36] who synthesized calcium
phosphate-coated liposomes (CaPELs) with aqueous solutions of sulforhodamine
B (SRB) trapped inside. SRB was incubated with lipids, and liposomes were formed

Fig. 6.19 The construction of SAO in silica nanoparticles for conversion of oxygen to singlet oxygen. (Adapted with permission from Xie et al. [70]. Copyright (2015) American Chemical Society.)
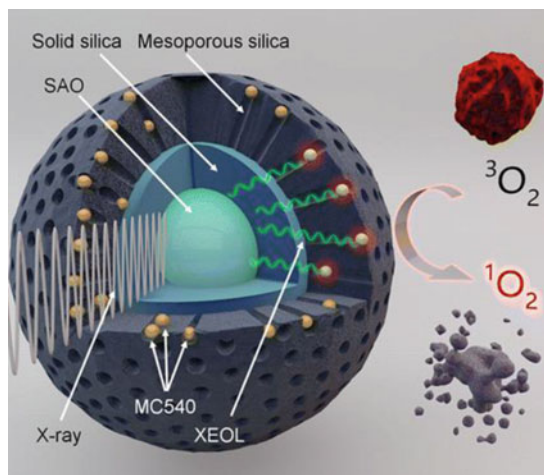
through micro-extrusion. Then, phosphoric acid and calcium chloride were used to deposit a calcium phosphate shell on the liposome surface at pH 10. The nanomaterials are shown in Fig. 6.9 and the synthetic method is given in Sect. 6.3.1.6. This nanomaterial can be used to detect type 2 physical enhancement because their size is approximately 100 nm in outer diameter and the solid calcium phosphate shell does not allow radicals to permeate. Other sizes of liposomes and CaPELs can be made, depending on the extrusion process.

Liu et al. [73] developed a new nanomaterial called BM@NCP(DSP)-PEG that had a bovine serum albumin protein-stabilized MnO_2 nanoparticle core wrapped by a polymer-linked cisplatin compound c,c,t-(diamminedichlorodisuccinato)Pt(IV) or DSP shell. Hafnium ions were also incorporated in the shell. This nanomaterial was then coated with dopamine followed by PEG. The overall size of the nanomaterial was slightly less than 110 nm. The Pt compounds were the prodrug.

Tung and Liu et al. [74] synthesized a new nanomaterial with which the authors studied the damage of *E. coli* under X-ray irradiation. The nanoparticle core was made of graphene oxide quantum dots (GQD), which were 3 nm in diameter. The quantum dots were then conjugated to multiple vancomycin molecules, which helped target bacteria, followed by attaching protoporphyrin to the surface of the quantum dots. The final product was a complex nanoparticle consisting of multiple quantum dots, and overall size was approximately 100 nm, based on TEM measurements.

6.4   Surfactants and Conjugation Reactions

Successful synthesis of nanoparticles relies on proper construction of the surface of these nanoparticles. Except for a small number of cases where the surface has the same composition as the core, most nanoparticles have different surface

compositions from the core. Further, the surface of nanoparticles is often modified post-synthesis to increase the functionalities of nanoparticles. These post-synthetic modifications have been developed and will be further explored in the future.

In this section, surfactants of the nanomaterials mentioned in this book and the chemical reactions used to generate these surfaces are described. Although many books have been published on the subject, this section mainly focuses on the discussion of nanomaterials used in X-ray enhancement measurements. Currently, many chemical reactions are used to link or conjugate surfactants to the surface of nanomaterials, and much more future work will undoubtedly expand types of surfactants and chemical means to conjugate surfactants to the surface of nanomaterials.

In the following, ligands or surfactants are listed in the context of X-ray enhancement measurements, followed by discussion of reactions with which one can conjugate surfactants to the surface of nanomaterials for X-ray enhancement measurements. A general discussion on the stability of surfactants is given in Sect. 6.4.3.

6.4.1   Surfactants of Nanomaterials

Surfactants of nanomaterials used in X-ray enhancement measurements have to simultaneously satisfy several requirements. First, surfactants have to make nanomaterials soluble in the media of interest, such as water, blood serum, or alcohol. Secondly, for X-ray enhancement, surfactants have to be non-scavenging toward reactive oxygen species or low-energy electrons if the goal is to cause physical enhancement. Lastly, surfactants may need to have affinity toward targets or probes used in X-ray enhancement.

Table 6.2 shows some of the ligands used as surfactants of nanomaterials employed in X-ray enhancement measurements described in this book. The methods

Table 6.2 List of surfactants of several nanomaterials used in X-ray enhancement measurements

Nanomaterials	Surfactants	MW (amu)
Gold nanoparticles	Citrate acid	50
	Polyethylene glycol (PEG)	2000–5000
	Trimethylammonium (TMA)	200
	Mercaptopropionic acid (MPA)	150
	DNA	Various
	Ethidium bromide	314
Silver nanoparticles	Citrate acid	50
Platinum nanoparticles	Polyvinylpyrrolidone (PVP)	10,000–50,000
Oxide nanoparticles	Silica (Si-OH or Si-O-Si)	18
Rare earth nanoparticles		
Micelles		
Liposomes	Phosphate groups	95
Calcium phosphate-enclosed liposomes	Ca^{2+} or PO_4^{3-}	40

of attaching these surfactants to the surface of nanomaterials will be discussed in
Sect. 6.4.2. The molecules range from simple citrate anions to complex
polyvinylpyrrolidone (PVP) and even DNA molecules. Almost all of these surfac-
tants are molecular.

6.4.2   Conjugation Reactions to Attach Surfactants
to the Surface of Nanomaterials

Conjugation of ligands to the surface of nanoparticles can be divided into at least
three general categories. Category I conjugation includes processes of attaching
surfactants to the surface of nanoparticles during the synthesis of nanoparticles.
Nanoparticle synthesis is terminated when all the feedstock of atoms or monomer
units are used. Category II conjugation is the replacement of the originally attached
surfactants with other surfactants. Category III conjugation includes reactions that
link different surfactants to what are already on the surface of nanoparticles.
Figure 6.20 illustrates these three conjugation processes. All three categories of
reactions are discussed in this section. The order of discussion follows the order of
nanomaterials discussed in the last section. The content is limited to nanomaterials
used in X-ray enhancement studies.

Since reactions defined in the first category are the most frequently occurring
reactions and the other two categories of reactions are usually derived from these
reaction products, it is critical to examine category I conjugation reactions. These
reactions can be represented by three types. The first type of reaction relates to
electrostatic attraction between gold atoms and ionic groups, such as citrate anions.
The second type of reaction relates to the formation of covalent bonds such as gold-
thiol bonds between thiol-terminated ligands and gold surface atoms. The third type
relates to interactions of long ligands or surfactants such as PVP that physically wrap
around gold nanoparticles. Figure 6.21 illustrates these three reactions between
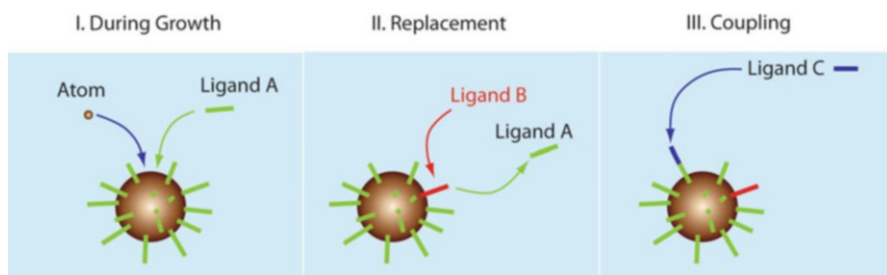
Fig. 6.20 Summary of three categories of chemical reactions linking surfactants to the surface of
gold nanoparticles. The first category is addition of surfactant or ligands during or after the growth
of nanoparticles. The second category is the replacement of existing surfactants or ligands with
other surfactants or ligands. The third connects surfactant ligands of different kinds to the existing
surfactants or ligands on the surface
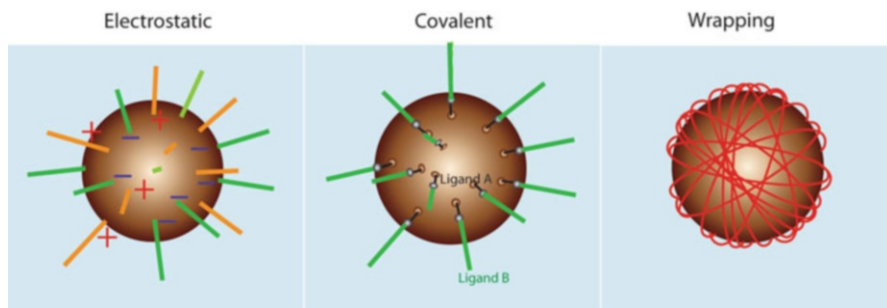
Fig. 6.21 Summary of three types of category I chemical reactions linking surfactants to the surface of gold nanoparticles. The first is addition of ligands during or after the growth of nanoparticles through electrostatic interactions. The second is the conjugation of new ligands to the existing ligands through covalent bonds. The third is addition of long polymeric ligands physically covering the surface

ligands or surfactants and the surface of the nanoparticle. The ligands conjugated to the surface using category I conjugation reactions can then be replaced using category II conjugation reactions or be linked to other ligands through category III conjugation reactions shown in Fig. 6.20.

In the following, published results are discussed based on the categories of reactions through which the surface of nanoparticles are covered. Gold nanoparticles are the most popular nanoparticles used in X-ray enhancement measurements. Synthesis of gold nanoparticles typically involves first or second or both categories of conjugation reactions defined in this section. For instance, only category I conjugation reactions are involved for citrate-covered gold nanoparticles. The average size of gold nanoparticles made this way ranges from 15 to 30 nm. Guo et al. [13] made 15 and 30 nm nanoparticles using citrate reduction and surfactant coverage methods. For smaller and larger gold nanoparticles, more complex synthetic methods were needed. Brust et al. [2] developed the thiol ligand coverage approach that transferred gold nanoparticles from aqueous to organic solvent once gold nanoparticles were covered with thiol ligands. Their method employed category I conjugation reactions. Another example is adding ligands other than the original coverage. For instance, folic acid can be added to the solution of citrate-covered gold nanoparticles. Due to its overwhelmingly high concentration, folic acid ligands are attached to the surface of gold nanoparticles. This approach belongs to category II since folic acid replaces citrate ligands.

To make gold nanoparticles more soluble, stable, or possessing targeting functions, categories II and III conjugation reactions are needed. For example, citrate-covered gold nanoparticles can be made in the first step. In a subsequent step, thiolated polyethylene glycol (PEG) ligands can be used to replace the citrate ligands. PEGylated gold nanoparticles are more soluble in water and more stable in blood serum, making these nanoparticles more suitable for animal studies that demand long circulation times. Guo et al. [13] used these PEGylated gold nanoparticles for type 1 physical and chemical enhancement measurements. Post-

synthesis modification of the surfactants is possible and is often needed in many applications. For example, Guo et al. [1] and Carter et al. [75] showed the switch of ligands to either positive or negative functional groups such as trimethylammonium or carboxylate. Similar methods have been developed by others, such as Rotello et al. [76]. Thiol-glucose ligands were used by several groups including Roa and Xing et al. [77] to improve uptake of gold nanoparticles by cells. DNA ligands can be attached to the surface of gold nanoparticles, a category of reactions that have been extensively studied by Mirkin et al. [78]. In another work in the framework of X-ray enhancement measurements, Su et al. [79] showed the results of ligand replacement reactions involving polyethylenimine (PEI), polysodium sulfonate, polydiallyl-dimethyl ammonium chloride (PDDA), and polydimethylsiloxane ligands.

Most of the third category conjugation reactions involve various click reactions between a ligand already on the surface of the nanoparticles and another incoming ligand. For gold nanoparticles used in X-ray enhancement measurements, click reactions were used by Guo et al. [17] to conjugate doxorubicin (DOX) to DNA bases through succinimidyl 4-(N-maleimidomethly)cyclohexane-1-carboxylate (SMCC). The synthesis conjugated hundreds of 12-mer DNA molecules onto a 15 nm gold nanoparticle, with approximately nine DOX molecules attached to each DNA molecule, resulting in thousands of DOX molecules attached to each gold nanoparticle. In this case, PEGylated gold nanoparticles were used because the nanoparticles were soluble in water during the synthesis. Many similar reactions belonging to thiol-ene click reactions have been extensively studied. Hoyle et al. [80] reviewed the thiol-ene reactions. Dondoni [81] also discussed this process. In another example, Latimer [82], in his MS thesis, discussed the attachment of PEG-CCP ligands onto gold nanoparticles. The modification was extensive, and the work showed the versatility of post-modification. With basic units such as thiol, amine, or carboxylate on the gold surface, other coupling reactions are possible. Castner et al. [83] discussed conjugation between DNA and the gold surface through thiol-ene click reaction. The surface was packed with maleimide ligands for DNA conjugation.

Cheng et al. [84] reported a gold-DOX nanoconjugate. Their method linked DOX to gold through disulfide bonds, which were formed between disulfide terminated PEG ligands on gold nanoparticles Au-PEG-SS and thiolated DOX DOX-SH. The PEG ligands were connected to the gold nanoparticles through thiol-gold bonding. The authors reported the release of DOX when the nanoconjugates were in cells, although it was unclear whether the release was caused by the cleavage of dithiol bonds as the authors claimed or through the cleavage of gold-thiol bond.

Vo-Dinh et al. [85] discussed a method of conjugating ligands to the surface of Y_2O_3 nanoparticles. The first step was to allow decomposed 2-chloroethylphosphonic acid to react with the oxide surface. This reaction belonged to the second category of conjugation reactions shown in Fig. 6.20. This chemical reaction established covalent bonding between the ligand and surface. In the second step, TAT ligands reacted with phosphate functional groups already on the surface of

the oxide nanoparticles. This step belonged to the third category of conjugation reactions shown in Fig. 6.20. As a result, oxide nanoparticles with Psoralen ligands on their surface were prepared. The reaction is shown in Fig. 2.42.

Micelles and liposomes have also been used to construct nanoparticles for X-ray enhancement. Micelles were used to construct gold nanoparticle aggregates. Liposomes were coated with calcium phosphate to prevent permeation of small molecules, such as reactive oxygen species, and the final products were used to study type 2 physical enhancement and X-ray-induced energy transfer (XIET) as studied by Guo et al. [36].

6.4.3   Stability of Ligands on Nanoparticles

As the ligands on the surface (i.e., surfactants) of nanoparticles at least share the control the functionality of nanomaterials, their stability is critical to the success of nanomaterial synthesis and applications. For example, single thiol-gold bonds may be easy to form, but they can also break at room temperature, as demonstrated in many reports. A possible solution is to use multiple thiol-gold bonds to anchor a ligand. For example, Mirkin et al. [86] demonstrated a method to synthesize multiple thiol-anchored DNA conjugates. They observed an approximate five degrees Celsius increase in DNA melting measurements when trithiols were used.

6.5   Characterization of Nanomaterials

Many physical methods can be used to characterize nanomaterials. Some of the most popular methods are listed in Table 6.3. In addition, detection ranges and purposes are given in Table 6.3 as well. Only acronyms of the methods are given. Special methods are being developed. For example, Rotello et al. [87] used mass spectrometry to detect ligands on nanoparticles that may prove useful in future research of nanomaterial synthesis and detection.

6.6   Nanomaterials for Physical, Chemical, and Biological Enhancement

Sections 6.3 and 6.4 describe the nanomaterials and their surfactants used in X-ray nanochemistry. A proper demonstration of each category and type of enhancement described in Chaps. 2, 3, 4, and 5 requires careful choice of these nanomaterials. Here, a number of nanomaterials that satisfy the basic requirements for supporting a particular enhancement are selected. It is important to point out that these

Table 6.3 Detection methods, range and detection purposes of the methods used to characterize nanomaterials

Method	Size range (nm)	Detection	Purposes
TEM	0.1–1000	Positions of atoms	Size, shape, and composition
SEM	1–1000	Positions of atoms	Size, shape, and composition
DLS	1–1000	Mobility of nanoparticles in solutions	Hydrodynamic radius
Mass spectrometry	1–10	Mass of particles or surfactants	Reaction yields or mass of particles
NMR	Any	Nuclear spin	Composition of particles or surfactants
EPR	Any	Unpaired electrons	Composition of particles or surfactants
FTIR	Any	Vibrational modes	Composition of particles, surfactants
UV-Vis	Any	Absorption peaks (valence electrons)	Resonance absorption, absorption profiles/finger print
XAS (EXAFS and XANES)	Any	Absorption spectra (core level)	Average coordination number, disorder, absorption edge, absorption finger prints

requirements are necessary but not sufficient conditions. Other nanomaterials that may not satisfy these conditions can still support these enhancements.

6.6.1   Physical Enhancement

There are at least three types of physical enhancement. Each type requires specific kinds of nanomaterials. General needs for the nanomaterials are discussed here. Although similar discussions are given in Chap. 2, the discussion below is given from the perspective of the nanomaterials that support a specific enhancement type.

6.6.1.1   Type 1 Physical Enhancement

Many nanomaterials can support just type 1 physical enhancement. As stated in Chap. 2, there are several requirements. A brief discussion is provided here relating to the nanomaterials that provide exclusive type 1 physical enhancement.

Silica-Covered 100 nm Gold Nanoparticles

Silica-covered large (>100 nm) gold nanoparticles are one of those that can generate exclusive type 1 physical enhancement, especially when the thickness of the silica

layer is great enough to suppress type 2 physical enhancement but not thick enough to significantly reduce type 1 physical enhancement. For <15 nm thick silica, the attenuation of energetic electrons emitted from the gold nanoparticle core irradiated by 40 keV X-ray energy is only a few percent.

Large Nanoparticles

Large gold nanoparticles (>100 nm) with inert surfactants are another choice. There is no need for silica coating if non-scavenging or weakly scavenging ligands are coated on the surface of these large nanoparticles to make them soluble in water or other media of interest. The reason that large nanoparticles can be used to support type 1 physical enhancement is that their total surface area per unit mass or WP is small; even if their surface is scavenging or catalytically active, as long as the probes are uniformly distributed in the whole sample volume, then it is still possible to generate high and dominating type 1 physical enhancement using large amounts of these nanomaterials. However, the ligand-covered gold surface is still scavenging, resulting in reduction to the enhancement. Non-fluorescent oxide nanoparticles that do not support type 3 physical enhancement can also support type 1 physical enhancement. However, in this case, type 2 physical enhancement still contributes to the measured enhancement, although it is only a small fraction of type 1 physical enhancement.

6.6.1.2 Type 2 Physical Enhancement

Type 2 physical enhancement can be generated by any size gold nanoparticles or nanostructures. As shown in Chap. 2, type 2 physical enhancement dominates in the surface region. The larger the nanomaterial or nanostructure, the greater the magnitude of peak type 2 physical enhancement is. For spherical nanoparticles, type 2 physical enhancement is strongest directly at the surface of the nanoparticle and quickly diminishes as the point of interest moves away from the surface.

Type 2 physical enhancement is more difficult to probe and therefore requires more elaborately designed nanomaterials. To date, the only nanomaterial that supports type 2 physical enhancement measurements was calcium phosphate-enclosed liposomes (CaPELs) with an aqueous solution of sulforhodamine B (SRB) molecules trapped inside, developed by Guo et al. [36]. The size of liposomes was approximately 60 nm in this experimental demonstration. Upon mixing with gold nanoparticles, CaPELs formed transient heterodimers with gold nanoparticles. The concentration of gold nanoparticles was high enough to generate a very strong type 2 physical enhancement signal. The CaP shell casing was thick and solid enough to prevent permeation of reactive oxygen species, but thin enough so that low-energy electrons could still penetrate through it to deposit energy inside CaPELs.

The synthetic approach to make type 2 physical enhancement probes employed by Guo et al. [36] can be expanded. For example, it is possible to use various sizes of

"inner tubes" such as micelles to replace liposomes so that smaller nanoscale probes may be synthesized. It is also possible to have multiple gold nanoparticles attached to a single nanoscale probe to generate much a higher type 2 physical enhancement. However, in this case, the size of gold nanoparticles will have to be smaller, and, consequently, the magnitude of type 2 physical enhancement is smaller, making it more difficult to observe type 2 physical enhancement. Future synthetic work is needed to improve linking multiple large gold nanoparticles to a single CaPEL.

Other attempts have been made to measure type 2 physical enhancement. One example was given by Guo et al. [75] in which gold nanoparticles were attached to supercoiled DNA. However, in that example, the small gold nanoparticles were catalytically active and therefore could be scavenging hydroxyl radicals or enhancing DNA stand breaks through catalytic reactions. Future work is needed to fully understand the results, starting with designing the nanomaterials that support only type 2 physical enhancement.

6.6.1.3   Type 3 Physical Enhancement

Type 3 physical enhancement is more complex than type 1 physical enhancement in the sense that nanomaterials that produce type 3 physical enhancement need to not only absorb X-rays but also need to convert the absorbed energy to UV-Vis photons, a process generally accomplished through the use of semiconductor or rare earth nanoparticles, as well as fluorescent molecules, as discussed in Sects. 2.4.4 and 6.3.1.11.

A number of nanomaterials can meet these requirements. For example, rare earth nanomaterials, quantum dots, and fluorescent semiconductor nanomaterials, such as tungsten oxide nanoparticles, can all meet these requirements. A list of nanomaterials was given in the review by Cai et al. [50]. Future work in the area of combining molecular fluorophores to X-ray absorbing and X-ray scintillating nanomaterials will help create much better type 3 physical enhancement nanomaterials. Nanomaterials that do not strongly absorb X-rays can also support type 3 physical enhancement when they can interact with Compton electrons produced in water under X-ray irradiation to generate UV-Vis photons.

6.6.2   Chemical Enhancement

Chemical enhancement requires completely different types of nanomaterials than type 1 or 2 physical enhancement, especially type 1 physical enhancement. This is because chemical enhancement derives from reactions involving the surface of nanomaterials and X-ray-generated species in media or other species. Therefore, it requires large surface areas as well as catalytically active surfaces. Type 2 physical enhancement does not require the use of an actual surface; it just needs to be close to the surface. Chemical enhancement may still occur even if the surface is covered

with ligands or surfactants, as long as these surfactants are permeable to the reactive oxygen species.

It is possible that certain nanoparticles can simultaneously satisfy the requirements for physical and chemical enhancement. Another option is to mix different nanoparticles that support different categories of enhancement to achieve a higher total enhancement. Guo et al. [88] showed algorithms governing how total enhancements were dependent on the individual enhancements, a topic covered in Chap. 5.

Semiconductor nanomaterials absorb X-rays to generate electron-hole pairs. If the pairs, in the form of exciton, can migrate to the surface of nanomaterials to enable catalytic reactions to produce reactive oxygen species, the nanomaterial can also cause chemical enhancement. Photocatalysis described in Chap. 11 belongs to this process. However, X-ray photocatalysis has not been extensively studied.

6.6.2.1   Anti-Enhancement

Although unintended, physical and chemical enhancement generally shun away from anti-enhancement. However, if no specific actions are taken during synthesis and purification process of nanomaterials, then nanomaterials are often radical scavengers because the surface material or the surfactants can scavenge reactive oxygen species responsible for enhancement. In many cases, anti-enhancement may dominate or even annihilate enhancement generated by nanomaterials. Figure 6.22 shows a few pathways through which nanomaterials can scavenge reactive oxygen species. Pathway A shows direct scavenging of ROS by the surface. Pathway B represents scavenging of ROS by a terminal group on the ligand. Pathway C
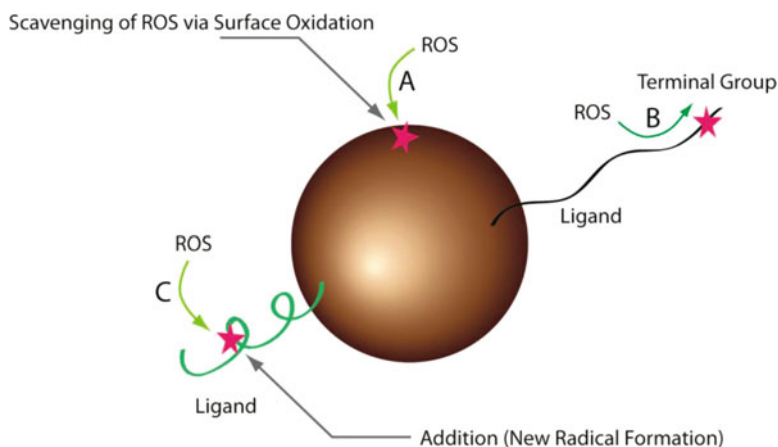
Fig. 6.22   Three different ways for a nanoparticle to scavenge reactive oxygen species (ROS). All three pathways lead to anti-enhancement. Pathway A is scavenging of ROS by the surface. Pathway B is the reaction of ROS with terminal functional groups of the ligand. Pathway C is the formation of a new radical after ROS react with the surfactant

illustrates ROS reacting with the ligand. If anti-enhancement is to be maximized, then these pathways can be utilized. On the other hand, many practices can help reduce anti-enhancement. Choice of surfactants, post-synthesis purification, selection of X-ray energy, choice of nanoparticle size, and the use of scavengers can all be used to control the degree of scavenging by nanomaterials.

6.6.3   Nanomaterials for Other Enhancements

Although biological enhancement is still a largely unknown process, many different types of nanomaterials can enable biological enhancement based on the existing understandings. According to the results presented in Chap. 4, biological enhancement exists when small nanoparticles or unprotected nanoparticles are used because these nanomaterials can bind to biomolecules and interfere with their functions, such as DNA repair, or cause oxidative stress. When large nanoparticles are used, they may not enter the nuclei of cells. For bacteria cells, chemical enhancement may exist for even large gold nanoparticles, and the enhancement may be amplified by cells to result in biological enhancement. In the case of bacteria, the requirement for the size is relaxed. There may be other requirements for nanoparticles to support biological enhancement, which will be studied in the future.

6.7   Nanoparticles for Applications in X-Ray Nanochemistry

Being able to create enhancement of the effectiveness of X-ray irradiation is the basic demand for nanomaterials used in X-ray nanochemistry. Enhancements discussed in Chaps. 2, 3, 4, and 5 have enabled many applications that are discussed in Chaps. 8, 9, 10, and 11. Mukherjee et al. [89] stated that gold nanoparticles were biologically viable and highly adaptable for conjugation with nearly any compound having an amine or thiol functional groups. It is to be seen whether other nanomaterials can surpass gold nanomaterials to dominate the application field of X-ray nanochemistry. In many of those applications, which are dominated by applications in medicine so far, there are additional requirements on the nanomaterials beyond the need for enhancement. These requirements, such as targeting tumors, are briefly discussed in Chap. 9. Requirements for nanomaterials used in imaging are different, which are discussed in Chap. 9 as well.

6.8 Conclusions and Future Work

One of the most important aspects of X-ray nanochemistry is the development of nanomaterials, which helps advance both basic and applied aspects of X-ray nanochemistry. Relevant nanomaterials and various ways to synthesize these nanomaterials are cursorily discussed here. The synthetic requirements for ideal nanomaterials used in X-ray nanochemistry are often more stringent than what are presented here because of the greater need for isolation, optimization, and combination of enhancements offered by these optimized nanomaterials. Currently there are many categories and types of enhancement, and there are nanomaterials that support each of them. This does not mean the nanomaterials are optimized for these enhancements—it simply means the nanomaterials developed to date can at least minimally support these basic enhancement categories and types.

Future efforts should be directed to the improvement of existing nanomaterials so that each category or type of enhancement can be isolated, optimized, and then recombined. These efforts will help improve understanding of the enhancement as well. For instance, better nanoscale probes will help detect type 2 physical enhancement when placed near nanostructures. Even more promising are the nanomaterials that can generate chemical enhancement by improving and incorporating new catalysis and catalysts. For example, more synergistic and catalytically active nanomaterials may enable much stronger chemical enhancement. The biggest breakthroughs in X-ray nanochemistry could happen in this area in the near future. Furthermore, advanced enhancement mechanisms may require nanomaterials to possess even more demanding and distinguished properties. In addition, all these studies can greatly benefit from more advanced theoretical approaches because currently no theoretical basis has been established to satisfactorily explain chemical and biological enhancement observed in X-ray nanochemistry. From these perspectives, X-ray nanochemistry will see a much more rigorous and exciting period of development in the next decade.

References

1. Foley, E., Carter, J., Shan, F., & Guo, T. (2005). Enhanced relaxation of nanoparticle-bound supercoiled DNA in X-ray radiation. *Chemical Communications*, 3192–3194.
2. Brust, M., Walker, M., Bethell, D., Schiffrin, D. J., & Whyman, R. (1994). Synthesis of thiol-Derivatised gold nanoparticles in a 2-phase liquid-liquid system. *Journal of the Chemical Society, Chemical Communications, 0*, 801–802.
3. Hainfeld, J. F., Slatkin, D. N., & Smilowitz, H. M. (2004). The use of gold nanoparticles to enhance radiotherapy in mice. *Physics in Medicine and Biology, 49*, N309–N315.
4. Chithrani, B. D., Ghazani, A. A., & Chan, W. C. W. (2006). Determining the size and shape dependence of gold nanoparticle uptake into mammalian cells. *Nano Letters, 6*, 662–668.
5. Hainfeld, J. F., Smilowitz, H. M., O'Connor, M. J., Dilmanian, F. A., & Slatkin, D. N. (2013). Gold nanoparticle imaging and radiotherapy of brain tumors in mice. *Nanomedicine, 8*, 1601–1609.

6. Ozin, G. A., & Arsenault, A. C. (2005). *Nanochemistry: A chemical approach to nanomaterials*. Cambridge, UK: RSC Publishing.

7. Dreaden, E. C., Alkilany, A. M., Huang, X. H., Murphy, C. J., & El-Sayed, M. A. (2012). The golden age: Gold nanoparticles for biomedicine. *Chemical Society Reviews, 41*, 2740–2779.

8. Brust, M., & Kiely, C. J. (2002). Some recent advances in nanostructure preparation from gold and silver particles: A short topical review. *Colloid and Surface A, 202*, 175–186.

9. Kim, B., Han, G., Toley, B. J., Kim, C. K., Rotello, V. M., & Forbes, N. S. (2010). Tuning payload delivery in tumour cylindroids using gold nanoparticles. *Nature Nanotechnology, 5*, 465–472.

10. Zhang, X. D., Luo, Z. T., Chen, J., Song, S. S., Yuan, X., Shen, X., Wang, H., Sun, Y. M., Gao, K., Zhang, L. F., et al. (2015). Ultrasmall glutathione-protected gold nanoclusters as next generation radiotherapy sensitizers with high tumor uptake and high renal clearance. *Scientific Reports UK, 5*, 8669.

11. Tien, J., Terfort, A., & Whitesides, G. M. (1997). Microfabrication through electrostatic self-assembly. *Langmuir, 13*, 5349–5355.

12. McIntosh, C. M., Esposito, E. A., Boal, A. K., Simard, J. M., Martin, C. T., & Rotello, V. M. (2001). Inhibition of DNA transcription using cationic mixed monolayer protected gold clusters. *Journal of the American Chemical Society, 123*, 7626–7629.

13. Cheng, N. N., Starkewolf, Z., Davidson, A. R., Sharmah, A., Lee, C., Lien, J., & Guo, T. (1950). Chemical enhancement by nanomaterials under X-ray irradiation. *Journal of the Chemical Society, Communications, 2012*(134), 1950–1953.

14. Duff, D., Baiker, A., Gameson, I., & Edwards, P. (1993). A new hydrosol of gold clusters .2. A comparison of some different measurement techniques. *Langmuir, 9*, 2310–2317.

15. Duff, D. G., Baiker, A., & Edwards, P. P. (1993). A new hydrosol of gold clusters .1. Formation and particle-size variation. *Langmuir, 9*, 2301–2309.

16. Turkevich, J., Stevenson, P. C., & Hillier, J. (1951). A study of the nucleation and growth processes in the synthesis of colloidal gold. *Discussions of the Faraday Society, 11*, 55–75.

17. Starkewolf, Z. B., Miyachi, L., Wong, J., & Guo, T. (2013). X-ray triggered release of doxorubicin from nanoparticle drug carriers for cancer therapy. *Chemical Communications, 49*, 2545–2547.

18. Perrault, S. D., & Chan, W. C. W. (2009). Synthesis and surface modification of highly monodispersed, spherical gold nanoparticles of 50-200 nm. *Journal of the American Chemical Society, 131*, 17042–17043.

19. Davidson, R. A., & Guo, T. (2014). Average physical enhancement by nanomaterials under X-ray irradiation. *Journal of Physical Chemistry C, 118*, 30221–30228.

20. Wang, C. H., Hua, T. E., Chien, C. C., Yu, Y. L., Yang, T. Y., Liu, C. J., Leng, W. H., Hwu, Y., Yang, Y. C., Kim, C. C., et al. (2007). Aqueous gold nanosols stabilized by electrostatic protection generated by X-ray irradiation assisted radical reduction. *Materials Chemistry and Physics, 106*, 323–329.

21. Liu, C. J., Wang, C. H., Chien, C. C., Yang, T. Y., Chen, S. T., Leng, W. H., Lee, C. F., Lee, K. H., Hwu, Y., Lee, Y. C., et al. (2008). Enhanced x-ray irradiation-induced cancer cell damage by gold nanoparticles treated by a new synthesis method of polyethylene glycol modification. *Nanotechnology, 19*, 1–5. Article ID 295104.

22. Liu, C. J., Wang, C. H., Chen, S. T., Chen, H. H., Leng, W. H., Chien, C. C., Wang, C. L., Kempson, I. M., Hwu, Y., Lai, T. C., et al. (2010). Enhancement of cell radiation sensitivity by pegylated gold nanoparticles. *Physics in Medicine and Biology, 55*, 931–945.

23. Kumar, R., Korideck, H., Ngwa, W., Berbeco, R. I., Makrigiorgos, G. M., & Sridhar, S. (2013). Third generation gold nanoplatform optimized for radiation therapy. *Translational Cancer Research, 2*, 228.

24. Wang, C. H., Chien, C. C., Yu, Y. L., Liu, C. J., Lee, C. F., Chen, C. H., Hwu, Y., Yang, C. S., Je, J. H., & Margaritondo, G. (2007). Structural properties of 'naked' gold nanoparticles formed by synchrotron X-ray irradiation. *Journal of Synchrotron Radiation, 14*, 477–482.

25. Merga, G., Saucedo, N., Cass, L. C., Puthussery, J., & Meisel, D. (2010). "Naked" gold nanoparticles: Synthesis, characterization, catalytic hydrogen evolution, and SERS. *Journal of Physical Chemistry C, 114*, 14811–14818.

26. Evanoff, D. D., & Chumanov, G. (2005). Synthesis and optical properties of silver nanoparticles and arrays. *Chemphyschem, 6*, 1221–1231.

27. Ziegler, C., & Eychmuller, A. (2011). Seeded growth synthesis of uniform gold nanoparticles with diameters of 15-300 nm. *Journal of Physical Chemistry C, 115*, 4502–4506.

28. Bastús, N. G., Comenge, J., & Puntes, V. (2011). Kinetically controlled seeded growth synthesis of citrate-stabilized gold nanoparticles of up to 200 nm: Size focusing versus Ostwald ripening. *Langmuir, 27*, 11098–11105.

29. Liu, X. K., Xu, H. L., Xia, H. B., & Wang, D. Y. (2012). Rapid seeded growth of monodisperse, quasi-spherical, citrate-stabilized gold nanoparticles via H_2O_2 reduction. *Langmuir, 28*, 13720–13726.

30. Song, H., Rioux, R. M., Hoefelmeyer, J. D., Komor, R., Niesz, K., Grass, M., Yang, P. D., & Somorjai, G. A. (2006). Hydrothermal growth of mesoporous SBA-15 silica in the presence of PVP-stabilized Pt nanoparticles: Synthesis, characterization, and catalytic properties. *Journal of the American Chemical Society, 128*, 3027–3037.

31. Porter, R., Shan, F., & Guo, T. (2005). Coherent anti-stokes Raman scattering microscopy with spectrally tailored ultrafast pulses. *The Review of Scientific Instruments, 76*, 043108.

32. Jin, R. C., Jureller, J. E., Kim, H. Y., & Scherer, N. F. (2005). Correlating second harmonic optical responses of single Ag nanoparticles with morphology. *Journal of the American Chemical Society, 127*, 12482–12483.

33. Solomon, S. D., Bahadory, M., Jeyarajasingam, A. V., Rutkowsky, S. A., Boritz, C., & Mulfinger, L. (2007). Synthesis and study of silver nanoparticles. *Journal of Chemical Education, 84*, 322–325.

34. Yu, X. J., Li, A., Zhao, C. Z., Yang, K., Chen, X. Y., & Li, W. W. (2017). Ultrasmall semimetal nanoparticles of bismuth for dual-modal computed tomography/photoacoustic imaging and synergistic thermoradiotherapy. *ACS Nano, 11*, 3990–4001.

35. Davidson, R. A., & Guo, T. (2012). An example of X-ray nanochemistry: SERS investigation of polymerization enhanced by nanostructures under X-ray irradiation. *Journal of Physical Chemistry Letters, 3*, 3271–3275.

36. Sharmah, A., Yao, Z., Lu, L., & Guo, T. (2016). X-ray-induced energy transfer between nanomaterials under X-ray irradiation. *Journal of Physical Chemistry C, 120*, 3054–3060.

37. Schulzendorf, M., Cavelius, C., Born, P., Murray, E., & Kraus, T. (2011). Biphasic synthesis of $Au@SiO_2$ core-shell particles with stepwise ligand exchange. *Langmuir, 27*, 727–732.

38. Shankar, C., Dao, A. T. N., Singh, P., Higashimine, K., Mott, D. M., & Maenosono, S. (2012). Chemical stabilization of gold coated by silver core-shell nanoparticles via electron transfer. *Nanotechnology, 23*, 245704.

39. Lien, J., Peck, K. A., Su, M. Q., & Guo, T. (2016). Sub-monolayer silver loss from large gold nanospheres detected by surface plasmon resonance in the sigmoidal region. *Journal of Colloid and Interface Science, 479*, 173–181.

40. Huang, C. W., Kearney, V., Moeendarbari, S., Jiang, R. Q., Christensen, P., Tekade, R., Sun, X. K., Mao, W. H., & Hao, Y. W. (2015). Hollow gold nanoparticles as biocompatible Radiosensitizer: An in vitro proof of concept study. *Journal of Nano Research Sw, 32*, 106–U140.

41. Huang, C. W., Jiang, J. C., Lu, M. Y., Sun, L., Meletis, E. I., & Hao, Y. W. (2009). Capturing electrochemically evolved Nanobubbles by electroless deposition. A facile route to the synthesis of hollow nanoparticles. *Nano Letters, 9*, 4297–4301.

42. Moeendarbari, S., Tekade, R., Mulgaonkar, A., Christensen, P., Ramezani, S., Hassan, G., Jiang, R., Oz, O. K., Hao, Y. W., & Sun, X. K. (2016). Theranostic Nanoseeds for efficacious internal radiation therapy of unresectable solid tumors. *Scientific Reports UK, 6*, 20614.

43. Milosavljevic, B. H., Pimblott, S. M., & Meisel, D. (2004). Yields and migration distances of reducing equivalents in the radiolysis of silica nanoparticles. *The Journal of Physical Chemistry. B, 108*, 6996–7001.

44. Nakayama, M., Sasaki, R., Ogino, C., Tanaka, T., Morita, K., Umetsu, M., Ohara, S., Tan, Z. Q., Nishimura, Y., Akasaka, H., et al. (2016). Titanium peroxide nanoparticles enhanced cytotoxic effects of X-ray irradiation against pancreatic cancer model through reactive oxygen species generation in vitro and in vivo. *Radiation Oncology, 11*, 91.

45. Chen, Y. Y., Song, G. S., Dong, Z. L., Yi, X., Chao, Y., Liang, C., Yang, K., Cheng, L., & Liu, Z. (2017). Drug-loaded mesoporous tantalum oxide nanoparticles for enhanced synergetic chemoradiotherapy with reduced systemic toxicity. *Small, 13*, 1602869.

46. Xing, M. M., Cao, W. H., Pang, T., Ling, X. Q., & Chen, N. (2009). Preparation and characterization of monodisperse spherical particles of X-ray nano-phosphors based on $Gd_2O_2S:Tb$. *Chinese Science Bulletin, 54*, 2982–2986.

47. Townley, H. E., Kim, J., & Dobson, P. J. (2012). In vivo demonstration of enhanced radiotherapy using rare earth doped titania nanoparticles. *Nanoscale, 4*, 5043–5050.

48. Elmenoufy, A. H., Tang, Y. A., Hu, J., Xu, H. B., & Yang, X. L. (2015). A novel deep photodynamic therapy modality combined with CT imaging established via X-ray stimulated silica-modified lanthanide scintillating nanoparticles. *Chemical Communications, 51*, 12247–12250.

49. Tang, Y. G., Hu, J., Elmenoufy, A. H., & Yang, X. L. (2015). Highly efficient FRET system capable of deep photodynamic therapy established on X-ray excited mesoporous LaF3:Tb scintillating nanoparticles. *ACS Applied Materials & Interfaces, 7*, 12261–12269.

50. Kamkaew, A., Chen, F., Zhan, Y. H., Majewski, R. L., & Cai, W. B. (2016). Scintillating nanoparticles as energy mediators for enhanced photodynamic therapy. *ACS Nano, 10*, 3918–3935.

51. Algar, W. R., Prasuhn, D. E., Stewart, M. H., Jennings, T. L., Blanco-Canosa, J. B., Dawson, P. E., & Medintz, I. L. (2011). The controlled display of biomolecules on nanoparticles: A challenge suited to bioorthogonal chemistry. *Bioconjugate Chemistry, 22*, 825–858.

52. Kang, Z. T., Zhang, Y. L., Menkara, H., Wagner, B. K., Summers, C. J., Lawrence, W., & Nagarkar, V. (2011). CdTe quantum dots and polymer nanocomposites for x-ray scintillation and imaging. *Applied Physics Letters, 98*, 181914.

53. Delage, M. E., Lecavalier, M. E., Cloutier, E., Lariviere, D., Allen, C. N., & Beaulieu, L. (2016). Robust shell passivation of CdSe colloidal quantum dots to stabilize radioluminescence emission. *AIP Advances, 6*, 105011.

54. Stodilka, R. Z., Carson, J. J. L., Yu, K., Zalman, M. B., Li, C. S., & Wilkinson, D. (2009). Optical degradation of CdSe/ZnS quantum dots upon gamma-ray irradiation. *Journal of Physical Chemistry C, 113*, 2580–2585.

55. Romero, J. J., Llansola-Portoles, M. J., Dell'Arciprete, M. L., Rodriguez, H. B., Moore, A. L., & Gonzalez, M. C. (2013). Photo luminescent 1-2 nm sized silicon nanoparticles: A surface-dependent system. *Chemistry of Materials, 25*, 3488–3498.

56. Gara, P. M. D., Garabano, N. I., Portoles, M. J. L., Moreno, M. S., Dodat, D., Casas, O. R., Gonzalez, M. C., & Kotler, M. L. (2012). ROS enhancement by silicon nanoparticles in X-ray irradiated aqueous suspensions and in glioma C6 cells. *Journal of Nanoparticle Research, 14*, 741.

57. Baldwin, R. K., Pettigrew, K. A., Ratai, E., Augustine, M. P., & Kauzlarich, S. M. (2002). Solution reduction synthesis of surface stabilized silicon nanoparticles. *Chemical Communications*, 1822–1823.

58. Ma, N., Li, Y., Xu, H. P., Wang, Z. Q., & Zhang, X. (2010). Dual redox responsive assemblies formed from diselenide block copolymers. *Journal of the American Chemical Society, 132*, 442.

59. Kirakci, K., Kubat, P., Fejfarova, K., Martincik, J., Nikl, M., & Lang, K. (2016). X-ray inducible luminescence and singlet oxygen sensitization by an octahedral molybdenum cluster compound: A new class of nanoscintillators. *Inorganic Chemistry, 55*, 803–809.

60. Liu, X., Zhang, X., Zhu, M., Lin, G. H., Liu, J., Zhou, Z. F., Tian, X., & Pan, Y. (2017). PEGylated Au@Pt nanodendrites as novel theranostic agents for computed tomography imaging and photothermal/radiation synergistic therapy. *ACS Applied Materials & Interfaces, 9*, 279–285.

61. Qu, Y. Q., Carter, J. D., & Guo, T. (2006). Silica nanocoils. *The Journal of Physical Chemistry. B, 110*, 8296–8301.

62. Qu, Y. Q., Carter, J. D., Sutherland, A., & Guo, T. (2006). Surface modification of gold nanotubules via microwave radiation, sonication and chemical etching. *Chemical Physics Letters, 432*, 195–199.

63. Bhattarai, S. R., Derry, P. J., Aziz, K., Singh, P. K., Khoo, A. M., Chadha, A. S., Liopo, A., Zubarev, E. R., & Krishnan, S. (2017). Gold nanotriangles: Scale up and X-ray radiosensitization effects in mice. *Nanoscale, 9*, 5085–5093.

64. Gole, A., & Murphy, C. J. (2004). Seed-mediated synthesis of gold nanorods: Role of the size and nature of the seed. *Chemistry of Materials, 16*, 3633–3640.

65. Dewi, M. R., Gschneidtner, T. A., Elmas, S., Ranford, M., Moth-Poulsen, K., & Nann, T. (2015). Monofunctionalization and dimerization of nanoparticles using coordination chemistry. *ACS Nano, 9*, 1434–1439.

66. Jain, P. K., & El-Sayed, M. A. (2007). Universal scaling of plasmon coupling in metal nanostructures: Extension from particle pairs to nanoshells. *Nano Letters, 7*, 2854–2858.

67. Al Zaki, A., Joh, D., Cheng, Z. L., De Barros, A. L. B., Kao, G., Dorsey, J., & Tsourkas, A. (2014). Gold-loaded polymeric micelles for computed tomography-guided radiation therapy treatment and radiosensitization. *ACS Nano, 8*, 104–112.

68. Zhang, P. P., Qiao, Y., Xia, J. F., Guan, J. J., Ma, L. Y., & Su, M. (2015). Enhanced radiation therapy with multilayer microdisks containing Radiosensitizing gold nanoparticles. *ACS Applied Materials & Interfaces, 7*, 4518–4524.

69. Fologea, E., Salamo, G., Henry, R., Borrelli, M. J., & Corry, P. M. (2010). Method of controlling drug release from a liposome carrier. US Patent: US8808733B2.

70. Chen, H. M., Wang, G. D., Chuang, Y. J., Zhen, Z. P., Chen, X. Y., Biddinger, P., Hao, Z. L., Liu, F., Shen, B. Z., Pan, Z. W., et al. (2015). Nanoscintillator-mediated X-ray inducible photodynamic therapy for in vivo cancer treatment. *Nano Letters, 15*, 2249–2256.

71. Fan, W. P., Shen, B., Bu, W. B., Zheng, X. P., He, Q. J., Cui, Z. W., Ni, D. L., Zhao, K. L., Zhang, S. J., & Shi, J. L. (2015). Intranuclear biophotonics by smart design of nuclear-targeting photo−/radio-sensitizers co-loaded upconversion nanoparticles. *Biomaterials, 69*, 89–98.

72. Fan, W. P., Wenbo, B., Bu, Z. Z., Shen, B., Zhang, H., He, Q. J., Ni, D. L., Cui, Z. W., Zhao, K. L., Bu, J. W., et al. (2015). X-ray radiation-controlled NO-release for on-demand depth-independent hypoxic radiosensitization. *Angewandte Chemie International Edition, 54*, 14026–14030.

73. Liu, J. J., Chen, Q., Zhu, W. W., Yi, X., Yang, Y., Dong, Z. L., & Liu, Z. (2017). Nanoscale-coordination-polymer-shelled manganese dioxide composite nanoparticles: A multistage redox/pH/H2O2-responsive cancer theranostic nanoplatform. *Advanced Functional Materials, 27*, 1605926.

74. Pan, C. L., Chen, M. H., Tung, F. I., & Liu, T. Y. (2017). A nanovehicle developed for treating deep-seated bacteria using low-dose X-ray. *Acta Biomaterialia, 47*, 159–169.

75. Carter, J. D., Cheng, N. N., Qu, Y. Q., Suarez, G. D., & Guo, T. (2007). Nanoscale energy deposition by x-ray absorbing nanostructures. *The Journal of Physical Chemistry. B, 111*, 11622–11625.

76. Rotello, V. M., Ghosh, P., Han, G., De, M., & Kim, C. K. (2008). Gold nanoparticles in delivery applications. *Advanced Drug Delivery Reviews, 60*, 1307–1315.

77. Zhang, X. J., Xing, J. Z., Chen, J., Ko, L., Amanie, J., Gulavita, S., Pervez, N., Yee, D., Moore, R., & Roa, W. (2008). Enhanced radiation sensitivity in prostate cancer by gold-nanoparticles. *Clinical and Investigative Medicine, 31*, E160–E167.

78. Demers, L. M., Ginger, D. S., Park, S. J., Li, Z., Chung, S. W., & Mirkin, C. A. (2002). Direct patterning of modified oligonucleotides on metals and insulators by dip-pen nanolithography. *Science, 296*, 1836–1838.

79. Zhang, P. P., Qiao, Y., Wang, C. M., Ma, L. Y., & Su, M. (2014). Enhanced radiation therapy with internalized polyelectrolyte modified nanoparticles. *Nanoscale, 6*, 10095–10099.

80. Hoyle, C. E., & Bowman, C. N. (2010). Thiol-Ene click chemistry. *Angewandte Chemie International Edition, 49*, 1540–1573.

81. Dondoni, A. (2008). The emergence of thiol-Ene coupling as a click process for materials and bioorganic chemistry. *Angewandte Chemie International Edition, 47*, 8995–8997.

82. Latimer, C. L. (2013). *Octaarginine labelled 30 nm gold nanoparticles as agents for enhanced radiotherapy*. In Department of Medical Biophysics, University of Toronto, Toronto, Vol. Master of science, p 81.

83. Lee, C. Y., Gong, P., Harbers, G. M., Grainger, D. W., Castner, D. G., & Gamble, L. J. (2006). Surface coverage and structure of mixed DNA/alkylthiol monolayers on gold: Characterization by XPS, NEXAFS, and fluorescence intensity measurements. *Analytical Chemistry, 78*, 3316–3325.

84. Gu, Y. J., Cheng, J. P., Man, C. W. Y., Wong, W. T., & Cheng, S. H. (2012). Gold-doxorubicin nanoconjugates for overcoming multidrug resistance. *Nanomedicine Nanotechnology, 8*, 204–211.

85. Scaffidi, J. P., Gregas, M. K., Lauly, B., Zhang, Y., & Vo-Dinh, T. (2011). Activity of psoralen-functionalized nanoscintillators against cancer cells upon X-ray excitation. *ACS Nano, 5*, 4679–4687.

86. Li, Z., Jin, R. C., Mirkin, C. A., & Letsinger, R. L. (2002). Multiple thiol-anchor capped DNA-gold nanoparticle conjugates. *Nucleic Acids Research, 30*, 1558–1562.

87. Zhu, Z. J., Tang, R., Yeh, Y. C., Miranda, O. R., Rotello, V. M., & Vachet, R. W. (2012). Determination of the intracellular stability of gold nanoparticle monolayers using mass spectrometry. *Analytical Chemistry, 84*, 4321–4326.

88. Davidson, R. A., & Guo, T. (2015). Multiplication algorithm for combined physical and chemical enhancement of X-ray effect by nanomaterials. *Journal of Physical Chemistry C, 119*, 19513–19519.

89. Kudgus, R. A., Szabolcs, A., Khan, J. A., Walden, C. A., Reid, J. M., Robertson, J. D., Bhattacharya, R., & Mukherjee, P. (2013). Inhibiting the growth of pancreatic adenocarcinoma in vitro and in vivo through targeted treatment with designer gold nanotherapeutics. *PLoS One, 8*, e57522.

90. Withers, N J., Plumley, J. B., Triño, N. D., Sankar, K., Akins, B. A., Rivera, A. C., Smolyakov, G. A., Timmins, G. S., & Osiński, M. (2009). Scintillating-nanoparticle-induced enhancement of absorbed radiation dose. *Proc. of SPIE, 7189*, 718917

Chapter 7
Techniques and Instruments for X-Ray Nanochemistry

The boundary condition determines the solution of second order differential equations - or as we commonly say: beauty is in the eye of beholder

7.1 Introduction

X-ray nanochemistry is in its infancy, and many instruments and techniques are still being developed. X-ray sources used in the currently available instruments for X-ray nanochemistry can be fairly compact, and with the addition of shielding and interfacing with other instruments, such as optical microscopes, an entire instrument can still be as small as a regular laser printer. One of such instruments was shown in the experiment of measuring absolute scintillation yield of rare earth nanoparticles performed by Guo et al. [1]. The same instrument has been used in many other recent studies. Another example was that used by Su et al. [2], which consisted of a mini X-ray source that is commonly used for X-ray imaging. A similar X-ray source was used by Cho et al. [3] for imaging nanoparticles with X-rays.

Despite of all these advancements in instrumentation for X-ray nanochemistry, the overall accomplishments in methodology and instrumentation in the area of X-ray nanochemistry are still limited because the majority of the publications in the area of X-ray nanochemistry focused on applications in medicine, which have generally employed existing methods to irradiate cells and animals. As the total enhancement becomes higher and the required dose is reduced, new instrumentation and methodologies with higher sensitivities will be needed. The existing body of work covering instruments and methodologies is evaluated here before further work is done. To fully reach its potential, development in theory, materials, methodology, and instrumentation will have to be coordinated. More efforts in basic studies are needed for X-ray nanochemistry to make long-term progress in addition to short-term gains. Future X-ray nanochemistry will likely advance far beyond the currently demonstrated augmentation of direct damage of cancer cells or tumors under X-ray irradiation.

This chapter discusses the physical methods used to measure enhancement. X-ray sources are central to instrumentation and are discussed here. The instruments and

related techniques include electron spin resonance (ESR) or electron paramagnetic resonance (EPR) spectroscopy, X-ray photoelectron spectroscopy (XPS), X-ray absorption spectroscopy (XAS), and a number of other analytical tools such as mass spectrometry and fluorimetry. Discussion on both techniques and instruments is aimed for researchers and students in the medical field and physical sciences.

7.2 Techniques for X-Ray Nanochemistry Enhancement Measurements

Table 7.1 summarizes the methods of enhancement detection used in X-ray nanochemistry to date. The order of presentation follows the published works chronologically. Discussion in the text of this section follows this order as well.

As Table 7.1 suggests, there are at least nine major techniques to date with which enhancement was measured. We will first describe these nine techniques together with their instruments.

7.2.1   Animal Models

The first measurement of enhancement was through the use of animal models by Hainfeld et al. [4]. The physical instrument was a regular X-ray irradiator, and mice were used as the animal model. Despite the complexity of using biological systems for the measurement of enhancement, results obtained from studying animal models were believed to be the closest to clinical trials and eventual human treatment. As a result, animal models are still being widely used to determine the efficacy of medicine or, in this case, the enhancement. Many works using animal models have been reported since this first work.

Table 7.1 Summary of the methods, in chronological order, used to measure enhancement defined in X-ray nanochemistry

Technique	Method to Measure	Readouts
Animal model	Tumor size	Survival fraction, delayed growth, tumor size
DNA strand breaks	Gel electrophoresis	Fluorescence of stained dyes
Fluorescence	Spectral profiles	Fluorescence intensity
SERS	Plasmonic response	Intensity and position
Biology	Assays (MTT, Clonogenic, γH2AX)	Colony numbers, fluorescence
NMR	Spectral profiles	Shift and peak profiles
EPR	EPR signal profiles	Peak height or integrated area
XPS	Spectral profiles	Peak position and height
UV-Vis	Spectral profiles	Peak position and height
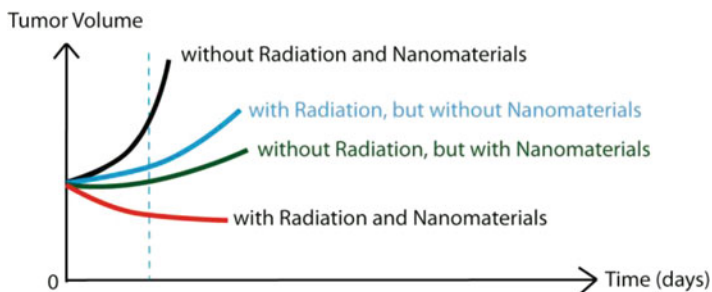
Fig. 7.1 Illustration of the existing methods of using animal models to determine the enhancement of X-ray effects by nanomaterials assuming the growth follows an exponential function. Tumor sizes are measured and used to determine the enhancement

As shown in Sect. 9.6, there are many reports of using nanoparticles to treat animals infected with tumors under the irradiation of X-rays to determine the effectiveness or dose enhancement factors. This is under the assumption that these nanoparticles only augment the dose effect, i.e., adding nanoparticles only causes physical enhancement and mainly type 1 physical enhancement. This is possible, but nanoparticles would have to be carefully synthesized and used as shown in Chaps. 2, 3, 4, and 5. Unfortunately, many studies reported in the literature did not meet this stringent requirement. As a result, other enhancements such as biological enhancement or anti-enhancement likely contribute to the enhancement. Therefore, it is difficult to validate the assumption that physical enhancement is the only enhancement mechanism responsible for the measured enhancement using animal models. Figure 7.1 and Eq. 7.1 together illustrate how the results of animal studies are quantitatively used to extract the magnitude of enhancement. In this case, tumor volumes are measured, and enhancement is calculated using tumor sizes at a specific time point.

Using the value at day t0 (marked by the dashed line), the absolute enhancement for data shown in Fig. 7.1 is equal to

$$\frac{(\ln red - \ln black)}{(\ln blue - \ln black) + (\ln green - \ln black)} - 1.0 \tag{7.1}$$

ln (color) is the natural logarithm of the value of the sizes of the tumor. The term on the numerator is the total effect caused by the addition of nanomaterials and X-rays alone. The first term in the denominator is the effect of irradiation, and the second term comes from toxicity of nanomaterials. The relative enhancement is the ratio of the total effect to the sum of the two effects. This definition is consistent to those given in Chaps. 2, 3, 4, and 5. When there is no toxicity, the second term in the denominator disappears. This calculation assumes that the growth of tumor follows an exponential function, which may not be true all the time.

7.2.2　DNA Damage or Strand Breaks and Electrophoresis

In the history of enhancement measurements in X-ray nanochemistry, DNA strand breaks were the second methodology appeared in the literature used by researchers to determine the enhancement, which was first demonstrated by Guo et al. [5]. Since then many works have been done using DNA strand breaks as the probe to measure enhancements, including both short DNA molecules and nuclear plasmid DNA. The former was done by Guo et al. as well as McMahon et al. [6], and the latter was done by Guo et al. [7] and several other groups. The results are covered in Chaps. 8 and 9.

DNA strand breaks are the consequence of a collection of chemical reactions involving many complex pathways. If catalysis involving nanomaterials is included, then reaction mechanisms are even more complicated. Strand breaks can be detected with gel electrophoresis or other methods, such as mass spectrometry. For gel detection, polyacrylamide or agarose gels are used to measure differently sized DNA. Figure 7.2 shows a typical way to use DNA strand breaks to measure enhancement. In this case, supercoiled DNA (scDNA) molecules are used. scDNA conjugated with small gold nanoparticles are shown in the left panel. After irradiation with X-rays, gel electrophoresis analysis is performed, which produces bands of DNA whose positions in the gel depend on the mobility of DNA in the gel. Here three bands are shown, corresponding to supercoiled (lower band), linear (middle band), and circular DNA (top band, all in the middle panel). Linear DNA is the result of a double-strand break (DSB), and circular DNA is the result of at least one single-strand break (SSB). The intensity profile of the bands obtained with staining DNA with dye molecules is used to determine the amount of DNA in the band. The amounts are then used to determine the damage and enhancement. A typical result is shown in the right panel of Fig. 7.2.
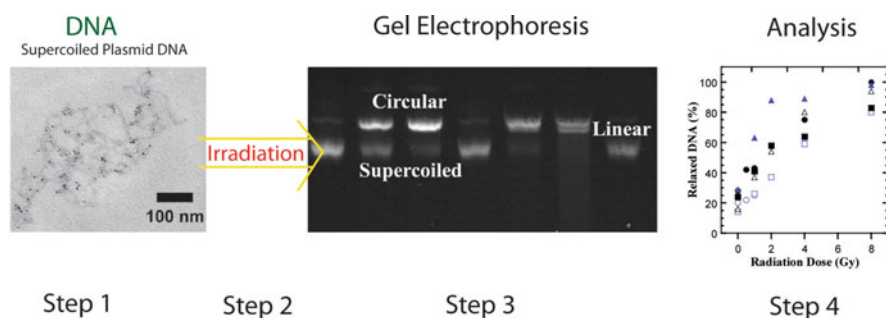
Fig. 7.2 DNA strand breaks used to measure enhancement. The left panel shows DNA conjugated to 3 nm gold nanoparticles. The middle panel shows a typical result of gel electrophoresis in which three bands are visible, representing supercoiled, linear, and circular DNA. The enhancement results are shown in the right panel. (Left panel: Adapted with permission from Guo et al. [8]. Copyright (2007) American Chemical Society. Right panel: Adapted from Guo et al. [5] with permission of the Royal Society of Chemistry.)

7.2.3   Fluorescence

The next probe used by researchers to determine enhancement is fluorometric assays. The first was used by Misawa et al. [9] and then independently by Guo et al. [10] around the same time. The two works were not related at the time, even though both were fluorescence-based. The explanations for the results were also different, which eventually led to the definition of types 1 and 2 chemical enhancement presented in Chap. 3. Type 1 chemical enhancement is defined as being caused by catalytic properties of nanomaterials enabled by the reactive oxygen species generated in water, whereas type 2 chemical enhancement relies on increased production of reactive oxygen species by nanomaterials. Type 1 chemical enhancement does not require increased production of reactive oxygen species.

Fluorescence spectroscopy is an extremely sensitive method to detect enhancement. Although single photon detection is possible, tens of thousands of photons are normally needed. One advantage of fluorescence detection is that it can occur in aqueous solutions. Figure 7.3 shows two typical procedures to detect enhancement using fluorescence spectroscopy. The first involves chemical reactions that convert originally nonfluorescent molecules to fluorescent molecules. It is shown in the top panel of Fig. 7.3. The second procedure shows the destruction of fluorescent molecules through reactions with reactive oxygen species created with X-ray irradiation of nanomaterial aqueous solutions (bottom panel). Results obtained by Guo et al., mentioned above, belonged to the fluorescence-increasing method. In another work, Guo et al. [11] showed an example of the fluorescence reduction method depicted in the bottom panel of Fig. 7.3.

In the following subsections, several fluorescent reactions are discussed.
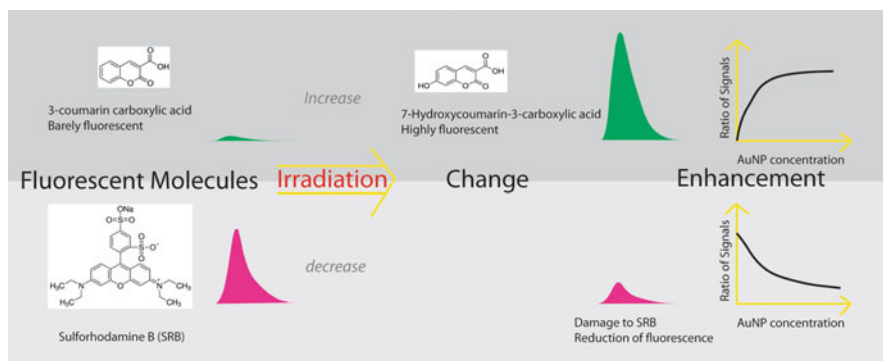
Fig. 7.3 Typical fluorescent assays to determine enhancement. Two approaches are shown. One of the two (top panel) shows increased fluorescence as a function of dose of X-rays or the gold nanoparticle concentration. Enhancement is the ratio of the increased intensity of fluorescence with gold nanoparticles to without gold nanoparticles. For decreased fluorescence (lower panel) as a function gold nanoparticle concentration, the enhancement can be calculated the same way

7.2.3.1   Coumarin-3-Carboxylic Acid (3-CCA)

One of the fluorescent reactions used to detect enhancement was the reaction between little fluorescent coumarin-3-carboxylic acid (3-CCA) with the hydroxyl radical to form highly fluorescent 7 hydroxycoumarin-3-carboxylic acid (7-OHCCA). The reaction mechanism is shown in Fig. 3.9. As described in Chap. 3, this complex reaction may be catalyzed by gold nanoparticles. As a result, one should be cautious when using this fluorescent assay to detect enhancement by nanomaterials. In addition to free 3-CCA, 3-CCA conjugates were also explored. Makrigiorgos et al. [12] studied the conjugation of 3-CCA to biomolecules and the fluorescent behavior of the conjugated 3-CCA under γ-ray irradiation. The authors found that 3-CCA could be conjugated through succinimidyl ester (SE), which did not affect the production of 7-OHCCA when the bound 3-CCA was irradiated.

7.2.3.2   Amino-Phenyl Fluorescein (APF) and Dihydroethidium (DHE)

Another molecule that can detect hydroxyl radicals and hence enhancement of hydroxyl radical production is APF. Misawa et al. [9] used APF to measure the enhancement by gold nanoparticles under X-ray irradiation. The reaction pathways were not presented. The fluorescence detection results were discussed by Misawa et al. A recent study by Sasaki et al. [13] also used APF to probe enhancement by titanium peroxide nanoparticles. No chemical enhancement was discussed. APF was used by Cohn et al. [14] to detect hydrogen peroxide and other species. Similarly, DHE was used to measure the amount of superoxide radicals. Kim et al. [15] also developed a gel using APF and DHE to probe the radicals generated from iron oxide nanoparticles under 4–15 keV synchrotron X-ray irradiation.

7.2.3.3   3-Benzoic Acid

Renault et al. [16] reported the results of their study of using benzoic acid as a scavenger to determine enhancement of transient radicals generated by X-ray irradiation of porous nanogold. Their porous gold was made via electrolysis. The hydroxylated forms, including 2-, 3-, and 4-hydroxy-benzonate, were more fluorescent than benzoic acid. The authors used the G value for hydroxyl radical production at 150 ps to determine the enhancement, which seems to be reasonable given the concentration of benzoic acid they used, which was between a few mM and 1 M. The results showed that at adequate concentrations of benzoic acid (i.e., at fast enough probing times after the production of radicals), up to 6 DEU enhancement was observed using porous nanogold. There was little enhancement when porous silica was used alone. Figure 7.4 shows the results.

Fig. 7.4 Benzoic acid detection of hydroxyl radicals generated by porous nanogold-assisted X-ray irradiation. (Adapted from Renault et al. [16] with permission of the Royal Society of Chemistry.)
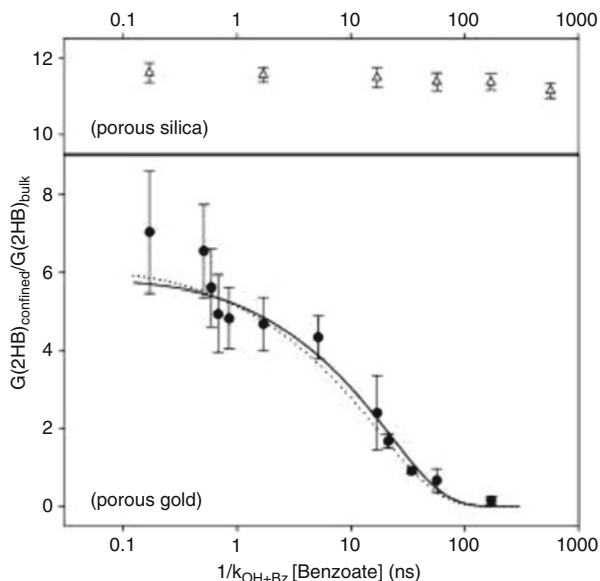
7.2.3.4   Sulforhodamine B (SRB)

As described in Fig. 7.3 (lower panel), another way to detect enhancement is to measure reduced fluorescence from fluorescent molecules damaged by reactive oxygen species. Due to the higher background signal, this method is less sensitive than reactions that make molecules more fluorescent. Moreover, a good dosimetric reaction requires the magnitude of the reduced fluorescence be linearly dependent on X-ray dose. Sulforhodamine B (SRB) was one such molecule among many tested. Reduction of fluorescence for many other dye molecules depends on the dose in complex manners. Figure 7.5 shows the response of free SRB in aqueous solutions and in CaPELs to X-ray irradiation. The steeper decay was found to be associated with free SRB in aqueous solutions, and the slow decay was associated with SRB aqueous solutions trapped inside the nanoscale probe CaPELs. The concentration range of SRB was 0.5 μM to 1 mM in these samples. Fluorescence detection has to be performed with diluted samples to avoid quenching.

7.2.3.5   X-Ray Photovoltaics

Another fluorescence technique utilizes thin-film photovoltaic (PV) cells to detect fluorescence from scintillators and nanoscintillators irradiated with X-rays. Absolute emission power was measured using this method, which was demonstrated by Guo et al. [1]. The authors were able to determine the absolute quantum efficiency of
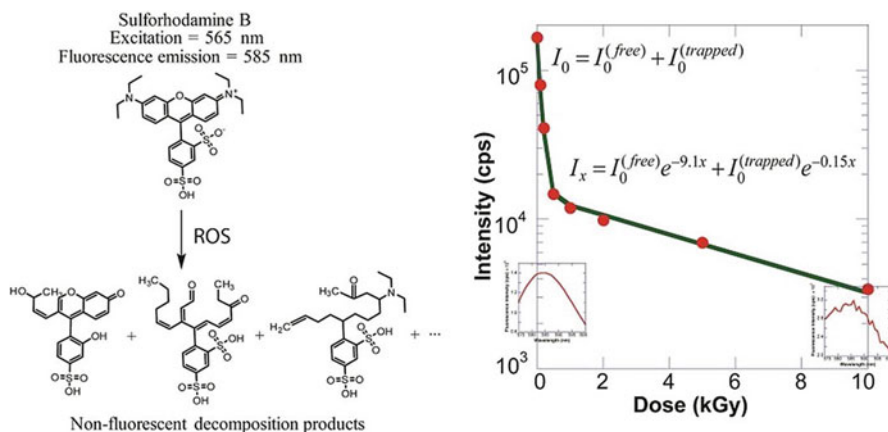
Fig. 7.5 SRB damage by X-ray irradiation through reaction with hydroxyl radicals to form various nonfluorescent products (left panel). The decrease in fluorescence is quantitatively shown in the right panel. The fast decay corresponds to hydroxyl radicals reacting with SRB in water, and the slow decay indicates the low reactivity between SRB trapped in the nanoscale probe CaPELs with hydroxyl radicals produced inside. (Reprinted with permission from Guo et al. [11]. Copyright (2016) American Chemical Society.)
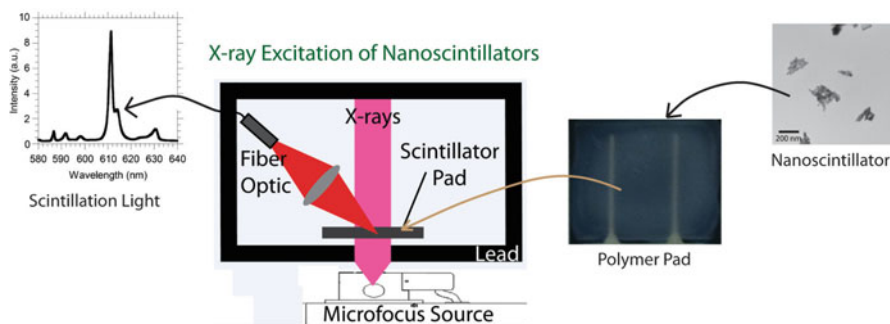
Fig. 7.6 Enhancement of X-ray-induced scintillation by nanoparticles. Here, only X-ray-induced scintillation measurement from nanoscintillators is shown. The apparatus was an X-ray source combined with an optical fluorescence detection system. Alternatively, thin-film photovoltaic cells were used to determine the absolute quantum yield of the nanoscintillator. (Reprinted with permission from Guo et al. [1]. Copyright (2014) American Chemical Society.)

nanoscintillators. The results are discussed in Sect. 2.4.4. Figure 7.6 shows a close-up of the PV cells and nanoscintillator materials. The measurement was performed in situ, meaning that emission was measured at the same time of X-ray irradiation of the nanoscintillators. A few hundred milligrams of the nanoscintillators were needed when a commercial multimeter was used to measure the voltage generated from the thin-film PV cells.
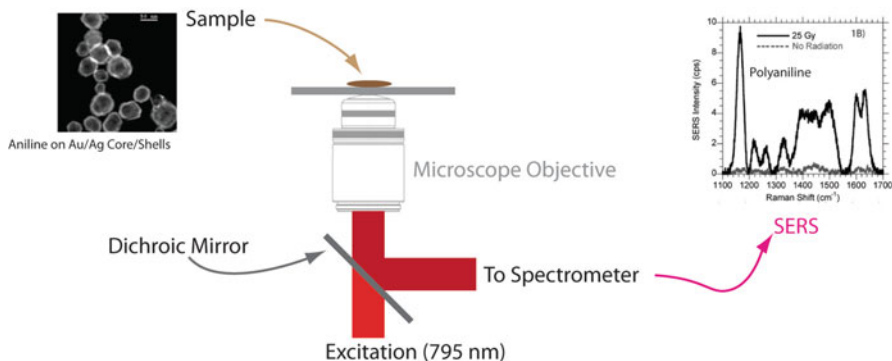
Fig. 7.7 A typical setup of surface-enhanced Raman spectroscopy (SERS). Samples were illuminated by light (usually monochromatic laser light), and Raman scattering light was collected and detected using a microscope and spectrometer. SERS spectra are obtained. The magnitude of the enhancement was calculated using signals from samples irradiated by X-rays to samples that were not irradiated. (Adapted with permission from Guo et al. [17]. Copyright (2012) American Chemical Society.)

7.2.4 Surface-Enhanced Raman Spectroscopy (SERS)

SERS can be extremely sensitive, detecting a monolayer of dye molecules on the surface of SERS substrates, which are often aggregated nanoparticles. Currently, only dye molecules (or highly fluorescent molecules) can support high SERS responses because of the so-called chemical enhancement (not to be confused with chemical enhancement in X-ray nanochemistry) or resonant energy transfer between surface plasmon of the aggregated nanoparticles and dye molecules. The aggregated nanoparticles produce another enhancement, which is created by local electrical fields near singular points around the aggregated nanoparticles.

The only example of using SERS to measure enhancements was given by Guo et al. [17] in which polymerization of the aniline monomers by X-rays was used to probe the enhancement. One form of polyaniline enantiomers was highly fluorescent and generated strong SERS signals. The proposed reaction pathways of polymerization are shown in Fig. 3.16. The experimental apparatus is shown in Fig. 7.7.

7.2.5 Biology

Biological reactions, such as DNA strand breaks and reactions that cause protein damages, were used to measure enhancement. These results are shown in Chap. 8. All categories of enhancement have been considered, although type 1 physical enhancement or physical enhancement was cited in most works, with occasional reference made to type 2 physical enhancement. Chemical enhancement was mentioned in DNA strand break studies. These reactions do not need to invoke biological enhancement discussed in Chap. 4.

In addition, many cell lines were used to determine the enhancement. Most of them were cancer cell lines. Chapters 8 and 9 describe these results. In these reports, physical enhancement again was often cited to be the main cause for the measured enhancement. However, as discussed in Chap. 4, there should be biological enhancement as well, especially for nanoparticles smaller than 10 nm in diameter.

Enhancement can be determined using many methods or assays. Survival fraction is one of the endpoints from which enhancement can be determined. Two general ways are used to calculate enhancement using the survival fraction data, as shown in Sect. 9.2.1.5. Subiel et al. [18] summarized several methods, including these two methods. Methods using different endpoints and assays and even those using the same survival fraction curves often give rise to different enhancement values because of the choice of different survival fraction values at different doses in the calculation.

A special case of using biology to detect enhancement was using *E. coli* to amplify enhancement. Sanche et al. [19] showed a new method of using transformation of supercoiled DNA into *E. coli* to produce proteins as a way to detect DNA damage. The method can be more sensitive than gel electrophoresis. Low-energy electrons were used to irradiate supercoiled plasmid DNA that caused single- and double-strand breaks (SSBs and DSBs). The breaks were caused by low-energy (0.5–20 eV) electrons emitted from nanoparticles under X-ray irradiation. Although the method was not used to directly measure the enhancement, it is foreseeable that it can be employed in those measurements. Figure 7.8 shows the procedure. This method was supposed to be able to isolate DNA damage from cellular functions.
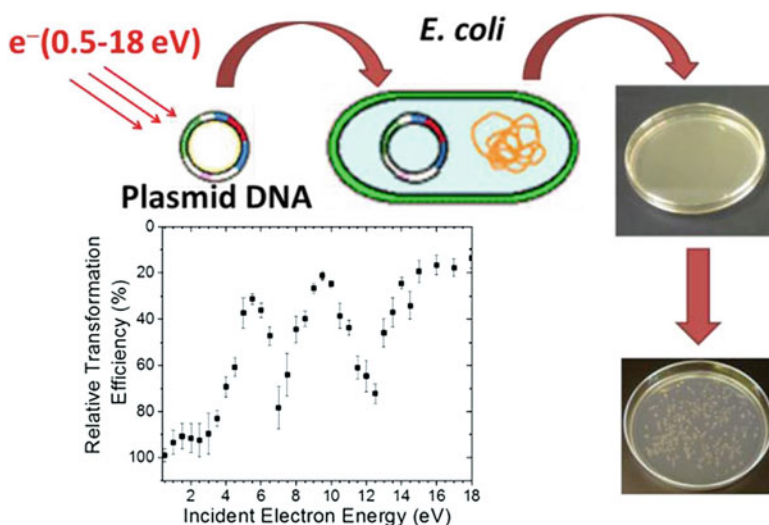
Fig. 7.8 *E. Coli* transformation of DNA damaged by low-energy electrons. Damaged DNA were not transformed as much as the undamaged DNA, therefore revealing the magnitude of DNA damage by low-energy electrons. The method can be an alternative to gel electrophoresis. (Adapted with permission from Sanche et al. [19]. Copyright (2015) American Chemical Society.)

7.2.6 Nuclear Magnetic Resonance (NMR) and Magnetic Resonance Imaging (MRI)

Marques et al. [20] showed a method of using nuclear magnetic transversal relaxation time R2 to quantify the enhancement by gold nanoparticles embedded in gels. The measured values were claimed to agree with theoretically predicted values, although upon a close examination, the measured values were more than an order of magnitude higher than what physical enhancement would support. Further clarification will be needed. Deyhimihaghighi et al. [21] reported an average MRI contrast enhancement of 27.1% upon using 0.01 mg/L 10 nm Pt nanoparticles irradiated by 6–25 Gy of 1.25 MeV ^{60}Co γ-rays. In another example, Sabbaghizadeh et al. [22] demonstrated NMR image-based enhancement of dose response in presence of 20 nm Ag nanoparticles after irradiation with 1.25 MeV ^{60}Co γ-rays. The authors observed an 11.8% increase in optical density when Ag nanoparticles were present.

7.2.7 Electron Paramagnetic Resonance (EPR) Spectroscopy

EPR spectroscopy relies on alignment of electron spin in a magnetic field. A free electron has two degenerate spin levels without the field, and the degeneracy is removed in the presence of a magnetic field. For a 3500 Gauss field, the split between the two energy levels corresponds to a transition enabled by a 9-GHz electromagnetic wave. Therefore, there is an absorption peak at 9 GHz for free electrons in a uniform magnetic field of 3500 Gauss. Figure 7.9 (middle panel) shows the diagram illustrating this process. Moreover, instead of sweeping the frequency of the electromagnetic wave across 9 GHz, data is obtained by sweeping
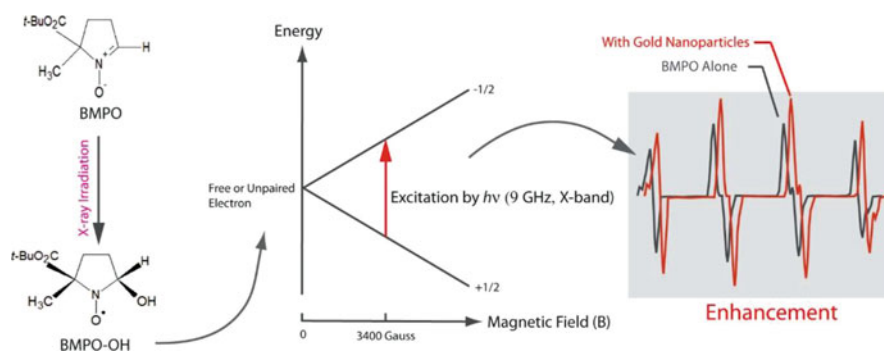
Fig. 7.9 EPR spectroscopic measurements of free or unpaired electrons. In the work described by Guo et al. [23], spin trap BMPO was used, which reacted with hydroxyl radicals to form spin adduct BMPO-•OH, which has a lifetime of approximately 40 min and can be detected by EPR. Enhancement can be calculated from the EPR signals with and without gold nanoparticles or other nanomaterials

the current through a small electrical coil around the sample amid an external permanent magnetic field set to 3500 Gauss and a microwave excitation frequency set to a fixed frequency of 9 GHz. The adjustable current through the coil creates a changing magnetic field on the order of 0.1–10 Gauss or 0.01–1 mT. In addition to free electrons, unpaired electrons in a radical can also be detected by EPR measurements. Absorption peaks at different magnetic fields created by the small coil are recorded. Figure 7.9 (left panel) shows a spin trap molecule BMPO reacting with a hydroxyl radical generated in X-ray-irradiated water to form a radical adduct. The lifetime of the spin adduct can be as short as few seconds or as long as a few hours. The molecule •BMPO-OH shown in Fig. 7.9 has a lifetime of approximately 40 min. Four EPR peaks appear within the sweeping range of the magnetic field (right panel). Multiple peaks are caused by the shielding of the nuclear spins (e.g., N or H) near the unpaired electron.

Three general methods were used to study enhancement using EPR spectroscopy. The first was to directly measure radicals, such as carbon radicals produced under ionizing radiation, as shown by Guidelli et al. [24]. Several EPR agents, such as formate and alanine, were often used. The concentration of radicals was supposed to increase as nanomaterials were added. The second method was to use spin traps such as BMPO to react with short-lived radicals such as hydroxyl radicals and then measure spin adducts with EPR spectroscopy. Examples belonging to this category included solvated electrons and reactive oxygen species. Common spin adducts and parameters are listed in Table 7.2. Guo et al. [23] performed measurements using this

Table 7.2 Common spin traps and their properties, as well as stable radicals and molecules that can produce stable radicals upon irradiated with X-rays

Spin traps	Spin labels	Radical-producing molecules	Adduct lifetime •OH/•O_2^- (min)	Trapping targets
DMPO			2.6/1.0	•OH, •O_2^-
DEPMPO			22.3/14.8	•OH, •O_2^-
DBPMPO			16/–	•OH, •O_2^-
EMPO			–/20.8	•OH, •O_2^-
BMPO			>30/15.7	•OH, •O_2^-
4-POBN				•OH, •O_2^-
DIPPMPO				•OH, •O_2^-
Cd-DIPPMPO				•OH, •O_2^-
Mito-DIPPMPO				•OH, •O_2^-
TEMP				$^1O_2$
	TEMPO			
	TEMPOL			
	^{15}N-PDT			
		Alanine		
		Lithium Formate		

For spin traps, the trapping efficiency for •OH and •O_2^- is different. Molecular names are shown in the Abbreviation

method. The third method was to measure spin labels under irradiation. These chemicals have unpaired electrons in their steady state. Meisel et al. [25] performed such measurements. Upon reaction with reactive oxygen species, the products became either EPR observable or silent. As gold nanoparticles could catalytically influence all three methods, chemical enhancement is possible in all three cases. Some of the three types of chemicals are shown in Table 7.2. Among many publications, the list is compiled based on Bacic et al. [26], Spasojevic et al. [27], Yin et al. [28], Peyrot et al. [29], and Wu et al. [30].

7.2.8   UV-Vis Spectroscopy

UV-Vis spectroscopy is a convenient method to detect the enhancement if the sample sizes are adequately large. Only recently has this method been used to probe the enhancement in X-ray nanochemistry. In the work performed by Guo et al. [31], the authors discussed a new nanomaterial that may be used to measure the enhancement. The nanomaterial was called Agu, which was made by coating a thin of silver onto the surface of large spherical gold nanoparticles. The silver layer was etched away by reactive oxygen species produced in water under X-ray irradiation. Surface plasmon resonance (SPR) profiles of Agu were obtained through UV-Vis absorption measurements. Typical spectra are shown in Fig. 7.10 (right panel). Silver was removed from Agu when the sample was irradiated with X-rays and SPR peak position shifted. This process was considered as X-ray etching, which is related to X-ray nanochemistry. Theoretically, several enhancements, such as types 1 and 2 physical enhancement, as well as chemical enhancement, may coexist in this process. In Fig. 7.10, the SPR peak position shifted to longer wavelengths as Ag was
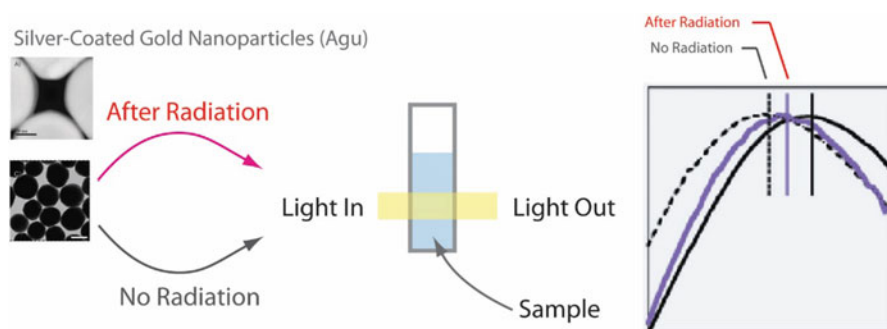
Fig. 7.10 UV-Vis measurements of X-ray-induced silver etching. Here, the sample was silver-coated gold spherical nanoparticles called Agu. The silver layer was thin, up to 2 nm on approximately 100 nm gold nanoparticles. The silver layer was etched away by the oxidizing species created by X-rays in water, and the surface plasmon resonance peak position was changed, as shown in the right panel. (Reprinted from Guo et al. [31]. Copyright (2016) with permission from Elsevier.)

etched from Agu. Although no enhancement was indicated in this work, in principle the enhancement can exist and be measured using the rate of etching measured with UV-Vis spectroscopy.

7.2.9   Electron and X-Ray Photoelectron Spectroscopy (XPS)

The most sensitive method to probe chemical species is through detection of charged particles, such as electrons or ions. The sensitivity allows for the detection of a single charged particle. However, detection of electrons emitted from nanomaterials upon X-ray absorption is tedious, difficult, and nearly impossible if nanomaterials are in liquids. As the enhancement is defined as the ratio of energy deposition in a medium with to without nanomaterials, one would have to measure electrons in a medium, a nearly impossible task for XPS. Nonetheless, if electron energy spectra and flux are known from vacuum measurements, then it is possible to benchmark the yield of electrons emitted from nanomaterials and then to theoretically predict energy deposition in solution. Another benefit of measuring electron emission from nanomaterials in vacuum is to validate the theoretically predicted electron spectra using the experimentally measured emission spectra.

An experimental exploration of XPS was performed by Casta el al. [32] who explored direct probe of electrons using XPS. This was possible because their goal was to confirm the theoretically simulated electron emission from nanoparticles under X-ray irradiation. The technique was to probe electrons in vacuum with microplate electron detectors. Figure 7.11 (top panel) shows the mechanism of study as well as the instrument. Also shown in Fig. 7.11 (bottom panel) are the XPS results.

An instrument developed by Huels et al. [33] was used as instruments to study the damage of DNA molecules in vacuum with ionizing radiation including X-rays, electrons, and especially low-energy electrons as shown by Cai et al. [34]. The work was relevant to X-ray nanochemistry because low-energy electrons were emitted from nanoparticles upon X-ray absorption by nanomaterials. However, the fraction of the damaged DNA by low-energy electrons in solutions was little known and could be much lower than the case of DNA damage in vacuum. As a result, the capability of using the instrument developed by Sanche et al. in regular enhancement measurements still needs to be explored.

7.3   X-Ray Sources and Instrumentation for X-Ray Nanochemistry

In addition to the techniques and instruments that have been used to detect enhancement, X-rays are needed for irradiation of samples. To this end, several types of X-ray sources were used in the reports appeared in the literature. Here, the X-ray
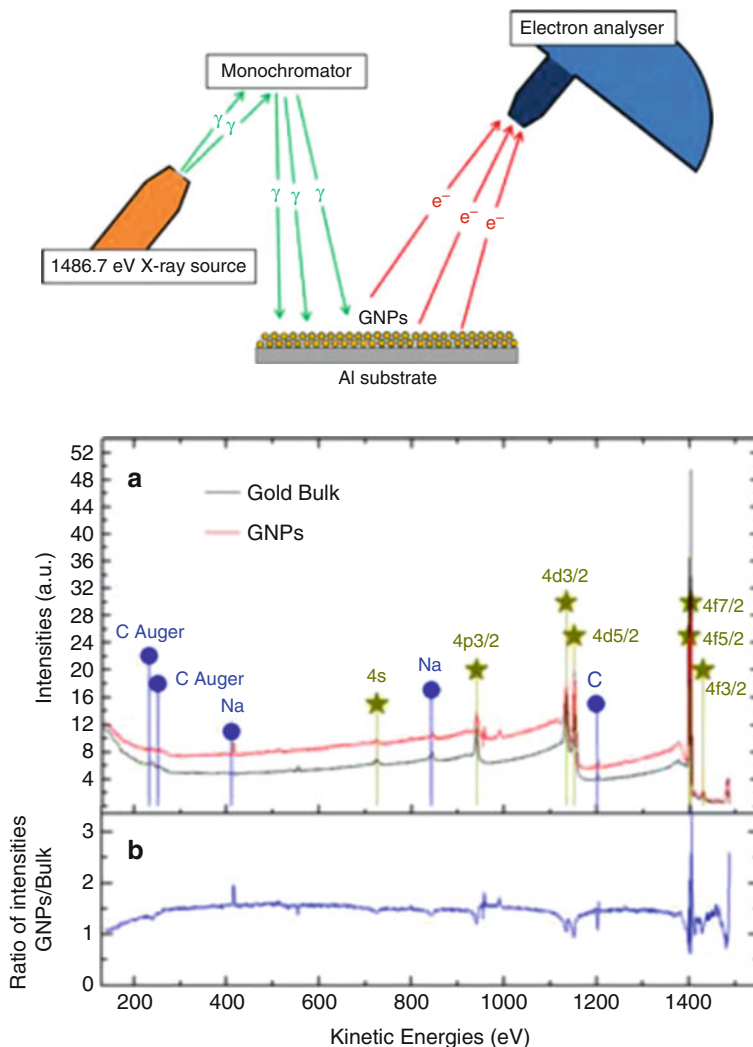
Fig. 7.11 X-ray photoelectron spectroscopy (XPS) used to probe emission of electrons from nanomaterials under X-ray irradiation. Although this is not the same as measuring the enhancement, the results can be used to compare with theoretical predictions. The top panel shows an experimental setup, and the bottom panel shows the results. The upper trace (**a**) in the bottom panel shows the electron emission spectra. The lower trace (**b**) in the bottom panel shows the relative electron yield (ratio) from gold nanoparticles compared with that from bulk gold bulk. (Casta et al. [32] With Permission of Springer.)

sources and several X-ray apparatuses used in the enhancement measurements are shown. The discussion is limited to the general description of the instruments, and readers who are interested in the details of the devices are encouraged to review the original publications or other technical descriptions available on the websites of various companies.

7.3.1 X-Ray Sources

The sources used in published enhancement measurements are discussed in this section.

7.3.1.1 Compact X-Ray Sources

There are several compact X-ray sources and some of them are smaller than a modern cell phone. One of the devices used in enhancement measurements was Mini-X made by Amtek. The rating of the source was 50 kVp and up to 80 μA, making it a 4-W source. Either silver or gold was used as the target material. The source and the energy spectrum in log and linear scale from the silver target are shown in Fig. 7.12. The source was used by Su et al. [2].

7.3.1.2 Microfocus X-Ray Sources

Microfocus X-ray sources are convenient to use. Figure 7.13 shows three similar commercial X-ray sources. The dimensions are available on the websites of these companies. Guo et al. used one of these sources in several of their enhancement measurements. Specifications of these sources are also given in Fig. 7.13 as well.

Compact X-ray sources as well as microfocus sources can be used in other more complex devices. For example, an apparatus called scanning focusing X-ray device is discussed in Chap. 9. A microfocus X-ray source or two of them can be mounted on motion stages in the device. Apertures can be used to collimate X-rays into needle thin X-ray beams. By quickly rotating and rocking the sources, a focused X-ray beam is formed. The concept and instrument are shown in Fig. 9.39.
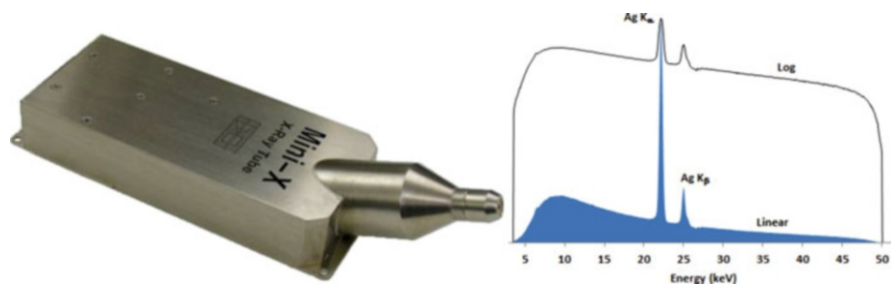
Fig. 7.12 The mini-sized X-ray source and spectrum from the source. (http://amptek.com/products/mini-x-ray-tube/)

Fig. 7.13 Microfocus X-ray source from Oxford Instruments (PX90, left panel), Hamamatsu Photonics (L94121, mid panel), and Thermo Fisher Scientific (PXS10, right panel). The product information is obtained directly from the websites of these companies. Highest X-ray energies and maximum powers of the sources are listed. Also shown are focus-to-object distances and focal sport sizes
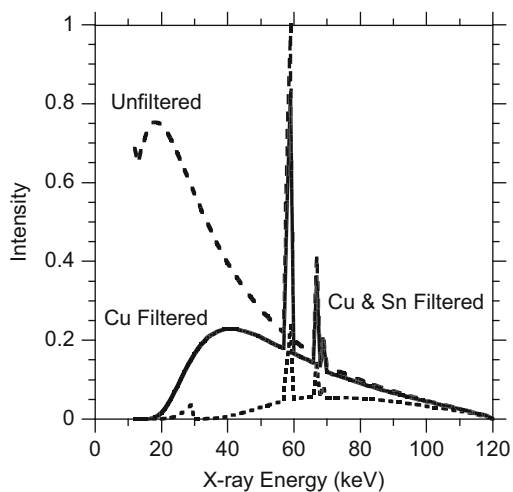
Fig. 7.14 X-rays emitted from a microfocus X-ray source without and with filters. When no filters are present, low-energy X-rays are abundant (dashed line). When both Cu and Sn filters are used, X-rays are over 40 keV (dotted line). Cu filter alone eliminates most of the X-rays below 20 keV (solid line). (Adapted with permission from Guo et al. [38]. Copyright (2015) American Chemical Society.)

7.3.1.3   Filtered X-Rays

X-rays emitted from microfocus or other X-ray tubes have a generic spectral profile that can be predicted by software such as SpekCalc, developed based on several publications by Poludniowski and Verhaegen et al. [35–37]. Figure 7.14 shows several spectra from a tungsten target operated at 100 kVp calculated by Guo et al. [38]. The unfiltered spectrum (dashed line) contains a large amount of

low-energy X-ray photons (i.e., below 15 keV). These X-rays are important to the production of reactive oxygen species in water. However, they have shallow penetration depths in water or tissues; even for a 5-mm thick of water, the unfiltered X-ray spectrum hardens significantly over the sample length. One way to avoid such a strong depth dependency is to use filtered X-rays. Figure 7.14 shows the same X-rays after passing through a Cu filter (solid line), as well as a spectrum of X-rays using a filter (dotted line) of Cu and Sn foil. Sn filters significantly reduce X-rays below 40 keV. The hard X-ray spectra after filtration through the Cu and Sn foils do not change significantly over water samples 1 cm thick, although they may be further hardened after going through water or tissues centimeters thick.

The spectra shown in Fig. 7.14 can be used to produce type 1 or 2 physical enhancement or type 1 chemical enhancement. The unfiltered X-rays can produce strong type 1 chemical enhancement, whereas the filtered X-rays can produce strong types 1 and 2 physical enhancement. It is worth pointing out is that filtration reduces the flux or the dose rate of X-rays from these sources.

7.3.1.4 Synchrotrons and Other X-Rays (Monochromatic)

Often, monochromatic X-rays are required to study mechanisms of enhancement because the enhancement depends on X-ray energy. In these cases, more advanced X-ray sources are employed, and some of them, such as Compton X-ray sources, are still under development. Synchrotrons are one of them and are now widely available. The parameters of a typical synchrotron source are compared with a microfocus source in Table 7.3.

Uesaka et al. [39] discussed a keV/MeV X-ray source. The source can fit in a small, 15 ft. × 15 ft. room. The authors used a YAG laser interacting with 10 MeV electrons emitted from an X-band linac at a single point in space. The scattering generated 22 keV or 44 keV X-rays in the traveling direction of the electrons. The energy spread was about 10% for X-rays, whose directionality remained within ±2.5 mrad of the electron beam. No experimental data was available on the energy spectrum.

Gokeri et al. [40] theoretically investigated irradiation of a gold-loaded tumor region in a realistic head phantom under an array of X-ray microbeams. The X-rays were between 30 and 600 keV, with a mean energy of 107 keV. This configuration can be realized by either traditional X-ray sources or accelerators.

Table 7.3 Comparison between a typical synchrotron and microfocus X-ray source

Parameters	Synchrotron	Microfocus
Energy	1–250 keV	10–250 kVp
Dose rate	Up to 5 kGy/min	Up to 100 Gy/min
Temporal profile	Nanosecond pulse	Continuous
Beam size	2 mm × 2 cm	10–100 μm
Sample size	2 mm × 2 cm	ϕ1 mm – 10 cm
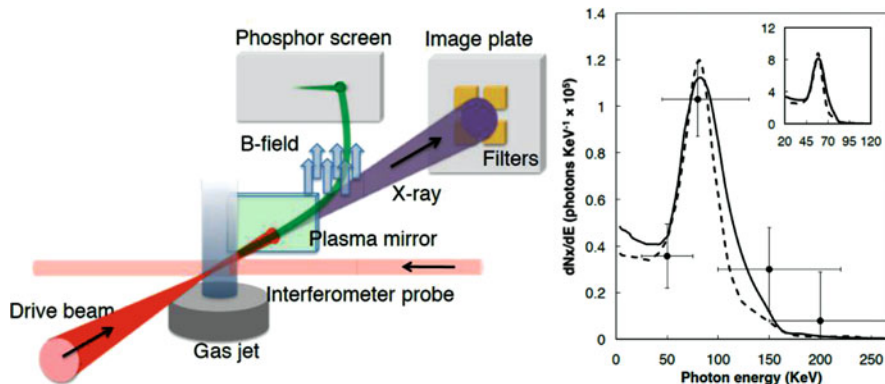
Fig. 7.15 Compton X-ray source (left panel) and its photon energy spectra (right panel). (Reprinted from Downer et al. [41], with permission of AIP Publishing.)

It is also possible to use other X-ray sources such as Compton sources. One such source was described by Downer et al. [41]. The source took advantage of ultrafast laser light scattering off energetic electrons. The source was ideal for creating enhancement by nanomaterials buried deep in a medium, a system resembling tumors in the body. Figure 7.15 shows such a source and the measured X-ray energy spectrum. No enhancement measurements were made using this source.

7.3.2 X-Ray Instruments

Various X-ray instruments can be built using these X-ray sources. Several of them are described in this section, ranging from top-down to bottom-up devices. Top-down is associated with X-rays irradiating samples from the top, while bottom-up is associated with X-rays traveling from below to irradiate samples positioned above. These two configurations are suited for different applications.

7.3.2.1 Bottom-Up Irradiation Methods

Bottom-up configuration requires X-rays to penetrate the bottom of sample containers. In this configuration, X-rays travel upward to irradiate samples positioned above the X-ray source. For still liquid samples, this configuration can be used as long as the bottom of containers is relatively thin. For containers with thick bottoms or complex supporting mechanisms, this configuration is not preferred. Figure 7.16 shows a typical device, as constructed by Guo et al. [10]. The same device was used in several works published by Guo et al. The X-ray source was a 65-W microfocus X-ray source (Thermo Scientific™ Kevex™ PXS10-65 W). Filters were placed right above the source to modify the spectrum of X-rays, with the final spectra similar to
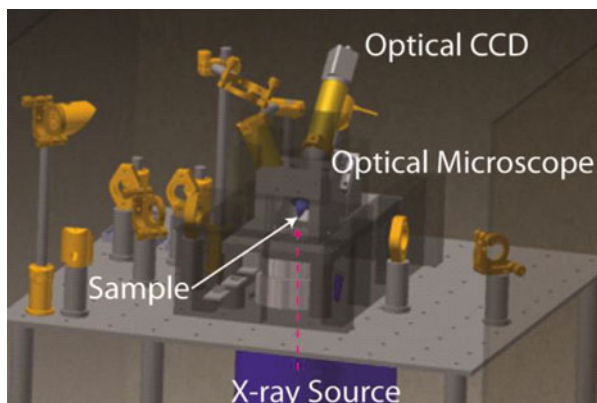
Fig. 7.16 An example of a bottom-up X-ray instrument. This homemade instrument was used in several publications. The microfocus X-ray source was under the breadboard that supported the optical parts, including a microscope objective to collect the visible light emitted from samples irradiated by X-rays and CCD to visualize the sample

those shown in Fig. 7.14. The device was interfaced with other instruments, such as an optical microscope. Fluorescent light was collected by a lens and focused onto an optical fiber that transmitted the light to a spectrometer equipped with a LN_2-cooled CCD detector. X-ray scintillation from nanomaterials was studied with this device, which was reported by Guo et al. [1].

7.3.2.2 Top-down Irradiation Methods

Another way to irradiate samples is from the top. In this case, X-rays travel downward to irradiate the sample. This configuration is suited for irradiating samples stored in thick bottom containers. It is also suited for irradiation of samples that require constant movement driven by large and complex platforms underneath the samples. When many accessories are needed to manipulate samples, this configuration is more convenient because it is easier to mount the accessories beneath the sample than to suspend them from above. Figure 7.17 shows one such instrument. The device was used by Guo et al. [42] in their demonstration of X-ray focusing. In this case, a thin needle beam of X-rays was formed using a microfocus X-ray source through an X-ray aperture in the top-down configuration. A phantom was mounted on a platform that was moved by two rotation stages so that the platform was rocked and rotated at the same time. This was equivalent to scanning the X-ray needle beam while pointing the beam at the same isocenter in space. The result was the same as focusing the X-ray beam to the isocenter. Instead of using X-ray focusing optics, which is difficult to make, focusing was achieved here by moving and reorienting the sample.

Fig. 7.17 An example of the top-down configuration of X-ray instruments. The microfocus X-ray source was mounted on the top. A scanning apparatus was shown in the bottom. A phantom is mounted on a platform that is rotated in two directions. (Reprinted with permission from Guo et al. [42]. Copyright (2016) by Radiation Research. All rights reserved.)
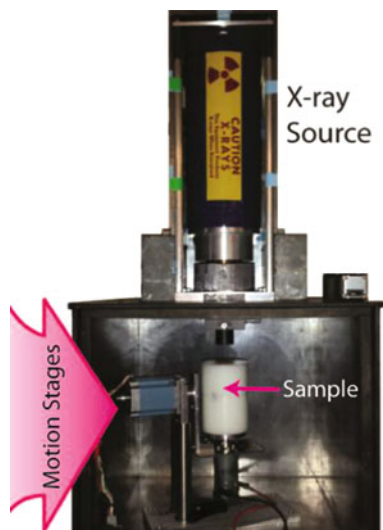
Table 7.4 Other X-ray sources or emitters

Source	Energy	Half-life	Particle	Dose rate
^{18}F	0.6335 MeV	109 min	Positrons	Various
^{60}Co	1.17 and 1.33 MeV	5.26 years	Photons	Various
^{90}Y	2.26 MeV	64 h	Photons	Various
^{103}Pd	21 keV	17 days	Photons	Various
^{137}Cs	0.512 and 0.662 MeV	30 years	Photons	Various
^{169}Yb	50–308 keV	32 days	Photons	Various
Faxitron	10–130 kVp, 0–3 mA	–	Photons	3 Gy/min, 3 shelf positions

7.3.2.3   Other X-Ray Sources

There are other ways to irradiate samples with X-rays. For example, brachytherapy often uses radioisotopes as its radiation sources. Table 7.4 lists some of these sources and their specifications. Reynoso et al. [44] used ^{169}Yb source for gold nanoparticle-aided radiation therapy. These sources have often been used for simulations and treatments. Conventional X-ray cabinets are also available. For example, Faxitron is a typical X-ray source that is used in many experiments.

7.3.2.4   Scanning Focusing of a Thin Needle Beam of X-Rays

The idea is to move/rotate a thin needle (pencil) X-ray beam to cover as large of a solid angle as possible while aiming the beam at a fixed point (focal point or isocenter) in space. Figure 7.18 illustrates the concept. The resulting effect is
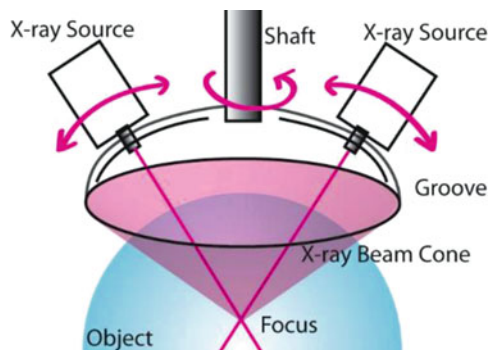
Fig. 7.18 The concept of scanning focusing of X-rays using apertured X-ray sources. Two microfocus X-ray sources are used here; both of them rotate while sliding up and down along the tracks on the spherical hemisphere. The integrated result is the focus of the X-ray beams at the focal spot. (Reprinted with permission from Guo et al. [42]. Copyright (2016) by Radiation Research. All rights reserved.)

equivalent to focusing the needle beam of X-rays at the isocenter or focal spot in space. This is the same as optically focusing through a lens, except that there is no lens here. There are two X-ray sources shown in Fig. 7.18. The purpose of using two sources is to balance the weight so that the two sources can move at high speeds. If one source is used, the eccentric force may be too great to maintain a tight focus.

7.4   In Situ Detection

There are many ways to detect the response of X-ray irradiation. To date, almost all measurements were performed ex situ, except for a couple of studies. Often chemical or biological methods were used when ex situ detection was needed because these reaction products were accumulated during the entire irradiation time, hence creating a time-integrated result. The only in situ measurement was performed using thin-film photovoltaic cells to detect scintillation from nanoparticles under X-ray irradiation shown by Guo et al. [1]. EPR spectroscopy can probe approximately in situ dynamics, although the example shown here is not exactly in situ.

7.4.1   X-Ray Photovoltaics

Section 7.2.3.5 discusses the setup that performs in situ measurements. In this section, the setup is shown to emphasize the in situ feature. In one configuration, which is shown in Fig. 7.19 (left panel), scintillation was detected by thin-film
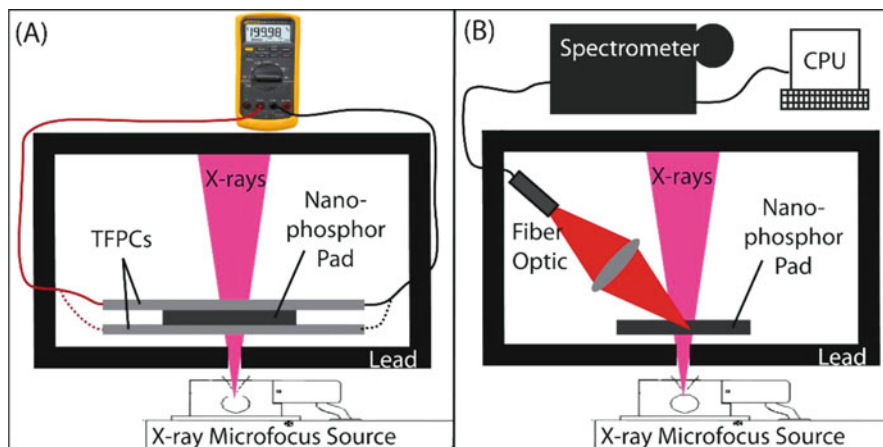
Fig. 7.19 In situ scintillation measurements. The left panel shows the in situ voltage measurement, and the right panel shows the in situ scintillation emission measurement with a spectrometer equipped with a LN_2-cooled CCD detector. (Reprinted with permission from Guo et al. [1]. Copyright (2014) American Chemical Society.)

photovoltaic cells and a multimeter. In another configuration, shown in the right panel of Fig. 7.19, the scintillation light was focused onto an optical fiber and then sent into a spectrometer equipped with a LN_2-cooled CCD detector. The overall optical detection efficiency was approximately 10%. The reading of the multimeter, as well as optical emission spectra, can be collected in situ. When X-rays are not illuminating the sample, there is no optical or photovoltaic signal.

7.4.2 In Situ EPR Spectroscopic Instrumentation and Experiments

Xu and Zhang et al. [43] reported the release of drug molecules trapped in micelles formed by block copolymers after γ-ray irradiation. The authors stated that there was little structural change to the micelles after irradiated with γ-rays. To investigate the mechanisms of release, the authors used in situ EPR spectroscopy to study hydroxyl radicals produced from UV-light irradiation of TiO_2 nanoparticles. EPR spectroscopic measurements were performed using 5,5-dimethyl-1-pyrroline N-oxide (DMPO) spin trap with a half-life of 40 seconds, indicating the experiment was not strictly in situ. The results showed reduction of hydroxyl radical yield when micelles were present, suggesting that hydroxyl radicals produced from γ-ray irradiation of water may react with diselenide polymer particles to release drug molecules (Fig. 7.20).
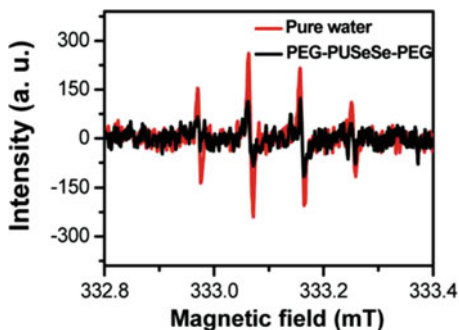
Fig. 7.20 EPR measurement of hydroxyl radicals using DMPO spin trap to study the releasing mechanisms of drug molecules from diselenide block copolymer micelles. (Reprinted with permission from Xu and Zhang et al. [43]. Copyright (2011) American Chemical Society.)

7.5   Conclusions and Future Work

The techniques for enhancement measurements are described here. Nine methods of detection are described. These methods are not exclusively designed for measuring any specific category or type of enhancement, so it is very possible that any of these methods can detect one or more than one category or type of enhancement. Future work involving mass spectrometry and other analytical methods can be developed to detect enhancement.

X-ray sources commonly used in enhancement measurements, as well as sources that can be used in the enhancement measurements, are briefly discussed. Several instruments are built based on these X-ray sources. Most of the devices are not originally created for X-ray nanochemistry, indicating a large potential market for this field may be created when basic and applied works are in full swing.

Many sources and devices are needed to advance X-ray nanochemistry. Future work is needed to develop these sources, instruments, and detection principles. Two main aspects that deserve scrutiny are in situ properties and ultrafast techniques, which are closely connected. The author of this book studied ultrafast X-ray spectroscopy between the mid-1990s and late 2000s, and much more progress has been made in this field in the last decade. It is foreseeable that many ultrafast measurements can be performed to conclusively identify the origins of enhancement, including physical and chemical enhancement.

Future work is also needed to fully track biological enhancement. This is challenging because most biological studies to date are conducted using kinetic measurements, with the data collected at the end of measurements. In the future, measurements will have to be done in situ. It is possible to develop new X-ray-based methods to accomplish this goal.

References

1. Davidson, R. A., Sugiyama, C., & Guo, T. (2014). Determination of absolute quantum efficiency of X-ray Nano phosphors by thin film photovoltaic cells. *Analytical Chemistry, 86*, 10492–10496.
2. Zhang, P. P., Qiao, Y., Wang, C. M., Ma, L. Y., & Su, M. (2014). Enhanced radiation therapy with internalized polyelectrolyte modified nanoparticles. *Nanoscale, 6*, 10095–10099.
3. Manohar, N., Reynoso, F., & Cho, S. (2012). Feasibility of direct L-Shell fluorescence imaging of gold nanoparticles using a Benchtop X-ray source. *Medical Physics, 39*, 3987–3988.
4. Hainfeld, J. F., Slatkin, D. N., & Smilowitz, H. M. (2004). The use of gold nanoparticles to enhance radiotherapy in mice. *Physics in Medicine and Biology, 49*, N309–N315.
5. Foley, E., Carter, J., Shan, F., & Guo, T. (2005). Enhanced relaxation of nanoparticle-bound supercoiled DNA in X-ray radiation. *Chemical Communications*, 3192–3194.
6. McMahon, S. J., Mendenhall, M. H., Jain, S., & Currell, F. (2008). Radiotherapy in the presence of contrast agents: A general figure of merit and its application to gold nanoparticles. *Physics in Medicine and Biology, 53*, 5635–5651.
7. Starkewolf, Z. B., Miyachi, L., Wong, J., & Guo, T. (2013). X-ray triggered release of doxorubicin from nanoparticle drug carriers for cancer therapy. *Chemical Communications, 49*, 2545–2547.
8. Carter, J. D., Cheng, N. N., Qu, Y. Q., Suarez, G. D., & Guo, T. (2007). Nanoscale energy deposition by x-ray absorbing nanostructures. *The Journal of Physical Chemistry. B, 111*, 11622–11625.
9. Misawa, M., & Takahashi, J. (2011). Generation of reactive oxygen species induced by gold nanoparticles under x-ray and UV irradiations. *Nanomedicine Nanotechnology, 7*, 604–614.
10. Cheng, N. N., Starkewolf, Z., Davidson, A. R., Sharmah, A., Lee, C., Lien, J., & Guo, T. (1950). Chemical enhancement by Nanomaterials under X-ray irradiation. *Journal of the Chemical Society, Communications, 2012*(134), 1950–1953.
11. Sharmah, A., Yao, Z., Lu, L., & Guo, T. (2016). X-ray-induced energy transfer between Nanomaterials under X-ray irradiation. *Journal of Physical Chemistry C, 120*, 3054–3060.
12. Makrigiorgos, G. M., Baranowskakortylewicz, J., Bump, E., Sahu, S. K., Berman, R. M., & Kassis, A. I. (1993). A method for detection of hydroxyl radicals in the vicinity of biomolecules using radiation-induced fluorescence of Coumarin. *International Journal of Radiation Biology, 63*, 445–458.
13. Nakayama, M., Sasaki, R., Ogino, C., Tanaka, T., Morita, K., Umetsu, M., Ohara, S., Tan, Z. Q., Nishimura, Y., Akasaka, H., et al. (2016). Titanium peroxide nanoparticles enhanced cytotoxic effects of X-ray irradiation against pancreatic cancer model through reactive oxygen species generation in vitro and in vivo. *Radiation Oncology, 11*, 91.
14. Cohn, C. A., Pedigo, C. E., Hylton, S. N., Simon, S. R., & Schoonen, M. A. A. (2009). Evaluating the use of $3'$-(p-Aminophenyl) fluorescein for determining the formation of highly reactive oxygen species in particle suspensions. *Geochemical Transactions, 10*, 8.
15. Jeon, J. K., Han, S. M., & Kim, J. K. (2016). Fluorescence imaging of reactive oxygen species by confocal laser scanning microscopy for track analysis of synchrotron X-ray photoelectric nanoradiator dose: X-ray pump-optical probe. *Journal of Synchrotron Radiation, 23*, 1191–1196.
16. Musat, R., Moreau, S., Poidevin, F., Mathon, M. H., Pommeret, S., & Renault, J. P. (2010). Radiolysis of water in nanoporous gold. *Physical Chemistry Chemical Physics, 12*, 12868–12874.
17. Davidson, R. A., & Guo, T. (2012). An example of X-ray Nanochemistry: SERS investigation of polymerization enhanced by nanostructures under X-ray irradiation. *Journal of Physical Chemistry Letters, 3*, 3271–3275.
18. Subiel, A., Ashmore, R., & Schettino, G. (2016). Standards and methodologies for characterizing radiobiological impact of high-Z nanoparticles. *Theranostics, 6*, 1651–1671.

19. Sahbani, S. K., Cloutier, P., Bass, A. D., Hunting, D. J., & Sanche, L. (2015). Electron resonance decay into a biological function: Decrease in viability of E-coli transformed by plasmid DNA irradiated with 0.5-18 eV electrons. *Journal of Physical Chemistry Letters, 6*, 3911–3914.

20. Marques, T., Schwarcke, M., Garrido, C., Zucolotto, O. B., & Nicolucci, P. (2010). Gel dosimetry analysis of gold nanoparticle application in kilovoltage radiation therapy. *Journal of Physics: Conference Series, 250*, 012084.

21. N Deyhimihaghighi, N., Mohd Noor, N., Soltani, N., Jorfi, R., Erfani Haghir, M., Adenan, M. Z., Saion, E., & Khandaker, M. U. (2014). Contrast enhancement of magnetic resonance imaging (MRI) of polymer gel dosimeter by adding platinum nano- particles. *Journal of Physics: Conference Series, 546*, 012013.

22. Sabbaghizadeh, R., Shamsudin, R., Deyhimihaghighi, N., & Sedghi, A. (2017). Enhancement of dose response and nuclear magnetic resonance image of PAGAT polymer gel dosimeter by adding silver nanoparticles. *PLoS One, 12*, e0168737.

23. Chang, J., Taylor, R. D., Davidson, R. A., Sharmah, A., & Guo, T. (2016). Electron paramagnetic resonance spectroscopy investigation of radical production by gold nanoparticles in aqueous solutions under X-ray irradiation. *The Journal of Physical Chemistry. A, 120*, 2815–2823.

24. Guidelli, E. J., Ramos, A. P., Zaniquelli, M. E. D., Nicolucci, P., & Baffa, O. (2012). Synthesis and characterization of gold/alanine Nanocomposites with potential properties for medical application as radiation sensors. *ACS Applied Materials & Interfaces, 4*, 5844–5851.

25. Zhang, Z. Y., Berg, A., Levanon, H., Fessenden, R. W., & Meisel, D. (2003). On the interactions of free radicals with gold nanoparticles. *Journal of the American Chemical Society, 125*, 7959–7963.

26. Bacic, G., Spasojevic, I., Secerov, B., & Mojovic, M. (2008). Spin-trapping of oxygen free radicals in chemical and biological systems: New traps, radicals and possibilities. *Spectrochimica Acta A, 69*, 1354–1366.

27. Spasojevic, I. (2010). Electron paramagnetic resonance – a powerful tool of medical biochemistry in discovering mechanisms of disease and treatment prospects. *Journal of Medical Biochemistry, 29*, 175–188.

28. He, W. W., Liu, Y. T., Wamer, W. G., & Yin, J. J. (2014). Electron spin resonance spectroscopy for the study of nanomaterial-mediated generation of reactive oxygen species. *Journal of Food and Drug Analysis, 22*, 49–63.

29. Abbas, K., Hardy, M., Poulhes, F., Karoui, H., Tordo, P., Ouari, O., & Peyrot, F. (2014). Detection of superoxide production in stimulated and unstimulated living cells using new cyclic nitrone spin traps. *Free Radical Biology & Medicine, 71*, 281–290.

30. Wen, T., He, W. W., Chong, Y., Liu, Y., Yin, J. J., & Wu, X. C. (2015). Exploring environment-dependent effects of Pd nanostructures on reactive oxygen species (ROS) using electron spin resonance (ESR) technique: Implications for biomedical applications. *Physical Chemistry Chemical Physics, 17*, 24937–24943.

31. Lien, J., Peck, K. A., Su, M. Q., & Guo, T. (2016). Sub-monolayer silver loss from large gold nanospheres detected by surface plasmon resonance in the sigmoidal region. *Journal of Colloid and Interface Science, 479*, 173–181.

32. Casta, R., Champeaux, J. P., Sence, M., Moretto-Capelle, P., Cafarelli, P., Amsellem, A., & Sicard-Roselli, C. (2014). Electronic emission of radio-sensitizing gold nanoparticles under X-ray irradiation: Experiment and simulations. *Journal of Nanoparticle Research, 16*, 2348.

33. Klyachko, D. V., Huels, M. A., & Sanche, L. (1999). Halogen anion formation in 5-halouracil films: X rays compared to subionization electrons. *Radiation Research, 151*, 177–187.

34. Cai, Z. L., Cloutier, P., Hunting, D., & Sanche, U. (2005). Comparison between x-ray photon and secondary electron damage to DNA in vacuum. *The Journal of Physical Chemistry. B, 109*, 4796–4800.

35. Poludniowski, G., Landry, G., DeBlois, F., Evans, P. M., & Verhaegen, F. (2009). SpekCalc: A program to calculate photon spectra from tungsten anode x-ray tubes. *Physics in Medicine and Biology, 54*, N433–N438.
36. Poludniowski, G. G., & Evans, P. M. (2007). Calculation of x-ray spectra emerging from an x-ray tube. Part I. Electron penetration characteristics in x-ray targets. *Medical Physics, 34*, 2164–2174.
37. Poludniowski, G. G. (2007). Calculation of x-ray spectra emerging from an x-ray tube. Part II. X-ray production and filtration in x-ray targets. *Medical Physics, 34*, 2175–2186.
38. Davidson, R. A., & Guo, T. (2015). Multiplication algorithm for combined physical and chemical enhancement of X-ray effect by nanomaterials. *Journal of Physical Chemistry C, 119*, 19513–19519.
39. Uesaka, M., Mizumo, K., Sakumi, A., Meiling, J., Yusa, N., Nishiyama, N., & Nakagawa, K. (2007). Pinpoint KEV/MEV X-ray sources for X-ray drug delivery system. In *PAC* (Vol. THPMN035, p. 2793). Albuquerque: IEEE.
40. Gokeri, G., Kocar, C., & Tombakoglu, M. (2010). Monte Carlo simulation of microbeam radiation therapy with an interlaced irradiation geometry and an au contrast agent in a realistic head phantom. *Physics in Medicine and Biology, 55*, 7469–7487.
41. Tsai, H. E., Wang, X. M., Shaw, J. M., Li, Z. Y., Arefiev, A. V., Zhang, X., Zgadzaj, R., Henderson, W., Khudik, V., Shvets, G., et al. (2015). Compact tunable Compton x-ray source from laser-plasma accelerator and plasma mirror. *Physics of Plasmas, 22*, 023106.
42. Davidson, R. A., & Guo, T. (2016). Nanoparticle-assisted scanning focusing X-ray therapy with needle beam X rays. *Radiation Research, 185*, 87–95.
43. Ma, N., Xu, H. P., An, L. P., Li, J., Sun, Z. W., & Zhang, X. (2011). Radiation-sensitive Diselenide block co-polymer Micellar aggregates: Toward the combination of radiotherapy and chemotherapy. *Langmuir, 27*, 5874–5878.
44. Reynoso, F. J., Manohar, N., Krishnan, S., & Cho, S. H. (2014). Design of an Yb-169 source optimized for gold nanoparticleaided radiation therapy. *Medical Physics, 41*(10), 101709.

Part IV
Development of Applications

Chapter 8
X-Ray Nanochemistry and Its Applications in Biology

The motivation to study biology is like watching the apple fall to Newton's head everyday.

8.1 Introduction

We have learned in Chaps. 2, 3, 4, and 5 that physical, chemical, and biological enhancement can be achieved using nanomaterials and the enhancement can be detected using chemical or biological reactions. As a result, chemical reactions are both a means (probes) and an end (target reactions). In Chaps. 2 and 3, the content is selected so that the physical or chemical enhancement can be measured as cleanly and easily to interpret as possible. Biological enhancement is formally described for the first time in Chap. 4 in which two types of biological enhancement are defined and several examples are given. However, the study of biological enhancement is far from complete or conclusive, or at least is not as conclusive as physical or chemical enhancement is because biological reactions are inherently more complex. For example, there are many endpoints that can be studied with multiple assays through different damage pathways, and each assay may yield a different magnitude of enhancement because the pathway associated with this assay is unique and different from others. One may say that the order in which these three categories of enhancement are ranked in terms of the completeness of their understanding is physical enhancement (PE) > chemical enhancement (CE) >> biological enhancement (BE).

The difficulties in studying biological enhancement make its study both challenging and exciting when compared with the other two categories of enhancement. Since the initial goal and one of the ultimate goals of using nanomaterials to enhance the effectiveness of X-ray irradiation in biological systems is to eradicate only tumor cells, biological targets are frequently used in X-ray nanochemistry studies. Reaching this goal definitely requires the study of enhancement mechanisms in biological systems. Chapter 3 discusses several relatively simple chemical reactions either employed to probe the enhancement or used as target reactions of enhancement. Chapter 4 cursorily describes biological enhancement. In this chapter, much more complex biological reactions involving proteins, nuclear DNA, and other cellular

organelles are used as the target of X-ray damage or modification. Understandably, enhancement measurements involving these biological molecules are much more complex than the relatively simple dosimetric chemical reactions discussed in Chap. 3. Many works reported in the literature are application-oriented rather than mechanis-oriented, partially because the damage mechanisms are far more complex in biological systems than dosimetric chemical reactions discussed in Chap. 3. Some of the published results, as shown in Chap. 4, suggest the existence of biological enhancement, although true causes for many of these measurements are still not completely understood and, in some cases, hardly understood at all, despite the fact that many or almost all the publications to date attribute the cause or origin of their measured damage to physical enhancement. Due to these difficulties, measured enhancements reported in this chapter are not assigned to any particular enhancement mechanisms. It would be difficult and incorrect to forcefully assign the reported enhancements to the enhancement mechanisms specified in Chaps. 2, 3, and 4 because those isolated enhancements may or may not be the true causes for the measured enhancements. Furthermore, it is unnecessary to affirm that all the enhancements observed in this chapter are caused by the enhancements described in Chaps. 2, 3, 4, and 5. Other mechanisms not discussed in this book may contribute to the observed enhancements. Damages discussed in this chapter are therefore categorized by the target or target reaction types and not by the category or type of enhancement.

Another reason of not assigning results shown in this chapter to specific categories or types of enhancement is that using biological targets to measure enhancement, as well as using X-ray nanochemistry and X-ray radiation to manipulate biological targets, demands careful work. The works performed to date have at least shown that enhancements did exist. When biological reactions, including cell apoptosis, are used to determine the enhancement or enhancements of X-ray-induced damage or changes, the measured enhancement depends on the pathways, endpoints, and assays, just as physical or chemical enhancement depends on the reactions and methods. Although there are many and almost too many pathways that could affect biological enhancement, results published to date only investigate certain pathways; as a result, at present time it is difficult to isolate biological enhancement from physical or chemical enhancement. To a degree, this may be a blessing because many uncorrelated works may help identify all possible pathways that can cause biological enhancement. As X-ray nanochemistry advances, the depth of understanding and degree to which we can manipulate the enhancement will be significantly increased.

Although mechanisms of enhancement are still unclear in most works, the main benefit of obtaining these enhancements without knowing the mechanisms is that the work is simpler and more straightforward; the downside is that the measured enhancement values could be far less than the maximum total enhancement one can possibly get. Therefore, applications that are directly based on these preliminary studies may lead researchers to wrong conclusions. However, science often progresses this way, i.e., through numerous trials and errors. Here, we will summarize the work in this area and show how X-ray nanochemistry is being used to generate damage to biological samples ranging from nuclear DNA molecule strand breaks to cell apoptosis.

Many reports that asserted the cause of enhancement to be physical enhancement would need further verification, as one has to exclude all other enhancements in order to confirm the origin of the enhancement. However, eliminating biological enhancement from the total enhancement in biological systems is difficult because biological reactions are intrinsically much more complicated than the simple one- or two-step chemical reactions. Currently there is no report that claims physical or chemical enhancement has nothing to do with the measured enhancement using biological systems. As it is shown in this chapter, as well as in Chap. 9, many experimental results of enhancement measurements using biological systems do not agree with theoretically predicted physical enhancement values. These facts strongly suggest the existence of many types of biological enhancement together with physical and chemical enhancement. For instance, it is possible that DNA strand breaks can be catalytically enhanced by gold nanoparticles. Therefore, the observed enhancement can very well come from enhancements of physical, chemical, and even biological nature or the combination of some or all of these enhancements.

Many different cell lines have been used in enhancement measurements. Results using healthy eukaryotic cells are given here, and results of studying cancerous cell lines are presented in Chap. 9. Results on bacterial cells are also given in this chapter. The radiation effects on bacterial cells are different from eukaryotic cells because of the structural differences between these two types of cells. As a result, enhancement for the two types of cells can be significantly different. The published results are reviewed here to highlight the differences.

8.2   X-Ray Nanochemistry on Biomolecules

Biological endpoints are complex to test, and damage pathways of biological targets are often complex. It is therefore prudent to specify all the experimental conditions, especially those used to describe nanomaterials so that researchers can more easily compare notes and learn from each other's efforts. Following this guideline, the main experimental conditions used in reports discussed in Chaps. 8 and 9 are listed, and results from different labs are compared. Often, authors may not be aware of all the conditions and parameters that are relevant. Being mindful of these parameters will help researchers working in the discipline to heed for important conditions in their future experiments.

A list of parameters is selected here to describe nanomaterials used in damaging biomolecules. These parameters can significantly influence enhancement to the effectiveness of X-ray irradiation on biological systems. These parameters are also important to damaging cells and tumors. More parameters may be added to this list in the future to define and specify experimental conditions, and some of those are listed in Chap. 9. Only after these parameters are specified, whenever possible, then can the enhancement results be meaningfully compared. Table 8.1 shows these parameters.

In the following, biological targets reported in the literature are reviewed.

Table 8.1 Parameters to describe nanomaterials (NMs) when testing enhancement using biological systems

Parameters	Range	Impact on biological systems	Purpose
Conc. of NMs	0.01–1000 nM	Uptake	Uptake
Solvent	Water, serum	Blood	Uptake
pH	2–10	Solubility of NMs	Uptake
Surfactants (high density)	PEG, Glu, folic acid, etc.	Stability and solubility	Targeting and uptake
Scavengers	DMSO, Tris, etc.	Little or no effect	ROS generation
Ligands (low density)	Antibody, peptide, etc.	T2PE or CE versus T1PE	Targeting
Composition	All elements	Toxicity and enhancement	Enhancement
Dimensions	<100 nm	Uptake, circulation, toxicity	Uptake

NMs nanomaterials

8.2.1   Proteins

Proteins account for 55% of non-water cellular weight in a cell and are the most abundant component of a cell. This means that it is critical to study protein damage by X-rays assisted by nanomaterials. The mass of individual proteins is as high as a few hundred thousand Daltons, and proteins are a few nanometers in size. In contrast, nuclear DNA molecules are much heavier and larger. Unless nanomaterials can target proteins and cause damage to only proteins under X-ray irradiation, damage to proteins is usually much less compared with nuclear DNA. Due to this, few studies have been devoted to studying protein damage by X-rays in the presence of nanomaterials. One of the few published reports available in the literature was presented by Sicard-Roselli et al. [1].

Protein damage mechanisms are only briefly mentioned here. Von Sontag [2] showed some of the popular thoughts on how proteins may be damaged by X-rays or reactive oxygen species. However, this is still an active area of research, and X-ray nanochemistry may help elucidate the damaging mechanisms.

Sicard-Roselli et al. [1] studied protein degradation using human centrin 2 (HScen2) proteins as a model system. This protein was chosen because it is known to be involved in DNA repair processes. The authors mixed the protein with gold nanoparticles and irradiated the mixture with X-rays. The average size of gold nanoparticles was 38 nm. Gel electrophoresis and colorimetry were used to determine the damage to Hscen2 proteins. The ratio of gold nanoparticle to protein ratio was 2×10^{-4}, and X-ray energy was 49 keV. Upon irradiation, optical absorption changed. The authors observed enhancement with proteins around μM and gold nanoparticles around 1–10 nM. 10 nM gold nanoparticle solutions corresponded to a 0.3 WP gold loading in water, which would create 0.3 DEU type 1 physical enhancement or 0.4 DEU physical enhancement. The measured
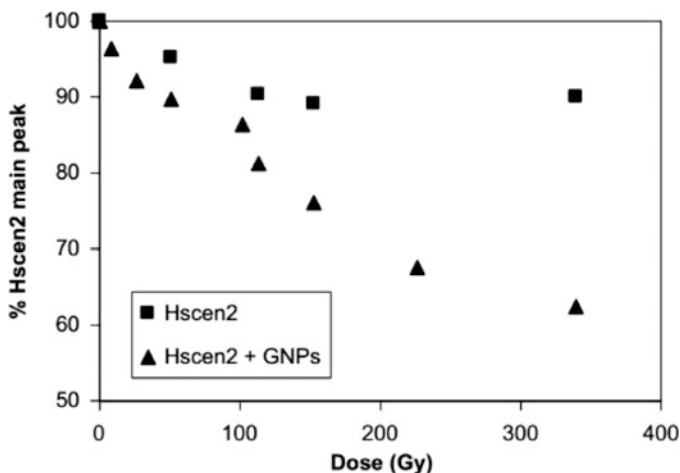
Fig. 8.1 Gold nanoparticles enhancing damage of proteins under X-ray irradiation. The trend with gold nanoparticles was different from that of proteins alone. The latter saturated above 150 Gy, whereas the former did not saturate even at 300 Gy. (Reprinted from Sicard-Roselli et al. [1], with permission from Elsevier.)

enhancement was 0.5 DEU, which was close to the magnitude of the theoretically predicted physical enhancement. The damage was not calibrated by other methods such as mass spectrometry or other biological assays. The results are shown in Fig. 8.1. It is worth pointing out that the dose dependency for the damage to proteins alone and to proteins with gold nanoparticles was different; in the case of protein alone shown in Fig. 8.1, the damage saturated at around 150 Gy. In contrast, gold nanoparticles seemed to be able to help the proteins to "overcome" this saturation, and the damage did not saturate even at 300 Gy. This suggested that the role of gold nanoparticles was not just to raise the amount of damage to the proteins but also somehow helped change how proteins response to X-ray irradiation. The damage could be facilitated by chemical enhancement as well, if physical enhancement could not fully explain the results. The magnitude of enhancement using the initial slopes of the protein damage at low doses (below 100 Gy) was 1.0 DEU. However, if the damages at 300 Gy were used, then the enhancement value would be 3.0 DEU.

8.2.2 Nucleotides

DNA molecules are a key component in the cell. Nuclear DNA in eukaryotic cells is massive in size and weight. When there are more than 250–2,500 double-strand breaks (DSBs) per nuclear DNA in mammalian cells within 24 h, which is 5 to 50 times the amount of endogenous DSBs and corresponds to 10–100 Gy of X-ray irradiation, the damage is considered to be beyond repair and can cause irreversible mutations and apoptosis. This estimation gives rise to approximately 8.3×10^{-9}

(/Gy bp) G values of DSBs of nuclear DNA in cells, each with 3×10^9 base pairs (bp). For this reason, DNA damage should be the most important biological reaction in the context of enhancing damage to cells by nanomaterials under X-ray irradiation. One of the earliest publications in the field of X-ray nanochemistry targeted plasmid DNA, and since then many groups have chosen DNA as the primary target for damage by nanomaterials under X-ray irradiation. Table 8.2 lists, in chronological order, the works of studying DNA damage enhanced by gold or other nanomaterials under X-ray irradiation.

Guo presented seminars around the country between 2002 and 2004 on the subject of using gold nanoparticles to enhance single-strand breaks of DNA molecules. Similar results were also shown at the ACS meeting in August 2004 [18]. Guo et al. [3] published the results of their first work on DNA strand breaks enhanced by gold nanoparticles under 100 kVp X-ray irradiation. In this work, 5600 base pair plasmid DNA molecules were used as the target, and the enhancement was provided by 5 nm gold nanoparticles coated with different surfactants. Gel electrophoresis was used to detect DNA strand breaks, and the supercoiled plasmid DNA (scDNA)

Table 8.2 List of works of using nanomaterials to enhance strand breaks of DNA molecules under X-ray irradiation

Authors Corresp/ First	Energy (kVp)	Dose (Gy)	Enhancement (DEU)	System	NMs (size, nm)
Guo et al. [3]	100	8	1–2	Supercoiled DNA	AuNPs (5.5)
Guo et al. [4]	100	4	1	Supercoiled DNA	AuNPs (3)
Butterworth et al. [5]	160 kVp	1000	12	Plasmid DNA	AuNPs
Sanche et al. [6]	60 keV (e⁻)		25	Plasmid DNA	AuNPs/film
Sanche et al. [7]	60 keV		0.44–6.48	Supercoiled DNA	AuNP/ cisplatin
Sicard-Roselli et al. [1]	17–70 keV	5	0.5–2.2	Supercoiled DNA	AuNPs
Lancomb et al. [8]	⁶⁰Co	1000	0.37–1.17	Plasmid DNA	PtNPs
Le Sech et al. [9]	2–11 (keV)	100	0.1	Plasmid	PtNPs
Sanche et al. [10]	60 keV (e⁻)		0.6–1.3	Plasmid DNA	Gd/AuNPs
Guo et al. [11]	100	4	1	DNA (12 mer)	AuNPs (15)
Yan et al. [12]	160	3	1.3	Nuclear DNA	AuNPs
Guo et al. [13]	100	4	2–15	Supercoiled DNA	AuNTs
Ma and Su et al. [14]	40		0.5	Nuclear DNA	AuNPs (13)
Zheng et al. [15]	10 eV (e⁻)		0.5–3.7	DNA (vacuum)	AuNPs (15)
Chow et al. [16]	150 keV	–	2.7 (theory)	DNA	AuNPs (100)
Sancey et al. [17]	220	8	0.3–1.0	DNA in B16F19	GdNPs

Only those results obtained using nanomaterials are chronologically listed here

AuNPs gold nanoparticles, *PtNPs* platinum nanoparticles, *GdNPs* gold nanoparticles
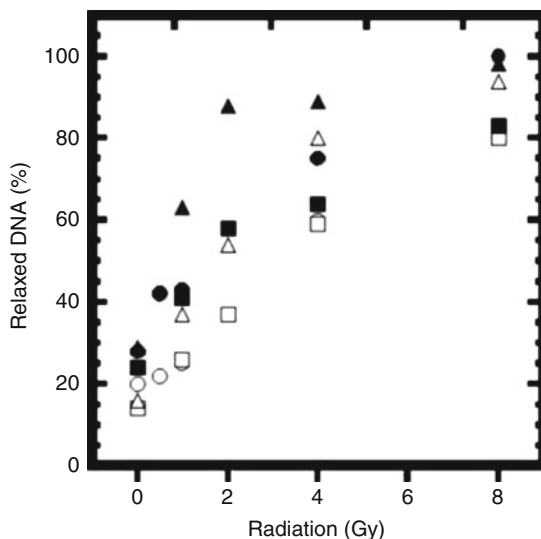
Fig. 8.2 Supercoiled DNA (scDNA) SSB results obtained using gel electrophoresis. SSBs with different concentrations of gold nanoparticles and X-ray doses are displayed. The ratio of slopes with gold to without gold was used to estimate the enhancement. The solid triangles (▲) are the irradiated scDNA with 5 nm gold nanoparticles. The empty squares (□) represent the irradiated scDNA without gold nanoparticles. Data taken below 2 Gy of irradiation was used for enhancement calculations and 1.0 DEU was obtained. (Adapted from Guo et al. [3] with permission of the Royal Society of Chemistry.)

molecules provided a sensitive probe to measure the enhancement. Surfactants used in this work could assist binding between the DNA molecules and gold nanoparticles. However, no direct evidence was provided with respect to whether there was DNA-gold nanoparticle conjugation.

The results of gold nanoparticle enhancement of single-strand breaks (SSBs) by Guo et al. are shown in Fig. 8.2. The empty squares (□) represent the irradiated scDNA without gold nanoparticles. The solid triangles (▲) are the irradiated scDNA with 5 nm gold nanoparticles. Detectable damage begins to show at low dose of 1 Gy. This is comparable to other results showing DNA damage in this dosage range. Linear damage-dose range occurred at up to 2 Gy. Depending on concentration of gold nanoparticles, the slope of SSBs as a function of dose was different. The ratios of slope with gold nanoparticles to without gold nanoparticles below 2 Gy were used to determine the magnitude of enhancement by gold nanoparticles. Based on the ratios of slopes, the unit WP enhancement was estimated to be 1.0 DEU WP^{-1}. This value was close to the theoretically predicted physical enhancement for 1 WP gold in water. This was reasonable because there was at least no intended conjugation between the gold nanoparticles and the DNA. As stated in Chap. 2, average type 2 physical enhancement is normally 1/6th of type 1 physical enhancement unless probes are preferentially attached to nanomaterials.

Guo et al. [4] employed scDNA again to study enhancement by nanoparticles under X-ray irradiation. The goal of this work was to test type 2 physical enhancement by conjugating nanoparticles to scDNA. The experiment was done in tris (hydroxymethyl)aminomethane (Tris) buffer using 3 nm gold nanoparticles. This time, the surface of the gold nanoparticles was covered with ethidium ligands that intercalate between DNA base pairs. This step significantly improved enhancement when compared with the results obtained by Guo et al. [3] because fewer gold nanoparticles were used. The interaction between scDNA and gold nanoparticles is shown in Fig. 2.39. The transmission electron microscope (TEM) image was obtained after ethidium ligated gold nanoparticles were incubated with scDNA in water for 24 h. scDNA was stained with uranyl acetate to increase imaging contrast. The image showed that all the nanoparticles were next to the DNA, which was in sharp contrast to the result of simply mixing the two (not shown here), revealing that most gold nanoparticles were at a significant distance from the DNA molecules without ethidium intercalation.

Figure 3.12 shows the results of SSBs, which are displayed as a function of hydroxyl radical scavenger Tris buffer concentration. The maximum measured enhancement was 2.0 DEU with 10–100 mM Tris. Type 1 physical enhancement was negligible because too small an amount of gold nanoparticles was used. For example, for gold loading below 100 ppm, and if probes were uniformly distributed in the whole sample, then the theoretically predicted type 1 physical enhancement should be below 0.01 DEU for the measured damage. If the damage was counted as physical enhancement, then the unit WP enhancement would be 2 DEU per 0.01 WP, or 200 DEU WP^{-1}, which was too high for type 1 physical enhancement based on the principles explained in Chap. 2. In addition, type 1 physical enhancement should be independent of scavengers, which contradicted the measured results. These results suggested that the measured enhancement could not be originated from type 1 physical enhancement. The results may be explained by average type 2 physical enhancement or chemical enhancement because the probing scDNA molecules were all conjugated to gold nanoparticles. Furthermore, both type 2 physical enhancement and chemical enhancement should be increased as more scavengers were added up to certain concentrations. Without Tris, the measured enhancement was 10 times smaller, of the order of 0.2 DEU. Under this experimental condition, the unit WP enhancement was 20 DEU WP^{-1}, which still could not support type 1 physical enhancement but was within the theoretical range of type 2 physical enhancement or chemical enhancement.

Theoretical simulations were performed to estimate the magnitude of type 2 physical enhancement. Taking the scavenging by Tris into consideration, simulations showed that contributions from average type 2 physical enhancement could explain approximately 20% of the observed enhancement, leaving 80% or the majority of the measured enhancement unexplained at the time of publication. This could be the first indication of chemical enhancement. As speculated in Chap. 3, strand breaks may be catalyzed by gold nanoparticles. The exact mechanisms are still unknown.

Guo et al. [13] used gold nanotubes with the intention of generating much higher type 1 physical enhancement to SSBs in scDNA. The amount of gold was 10^5 times

more than the conjugated case mentioned above. However, because the gold surface was bare without ligand protection, reactive oxygen species such as hydroxyl radicals were readily scavenged by the gold surface. Although the dimensions of the gold nanotubes were large (100 nm in diameter and many microns in length), the surface area for 100 WP was still large enough to scavenge a significant fraction of hydroxyl radicals. As a result, the measured enhancement was only 2–3 DEU, whereas the predicted type 1 physical enhancement was nearly 100 DEU. This was an example of both enhancement and anti-enhancement using biochemical targets. When hydroxyl radical scavengers such as Tris were added, enhancement was approximately 15 DEU due to suppression of scavenging by the gold surface.

Butterworth et al. [5] studied DNA strand breaks in plasmid DNA with high-Z metal nanoparticles under irradiation of 160 kVp X-rays. They used 5 nm, 20 nm, and 1.5 μm diameter gold particles as well as 30 nm silver nanoparticles. Loading of gold nanoparticles was 50 μg/mL, which was equivalent to 0.005 WP. This loading would generate approximately 0.005 DEU type 1 physical enhancement. Gel electrophoresis was used to detect single-strand breaks in Tris-EDTA buffer. The dose used in the study was very high, up to 1000 Gy, which was much higher than what was used by Guo et al. [3]. The authors obtained the results of single- and double-strand breaks (SSBs and DSBs). Enhancement was only observed when gold nanoparticles were added into Tris-EDTA buffer solutions. SSBs were more than doubled for 5 and 20 nm gold nanoparticles, giving rise to 0.29 and 0.12 DEU enhancements. Adding DMSO significantly reduced the measured enhancement. The observed enhancement results are shown in Fig. 8.3. Due to the high dose (see Fig. 8.3) used in the experiments, it is possible that other processes played a role in the measured systems.

Sicard-Roselli et al. [19] studied how citrate-covered gold nanoparticles of different sizes helped increase the damage to scDNA under X-ray irradiation. The sizes were 8–92 nm in diameter. The damage was studied with different effective, not monochromatic though, X-ray energies between 17 and 70 keV with various filters. Gel electrophoresis was used to determine the scDNA strand breaks. The dose was up to 5 Gy, close to what Guo et al. [3] used. The DNA was scDNA, which become circular after single-strand breaks (SSBs). Figure 8.4 shows the results using 37.5 nm gold nanoparticles with a 1:1 ratio of gold nanoparticles to DNA. Type 1 physical enhancement should dominate here because there was no conjugation between DNA and gold nanoparticles. The DNA concentration was 5 nM, and the concentration of gold nanoparticles was 5 nM as well, which corresponds to 8×10^{-3} WP of gold in water. This loading of gold would generate a 0.01 DEU enhancement, which was clearly less than the 0.5–2.2 DEU measured in their work shown in Fig. 8.4. This seemed to be another example that indicated the existence of chemical enhancement. The energy dependency, though, could be the revelation of chemical or physical or both enhancements.

In a series of papers, Sanche et al. systematically investigated how low-energy electrons interacted with films of molecules, such as dry DNA molecules, in vacuum. The authors used a beam of low-energy electrons, or X-ray-generated low-energy electrons from X-rays interacting with metals including nanoparticles. For example,
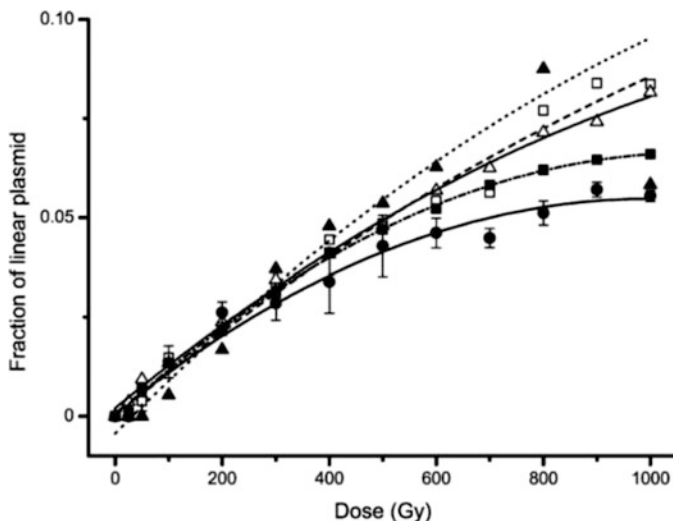
Fig. 8.3 Plasmid DNA single-strand breaks in terms of linear plasmid fraction. Large doses of radiation were used, up to 1000 Gy. Enhancements were mild, ranging from 0.12 to 0.29 DEU. (Reprinted with permission from McMahon et al. [5]. Copyright (2008) by Radiation Research. All rights reserved.)
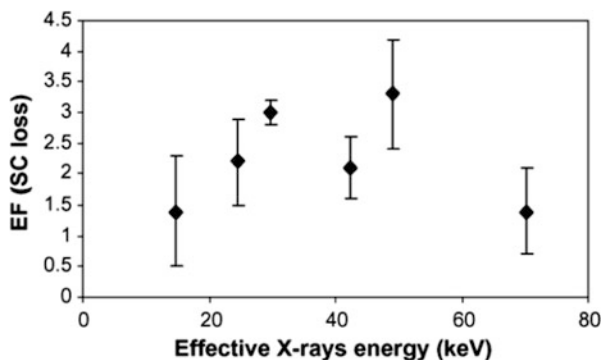
Fig. 8.4 Enhancement to plasmid DNA single-strand breaks as a function of effective X-ray energy. Energy dependency is observed, and the enhancement ranged from 0.5 to 2.2 DEU (Reprinted from Sicard-Roselli et al. [19]. Copyright (2009) with permission from Elsevier)

Sanche et al. [6] reported radiosensitization of DNA damage, or strand breaks by gold nanoparticles, under low- or high-energy electron irradiation. The electron interaction with DNA was related to the field of X-ray nanochemistry, although electrons interacting with films of dry DNA molecules deposited on metals in vacuum were different from electrons interacting with water or DNA molecules dissolved in water. The former allows electrons to directly interact with DNA, whereas the latter relies on reactive oxygen species generated in water to damage DNA molecules.

Fig. 8.5 Strand breaks of
scDNA as a function of
electron energy between
0 and 4 eV. Resonance
features were observed.
(Reprinted with permission
from Martin et al.
[21]. Copyright (2004) by
the American Physical
Society.)
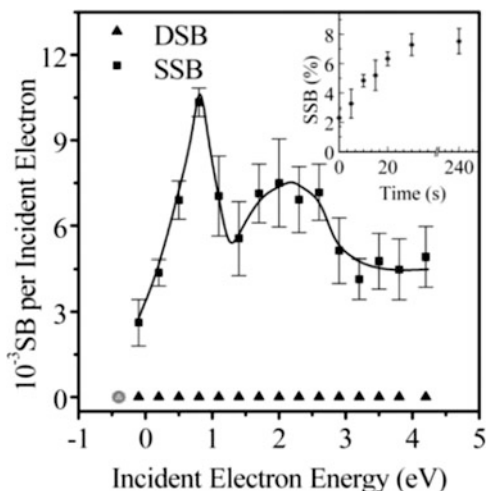
The first work of electrons, not X-rays, interacting and damaging DNA molecules
in vacuum, without the use of nanoparticles, was reported by Huels et al. [20], who
found resonant interactions between 3 and 20 eV electrons and molecules such as
DNA in the form of thin films in vacuum. Sanche et al. [21] performed a similar
study, but the energy of electrons was lowered to 0–4 eV. Again, resonant damage to
DNA thin films was observed in vacuum. Figure 8.5 shows the results with clear
resonance structures.

After these works, Sanche et al. [22] investigated the damage to 3197 base pair
plasmid DNA in vacuum by X-rays and electrons. No nanoparticles were used. X-
rays were 1.5 keV from Al K_α. The electrons were those emitted from a tantalum
target irradiated with Al K_α X-rays. If the damage was caused by low-energy
electrons (LEE) and not by X-rays, direct damage to DNA by X-rays could be
extrapolated to be between 10 eV and 150 keV using the electron energies matching
those emitted from the tantalum. The predicted damage is shown in Fig. 8.6. Keep in
mind the data was not experimentally obtained but extrapolated from experimental
data. The enhancement factor was high, ranging from 15 to 30 DEU for photons
between 25 eV and 150 keV. Given the mass of tantalum film adjacent to the DNA
film, this magnitude of enhancement factor was reasonable based on peak type
2 physical enhancement described in Chap. 2. The impact to the aqueous solution
case needs further investigation because the experiments were performed in dry
conditions.

The first case in which Auger electrons were used to assist damage of DNA
molecules was reported by Sanche et al. [6]. In this experiment, the authors irradiated
plasmid DNA with 60 keV electrons. Gold nanoparticles were used, but there was no
discussion on how gold nanoparticles interacted with DNA, which was assumed to
be via electrostatic interaction based on TEM images. The size distribution of gold
nanoparticles was between 1 and 12 nm in diameter. No ligand was used to terminate
the surface of gold in the gold nanoparticles. The nanoparticles were not purified and
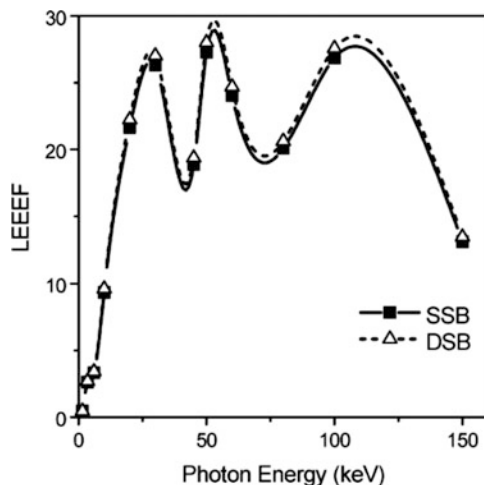
Fig. 8.6 Plasmid DNA single-strand breaks in terms of linear plasmid fraction. The enhancement was explained as caused by low-energy electrons (LEE); hence it is called the LEE enhancement factor (LEEEF), which was obtained using the ratio of the amount of DNA breaks deposited on a tantalum substrate irradiated by X-rays to that by X-ray photons without the tantalum substrate (Reprinted with permission from Sanche et al. [22]. Copyright (2005) American Chemical Society)

hence residual chemicals could be present. The authors then mixed the DNA with gold nanoparticles for irradiation experiments. The damage, which includes SSBs and DSBs, was detected using gel electrophoresis, and an enhancement of 2.5 DEU was measured when gold nanoparticles were used. The percentage of SSBs with gold nanoparticles reached 30–45%. The authors also deposited a monolayer of DNA on thin gold films, and enhancement was found to be 10 times higher, on the order of 25 DEU. Based on these results, the authors concluded that the higher enhancement was caused by low-energy (secondary) electrons emitted from the gold thin film. The authors noted that: "Although the detailed mechanisms leading to tumor regression in the study of Hainfeld et al are not known, it is obvious that a larger portion of the energy of the primary ionizing photons is transferred to the tumor due to the increased absorption of X-ray by gold nanoparticles."

Sanche et al. [7] studied the radiation damage to plasmid DNA by 60 keV electrons. The average size of the gold nanoparticles used in this work was 5.2 nm. The concentration of gold nanoparticles was estimated to be 0.2 μM, and there were approximately 3000 nanoparticles per DNA. This ratio was about 300 times higher than what was used by Guo et al. [4]. The gold nanoparticles were not covered with any ligands, and could interact strongly with the DNA molecules to form conjugates. The gold loading in water was 0.015 WP, so the highest X-ray-generated average enhancement should be less than a few percent. The measured enhancement was between 0.44 and 1.3 DEU for single-strand breaks, which was much higher than the theoretically predicted maximum X-ray-induced damage enhancement by 0.015 WP gold in water. Although electron-generated

enhancement was different from that generated by X-rays, the highest enhancement can only be smaller for electron irradiation because of smaller absorption cross-section differences between gold and water for electrons unless special processes such as resonance absorption occur. This means the observed enhancement could come from local enhancement such as type 2 physical enhancement or chemical enhancement.

Sanche et al. [23] then systematically examined damage to DNA by low-energy electrons. In this work, they studied the dependence of DNA damage on DNA sequence. A twofold difference was found among several tested DNA sequences, ranking from TTT to TGT. For low-energy electron irradiation, their results suggested that the most vulnerable base was TTT. Sanche et al. [24] investigated how soft X-rays and low-energy electrons damaged DNA. In this case, they used soft X-rays and low-energy electrons from a low-energy electron diffraction (LEED) device. The authors deposited a few layers of DNA onto tantalum and glass sub-strates and exposed the composite materials to soft X-rays of 1.5 keV. The electron energy spectrum peaked at 1.4 eV, but with a long tail that extended to 1.4 keV. The enhancement was estimated based on the amount of SSBs for the two films. They found that in a N_2 and O_2 environment, low-energy electrons cause a 3–4 DEU enhancement in strand breaks using the metal film. They also found that adding O_2 could enhance damage of DNA by 80% to 90% over N_2. The authors argued that the enhancement was derived from the increased production of low-energy electrons released from tantalum compared to silica. This seemed to suggest low-energy electrons and soft X-rays damaged DNA via cooperative pathways that involved O_2, which was possible as Hecht et al. [25] showed that O_2-mediated DNA damage.

Sanche et al. [10] improved gold nanoparticle synthesis by attaching Gd atoms to the surface of gold nanoparticles through chemical reactions. The authors used 3197 base pair plasmid DNA, and no conjugation occurred between DNA and nanoparticles. They used two types of gold nanoparticles, one without any ligand and one with thiol undecane or dithiolated diethylene-triamine-pentaacetic (DTDTPA). Their goal was to study the effect of the thickness of the molecular layer between DNA and the surface of gold nanoparticles on DNA strand breaks. Dry thin films of gold nanoparticle-DNA mixtures were irradiated with 60 keV electrons, and the authors observed decreased enhancement, from 2.3 DEU to 1.6 DEU, as the ligand length increases from bare gold nanoparticles to gold nanoparticles coated with the longest ligand of undecane thiol S-$C_{11}H_{23}$. When gold nanoparticles were coated with ligand DTDTPA:Gd, no enhancement was observed. However, the experiment could not rule out chemical enhancement, as bare surface can provide the strongest chemical enhancement.

More recently, a few reviews were written by Sanche et al. For example, Sanche et al. [26] discussed the role of solvated electrons. The authors evaluated the role of secondary electrons produced in water under ionizing radiation in damaging DNA molecules in water. The authors argued that experimental data obtained in high vacuum may shed light or even directly impact on the understanding of how DNA molecules are damaged in aqueous solutions. A recent review by Sanche et al. [27] discussed how electrons may damage biological molecules. In another recent

publication, Sanche et al. [28] suggested that low-energy electrons may resonantly interact with L-cysteine films in ultrahigh vacuum as well. In another review, Sanche [29] discussed the impact of low-energy electron interactions with DNA on cancer radiation therapy.

Lacombe et al. [8] compared 3 nm platinum nanoparticles with platinum atoms of the same weight percentage in causing single- and double-strand breaks. The authors found that although single-strand breaks favored the use of platinum atoms (0.63 DEU) over the platinum nanoparticles (0.37 DEU), the nanoparticles caused more double-strand breaks (1.17 DEU) than platinum atoms (0.63 DEU). The authors hypothesized that platinum nanoparticles played catalytic roles in terms of causing double-strand breaks, a result that could also be explained by chemical enhancement defined in Chap. 3. In another work, Le Sech et al. [9] employed low-energy X-rays at the M and L edge of platinum (Pt) to irradiate Pt terpyridine chloride (PtTC) and Pt nanoparticles mixed with plasmid DNA. They observed increased SSB slopes when either platinum nanoparticles or the molecular platinum complex was in the mixture. The later caused an up to 1-DEU enhancement. For the Pt complex, there was approximately one SSB per free DNA after 100 Gy of irradiation. This was in agreement with Guo et al. [3] who observed 10% SSBs with less than 10 Gy of irradiation with gold nanoparticles. However, the platinum nanoparticle result obtained by Le Sech et al. showed little enhancement, which was an order of magnitude less than Guo et al. [3]. The results given by Le Sech et al. also showed that L and M shell X-rays presented different trends. Table 8.3 shows the results.

Yan et al. [12] developed a doxorubicin (DOX) gold nanoparticle complex and used it to destruct cells under X-ray irradiation. The average size of the gold nanoparticles was 10 nm. Three ligands were coated onto the surface of gold nanoparticles. These ligands included a drug encapsulation ligand *1*, a targeting ligand *2*, and a targeting enhancing ligand *3*. No covalent linkage existed between DOX and gold nanoparticles. The drugs were encapsulated in cyclodextrin (CD) drug carriers (*1*). X-ray source used in the work was operated at 160 kVp and 0.27 Gy/min, and a 3 Gy exposure was used in their work. The authors examined nuclear DNA DSBs using γ-H2AX assay and found a 2.3 DEU enhancement. Figure 8.7 shows the results. DOX alone was 0.1 μM and was 12 times lower than the IC_{50} dosage. Without targeting, gold nanoparticles played an anti-enhancing role, and DOX on gold nanoparticles was less damaging than 0.1 μM DOX.

Table 8.3 DNA damage by Pt molecular complex and nanoparticles under X-ray irradiation

	With PtTC	With PtNPs	Without PtNPs	Free DNA	Enh (PtTC)
SSB – L Shell ($\times 10^{-3}$)	13.6	8.6	8.4	7.7	*0.76*
SSB – M Shell ($\times 10^{-3}$)	6.5	5.5	5.4	2.9	*1.24*
DSB – L Shell ($\times 10^{-3}$)	13	9	8.4	6.7	*0.94*
DSB – M Shell ($\times 10^{-3}$)	10.6	9	8.6	5.5	*0.92*

Results are adapted from Le Sech et al. [9]. Calculated enhancements (Enh) are shown in the last column

Fig. 8.7 Nuclear DNA damage by gold nanoparticles (GNP) coated with DOX and irradiated with X-rays. The endpoint was nuclear DNA damage and the assay was γ-H2AX. Anti-enhancement was detected without targeting ligands on GNP. (Adapted from Yan et al. [12] with permission of the Royal Society of Chemistry.)
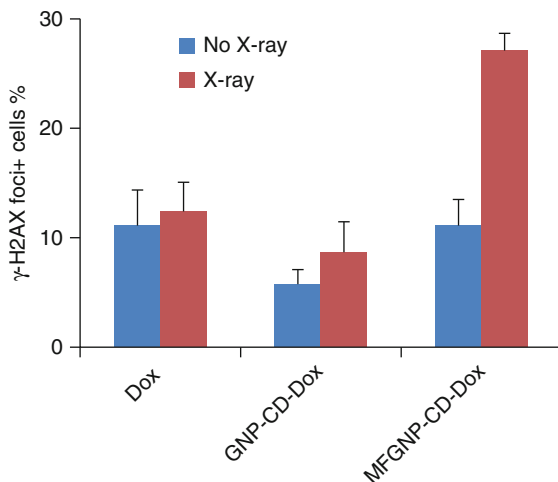
Enhanced damage to nuclear DNA was only observed when both ligands *2* and *3* were on the surface of gold nanoparticles.

Ma and Su et al. [14] studied cellular DNA damage after irradiating cells incubated with gold nanoparticles coated with different polyelectrolytes. The average size of gold nanoparticles was 13 nm. The X-rays were 40 kVp and dose rate was 0.08 Gy/min. The cells were A172 human glioblastoma cells. They found that particles coated with a cationic layer were more internalized. Nuclear DNA damage was detected by the alkaline halo assay. The loading of gold nanoparticles after incubation was not calibrated, although cell responses after X-ray irradiation of gold nanoparticle-treated cells showed little change for negatively charged ligand-coated gold nanoparticles. The results showed DNA damage was more than doubled for gold nanoparticles coated with positively charged ligands based on the results obtained with γ-H2AX assay. Figure 8.8 shows the results. The top two panels show the DNA damage assay results, and the bottom two panels show the enhancement results. Even though cancer cells were used here, the nuclear DNA damage studied here could be easily expanded to studying healthy cells.

Zheng et al. [15] studied the impact of the size and surface of gold nanoparticles on DNA strand breaks under X-ray irradiation. The DNA-gold nanoparticle samples were prepared in solutions and lyophilized for measurements in vacuum. For positively charged ligand bound to gold nanoparticles, DNA damage increased as the amount or number of gold nanoparticles increased. For negatively charged ligand-covered gold nanoparticles, there was no such increase. The authors attributed the damage to be caused by low-energy electrons.

Chow et al. [16] theoretically estimated energy deposition enhancement from a gold nanoparticle near a DNA strand. The authors used dose enhancement ratios (DER) to represent the enhancement. The estimated enhancement was 2.7 DEU for a 100 nm gold nanoparticle placed 30 nm away from the DNA molecules under 150 keV X-ray irradiation, which was in close agreement with the values given in
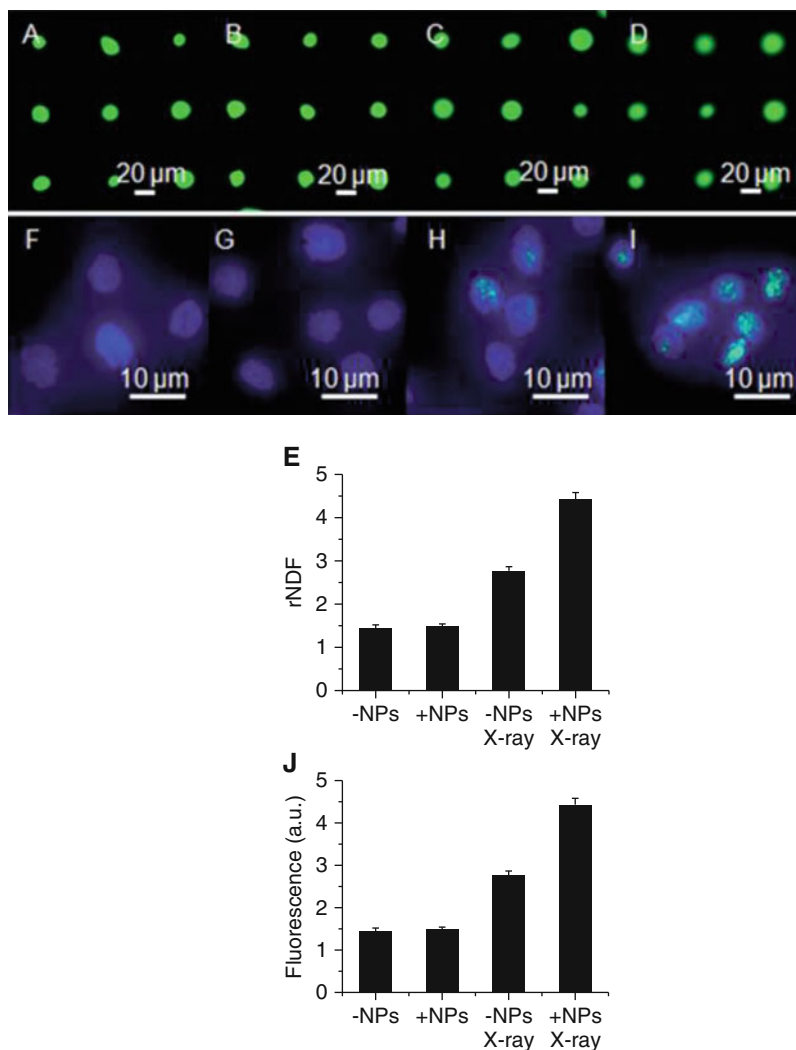
Fig. 8.8 Nuclear DNA damage by gold nanoparticle multilayers under X-ray irradiation. The endpoint was DNA damage. One assay was HaloCHIP assay, which involved diffusion of damaged nuclear DNA in gel matrix and detection of the damage DNA using relative nuclear diffusion factor (rNDF) as shown in panel **E**. Panels **A–D** show the fluorescence images. γ-H2AX assay was used for assessing double-strand breaks, with images shown in panels **F–I**, and the results are shown in panel **J**. (Adapted from Ma and Su et al. [14] with permission of the Royal Society of Chemistry.)

Chap. 2 and was consistent with type 2 physical enhancement. No chemical enhancement was considered.

Sancey et al. [17] studied DNA damage in brain tumor cells B16F10 after treated with gadolinium-based nanoparticles AGuIX and X-rays. γ-H2AX immunofluorescence assay was used to measure DNA damage. DNA molecules were irradiated

with X-rays from a 220 kVp X-ray generator with a 2 mm Al filter with up to 8 Gy of radiation. DNA damage was evaluated after 2 Gy of irradiation, and the enhancement was between 0.1 DEU (0.5 h after incubation) and 0.3 DEU (24 h after incubation) for X-ray irradiation with the assistance of nanoparticles. The reason why this result is shown here is because DNA damage was measured, which may be extended to the study of health cells.

8.2.3 Other Targets and Biological Reactions

Other biological targets include carbohydrates. Molecules such as hyaluronic acid may be possible targets. These molecules should be highly reactive toward reactive oxygen species, although preliminary results suggested the damage of hyaluronic acid by X-ray radiation was not extensive or could not be sensitively detected. Future work is needed. Similarly, other molecular targets, or even cellular organelles such as mitochondria, may be targeted for damage. Butterworth et al. [30] measured mitochondria oxidation using flow cytometry when the cancer cells were irradiated with 225 kVp X-rays in the presence of 1.9 nm gold nanoparticles. Although no targeting was performed, it was the first case in which mitochondria damage was assessed within the scope of X-ray nanochemistry research. Liu and Ma et al. [31] studied the damage by mitochondria-targeting gold nanoclusters and found cancer cell death as a result of damage. An approximately 0.3 DEU enhancement was observed. McMahon et al. [32] theoretically investigated this topic and found enhanced damage through a type 2 physical enhancement-like mechanism.

8.3 Cells

Damage to cells by ionizing radiation has been studied for nearly a century. However, understanding the damaging mechanisms and systematic studies at the molecular level is still lacking due to the complexity of the cellular systems. There are many proposed mechanisms, such as the bystander effect, the threshold effect, as well as the linear dose effect (see, e.g., Hei [33] and Cohen [34]). When nanomaterials are involved, an extra layer of knowledge, such as uptake and toxicity of nanomaterials to the cell, has to be considered. In this section, results of cell damage by X-rays in the presence of nanomaterials are discussed. The results of damage to mainly healthy cells are summarized and compared here. The results are divided into two sections: eukaryotic cells and bacteria. Within each section, the results are summarized chronologically according to the corresponding authors.

8.3.1   Damage of Eukaryotic Cells by X-Rays Assisted by Nanomaterials

In Chap. 4, cellular works on biological enhancement are discussed when uptake data is available. Healthy, noncancerous cell lines are the focus of discussion here. Results on using tumor cells are reviewed in Chap. 9. The damage is divided according to the means of damage claimed by the authors, whether the damage is direct or indirect. Direct damage means nanomaterials directly absorb X-rays and cause damage to biological targets. Indirect means the damage is caused by the addition of nanomaterials, but may not be caused by absorption of X-rays by nanomaterials. For instance, damage is indirect if nanomaterials are to carry drugs into the cells, and upon irradiation drugs are released from the nanoparticles and cells are damaged.

8.3.1.1   Direct Interaction

Prior to nanomaterial enhancement to damage to cells under X-ray irradiation, Das et al. [35] first showed that cell apoptosis increased by 42%, equivalent to a 0.42 DEU enhancement, when cells were irradiated with 200 kVp X-rays with 1 WP gold microspheres in the cell. Three cell lines were used. Their results generally agreed with the magnitude of damage predicted by physical enhancement shown in Chap. 2. Even though the work was not done with nanomaterials and cancer cell lines were used, it was the most closely related work to demonstrating physical enhancement with nanomaterials in cellular systems.

Since then, many works have been published on using nanomaterials to enhance the damage to cells under X-ray irradiation. Table 8.4 shows the summary of healthy eukaryotic cell studies using X-ray nanochemistry.

Chen and Xing et al. [36] employed a nonmalignant breast cancer cell line (MCF-10A) to investigate X-ray effects with the assistance of gold nanoparticles. The average size of the gold nanoparticles was 10 nm, and the nanoparticles were coated with two types of ligands, cysteamine (AET) and thioglucose (Glu). 10 Gy of 200 kVp X-rays were used. The authors found that X-ray irradiation alone caused a 20% reduction in cell viability to MCF-10A cells. The same dose of irradiation, however, caused cancerous MCF-7 cells to become 15% more viable than without irradiation. The results showed differences between healthy and cancerous cells under irradiation, although no clear explanation was given. After Glu-coated gold nanoparticles were incubated with MCF-10A cells, radiation sensitivity stayed the same. They found that AET-coated gold nanoparticles generated higher uptake, with nearly 120,000 particles per cell. This was about 20-fold higher than the 50 nm case and was equivalent to approximately 1 WP of gold in the cell. For the 200 keV X-rays, no enhancement was found after irradiation of MCF-10A with X-rays in presence of gold nanoparticles. In contrast, enhancement was detected for cancer cell MCF-7 incubated with Glu-coated gold nanoparticles after X-ray irradiation. The

Table 8.4 Cell damage by nanoparticles under X-ray irradiation

Ref.	Cells	NMs	Assay	Dose (Gy)	Energy	Enhancement (DEU)
Das et al. [35]	CHO-K1	AuNPs (1500 nm)	Clonogenic	8	140,200, 240	0.4
Chen and Xing et al. [36]	MCF-10A	AuNPs (10 nm)	MTT	10	200 kVp	Negligible
Geso et al. [37]	BAEC	AuNPs (1.9 nm)	Survivability	~5	80, 150	20–25
Butterworth et al. [38]	Fibroblast	AuNPs (1.9 nm)	Clonogenic	1	160 kVp	−0.15 to 1.0
Rahman et al. [39]	BAEC	AuNPs	Trypan blue exclusion	10	150 KeV	1.5
Geso et al. [40]	BAEC	AuNPs (1.9 nm)	Survivability	~5	80, 150	0.3–2.5
Kunjachan and Berbeco et al. [41]	Endothelial	AuNPs (2–3 nm)	Crystal violet	5–10	220 kVp	1–2

The results are arranged chronically
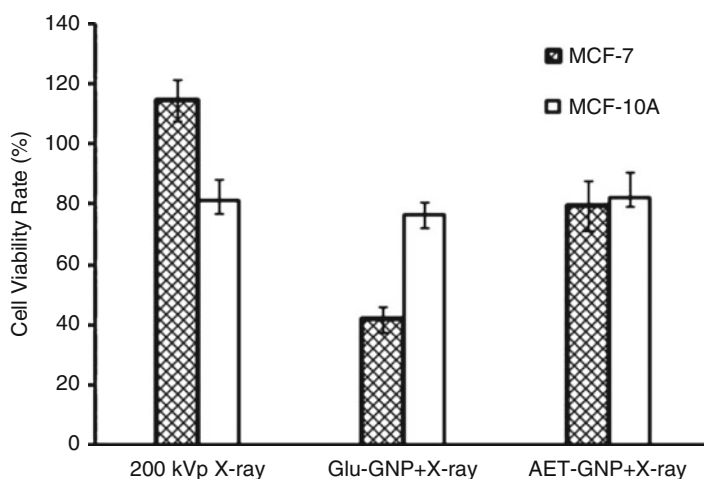
Fig. 8.9 Normal breast cell line MCF-10A in comparison with cancerous cell line MCF-7. Glu-coated gold nanoparticles under X-ray irradiation produced best result of enhancement only in MCF-7 cells. No effect occurred to MCF-10A cells. (Reprinted with permission from Chen and Xing et al. [36]. Copyright (2008) by John Wiley and Sons.)

results clearly showed there was a radiosensitization difference between healthy and tumor cells when treated with radiation assisted with gold nanoparticles. The effect can come from more than just physical enhancement because 10 nm gold nanoparticles could go into the nucleus of the cell. Figure 8.9 shows the results.

Geso et al. [37] studied enhanced damage to bovine aortic endothelial cells (BAECs) with 1.9 nm gold nanoparticles under X-ray and electron irradiation. The authors measured uptake and cytotoxicity of these nanoparticles. However, the uptake data was not strictly quantitative because only TEM images were available. The incubation concentrations were up to 1 mM gold ions/atoms in water, which was equal to 0.02 WP gold in water for the incubation concentration of 1.9 nm gold nanoparticles. These gold nanoparticles were apparently toxic to BAECs, reducing cell survivability by 30% at 0.01 WP incubation concentration. Judging from cellular toxicity, there should be a high loading of these gold nanoparticles, on the order of 1–10 WP in the cell. Up to 5 Gy of X-ray radiation was delivered to the cells. For 80 keV X-rays, they observed a 4.0 DEU enhancement at 0.005 WP incubation concentration. This was extremely high for such a low concentration of gold; however, because uptake concentration may be much higher than the incubation concentration, it is still possible that the measured enhancement was caused by physical enhancement. At 0.02 WP incubation concentrations, the enhancement was 24 DEU. As no data on direct measurement of uptake was available, it was difficult to estimate the origin of enhancement and therefore impossible to estimate the unit WP enhancement. The authors stated that 10 DEU was expected for 0.5 mM gold concentration, which was 0.01 WP of gold in water. This expectation was much higher than those supported by type 1 physical enhancement. The measured enhancement represented the highest enhancement (not unit WP enhancement) in eukaryotic cells to date. Figure 8.10 shows the results. The enhancement calculated from the experimental data shown in Fig. 8.10 can be done in several ways and all
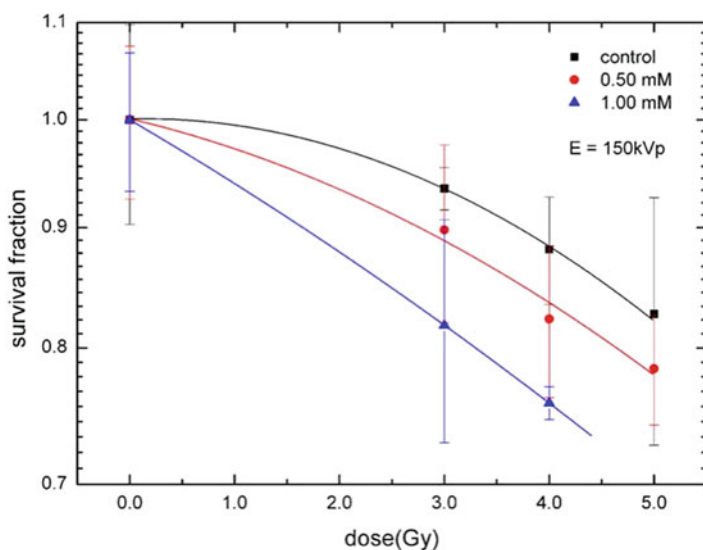
Fig. 8.10 Enhanced damage to BAECs with gold nanoparticles. The magnitude of enhancement is less than 1.0 DEU based on the data (at 85% surviving fraction or 3 or 4 Gy) shown here. The enhancement value cited by the authors was 24 DEU. (Reprinted from Geso et al. [37]. Copyright (2009) with permission from Elsevier.)

the values, however, are approximately 0.5–0.8 DEU. It is worth noting that these values were close to those reported in other publications using similar gold nanoparticles and cell lines (vide infra).

Rahman and Geso et al. [40] described the outcome of their study using monochromatic X-rays from synchrotrons and 1.9 nm gold nanoparticles to treat BAECs. The X-ray energy ranged from 30 to 100 keV in 10 keV steps. The incubation concentration was 0.1 mM or 0.02 WP gold in water. This loading could produce a 0.02 DEU or 0.03 DEU enhancement according to Chap. 2 if type 1 physical enhancement or physical enhancement was considered. This estimation also agreed with the calculated enhancement shown in the publication. The measured enhancement, however, ranged from 0.3 to 2.5 DEU, which was much lower than what the authors stated in 2009, as shown above, but still significantly greater than the theoretically predicted physical enhancement. Both experimentally obtained and theoretically predicted dose enhancement factors as a function of X-ray energy were obtained. Although the absolute values of these two sets of data shown here were different, the trends were close to each other. As stated in Chap. 4, experimentally measured enhancement values could be due to biological enhancement or chemical enhancement or both. The energy dependencies for both enhancements were clear, although the standard deviation data was missing, making it difficult to gauge the true meaning of the two data sets.

Butterworth et al. [38] studied both cancer cell lines and healthy cell lines. Only the healthy cell line results are presented here. The authors used 1.9 nm gold nanoparticles. No direct uptake data was available. Their incubation concentration was 0.01 WP, similar to that by Geso et al. discussed above. They found that enhancement was a function of cell lines and gold concentration. The enhancement ranges from a slight anti-enhancement of −0.15 DEU to an enhancement of nearly 1.0 DEU.

In another report, Rahman et al. [39] showed enhanced cell destruction by irradiating gold nanoparticles mixed with BAECs with 25 μm diameter microbeams of 150 keV X-rays from a synchrotron source. The results showed decreased cell viability for increasing concentrations of gold nanoparticles in the incubation solutions after a 10 Gy of X-ray irradiation. The percentage was 50% at 1 mM gold. When the concentration was doubled, viability decreased from 50% to 18%.

Kunjachan and Berbeco et al. [41] reported damage to epithelial cells using vessel-targeted gold nanoparticles, which were 2–3 nm gold nanoparticles coated with Arg-Gly-Asp ligands for targeting, as well as conjugated to a fluorophore for imaging purpose. The overall hydrodynamic size of the nanoparticles was 8–10 nm. Human umbilical vein endothelial cells were treated in this study. In vivo results of the study were given in Chap. 9. The doses were 5 and 10 Gy, and X-ray energy was at 220 kVp. A 1–2 DEU enhancement in survival fraction was observed when both gold nanomaterials and X-rays were applied. Figure 8.11 shows the results. The left panel illustrates mechanisms and the right panel shows in vitro data. The data shows that cell survival decreases from 95% for untreated cells to 33–41% for nanoparticle treated cells.
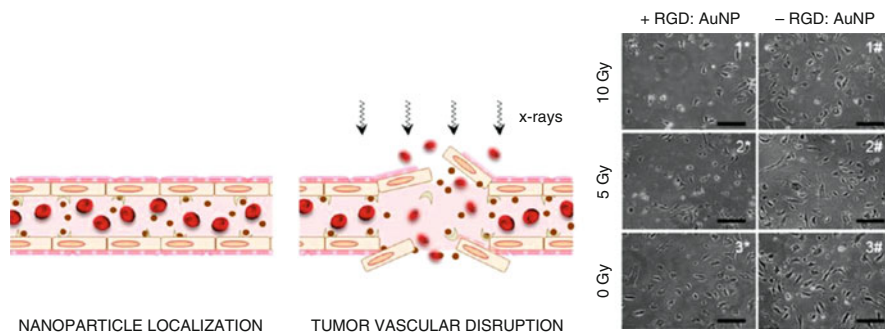
Fig. 8.11 X-ray irradiation of epithelial cells in the presence of gold nanoparticles. The left panel illustrates the proposed mechanism and the right panel shows the results, which shows fewer cells survived when greater doses and gold nanoparticles (AuNP) were used. (Reprinted with permission from Kunjachan and Berbeco [41]. Copyright (2015) American Chemical Society.)

8.3.1.2   Indirect Damage to Cells

The definition of indirect damage to cells is reserved for damage that is not directly caused by the nanoparticles themselves under X-ray irradiation. Instead, the damage is caused by X-ray-generated species in water or the environment. An example of indirect damage is the damage of the cell by drugs released from drug-carrying nanomaterials triggered with X-rays or X-ray-generated reactive oxygen species. Other indirect damage is possible. For example, nanomaterials may bind to repair proteins, therefore inhibiting their function. Without X-rays, cells behave normally with nanomaterials around because the work of the repair proteins is not needed. After X-ray irradiation, cellular components, including nuclear DNA molecules, are damaged by X-ray-generated ROS. Normally, repair proteins can repair the strand breaks. However, in the presence of nanoparticles, repair proteins are hindered and cannot properly function because they are bound to or blocked by the nanoparticles, leading to increased cell death. There may be more ways to indirectly damage cells using nanomaterials under X-ray irradiation.

Guo et al. [11] demonstrated X-ray triggered release of drugs from nanoparticles delivered into cells. Cells used in this work were from a breast cancer cell line although healthy cells should also be damaged this way. The nanoparticles were 15 nm gold nanoparticles, and doxorubicin (DOX) molecules were conjugated to short-strand DNA molecules linked to the surface of gold nanoparticles. The process was understood as being a form of controlled release of drugs. The increased damage was caused by DOX released after X-ray irradiation. In this study, the dose of X-rays was 10 Gy, at which the survival fraction was 11%. After adding the drug-loaded nanoparticle complex, survival fraction decreased to 4%. The result suggested that subjecting nanoparticle-drug complex to a 10 Gy radiation created an effect equivalent to a 14 Gy of irradiation. The results were also shown as the triggered release of drugs in cells in Chap. 9, and the data is shown in Fig. 9.45.

Another example of indirect damage was given by Xu and Zhang et al. [42] who created selenium block copolymer aggregates with chemotherapy drugs entrapped. The authors used ionizing radiation to release the drugs by cleaving selenium-selenium bonds. A schematic is shown in Fig. 9.43. HepG2 cells were used for in vitro work. The X-ray source was ^{60}Co, and 70% of the drug DOX was released at around 50 Gy of radiation. At 5 Gy dose, approximately 40% of the drug was released nearly 3 h after irradiation. The reduction in viability was ca. 20%. Even though this work employed cancer cells, it is reasonable to believe that healthy cells can be damaged in the same manner as well.

Most of these indirect damage studies are still in design phase and will require more research before they can be used in practical cancer treatment. However, the long-term benefits clearly outweigh the extra effort. If efficient release mechanisms can be developed, then it is possible to significantly reduce the X-ray dose needed to release lethal doses of drugs at only desired locations, therefore overcoming both the drawbacks and severe side effects of radiotherapy and the systematic toxicity of chemotherapy.

8.3.2   Damage to Prokaryotic or Bacterial Cells

Prokaryotic cells have several major differences from eukaryotic cells. For example, the uptake of nanoparticles may be different for the two types of cells because of the higher surface-to-volume ratio for prokaryotes. Another difference is that prokaryotic cells do not have cellular nuclei, making their DNA and other cellular components accessible to nanoparticles of any size. In the framework of X-ray nanochemistry, bacterial cells should be much more easily subjected to type 2 physical enhancement and chemical enhancement, as well as possible biological enhancement because targets of damage in bacterial cells are accessible to nanoparticles of any size, which is in contrast to eukaryotic cells that have a nuclear envelope to prevent direct nanoparticle access unless the nanoparticles are small enough to enter the nuclei. As stated in Chap. 2, in eukaryotic cells, large nanoparticles are kept outside of the nuclei, and type 2 physical enhancement from these large nanoparticles produces little enhancement to damage nuclear DNA microns away. For small gold nanoparticles or similarly sized nanoparticles, unfortunately, physical enhancement is usually negligible unless large amounts of such nanoparticles are present, at which point chemical enhancement, including anti-enhancement, dominates. In bacterial cells, these limitations are removed and the total enhancement can be much higher, especially if multiplication of physical, chemical, and possibly biological enhancement as shown in Chap. 5 is possible. These differences make the two types of cells respond differently to ionizing radiation in the presence of nanomaterials.

Sicard-Roselli et al. [43] studied the damage to *E. coli* (CGSC 7740) using gold nanoparticles and X-rays. They used the Turkevich method to synthesize gold nanoparticles in the presence of citrate ligands. The size of gold nanoparticles was

Fig. 8.12 Damage of *E. coli* by gold nanoparticles under X-ray irradiation. This strain of *E. coli* is highly radiation-resistive. An enhancement was observed when gold nanoparticles were used. (Sicard-Roselli et al. [43] is an open access article published by Gold Bulletin.)
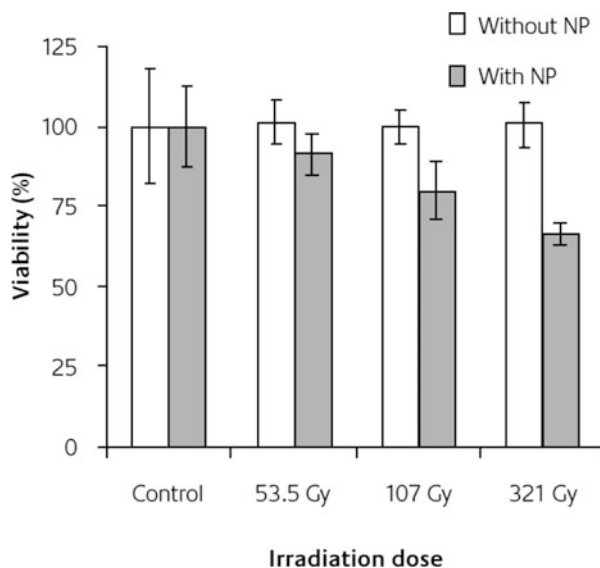
37.5 ± 5.6 nm. TEM results did not show any gold nanoparticles inside *E. coli* due to negative surface of both the nanoparticles and bacteria. The X-ray source was operated at 40 KV and 20 mA, with the predominant X-rays at 8 keV. No damage was detected to *E. coli* at up to 321 Gy without gold nanoparticles, and damage increased to 30% by adding gold nanoparticles. Based on their data, the D_{37} (37% short-term (<6 days) viability) would be 954 Gy, which was still less than 2000 Gy of the normal value for *E coli*. The results indicated that the gold nanoparticles enhanced the damage of *E. coli* by 1 DEU. However, when long-term (18–24 days) viability was used as the endpoint, the authors stated that enhancement with gold nanoparticles was not statistically significant. These results confirmed that endpoints and assays influence the outcome of enhancement measurements. Figure 8.12 shows the results, which clearly show an enhancement by the gold nanoparticles under X-ray irradiation when short-term viability endpoint was used.

Battista et al. [44] showed that it took 300–1300 Gy to reach D_{37} level for *E. coli*, (strain MG1655) although these damage values were not directly offered by the authors. Valizadeh et al. [45] investigated how gold nanoparticles affected radiotherapy using 140 kVp X-rays. Using *E. coli* clinical strains and with a gold loading of 0.04 WP, *E. coli* inhibition zone diameter was affected. 0.04 WP of gold should generated a very low relative enhancement value if type 1 physical enhancement was the cause for enhancement. The size range of gold nanoparticles was from 57 to 346 nm, and at 400 ppm, 57 nm gold nanoparticles produced a 0.21 DEU enhancement measured with NMR R_2 change to the gold nanoparticles in gels.

Su et al. [46] performed an enhancement study on bacteria *Pseudomonas aeruginosa*. The nanoparticles were bismuth nanoparticles with an average diameter of 30 nm. A mini X-ray source operated at 40 keV and 100 µA using a silver target was used. The authors also used a 0.25 mm Al and 25 µm Ag filter to reduce

0–15 keV X-rays. The energy spectrum used in this work carried a large amount of low-energy X-rays that could cause strong chemical enhancement or generate a large amount of reactive oxygen species, which could complicate the damage process. The dose was 0.4 Gy/min, and irradiation time is 10 min, resulting in a 4 Gy total dose. Their results showed only a 10% reduction in colony number after 4 Gy, suggesting the LD_{50} value was on the order of 10 Gy, which was at least two orders of magnitude less than value reported in the literature for *P.A.* ATCC 27853 by Li et al. [47]. The highest enhancement stated by the authors was 37 DEU with 0.2 mg/mL or 0.02 WP loading of gold in water. Bismuth nanoparticles themselves did not cause much toxicity, even for loading up to 5 WP. In contrast, only 5% of the cells were left when bismuth nanoparticles were added under X-ray irradiation. The 37 DEU enhancement was one of the highest enhancements reported in the literature to date. As discussed in Chaps. 2 and 3, this could not be type 1 physical enhancement. It was possible that type 2 physical enhancement played an important role, but only if aggregates of nanoparticles were next to DNA. However, no high-resolution TEM images were available, making it difficult to determine the significance of type 2 physical enhancement. It was possible that the enhancement could originate from chemical, biological, or other enhancement. Figure 8.13 shows the results, which include the images of colonies (panels **A–D**), the cell colony counts (middle panel to the right of panels **A–D**), and the comparison of enhancements at different gold nanoparticle concentrations (panel **E**).

Tung and Liu et al. [48] studied the effect of a new nanomaterial on damaging *E. coli*. The nanomaterials were protoporphyrin IX attached graphene oxide quantum dots (GDQs) and are discussed in Chap. 6. The nanomaterial was called Van-GQDs/PpIX. Bacteria-targeting ligand vancomycin was conjugated to the surface of the particles. The strain of the *E. coli* was ATCC25922, which could be damaged by the nanomaterial Van-GQDs/PpIX without X-rays. At the highest loading of the Van-GQDs/PpIX, irradiation of 2 Gy of 6-MV X-rays reduced the viability of *E. coli* by nearly 50%.
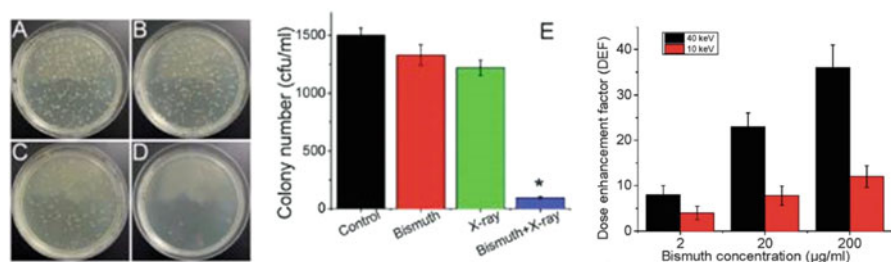
Fig. 8.13 Killing of bacteria with bismuth nanoparticles under X-ray irradiation. Images of colonies are shown in panels **A–D**. Based on the colony number shown in the middle panel, the cited enhancement was 37 DEU, and is calculated to be 11 DEU using the data shown in the middle panel. Enhancement values given by the authors are shown in panel **E**. (Adapted in part from Su et al. [46] with permission of the Royal Society of Chemistry.)

8.4   Summary of the Results

All the results shown in this chapter are displayed in Fig. 8.14, which shows the
enhancement values as a function of weight percentage (WP) of gold or other
nanoparticles in water. Vertical lines are used to show the range of enhancement at
a specific loading of gold. The results without the uptake data are not shown here. As
is shown in Fig. 8.14, the majority of the enhancement is between 0.1 and 3.0 DEU,
regardless of the uptake, except for a couple of studies. This may be a coincidence or
by design, as biological systems offer a great control over the output signal. Future
work will be needed to conclusively determine the true cause. A similar graph, with
much narrow range of enhancement observed, was created by Rosa et al. [49], in
which the cited enhancement values were between 1.2 and 2.0 DEU over five orders
of magnitude of loadings of gold in water.

8.5   Conclusions and Future Work

Results of the enhanced damage to biomolecules, cellular organelles, and healthy
cells assisted by nanomaterials under X-ray irradiation are presented and discussed
here. These results are reported in the literature during the past decade. As summa-
rized in Fig. 8.14, most of the measured enhancements are distributed between 0.1
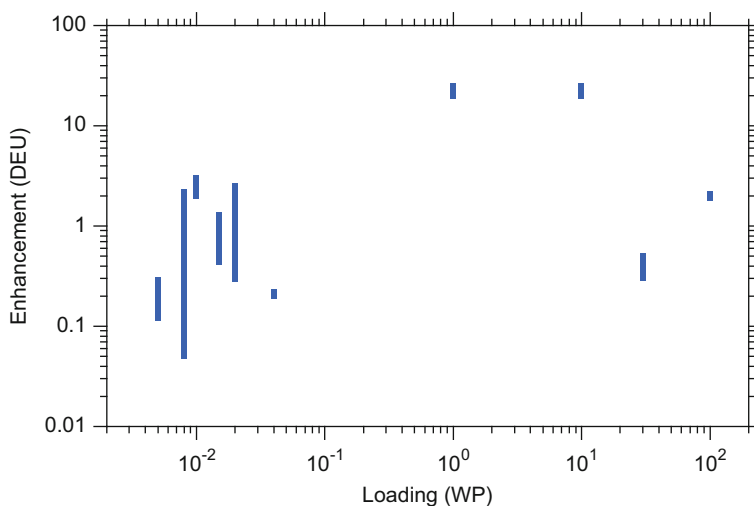
Fig. 8.14 Summary of the enhancement measured using biological samples including biomole-
cules, healthy cells, and prokaryotes. Range of enhancement is shown at each known loading.
Majority of the measurements lies in the range of 0.1–2.5 DEU, with two exceptions from two
measurements that put the enhancement magnitude between 20 and 40 DEU

and 3.0 DEU. This conclusion is also recognized by Rosa et al. [49]. Future work is needed to understand whether this is a coincidence or by design of the cellular system.

To date, only simple responses to X-ray irradiation, such as damage to the cell, have been investigated. However, it may be more important to develop methods to fully investigate how cells respond to damage by ionizing radiation and how to use X-ray nanochemistry to pinpoint the location of damage. These new methods may help improve understanding of biology as well. For instance, is it possible to use X-ray nanochemistry to trigger DNA repair systems with no side effect? One process that may demand great scrutiny is biological enhancement. Another great potential is the combination of nanobiology and X-ray nanochemistry.

X-ray nanochemistry may also help study biology, or more precisely nanobiology. The interplay between nanotechnology and biology can be strengthened through X-ray nanochemistry because it offers many tools, or otherwise difficult-to-find pathways, of energy delivery and imaging methods. It is foreseeable that X-ray nanochemistry and chemical biology may help each other in the near future.

The impact of X-ray nanochemistry on biology described in this chapter may be more far reaching than cancer treatment shown in Chap. 9. Currently, though, medical applications dominate the study of X-ray nanochemistry, which is understandable because most researchers view the utility of X-rays as being related to medical imaging and radiotherapy. However, when the potential of X-ray nanochemistry is fully reached, it is expected that the greatest impact of X-ray nanochemistry to medicine may be X-ray triggered release, as demonstrated in a primitive manner by Guo et al. [11]. Much more work is needed before that goal can be realized.

The fundamental study of X-ray nanochemistry in biology is necessary even though such a goal may temporarily be overwhelmed by the more practical desire of finding drugs to treat cancer; the work of studying fundamental physical, chemical, and biological processes is now being temporarily overlooked. However, as it will be proven, successfully studying these fundamental processes will be the only path to revolutionize cancer treatment because X-ray nanochemistry is powerful enough to offer much greater potentials and rewards after X-ray nanochemistry and its application in biology are properly and adequately studied.

References

1. Brun, E., Duchambon, P., Blouquit, Y., Keller, G., Sanche, L., & Sicard-Roselli, C. (2009). Gold nanoparticles enhance the X-ray-induced degradation of human centrin 2 protein. *Radiation Physics and Chemistry, 78*, 177–183.
2. von Sonntag, C. (1987). *The chemical basis for radiation biology*. London: Taylor and Francis.
3. Foley, E., Carter, J., Shan, F., & Guo, T. (2005). Enhanced relaxation of nanoparticle-bound supercoiled DNA in X-ray radiation. *Chemical Communications*, 3192–3194.

4. Carter, J. D., Cheng, N. N., Qu, Y. Q., Suarez, G. D., & Guo, T. (2007). Nanoscale energy deposition by x-ray absorbing nanostructures. *The Journal of Physical Chemistry. B, 111*, 11622–11625.

5. Butterworth, K. T., Wyer, J. A., Brennan-Fournet, M., Latimer, C. J., Shah, M. B., Currell, F. J., & Hirst, D. G. (2008). Variation of strand break yield for plasmid DNA irradiated with high-Z metal nanoparticles. *Radiation Research, 170*, 381–387.

6. Zheng, Y., Cloutier, P., Hunting, D. J., & Sanche, L. (2008). Radiosensitization by gold nanoparticles: Comparison of DNA damage induced by low and high-energy electrons. *Journal of Biomedical Nanotechnology, 4*, 469–473.

7. Zheng, Y., & Sanche, L. (2009). Gold nanoparticles enhance DNA damage induced by anti-cancer drugs and radiation. *Radiation Research, 172*, 114–119.

8. Porcel, E., Liehn, S., Remita, H., Usami, N., Kobayashi, K., Furusawa, Y., Le Sech, C., & Lacombe, S. (2010). Platinum nanoparticles: A promising material for future cancer therapy? *Nanotechnology, 21*, 085103.

9. Porcel, E., Kobayashi, K., Usami, N., Remita, H., Le Sech, C., & Lacombe, S. (2011). Photosensitization of plasmid-DNA loaded with platinum nano-particles and irradiated by low energy X-rays. *Journal of Physics: Conference Series, 261*, 012004.

10. Xiao, F. X., Zheng, Y., Cloutier, P., He, Y. H., Hunting, D., & Sanche, L. (2011). On the role of low-energy electrons in the radiosensitization of DNA by gold nanoparticles. *Nanotechnology, 22*, 465101.

11. Starkewolf, Z. B., Miyachi, L., Wong, J., & Guo, T. (2013). X-ray triggered release of doxorubicin from nanoparticle drug carriers for cancer therapy. *Chemical Communications, 49*, 2545–2547.

12. Zhou, H. Y., Zhang, Y., Su, G. X., Zhai, S. M., & Yan, B. (2013). Enhanced cancer cell killing by a targeting gold nanoconstruct with doxorubicin payload under X-ray irradiation. *RSC Advances, 3*, 21596–21603.

13. Carter, J. D., Cheng, N. N., Qu, Y. Q., Suarez, G. D., & Guo, T. (2012). Enhanced single strand breaks of supercoiled DNA in a matrix of gold nanotubes under X-ray irradiation. *Journal of Colloid and Interface Science, 378*, 70–76.

14. Zhang, P. P., Qiao, Y., Wang, C. M., Ma, L. Y., & Su, M. (2014). Enhanced radiation therapy with internalized polyelectrolyte modified nanoparticles. *Nanoscale, 6*, 10095–10099.

15. Yao, X. B., Huang, C. N., Chen, X. P., Zheng, Y., & Sanche, L. (2015). Chemical radiosensitivity of DNA induced by gold nanoparticles. *Journal of Biomedical Nanotechnology, 11*, 478–485.

16. He, C., & Chow, J. C. L. (2016). Gold nanoparticle DNA damage in radiotherapy: A Monte Carlo study. *Bioengineering, 3*, 352–361.

17. Kotb, S., Detappe, A., Lux, F., Appaix, F., Barbier, E. L., Tran, V. L., Plissonneau, M., Gehan, H., Lefranc, F., Rodriguez-Lafrasse, C., et al. (2016). Gadolinium-based nanoparticles and radiation therapy for multiple brain melanoma metastases: Proof of concept before phase I trial. *Theranostics, 6*, 418–427.

18. Guo, T. Nanoparticle enhanced X-ray therapy. In *ACS annual meeting*, Philadelphia, August 2004.

19. Brun, E., Sanche, L., & Sicard-Roselli, C. (2009). Parameters governing gold nanoparticle X-ray radiosensitization of DNA in solution. *Colloid Surface B, 72*, 128–134.

20. Boudaiffa, B., Cloutier, P., Hunting, D., Huels, M. A., & Sanche, L. (2000). Resonant formation of DNA strand breaks by low-energy (3 to 20 eV) electrons. *Science, 287*, 1658–1660.

21. Martin, F., Burrow, P. D., Cai, Z. L., Cloutier, P., Hunting, D., & Sanche, L. (2004). DNA strand breaks induced by 0-4 eV electrons: The role of shape resonances. *Physical Review Letters, 93*, 068101.

22. Cai, Z. L., Cloutier, P., Hunting, D., & Sanche, U. (2005). Comparison between x-ray photon and secondary electron damage to DNA in vacuum. *The Journal of Physical Chemistry. B, 109*, 4796–4800.

23. Li, Z. J., Cloutier, P., Sanche, L., & Wagner, J. R. (2010). Low-energy electron-induced DNA damage: Effect of base sequence in oligonucleotide trimers. *Journal of the American Chemical Society, 132*, 5422–5427.

24. Alizadeh, E., Cloutier, P., Hunting, D., & Sanche, L. (2011). Soft X-ray and low energy electron-induced damage to DNA under N-2 and O-2 atmospheres. *The Journal of Physical Chemistry. B, 115*, 4523–4531.

25. Nagai, K., Carter, B. J., Xu, J. W., & Hecht, S. M. (1991). DNA cleavage by oxygen radicals produced in the absence of metal-ions or light. *Journal of the American Chemical Society, 113*, 5099–5100.

26. Alizadeh, E., & Sanche, L. (2012). Precursors of solvated electrons in radiobiological physics and chemistry. *Chemical Reviews, 112*, 5578–5602.

27. Alizadeh, E., Orlando, T. M., & Sanche, L. (2015). Biomolecular damage induced by ionizing radiation: The direct and indirect effects of low-energy electrons on DNA. *Annual Review of Physical Chemistry, 66*, 379–398.

28. Alizadeh, E., Massey, S., Sanche, L., & Rowntree, P. A. (2016). Low-energy electron-induced dissociation in condensed-phase L-cysteine II: A comparative study on anion desorption from chemisorbed and physisorbed films. *European Physical Journal D, 70*, 75.

29. Sanche, L. (2016). Interaction of low energy electrons with DNA: Applications to cancer radiation therapy. *Radiation Physics and Chemistry, 128*, 36–43.

30. Taggart, L. E., Mcmahon, S. J., Currell, F. J., Prise, K. M., & Butterworth, K. T. (2014). The role of mitochondrial function in gold nanoparticle mediated radiosensitisation. *Cancer Nanotechnology, 5*(12), 1.

31. Fang, X., Wang, Y. L., Ma, X. C., Li, Y. Y., Zhang, Z. L., Xiao, Z. S., Liu, L. J., Gao, X. Y., & Liu, J. (2017). Mitochondria-targeting Au nanoclusters enhance radiosensitivity of cancer cells. *Journal of Materials Chemistry B, 5*, 4190–4197.

32. McMahon, S. J., McNamara, A. L., Schuemann, J., Prise, K. M., & Paganetti, H. (2016). Mitochondria as target for radiosensitization by gold nanoparticles. *Journal of Physics: Conference Series, 777*, 012008.

33. Hei, T. K. (2016). Radiation bystander effects. *Environmental and Molecular Mutagenesis, 57*, S52–S52. 47th Annual Meeting of the Environmental-Mutagenesis-and-Genomics-Society. Kansas City, MO. SEP 24–28.

34. Cohen, B. L. (1999). Validity of the linear no-threshold theory of radiation carcinogenesis at low doses. *Journal of British Nuclear Energy, 38*, 157–166.

35. Herold, D. M., Das, I. J., Stobbe, C. C., Iyer, R. V., & Chapman, J. D. (2000). Gold microspheres: A selective technique for producing biologically effective dose enhancement. *International Journal of Radiation Biology, 76*, 1357–1364.

36. Kong, T., Zeng, J., Wang, X. P., Yang, X. Y., Yang, J., McQuarrie, S., McEwan, A., Roa, W., Chen, J., & Xing, J. Z. (2008). Enhancement of radiation cytotoxicity in breast-cancer cells by localized attachment of gold nanoparticles. *Small, 4*, 1537–1543.

37. Rahman, W. N., Bishara, N., Ackerly, T., He, C. F., Jackson, P., Wong, C., Davidson, R., & Geso, M. (2009). Enhancement of radiation effects by gold nanoparticles for superficial radiation therapy. *Nanomedicine Nanotechnology, 5*, 136–142.

38. Butterworth, K. T., Coulter, J. A., Jain, S., Forker, J., McMahon, S. J., Schettino, G., Prise, K. M., Currell, F. J., & Hirst, D. G. (2010). Evaluation of cytotoxicity and radiation enhancement using 1.9 nm gold particles: Potential application for cancer therapy. *Nanotechnology, 21*(295101), 1–9.

39. Rahman, W.N., Wong, C.J., Yagic, N., Davidson, R., & Geso, M. (2010). Dosimetry And Its Enhancement Using Gold Nanoparticles In Synchrotron Based Microbeam And Stereotactic Radiosurgery. *AIP Conference Proceedings, 1266*, 107–110.

40. Rahman, W. N., Corde, S., Yagi, N., Aziz, S. A. A., Annabell, N., & Geso, M. (2014). Optimal energy for cell radiosensity enhancement by gold nanoparticles using synchrotron-based monoenergetic photon beams. *International Journal of Nanomedicine, 9*, 2459–2467.

41. Kunjachan, S., Detappe, A., Kumar, R., Ireland, T., Cameron, L., Biancur, D. E., Motto-Ros, V., Sancey, L., Sridhar, S., Makrigiorgos, G. M., et al. (2015). Nanoparticle mediated tumor vascular disruption: A novel strategy in radiation therapy. *Nano Letters, 15*, 7488–7496.
42. Ma, N., Xu, H. P., An, L. P., Li, J., Sun, Z. W., & Zhang, X. (2011). Radiation-sensitive Diselenide block co-polymer Micellar aggregates: Toward the combination of radiotherapy and chemotherapy. *Langmuir, 27*, 5874–5878.
43. Simon-Deckers, A., Brun, E., Gouget, B., Carriere, M., & Sicard-Roselli, C. (2008). Impact of gold nanoparticles combined to X-ray irradiation on bacteria. *Gold Bulletin, 41*, 187–194.
44. Harris, D. R., Pollock, S. V., Wood, E. A., Goiffon, R. J., Klingele, A. J., Cabot, E. L., Schackwitz, W., Martin, J., Eggington, J., Durfee, T. J., et al. (2009). Directed evolution of ionizing radiation resistance in Escherichia coli. *Journal of Bacteriology, 191*, 5240–5252.
45. Kamiar, A., Ghotalou, R., & Preparation, H. V. (2013). Physicochemical characterization and performance evaluation of gold nanoparticles in radiotherapy. *Advanced Pharmaceutical Bulletin, 3*, 425–428.
46. Luo, Y., Hossain, M., Wang, C. M., Qiao, Y., An, J. C., Ma, L. Y., & Su, M. (2013). Targeted nanoparticles for enhanced X-ray radiation killing of multidrug-resistant bacteria. *Nanoscale, 5*, 687–694.
47. Li, Y. Y., Wang, Z. L., Liu, X. X., Tang, J. Y., Peng, B., & Wei, Y. Q. (2016). X-ray irradiated vaccine confers protection against pneumonia caused by pseudomonas Aeruginosa. *Scientific Reports UK, 6*, 18823.
48. Pan, C. L., Chen, M. H., Tung, F. I., & Liu, T. Y. (2017). A nanovehicle developed for treating deep-seated bacteria using low-dose X-ray. *Acta Biomaterialia, 47*, 159–169.
49. Rosa, S., Connolly, C., Schettino, G., Butterworth, K. T., & Prise, K. (2017). Biological mechanisms of gold nanoparticle radiosensitization. *Cancer Nanotechnology, 8*(1), 2.

Chapter 9
Medical Applications of X-Ray Nanochemistry

All living things have inertia too – once they start, it is hard to stop

9.1 Introduction

Medical applications have been the central theme of X-ray nanochemistry from the very beginning. Prior to the conception of the idea of using nanoparticles to improve X-ray imaging or radiotherapy, many efforts had been given to studying how to increase radiation effects using various materials. One of the most noticeable therapeutic efforts involving ionizing radiation and new materials was Auger therapy using iodine labeled nucleotides such as IUdR, as discussed by Kasis [1]. However, the enthusiasm of employing IUdR quickly dissipated after the first wave of demonstrations using nanomaterials to improve radiotherapy that began in 2004 and 2005, and little happened until a recent theoretical work by Ye et al. [2] showed that it is possible to combine Auger therapy with X-ray nanochemistry. Other therapeutic methods, such as proton therapy using boron species, will not be discussed here, though it is perceivable that discoveries made within X-ray nanochemistry will help these methods as well.

   The original idea of using nanomaterials to enhance radiotherapy was straightforward, meaning no special care was needed except for passively mixing nanoparticles with, or delivering them to, targets that receive X-ray irradiation. The first account on record describing X-ray enhancement through the use of nanomaterials in medical applications was an ACS annual meeting report in August 2004 by Guo [3] in which the phrase "nanoparticle-enhanced X-ray therapy" (NEXT) was mentioned. Guo [4] used the same term in a patent application. The first publication of using nanoparticles under X-ray irradiation to improve the effectiveness of X-rays was contributed by Hainfeld et al. [5], who reported the first case of using gold nanoparticles to treat tumors in mice. Their patent was issued in 2009, with the priority date set in 1998; the earlier date was more than a decade after the authors had been exploring gold nanoparticles as a transmission electron microscope contrast agent. The work by Hainfeld et al. made a clear and strong case

of supporting the concept of nanoparticle-enhanced X-ray therapy. Based on the idea proposed by Guo in 2001, Guo et al. [6] published their result in early 2005 using strand breaks of plasmid DNA as the reporter reaction to measure enhanced damage to supercoiled plasmid DNA molecules in the presence of gold nanoparticles irradiated with X-rays. The original intention of works by Hainfeld et al. and Guo et al. was to use relatively simple nanomaterials (i.e., first-generation nanomaterials in Roco's NNI definition [7]) to increase X-ray absorption and improve the efficacy of radiotherapy for cancer treatment. It is fair to say that these works marked the beginning of X-ray nanochemistry research, even though X-ray nanochemistry was not formally established until about 8 years later.

   In the medical field, the most direct way to prove that a method or a drug can effectively destroy cancer cells without lethal side effects is to run clinical trials. However, it is difficult to do so for new ideas like nanomaterial-assisted or nanomaterial-enhanced X-ray therapy. This is because the therapeutic method, as it stood a decade ago, was too primitive and was far from being understood, let alone optimized. A more appropriate approach would be to first carry out careful work in chemistry and biology laboratories to assure that materials or methods are optimized before performing animal studies. In this sense, what Hainfeld et al. did as described in their first publication of using small gold nanoparticles to increase the efficacy of X-ray treatment of cancerous mice was both premature and revolutionary because such a novel idea was never tested anywhere, not even in a chemistry research lab. The idea was only proposed starting in 2001 by Guo and no work was done in chemistry laboratories until 2003. However, as Chap. 2 shows, a relatively simple calculation would suggest that there should be detectable physical enhancement with a sufficient amount of gold in the target volume. If one has enough experience working with nanomaterials in animals, then a biological experiment using the animal model seemed reasonable.

   In reality and as shown in Chaps. 2, 3, 4, and 5, even the enhancement to the yield of a relatively simple chemical reaction can be quite complex to understand, let alone damaging cells or treating tumors in animals with nanomaterials under X-ray irradiation. The latter two systems contain many more reactions and pathways. It seems unfathomable to directly use animal models before understanding every possible pathway. However, in biology and medical practices, focusing on the destruction of cells is often much simpler to do than understanding mechanisms. To many researchers, the most accessible and prudent or even scientifically sound method to show an enhancement is to prove that neither nanomaterials nor radiation is too toxic to cells and that the combination of the two causes significantly more destruction than the sum of the two acting alone. Many works have shown that gold nanoparticles indeed help improve the destruction of cells when irradiated with X-rays. Unfortunately, this does not mean that enhanced destruction is actually caused by enhanced absorption of X-rays by the added gold nanoparticles. The observed enhancement may arise from other mechanisms, such as biological enhancement shown in Chap. 4, that have little to do with X-ray absorption by the added nanomaterials. That being said, the experimental outcomes are still true and impactful, even if the results may or may not be completely caused by the expected

mechanisms. Understanding of the enhancement mechanisms and optimization of enhancement may progress slowly and demand greater efforts over many years. Readers should be aware that explanations or interpretations of the results may be complex, and proper experiments, new nanomaterials, and methodologies have to be developed before the true origins of enhancement can be identified.

Considering X-rays can both image and treat tumors, it is reasonable to deploy X-ray nanochemistry in both areas. Many methods have been developed, and much progress has been made in nanomaterial-assisted X-ray imaging. In addition, new imaging methodologies are being developed as well. Studying imaging also promotes exploration of delivering nanomaterials to target tumors, as shown in Sect. 9.3, which helps current treatment methods and future use of X-ray nanochemistry in cancer treatment. These publications lay the foundation to guide the use of primitive nanomaterials in radiotherapy and X-ray imaging. As discussed in Sect. 9.8, future use of X-ray nanotechnology will probably rely much more on X-ray-triggered release than on the current radiotherapy.

For the purpose of cancer treatment, many in vitro and in vivo enhancement measurements have been performed using relatively simple nanomaterials or nanochemistry. IUdR and BUdR were also used to improve radiosensitization, but their contribution to cancer therapy has been limited. While nanomaterials have not yet met the same fate as other originally promising materials such as BUdR and IUdR, little value has been added to the overall cancer treatment paradigm so far through the use of nanomaterials under X-ray irradiation. This is probably why only incremental improvements have been made more than a decade after several important papers were published and a first round of patents were granted. The main advantage of using nanomaterials to date seem to be that moderate gains in the effectiveness of radiotherapy can be achieved from using high loadings of these nanomaterials without severe toxicities.

Publications to date suggest that the original hypothesis of using gold nanoparticles to enhance radiotherapy is largely validated, but the exact technologies as they stand now have not generated the impact originally envisioned. Fortunately, unlike IUdR that had limited potential but significant cytotoxicity, gold nanoparticles have much less cytotoxicity, and there are many ways to improve their performance. Currently, efforts are being devoted to developing nanomaterials for various enhancements, and some of the developments have been used clinically. Movement from using nanoparticles to enhance radiotherapy in research labs to practical medical applications including clinical settings is happening, albeit slowly. The review of these works presented here and elsewhere using nanomaterials under X-ray irradiation for medical applications might inspire new approaches.

The intent of this chapter is therefore to discuss publications that apply X-ray nanochemistry to medicine. Among the topics covered in this chapter is a section that discusses theoretical studies related to medical applications of X-ray nanochemistry, which is given in Sect. 9.4. The rest of the chapter are divided into three main sections.

The first section of this chapter, i.e. Sect. 9.3, intends to systematically discuss papers in the area of imaging using nanomaterials under X-ray irradiation. Imaging

work has been expanded in many directions by researchers, and many findings are reviewed and discussed in this section.

The second section, Sect. 9.5–9.7, deals with the treatment of cells and tumors. As shown in Chaps. 2, 3, 4, and 5, it is even difficult to perform clean physical enhancement studies in controlled environments of pure water. It is conceivable that high loadings of small metallic or semiconductor nanoparticles in cells or animals may have many unintended consequences. For cellular work, this chapter only covers work using cancer cell lines. The results of studying healthy cell lines are given in Chap. 8, despite the fact that results on healthy cells are equally useful in medical applications. Instead of assigning different categories of enhancement to the results, this chapter summarizes all the efforts of using nanomaterials to enhance imaging or treatment of cancer cell lines (in vitro) and tumors (in vivo) under X-ray irradiation. Several methods of treating cancer cell lines with drugs and X-ray radiation are included as well. In addition, clinical trials are mentioned in this section. Although a majority of work published to date in the area of enhancing the effectiveness of X-ray irradiation with nanomaterials only scratches the surface of X-ray nanochemistry, the field is advancing. It is expected that increasingly advanced nanoscale systems will help advance medicine in the next decade, much more than simple nanomaterials did in the past decade.

The third section of this chapter, Sect. 9.8, covers X-ray-triggered release of drugs. Most of the work in the area of medical applications of X-ray nanochemistry intends to use nanomaterials to directly enhance the effectiveness of X-ray irradiation, e.g., to use nanomaterials to cause more damage to cancer tissues than X-rays alone. In this regard, current X-ray nanochemistry may have a limited impact. A more promising approach is to use X-ray nanochemistry to support the use of a subacute dose of X-rays to trigger the release of a lethal dose of drugs to annihilate tumors. In this area of research, X-ray nanochemistry may help uncover underlying mechanisms and push for more advanced chemical systems for cancer treatment. One such work was shown by Guo et al. [8] in which X-rays were used to trigger the release of doxorubicin from the surface of gold nanoparticles, by way of radicals produced in cells reacting with and cleaving DNA linkers to which the drug molecules were attached. Their work represented the first attempt to use nanomaterials in a sophisticated manner to achieve enhancement. Several other publications demonstrated a similar proof of concept. For example, Xu and Zhang et al. [9] created a diselenide nanomaterial responsive to ionization radiation. X-ray-triggered release of drugs, as defined in X-ray nanochemistry, may reshape the landscape of radiotherapy by largely eliminating it and replacing it with X-ray-triggered therapy, a new approach sans any radiation side effects. X-ray nanochemistry may also change chemotherapy by allowing the triggered release of extremely potent chemotherapy drugs at designated locations in the body. Although there are still many obstacles to overcome, future work in this area is exciting.

An X-ray nanochemistry application closest to creating a real therapy uses rare earth nanomaterials for physical enhancement and cancer treatment. Maggiorella et al. [10] published the results, and a company, Nanobiotix Inc., was formed and has been carrying out clinical trials using these nanomaterials. Future work will need to identify the actual mechanisms and causes of the enhancement.

9.2   General Approaches and Procedures Used in Medical Applications

In vitro and in vivo works are laborious and difficult to perform, with many variables being able to affect the outcome. In this section, generic guidelines on cell and animal work are described to help reduce inconsistencies due to ambiguities among works by different research groups. Enhancements are often measured using assays that probe endpoints, and both assays and endpoints are discussed. This discussion is placed before the main sections of imaging and treatment so that these practices can help guide readers and researchers to navigate through many different results reported in the literature and discussed in this book. Due to largely varying procedures and conditions throughout the literature, we try to briefly summarize all the major and most relevant information and conditions.

9.2.1   Cell Work

9.2.1.1   Types of Cells

Many cell lines have been used in medical applications of X-ray nanochemistry. They have different dose response curves, and there are advantages or disadvantages for using a specific cell line. Table 9.1 lists many cell lines used in X-ray nanochemistry works and their lethal dose, LD_{37}, either directly available from their work or calculated by the author of this book based on the survival fraction curve. As tumor cells divide faster than healthy cells, one would expect that tumor cells might have lower LD_{37} values. The difference is not obvious, however, possibly because the standard deviations associated with each of the two categories of cells are large, hence making such a differentiation difficult. Nonetheless, the difference exists between some of these two types of cell lines, as shown in Chap. 8.

9.2.1.2   Cell Preparation

The cells are generally incubated in CO_2 (5%) at 37 °C prior to treatment with nanoparticles and X-rays. In many studies, the cells are placed at the bottom of a Petri dish for a few days prior to incubation with nanoparticles and X-ray irradiation. The incubation concentration of nanoparticles ranges from nanomolar to micromolar of nanoparticles, depending on the type and size of nanoparticles. Instead of reporting nanoparticle concentrations, many researchers use the concentration of gold atoms or ions (salt), which ranges from micromolar to millimolar. However, in many cases it is preferable to provide nanoparticle concentrations as well as atomic or ionic concentrations. After incubation, nanoparticles outside cells are washed away before irradiation.

Table 9.1 Cell lines used in X-ray nanochemistry work. Only one reference is given to each cell line. The results are ordered alphabetically according to the cell names. Cell type, name, and their LD_{37} (1/e) dose are also given

Cell name	Cell type	LD_{37} (Gy)[b]	Ref.
4T1	Murine breast cancer	4.0	Yang et al. [11]
9L	Brain cancer	3.5	Tehei et al. [12]
A375	Skin cancer		Chen et al. [13]
A-431/MDA-MB-231/DU-145/PC-3	Various cancers		Mikkelsen et al. [14]
A549	Lung cancer	2.0	Jiang et al. [15]
A549/KB	Human epidermal	>10	Yan et al. [16]
Bovine aortic endothelial cell	Endothelial	>10	Geso et al. [17]
C3H 10T1/2	Fibroblast	–	Regulla et al. [18]
C6	Glioma	6.1[a]	Kotler et al. [19]
CHO-K1 /EMT-6 / DU-145	Hamster ovary	2–4	Das et al. [20]
CT26	Colon cancer	–	Choi et al. [21]
CT26	Colorectal	3.0	Hwu et al. [22]
CT26	Colon cancer	–	Guo et al. [23]
DU145	Prostate	40	Juzenas et al. [24]
DU145/HaCaT	Prostate	6–8/2–4	Geso et al. [25]
Du145/MDA-MB-231/T98G	Prostate	6.0	Taggart et al. [26]
E. coli	Bacteria	100	Liu et al. [27]
EMT-6/CT26	Murine breast cancer	6.0/3.0	Hwu et al. [28]
F98 and B16	Glioma	4.0	Pradhan et al. [29]
GBM (MCF-7)	Human glioblastoma	–	Krishnan et al. [30]
GL261	Brain tumor		Hallahan et al. [31]
H1299-Luc	Lung, lymph	8	Xie et al. [32]
H460	Lung cancer	3.5	Sheng et al. [33]
HCT116/HT1080	Colorectal tumor/fibrosarcoma	5.0	Maggiorella et al. [10]
HCT116	Colorectal tumor	3.0	Paquette et al. [34]
HeLa	Cervical cancer	4.0	Chirthrani et al. [35]
HeLa/BEL-7402	Cervical cancer/liver carcinoma	10	Zhao et al. [36]
HepG2	Liver	1.0	Li et al. [37]
HT1080	Human fibrosarcoma	3.0	Tsourkas et al. [38]
HT29	Colorectal cancer	6.0	Arab-Bafrani et al. [39]
HTB-72	Skin melanoma	4.2	Kim et al. [40]
K562	Glioma	–	Su et al. [41]
KB	Cervical cancer	6.0	Chen et al. [42]
MCF-7	Breast cancer	4.0	Liu et al. [43]
MCF-7	Breast cancer		Chen et al. [44]
MCF-7 (nine total)	Breast cancer (eight others)	2.0	Butterworth et al. [45]

(continued)

Table 9.1 (continued)

Cell name	Cell type	LD$_{37}$ (Gy)^b	Ref.
MCF-7/Caco-2/3T3	Breast cancer	–	Kryschi et al. [46]
MCF-7/Hep G2	Breast cancer, human liver cancer	–	Ito et al. [47]
MCF-7/SKOV-3	Breast/ovarian cancer	–	Cook et al. [48]
MCG803	Gastric carcinoma	–	Cui et al. [49]
MDA-231 (nine)	Breast cancer	4.5	Jain et al. [50]
MDA-MB-231	Breast cancer	4.3	McMahon et al. [51]
MDA-MB-231/T47D	Breast cancer	5/4	Latimer [52]
CT26	Colon cancer	–	Kim et al. [53]
OECM1	Human cancer	–	Hwu et al. [54]
OVCAR-3	Ovarian	–	Chen et al. [55]
Panc1	Pancreas	>50^a	Goldys et al. [56]
PC-3	Prostate	–	Vo-Dinh et al. [57]
RG2	Glioma	~10	Geso et al. [58]
S2	Glioblastoma	–	Welland et al. [59]
U251	Brain cancer	–	Wen et al. [60]
U87	Glioblastoma	14^a	Retif et al. [61]

^{a}Predicted by the author of the book based on the data in the report
^{b}LD$_{50}$ = 0.70 × LD$_{37}$

9.2.1.3   Uptake

Most of the published works only specify incubation concentrations and times. However, it is important to have the uptake measured so that experimentally measured enhancements can be calibrated against theoretically predicted enhancement values, at least for physical enhancement. Uptake is usually determined with the help of atomic absorption spectroscopy (AA) or other mass spectrometry methods, such as inductively coupled plasma mass spectrometry (ICP-MS). The difference between incubation and uptake concentrations is often significant. Table 9.2 summarizes results for studies that have measured uptake. The size dependency of uptake is also studied and the results are given in the table as well.

Two of the most important parameters affecting the uptake of nanoparticles by cells are the size and surface coating (surfactant) of nanoparticles. With regard to size, several studies focused on the effect of size. Chan et al. [75] studied the uptake of five different sizes of gold nanoparticles, ranging from 14 to 100 nm for three different cell lines. They found that 50 nm gold nanoparticles had the highest uptake. Chithrani et al. [35] studied the radiation damage enhancing capability of gold nanoparticles ranging from 14 to 74 nm in diameter. The authors also found that 50 nm nanoparticles had the highest uptake. Chang et al. [76] showed that among

Table 9.2 Uptake of nanoparticles for different cell lines. The works are arranged based on the magnitude of uptake, from the lowest (1 ppm or 0.0001 WP) to highest (40 WP). Ligands or surfactants on the surface of nanoparticles are shown as well

Composition	Size (nm)	Ligand name	Cell name	Uptake amount (WP)	Ref.
Au/Fe$_3$O$_4$	50	Folic acid	A549	0.0001	Mei et al. [62]
Au	14, 50, 74	CTAB	HeLa	0.00005, 0.005, 0.016	Chan et al. [63]
Van-GQD/PpIX	100	Vancomycin	E. coli	0.01	Liu et al. [27]
Au	7	Glucose	Du145	0.023	Xing et al. [64]
Au	10	Cysteamine	MCF-7	0.03	Xing et al. [65]
AuNPs	1.9/28–142	Micelles	HT1080	0.057	Tsourkas et al. [38]
Au	10.8	Thiol-glucose	DU-145	0.081	Roa et al. [64]
Au	10.8	6-Deoxy-6-fluoro-1-thio-D-glucose	DU-145	0.081	Roa et al. [66]
Bismuth oxide	μm plates	PEG	9L	0.1	Tehei et al. [12]
Au	1.4	pHLIP	A549	0.11	Reshetnyak et al. [67]
Au@SiO$_2$	45.97/1.16	CTAB	MCG-803	0.3	Cui et al. [49]
Au	47.3 ± 8.7	HS-mPEG	MDA-MB-231 MDA-MB-436	0.44 and 0.20	Allen et al. [68]
Se	100–500	PEG	HeLa	0.46 μM/10 cells	Chen et al. [69]
Pt	–	Terpyridine	F98 B16	0.7	Pradhan et al. [29]
Au	14–74	Citrate	HeLa	0.7	Chirthrani et al. [35]

Au	2–50 nm	–	MDA-MB-231	0.88	McMahon et al. [70]
Gd$_2$O$_3$	42 ± 3	Polysiloxane	CT26	0.9	Kim et al. [53]
Au	3000	–	EMT-6	1	Das et al. [20]
Au	1.9	–	Du145, MDA-MB-231, T98G	0.07–1.5	Taggart et al. [26]
Bi	3.6	LyP-1	4 T1	1.72	Li et al. [71]
Au-Se	100	Chitosan	A375	2	Chen et al. [72]
Au	3	Tiopronin	HCT116	3.3	Paquette et al. [34]
Au	47	Foliate	HeLa	3.4	Khoshgard et al. [73]
Au	50	(Purchased from sigma-Aldrich)	HT29	5	Arab-Bafrani et al. [39]
Au	4–5	Glucose	A549, KB	6	Yan et al. [16]
Au	16–17	Thioctic acid-β-cyclodextrin	HeLa, A549	12	Yan et al. [74]
FeO$_x$	13	Alginate	CT26	17	Choi et al. [21]
Au	15	DNA/DOX	MCF-7	30	Guo et al. [8]
Au	30	CPP-PEG	MDA-MB-231 T47D	5–40	Latimer [52]

CPP cell-penetrating peptides, *CTAB* cetyltrimethylammonium bromide, *DNA* deoxyribonucleic acid, *DOX* doxorubicin, *PEG* polyethylene glycol, *pHLIP* pH low-insertion peptides.

3 to 50 nm gold nanoparticles, 13 nm gold nanoparticles were found to be the best for maximum uptake. Xing et al. [77] studied the uptake of several gold nanoparticles by two cancer cell lines. They discovered that cysteamine covered 10 nm gold nanoparticles had the highest uptake rate of 1.2×10^5 nanoparticles/cell, corresponding to approximately 0.1 WP of gold in the cell.

Many works have studied the effect of surfactants on uptake. For example, Mukherjee et al. [78] showed the uptake of gold nanoparticles on the order of 0.2 WP at different locations after incubation/circulation. Their nanoparticles were coated with various ligands, including antibodies and gemcitabine. Su et al. [79] used polyelectrolyte ligands on gold nanoparticles to improve nanoparticle internalization. No quantitative results were presented, although increased damage to nuclear DNA was observed with positively charged ligands on the surface of gold nanoparticles. Latimer [52] found that cell-penetrating peptides (CPPs) improved uptake. The author used clonogenic assays to determine the enhancement, and values between 1.3 and 2.1 DEU were measured using between 0.03 and 1.6 million ca. 30 nm gold nanoparticles per cell. These uptake levels corresponded to 0.8 to 43 WP of gold in a cell, and physical enhancement of 0.8 to 43 DEU is expected for such uptake. Coatings of other ligands could also improve uptake. Although no absolute uptake data was given, an acidity sensing peptide, pHLIP (pH low-insertion peptide), was found by Cooper and Reshetnyak et al. [67] to significantly improve uptake. TEM images showed the presence of significant amounts of 1.4 nm pHLIP functionalized gold nanoparticles in the cell. Kim et al. [40], however, found no 1.9 nm gold nanoparticles in the cell. In contrast, significant uptake of 50 nm gold nanoparticles was observed in the same work. Further studies are needed to reconcile all these diverging uptake results.

9.2.1.4   Endpoints and Assays

Endpoints and assays are two closely connected concepts. Many endpoints can be used to estimate the enhancement, and the results of enhancement measurements can be quite different, depending on the endpoint. Table 9.3 shows several endpoints and assays used to measure the enhancement. Some endpoints are easier to employ than others. For example, MTT assay is much less time consuming than clonogenic assay. However, data from clonogenic assays can be more reliable in terms of assessing the viability of the cell because the cell has adequate time to respond to the treatment.

Table 9.3 Endpoints and assays used in X-ray nanochemistry to inspect enhancement

Endpoint	Assay
Apoptosis, sub-G1	Flow cytometry
Cell death	Clonogenic
Cell viability	Clonogenic, MTT, MTS, caspase-3
DNA SSBs	γ-H2AX, gel electrophoresis
DNA damage	Comet assay
Oxidative stress	Fluorescence dye/flow cytometry

9.2.1.5 Cytotoxicity

After selecting the cell line, incubation conditions, and the assay to probe an endpoint, it is important to assess the cytotoxicity of a nanomaterial to the cell before enhancement can be measured. Nanoparticles and especially surfactants may pose toxicity to cells. It is possible, for example, for nanoparticles themselves to be nontoxic, while the ligands on the surface exhibit toxicity. As a result, cell viability may be reduced when ligands are detached from the surface of nanoparticles in the cell. Depending on the assay used to measure enhancement, this toxicity may or may not be evident before irradiation. Rotello and Vachet et al. [80] studied the stability of gold nanoparticles in cells using mass spectrometry. Their study found that biothiols on gold nanoparticles were more stable in cells, which may render thiol-protected gold nanoparticles more stable in cells. Even if nanoparticles themselves and their surfactants are not toxic, nanoparticles may disintegrate in cells, releasing toxic ions or atoms. Selenium or cadmium nanomaterials belong to this category.

9.2.1.6 Irradiation with X-Rays and Enhancement Measurements

Cells are typically irradiated for up to tens of minutes to obtain a total dose of 1–10 Gy. Typical cell survivability curves, with and without gold nanoparticles, are shown in Fig. 9.1. This can be obtained from clonogenic, MTT or other assays, and different assays usually generate different surviving fraction curves and hence enhancement values. DNA damage curve is different, counting the damaged DNA rather than the percentage of intact DNA after irradiation. Enhancement values are derived by comparing the curve with nanoparticles under X-ray irradiation to the
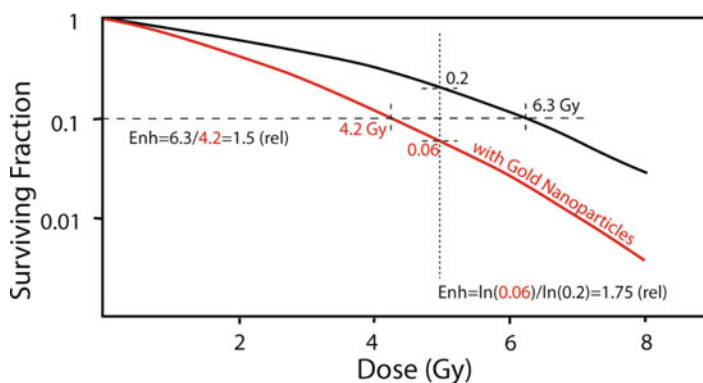
Fig. 9.1 Two typical cell survival curves, with and without nanoparticles are shown here. There are two ways to calculate the magnitude of enhancement. One uses the ratio of survival fractions at the same dose (shown here at 5 Gy, marked by the dotted line), and the other uses the ratio of doses at the same survival fraction (shown here at 0.1 surviving fraction, marked by the dashed line). The two values should be close, although there is no guarantee for them to be identical. Other methods have also been used to determine the magnitude of enhancement

curve without nanoparticles under X-ray irradiation. If nanoparticles are toxic, then the toxicity has to be included as well. Figure 9.1 shows two quick methods of calculating the magnitude of enhancement using in vitro data. Similar methods of enhancement calculation have been discussed in the literature. The first method uses the doses without and with gold nanoparticles at the same surviving fraction. For example, if 10% surviving fraction is used, as shown by the horizontal dashed line in Fig. 9.1, the dose without gold nanoparticles needed to cause this amount of damage is 6.3 Gy, while the dose needed to cause the same magnitude of damage with gold nanoparticles is 4.2 Gy. The enhancement is 6.3/4.2 − 1 = 0.50 DEU. The second method, shown by the vertical dotted line in Fig. 9.1, is to use surviving fractions at the same dose of X-ray irradiation to compute the enhancement. The enhancement value is calculated as the ratio of the natural log of the surviving fraction with nanomaterials under X-ray irradiation to X-rays without nanomaterials minus 1, which is ln(0.06)/ln(0.2) − 1 = 0.75 DEU. It is worth pointing out that ratios of doses or surviving fractions give rise to relative enhancement. Absolute enhancement is equal to relative enhancement minus one. The two enhancement values obtained using these two methods are close. Although these methods are simple to use, they are dependent of the surviving fraction or dose of choice and therefore need to be used with caution. For the purpose of destruction of tumor cells, 10% or even 1% surviving fraction should be used.

A third method of enhancement computation using the survival curves is to use ratios of α or β or both, the coefficients of the fitted survival fraction exponential equations. The enhancement is the ratio of α or β with nanoparticles to without nanoparticles, whichever has the larger coefficients in front of them. This method also yields different results due to the choice of doses and survival fractions. Subiel et al. [81] reviewed and discussed several standard methodologies used to determine the enhancement factor based on survival fraction data. Several different ways were provided, and two of them, radiation enhancement factor and radiation enhancement ratio, are similar to those given here. At least two additional methods of evaluating enhancement using the survival fraction curves exist in the literature, which can be derived from (1) linear-quadratic model and (2) mean inactive dose.

9.2.2   Animal Work

There are similarities between the use of cellular models and animal models for enhancement studies. In general, animals are infected with tumor cells and then treated with nanoparticles and radiation. The tumor sizes or life span changes at the end of treatment are commonly used to obtain the magnitude of enhancement or improvement. Compared with cellular models, animal models have even more variables. The established procedures, regardless of their effectiveness and validity in simulating human diseases, are given here so that researchers have a general guideline to follow as they go through the rest of this chapter.

9.2.2.1   Animals

Mice or rats are most frequently employed, although other animals such as swine are used as well. There are two general methods to infect animals with tumor cells. One is to purchase the infected animals and then treat them with nanoparticles and radiation. The other is to purchase healthy animals and then infect them with cancerous cells. Tumors are allowed to grow to a certain size before the planned treatment experiments.

9.2.2.2   Nanoparticle Delivery/Tracking

There are several methods to deliver nanomaterials to tumors in animals. One is through intravenous injection, usually through the tail veins. The other is to inject nanomaterials directly into the tumor, a method employed less often. Irradiation follows, after which animals are euthanized and tumor size is measured. Nanoparticles are generally in aqueous solutions, but in several cases, they are in serum. The method of delivery, however, is the same for these different solutions.

9.2.2.3   Targeting

X-ray nanochemistry benefits from and contributes to delivery and targeting of nanomaterials to biological targets because applications of X-ray nanochemistry rely on the development of these chemical and biological methods. For example, nanodrugs should not only be triggered by X-rays to release payloads but also be easily taken up by tumors or be actively targeting tumors and other biological entities. Other factors include that the release of drugs from nanomaterials uses bio-orthogonal chemistries so that drugs are not released without external triggering. These are important aspects of X-ray nanochemistry.

Tumors may be targeted both actively and passively. In active targeting, ligands such as peptides or antibodies are coated on the surface of nanoparticles so that nanomaterials can seek and bind to tumor cell surfaces and eventually, preferentially enter tumor cells. For example, Hallahan et al. [82] reported the use of a recombinant peptide, HVGGSSV, that binds to irradiated tumors to help improve the delivery of nab-paclitaxel to tumors. Even without these targeting agents, passive targeting is possible because the size and charge of the nanoparticles may be suitable to facilitate their entry into tumors by relying on the so-called epidermal permeation and retention (EPR) effect. These processes are important to both imaging and treatment of tumors. Although targeting and delivery are not a central topic in X-ray nanochemistry, these two aspects are of paramount importance to X-ray nanochemistry applications in medicine. A list of the surfactants, including targeting and delivery reagents, is given in Table 6.2. There are several review articles on this topic as well. For example, El-Sayed et al. [83] examined a targeting mechanism through the use of nuclear localization signal (NLS) peptide, a popular method.
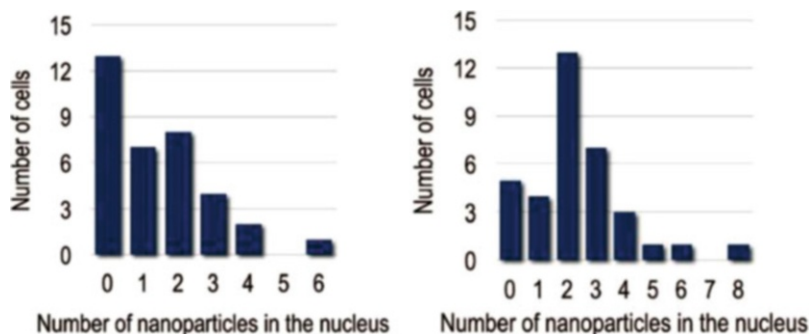
Fig. 9.2 Uptake and nuclear targeting studied by Brust et al. [84]. The numbers of gold nanoparticles per nucleus with only cell-penetrating peptide (CPP) ligands are less than those with both CPP and nuclear location signal (NLS) ligands on gold nanoparticles. Those with CPP are shown in the left panel, and those having both CPP and NLS ligands are shown in the right panel. (Reprinted with permission from Brust et al. [84]. Copyright (2008) American Chemical Society.)

Cell-penetrating peptide (CPP) was another example. Brust et al. [84] studied the uptake and intracellular fate of gold nanoparticles with several different types of surfactants, including NLS peptides. They used HeLa cells as the platform and 16 nm gold nanoparticles, which were close to the size limit of nanoparticles that can move through nuclear envelope pores of less than 20 nm in diameter. Figure 9.2 shows typical results obtained with NLS but without CPP (left panel) and those obtained with both CPP and NLS (right panel). The authors showed the result of increased occurrence of cell nuclei containing gold nanoparticles when both CPP and NLS ligands were conjugated to the surface of these gold nanoparticles. Jon et al. [85] provided an extensive review of the current literature on targeting for imaging and therapy. More recently, Su et al. [86] employed CPP-modified gold nanoparticles to improve the effectiveness of radiotherapy.

Although nuclear targeting is different from cell or tumor targeting, many groups found that the surfactant on nanoparticles can affect both cell uptake and nuclear penetration. For instance, Hainfeld et al. [87] and Su et al. [79] found that positively charged ligands on gold nanoparticles increase their uptake by cells and nuclei.

9.2.2.4 Biodistribution of Nanomaterials in Animals

Similar to the importance of uptake data to cellular work and enhancement measurements, it is important to know the biodistribution information of nanomaterials in animals. Mass spectrometry is usually used to determine biodistribution of nanomaterials in animals. Biodistribution in animal work is also discussed in Sect. 9.3 using X-ray imaging tools, which require adequate amounts of nanomaterials within the targeted volume in animals. Biodistribution and pharmacokinetics are critical to the study of the fate and effect of nanomaterials in animals.

9.2.2.5   Irradiation Protocols

Animals are irradiated with X-rays, either by single irradiations or in fractionations, depending on the required dose. If a dose of less than 10 Gy is needed, then a single irradiation is commonly used. For greater doses, fractionations may be used by administering a moderate dose multiple times. Many researchers, especially those performing in vitro studies, used a single dose of irradiation. X-ray filters are used to remove low-energy X-rays when needed. Other important factors are irradiation timing and duration, as nanoparticles may quickly clear the tumor, as shown in Fig. 4.3.

9.2.2.6   Enhancement Measurements and Calculations

Delayed tumor growth is often used to evaluate the effectiveness of treatment. The method shown in Fig. 7.1 is used to determine enhancement in in vivo work. If there is no toxicity from the nanomaterials, the magnitude of the enhancement can be calculated using the formula:

$$\frac{\ln(\text{tumor size without any intervention}) - \ln(\text{tumor size with X}-\text{ray}+\text{nanoparticles})}{\ln(\text{tumor size without any intervention}) - \ln(\text{tumor size with X}-\text{ray only})}$$

$$(9.1)$$

An example is given here for a tumor that has grown to 11 times its original size at the time of inspection. If the size is reduced to seven times its original size after X-ray irradiation alone and to two times its original size after irradiation with X-rays in the presence of nanomaterials, then the enhancement is:

$$\frac{\ln(11) - \ln(2)}{\ln(11) - \ln(7)} = \frac{2.40 - 0.69}{2.40 - 1.95} = 3.80 \text{ DEU (rel)} \qquad (9.2)$$

The absolute enhancement is 2.8 DEU. This calculation assumes there is no toxicity from the nanomaterial and the growth of tumor follows an exponential function. The results shown here are consistent with the magnitude of enhancement calculated using Eq. 7.1.

9.2.3   Clinical Work

There are several cases of clinical work involving nanomaterials in the context of X-ray nanochemistry. Stage II/III clinical trials are being conducted by a French company Nanobiotix Inc. using hafnium oxide nanoparticles and X-rays for enhanced cancer treatment. The work is described in this chapter as well.

9.3   Imaging and Detection of Tumors with X-Rays Assisted by Nanomaterials

Imaging with X-rays has been an important tool in medical research and medicine for more than a century since the discovery of X-rays by Rötengen in 1895. Enhanced absorption by the added nanoparticles made of heavy elements can further improve imaging contrast when nanoparticles are delivered to tumor sites through active or passive targeting.

Many new nanomaterials have been developed to improve X-ray imaging. Even though most of the current imaging studies use only the most straightforward principles of X-ray attenuation by nanomaterials as the basis for guiding their imaging improvement, it is foreseeable that other enhancement mechanisms, such as X-ray-induced energy transfer (XIET) discussed in Chap. 2, may be used in the future to enrich nanomaterial-assisted X-ray imaging.

In practice, the sensitivity of X-ray imaging is moderate, whereas state-of-the-art positron emission tomography (PET) and magnetic resonance imaging (MRI) offer better sensitivity. Nonetheless, computed tomography (CT) and regular transmission imaging such as chest X-rays are popular and useful because of their low costs and adequate sensitivity. The number of studies using nanoparticle-based contrast agents to improve CT and other X-ray imaging techniques has grown quickly in the past decade. Figure 9.3 shows the number of works published per year for the last 20 years that have the combination of keywords of "nanoparticle + X-ray + imaging." A similar graph is presented by Cormode et al. [88]. The growth rate is similar to the number of publications in the area of X-ray nanochemistry shown in Fig. 1.1. It is worth noting that Fig. 1.1 is obtained through the papers cited in this book, whereas Fig. 9.3 is obtained through literature searches using keywords.

Five areas related to imaging are briefly reviewed and discussed in this section. The first is the method of imaging. Several new imaging methods are included. The second is the object of imaging, ranging from mice to swine. The third area
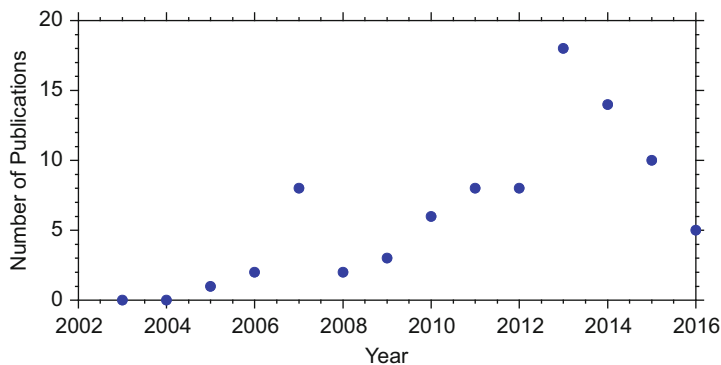
Fig. 9.3 Number of publications per year on the subject of "nanoparticle + X-ray + imaging" provided by the search program *Web of Science*

encompasses the core material of contrast agents, which can be gold nanoparticles or micelles. Fourth is the surface coating of contrast agents, which can be peptides or silica shells. The fifth and final area is the method of delivery, including injection and inhalation. Targeting and biodistribution analysis are also included in this subsection. All these five areas have been investigated in recent years. There are no known clinical trials using nanoparticles as imaging contrast agents to date.

9.3.1   New Imaging Methods

The first topic of this section covers new methods developed in the area of nanoparticle-enhanced X-ray imaging in recent years. Although other techniques may be relevant, the focus here is on techniques that support the use of nanomaterials as contrast agents in X-ray imaging. One common parameter that can be used to gauge the capability of these techniques is the unit weight percent contrast increase (UWPCI, in units of HU WP^{-1}) resulting from the introduction of nanomaterials. The units for contrast is HU, or Hounsfield Units. Whenever possible, the value of UWPCI is specified for each work, and all the values found in the publications cited are summarized at the end of this section in Fig. 9.15. If the detection method is based on fluorescence rather than absorption, then unit weight percent signal-to-noise ratio (S/N) (UWPSN) instead of unit WP contrast increase is given. However, due to infrequent references to S/N in reports, this figure of merit is seldom used.

Sun et al. [89] explored the use of gold nanoparticles for the purpose of performing computed tomography (CT). The nanoparticles employed ranged from 4 to 60 nm in diameter. The uptake and cell viability of gold nanoparticles by HeLa S3 cells were studied. Using 4, 20, 40, and 60 nm gold nanoparticles, X-ray attenuation was measured. 4 nm gold nanoparticles had the greatest uptake. The results showed that the equivalent attenuation was 600 HU for 0.1 mol/L gold loading or 300 HU WP^{-1} in terms of UWPCI. This magnitude of UWPCI was the average value for gold nanoparticle contrast agents.

Cui et al. [49] investigated the use of silica-coated gold nanorods for enhancing the contrast of X-ray imaging. Their results showed that silica-coated gold nanorods increased the contrast of CT at the rate of 15 HU for a 3 mg/mL loading, equivalent to 50 HU WP^{-1}. This value was at the low end of the spectrum of UWPCI for nanomaterials as contrast agents. CT results are shown in Fig. 9.4. Based on the contrast increase, the loading of nanomaterials at the tumor site was approximately 54 mg/mL. The authors reported a 10 mg/mL loading at the tumor site.

Cho et al. [90] investigated the potential of using gold nanoparticles to assist X-ray imaging by using X-ray fluorescence from gold irradiated with 110 kVp X-rays. This was the first fluorescence-based CT work using nanoparticles. A conventional X-ray source equipped with an X-ray hard aperture was used to excite 1 cm diameter gold solution targets filled with 1 and 2 WP gold. A CdTe photodiode detector was used to probe X-ray fluorescence. For 2 WP gold solutions, the fluorescence signal was around 600 counts on top of 2000 counts due to background
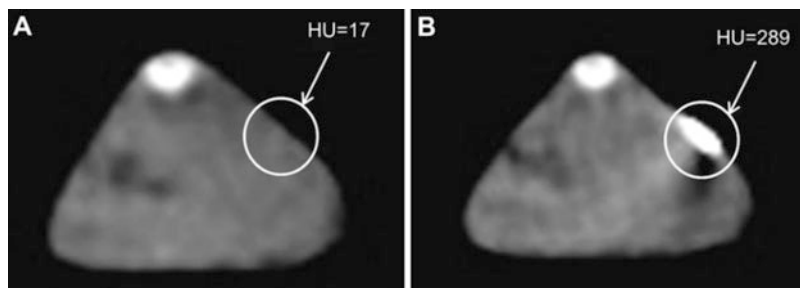
Fig. 9.4 Images of mice without (**a**) and with (**b**) silica-coated gold nanorods. (Reprinted from Cui et al. [49]. Copyright (2008) with permission from Elsevier.)

(scattering). Background removal gives higher contrast images. These results were simulated by Cho et al. [91], providing guidance for their subsequent imaging work. It is possible to use UWPSN to quantify the images of nanomaterials. However, unlike HU that is widely used in transmission imaging, most works in fluorescence imaging do not specify their S/N values, making it difficult to quantify figure of merit of fluorescence-based imaging methods using this parameter.

Cho et al. [92] again studied tumor imaging with the assistance of nanoparticles in the framework of X-ray fluorescence computed tomography (XFCT). The authors used a traditional X-ray tube with a conically shaped lead aperture or collimator. Three gold nanoparticle-loaded regions were embedded in a phantom made of poly (methyl methacrylate) (PMMA). CdTe X-ray detectors located behind the apertures were used to detect X-ray fluorescence at 90° from the incoming X-rays. For the 3 cm diameter phantom, the embedded 0.5 cm diameter gold-loaded samples were detected with a 0.5 WP gold loading, and the 2 WP gold-loaded region was clearly visible. Cho et al. [93] used fluorescent X-rays emitted from the L-shell of gold nanoparticles near 10 keV for imaging. A signal-to-noise ratio (S/N) of 8 was achieved with 2 WP of gold in the water phantom, giving rise to 4.0 UWPSN. A year later, Cho et al. [94] used a Monte Carlo method to theoretically study how to best detect tumors using XFCT. The authors found that the use of X-ray filters could increase S/N and obtained a S/N of 20 when 1 mm Pb filters were used in conjunction with 81–100 keV X-rays.

In a work by Meng et al. [95], sheetlike 15 keV X-ray beams from Advance Photon Sources (APS) were used to excite samples to induce X-ray fluorescence. The beam was as thin as a few microns and arrays of beams were used, either in the form of 15 beams (3 × 5 array) of 0.3 mm diameter or 35 beams of 0.1 mm diameter. The phantoms were comprised of Fe (25 mM), Zn (50 mM), and Br (25 mM) solutions which filled three plastic tubes of 0.75 mm diameter. Fluorescence was measured using a CCD detector with 250 eV energy resolution. The most visible sample was the tube filled with Br solution. Figure 9.5 shows the image of three tubes. Although no nanomaterials were used, it was expected that the imaging method could be readily extended to detecting nanomaterials as contrast agents.

Fig. 9.5 XFCT image of three tubes of 0.75 mm diameter using 35 beams of 0.1 mm diameter. Colors were added to differentiate the three tubes filled with three samples of Fe, Zn, and Br solutions. (Permission of SPIE and Meng [95].)
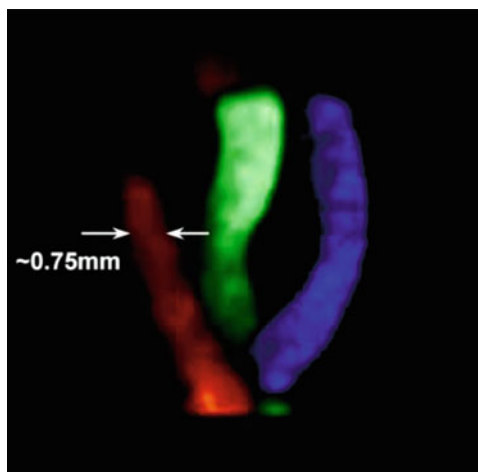
Wen et al. [96] discussed a method of using conventional X-ray sources to perform coherent X-ray imaging of several objects including vials of solution of water and oil. The X-rays were 17.48 keV from a molybdenum target. The authors observed the first harmonic of the Fourier transformed images, which could be used to derive the scattered images of the samples. Fine features on the order of 60–200 nm were observed, suggesting that it is possible to image nanomaterials in solution. They also observed scattering with some unusual images.

Bazalova et al. [97] theoretically studied fluorescence CT principles for X-ray imaging of gold targets in theoretical phantoms. X-ray dose, gold loading, target dimension, and location in the phantoms were all taken into consideration. The authors demonstrated that XFCT was superior because it does not depend on the surrounding tissues, whereas conventional CT does. A scanning beam configuration was also employed by Bazalova et al. [98], and the authors called the technique scanning beam digital X-rays. In another effort, Xing et al. [99] demonstrated the imaging of embedded gold, gadolinium, and barium targets in phantoms using XFCT. Their experimental setup was similar to Cho et al. [92], and the results suggested that gadolinium provided high contrast as well.

Shi et al. [100] reported the results of their study of CT imaging using gold nanoparticles entrapped in dendrimers in a mouse model. The size of gold nanoparticles was between 2 and 4 nm. The amine-terminated fifth-generation dendrimers were slightly larger, although no data on the exact size was available. A clear image was obtained, showing the injected gold nanoparticles in mice. The loading was 10 μL of 20 mM dendrimer-entrapped gold nanoparticles. No toxicity data was available. Their results showed an increase of 1000 HU with a 2 WP gold loading, resulting in a UWPCI of 500 HU WP^{-1}.

Hallahan et al. [101] synthesized multifunctional FePt nanoparticles for targeting and imaging of cancer. The particle size was 2.7 ± 1.0 nm, and the surface was further modified by adding polyethylene glycol (PEG) and then HVGGSSV peptide

ligands. This specific peptide targeted irradiated tumor microvascular cells. The mice were treated with 3 Gy of 300 kV X-rays from a linear accelerator, and the nanoparticles were administered 4 h after irradiation. The authors showed localization of the targeted nanoparticles in tumors using near-infrared (NIR) imaging in lung cancer-bearing mice and quantified the uptake. The control peptide SGVSGHVN-FePt nanoparticles did not show any localization. This work did not use X-ray imaging in the conventional sense.

Ren et al. [102] demonstrated that it was possible to use CT to probe silica-coated gold nanorods in xenograft mice. The initial gastric tumor size was 5 mm. The injection solution had a 3 mg/mL or a 0.3 WP gold loading. The average size of gold nanorods was 44 nm long with an aspect ratio of 2.9. The thickness of silica coating was 15 nm. The loading in the tumor was estimated to be 0.2 WP, and the imaging yielded a contrast of 56 HU, resulting in a UWPCI of 280 HU WP^{-1}. The X-ray images prior to and post gold nanorod injection showed a slight change. In contrast, the same amount of gold nanorods generated a better contrast when near-infrared light (NIR) was used. Physical enhancement, which is close to but lower than attenuation enhancement based on the discussion given in Chap. 2, would be 0.2–0.3 DEU for 0.2 WP uptake. Figure 9.6 shows the imaging results.

Rose-Petruck et al. [103] developed a new method to image gold nanoparticles in solutions. The authors first obtained an X-ray absorption image of the sample, followed by Fourier transformation of the image to the reciprocal space. Their X-ray microfocus source was 20 W and sample exposures were 3 min. Their uptake data showed less than 3 pgs of gold per cell for 10 or 50 nm gold nanoparticles, which was equivalent to a 6 ppm fraction of the sample volume or a 0.012 WP gold loading in the cell (1 ng). Figure 9.7 shows the transmission images and Fourier transform pattern. Based on the S/N shown in the figure, much lower loadings of
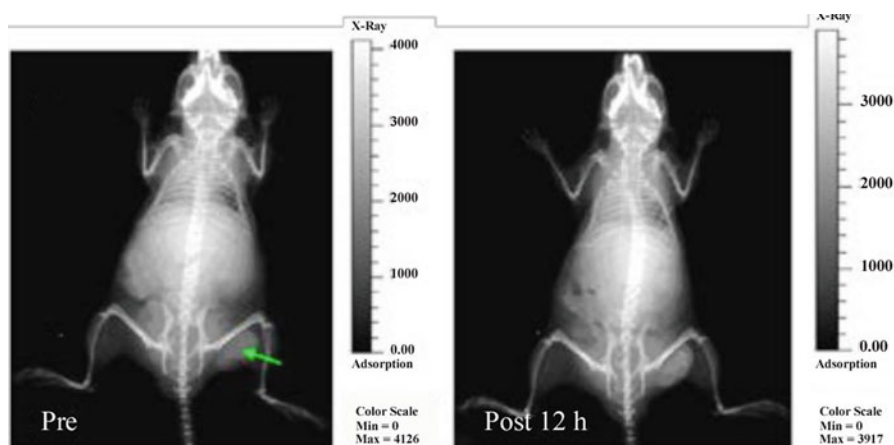
Fig. 9.6 CT imaging of a gastric tumor with silica-coated gold nanorods in mice. The loading was 0.2 WP in the tumor. The arrow shows the 5 mm tumor prior to (left) and after (right) injection of gold nanomaterials. (Reprint with permission from Ren et al. [102]. Copyright (2011) of Optical Society of American.)
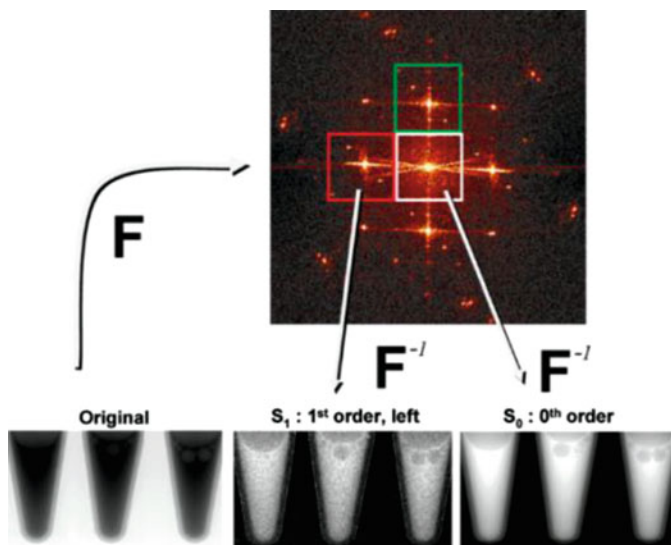
Fig. 9.7 Fourier transformation of transmission imaging for gold nanoparticles in solutions. The detection sensitivity was about 0.01 WP of gold in water. (Reprinted with permission from Rose-Petruck et al. [103]. Copyright (2011) American Chemical Society.)

gold in the sample can be detected. The authors proposed to use this method for cancer imaging.

Another method of X-ray fluorescent imaging was developed recently by Guo et al. [104], who discussed the results of X-ray imaging of tumor phantoms buried in large water phantoms with the assistance of nanoparticles. Figure 9.8 illustrates the principle. The idea was to use a needle X-ray beam to irradiate a sample while detecting X-ray fluorescence emitted from nanoparticles in the sample in the direction perpendicular to the needle X-ray beam path, a practice similar to the detection configurations used in several other reports. Apertures in front of the detectors were used to allow only X-rays emitted from certain points in the sample to enter the energy-dispersive detectors. This way, fluorescent X-ray photons emitted from the nanoparticles was measured with minimal interference from scattered X-rays.

Figure 9.9 shows the results of imaging a volume of interest embedded in a water cube. The loading of gold in the simulation was 1 WP and the shapes were cylindrical disks. Panel A shows the overall imaging result, which shows the location of the nanoparticle-loaded volume. Panels B and C show the side views of silver- and gold-loaded target volumes. Panel D shows the whole sample volume. Panels E and F shows the top views of the imaging. For 33 keV X-rays, Ag was more visible than Au.
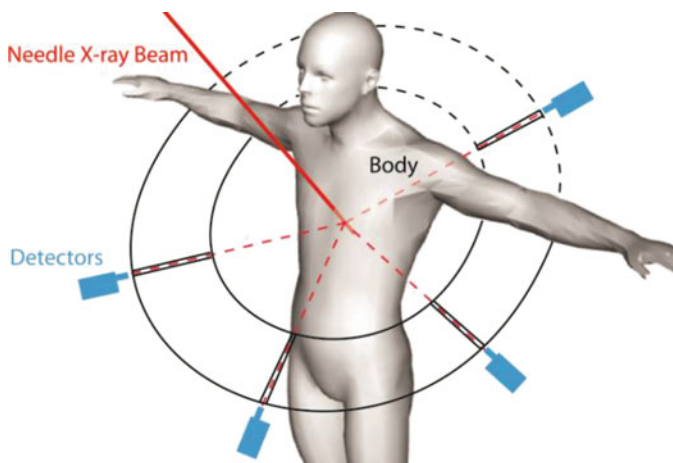
Fig. 9.8 Illustration of using X-ray fluorescence to detect nanoparticles in tumors in the human body. Multiple detectors were used to detect the nanoparticles at the targeted point in the body irradiated with an X-ray beam. The X-ray beam, the detectors, and the apertures were aligned before imaging [105]
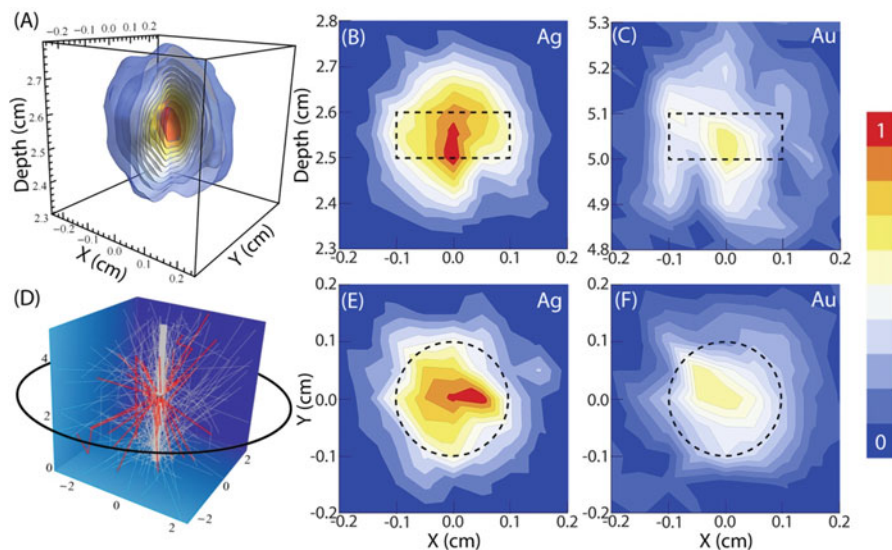
Fig. 9.9 Simulated results of detection of gold nanoparticles in tumor phantoms. A 10 cm water cube was used as the phantom. The results showed that it was possible to detect a 1 WP silver- and gold-loaded 2 mm diameter and 1 mm height disk-shaped tumor using the detection setup shown in Fig. 9.8

Table 9.4 List of animal types and nanomaterials used in imaging works

Objects	Nanomaterials	Refs.
Mice	AuNPs	Hainfeld et al. [5]
Rats	AuNPs	Pradhan et al. [29]
Juvenile swine	AuNPs	Boote et al. [106]

9.3.2   Imaging Objects

The second area is the object of imaging. Only a few kinds of objects have been used, which include mice, rats, and swine. Table 9.4 lists all of the objects reported in the literature. Nanomaterials used in these animal studies are also listed. All objects are small compared with the human body. Representative references are given.

9.3.3   Core of Contrast Agents

Nanomaterials as contrast agents have been developed quickly in the last decade. Table 9.5 lists the core materials of the nanomaterial contrast agents for X-ray imaging reported in the literature. The discussion in this subsection follows chronologically the groups who performed the work.

Hainfeld et al. [107] used gold nanoparticles as a contrast agent for X-ray imaging. Their results, which were also shown in their 2004 publication [5], clearly revealed mouse veins after injection of gold nanoparticle solutions into the tail veins. Figure 9.10 shows the images before injection (left panel) and 2 min after injection (right panel). The veins were clearly visible with the injection of gold nanoparticles. The diameter of the vein shown in the right panel was approximately 0.2 mm. Since 30 HU (or 7 HU) was the minimum contrast difference needed to differentiate two objects, and the image in the right panel shows a contrast much higher than the minimal needed for differentiation, the contrast change should be greater than 30 HU. The loading, as claimed by the authors in their 2004 publication, was higher than 0.2 WP. Combining these two pieces of information, UWPCI should be on the order of 150 HU WP^{-1}.

Hainfeld et al. [108] employed gold nanoparticles to image brain tumors in mice. The average size of gold nanoparticles was 11 nm and gold loading in the tumor was 1.5 WP. The results suggested that nanoparticles crossed the blood-brain barrier and were taken up by the tumor more effectively than healthy brain tissues, resulting in a ratio of 19:1 nanoparticles in tumor to healthy tissue. The X-rays were 100 kVp with a 1.7 mm Al filter. The authors found that the toxicity LD_{50} for gold nanoparticles alone was 5 g/kg or 0.05 WP, which is low compared to the loadings used in many reports. Although unspecified, this loading should be the value for the whole volume of the animal, as the tumor loading of gold was much higher than this value. It was also unclear as to whether this LD_{50} was with respect to healthy mice or cancer-bearing mice. The authors used a loading of 4 g/kg or 0.04 WP injection dose of gold nanoparticles for imaging. The contrast change was 1050 HU at 15 h after injection

Table 9.5 List of nanomaterials used in X-ray nanochemistry imaging. Composition, size, uptake and X-ray energy are given. Contrast chance or increase is listed and UWPCI is calculated based on contrast change and uptake. The results are arranged chronologically according to the corresponding authors. Multiple papers from the same group are grouped together

Composition	Size (nm)	Uptake amount (WP)	X-ray energy	Fluo	Contrast increase (HU)	UWPCI (HU/WP)	Ref.
Au	1.9	0.3	22 kVp	–			Hainfeld et al. [107]
Au	11	1.5	45 kVp	–	1050	875	Hainfeld et al. [108]
Au/Gd	2.4	1	40 kV	–	1287	1287	Roux et al. [109]
Au	4–60	2	120 kVp	–	600	300	Sun et al. [89]
C	–	Pure	30 kV	–			Wen et al. [96]
Au (theory)	–	0.1–1.0	60–140 keV	–	–	–	Yusa et al. [110]
Au	20	0.038	80, 140 kVp	–	2.2–13	130	Boote et al. [106]
Au	1.9	1.0–2.0	110 kVp	Yes			Cho et al. [90]
Theory		<2	110 kVp	Yes			Cho et al. [91]
Au	1.9	0.5–2.0	105	Yes			Cho et al. [111]
Au		<2	62 kVp	Yes			Cho et al. [93]
Au	Theory		105 kVp	Yes			Cho et al. [94]
Au	12–29		80 kVp	–	130		Jon et al. [112]
Fe, Zn, Br	Solutions		15 keV	Yes			Meng et al. [95]
Au	2–4	0.15	80 kV	–	>7	>50	Shi et al. [100]
AuNP@SiO$_2$	88		110 kVp	–	20	300	Mulder et al. [113]
Au@SiO$_2$	18/46		10–40 Kv		300		Cui et al. [49]

Au	Theory		110 kVp	Yes	56	280	Manohar et al. [114]
SiO$_2$-covered AuNRs	15/44	0.2	130 (kVp)	–			Ren et al. [102]
Au	10–50	6 ppm	95.6 kV	Special	–	–	Rose-Petruck et al. [103]
Gd oxide	1.1	5–6 ppm	>50.2 keV	–			Roux et al. [115]
TiO$_2$	2–3	1.5	50, 125 kVp	–	26.6	17.7	Kuncic et al. [116]
Au (saline solutions)	–	2	150 kVp	Yes			Bazalova et al. [99]
Au	15	0.05	20–100 kV				Kunzel et al. [117]
Au	1.9	14.1	120 kVp	–	3000	114	Tu et al. [118]
Bi^{3+}/SWCNTs		0.1	110 kVp	–	36	360	Wilson et al. [119]
Au		0.05–0.5	45 kVp	–	60–225	1200–450	Cole et al. [120]
Pt	10 nm	5–30 ppb	1.25 MeV	–	0.27	Optical density	Deyhimihaghighi et al. [121]
Au/SiO$_2$	17/60/12	3.6	50 kVp	–	1100	306	Zhao et al. [122]
Au		1	100 kVp	Yes			Guo et al. [105]
Au	30/90		45 kV	–	220		Kannan et al. [123]
Au	10, 50	0.002	80–100 kV	–			Rose-Petruck et al. [124]
Au/FeOx NPs	100	0.3 (0.0003–0.3)	55 kVp	–	110	366	Casey McQuade et al. [125]
LF3:Tb/Si$_2$O/Dye	40	24.9	<45 kV	–	3000	121	Yang et al. [126]
Gd/Yb/SiO$_2$	280/500		120 kV	–	2144	1230	Yang et al. [127]
Au	3.9–41			–	60		Chang et al. [76]
Au/Fe$_3$O$_4$	50 nm	0.8	50 kVp		700	875	Mei et al. [62]
Au	7, 9, 19, 38	1			900	900	Bulte et al. [128]
Bi	3.6	1.72	80 kV	–	1193	690	Li et al. [71]
Au nanorods	10 × 50	2	60 kVp	–	300	150	Xu et al. [129]

Fig. 9.10 Image of mice without nanoparticles (left panel) and injected with 1.9 nm gold nano-particle solutions (right panel). A vein only a fraction of mm in diameter was visible in the right panel (marked by the arrow). (From Hainfeld et al. [5]. doi: https://doi.org/10.1088/0031-9155/49/18/N03. © Institute of Physics and Engineering in Medicine. Reproduced by permission of IOP Publishing. All rights reserved.)

and the half-life was 24 h. UWPCI was 875 HU WP^{-1} for a 1.2 WP loading (in tumor) given by the authors.

Roux et al. [109] developed a chelate surfactant layer on gold nanoparticles for combined X-ray and MRI imaging of animals that can potentially be used in clinical applications. The ligands included DTPA, DTPADA, and DTDTPA. The average size of the gold nanoparticles was 2.4 nm. The X-rays were from synchrotrons and both CT and microbeam configurations were used. Fifty-one beams of 25 μm diameter X-ray beams, whose energy were as high as 100 keV, from the European Synchrotron Research Facility (ESRF) were used. Rats injected with gold nanoparticles irradiated with X-rays survived almost twice as long as those that were not treated with gold nanoparticles, suggesting that gold nanoparticles irradiated with X-rays inhibit tumor growth.

Boote et al. [106] performed CT imaging of a phantom and juvenile swine using gold nanoparticles as a contrast agent. The average size of gold nanoparticles was 50 nm. The uptake was found to be 0.38–0.68 mg/g in the liver and spleen, which corresponds to gold loadings of 0.038–0.068 WP. Images obtained by the authors with the gold contrast agent showed an average increase of contrast of 7 HU, which was lower than the normally required minimal 30 HU to separate two objects. The average UWPCI was 180 HU WP^{-1}, similar to other results obtained with mice models. Given the size of swine being an order of magnitude larger than mice, the results were encouraging.

Jon et al. [112] used a specially prepared gold nanoparticle as both a contrast agent and therapy enhancer. The authors coated the gold nanoparticles with a prostate-specific membrane antigen RNA aptamer, which targeted prostate cancer cells that expressed the antigen proteins. The results showed a 4× increase in CT imaging contrast for the targeted results compared to a non-targeted control imaging measurement.

Kannan et al. [130] showed that gold nanorods were an effective X-ray image enhancer. The nanorods had an average diameter of around 30 nm and a length of 90 nm, giving rise to an aspect ratio of 3. The uptake was rapid, and an increase in

contrast of 90 HU was observed after one injection and 200 HU after the second injection. No unit mass contrast increase was available. Zhao and Ma et al. [122] demonstrated the use of folic acid conjugated silica-coated gold nanorods for CT imaging. The dimensions of the nanorods were 60 nm long and 17 nm in diameter. The thickness of the silica costing was 12 nm. At 36 mg/mL concentration, which was 3.6 WP, the contrast increase was 1100 HU, corresponding to a 306 HU WP^{-1} UWPCI.

Roeder et al. [120] developed bisphosphate-functionalized gold nanoparticles as an X-ray contrast agent. The ligand had an amine group that can bind to gold surface and a phosphonate group that binds to calcium ions on hydroxyapatite crystal surface. The gold nanoparticles were 12 nm in size. Up to 225 HU increase was detected using a three-dimensional CT imaging method, although approximately 20 WP of gold was found in the targeted region. UWPCI obtained in this work was only 11 HU WP^{-1}, which was approximately an order of magnitude less than the lowest obtained by others. A similar work by the group is mentioned later in this section when surfactants are discussed.

Yang et al. [126] produced LaF_3:Tb nanoparticles covered with silica and tethered with organic dye molecules. A LaF_3:Tb core was used to absorb X-rays for CT imaging purposes as well as for scintillation so that the emitted photons transferred their energy to the dye molecules through FRET. Although not explicitly expressed, the average size of the core was 40 nm, and the authors claimed the silica layer thickness ranged from 3 to 45 nm. The contrast increase was 3000 HU per 0.7 M of LaF_3:Tb. UWPCI was 121 HU WP^{-1}, calculated based on the contrast increase and the molecular mass of 355 g/mol, which resulted in a 24.9 WP loading. Figure 9.11 shows the results.

Yang and Lin et al. [127] studied a multimodal imaging approach to image nanomaterials in vivo. This time the authors employed Gd and Yb nanomaterials. Similar to their work mentioned above, the contrast increase reached 3000 HU but
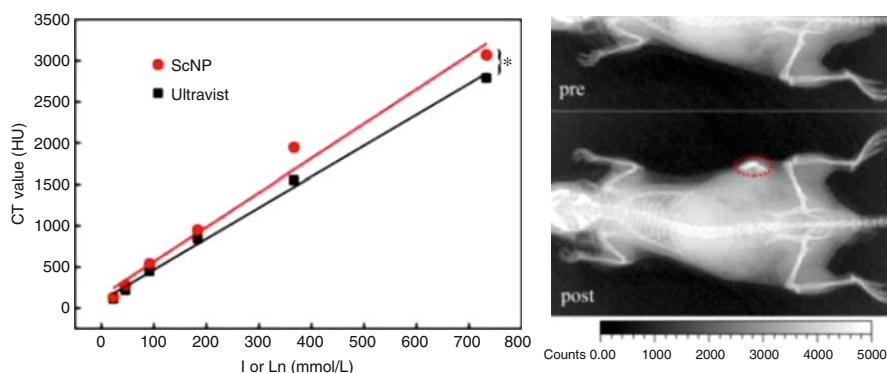
Fig. 9.11 Image contrast (left panel) and images of animals (right panel) using LaF_3:b nanoparticles to enhance X-ray imaging. (Adapted in part from Yang et al. [126] with permission of the Royal Society of Chemistry.)

with only 25 mg/mL loading. This was equivalent to 1200 HU WP^{-1}, which was one of the highest UWPCI reported in the literature.

Tu and Lo et al. [118] studied gold nanoparticles as a contrast agent in CT planning for radiotherapy. The size of gold nanoparticles was 1.9 nm. The loading of gold nanoparticles in media in their experiments ranged from 28 to 141 mg gold per mL. The increase of imaging contrast was 322 HU for 28 mg/mL and 1608 HU for 141 mg/mL. These increases translated to 114 HU WP^{-1} UWPCI for gold in tissue. They also calibrated the gold nanoparticles against a standard of Conray 60, an iodine-based contrast agent. The authors suggested to use 22.5 mg/mL gold in clinical cases, which was over 2 WP (in tumor) and could cause more than twofold radiation enhancement if physical enhancement was considered.

Wilson et al. [119] discussed the work of using a new type of bismuth nanomaterial, i.e., evaporated bismuth trapped in or embedded in single-walled carbon nanotubes, for CT imaging. The X-ray energy was 110 kVp. Single-walled carbon nanotubes with bismuth showed an increase of 36 HU over imaging without bismuth, which was greater than the 30 HU difference required for distinguishing adjacent tissues. Bi^{3+} loading was 1 g/kg or 0.1 WP. The technique thus generated a 360 HU WP^{-1} UWPCI using their bismuth nanostructures.

Tsourkas et al. [38] used micelles-containing gold nanoparticles for imaging (and treatment) of tumors in mice. The micelle size was between 25 and 150 nm and gold nanoparticles in the micelles were 1.9 nm in diameter. The CT images showed gold contrast agent in HT1080 flank tumors 24–48 h after injection of nanoparticles. Nearly 6% of the injected dose of gold nanoparticle micelles was found in the tumor 48 h after nanoparticle administration, which corresponded to 0.57 mg/mL or 0.057 WP. The authors mentioned that the detection limit of using gold as contrast agent was 0.5 mg/mL, which was 0.05 WP gold in water. According to results acquired here, the contrast increase for adding gold was between 120 and 800 HU WP^{-1}, which means that 0.05 WP would generate a contrast increase between 7 and 40 HU. Tsourkas et al. [125] improved the imaging and therapy by incorporating magnetic nanoparticles into the micelles so that CT imaging could be performed in practical radiotherapeutic settings. The magnetic nanoparticles, or superparamagnetic iron oxide nanoparticles, were used to enable magnetic resonance imaging (MRI). Gold nanoparticles were used to provide radiosensitization.

Wang and Mei et al. [62] synthesized iron oxide nanoparticle-functionalized gold nanocages for simultaneous CT and MRI imaging. Moreover, T1- and T2-weighted MRI imaging were obtained. UWPCI was on the order of 500 HU WP^{-1}. In another work, Tian and Pan et al. [131] employed Au@Pt nanodendrites synthesized for the purpose of imaging and treatment of tumors. The gold core had a diameter of 8 nm and the platinum nanobranches, as the authors called them, on the surface of the gold cores were approximately 10 nm long, making the whole nanodendrites nearly 30 nm in diameter. The nanodendrites were then PEGylated. CT imaging showed nearly 1800 HU increase at 10 mg/mL loading, giving rise to an 1800 HU WP^{-1} UWPCI. The nanodendrites were also used for tumor treatment, and the best results were obtained when both near-infrared and X-ray irradiation were present.

Yang and Li et al. [71] used 3.6 nm bismuth nanoparticles coated with LyP-1 peptide ligands to increase contrast in tumor imaging. Their calibrated unit concentration contrast increase was 13.8 HU mM^{-1}, which was equivalent to 690 HU WP^{-1}. Zhao and Xu et al. [129] developed gold nanorod-based nanoparticles for CT imaging. A silica shell was coated onto the nanorod core, and ethanolamine-modified poly(glycidyl methacrylate) ligands were conjugated to the surface of the silica shell. Glioma tumor-bearing mice, after injection of the nanomaterial, were imaged and up to 300 HU contrast increase was measured with nearly 20 mg/mL incubation concentration. No uptake data was available.

Several review articles on contrast agents have been published in recent years. The applications of these agents are not limited to X-rays. Most of the reviews covered more materials than what is discussed here, so readers interested in contrast agents for modalities other than X-rays can read these reviews. The chemistry involving synthesis and functionalization of the nanoparticle-based contrast agents share a common knowledge base with X-ray nanochemistry.

Among these reviews, Cormode et al. [132] summarized the results of using gold nanostructures for diagnosis and therapy. Cormode et al. [88] reviewed contrast agents developed from micelle and liposomes. Anton et al. [133] reviewed inorganic nanoparticles as contrast agents. Cole et al. [134] summarized the results of using gold nanoparticles as contrast agents for X-ray imaging. There have also been systematic efforts to improve contrast agents, such as employing ytterbium nanoparticles. For example, Liu et al. [135] reviewed the use of ytterbium-nanoparticles for X-ray imaging. Li et al. [136] reviewed the use of several gold nanostructures including nanoparticles and nanorods for CT imaging and imaging guided therapy.

9.3.4   Surfactants of Contrast Agents and Impact on Targeting, Delivery and Biodistribution

Surfactants are an important component of nanomaterial-assisted X-ray imaging. Although the contrast often originates from the nanomaterial core, its surface can influence uptake, targeting, and other properties of contrast agents, such as delivery and biodistribution. Many groups have worked on formulating nanomaterials for medical applications. These efforts have also helped advance X-ray nanochemistry. The current focus of X-ray nanochemistry is to learn about the fundamental processes, such as to enhance the effectiveness of X-ray irradiation through defining a number of chemical, biological, and nanochemical reactions, and these reactions are influenced by the surfactants as well. It should soon be clear that delivery and targeting of the nanomaterials will be needed not only for imaging but also for more advanced X-ray nanochemical applications, such as triggered release, because targeting and delivery will be important for practical applications once the fundamental enhancement mechanisms of triggering are understood and developed.
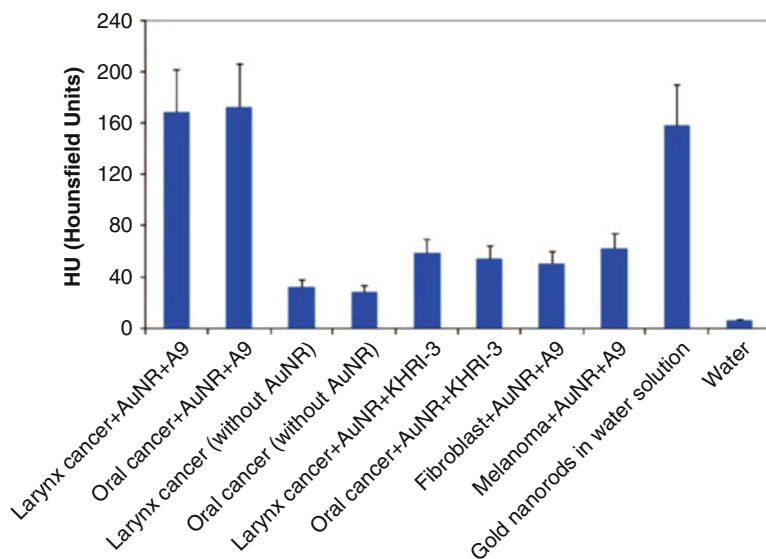
Fig. 9.12 Effect of targeting of gold nanorods (AuNR). The first two bars are about five times the third and fourth, demonstrating the effect of targeting. (Reprinted (adapted) with permission from Popovtzer et al. [139]. Copyright (2008). American Chemical Society.)

Many chemicals can help improve selective binding of nanomaterials to targets. For example, cell-penetrating peptides (CPP) on the surface of nanomaterials can facilitate the delivery of nanomaterials into the cell. There are many reviews on this subject and readers are encouraged to read them if interested. For example, Shen et al. [137] reviewed the work on CPPs. Sée et al. [138] reviewed the literature on delivering gold nanoparticles into mammalian cells.

A large number of groups have worked on targeting, and many demonstrations are available to show the effectiveness of targeting in terms of increasing the imaging contrast of and damage to tumors. For example, Kopelman et al. [139] showed a proof of concept of targeting to improve CT contrast. A fivefold improvement was recorded when gold nanorods (AuNR) were used. Figure 9.12 shows the results. Many other cellular surface components such as hypoxia-inducible factor (HIF-1) can be targeted.

Roeder et al. [140] discussed the use of bisphosphate-functionalized gold nanoparticles as a contrast agent for detection of breast microcalcification. This type of nanoparticles selectively concentrated at the reacting or tumor sites and increased the contrast to facilitate detection of these sites because phosphate functional groups targeted and reacted with hydroxyapatite (HA) in the breast. The authors found that the contrast increased by 300 HU with a 25 mg/mL or 2.5 WP HA loading at the tumor site. Gold loading was not specified. The results obtained by Cole et al. are shown in Fig. 9.13. Targeting therefore further improved the performance of high contrast nanomaterials, and minimized the total amount of nanomaterials used in imaging.
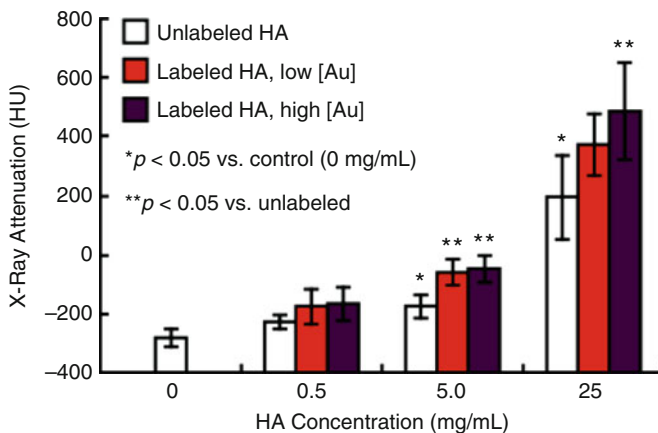
Fig. 9.13 Bis-phosphate functionalized gold nanoparticle contrast agent reported by Roeder et al. [140]. HA loadings are shown, although gold loading was not quantitatively determined and shown. (Reprinted from Cole et al. [140]. Copyright (2014) with permission from Elsevier.)
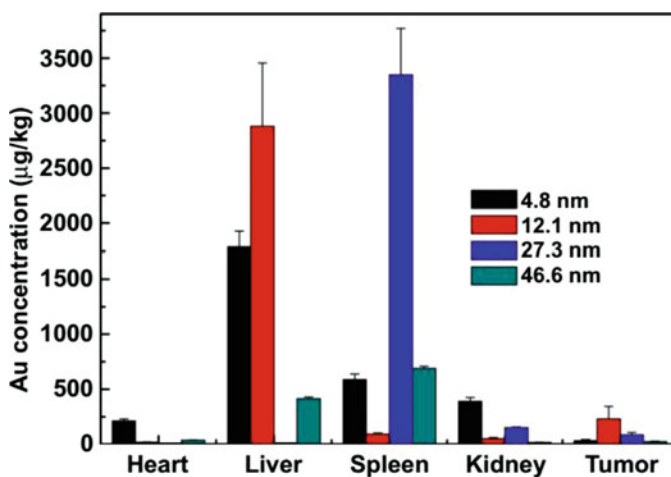
Fig. 9.14 Biodistribution results after delivery of gold nanoparticles into animals. Four sizes of gold nanoparticles were used, and most of the nanoparticles were found in the liver and spleen. (Reprinted from Zhang et al. [141]. Copyright (2012), with permission from Elsevier.)

Results on biodistribution have been provided by many groups. The data are critical to the determination of the cause for the enhancement as well, although not all the published reports contained this important piece of data. Biodistribution information is usually obtained through elemental analysis of different organs using mass spectrometry. A typical result is shown in Fig. 9.14, which was obtained by Zhang et al. [141].

9.3.5 Summary of Imaging

Imaging, when combined with other more direct methods of measuring the uptake such as ICP-MS, can also be used to evaluate or predict physical enhancement based on the difference between mass energy absorption coefficients μ_{en}/ρ and mass attenuation coefficients μ/ρ as discussed in Sect. 2.2. This is because imaging can be used to obtain mass attenuation coefficients μ/ρ, and since mass attenuation coefficients μ/ρ has a fixed relationship with mass energy absorption coefficients μ_{en}/ρ, which determine physical enhancement, it is therefore possible to predict physical enhancement using imaging contrast. In addition, as shown above, imaging can be used to provide information on biodistribution, both qualitatively and quantitatively.

As indicated above, nanomaterial-assisted X-ray imaging has been mainly used in small animal models and rarely in large-size animals or human phantoms. Further, toxicity issue has to be addressed before human imaging is possible. The work done so far has established the baseline for loadings of nanomaterials as well as X-ray energy and other parameters such as targeting and delivery. These studies have paved the way for imaging larger objects.

Figure 9.15 summarizes most of the results mentioned in this section. Loading in the units of WP is used in the horizontal axis and UWPCI in the units of HU WP^{-1} is
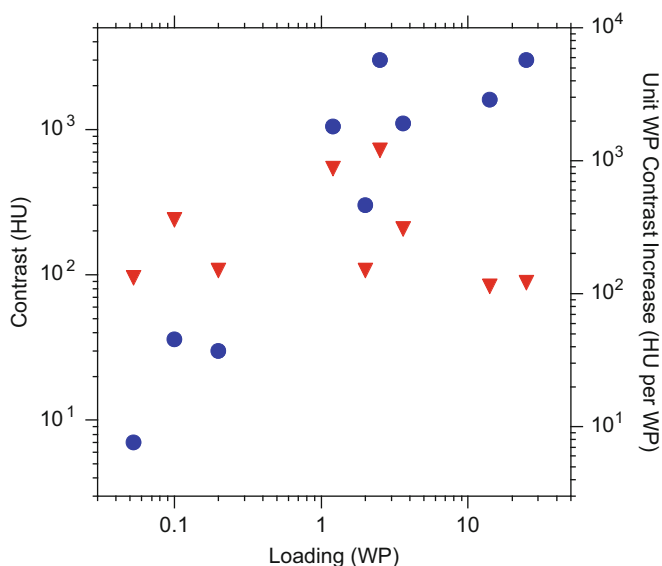
Fig. 9.15 Summary of the results of nanoparticle-enhanced X-ray imaging. Contrast results are given (blue circles). The values of unit WP contrast increase (UWPCI) in HU WP^{-1} (red triangles) from adding nanomaterials are also given, which are greater than 100 HU WP^{-1} for all the results reported in the literature

used for the right vertical axis (red triangles). Contrast change in units of HU is shown in the left vertical axis (blue circles). As it is shown here, all the works shown in this section, with the exception from one study, generated UWPCI between 120 and 800 HU WP^{-1}. Using 30 HU as the minimum contrast difference between adjacent tissues, the minimum loadings for these new imaging contrast agents are between 0.0375 and 0.25 WP, which are below the LD_{50} toxicity level for most nanoparticles. However, since most results shown here are acquired using small animal models, these criteria will have to be revised upward in clinical trials and treatment of patients if the imaging objects are much larger than the tested objects described here. Loadings would have to be orders of magnitude higher because of the much greater thickness of human body unless sectional images are taken. It is very likely that 1 WP nanomaterials are needed for imaging large objects. At this level, many nanomaterials are toxic. If there is no guarantee that nanomaterials only target tumors or only large amounts of nanomaterials accumulate at tumors, then either more sensitive imaging methods such as X-ray fluorescence-based approaches have to be used, or only small objects are imaged.

When high loadings (>1 WP) of nanomaterials are needed for imaging, then most likely the same nanomaterials can be used to effectively enhance the efficacy of X-ray treatment. If only physical enhancement is involved, then about a 1.0 DEU enhancement can be reached. On the other hand, if efficient X-ray-triggered drugs are developed and used, the dose requirement for the treatment may be lowered to 0.1 Gy or even 0.01 Gy, which is far less than even the acute dose of 1 Gy for the human body. In this section, no dose information is given. For CT of human bodies, the dose is usually kept below 0.1 Gy or 10 rem (head CT) or even below 0.01 Gy or lower (chest). It would be convenient to use the same nanomaterials and similar doses to both image and treat tumors with X-rays in human bodies.

In the next section, results of theoretical studies of enhancement of energy deposition are reviewed.

9.4   Theoretical Work on Cancer and Animal Treatment

The theory used here is based on physical enhancement described in Chap. 2, not full quantum simulations of molecular or biological events. Many of the theoretical works have already been presented in Chap. 2, so here only those that are closely related to medical applications but not fully described in Chap. 2 are summarized. Even though no quantum or molecular dynamics simulations are involved, the theoretical results shown both here and in Chap. 2 can still help explain experimental in vivo and in vitro results in the form of predicting the magnitude of physical enhancement. While biological systems are complex and often the measured enhancement values are heavily influenced by biological processes or pathways, at least it is still possible to conduct these theoretical works to help discern whether the observed enhancements can be interpreted by the increased absorption of X-rays

from the added nanomaterials. If the magnitude of the theoretically predicted physical enhancement is far different from the experimentally measured enhancement values, then chemical or biological enhancement or other processes could dominate. Such revelation may promote researchers to work toward uncovering the true causes of enhancement.

Table 9.6 lists the groups that have reported the results of theoretical prediction of the enhancement of using nanoparticles on cancer treatment. Many nonmedical studies are discussed in Chap. 2. The desired enhancement calculations for medical applications address situations closely related to the in vitro and in vivo experiments. As discussed in Chap. 2, the magnitude of physical enhancement, which is the only enhancement that can be accurately simulated theoretically to date, is approximately 1.4 DEU WP^{-1} of gold in water under 33 keV X-ray irradiation. Table 9.6 includes calculations that showed much greater enhancement factors, as high as 10,000 DEU WP^{-1} of gold in water. The causes for such a large disparity of enhancements reported in the literature are explained in Sect. 2.3.3.3 and Fig. 2.19.

Cho [142] employed a BEAMnrc/DOSXYZnrc code and simulated the enhancement by gold in phantoms under X-ray irradiation. The results are discussed in Chap. 2. The main conclusion was that there was enhanced energy deposition in water to which gold was added. The magnitude of enhancement was 1.0 DEU for 0.7 WP gold in water, a value that agreed with many studies reported in the literature.

McMahon et al. [143] calculated enhancement of energy deposition by gold contrast agents under 150 kVp and 15 MV X-ray irradiation. A loading of 10 mg/mL or 1 WP was used in their calculations. The authors proposed a "figure of merit," which was the ratio of total dose in the tumor to the highest dose in nearby healthy tissues. Their results are shown in Fig. 9.16, which indicate approximately an enhancement of 1 DEU WP^{-1} for 150 kVp X-rays either with (dashed line) or without (solid line) Al foil filter. X-rays reached the enhancement site had to traverse through a 50 mm thick tissue, which was a de facto filter that made X-rays harder (more energetic) even without the use of filters. The predicted enhancement values were close to those predicted by other calculations shown in Chap. 2. The enhancement was negligible for 15 MV X-rays (dotted line). The results on high-energy MV X-rays were also close to those obtained by others. These results suggested again that if significant unit WP enhancement was observed using MV X-rays, then the enhancement should be caused by chemical or biological enhancement.

Yusa et al. [110] theoretically studied the role of colloidal gold as a contrast agent. The authors found that with 1 WP gold in tissues, the contrast increase was 70% of the contrast obtained with bone in tissues of the same dimensions irradiated with 88 keV monochromatic X-rays. Assuming the bone model is cancellous, then the UWPCI is approximately 490 HU WP^{-1}. The results, however, could not be directly used to infer energy deposition enhancement because the calculated 70% increase was an attenuation increase, not the energy deposition increase. The two values are not close to each other at 88 keV based on the discussion given in Chap. 2.

Gokeri et al. [144] theoretically investigated irradiation of a gold-loaded tumor region in a realistic head phantom irradiated with an array of X-ray microbeams. Their method used an array of parallel microbeams of X-rays and a gold contrast

Table 9.6 List of works in theoretical studies of physical enhancement in biological systems. The results are arranged chronologically, from the earliest to the most recent. Composition and size of nanomaterials are given, as well, X-ray energy, the package used in the simulation and targets are given

Composition	Size (nm)	Cell/target	X-ray energy	Package	Ref.
Au	Atoms	Phantoms	140 kVp, 6 MV	BEAMnrc/DOSXYZnrc	Cho [142]
Au	Atoms	Phantoms	150 kVp,15 MV	Geant4	McMahon et al. [143]
Au	Atoms	Contrast agent	60–140 keV	EGS5	Yusa et al. [110]
Au	Atoms	Phantoms	30–600 keV	MCNPX	Gokeri et al. [144]
Au	1.9, 5, 30, 100	Water	20–157 keV, 6 MV	MCNP-5	Pignol et al. [145]
Au	2–50	MDA-MB-231	20–150 keV, 160 keV	Geant4/Geant4-DNA/LEM	McMahon et al. [51]
Au	2	MDA-MB-231	6 and 15 MV	Geant4/C4DNA/LEM	McMahon et al. [70]
Z = 53–81	Atoms	Phantoms	50–600 keV	PENELOPE	Martinez-Rovira et al. [146]
Au	1.9	Slab models	80–120 kVp	Homemade based on Cole (ref)	Ngwa et al. [147]
Au	30	PC-3	300 kVp	MCNP-5/PENELOPE	Pignol et al. [148]
Au	Atoms	Tumor capillary vessels	150 kV	Geant4	Amato et al. [149]
Au	30, 50, 100	Phantoms	50–120 keV, 1.3–18 MV	MCNPX	Mesbahi et al. [150]
Au	50	Bladder cancer cells	200 keV	Geant4	Jeynes et al. [151]
Au	2, 15, 50, 100, 200	Water	60–150 kVp	PENELOPE/Geant4/ENSnrc	Li et al. [152]
Terpyridine-Pt complex	Atoms	F98 and B16	160 kVp/6 MV	Geant4	Pradhan et al. [29]
Ag, Au	5–250	Liquid	40 kev	Homemade	Wardlow et al. [153]
Au	100	Generic spherical cells	60 kVp	PARTRAC	Xie et al. [154]
Au	3–50	HeLa	keV, MeV	Geant4	Chang et al. [76]
FeOx, Au	20, 50	U87	6 MV	Geant4-GATE.7.0	Retif et al. [61]
Au	2	MDA-MB-231	160 kVp, 6 MV, 15 MV	Geant4-G4DNA	Attilli et al. [155]
Au	2, 15, 20 50	MDA-MB-231, F-98	51, 150 keVp, 6 MV	LEM	Schuemann et al. [156]

The packages are discussed in Sect. 2.3.3
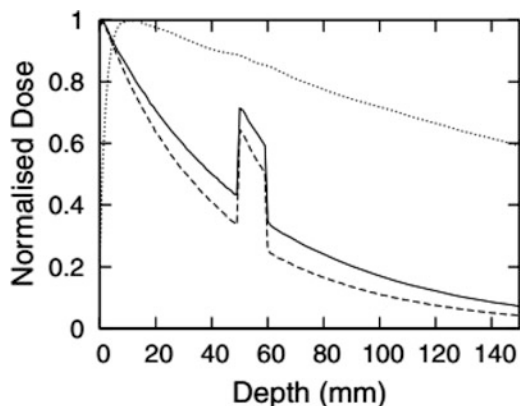
Fig. 9.16 Calculated enhancement for 150 kVp and 15 MV X-rays. Nearly 1.0 DEU was obtained when 1 WP gold nanoparticles were irradiated with 150 keV X-rays (solid and dashed lines). Enhancement was negligible for 15 MV X-rays (dotted line). (From McMahon et al. [143]. doi: https://doi.org/10.1088/0031-9155/53/20/005. © Institute of Physics and Engineering in Medicine. Reproduced by permission of IOP Publishing. All rights reserved.)

agent for therapy. Although no nanomaterials were used, similar therapeutic effects exist regardless of the form of gold, whether it was in the form of atoms or nanoparticles. The form of materials would affect the delivery or targeting of the material. In the work by Gokeri et al., up to 20 beams of 0.68 mm diameter were employed to irradiate a head phantom. 7 mg/g or 0.7 WP gold in tumor was loaded in the tumor, and an approximately 40% increase in dose enhancement or a 0.4 DEU enhancement was observed in in-beam dose. The average X-ray energy was 107 keV with the spectrum of X-ray covering 30–600 keV. The calculated enhancement of 0.57 DEU WP^{-1} for the spectrum was close to the experimentally measured enhancement using a mice model, suggesting that the observed enhancement could be caused by physical enhancement.

Pignol et al. [145] explored the potential of using gold nanoparticles in clinical scenarios. The codes the authors used were MCNP-5 with cross-section data from ENDF/B-VII and PENELOPE 2008.1. The size of the nanoparticles ranged from 1.9 to 100 nm. The results included detailed contributions from different types of electrons such as photoelectrons and Auger electrons. The calculations also considered energy absorbed internally by gold nanoparticles. Figure 9.17 shows the trajectories of electrons emitted from gold nanoparticles. The results showed that for 6 MV radiation, more than 100 WP of gold in cells was needed to generate a measureable enhancement, which was not clinically possible or achievable. For 300 kVp, only a 0.5 WP gold loading in water was needed to generate a measureable enhancement, which is possible in clinical settings. These results agree with those shown in Chap. 2.

Ngwa et al. [147] discussed a method of using gold nanoparticles to improve radiosurgery for neovascular age-related degeneration. Their modeling configuration is shown in Fig. 2.20 in Chap. 2. The authors reported an enhancement of 1.5 DEU
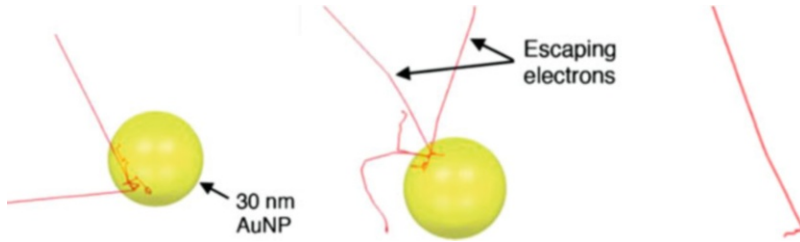
Fig. 9.17 Calculated electrons tracks in water from those emitted from a 30 nm gold nanoparticle irradiated by 6 MV X-rays (left and middle panels) and I-125 source (right panel, maximum 35 keV X-rays). One noticeable difference is that the track shown in the right panel is over 10 μm long (the 30 nm nanoparticle is invisible), whereas the tracks shown in the left and middle panels are only tens of nanometer long. (From Pignol et al. [145]. https://doi.org/10.1088/0031-9155/56/15/001. © Institute of Physics and Engineering in Medicine. Reproduced by permission of IOP Publishing. All rights reserved.)
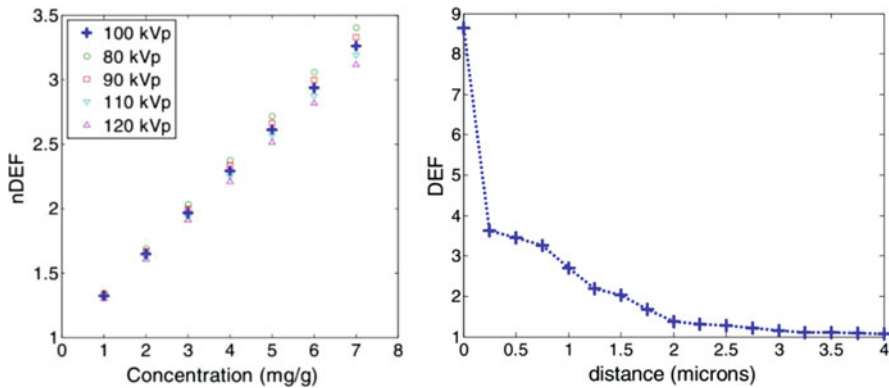
Fig. 9.18 Nuclear dose enhancement factors (nDEF) at different concentrations of gold calculated for gold nanoparticles irradiated with X-rays at energies between 80 and 120 kVp (left panel). The right panel shows the spatial profile of nDEF. (From Ngwa et al. [147]. https://doi.org/10.1088/0031-9155/57/20/6371. © Institute of Physics and Engineering in Medicine. Reproduced by permission of IOP Publishing. All rights reserved.)

per 0.5 WP gold in water for several X-ray energies between 80 and 120 kVp. This was equivalent to 3.0 DEU WP^{-1} unit weight percentage enhancement, which was higher than the typical 1.0 WP^{-1} enhancement based on type 1 physical enhancement or 1.4 DEU WP^{-1} physical enhancement. The increase was possibly due to type 2 physical enhancement, as the authors labeled the dose enhancement as nuclear dose enhancement factor (nDEF). Figure 9.18 shows the results of nDEF and dose enhancement factors near a 500 nm thick slab using 100 kVp X-rays, which clearly show type 2 physical enhancement.

In one of several publications, Amato et al. [149] estimated enhancement from gold in capillary phantoms under X-ray irradiation. They employed large amounts of gold, including 10, 20, 50, 100, and 200 mg/g in the phantom, which corresponded

to 1–20 WP gold loadings in tissue. They modeled several paths of gold diffusion through the capillary vessel as well as the depth effect. The X-ray energy was 150 kVp. The authors calculated unit WP enhancement for gold in phantom, and the results showed 0.65–1.0 DEU WP^{-1}. This range of magnitude of enhancement agreed reasonably well with the type 1 physical enhancement of nearly 1 WP^{-1} for 40 keV X-rays shown in Chap. 2.

Mesbahi et al. [150] theoretically modeled dose enhancement from gold nanoparticles under ionizing radiation of 50–120 keV to MeV photons. They obtained 0.4–2.7 DEU for monochromatic kilovoltage X-rays. The optimal energy was found to be 90 keV. For 0.7 WP, the enhancement was 1.0 DEU for 90 keV X-rays, corresponding to unit WP enhancement of 1.4 DEU WP^{-1}. This value is identical to the values obtained in Chap. 2 as well as those shown in this section. In contrast, the predicted enhancement was only 0.03 DEU for MeV X-rays, which also agrees with other results.

Li et al. [152] used three Monte Carlo packages, PENELOPE-2011, GEANT4, and EGSnrc, to simulate dose enhancement by gold nanoparticles. Four sizes of gold nanoparticles under X-rays at four energies between 60 and 150 kVp were used. Twenty water shells whose thicknesses are between 10 nm and 1 μm around the gold nanoparticle were used to evaluate the enhancement. All three packages predicted local enhancement near the surface of gold nanoparticles, as suggested in Chap. 2. The enhancement values predicted in this work were higher than those shown in Fig. 2.35. For a 100 nm diameter gold nanoparticle, over 1000 DEU enhancement was predicted within the first 10 nm water shell using PENELOPE. This high enhancement value was caused by the irradiation configuration of X-rays, illuminating only a small cross-section of water matching the size of gold nanoparticles, as explained in Fig. 2.19. Such artificial reduction of the denominator in enhancement calculation increased the magnitude of enhancement because enhancement is the ratio of energy deposition by electrons released from gold to from water as shown in Eq. 2.1. A significant reduction in the amount of energy deposited in water by electrons produced from X-rays interacting with water resulted in a significant reduction to the denominator.

Jeynes et al. [151] theoretically estimated the influence of secondary electrons emitted from gold nanoparticles in cells under both X-ray and proton irradiation. X-ray energy was up to 200 keV and proton energy was up to 250 MeV. Geant4.10. p01 together with CLHEP2.1.3.1 and ROOT 5.28.00 were used. RT112 bladder cancer cell line was used to obtain the experimental results. Significant increase of secondary electron emission was found with X-ray irradiation of gold nanoparticles, whereas only 10–20% increase was found with protons.

Xie and Li et al. [154] employed a PARTRAC code to simulate nuclear DNA damage and enhancement factor with 100 nm diameter gold nanoparticles positioning in a spherical cell and surrounding, but without entering, the spherical nucleus in the middle of the cell. 60–200 kVp X-rays were used in the simulation. The overall DNA strand break enhancement factor, however, was less than 20% (0.2 DEU) for 100 nm gold nanoparticles and 60 kVp X-rays. Higher enhancement occurred when the gold nanoparticles were on the nucleus surface than in the

cytoplasm. Pradhan et al. [29] compared enhancement by 1 and 7 mg/g Pt loadings in tumor phantoms under irradiation of 160 kVP and 6 MV X-rays. For 7 mg/g loading or 0.7 WP Pt in tumor, the enhancements were 0.81 DEU and 0.14 DEU for 160 kVp and 6 MV, respectively, calculated using a Monte Carlo method (Geant4). The unit WP enhancements were therefore 1.15 DEU WP^{-1} at 160 kVp and 0.2 DEU WP^{-1} at 6 MV. These values generally agreed with the results shown in Chap. 2.

Moshirian et al. [157] theoretically studied homogeneous and inhomogeneous distribution of gold in tumors deep in tissues. The authors found that 55 keV X-ray energy was optimal for maximal dose enhancement in the tumor. The maximum enhancements in various settings were much greater than approximately 1 DEU WP^{-1}. For example, the highest enhancement was 17.5 DEU in the inhomogeneous loading of 0.7 WP gold in water phantoms. These results demonstrate the utility of using type 2 physical enhancement to damage nearby targets.

Zygmanski et al. [158] reviewed the modeling of dose enhancement calculations in clinical X-ray irradiation settings. The authors provided a general discussion of the enhancement and compared the results of dose enhancement ratio (DER) obtained using two theoretical packages, CEPXS and GEANT4, and found the two results agreed with each other. For a 100 nm gold slab under 100 keV X-ray irradiation, an experimental condition reachable with metal implants, DER was as high as 30 DEU. DER at the surface of the gold slab was 110 DEU for 20 keV X-rays, which suggested that the enhancement was largely type 2 physical enhancement.

Retif et al. [61] described a new theoretical method that helped rank the effectiveness of organometallic nanoparticles in enhancing radiation effects, which were not limited to DNA damage originated from radiation induced energy deposition. In addition, the authors considered irregular distributions of nanoparticles in cells, similar to what Moshirian et al. observed. Although the authors claimed that the method was not to estimate the enhancement itself, they also asserted that the outcome agreed with the results of in vitro measurements. Their results suggested that the ranking of the nanoparticles should be 20 nm iron nanoparticles (best), 20 nm gold nanoparticles (middle), and 50 nm gold nanoparticles (worst).

Thomson et al. [159] investigated theoretically the influence of multiple cellular structures on enhanced energy deposition in nuclei. The geometric arrangement was similar to what was known as the lattice effect described by Guo et al. [160]. No nanoparticles were used. 20–370 keV X-rays were considered. The results and method are applicable to the cases where nanoparticles are embedded in the cells.

Schuemann and Ye et al. [156] theoretically studied enhancement of energy deposition in two types of cell by four sizes of gold nanoparticles coating the surface of the cells. The enhancement was caused by local effect model (LEM) and was close to type 2 physical enhancement defined in Chap. 2. Only a single cell was considered in this study, so the configuration was set up to study type 2 physical enhancement. Three energies of X-rays at 51 keV, 150 kVp, and 6 MV were used. The sizes of gold nanoparticles were 2, 15, 20, and 50 nm. The gold nanoparticles were all outside the cell. The results showed less than 1.0 DEU for 2 WP gold around

the cells for both 51 keV and 150 kVp X-rays and negligible enhancement for 6 MV X-rays. These results are in agreement with those obtained by others as shown in Chap. 2.

Attili et al. [155] theoretically simulated the enhancement of energy deposition by electrons in the nuclei of MDA-MB-231 cells. The authors also used LEM to describe their scenario, which was similar to type 2 physical enhancement described in Chap. 2. Gold nanoparticles were 2 nm in dia., and a Monte Carlo method using Geant4 version 10.1 toolkit was employed to simulate the energy deposition. X-rays were 160 keV, and 6 and 15 MV. The results showed that ionization probabilities per Gy for these 2 nm gold nanoparticles in water at these energies were 4.35×10^{-7}, 2.35×10^{-7}, and 2.25×10^{-7}, respectively. The authors did not specify whether these ionization events were ionization of core electrons. The first value was similar to what is given in Chap. 2. However, the last two values were high, which were within a factor of two of that at 160 kVp. Given the fact that X-ray absorption by gold at 6 MV was nearly three orders of magnitude less than at 160 kVp, the ionization for these small nanoparticles at 6 and 15 MV must be caused by charged particles generated from Compton scattering or pair production when X-rays interacted with water. Under such conditions chemical enhancement described in Chap. 3 should dominate because water absorption of X-rays dominated. If this is correct, then physical enhancement at these high MV X-ray energies should be much less than that by X-rays at keV energies, as reported in a large number of studies. The authors then compared the simulated survival fraction data with the experimentally measured results and found a good agreement at all these three energies.

The results shown in this section confirm that the magnitude of originally conceived physical enhancement in the form of the sum of average types 1 and 2 physical enhancement can only produce an approximately 1.4 DEU WP^{-1}. Potential medical applications would follow this guideline if physical enhancement is the source of enhancement. When much higher physical enhancement values are needed, then it is necessary to use peak type 2 physical enhancement described in Chap. 2, which can reach 10–50 DEU or even higher but requires large nanoparticles or aggregates of nanoparticles. However, such enhancement only exists in a region close to the surface of nanoparticles.

9.5   Treatment of Cancer (In Vitro) Cell Lines with Nanomaterials and X-Rays

9.5.1   Survey of In Vitro Work

Many efforts have been devoted to studying the enhancement of damage to cancer cells. Although cellular work is not as impactful or direct as animal models or even human clinical trials, cellular work does provide the necessary foundation and guidance for animal and clinical work. Logically there have to be some

understanding about the chemical systems such as nanomaterials even before the cell work, thereby fundamental chemical and physical works are needed before the cell work. The approach of going directly to animal may leave many issues unresolved, but at the same time, such an approach with positive results may inspire basic work. The significance of the cell work is that it bridges fundamental studies and animal and clinical work.

Chapter 8 covers cell work using healthy cells. In this chapter the target is cancer cell lines. The fast-growing nature of cancer cells should make them more susceptible to enhanced radiation effects, which is shown in Table 9.1. However, when compared with Table 8.4, the difference is not obvious.

Most of the discussion on enhancement effects cites the "traditional" enhancement or physical enhancement of the effectiveness of X-ray irradiation by nanoparticles under X-ray irradiation. This type of enhancement leads to release of electrons, followed by increased energy deposition in cells, which then converts to generation of additional reactive oxygen species. On the other hand, work has begun to create next generations of chemical and nanochemical systems following X-ray nanochemistry principles such as using triggered release of targeted delivery of highly potent drugs for ultimate enhancement of cell killing. In vitro work help test these promising possibilities. The triggered release results are given in Sect. 9.8.

Table 9.7 shows the groups that used cell work to examine the effect of nanomaterials. Another way to look at these results is that they are the applications of X-ray nanochemistry in damaging tumor cells by X-rays assisted with nanomaterials. X-ray-triggered release of drugs is not shown here. Table 9.7 also lists parameters important to performing cell work. The information includes cell lines, assay types, uptake/loading and nanoparticle compositions, X-ray dose and energy, enhancement, and the groups that performed the study. These parameters are described in the text as well.

Most work used purchased gold nanoparticles to test the damaging power of nanomaterials to cells under X-ray irradiation. More advanced nanomaterials are being synthesized to improve targeting tumor cells and damage because the unit WP enhancement from gold or other elements is usually fixed. Primitive nanoparticles only provided limited benefits and will not be commercially competitive, and future cancer treatment will have to use more advanced nanomaterials or mechanisms to assist cancer treatment. Nonetheless, the work published to date has helped establish a foundation for future endeavors.

The cited reasons in the literature for damage to cancer cells have generally been physical enhancement, which then causes the subsequently increased production of reactive oxygen species (ROS) in tumor cells. To date little effort had been devoted to demonstrating the existence of other damaging mechanisms in cells although those alternative mechanisms were suggested in several reports. For instance, biological enhancement is described in Chap. 4. There is also the possibility of chemical enhancement shown in Chap. 3. These possible mechanisms will have to be investigated in the future with improved synthesis of nanomaterials and more advanced instruments and methodologies.

Table 9.7 In vitro studies of enhancement of radiation damage of cancerous cells by nanoparticles under X-ray irradiation. The results are arranged alphabetically for the corresponding authors

Cell line	Assay	Uptake (WP)/ (#NPs)	X-ray Energy/dose (Gy)	NMs/surface	Enh (DEU)	Ref.
Colon cancer cells (HT-29)	MTS	>5	9 MV/8	50 nm AuNPs	0.90	Arab-Bafrani et al. [39]
DU-145, MDA-231-MB	Clonogenic, γ-H2AX	–	160 kVp/2	1.9 nm AuNPs	-0.19–0.97	Butterworth et al. [45]
MCF-7 breast cancer	MTT	$0.3/(1.21 \times 10^5)$	200 kVp, 1.3 MeV/ 10	10 nm AuNPs/cysteamine, Glu		Chen et al. [65]
MCF-7	Clonogenic	–	Cs-137/4	2.0–2.5 nm AuNPs/SUMO2/3	0.49, 7.88	Chen et al. [44]
HepG2	Clonogenic, γ-H2AX	0.00173	50 kVp/1–6	16 nm AuNPs/tirapazamine-conjugated PEG	0.25	Chen and li et al. [37]
PC3	MTT	–	120 kVp/2	4 nm Cu&Co doped ZnS/PEG w/wo TBrRh123	0.03–1.4	Chen et al. [161]
HeLa, EMT-6	MTT, clonogenic	$/10^9$	73 keV[a]/10	FeOxNPs	0.33–0.6	Chen and Margaritondo et al. [162]
HeLa, NIH3T3	MTT	3.6	–/8	500 Se NPs/PEG	0.5	Chen et al. [69]
PC3				Ce doped LaF_3		Chen et al. [163]
HeLa	γ-H2AX, clonogenic	0.7	105 keV, 6 MV/	14–74 nm AuNPs/citrate	0.66, 0.17	Chithrani et al. [35]
MCF-7, SKOV-3	Cell viability assay	–	No X-ray irradiation experiment	10.4 nm AuNPs/lipoic PAA with cisplatin	–	Cook et al. [48]
A549	–	–	250 kVp/3 Gy	1.4 nm AuNPs/pHLIP	<10%	Cooper et al. [67]
MDA-MB-231	γ-H2AX	0.7	20–70 keV/1.5	1.9 nm AuNPs	0.95	Currell et al. [164]
A549	Clonogenic, γ-H2AX, 53BP1 foci	–	6 MV/8	Bi^{3+} on 5 nm $Gd_2O_3NP@SiO_2$/ DOTAGA	1.0	Detappe & Berbeco et al. [165]
U87	γ-H2AX, clonogenic	Optical	^{60}Co	3 nm GdNPs	0.14–1.83	Falk et al. [166]

RG2 glioma	Mobility	TEM	125 keV	1.9 nm AuNPs		Geso et al. [58]
Panc 1 cells	MTS	–	6 MeV/6	12 nm Au NPs/ PEG and verteporfin	0.14	Goldys et al. [167]
Glioma C6	CM-DCF fluorescence	1 (attenuation of X-rays)	4 MeV/3	<5 nm SiNPs	6	Gonzalez & Kotler et al. [19]
HeLa	MTT, clonogenic	–	120–250 kVp, ^{60}Co/2 Gy	AuNPs 47 nm/FA/4-ATP	0.35–0.64	Hashemi et al. [73]
CT26 colorectal	Clonogenic	$0.1/(1 \times 10^6)$	6 MV/2	4.7 nm AuNP/PEG	0.13	Hwu et al. [22]
EMT-6 and CT26	MTT, clonogenic, γ-H2AX	N/A	6.5, 8, 73 keV, 6 MeV/10	AuNP	<0.45	Hwu et al. [28]
MDA-231 breast cancer	Clonogenic		160 kV, 6, 15 MeV/6	1.9 nm AuNPs	0.41	Jain et al. [50]
A549 lung cancer	MTT, clonogenic	–	6 MV/6	Cisplatin nanoliposomal	0.5	Jiang et al. [15]
Du-145	Methylene blue	–	160 kVp/0–25	60 nm C-Ag/PEG	0.6	Juzenas et al. [24]
HeLa, PC3	MTT	–	200 kV (average 60–70 keV)/1,5–6	8–9 nm Eu or Gd doped ZnO	2	Kharrazi and Amani et al. [170]
Du-145	Colony formation assay	2.7×10^3 (Fe)	6 MV/2–8	20 nm Fe_3O_4/ amino-group dextran	0.2	Khoei et al. [171]
CT26 colorectal	MTT	3–17/	7.1 keV/5, 20	10.6 nm FeONP/alginic acid	–	Choi et al. [21]
HTB-72 skin melanoma	Clonogenic	–	150 kVp, 450 kVp/8	1.9 nm (water-soluble organic shell), 50 nm Au NPs	0.12–0.62	Kim et al. [40]
9 L gliosarcoma	Clonogenic	–	10 MV/8	Rare earth (0.05–0.5%)	0.33	Konstantinov et al. [172]
Caco-2, MCF-7, 3 T3	DCF	–	120 kV/1–3	9–20 nm $(\gamma\text{-}Fe_2O_3)_{1-x}(Fe_3O_4)_x$ (SPIONs)/malate or citrate	0.11–3.86	Kryschi et al. [46]
HeLa	Clonogenic, MTS	Confocal imaging	220 kVp	2–3 nm AuNP/PEG	2.8	Kumar et al. [173]
MCF-7, T47D, MDA-MB-231	Clonogenic	$30/(1.6 \times 10^6)$	300 kVp/8	30 nm AuNPs/CPP-PEG	1.3–2.1	Latimer [52]

Table 9.7 (continued)

Cell line	Assay	Uptake (WP)/(#NPs)	X-ray Energy/dose (Gy)	NMs/surface	Enh (DEU)	Ref.
Hela	Colony formation essay	–	^{137}Cs (662 keV)/1–8	4.8, 12.1, 27.3, 46.6 nm Au NPs/PEG	0.41	Liang et al. [141]
HT1080 fibrosarcoma	Clonogenic	TEM	200 keV, 1 and 6 MeV/8 or 2×4	MBTXR3 (50 nm HfONP)/biocompatible	0.12 (at 10% SF)	Maggiorella et al. [10]
F98	Alexa annexin V/dead cell apoptosis kit	–	90 keV/0–20	3 nm GdNPs (AGuIX®)	0.045	Martinez-Rovira et al. [172]
MDA-MB-231 breast cancer		0.88/(1.3 × 10^8)	6, 15 MeV/5	2 nm AuNPs	0.18–0.24	McMahon et al. [70]
HeLa	WST-1/CFU		100 kV/5 Gy	TiO$_2$, ZnS:Ag, CeF$_3$, CdTe QDs	1.0	Misawa et al. [173]
HeLa	γ-H2AX	–	28 keV/1.0	50 nm AuNPs/methyl polymer	0.7–1.3	Ngwa et al. [174]
HCT116 colorectal	γ-H2AX	3.3	80 kV/10	3 nm AuNPs/tiopronin	1.0	Paquette et al. [34]
HeLa	MTT	0.1	6 MV/8	3 nm FePtNPs/cysteamine	<0.1	Quan and Jiang et al. [175]
HeLa	MVP	–	5–60 keV (max intensity at 10 keV)	La in micelle (Hyp-GdEuC12 micellar particles)	No cell damage experiment	Réfrégiers et al. [178]
DU-145 prostate cancer	MTT, CG	0.023/(6.7 × 10^4)	200 kVp/2	7 nm AuNPs/Glu	0.5–1.4	Roa et al. [64]
DU-145	MTT, CG	0.024 (7 × 10^4)	1176 keV/2 and 4	7 nm AuNPs/Glu	0.2–0.35	Roa et al. [66]
A549	Clonogenic	–	6 MV/2	SiC (20 nm)/SiO x (20 nm thick) nanowire/porphyrin	2.53	Salviati et al. [177]
MIAPaCa-2	Colony formation essay, γ-H2AX	–	150 kVp with 1 mm Al filter/0–5	50–100 nm TiOxNPs/PAA	0.40 (at 10% survival)	Sasaki et al. [178]

Cell line	Assay	Concentration	X-ray	Nanomaterial	Enhancement	Reference
H460	Clonogenic	–	6 MV/8	CdSe/ZnS/PEG	0.2	Sheng et al. [33]
K562	Nuclear diffusion factor	None	40 kV/3	13 nm AuNPs microdisks	<0.4	Su et al. [41]
MDA-MB-231	Clonogenic	–	225 kVp, 6 MV/6	100 nm hollow Au (inner 50 nm)/PEG	0.5, 0.1	Sun, Mao and Hao et al. [181]
T98G, Du145, MDA-MB-231	Clonogenic	0.07–1.5/ (2.2×10^8)	/8	1.9 nm AuNPs	0.14–0.92	Taggart et al. [26]
9L gliosarcoma cells	Clonogenic	–	125 kVp, 10 MV/1–8	50–70 nm Bi_2O_3 NPs	0.48, 0.25	Tehei et al. [12]
HT1080 fibrosarcoma	Clonogenic, γ-H2AX	–	150 kVp/6	Micelles of 1.9 nm AuNPs/PEG	0.7	Tsourkas et al. [38]
PC-3	Methylene blue	–	160, 320 kVp/2	12 nm Y2O3 NPs/TAT peptide or psoralen-functionalized TAT	0.92, 1.44	Vo-Dinh et al. [57]
U251	CCK-8 assay (cell viability)	–	6 MV/4	15.38 nm Ag NPs/PVP	0.5	Wen and Gu et al. [60]
HepG2 liver cancer	MTT	–	^{60}Co/5	Se aggregates/DOX	0.2	Xu and Zhang et al. [9]
A549, KB	XTT	6/	100 kV/10	4 nm AuNPs/Glu, FA	2.6–15[b]	Yan et al. [16]
4 T1	Clonogenic	5 µg/mL	/0–8	3.6 nm Bi NPs/PEG, Lyp-1	0.26	Yang and li et al. [71]
4 T1	MTT, clonogenic, γ-H2AX	–	/2–8	100 nm Au (20 nm) @FeS/PEG	0.37	Yang, Wu and Yang et al. [11]
MCF-7	Clonogenic	0.00075–0.0315	6 MV/2.25	2 nm Au NPs/glutathione(GS) or PEG	–0.16, 0.44, 0.27–0.50	Zheng et al. [180]
K562	–	–	662 keV/20–100	14–16 nm AuNPs	–	Zhang et al. [181]

NPs nanoparticles, *NMs* nanomaterials, *AuNPs* gold nanoparticles, *CG* clonogenic, *Glu* glucose, *PEG* polyethylene glycol, *SF* surviving fraction, *FeONP* iron oxide nanoparticles, *DOX* doxorubicin, *FA* folic acid, *pHLIP* pH-sensitive low-insertion peptide, *4-ATP* 4-aminothiophenol, *DOTA* tetraazacyclododecane tetraacetic acid

[a]Reported by the authors

[b]Calculated enhancement based on the reported data

From the presentations given in this section, it will become clear that uptake is critical to understanding the origin of enhancement. Uptake information, however, is not available in many studies, and even with uptake data, the measured enhancements could not often be satisfactorily explained by the added nanomaterials through only physical enhancement. As stated before, incubation concentration is not the same as uptake concentration, as cells often regulate the uptake of nanoparticles depending on the size, shape, and surfactants of nanomaterials.

9.5.2 Enhancement of Damage to Tumor Cells Assisted by Nanomaterials under X-Ray Irradiation

The published results are reviewed chronologically, following the same protocol used in other chapters in the book. Publications from the same research group are discussed together.

Publications of studying cancer cell damage assisted by nanomaterials under X-ray irradiation began to appear in the literature in 2007. Misawa et al. [175] investigated HeLa cell damage under X-ray irradiation using several nanomaterials to enhance the effectiveness of X-ray irradiation. The nanomaterials included TiO_2 nanoparticles, ZnS doped with Ag particles, CdTe quantum dots, and CeF_3 particles. X-ray energy range was between 20 and 170 keV and X-ray dose was up to 5 Gy. No quantitative uptake data was available although images obtained in this work do suggested efficient uptake of CdSe quantum dots. The enhancement was significant as well—the results showed that survival fraction dropped down to 10% with only 2–3 Gy of 100 kVp X-rays, and LD_{50} was around 1 Gy for quantum dot-treated HeLa cells, which suggested a greater than 1.0 DEU enhancement for these nanoparticles.

Roa and Xing et al. [64] used gold nanoparticles in prostate cancer cells to demonstrate the utility of gold nanoparticles in cancer therapy. The authors showed that glucose-coated gold nanoparticles improved the uptake over other nanoparticles such as neutral gold nanoparticles. The size of their nanoparticles was ca. 7 nm in diameter. The authors used DU-145 prostate cancer cell line. The radiation was 200 kVp X-rays and dose was 2 Gy. The uptake data showed 6.73×10^4 gold nanoparticles per cell, which was equivalent to 0.023 WP of gold in water. This would only give rise to a 2–3% increase in radiation damage if physical enhancement dominated. Radiation alone inhibited 16% of the tumor cell growth, whereas inhibition increased by 30% and 45% when gold nanoparticles were added, suggesting a 1.4 DEU enhancement. This experimental measured enhancement was much higher than the value predicted by physical enhancement shown in Chap. 2. The authors did not predict the enhancement themselves. However, the authors did note that tumor killing did not completely correlate with the uptake concentrations of nanoparticles. The observed results might be explained by biological enhancement because the size of nanoparticles was 7 nm, making it possible for

these nanoparticles to enter the nuclei, although chemical enhancement could not be ruled out either.

Roa and Xing et al. [66] studied Du-145 incubated with glucose-coated 7 nm gold nanoparticles and irradiated with γ-rays emitted from ^{137}Cs. The uptake was determined to be 7.0×10^4 nanoparticles per cell, which was only 0.024 WP, similar to what mentioned above. The observed enhancements using MTT assay at 2 and 4 h after irradiation were 0.22 and 0.35 DEU. Hence the enhancement per unit WP was 9 and 16 DEU WP^{-1}, much higher than the average 1.0 DEU WP^{-1} offered by physical enhancement for keV X-rays. This implied that type 2 physical enhancement or other categories of enhancement such as chemical or biological enhancement might play an important role.

Chen and Xing et al. [65] studied the enhancement of radiation damage to breast cancer cell line MCF-7 by 10 nm gold nanoparticles coated with several different surfactants. Among the ligands, cysteamine was found to generate maximal uptake, reaching 1.2×10^5 gold nanoparticles or 0.03 WP of gold in a cell. However, glucose-covered gold nanoparticles did not have the highest uptake (3.0×10^4) but caused the most damage to the cells. The X-ray energy used in the work included 200 kVp X-rays as well as γ-rays from ^{131}Cs and ^{60}Co sources. The total dose was 10 Gy for each irradiation and the assay was MTT. 200 kVp was the most effective X-ray energy for generating enhancement. These results suggested that a different enhancement mechanism from physical enhancement should be in control. Figure 9.19 shows the uptake and cell viability results.

Hwu et al. [22] used 4.7 nm gold nanoparticles for the purpose of enhancement of radiation damage to mice tumor cells CT26. They observed approximately 1×10^6 gold nanoparticles per cell, which corresponded to 0.1 WP of gold in those cells. Synchrotron X-rays between 8 and 15 keV with an average of 12 keV were used and an approximately 0.13 DEU enhancement was observed, which gave rise to a 1.1 DEU WP^{-1} unit WP enhancement. Hwu et al. [28] investigated enhancement by PEGylated gold nanoparticles under the irradiation of several X-ray sources,
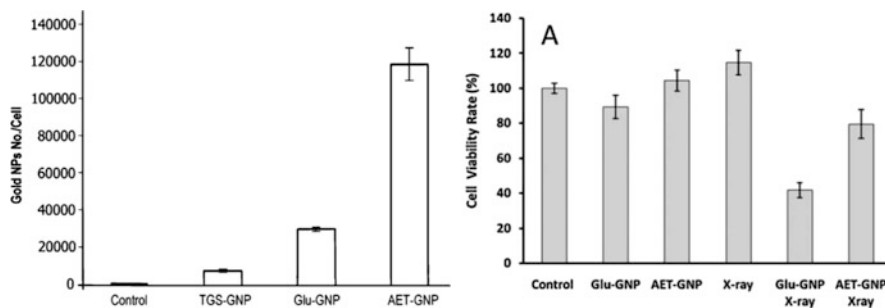
Fig. 9.19 Uptake (left panel) and enhancement results (right panel) using MCF-7 breast cancer cell line and 200 kVp X-rays with 10 nm gold nanoparticles. Damage by Glu-GNP was the highest even though uptake of AET-GNP was the highest, proving uptake was not the only parameter that controlled the outcome. (Reprinted with permission from Chen and Xing et al. [65]. Copyright (2008) by John Wiley and Sons.)

including a Cu Kα X-ray source, a commercial biological radiator with an average X-ray energy of 73 keV and a 3 MV X-ray source. Compared to X-ray irradiation alone, survival rates were lowered by up to 45% for cells incubated with gold nanoparticles and irradiated with X-rays.

Sheng et al. [33] showed the results of their study of quantum dots conjugated with photofrin under 6 MV X-ray irradiation. H460 cells were used in the test. The authors suggested that energy transfer efficiency approaches 100% from the excited quantum dots to a high coverage of photofrin molecules on the surface. Increased cell damage was observed with both radiation and nanomaterials treatment.

Geso et al. [58] employed microbeams from synchrotron X-rays to irradiate gold nanoparticles and endothelial cells deposited on a flat surface. The average X-ray energy was 125 keV. 1.9 nm gold nanoparticles and rat glioma RG2 cells were used. The microbeam irradiation was beneficial for the healthy cells near the tumor cells to recover, similar to "wound healing," a process that is not well understood. The authors confirmed that healthy cells tend to spill to the irradiated strips very quickly and found that tumor cells also tended to help neighboring dying cells, but at a much slower rate than the healthy cells. This finding suggested that at the tissue level, microbeam approach might be more beneficial than at the cellular level.

Zhang et al. [183] investigated interactions of gold nanoparticles with K562 cells under irradiation of 662 keV X-rays. The dose range was 2–10 kR or 20–100 Gy. Surface plasmon resonance profiles were measured to determine the impact of X-ray radiation on the nanoparticles. The authors argued that radiation produced species such as electrons and radicals changed the plasmonic response. Cytotoxicity was measured with different incubation concentrations, although no direct X-ray irradiation of gold nanoparticles in K562 cells were carried out.

Since 2009, as described in Sect. 9.6.3, Nanobiotix Inc. has been working on a nanoparticle-based drug that can absorb X-rays and destruct tumor. The company used at least two cancer cell lines, HC116 and HT1080. A patent issued to Levy et al. [184] had a priority date of June 5, 2008. The nanomaterials were known to be crystalline HfO_2 nanocrystals. X-rays were 200 kVp with a 0.2 mm Cu filter. For cells, 4 Gy of radiation was used. Similar studies were carried out by Maggiorella et al. [10] in which the two types of cells were irradiated with 0.38 MeV, 1.25 MeV, and 6 MV X-rays for 8 or 2×4 Gy. The estimated enhancement was 0.12 DEU based on clonogenic assay results.

Butterworth et al. [45] studied dose enhancement using nine cell lines and several endpoints including DNA damage. Their dose enhancement factor was the ratio of 2 Gy to the dose required to produce the same surviving fraction in the presence of gold nanoparticles as that of 2 Gy radiation alone. This was one of the two ways to calculate enhancement using the surviving curve shown in Fig. 9.1. The X-rays were 160 kVp. The incubation concentrations were between 10 and 100 μg/mL of 1.9 nm gold nanoparticles. They observed cell dependent dose enhancement factors. Except for Agg-1552B and T98G, higher incubation concentrations (not the uptake) did not yield higher magnitude of enhancement. Not all the cells experienced enhancement. This study demonstrated the need for scrutiny of enhancement mechanisms as well as the experimental protocol. The results are listed in Table 9.8, which shows the

Table 9.8 Dose enhancement results obtained by Butterworth et al.

Cell	DEF (10 μg/mL)	DEF (100 μg/mL)
AGG-1552B	1.16	1.97
Astro	1.04	0.96
DU-145	0.98	0.81
L132	0.86	0.87
MCF-7	1.41	1.09
MDA-231-MB	1.67	1.11
PC-3	1.07	1.02
T98G	1.30	1.91

Adapted from Butterworth et al. [45]

enhancement is from anti-enhancement (-0.19 DEU) to an enhancement of 0.97 DEU. The values listed in the table are DEFs, which is the relative enhancement.

Chen and Margaritondo et al. [162] studied cell survival after irradiating HeLa and EMT-6 cells incubated with iron oxide nanoparticles decorated with dextran molecules. The uptake of nanoparticles was studied, both qualitatively with TEM imaging and quantitatively with ICP-MS. The enhancement, however, was less than 0.1 DEU. Kong et al. [185] used gold nanoparticles to enhance the efficacy of radiotherapy of ovarian cancer cells. The authors used both X-ray and γ-rays and glucose-coated as well as naked gold nanoparticles. Ten sizes of gold nanoparticles between 12 and 17 nm were used, and 13 nm gold nanoparticles were found to produce the highest uptake, and 160,000 nanoparticles were found per cell, corresponding to a 0.4 WP loading of gold in the cell. LD_{50} for the cell was 5 Gy, but the authors used up to 25 Gy in their work. Glucose-coated gold nanoparticles were found to generate better uptake than the naked nanoparticles. An enhancement between 0.2 and 0.4 DEU was measured, suggesting that the cause for the enhancement could come from physical enhancement by 0.4 WP gold.

Chithrani et al. [35] used gold nanoparticles of different sizes, ranging from 14 to 74 nm in diameter, in their radiation dose enhancement study. The gold nanoparticles were synthesized with a citrate reduction method, and no further treatment was performed to the nanoparticles. Uptake of gold nanoparticles into cells was measured, and incubation of 8 h was found adequate. The highest uptake was achieved for 50 nm gold nanoparticles, and 6000 gold nanoparticles per cell were detected. This loading corresponded to a 7 mg/g or 0.7 WP of gold in the cell if the cell mass is 1 ng. HeLa cells were used and γ-H2AX assay was used to detect cellular DNA damage. Figure 9.20 shows the results of uptake (left panel) and survival (right panel). Using the doses at 0.1 surviving fraction, the enhancement is estimated to be 0.5 DEU. Chithrani et al. [186] improved the uptake of 14 nm gold nanoparticles by conjugating peptides to the surface of the nanoparticles. The uptake was improved from 1000 nanoparticles to 2500 nanoparticles per cell. Increased damage to DNA was observed with the peptide-conjugated 14 nm gold nanoparticles.

The results of nuclear DNA damage obtained by Chithrani et al. in terms of double-strand breaks by gold nanoparticles incubated with HeLa cells are shown in Fig. 9.21. Based on two assays of γH2AX and 53BP1, the enhancement of DSBs
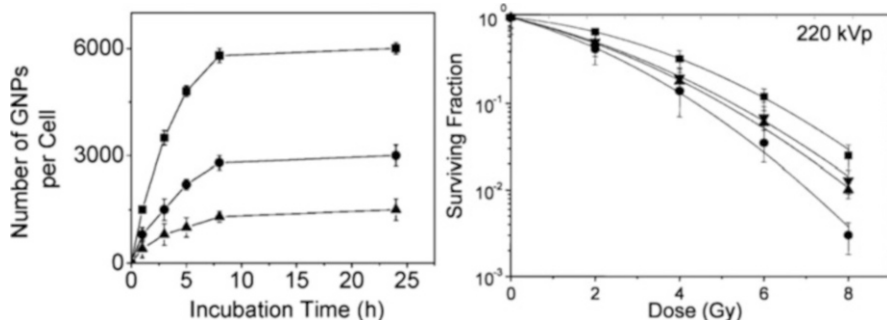
Fig. 9.20 Results of three size gold nanoparticles for enhancement. 14 (triangle), 50 (round), and 74 (square) nm gold nanoparticles were used. The left panel shows the uptake data and the right shows the survival data. An enhancement of 0.5 DEU is deduced from the surviving data using doses at 10% fraction. (Reprinted with permission from Chithrani et al. [35]. Copyright (2010) by Radiation Research. All rights reserved.)

Fig. 9.21 DNA damage by gold nanoparticles and X-ray radiation. More damage occurred to DNA when the cells were irradiated 4 h after incubation than 24 h. (Reprinted with permission from Chithrani et al. [35]. Copyright (2010) by Radiation Research. All rights reserved.)
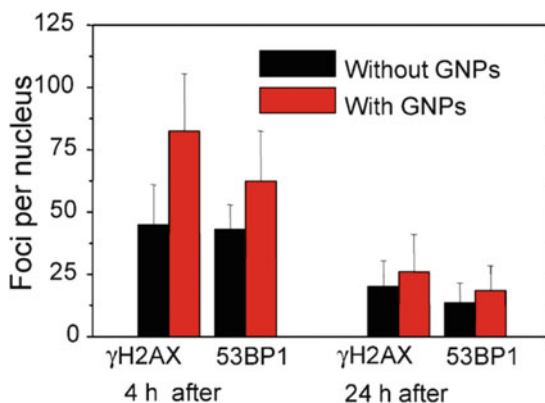
was between 0.1 and 1.0 DEU. The results suggested a maximum enhancement of about 1.0 DEU was reached when irradiation was given 4 h after incubation. It is interesting to note that DNA damage was reduced to half in the control sample 24 h after incubation, as shown in Fig. 9.21.

Jain et al. [50] used linear accelerators (LINAC) at 6 and 16 MeV and 160 keV X-rays to irradiate MDA-MB-231 and two other cell lines for enhancement. The cells were exposed to up to 6 Gy of radiation. LD_{50} dose was about 4 Gy and 1.9 nm gold nanoparticles were used. No uptake results were shown. At 4 Gy dose, the surviving fraction (SF) was about 40%. With gold nanoparticles, the enhancement to the damage was 0.05–0.45 DEU for 160 kV and negligible at 6 MeV. The results are given in Fig. 9.22.

Chen et al. [44] reported the damage to MCF-7 cells by gold nanoparticles under X-ray irradiation. Their intended damage mechanism was through blocking the DNA repair pathways. The gold nanoparticles were 2.0–2.5 nm and were conjugated with surface ligands bound to the DNA repair proteins. With 4 Gy of radiation and incubation concentration of 0.1 μM, the damage was increased by approximately 30%.
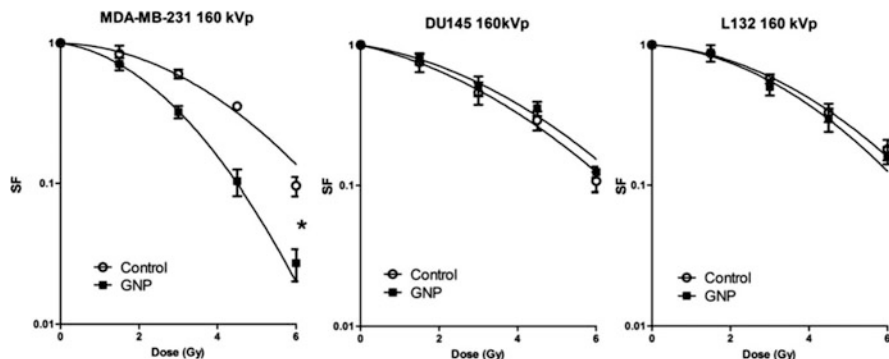
Fig. 9.22 Damage to three cell lines using 1.9 nm gold nanoparticles under irradiation of 160 keV X-rays. Enhancement is observed only with MDA-MB-231 cells. (Reprinted from Jain et al. [50]. Copyright (2011) with permission from Elsevier.)

Jiang et al. [15] conducted a study of A549 human lung cancer cell damage using cisplatin embedded nanoliposomes under irradiation of up to 6 Gy of 6 MV X-rays. The survival fraction was 2–3% at 6 Gy and LD_{50} was 1.5 Gy. Upon adding the formulated drug, LD_{50} decreased to 1 Gy, producing an enhancement of 0.5 DEU. In their in vivo data, the authors used 6 Gy and formulated nanodrugs and observed delayed growth of tumors. The in vivo results will be shown in the next section.

Yan et al. [16] found that dual ligand-coated gold nanoparticles increased the uptake of nanoparticles by cells. The two ligands on the gold nanoparticles were glucose (Glu) and folic acid (FA). The average size of the gold nanoparticles was 4–5 nm in diameter, although there were much smaller gold nanoparticles in the mixture. The increase of uptake due to the coverage of FA on the nanoparticles was 3.9- to 12.7-fold. The experiments were done using cell lines KB and A549. The highest uptake was 6×10^{-11} g in a 10^{-9} g cell, which was equivalent to 6 WP gold in water. X-rays were from a cabinet source operated at 100 kV, 3 mA and at 1.46 Gy/min dose rate. The cells were exposed to 10 Gy of radiation. If only physical enhancement existed, then an enhancement of 6–8 DEU was expected. The authors found that A749 cell line responded poorly to treatment with gold nanoparticles, whereas KB responded favorably. Viability of A549 cells was barely reduced after irradiation with 10 Gy of radiation. Viability of KB did not decrease with only X-ray irradiation. With 6 WP gold, cell viability was only reduced to 80% for A549 and 20% for KB. The results clearly showed the disparity of cells vulnerability toward X-ray radiation or reactive oxygen species generated from X-ray irradiation.

McMahon et al. [70] studied the nanoscale energy deposition within cells using 2 nm gold nanoparticles and 6 and 15 megavoltage X-rays. Breast cancer cell line MDA-MB-231 was used. 1.3×10^{8} gold nanoparticles were found in each cell, corresponding to a loading of 0.88 WP. No toxicity data was available. The enhancement was 0.18 DEU for 15 MeV X-rays and 0.24 DEU for 6 MeV X-rays. These give a unit WP enhancement of 0.25 DEU WP^{-1} for these high-energy X-rays. The authors also measured the X-ray and electron energy spectra beneath a 5 cm water sample for 6 MeV X-rays. They then used the electron energy spectra to
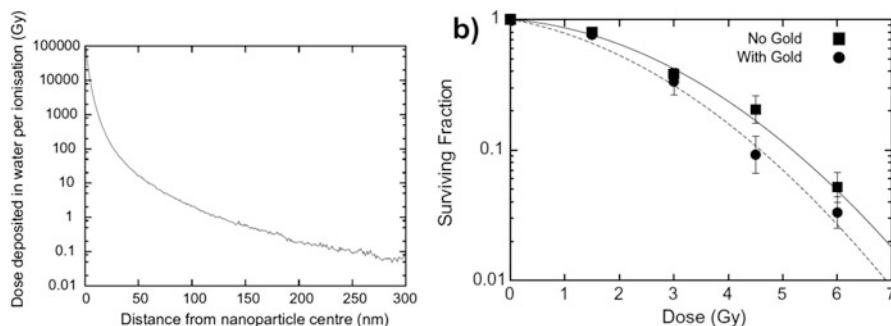
Fig. 9.23 Radiation enhancement by 2 nm gold nanoparticles under 15 MeV X-ray irradiation. The results show a small enhancement of 0.18 DEU, which agreed with the theoretically predicted physical enhancement for X-rays at this energy. (Reprinted from McMahon et al. [70]. Copyright (2011) with permission from Elsevier.)

calculate energy deposition in water around 2 nm gold nanoparticles. For irradiation with 1 Gy of 6 MeV X-rays, only 2.3×10^{-7} gold nanoparticles were directly ionized. This meant there were about 150 ionized gold nanoparticles per cell with 5 Gy of radiation using the uptake data obtained by the authors. The authors also calculated energy deposition profiles for the gold nanoparticle and found that the magnitude of energy deposition decreases exponentially as a function of distance from the nanoparticle. The decay constant was approximately 5.4 nm based on their calculation results, which was similar but greater than the one obtained by Guo et al. [187]. The left panel of Fig. 9.23 shows the local effect of energy deposition, and the right panel shows the clonogenic results. There was a reasonably good agreement between the theoretically predicted physical enhancement and measured enhancements, as shown in the right panel of Fig. 9.23. As pointed out in Chap. 4 and other places in the book, physical enhancement may not generate the measured enhancement when large amounts of small catalytically active gold nanoparticles are used. It will be interesting to see in the future whether the agreement observed here is coincidence.

Xu and Zhang et al. [9] investigated a doxorubicin trapping diselenide polymer aggregate under γ-ray irradiation. They used HepG2 cell (human liver cancer) line in their work. The authors studied the drug release under X-ray irradiation. The results are discussed in Sect. 9.7 as well. After 5 Gy of irradiation, nearly 20% reduction in cell viability was observed. The authors quantified hydroxyl radical generation and observed an increase of hydroxyl radical production upon adding the di-Se block copolymer aggregates into the samples under X-ray irradiation.

Vo-Dinh et al. [57] designed a nanosystem that absorbed X-rays and converted the absorbed X-ray energy into fluorescence that helped generate singlet oxygen. The nanoscintillator was Y_2O_3, which emitted UVA light after absorption of X-rays. Fluorescent molecule psoralen was tethered to the surface of Y_2O_3 nanoparticles. Psoralen absorbed UVA emitted from Y_2O_3 and generated singlet oxygen, a known process. Prostate cancer line PC-3 was used in the study. The incubation concentration was up to 100 ppm of Y_2O_3, although no data of uptake was available. The dose
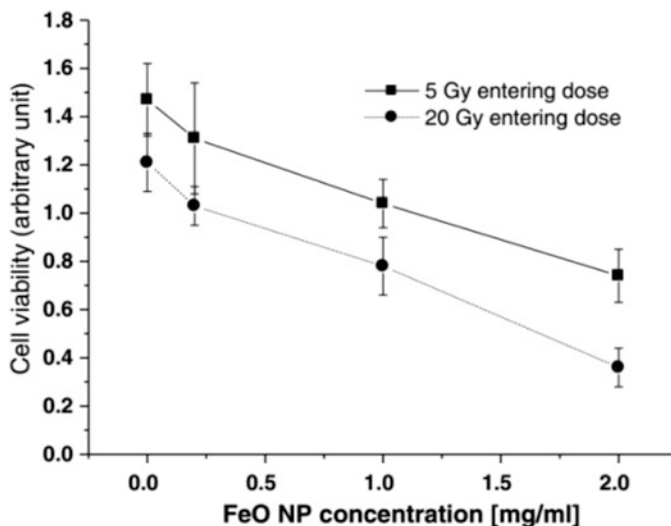
Fig. 9.24 Cell viability after irradiation with 7.1 keV X-rays in the presence of 13 nm iron oxide nanoparticles. Two doses were used, and the trends were similar. (Used with permission from Choi et al. [21] under CC BY 2.0 license.)

was 2 Gy for 160 keV and 320 keV X-rays. The survival was lowered by approximately 10–30% at a 100 ppm incubation concentration.

Choi et al. [21] studied damage to cells and tumors using FeO_x nanoparticles under synchrotron X-ray irradiation. The authors used X-rays at 7.1 keV to irradiate nanoparticles in CT26 tumor cells. The size of nanoparticles was 13 nm. The authors called the method photo-activated therapy (PAT). The incubation concentrations were between 0.2 and 2 mg/mL. The uptake was between 30 and 169 μg Fe in 10^6 cells. If the average of cell mass is 1 ng, then the loading of Fe per cell was 3–17 WP. The cell viability data showed decreased viability at increased FeO_x incubation concentrations, and a similar trend was observed between two doses of 5 and 20 Gy. Based on the data, a 17 WP loading of Fe in a cell increased the reduction of the viability by 50% when irradiated with 5 Gy of radiation. No data showed the effect of radiation only. Figure 9.24 shows the results of cell viability at two doses.

Liang et al. [141] studied cell viability after irradiating the cells with X-rays in the presence of gold nanoparticles. Four different sizes of PEGylated gold nanoparticles were used, including 4.8, 12.1, 27.3, and 46.6 nm. Two different incubation concentrations were used with HeLa cells. Up to 8 Gy of X-ray irradiation was used. 4.8 nm nanoparticles were found to pose mild cytotoxicity after 48 h at 0.1 mM or higher gold concentrations. 12.1 nm gold nanoparticles were found to be the most effective in destroying HeLa cells under X-rays. Survival fraction decreased to 10% at 4 Gy with 12.1 nm gold nanoparticles (0.1 mM gold), which was 50% less than that incurred with 6 Gy irradiation without gold nanoparticles. The authors also performed in vivo tests, whose results are shown in the next section.

Gonzalez and Kotler et al. [19] studied MeV irradiation of <5 nm silicon nanoparticles incubated with glioma C6 cells. Dynamic light scattering

measurements showed 2–3 nm diameter, and transmission electron microscopy showed a much larger size distribution of 3–90 nm. Photoluminescence of the particles was at 420 nm. Using fluorescence assays, authors studied the production of hydroxyl radicals, superoxide radicals, and singlet oxygen and found their yields were enhanced by 9 to 22 times. Uptake was measured in a relative manner, which showed higher uptake at longer incubation times. For 6-h incubation, attenuation of 4 MeV X-rays was doubled by the cells with the nanoparticles. Under the same condition, six times more reactive oxygen species were generated with silicon nanoparticles than without the nanoparticles. It is speculated by the authors that the observed 6 DEU enhancement was caused by biological processes triggered by increased amounts of reactive oxygen species. The 100% increase in absorption only supported an up to 2 DEU physical enhancement. The observed 6 DEU enhancement therefore must be caused by other mechanisms. A likely reason is silicon nanoparticles interacting with DNA repair proteins and blocking their functions, as mentioned in Chap. 4.

Ngwa et al. [174] employed low-dose-rate X-rays to interact with gold nanoparticles in HeLa cells. The incubation concentration was 0.02 WP. The nanoparticles were 50 nm in diameter and covered with methyl polymer. The dose was provided from a I-125 (emitting X-rays at 3.6 keV and 30.5–35.3 keV) source and activity was 2.6 mCi, which corresponded to a dose rate of 2.1–4.5 cGy/h. The total dose was up to 1 Gy. The enhancement was between 0.7 and 1.3 DEU. No uptake data was available, making it impossible to determine whether the measured enhancement matched the theoretically predicted physical enhancement at this specified X-ray energy.

Cook et al. [48] demonstrated an interesting system in which cisplatin was conjugated to the surface of gold nanoparticles. The formulation was used for chemoradiation therapy, and the authors suggested that Auger electrons emitted from gold played a vital role. The authors observed enhanced cell destruction of both MCF-7 and SKOV-3 cancer cells using the formulation under X-ray irradiation. Figure 9.25 shows the formulation and the survivability data. No attempts were made to determine the enhancement values.
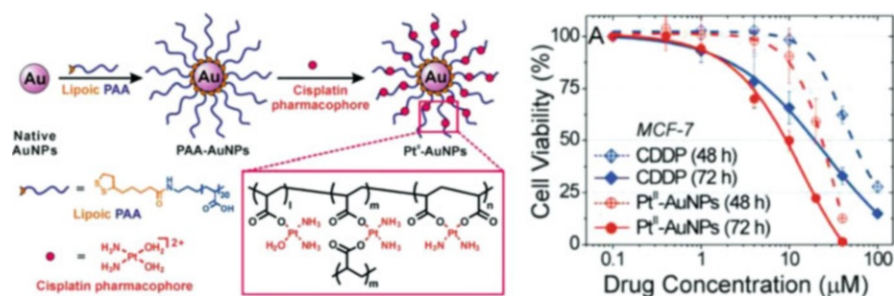
Fig. 9.25 Results of cell viability after treatment with formulated cisplatin using gold nanoparticles (AuNPs) covered with poly acrylic acid (PAA) ligands irradiated with X-ray radiation. (Adapted in part from Cook et al. [48] with permission of the Royal Society of Chemistry.)

Kumar et al. [171] reported a third-generation gold nanoparticles covered with several ligands for optimal radiation therapy. The authors chose HeLa cell line in their study. The uptake was visualized with attached fluorophores, but without direct quantification in terms of weight percentage. The average size of the gold nanoparticles was 2.5 nm. The X-ray energy was 220 kVp and the dose rate was 5.45 Gy/min. 0.5 mg/mL and 2.0 mg/mL incubation concentrations were used. The authors employed a clonogenic assay to determine the enhancement, and an enhancement up to 2.8 DEU was measured.

Juzenas et al. [24] discussed a new nanomaterial with a silver shell and a carbon core for cancer therapy. The authors used cancer cells including prostate cancer cells Du145 and irradiated the cells with 160 kVp X-rays. The X-ray source was a Faxitron source, running in CW mode at 160 kV/6.3 mA. The dose rate was 1 Gy/min. The size of the nanomaterial ranged from less than 10 nm to greater than 100 nm, with an average size of 60 nm. The authors called the nanomaterial C-Ag-PEG. The cell survival test was performed 24 h after irradiation. Only incubation concentrations were given and no uptake data was available. If the doses at 70% cell survival fractions were used to determine the enhancement, then adding C-Ag-PEG nanomaterial created a 0.6 DEU enhancement. Figure 9.26 displays the results of cell damage.

Latimer [52] investigated enhanced radiotherapy using 30 nm gold nanoparticles conjugated to polyethylene glycol (PEG) and then cell-penetrating peptides (CPP). The author used three cell lines including MDA-231-MB and obtained the uptake and cell survival data. The results showed enhanced uptake for 30 nm nanoparticles,

Fig. 9.26 Enhancement from silver-coated carbon nanoparticles under X-ray irradiation. (From Juzenas et al. [24]. doi: https://doi.org/10.1088/0957-4484/24/32/325103. © Institute of Physics and Engineering in Medicine. Reproduced by permission of IOP Publishing. All rights reserved.)
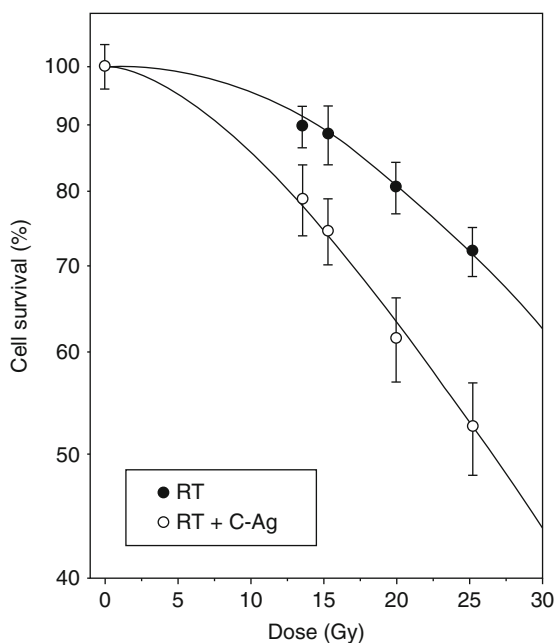
which agreed with the literature data shown in this chapter. The uptake amplification factor ranged from nearly 2 times to more than 11 times. The highest uptake occurred to T47D cells, which had more than 1.6×10^6 30 nm gold nanoparticles per cell and corresponded to over 40 WP of gold in the cell. This amount of gold was supposed to generate 40 DEU physical enhancement of damage for 40 keV X-rays. The experimental results showed 0.1 DEU WP^{-1} for PEG-AuNPs and 0.3 DEU WP^{-1} for CPP-PEG-AuNPs in T46D cells, which were lower than the predicted enhancement for 300 keV X-rays. It was unclear as to what caused the discrepancy, although scavenging can be a reason. For MCF-7 cells, the uptake was 1.9×10^5 of 30 nm gold nanoparticles per cell or 5 WP of gold in the cell. The measured enhancements are 0.9 DEU WP^{-1} for PEG-AuNP and 1.1 WP^{-1} for CPP-PEG-AuNPs. These results were higher than those predicted by theory for 300 keV X-rays. The results suggested that parameters such as cell types other than the amount of nanoparticles and their surface may play important roles in determining the enhancement of cellular destruction by nanoparticles under X-ray irradiation.

Chen et al. [163] reported the use of Ce^{3+}-doped lanthanum(III) fluoride nanoparticles as an X-ray-driven photodynamic therapeutic agent. The authors used several assays to measure the damage, including oxidative stress, mitochondrial damage, and DNA fragmentation on prostate cancer cells (PC3) after exposed to 90 kVp X-rays.

Konstantinov et al. [170] claimed that they observed a 0.33 DEU enhancement to cancer cells with 50–500 μg/mL loading of tantalum pentoxide nanoparticles. The X-ray energy was 10 MeV. If physical enhancement were considered, then for a 0.005–0.05 WP loading, the enhancement would be less than 1%. However, the specified loading was the incubation concentration, not uptake, meaning cells might have much high concentrations of nanomaterials in them. The authors also speculated that photoelectric and/or pair production processes may contribute to the observed enhancement. Without the uptake data, however, one could not determine the origin of enhancement.

Khoei et al. [169] showed the results of their cancer cell damage study with iron oxide nanoparticles irradiated with 6 MeV X-rays. The cell line was Du-145 prostate carcinoma cell line. The authors obtained a 0.2 DEU enhancement in the range of 2–8 Gy of irradiation. The nanoparticle incubation concentration was 0.1 WP. No uptake information was available. Their cell survival fraction was 80% at 2 Gy and 10% at 4 Gy. This result shows that LD_{50} can be different even for the same cell line but in different experiements.

Tsourkas et al. [38] used HT1080 human fibrosarcoma cells to test the effectiveness of dicoblock copolymer PEG-PCL formulated micelles filled with 1.9 nm gold nanoparticles. The size of the assemblies ranged from 28 to 142 nm measured by DLS, and a similar size range was detected using TEM. The authors also performed animal tests (shown in Sect. 9.5). The authors did not examine the form of micelles at the end of the experiments, whether gold nanoparticles were still in the micelles or released from the micelles. Survival fraction was at 10% after 5 Gy of irradiation. The enhancement was 0.32 DEU (using 50% survival fraction with and without gold). No uptake data was available.

Superparamagnetic iron oxide nanoparticles were synthesized and used by Kryschi et al. [46] to destruct cancer cells. The size of the nanomaterial was on the order of 10 nm. Two coatings were used, which were malate and citrate. Three cell lines were used, which were Caco-2, MCF-7, and 3 T3. 1 or 3 Gy X-ray irradiation was administered, and fluorescence assay was used to measure the cellular reactive oxygen species. The results were complex as nonlinear dose dependency was observed in the 1–3 Gy dose range.

Chen et al. [161] synthesized a new afterglow nanoparticle upon X-ray irradiation. The nanoparticles were Cu and Co co-doped ZnS and had an average size of 4 nm. The afterglow emitted at 550 nm. The lifetime of the afterglow was 8 sec (1/e). They authors then conjugated photosensitizer tetrabromorhodamine-123 to the surface. The ligand was known for its photodynamic therapy (PDT) properties. PC3 cells were used to gauge the PDT capability of the whole complex. Enhancement could not be determined due to lack of X-ray-only results.

Hashemi et al. [73] used gold nanoparticles coated with folate ligands in their enhancement study of radiotherapy of HeLa cells. The average size of gold nanoparticles was 47 nm. ^{60}Co and an X-ray source operated between 120 and 250 kVp were used. The dose range was between 1.18 and 3.43 Gy. The authors noticed a nearly eigthfold increase in uptake for foliate-conjugated gold nanoparticles compared to as-synthesized PEGylated nanoparticles. The uptake of these gold nanoparticles into HeLa cells was measured, and at the 24-h incubation time, more than 3×10^4 gold nanoparticles were in each cell, giving rise to a 3.4 WP gold loading in the HeLa cell using 1.0 ng cell weight. If physical enhancement dominates, then the enhancement should be around 3.4 DEU for 33 keV X-rays, less so for 120 keV, and only a fraction of it for ^{60}Co. According to the authors, the enhancement was higher for folate-conjugated gold nanoparticles. The enhancement was 0.6 DEU for 120 kVp X-rays using 60% survival fraction. The nanomaterials may pose anti-enhancement in addition to physical enhancement for the 47 nm gold folate-coated gold nanoparticles because the measured enhancements were lower than the predicted physical enhancement.

Su et al. [188] employed bismuth nanoparticles conjugated to iron oxide magnetic nanoparticles with folic acid surfactants to target circulating tumor cells (HeLa) in the blood. The tumor-bound nanoparticles were collected with permanent magnets. 40 kVp X-rays were used. Dose and dose-rate information was not provided. MTT and comet assays were used to detect cell viability and DNA damage. Enhanced damage in the presence of bismuth nanoparticles was observed.

Ma and Su et al. [79] investigated the use of gold nanoparticles for enhancing the effect of radiation damage to human glioblastoma cells under X-ray irradiation. 13.5 nm diameter gold nanoparticles coated with several different surfactants were synthesized to improve uptake of nanoparticles. The authors observed more DNA damage with positively charged surfactants on gold nanoparticles, although no quantitative results were given with respect to the uptake and damage. Ma and Su et al. [41] developed a unique nanosystem to study the effect of nanostructures on damage to cells under X-ray irradiation. They created microdisks using multiple layers of gold nanoparticles (13 nm diameter) on glass slides. Several cell lines

including K562 cells attached to the microdisks were irradiated with 40 kV X-rays. The enhancement ranged between zero and approximately 0.4 DEU. Due to irregularity of the microdisks, gold loadings next to cells were difficult to quantify. However, a clear advantage of this approach was the cleanness of the pathway to identify the origin of enhancement because unless nanoparticles diffuse away from the microdisk, enhancement, albeit small, should all come from only physical enhancement.

In their latest work, Su et al. [86] reported enhanced cancer treatment with cell-penetrating peptide (CPP)-modified gold nanoparticles. The gold nanoparticles were 10 nm in diameter with large standard deviations. Two cell lines, HeLa and human fibroblasts, were used. Production of reactive oxygen species was measured, and CPP-conjugated gold nanoparticles were found to enhance the yield by more than twofold. Nuclear DNA damage was measured with and without X-ray irradiation, but no significant differences were found. The overall results suggested some effectiveness of using CPP-conjugated gold nanoparticles.

Sun, Mao, and Hao et al. [179] reported the use of hollow gold nanoparticles as radiosensitizers. The hollow gold nanoparticles had a 50 nm inner and 100 nm outer diameter. The particles were covered with PEG ligands. MDA-MB-231 breast cancer cell line was used in the study, and the endpoint of cell viability in terms of its metabolic activity was measured with MTT assay. The authors found little toxicity for up to 0.35 mM gold in solution. Less than 4 Gy of radiation was used at 225 kVp and 3.9 Gy/min dose rate. High-energy X-rays at 6 MV and 14 Gy/min was also used. The enhancement for keV and MV X-rays were 0.5 and 0.1 DEU, respectively. It was difficult to compare the measured enhancements with expected enhancements because no uptake data was available.

Salviati et al. [179] used porphyrin conjugated to silicon carbide/silica (SiC/SiO_x) nanowires in X-ray excited photodynamic therapy. They used click reactions to link porphyrins to the surface of the nanowires. 6 MeV X-rays (γ-rays) were used, which relied mainly on pair production and Compton scattering processes to generate secondary electrons to excite porphyrins and produce singlet oxygen. Low doses (0.4–2 Gy) of X-rays and lung adenocarcinoma cells were used. The enhancement was a 75% reduction in cell population when treated with porphyrin conjugates compared to the control without porphyrin. The authors also compared the results of using nanomaterials and X-rays with those without using them. Enhancement due to the combination of the nanomaterials and X-rays was subtle but measurable.

Cooper and Reshetnyak et al. [67] reported using 1.4 nm gold nanoparticles tethered to pH-sensitive low-insertion peptide (pHLIP) to treat lung carcinoma A549 cells under X-rays. They found enhanced damage to the cell treated with gold nanoparticles. The X-rays were 250 kVp. The uptake data was not available, and enhancement was 0.1–0.2 DEU when samples were exposed to a low dose of 1.5 Gy of X-rays.

Réfrégiers et al. [176] reported a study of HeLa cell damage using lanthanide trapped in micelles to produce singlet oxygen for X-ray-induced radiophotodynamic therapy (RPDT). The lanthanide (Gd and Eu in their study) in the form of ions were chelated to C12 ligands to form the micelles. The authors showed fluorescence from

lanthanides when micelles were in HeLa cells and measured the production of singlet oxygen. No enhancement data was available.

Detappe and Berbeco et al. [187] studied the response of pancreatic cancer cells to the treatment of gadolinium-based nanoparticles under 220 kVp and 6 MeV X-ray irradiation. The nanoparticles were called AGuIX®, which were used in many imaging studies. The authors found that 6 MeV X-rays provided the best trade-off between penetration depth and enhancement. At 10 cm depth, the measured enhancement was 0.3 DEU, which was promising.

Chen et al. [69] studied selenium particles for enhancement under X-ray irradiation. The authors used both commercial and homemade selenium nanoparticles covered with polyethylene glycol (PEG) ligands and found that commercially made particles disintegrated under X-ray irradiation. The particle sizes were large, on the order a few hundred nanometers. HeLa cells were used, and MTT assay was used to determine the cell viability. X-ray information was not found, although the dose was specified to be 8 Gy, which was relatively high for HeLa cells. The highest enhancement was obtained using the commercial selenium particles. The authors attributed the damage to fragmentation of selenium particles, which according to the authors led to the generation of reactive oxygen species and oxidative stress detected by the authors using dichlorofluorescein (DCF) assay. The results are shown in Fig. 9.27. Enhancement was estimated to be 0.5 DEU. Uptake was determined with ICP-MS.

Falk et al. [166] studied the effect of gadolinium (Gd) nanoparticles under γ-rays (^{60}Co) on treating U87 cells. The diameter of the Gd nanoparticles was 3 nm, and the molecular weight was 8.5 kDa, corresponding to a density of approximately 1.0 g/cm^3, which was identical to water. Incubation was conducted and uptake was studied with optical detection of the nanoparticles conjugated with cy5.5 dye molecules. Gd nanoparticles were found in cytoplasm of U87 cells although no Gd nanoparticles were found in the nuclei. No quantitative data on uptake of the nanomaterials was available. The assay was γ-H2AX to detect nuclear DNA damage as well as clonogenic assay to detect cell reproduction ability. After 1 and

Fig. 9.27 Reactive oxygen species generated by the introduction of selenium particles under X-ray irradiation. (Reprinted from Chen et al. [69]. Copyright (2016) with permission from Elsevier.)
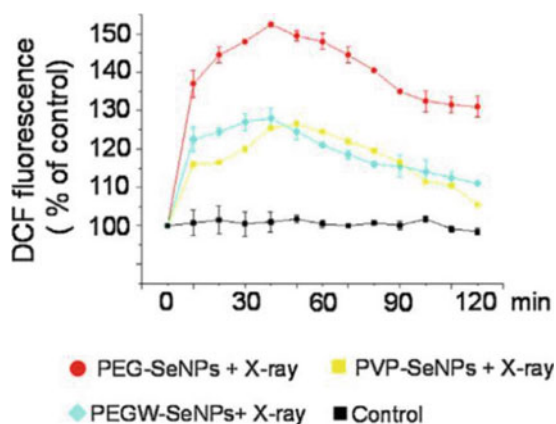
4 Gy of irradiation, the authors measured moderate enhancements due to the addition of Gd nanoparticles. DNA damage was found to be dependent on the incubation time. Based on the data, enhancement values were 1.83 DEU at 1 Gy (at 0.55 survival) and 0.14 DEU at 4 Gy (at 0.37 survival). It was more likely that higher doses of radiation were needed in practice, and the enhancement values under those conditions could be even smaller because survival fractions would be lower. On the other hand, the density of the Gd nanoparticles was close to water, suggesting that the observed enhancement could further increased if higher density Gd nanomaterials are used without causing significantly higher toxicity.

Taggart et al. [26] investigated the effect of 1.9 nm gold nanoparticles. Three cancer cell lines, MDA-MB-231, DU-145, and T98G, were used. Four cell assays of detecting reactive oxygen species level, mitochondrial oxidation, mitochondrial polarization, and cell survival were used. The uptake was between 1×10^7 and 2.2×10^8 nanoparticles per cell, corresponding to 0.07–1.5 WP of gold in these cells (assuming 1 ng cell mass). The lowest uptake occurred to DU-145 and highest for T98G. After 24 h of incubation, the uptake for Du-145, MDA-MB-231, and T98G was 1.0×10^8, 1.5×10^8, and 2.2×10^8, respectively. 2, 4, and 8 Gy of radiation doses were administered, and enhancements were between 0.92 DEU at 2 Gy for T98G and 0.14 DEU at 8 Gy for MDA-MB-231 using clonogenic assay. Based on these results and the results of reactive oxygen species scavenging reactions, the authors suggested that the use of these nanoparticles caused oxidative stress and eventual damage to mitochondria, which led to cell death. The measured enhancements were within the range of predicted physical enhancement values for the loadings of gold in the cells.

Quan and Jiang et al. [175] studied the sensitivity of HeLa cells to FePt nanoparticles under X-ray irradiation. The authors claimed that the nanoparticles possessed a chemoradiotherapeutic effect. The size of nanoparticles was close to 3 nm and had different compositions, ranging from $Fe_{26}Pt_{74}$ to $Fe_{77}Pt_{23}$. It turned out that these nanoparticles were toxic to the cell. At 10 μg/mL incubation concentration, cell viability was reduced to half. With X-ray irradiation and nanomaterials, viability was further reduced over the sum of radiation and nanomaterials acting separately, albeit insignificantly. At 8 Gy, the viability was 32% with X-ray and nanomaterials, which corresponded to an enhancement of less than 0.1 DEU. Cellular uptake of Pt was measured and was only 0.1–0.2 μg/100 μg or 0.1 WP. Physical enhancement should be around 0.1–0.2 DEU at this Pt loading, which agrees with the experimental value.

Sasaki et al. [178] synthesized titanium peroxide nanoparticles (shown in Chap. 6) and used them to generate hydroxyl radicals. The peroxide nanoparticles apparently were found to be much more efficient, by at least 20-fold, in generating hydroxyl radicals under X-ray irradiation than TiO_2 nanoparticles. However, in the presence of glutathione, hydroxyl radial production yield was severely reduced. DNA damage detected by γ-H2AX assay was enhanced by more than 100%. X-ray irradiation alone (5 Gy) used in the animal work did not reduce tumor size at all. When X-ray irradiation was combined with the nanoparticles, a 2.4 DEU enhancement was measured, using the tumor sizes given by the authors.

Wen and Gu et al. [60] used silver nanoparticles to enhance the effect of cell destruction under X-ray irradiation. U251 cells and 6 MV X-rays were used. 3-Methyladenine (3-MA) autophagy inhibitor and antioxidant N-acetyl cysteine (NAC) were used to determine the role of reactive oxygen species. It was found that silver nanoparticles were toxic, and the enhancement was about 0.5 DEU based on caspase-3 assay without NAC and became nearly zero with NAC. When 3-MA was used, enhancement was close to 2 DEU without NAC and was still 1.0 DEU with NAC. The results could be useful to other in vitro and in vivo work.

Martinez-Rovira et al. [172] discussed the use of gadolinium nanoparticles under X-rays to treat glioma cells. Fourier Transform Infrared (FTIR) spectroscopy was used to measure the response or enhancement. The gadolinium nanoparticles were purchased, which consisted of gadolinium compound-decorated nanoparticles. The size was 3 nm. Average X-ray energy was 90 keV and dose rate was 1.1 Gy/min. The responses were analyzed and identified as changes to DNA backbone phosphate groups. Metabolic activity measurements showed the effect of the nanoparticles, which was the most prominent after greater than 5 Gy of irradiation. The measured LD_{50} dose for F98 cells was greater than 20 Gy, which was higher than most of the LD_{50} values reported in the literature.

Currell et al. [163] used 1.9 nm gold nanoparticles on MDA-MB-231 cells and performed both DNA damage and theoretical simulations of the damage. Imaging of the nanoparticles suggested that detectable nanoparticles largely remained outside the nuclei. However, the results did not completely exclude the possibility of the nanoparticles entering the nuclei because the detection method was through surface plasmon resonance using two-photon excitation, and no calibration was given. Results of simulations using the local effect model (LEM) mentioned in Chap. 2 suggested that these nanoparticles outside the nuclei in the amount of 0.7 WP could be responsible for the damage of DNA measured in the work. The results suggested a strong energy dependency of nuclear DNA damage under monochromatic X-ray irradiation, with the peak of damage occurring at 55 keV (experimentally) or 40 keV (simulation). According to the measurements, there was little or no enhancement for X-rays below 20 keV or above 70 keV, agreeing with the claim made in Chap. 2, stating that enhancement peaks around 50 keV.

Tehei et al. [12] reported the study of using bismuth oxide nanoparticles to assist radiotherapy. 9 L gliosarcoma cell line was used, and X-ray energies were 125 kVp and 10 MV. Incubation concentration was 50 μg/mL although no uptake data was available. A moderate enhancement of 0.48 and 0.25 DEU were observed at these two energies. In another report, bismuth nanoparticles (3.6 nm) were synthesized and used to explore their enhancement potential to radiotherapy by Yang and Li et al. [71]. The nanoparticles were PEGylated and targeting peptide LyP-1 ligands were conjugated to the surface. 4T1 cells were used in the study. Approximately 5 μg/mL was found in the cell for Lyp-1 covered nanoparticles, which was only 5 ppm. PEGylated nanoparticles had only 40% of the uptake of the LyP-1 covered nanoparticles. However, both uptake values were low and there should be no measurable physical enhancement. The authors showed an approximately 2 DEU enhancement, which was unexplainable using physical enhancement mechanisms shown in Chap. 2.

Zheng et al. [180] reported that ligands on 2 nm gold nanoparticles were critical to determination of their sensitizing properties. If the ligand was PEG, then the nanoparticles were basically radioprotectors, i.e., scavenging radicals in the MCF-7 cell. If the ligand was zwitterionic glutathione, then the nanoparticles functioned as sensitizers. The authors also studied the uptake and found that glutathione-coated gold nanoparticles were 20 times better than PEG-coated gold nanoparticles in terms of being able to enter the cell. The authors also pointed out that uptake did not affect the enhancement or scavenging properties of these nanoparticles. This outcome is in agreement with the conclusions shown in Chaps. 2 and 3, stating that very small nanoparticles are unlikely to produce physical enhancement, and if any enhancement is found, it is more likely to be chemical enhancement, which depends on the surface structure.

Kharrazi and Amani et al. [168] reported the synthesis of lanthanide-doped ZnO-based nanoparticles and application of this nanomaterial in treating HeLa and PC3 cancer cells. Therefore, this was at least a case of type 3 physical enhancement described in Chap. 2. The average size of the nanoparticles was between 4 and 10 nm. The authors also conjugated rhodamine B molecules to the surface of nanoparticles. Mild toxicity was observed with ZnO nanoparticles and rare earth-doped ZnO nanoparticles. When combined with X-ray or γ-ray irradiation, decreased cell viability was observed. It is interesting to note that the viability was about 10% with a single 6 Gy X-ray irradiation. The viability was near 40% when under three fractions of 2 Gy X-ray irradiation, suggesting that fractionation irradiation was less lethal than a single dose. The authors observed that a 2 Gy X-ray irradiation of 20 μg/mL loading of Eu-doped ZnO nanomaterials was equivalent to a three-fractionation of 2 Gy X-ray irradiation, both reducing the viability to 30%. If enhancement is calculated based on the accumulated dose, which is clearly inaccurate, then a 2.0 DEU enhancement is observed here.

Paquette et al. [34] studied the effect of tiopronin-coated gold nanoparticles on the destruction of HCT116 cells. The ligand was chosen to maintain the nanoparticles soluble and stable at high gold nanoparticle concentrations. The average X-ray energy was 26 keV. LD_{50} dose was only 1.5 Gy, indicating HCT116 cells were radiosensitive to 26 keV X-rays. The nanoparticles were around 3 nm. γ-H2AX assay was used to measure the enhancement to DNA damage. Uptake measurements revealed up to a 3.3 WP gold loading in cell using 1 ng cellular weight. Nearly 1.0 DEU was measured using the DNA damage assay, which corresponded to a unit WP enhancement of 0.3 DEU WP^{-1}. The results suggest that these nanoparticles are scavenging as well as generating enhancement.

Chen and Li et al. [37] explored the effect of tirapazamine-conjugated gold nanoparticles on liver cancer cell HepG2 under X-ray irradiation. Tirapazamine was known to produce hydroxyl radicals in the presence of a very low level of oxygen. The gold nanoparticles were 16 nm. LD_{50} was only 1 Gy for the cell line, and enhancement was on the order of 0.2 DEU for hydroxyl radical production in water and 0.3 DEU for surviving fraction reduction.

Kim et al. [40] compared two sizes of gold nanoparticles for therapeutic purpose. The authors employed 1.9 and 50 nm gold nanoparticles and 150 and 450 kVp

X-rays. The cell line was HTB-72 skin melanoma. Incubation concentration was around 0.01 WP. Although no quantitative uptake data was available, TEM images were available to show that uptake of 50 nm gold nanoparticles was much higher than 1.9 nm gold nanoparticles. Enhancements was 0.3 and 2.7 DEU for 1.9 and 50 nm gold nanoparticles at 2 Gy of 150 kVp X-rays. Greater enhancements were observed at higher doses, reaching 6.8 DEU at 7 Gy. This trend was counterintuitive because usually the enhancement decreases as the dose of irradiation increases.

Goldys et al. [167] explored the use of verteporfin-conjugated 12 nm gold nanoparticles in X-ray-mediated photodynamic therapy. Verteporfin was a porphyrin derivative. Light excitation at 690 nm of the nanomaterial in Panc 1 cells apparently reduced the cellular viability by more than 50%, demonstrating that singlet oxygen generation ability of verteporfin was not reduced by gold nanoparticles. However, the effect of 6 Gy of X-ray excitation was minimal, showing only a 0.05 DEU enhancement.

Arab-Bafrani et al. [39] studied the treatment of colon cancer cells with 50 nm gold nanoparticles and 9 MeV radiation. Cell viability or survival fraction was evaluated using MTS assay. 6×10^4 gold nanoparticle uptake was measured with atomic absorption (AA) spectroscopy. This level of uptake corresponded to over 5 WP of gold in cells, which was supposed to generate at least a 5 DEU enhancement if only physical enhancement, was considered. Using LD_{50} for HT29 cells without and with gold nanoparticles, an enhancement of approximately 1.0 DEU was obtained. This result again suggests that gold nanoparticles without special treatment would scavenge, reducing the enhancement caused by these nanoparticles.

Yang, Wu, and Yang et al. [11] developed a similar approach employed by Li et al. [188]. The latter used WS_2 nanodots instead of Au@FeS nanomaterials. In Yang's work, gold nanoparticle core-FeS shell nanostructures coated with PEG ligands were synthesized and used in the mouse model. The gold core was approximately 20 nm, and after FeS shell wrapping, the overall size of the nanoparticles was approximately 100 nm. Laser light at 808 nm was used to heat the samples, and up to 70 °C was measured using irradiance of 1 W cm^{-2}. 4T1 cell line was used in the in vitro experiments and a 4 Gy X-ray dose was used, which caused a 20% reduction in surviving fraction. These results suggested that LD_{50} was 12 Gy for 4T1 cells, which was higher than normal cells. The nanomaterial caused only a 0.1 DEU enhancement. The largest enhancement occurred when laser and X-ray irradiation of the nanomaterials were combined.

Geso et al. [25] tested titanium dioxide nanoparticles as radiosensitizers. The size of the nanoparticles was about 30 nm and the surface was modified with amine or PEG, and 80 kV and 6 MV X-rays were used. Up to 8 Gy of X-ray dose was used. HaCaT and DU-145 cells were used in the study. Results from MTS assay suggested LD_{50} for both cell lines were the same, which was about 6–8 Gy. Clonogenic results, however, suggested the LD_{50} was 2–4 Gy for both cells. The results suggested that not only enhancement measurements depended on assays; LD_{50} also depended on the assay as well. The particles were found to be not toxic to the cells. The enhancements at two energies were similar, ranging from 0.56 to 0.77 DEU for 80 kV X-rays and 0.37 to 0.67 DEU for 6 MV X-rays at 4 mM titanium dioxide

nanoparticle incubation concentration. Reactive oxygen species generation was considered to be the cause for the enhancement. If the ionization of nanoparticles was caused by the electrons produced from X-rays interacting with water, then the closeness of the two enhancement magnitudes at two energies can be explained.

Detappe and Berbeco et al. [165] engineered a hybrid nanomaterial that had a Gd_2O_3 core and SiO_2 shell covered with DOTAGA ligands whose terminal groups trap Bi^{3+} ions. The final size was less than 5 nm in diameter measured with DLS. The nanomaterial was called SiBiGdNP. The radiation was 6 MV X-ray. Clonogenic assay was used to measure the survival fraction of A549 cells. Without the nanomaterials, LD_{50} was 6 Gy. With the nanomaterials LD_{50} was 3 Gy, giving rise to a 1.0 DEU enhancement. No uptake data was available.

9.5.3   Summary

All these results shown in this section, despite variations and fluctuations from report to report, reveal three general trends. First, there is usually an enhancement to the destruction of cancerous cells under X-ray irradiation when gold nanoparticles are added. All the reported studies show some enhancement. The second trend is that the measured enhancements are similar, of the order of 0.5–1.0 DEU. This may be caused by how the experiments are performed or by something more profound. The third trend is that based on the uptake and enhancement data, which are summarized in Fig. 9.28, a small number of reports show the value of the measured enhancement being close to the theoretically predicted physical enhancement. However, this agreement happens to occur only when the predicted physical enhancements are close to 0.5 DEU, essentially the same as the average enhancement for most
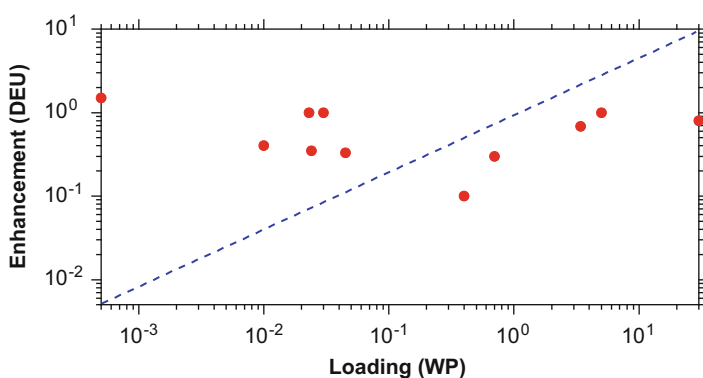
Fig. 9.28 Experimentally measured enhancements (round dots) for actual loadings of gold or other nanoparticles in the cell. Also shown is the predicted physical enhancement at the corresponding uptake or gold loading (dashed line). The enhancement uses dose enhancement units (DEU); the loading has the unit of weight percentage of gold (WP) in the cell

measurements. This implies that this agreement is possibly just a coincidence than a true cause-effect agreement.

Unfortunately, there are almost no mechanistic studies to conclusively explain the origin of enhancement. It is difficult to isolate enhancement mechanisms unless experiments are extremely well controlled because cellular responses are complex. One example of a better-controlled experiment is to use γ-H2AX assay to measure nuclear DNA damage by large nanoparticles. If the size of gold nanoparticle is larger than 30 nm, and if the end point is nuclear DNA damage, then it is most likely the enhancement is physical enhancement because gold nanoparticles are located outside the nuclei and hence cannot cause chemical or biological enhancement—these gold nanoparticles can only remotely deposit energy in the nuclei to damage nuclear DNA. These studies show that carefully designed nanomaterials and irradiation experiments are needed to isolate individual enhancements and determine enhancement mechanisms.

Figure 9.28 summarize the experimentally measured enhancements cited in this section, and it is evident that most of them have enhancement magnitude around 0.5 DEU or between 0.1 and 1.0 DEU, even though uptake are as low as 10^{-3} WP and as high as 40 WP. As a reference, the predicted physical enhancement as a function of gold loading is also shown in Fig. 9.28 (dashed line). The two trends are clearly uncorrelated, which suggests that the measured enhancement does not depend on physical enhancement. It seems the cells have an internal regulating mechanism. Several articles and Chap. 4 discuss the possibility and various forms of biological enhancement. Future work is needed to uncover the true causes for the measured enhancements.

9.6   Treatment of Tumor (In Vivo) Tissues with Nanomaterials and X-Rays

This section contains two parts. The first addresses in vivo work. The second part discusses preclinical or clinical trials.

9.6.1   Survey of In Vivo Work

The works published in the area of using X-ray nanochemistry to treat animals are listed in Table 9.9. The first publication in this area was done by Heinfeld et al. [5]. Unlike the study of other experimental drugs, this first work used an animal model, although to this date it is still unknown whether the effect measured in this work was solely caused by the predicted physical enhancement.

Hainfeld et al. [5] used Balb/C mice (average weight 35 g) infected with mammary carcinoma cells as their animal model to determine the effect of gold

Table 9.9 List of *in vivo* studies of enhancement of radiation damage by nanoparticles to tumors in animals. The results are ordered chronologically according to the corresponding authors and clustered for the each corresponding author when multiple papers are published by the same group. Enhancement (Enh) values are calculated by the author of this book if not given in the published reports

Animal type	Uptake amount (WP)	Composition	Size (nm)	Ligand name	X-ray energy/dose (Gy)	Enh (DEU)	Ref.
Mice	0.23/1.8	Au	1.9		30	0.59/5.5^a	Hainfeld et al. [5]
Mice		Au			250 kVp		Hainfeld et al. [191]
Mice	1.5	Au	11	– (from nanoprobes)	100 kVp/30	2.00	Hainfeld et al. [108]
Mice	–	–	–	HVGGSSV	/3Gy^b	–	Jaboin et al. [190]
Mice	7.4	Au	13	Citrate	6 MeV/50	0.50	Chen et al. [191]
Mice		Au	4.7	PEG	6 MV		Hwu et al. [22]
Mice	6 mg	Au	30 nm	PEG	6 MV/25	0.40	Popovtzer et al. [139] and [192]
Mice	–	PtFe		GIRLRG	/3		Hallahan et al. [31]
Mice/Lung		Nab-paclitaxel	–	HVGGSSV	300 kV/3		Hallahan et al. [82]
Mice	–	Cisplatin@liposome	100	–	6 MV/6–28	0.50	Jiang et al. [15]
Rats		Gd$_2$O$_3$@SiO$_2$	1.1 core, 0.5 shell	DTPADA	50–350 keV (mean 90 keV)/		Roux et al. [115]
Mice		Au	15–20	PEG diacrylate			Hwu et al. [196]
Mice	0.004 (Fe/tumor)	FeOx	13–15	Alginic acid	7.1 keV/10–40		Choi et al. [21]
Mice	Measured 24 days after	Au	4.8–46.6	PEG-SH	137–Cs/5	−0.28–3.73	Liang et al. [141]
Mice	0.7	Au	50	(Commercial product, unknown)	6,18 MV/20	0.10	Anijdan et al. [197]

Mice	0.7–3.0	Au (nanorods)		PEG/cetuximab	140kVp/10	0.05–0.33	Krishnan et al. [198]
Mice	0.043	Au	2	PEG,RGD, AF647	220 kVp/10	3	Berbeco et al. [199]
Mice		Lu, Au, NaYF$_4$; Yb/Er/Tm/Gd		PEG5000			Bu et al. [200]
Rat	0.7	Terpyridine-Pt complex	Molecules	–	160 kVp, 6 MV/15		Pradhan et al. [29]
Mice	0.055 ± 0.017	Au NP SuperPara FeOx@PEG-PLC micelle	2.2 Au, 14 FeO, 100 by DLS	–	150 kVp/6		Tsourkas et al. [125]
Mice	0.00066, 0.00038	Au	18	BSA	160kVp/3 + 2	0.10	Tu et al. [198]
Mice	–	SrAl$_2$O$_4$:Eu (SAO)@SiO2	400	Merocyanine 540 loaded in shell	50 kV/0.5	181.09	Xie et al. [199]
Mice	0.00095	Au	<2	Glutathione	662 keV (137-Cs) /5	1.65	Xie et al. [200]
Mice	2.5	Gd/Yb/Ln/SiO$_2$	280 width/500 length	ZnPc, folic acid			Yang et al. [127]
Mice		Au	3–50	SH-PEG-COOH	keV, MeV	3.55	Chang et al. [76]
Mice/U14		Au	60	PEG	6 MV	0.07	Chen et al. [42]
Mice		Au, SiO$_2$	20–200 nm	PEG, CTAB, DNA, RNA	80.7 keV	1.00	Li et al. [136]
Mice	–	Au@MnO$_2$	50	PEG	160 keV/6	3.98	Yang et al. [204]
Mice	0.0001	Au/Fe$_3$O$_4$	70	PEG, folic acid	50 kVp		Mei et al. [62]
Mice		Perfluorohexane@liposome	100	–	6 MV/0–10		Hu et al. [23]
Mice	1	Au	1500–3000		200 kVp/8	0.40	Das et al. [20]
Mice	–	SrAl$_2$O$_4$:Eu@SiO$_2$	73.5 ± 26.9	–	50 kVp/5	2.26/4.02	Xie et al. [32]

(continued)

Table 9.9 (continued)

Animal type	Uptake amount (WP)	Composition	Size (nm)	Ligand name	X-ray energy/ dose (Gy)	Enh (DEU)	Ref.
Mice	0.00074, 0.00222	Au rod@mSiO$_2$	57.70 × ϕ14.44	PEG, RGD	6 MV/10	0.80, 3.44	Fu et al. [202]
Mice	3.3	Au	3	Tiopronin	26 keV	2.00	Paquette et al. [34]
Mice		Au in MnS in ZnS	30–40	PEG	/4, 6	2.60 (4 Gy), 1.25 (6 Gy)	Yang et al. [203]
Mice	0.00013 (Au), 0.00115 (Se)	Au-Se	120	RGD and ACPP	6 MV/40 (fractional)	0.15 (IV) 0.37 (IT)	Chen et al. [13]
Mice		WS$_2$ in polyaniline shell	6.1	Hyaluronic acid and chlorin e6	/6	0.20	Li et al. [188]
Mice		BSA/MnO$_2$/Hf/DSP	150	PEG	/6	1.79	Liu et al. [204]
Mice	–	GdW$_{10}$ (polyoxometalate) @chitosan	30	siRNA HIF-1α	–/10	2.47	Zhao et al. [36]

[a]Reported by the authors of the publications
[b]Dose to activate tumor targeting

nanoparticles on radiotherapy. Following a week of tumor growth, animals were treated with 1.9 nm gold nanoparticles and then irradiation of 250 kVp X-rays. The dose was a single dose of 30 Gy. Based on the values given in the paper, gold loading in the tumor after gold nanoparticle administration was $(4.9/100) \times 1.35$ g/kg = 6.6 mg/g or 0.7 WP. The peripheral had $(10/100) \times 1.35$ g/kg = 20 mg/g or 2 WP. Blood had a gold loading of $(10/100) \times 1.35$ g/kg = 20 mg/g or 2 WP. The estimated enhancement using 33 keV X-rays, which should produce highest physical enhancement allowed, was 1.0 DEU at the tumor and 2.8 DEU in the peripheral and blood. For 250 kVp, the predicted enhancement was close to 0.5 DEU, which was close to the measured enhancement of 0.4 DEU calculated by the author of the book using exponential growth models, although the authors reported an enhancement of 5.5 DEU. The results are shown in Fig. 2.21.

Hainfeld et al. [191] showed their results of gold nanoparticle treatment of cancer-bearing mice. The experimental setup was similar to what was described in their 2004 publication, i.e., 3 g kg^{-1} gold loading and irradiated with 250 keV for 30 Gy. In another similar study, Smilowitz et al. [208] studied the enhancement of radiation therapy by gold nanoparticles under X-ray radiation. They used murine squamous cell carcinoma. The authors found that 68 keV X-rays were more effective than 157 keV X-rays. This energy dependency result implied that gold absorption of X-rays played an important role. The authors also found that gold nanoparticles worked better with 42 Gy dose than 30 Gy. This suggested that enhancement obtained using the surviving curve was a valid assessment because enhancement calculated thereby was usually higher at lower doses. Hainfeld et al. [108] used 11 nm gold nanoparticles for intravenously injection for both imaging and treatment of brain tumors. The loading was 1.5 WP and the enhancement was approximately 2.0 DEU. The results are shown in Fig. 9.29. This enhancement was close to the theoretically predicted physical enhancement caused by the gold loading for 100 kVp X-rays. The chance for the nanoparticles to enter nuclei was small because of the relatively large size of gold nanoparticles of 11 nm, which reduced the probability of having chemical or biological enhancement. The half-life of the 11-nm gold nanoparticles was 24 h, which was much longer than the 42 min half-life for 1.9 nm gold nanoparticle mentioned earlier.

Chen et al. [209] studied scintillation from nanoparticles that helped increase the production of singlet oxygen. Porphyrins were the molecules of their choice. Various lanthanides were tested as well. Specifically, LaF_3: Ce^{3+} nanoparticles were studied. As discussed in Chap. 2, scintillation belongs to type 3 physical enhancement, which is related to photons released from the added nanoparticles. Even though it was possible to measure the absolute quantum yield of the added scintillation nanomaterials as shown by Guo et al. [210], the parameter was not commonly measured in applications of these nanomaterials. Instead, measuring the yield of singlet oxygen was commonly performed. If there were no other nonlinear processes involved, then the two measurements should yield the same result.

Halllahan et al. [31] reported a method of using Pt compounds under 3 Gy X-ray irradiation to study radiation treatment of GL261 brain tumor xenografts as well as mice treated with other cancer cells including breast cancer cells MDA-231 and lung
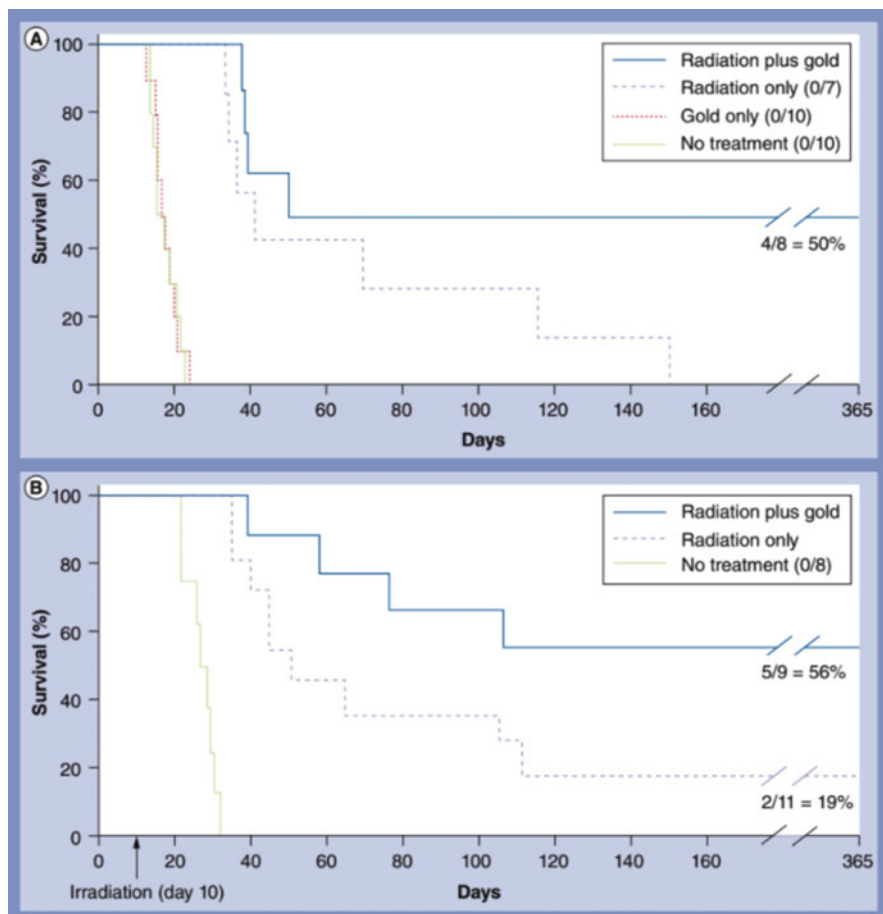
Fig. 9.29 Survival of mice treated with gold nanoparticles under X-ray irradiation. (Used with permission from Hainfeld et al. [107] under CC BY 3.0 license.)

cancer cells H460. The authors conjugated peptides to the surface of PtFe particles and investigated biological effects. In terms of accumulating in breast cancer tumors, GIRLRG peptide appeared to be an effective ligand when coated on the surface of PtFe particles. Hallahan et al. [82] again used peptides conjugated to nab-paclitaxel nanoparticles to bind to the radiation-inducible receptor in irradiated tumors. In this study, the authors used a mice model for lung cancer treatment. X-rays were used to activate the receptor to which peptide bound nanoparticles targeted. Optical imaging was used to confirm targeting of the nanoparticles. Hallahan et al. [101] reported on radiation-guided delivery of FePt nanoparticles coated with peptide for cancer treatment. The average size of FePt nanoparticles was 2.7 ± 1.0 nm. Accumulation of the nanoparticles at tumor sites after irradiation was observed, indicating the nanoparticles indeed targeting the radiation treated tumors.
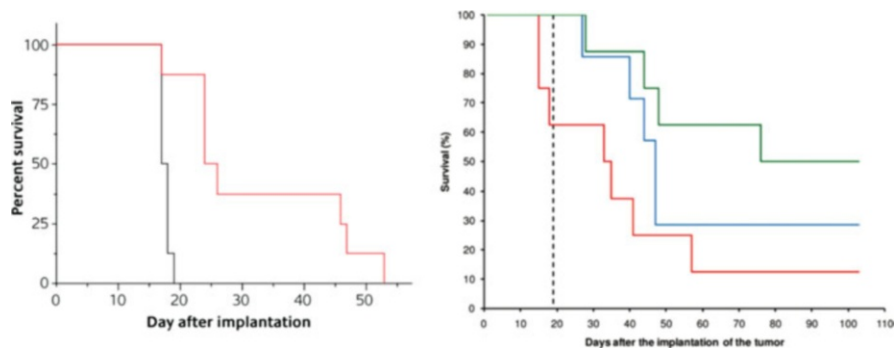
Fig. 9.30 Results of nanoparticle-enhanced therapy on treating 9L gliosarcoma-bearing rats. Percentage survival results using gold nanoparticles (left panel) are shown. Effect of rare earth-doped titania on the enhancement of radiation is shown in the right panel. (Left panel: Roux et al. [208]. Open access made possible by Gold Bulletin. Right panel: Adapted with permission from Roux et al. [115]. Copyright (2014) American Chemical Society.)

Chen and Wu et al. [191] employed cancer-bearing mice to investigate the effect of 13-nm gold nanoparticles under 6-MeV electron irradiation. Gold nanoparticles under irradiation showed a 25–50% improvement for a gold loading of 74 μg/mg in tumor tissues using the survival fraction measurements performed over a 100-day study. This translated to a 0.25–0.5 DEU enhancement for or 7 WP gold in tumor loading. 7 WP gold nanoparticles in water is supposed to produce only 0.2 DEU enhancement because electron interaction cross-sections with gold is only three times that with water, which suggests that the observed enhancement could be caused by physical enhancement.

Roux et al. [208] developed chelate surfactants on gold nanoparticles for combined X-ray and MRI imaging of animals and potentially for clinical applications as well. Further, they evaluated the therapeutic impact of their nanoparticles. The average size of gold nanoparticles was 2.4 nm. X-rays were from synchrotrons and a microbeam configuration was used. Although no direct and quantitative data was available showing the uptake and enhancement, the authors used fisher rats and doubled the survival time for the treated animals. The authors showed evidence of using gold nanoparticles as both a contrast agent to detect and a therapeutic agent to treat 9L gliosarcoma tumors in mice. The results are shown in Fig. 9.30 (left panel). Roux et al. [115] used microbeam radiation to irradiate Gd-based nanoparticles for therapeutic purpose. Gd nanoparticles were used as a contrast agent for MRI. The authors found that with sufficient amounts of Gd in the tumor, cancer-bearing mice could stay alive longer after Gd nanoparticle-treated mice were irradiated with X-rays. 9L gliosarcoma-bearing rats were used, and the treatment results are shown in Fig. 9.30 (right panel). The skin entrance dose was set at 400 Gy, which was significantly higher than normal animal work.

Hunting et al. [209] used MRI to visualize nanoparticles for enhanced radiotherapy of cancer-bearing mice. Their 5 nm average-size gold nanoparticles, covered with gadolinium capturing ligands of dithiolated diethylenetriaminepentaacetic,
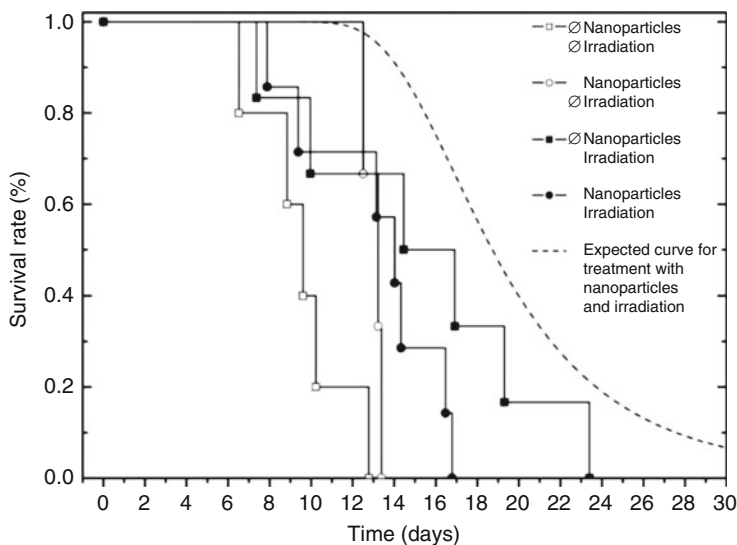
Fig. 9.31 Survival of mice treated with gold nanoparticles under X-ray irradiation. Experimental results are compared with the theoretical predictions (dashed line). (Adapted from Hunting et al. [209], reprinted by permission of Taylor & Francis Ltd. http://www.informaworld.com)

were injected into the mice in the tail veins. The radiation dose was 10 Gy at 150 kVp. The MRI results showed 10 μg gold nanoparticles in 30 μL or 30 μg of tumors, giving rise to a 33 WP gold loading in tumor. If the average physical enhancement existed, then a 33 DEU maximum physical enhancement was expected. Figure 9.31 shows the results, which indicate that the measured enhancement is lower than the expected enhancement. Nonetheless, there was enhancement by gold nanoparticles when irradiated with X-rays.

Jiang et al. [15] conducted treatment of tumor in mice with cisplatin-packed nanoliposomes. Single dose of up to 28 Gy was administrated to both A549 cells and Lewis lung carcinoma. The authors counted the jejunal crypts after sacrificing the mice. Tumor growth delay (TGD) (in vivo) and cell survival curve (CSC) (in vitro) were obtained and used to estimate the efficacy of the combination of radiation and drugs. Irradiation was carried out 72 h after drug administration, at which time the drugs were distributed to the tumor sites. Jejunal crypt survival curves were determined using the linear-quadratic model (L-Q). Nanoliposomes were nontoxic, but their drug-containing versions showed inhibition of A549 cell growth/colony formation. Tumor growth was delayed with X-ray irradiation and with drug bearing nanoliposomes, and tumor growth delays were more pronounced than jejunal crypt cells in mice. The cell survival fraction was 2–3% at 6 Gy. The best result was obtained with a 72-h delay between the injection of nanodrugs and irradiation. Tumor growth was delayed up to 26 days upon treatment with nanodrugs and radiation.
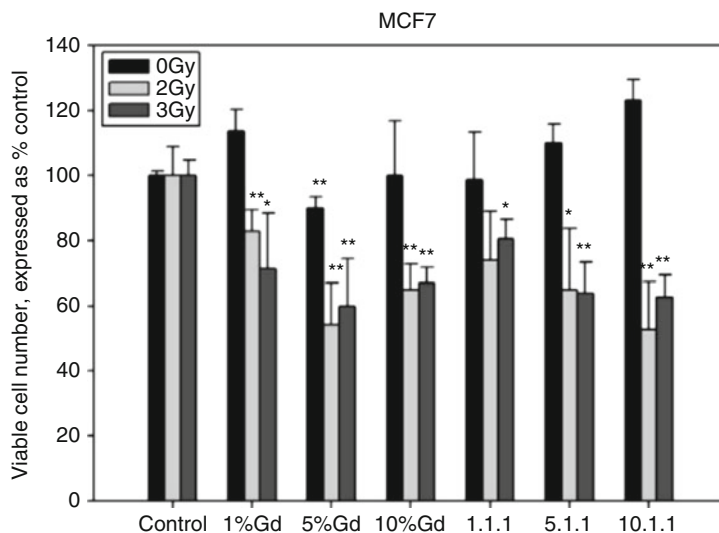
Fig. 9.32 Effect of rare earth-doped titania on the enhancement of the effect of radiation. (Reprinted from Townley et al. [210]. Copyright (2012) with permission from Elsevier.)

Townley et al. [210] reported using X-rays to activate lanthanide (Gd and other elements)-doped titania nanoparticles for cell killing. The authors stated that the average size was 60 nm with multiple grains of 3–10 nm. They also coated the nanoparticles with a layer of silica and estimated the thickness to be around 1–2 nm. The dose of irradiation was 3 Gy from X-rays with an 80–90 keV average energy. Cell proliferation was reduced by 75% after treatment. The authors attributed the enhancement to increased production of reactive oxygen species in the presence of these nanomaterials. Figure 9.32 shows the results of enhancement measurements.

In addition, Townley et al. [211] studied rare earth element-doped TiO_2 nanoparticles for radiation therapy. They also coated a 1–2 nm layer of silica on the outside of the nanoparticles. They irradiated animals using X-rays emitted from an X-ray tube operated at 200 kVp. Emission from rare earth elements under X-ray irradiation was used for excitation to produce reactive oxygen species. The results confirmed that X-ray irradiation of the said nanomaterials reduced the tumor size by half.

Choi et al. [21] discussed their work of using synchrotron X-rays at 7.1 keV to irradiate FeO_x nanoparticles in a mouse tumor model. This was a unique study because the X-ray energy was low and X-rays were resonantly absorbed by the nanoparticles, similar to what was done by Townley et al. mentioned above. The authors called the method photo-activated therapy (PAT). They treated CT26 tumors and CT26 tumor-infected mice. Tumor regression assay was used to estimate enhancement. A similar set of in vitro results are presented in Sect. 9.5.3. The size of the nanoparticles was 13 nm. Cytotoxicity of FeO_x nanoparticles was observed at 0.2 WP, which was the incubation concentration. After uptake, the concentration in

the cell was 30 pg or about 0.3 WP (30 pg in a cell weighing 1 ng). FeO_x nanoparticles alone already significantly delayed the growth of the tumor. The loading of FeO_x nanoparticles was verified to be 40 ppm (40 μg/g) in tissue. This loading was low compared with the gold loading in gold nanoparticle sensitized X-ray treatment of cancer-bearing animal models. The total X-ray dose was 40 Gy, delivered over 10 days. Their results are shown in Fig. 9.33. The combination of X-rays and FeO_x nanoparticles had the best effect. Radiation alone also showed significant improvement, almost as good as the combined radiation and nanoparticle
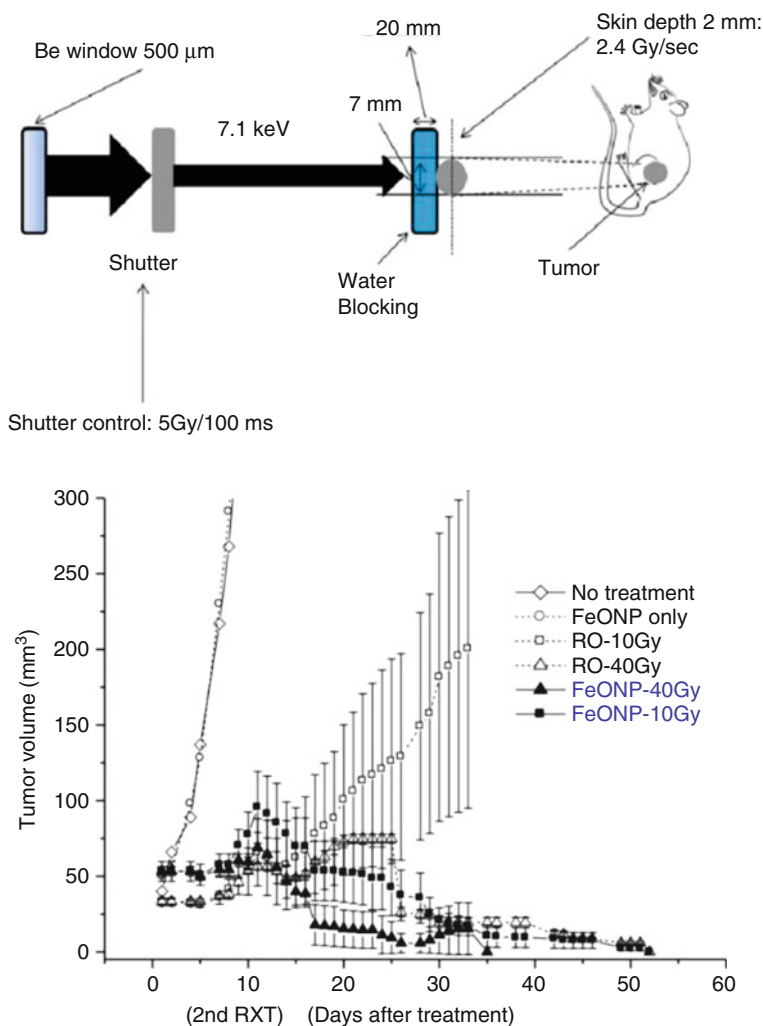
Fig. 9.33 Resonant interactions of X-rays and iron oxide nanoparticles in mouse tumors for radiotherapy. 10 and 40 Gy doses were used. The top panel shows the experimental setup, and the bottom panel shows the results. (Adapted from Choi et al. [21]. Used with permission under CC BY 2.0 license.)

effect. The results indicated 100% mice survived after 40 Gy treatment with FeO_x nanoparticles. On the other hand, only 20% survived after a 10 Gy irradiation. The authors also performed enhancement studies with high-energy X-rays emitted from accelerators, but no enhancement was detected.

Liang et al. [141] reported the results of their study on the effect of the size of gold nanoparticles on treating cancerous cells and mice. They used PEGylated gold nanoparticles for radiation therapy. γ-rays, U14 mice model, and 5 Gy of radiation were used in their work. The sizes of the gold nanoparticles were 4.8, 12.1, 27.3, and 46.6 nm. The results showed that 4.8 nm gold nanoparticles had the highest toxicity. The mice were monitored up to 28 days. Tumor size was used for determination of enhancement of treatment efficacy. They observed size dependency and found that 12 and 27 nm gold nanoparticles were better than 4.8 and 46 nm for slowing down the growth of cancer cells.

Anijdan et al. [194] used MV X-rays to irradiate tumor-bearing mice administered with gold nanoparticles. 6 and 18 MV X-rays were used at a dose of 20 Gy. 50 nm gold nanoparticles were used. The accumulation of gold in tumor was reported to be 7 mg/g, similar to what Hainfeld et al. [5]. The enhancement based on survival probability was on the order of 0.1 DEU.

Krishnan et al. [195] published their patent application of using targeted gold nanorods (AuNR) for treatment of cancerous cells and animals. The animal model results using tumor volume as a gauge of enhancement showed the best outcome with inhibitor cetuximab conjugated C225-AuNR under X-ray irradiation. The results of using PEGylated AuNR (PEG-AuNR) under X-ray irradiation were similar to that of irradiation alone. Results from cellular work were also presented in the application.

Tsourkas et al. [38] used a tumor-bearing animal model to study the effectiveness of 1.9 nm gold nanoparticles in micelles made of amphiphilic dicoblock copolymer poly(ethylene glycol)-b-poly(ε-caprolactone) PEG-b-PCL. The size of the assemblies ranged from 28 to 142 nm measured by DLS, and similar sizes were measured with TEM. The dose used by the authors was 6 Gy at 150 kVp. Treatment of HT1080 flank tumors using X-rays and the gold nanoformula showed a 0.7 DEU enhancement with 0.57 mg/mL or 0.057 WP gold loading in tumors measured with ICP-PES. This level of gold loading was supposed to produce only a few percent of physical enhancement, which was 10% of the measured enhancement. The loading of gold in the tumor and X-ray dose was lower than what others used in other animal models. Figure 9.34 shows the results by Tsourkas et al.

Tu et al. [198] performed both in vitro and in vivo measurements on glioblastoma tumors. The cellular apoptosis data suggested some enhancement when BSA-coated 18 nm gold nanoparticles were irradiated with X-rays. The in vivo data was mildly encouraging, showing that X-rays plus gold nanoparticles were slightly more effective than X-rays alone.

Guo and Xie et al. [200] studied the radiotherapeutic effect of ultrasmall gold nanoparticles, each containing only 29–43 gold atoms. The nanoparticles were covered with glutathionate ligands. The nanoparticles were injected into mice, and the loading in the tumor was of the order of 8–10 μg/g, which was too low to create
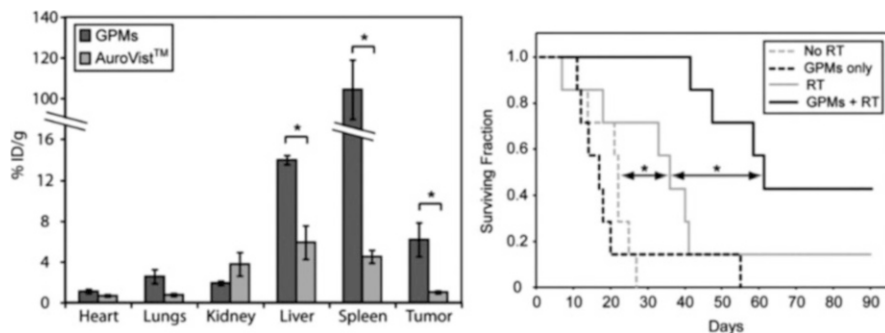
Fig. 9.34 Enhancement in terms of survival fraction increase after treatment with nanoliposomal 1.9 nm gold nanoparticles and radiation. The left panel shows the biodistribution and the right panel shows the surviving fraction results. (Reprinted in part with permission from Tsourkas et al. [38]. Copyright (2015) American Chemical Society.)
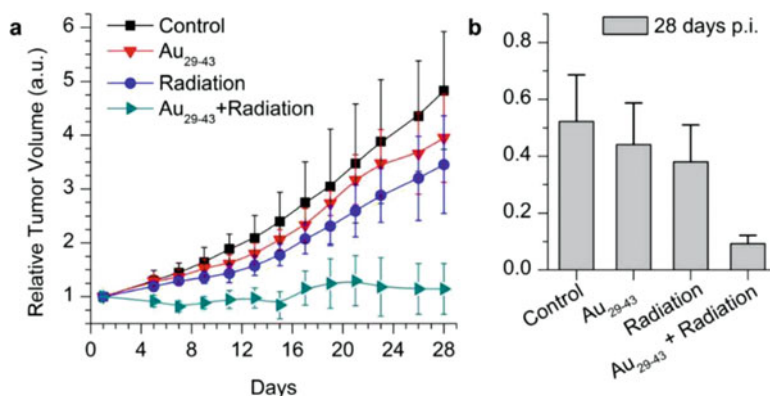
Fig. 9.35 Ultrasmall gold nanoparticles for radiation therapy. The time-course study of the tumor volume is shown in the left panel, and the right panel shows the results of weight study. The effect of enhancement is clearly visible in both studies. (Adapted from Guo and Xie et al. [200]. Used with permission under CC BY 4.0 International license.)

any physical enhancement. On the other hand, the authors observed a clear impact of the combination of X-ray radiation and the nanoparticles—after 28 days, there was almost no tumor growth among mice exposed to both ingredients, whereas the tumor grew fivefold among the mice without the treatment. Figure 9.35 shows the enhancement results, which showed a much higher enhancement than physical enhancement caused by a 10 ppm loading of gold in tissues. The calculated enhancement using Eq. 9.1 is 1.6 DEU, after taking both toxicity of the nanoclusters and X-ray damage into account.

Kunjachan and Berbeco et al. [196] reported tumor vascular damage to Panc-1 tumor xenografts using vessel-targeted gold nanoparticles. 2–3 nm gold

nanoparticles were coated with Arg-Gly-Asp ligands for targeting and imaging purposes. The overall hydrodynamic size was 8–10 nm. In vitro study results are given in Chap. 8. Animal model results are given here. The authors employed a Small Animal Radiation Research Platform to deliver localized dose at the small tumors with two orthogonal and collimated beams of X-rays. The dose was 10 Gy from 220 kVp X-rays. The local dose was about four times higher than the rest of the animal because of the irradiation configuration. 3.0 DEU enhancement in γ-H2AX assay results was observed when both gold nanomaterials and X-rays are applied. However, no quantitative biodistribution data was available, making it difficult to assess the origin of enhancement.

Xie et al. [199] studied a nanoscintillator for its X-ray-induced photodynamic therapy properties. The nanoscintillator was mechanically ground $SrAl_2O_4:Eu^{2+}$ bulk materials. The authors named the nanomaterials SAO and mesoporous SAO was called M-SAO. The luminescence was emitted from Eu^{2+}. The grinding produced approximately 80 nm nanoparticles. The nanoparticles were coated with a silica layer of different thicknesses because the nanoparticles were highly hydrolytic. The final size was near 400 nm. Photoluminescence was at 520 nm and its intensity decayed quickly to less than 10% after 3 days. Figure 9.36 shows the results. The left panel shows the results of singlet oxygen measurements, which suggested that only M-SAO produced significant amounts of singlet oxygen. The right panel shows the in vivo data. Again, only the M-SAO nanoscintillator under X-ray irradiation suppressed tumor growth. The enhancement value is significant if the volumes of tumors shown in Fig. 9.36 are used together with Eq. 7.1 or Eq. 9.1 because of the closeness of the effects of radiation or nanoparticles alone to the control.

Liu and Yang et al. [203] developed a new nanomaterial Au@MnS@ZnS-PEG that was used for MRI imaging and X-ray sensitization. The nanomaterial consisted of a gold core of a few nm in diameter that was in a MnS shell followed by a coating of ZnS on the outside. The nanoparticles were then conjugated with PEG ligands.
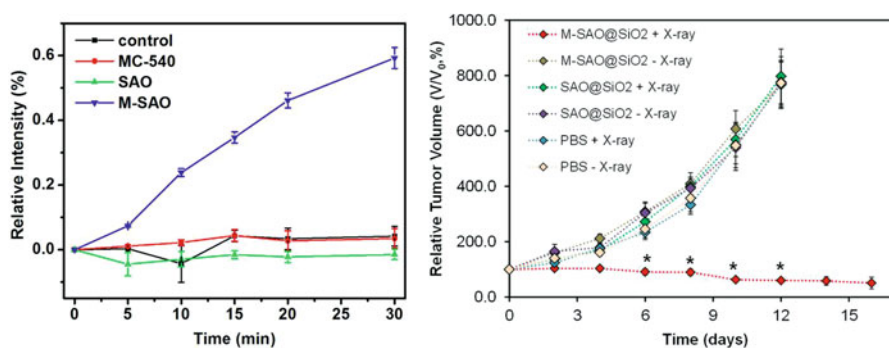
Fig. 9.36 Singlet oxygen production (left panel) and summary of in vivo radiation therapy (right panel) using M-SAO nanomaterials developed by Xie et al. An enhancement of close to 200 DEU is obtained using the data shown in right panel. (Adapted with permission from Xie et al. [199]. Copyright (2015) American Chemical Society.)

The overall size was on the order of 100 nm. Both in vitro and in vivo experiments were performed. 4T1 cells were used, and LD_{50} was 3.5 Gy, which decreased to 2.5 Gy with the use of the nanomaterial, resulting in a 0.7 DEU enhancement. In vivo results showed a 1.3 DEU enhancement using a 4 Gy dose of X-ray irradiation. 6 Gy irradiation together with the nanomaterial nearly completely suppressed tumor growth. No toxicity was available for the nanomaterial.

Zhao and Yang et al. [202] synthesized silica-coated gold nanorods and employed the nanomaterial to treat tumor-bearing mice exposed to 6 MV X-ray radiation. The nanorods were 58 nm long and 14 nm in diameter and the coating thickness was 18 nm. Arginine-glycine-aspartic acid (RGD) peptides were then conjugated to the surface of the silica-coated nanorods for targeting. Both in vitro using MDA-MB-231 cells and in vivo studies were performed. Cellular survival fraction data showed improvement when RGD peptide-conjugated nanorods were used with X-rays, resulting in a moderate 0.4 DEU enhancement using X-ray doses to cause a 10% surviving fraction. In vivo data was more promising, reaching 2.5 DEU when RGD peptide-conjugated nanomaterials were used with X-rays compared with radiation alone.

Liu and Gu et al. [212] compared the radiosensitizing property of ca. 15 nm silver and gold nanoparticles using both in vitro and in vivo models, and the authors found that silver nanoparticles were more lethal in both models. This outcome should not be surprising as silver nanomaterials tend to disintegrate under redox and X-ray irradiation environment, as shown by Guo et al. [213].

Paquette et al. [34] investigated the effect of a tiopronin-coated gold nanoparticle on killing tumors in mice. The average X-ray energy was 26 keV. The nanoparticles were around 3 nm. Tumor volume was used to determine enhancement. Biodistribution measurements showed only 0.05 WP gold in tumor tissues, which was inadequate to cause any significant physical enhancement. Nearly 1.0 DEU was calculated using tumor volumes at the 10-day point after X-ray irradiation, which was similar to the in vitro enhancement in treating colorectal tumors.

Yu and Chen et al. [13] synthesized a gold nanorod core-selenium spherical shell nanomaterial covered with chitosan ligands as well as peptide targeting ligands. The authors conducted in vitro and in vivo work to determine the effect of these nanomaterials on X-ray radiotherapy. They used A375 cell line and A375-bearing mice to measure the enhancement. Based on their results, the calculated enhancement of using X-rays and the nanomaterials was approximately 0.3 DEU. The nanomaterials themselves were more than twice as toxic as 4 Gy X-rays. The cytotoxicity may be caused by dissolution of Se nanomaterials in cells.

Yang and Li et al. [71] studied the radiosensitizing properties of their 3.6 nm dia. Bismuth nanoparticles. The nanoparticles were conjugated with LyP-1 tumor targeting peptide ligands. The relative tumor volume was measured to determine the enhancement. No toxicity was found with the bismuth nanoparticles. The calculated enhancement based on the tumor size measurements was 0.8 DEU. Using contrast increase of 1193 HU and the calibrated unit mass contrast increase of 13.8 HU mM^{-1}, bismuth concentration was 86 mM, which correspond to 1.72 WP. If this amount of bismuth was accumulated in the tumor and only physical

enhancement was responsible for the increased damage observed by the authors, then up to 2.4 DEU enhancement would be seen for 33 keV X-rays.

Detappe and Berbeco et al. [165] synthesized a nanomaterial that had a Gd_2O_3 core and SiO_2 shell covered with DOTAGA ligands with Bi^{3+} ion trapping terminal groups. The final size was 4.5 nm, measured with DLS. The final nanomaterial product, called SiBiGdNP, was irradiated with 6 MV X-rays after intravenous injection into the animals infected with A549 lung tumor. Tumor growth or percentage survival data was used to estimate the enhancement. The control showed linear growth over 60 days. Radiation alone seemed to suppress tumor growth till 60 day, beyond which the volume grew exponentially. The biodistribution measurements showed small amounts of the nanomaterials in the tumor. The results again proved that biological experiments with small nanomaterials did not follow physical enhancement predictions.

As shown in Chap. 6, Liu et al. [204] developed a new nanomaterial called BM@NCP(DSP)-PEG with a bovine serum albumin protein-stabilized MnO_2 nanoparticles core that was wrapped by a polymer-linked cisplatin compound shell. This nanomaterial was then coated with dopamine and then PEG. The authors used this nanomaterial to treat 4T1 cells and measured cell damage using γ-H2AX assay for DNA damage and MTT for cell viability. 6 Gy of radiation was used. Enhanced DNA damage was observed with the nanomaterial under X-ray irradiation. However, since no data on radiation alone was available, it was impossible to calculate the enhancement. Based on the results presented by the authors, it seemed that the nanomaterial was toxic to cells. However, no such toxicity was shown in the animal model. If the result of cisplatin in combination with X-ray was used to calculate the enhancement with the nanomaterial plus X-rays, then the enhancement was approximately 1.0 DEU.

9.6.2   Preclinical and Clinical Trials

There have been only a few preclinical and clinical trials using nanomaterials to enhance the efficacy of radiotherapy. These studies are summarized here. Jain et al. [214] reviewed the preclinical trials of gold nanoparticles. The authors also discussed the gold nanoparticles as drug carriers, contrast agents, thermal drugs, and as radiosensitizers. The authors did not include certain nanoparticles such as those used by Nanobiotix in their clinical trials as discussed below.

Nanobiotix Inc. is a French company that has been developing radio-enhancers using nanomaterials. The company first reported its product NBTXR3 in 2009. NBTXR3 was claimed to contain crystalline nanomaterials that are inert and absorb X-rays and release electrons as the primary reason for its cancer treatment effectiveness. The company patented a drug platform called NanoXray Therapeutics, which includes the drug NBTXR3. The company tested the drug on several tumors including HCT116 colon cancer tumor and HT1080 fibrosarcoma tumor. Maggiorella et al. [10] investigated the radiotherapeutic effect of hafnium oxide

nanoparticles, which were NBTXR3. Negatively charged surface ligands were coated on the surface of the nanoparticles. DLS measurements suggested a 50 nm average diameter. Both in vitro measurements using HT1080 cells and clonogenic assay and in vivo studies were performed. TEM images showed aggregated nanoparticles in the cell, albeit not in the nuclei. Clonogenic assay results show higher enhancement at cobalt-60 energy than 6 MV γ-rays. The enhancement at cobalt-60 was less than 0.5 DEU. In vivo data were collected using HCT 116 tumor model. The authors claimed a ninefold or 9.0 DEU enhancement. Enhancement caused by direct X-ray absorption by nanomaterials should play a negligible role because high-energy X-rays were used. The company has been conducting a phase III clinical trial using its latest product NBTXR3. The latest news, which was shown online on July 6, 2016, indicated "promising signs of tumor volume response." The trial used 70 Gy to treat neck cancers and the results showed shrinkage of tumor after treatment with NBTXR3 and X-ray radiation.

Sancey et al. [215] reported using gadolinium-based nanoparticles to treat brain melanoma metastases under X-ray irradiation. The authors called the study proof-of-concept before phase I trial. The idea was to use gadolinium compound surrounding nanoparticles to absorb X-rays and then release reactive oxygen species to kill tumor cells. The study included in vitro and in vivo component. Brain tumor-bearing mice were used as the animal model and skin melanoma cells were used as in the in vitro study. Radiation was 220 kVp X-rays with Al filters. The average size of the nanoparticles was 3 nm. The loading of gadolinium in the nanoparticles was 20%. The authors called the nanoparticles AGuIX. No quantitative uptake or biodistribution data was available. Dose enhancement factor using the in vitro data was 0.3 DEU with 0.6 mg/L incubation concentration of the AGuIX. In vivo data showed more than a 2.0 DEU enhancement using the survival fraction after 7 Gy and 10 mg treatment. Although this was labeled as preclinical, the scope of work was similar to many of those presented in Sect. 9.6. Long-term cytotoxicity data is not available.

Magné et al. [216] reviewed the status of field of using nanoparticles in radiation oncology. The review covered bench work as well as clinical work. The authors discussed the physical and biological aspects of nanoparticles when they interact with biological systems. Both aspects share similarities with the physical and biological enhancement discussed in this book. The review listed all the recent clinical trials in the world that employ technologies related to using nanomaterials to assist radiotherapy.

9.6.3 Summary

The in vivo enhancement results are summarized in Fig. 9.37. For the work showing uptake results, the corresponding enhancements are shown in solid symbol. The enhancement factors are clustered around 0.5 DEU, meaning that the effect is almost the same regardless of the amount of nanoparticles introduced into the animals. This
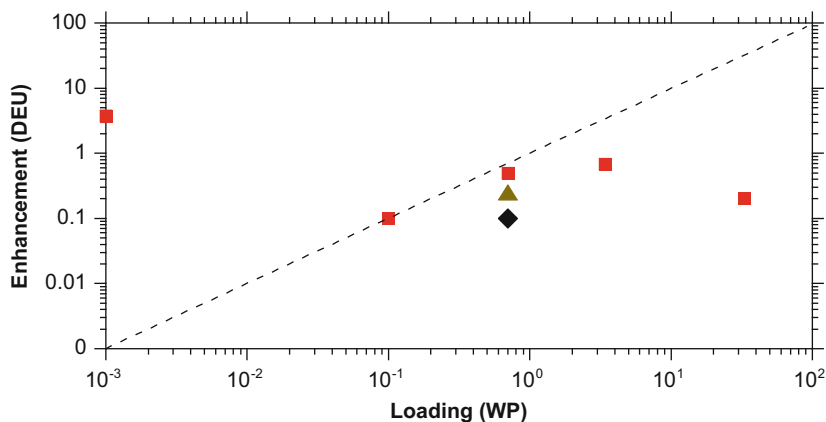
Fig. 9.37 Summary of the results of in vivo work of using nanomaterials to improve radiation therapy (red squares). The trend is similar to the in vitro results shown in Fig. 9.28, i.e., the measured enhancements are clustered around the value of 0.5–1.0 DEU regardless of the loading of the nanomaterials in the animals, which varied over five orders of magnitude. MV irradiation results are also shown here (brown triangles and black diamonds)

is similar to what is shown in Fig. 9.28 for the in vitro enhancement studies. Therefore, it is possible that the observed enhancements do not originate from physical enhancement as researchers have originally envisioned. Chemical enhancement may be more likely, and biological enhancement may be the most likely source for the observed enhancements. Although the impact of these experiments is too early to tell, it is prudent to state that animal models are a complex system, and many features such as pharmacokinetics still need to be carefully investigated. Knowing what is shown in Fig. 9.37, an immediate benefit may be that only small loadings are needed to achieve the average 0.5 DEU enhancement.

9.7   Other Methods to Improve X-Ray Treatment of Cancer with Nanomaterials

Several reports in the literature have described the results that are beyond the scope of the work discussed in the last three subsections. Here, these results are briefly discussed because they can be readily used in medical applications of X-ray nanochemistry. This part covers miscellaneous methods that can be used with nanomaterial-assisted X-ray treatment. For example, a new method is shown that can deliver hundreds and even thousands of times more dose to a target deep in the body than the surface dose using a continuous scanning focusing X-ray beam configuration.

One way to enhance the effectiveness of X-ray irradiation is to manipulate X-rays to increase the local dose at a target in the middle of an object. There were several methods reported in the literature to achieve this goal. For example, Norman et al. [220] invented a multiple beam scanner to improve X-ray therapy. These X-ray beams were on the same plane and each beam pointed at the same point on the plane. The configuration effectively focused these beams to the point, forming a focal spot a few millimeters in diameter. The dose was enhanced a few times at the focus. Uesaka et al. [218] discussed a concept using multiple 10 MeV X-ray stationary beams. The footprint of the device was relative large, around 5 m × 5 m. Gokeri et al. [144] used multiple parallel beams of X-rays, each with a 0.68 mm diameter and energies from 30 keV to 600 keV available at the ESRF synchrotron source. The beams delivered high dose deep in the head by pointing the beams at the same point from many directions. The authors also calculated enhancement by adding gold into the region of interest. For 7 mg/g or 0.7 WP gold loading, they observed an approximately 30% increase, which was lower than the 1.4 DEU WP^{-1} physical enhancement for 33 keV X-rays.

Jaboin et al. [190] reported a radiation-guided nanoparticle drug delivery system to treat pancreas cancer cells in mice. The authors coated the nanoparticles with HVGGSSV peptides on the surface of nanoparticles, which also had several other ligands coated on the surface including an optical fluorescence label for near-infrared imaging. Upon irradiation with a 3 Gy dose of ionizing radiation, the peptide-conjugated nanoparticles were administered into mice, and it was found that these nanoparticles targeted tumors because of the selective binding between the peptide- and radiation-activated receptors. Without irradiation, there was no localization of nanoparticles at the tumors. This method may prove useful in delivering drugs only to tumor sites after being irradiated with X-rays.

Pradhan et al. [219] theoretically predicted effects of Auger processes in highly ionized gold atoms and their applications in nanotheranostics. Their work was based on resonant absorption of X-ray photons by highly ionized gold ions that allowed K to L transitions, meaning all the electrons above L shells were ionized prior to this simulated process. The authors predicted the energy deposition by electrons released from gold irradiated with 68 and 82 keV as well as 2 MeV X-rays and found a high enhancement from resonant absorption by these highly charged ions. However, in order for this to work, the gold species under investigation have to be nearly fully ionized, up to Au LXXVII or Au^{77+}. The lack of electrons for the subsequent Auger processes makes this ambitious design difficult to implement practically. An alternative may be using intense ultrafast X-ray pulses to resonantly remove just an L-shell electron, which would be similar to pulsed laser irradiation as suggested by the authors.

It is possible that other mechanisms of enhancement exist. For example, Nadeau et al. [220] demonstrated doxorubicin on small gold nanoparticles (<2.7 nm) could effectively kill even apoptosis-resistant cancer cells. The authors attributed the enhancement, which was 20 DEU, to the ability of these small nanoparticles being able to enter the nuclei. Such a process may prove to be useful in X-ray-induced enhancements.

Tu and Lo et al. [118] used gold nanoparticle contrast agents for radiotherapy planning. They compared the gold nanoparticles against a standard of Conray 60, an iodine-based contrast agent, and for the same concentration, gold nanoparticles were about 20% better. This work indirectly showed that gold nanoparticles were viable materials that could be imaged and then employed for treatment once the location is confirmed.

Welland et al. [59] used a new nanomaterial that had cisplatin conjugated to the surface of gold nanoparticles (AuNPs). They used S2 cells and three assays including the MTS cell viability assay, nuclear DNA damage γH2AX and caspase-3 assay to determine the effectiveness of cell killing. Gold nanoparticles covered with human serum albumin (HAS) or polyethylenimine (PEI) were also used. PEI-AuNPs had much higher uptake and could cause more DNA damage than HAS-AuNPs. AuNPs with cisplatin conjugated to their surface were found to be much more effective in causing nuclear DNA damage ($>10\times$) and cell death ($\sim3\times$) than AuNPs without cisplatin.

Guo et al. [221] showed the advantage of using a continuously rastering X-ray beam over even 65 stationary X-ray beams. The authors performed both theoretical simulations and experimental prototype work. Two possible experimental setups are shown in Fig. 9.38. The left panel shows a proposed design that employs two moving X-ray sources. The right panel shows a microfocus X-ray source mounted on the top of a lead chamber in which two rotary motors were mounted to manipulate a platform. A plastic phantom was mounted on the platform, which rotated in one direction and rocked in another, creating a truncated 3D spherical cap motion.

The simulated data of continuous scanning focusing is shown in Fig. 9.39, which displays delivered dose profiles in two directions, one along the central X-ray beam path or axial direction and another in the perpendicular direction. The left panel of Fig. 9.39 shows the dose profile in the axial direction. Three beam configurations were used: 9 beams, 65 beams, and continuous rastering beam. The results showed a clear advantage of using the continuous rastering beam, depositing most energy at the focal point deep in the tissue. The increase over the surface dose was nearly 200-fold for the X-ray spectrum shown in the inset in the top panel. Figure 9.39
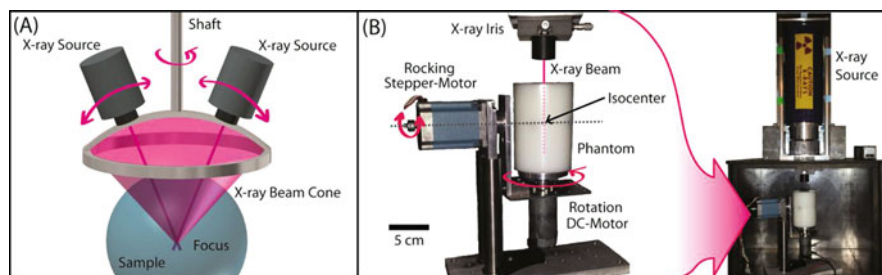
Fig. 9.38 Apparatuses of the continuous scanning focusing X-ray needle beam. The left panel shows a design using two microfocus X-ray sources and a stationary sample configuration. The right panel describes an experimental setup of a single X-ray source, a moving or rastering sample configuration using two motors. (Reprinted with permission from Guo and Davidson. [222]. Copyright (2016) by Radiation Research. All rights reserved.)
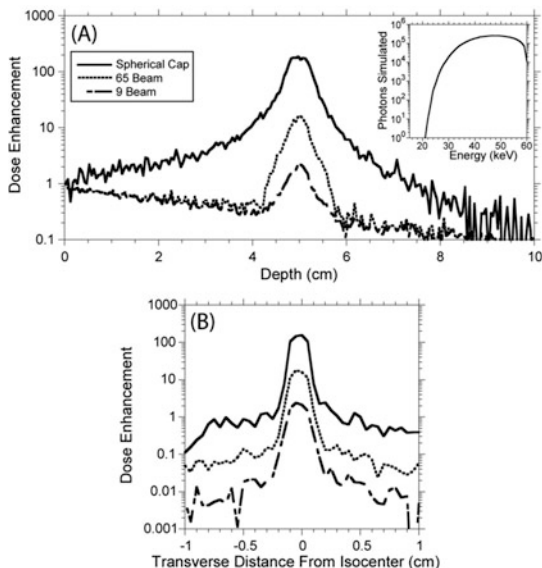
(bottom panel) shows the dose enhancement in the radial direction. Again, the enhancement at the focus was 100-fold more than the peripheral. With the addition of gold nanoparticles, it was possible to further increase the dose deposited at the focus, and an enhancement of up to 3000 DEU was possible when scanning focusing technique was combined with multiplication of physical and chemical enhancement shown in Chap. 5. These results demonstrated the benefit of using the rastering focusing configuration to increase local dose without even using nanoparticles. For example, if only a 0.5 DEU or even 5 DEU enhancement is needed, then continuous rastering with a narrow beam of X-rays can deliver without using radiosensitizers. When higher enhancements such as 1000 DEU are needed, then nanomaterial-assisted methods may be employed in addition to the continuous rastering beam approach. If targets at shallower depths need to be treated, larger solid angle rastering focusing may be used to achieve the same effect of dose enhancement at the target.

Lapotko et al. [222] showed an interesting method which the authors claimed lowered the X-ray dose needed to treat cancer cells by 100-fold and tumors by 17-fold. Totally four modalities were used in their approach to treat cells or tumors. Gold nanoparticles were used as one of the four modalities, and the other three were X-rays, encapsulated drugs, and near-infrared laser pulses. Prior to X-ray irradiation, laser light was used to irradiate gold-loaded cells or tumors to create plasmonic nanobubbles, which can help rupture the encapsulation to release drugs. The authors then applied X-rays to work synergistically with the released drugs. The authors called the process amplification because the X-ray dose needed to kill the cells was reduced significantly, down to 2–4% of what was normally needed in X-ray radio-therapy. However, the dose employed by the authors was 4 Gy, similar to what was used to destroy cells with only X-rays, not 0.04 Gy. The amplification obtained at

Fig. 9.40 Results of combination of four methods, a drug, infrared laser light, X-rays, and gold nanoparticles, to kill tumor cells. The optimal results were obtained when all four modalities were used and X-ray irradiation occurred 6 h after laser treatment. (Reprinted by permission from Macmillan Publishers Ltd.: Nature Medicine Lapotko et al. [222], copyright (2014).)
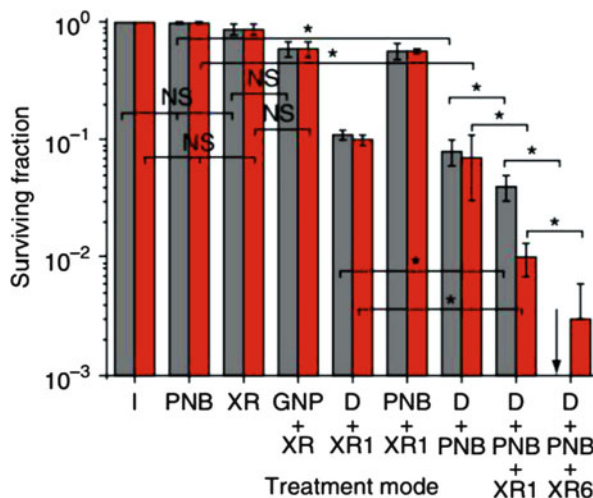
this dose was visible in lowering the surviving fraction, which was much less than what was caused by 4 Gy of irradiation alone due to the actions of the drugs. Figure 9.40 shows their results. The authors used the term intracellular amplification, suggesting the amplification was at least partially achieved through cellular activities. As a result, the process may be understood as equivalent to biological enhancement. The authors did not explain the amplification. The loading of gold was nonuniform in the cell, and quantitative uptake data was not available. The gold nanoparticle and X-ray data suggested that the loading of gold nanoparticles was low because the enhancement from this combination (GNP+XR in Fig. 9.40) was low.

A similar method was developed by Wu and Chen et al. [42]. The nanomaterials were hollow gold nanoshells synthesized from silver seed nanoparticles. The outside diameter was ca. 60 nm. The nanoshells absorbed near-infrared (NIR) light. KB cells were used in in vitro work and mice with U14 xenograft tumors were used in in vivo work. Surviving fraction was used to determine the in vitro enhancement, and tumor size was used to determine the in vivo enhancement. No quantitative data was available for the uptake or biodistribution, so it was impossible to predict the magnitude of physical enhancement. 6 MV X-rays were used, so it was unlikely the enhancement was caused by physical enhancement. The results suggested a 0.2 DEU in vitro enhancement using the gold nanomaterials and 6 MV X-rays. Based on the tumor sizes, in vivo enhancement of 0.07 DEU was obtained. NIR together with MV X-rays produced better results, similar to what is shown in Fig. 9.40.

Shi et al. [223] studied the effect of adding nuclear targeting ligands to the surface of gold nanoparticles for enhanced X-ray irradiation damage to cells and tumors. The nanomaterials were silica-coated rare earth nanoparticles with nuclear targeting TAT ligands conjugated to the surface. The size of the nanomaterials was between 40 and 81 nm, measured with TEM and DLS, respectively. The authors claimed that these nanomaterials entered the nuclei with pores of 50–70 nm, which was different from statements in other publications. HT-1080 cells were used in in vitro work, which

showed a 0.77 DEU enhancement without TAT, and the enhancement increases to 1.2 DEU with TAT. NIR irradiation was used synergistically. Tumor volume measurements showed a 1.9 DEU enhancement. Again in vivo data suggested that NIR irradiation was more effective than X-rays.

Bu and Shi et al. [197] investigated a method to release NO using X-rays, which was used to treat tumors under hypoxic conditions. The synthesis was conducted with the aid of nanochemistry because multiple step reactions were involved in constructing the nanomaterials. The authors called the rare earth nanoparticles upconversion nanoparticles (UCNPs) and mesoporous silica-covered UCNPs USMSs. When the nanoparticles contained S-nitrosothiol, an NO donor, the nanomaterial was called USMS-SNO. NO was released under X-ray irradiation. NO production was on the order of 8.5 µM over 23 h even without USMS-SNO. With irradiation of 5 Gy X-rays and in the presence of nanomaterials, the amount increased to 10 µM, representing a 30% increase. In vivo data was used to calculate the enhancement, and a 0.4 DEU enhancement was obtained using tumor volumes at 15-day point, which agreed well with the NO amount increase for 5 Gy irradiation. In another report, Shi et al. [224] described the results of synthesis and application of a rare earth nanoparticles core covered with porphyrin IX-embedded PEG and conjugated with TAT targeting ligands. TAT ligands significantly improved the performance of the nanomaterials in killing tumor cells and tumors.

Koger et al. [225] theoretically model the irradiation of gold nanoparticles embedded tissues similar to Guo et al. [221]. The authors called their method arc radiation therapy. PENELOPE (v 2011) was used to help predict the results, which showed a similar energy dependency as that predicted by the ratio of X-ray mass energy absorption coefficients of gold to water shown in Fig. 2.1 (right panel). With the gold nanoparticles embedded in the tissue, a much better defined spatial profile was obtained, similar to that shown in Fig. 9.39.

Yang et al. [201] found that coating a layer of MnO_2 on gold nanoparticles helped increase the amount of oxygen in hypoxic cells. MnO_2 reacted with endogenous H_2O_2 in the cell to generate oxygen, which was believed to be an important component for effective radiotherapy. The nanoparticles were then coated with PEG ligands to form Au@MnO_2-PEG. The gold core was 30 nm in dia., and the MnO_2-coated gold nanoparticles had an average diameter of 50 nm. Dissolved oxygen amount increased when the nanomaterial was used with H_2O_2. 4T1 cells were used and the best result of DNA damage using γ-H2AX assay was achieved through using Au@MnO_2-PEG and X-rays, which caused more than three times the amount of DNA damage by X-rays alone. In vivo results were equally encouraging. Figure 9.41 shows the results.

Ogino et al. [226] discovered a unique way to counter hypoxic conditions in tumor treatment. The idea was to treat titanium dioxide (TiO_2) nanoparticles with hydrogen peroxide (H_2O_2) so that the new nanomaterials slowly released H_2O_2 and therefore oxygen in the cells or tumors. The presence of oxygen hence sensitized the destruction of cancerous cells or tumors by X-ray irradiation. The titanium nanoparticles were first modified with polyacrylic acid and then hydrogen peroxide. The particle size characterized by DLS was on the order of 100 nm. Release of H_2O_2

Fig. 9.41 Combination of Au@MnO$_2$ and X-rays to kill tumor cells. The results were obtained by Yang et al. [201]. (Reprinted by permission from Macmillan Publishers.)
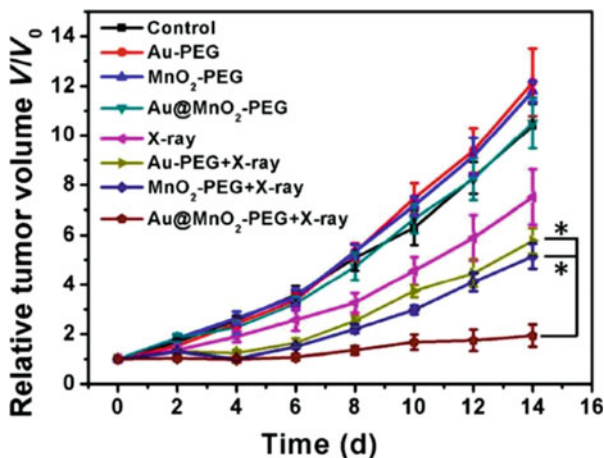
was measured both electrochemically and with enzyme-chemiluminescence detection. Although no direct in vitro or in vivo data was available, the method showed potential to sensitize radiotherapy under hypoxic conditions.

Wu, Hu, and Guo et al. [23] employed liposome encapsulated perfluorohexane under X-ray irradiation to treat tumors. Perfluorocarbons (PFCs) were known to supply oxygen to hypoxic locations such as tumors, and abundance of oxygen was beneficial to radiation damage of biological targets such as cells and tumors. The size of liposomes was ca. 100 nm. NIR imaging showed accumulation of approximately one-third of the liposomes in the tumor. Only a mild improvement was observed.

An interesting method was developed by Hao and Sun et al. [227] in which palladium-103 brachytherapy radioisotope was embedded in the coating of hollow gold nanoparticles. The authors called the new nanomaterial nanoseeds. The overall size of the nanoparticle was 120 nm. Both in vitro and in vivo studies were performed. Single-photon emission computed tomography (SPECT) was used to image the distribution of the nanomaterial in prostate cancer xenograft mice. Tumor suppression over 35 days was observed.

Li et al. [188] synthesized a complex nanoparticle nanomaterial that had a WS$_2$ nanodot core (6.1 nm dia.) and polyaniline shell covered with PDT agent chlorin e6 and hyaluronic acid targeting ligands. This nanomaterial (30 nm dia.) together with X-rays and NIR light was used to cause enhanced damage to 4T1 mouse breast tumor cells and tumors in animals. γ-H2AX assay and tumor size were used to determine the enhancement. A 0.2 DEU enhancement was observed with the nanomaterials and 6 Gy X-ray irradiation. In vivo results showed a similar enhancement with the use of the nanomaterials with X-rays and without NIR light. With NIR light and especially combination of 670 and 808 nm, the enhancement was much higher.

Liu et al. [228] synthesized a composite made of mesoporous tantalum oxide nanoparticles loaded with doxorubicin. The overall size was about 100 nm. The mass unit surface area was on the order of 90 m^2/g, and the average pore size was

4 nm. The authors preformed both in vitro and in vivo studies using 4T1 cells and tumor-bearing mice. Uptake data was not available, but biodistribution data was available. It was impossible to calculate LD_{50} from the surviving fraction data shown in the publication, but DNA damage was minimal after 6 Gy of irradiation alone. The enhancement of using the nanomaterials and radiation was strong, which reached more than 10 DEU. In vivo data showed best result for doxorubicin-loaded nanomaterials under X-ray irradiation. However, enhancement was only about 2.0 DEU, much lower than the in vitro case.

9.8   X-Ray-Triggered Released Drugs and X-Ray Nano-Prodrugs

The biggest benefit of radiosensitizers is that they are readily used in conjunction with radiotherapy. The downside is that to date the magnitude of enhancement from using nanoparticle sensitizers is limited, and large amounts of nanomaterials are required—in many cases, these nanomaterials cause cytotoxicity. A completely different approach is to use X-rays and especially focused X-rays such as those described in the last section to trigger the release of drugs that are securely stored in delivery vehicles. Upon irradiation with the focused X-rays, the drugs are released. The biggest advantage of doing it this way is that the triggering mechanisms can be developed away from complex cellular chemistry, making it possible to use low doses of X-rays to trigger the release of a lethal dose of potent drugs. The biggest challenge is how to develop efficient triggering mechanisms to meet the low-dose requirement. Here, several publications are reviewed. It seems possible to develop efficient chemical and biological mechanisms to reach the goal of using low doses of radiation to trigger the release of large amounts of payload. The main difference between X-ray-triggered therapy and radiotherapy is that the former uses X-rays to trigger the release of drugs rather than to use X-rays to destruct cells.

X-rays have been used in conjunction with drugs to increase the efficacy of cancer treatment. Synergistic results are obtained through simultaneous or delayed X-ray irradiation with drug administration, as reported by Coppey et al. [229] who observed increased cytotoxicity from irradiation 24 h after drug administration. However, the enhancement achieved this way still depends on radiotherapy because destruction is still partially caused by radiation.

X-ray and other ionizing radiation triggered prodrugs were also studied in the past. For example, Nishimoto et al. [230] showed a fluorouracil-based prodrug activated with MeV radiation. The drug, a derivative from fluorouracil, reacted with solvated electrons produced in water by ionizing irradiation in absence of oxygen to form 5-fluorouracil, a compound of greater cytotoxicity. Less than 10 Gy was used for activation. Tumor growth delays were observed with the combination of radiation and prodrugs under hypoxic conditions, whereas cytotoxicity under aerobic conditions was much less.

When nanomaterials are used, the situation may be fundamentally changed and improved. What may prove to be revolutionary is the use of X-rays to trigger the release of an otherwise safely bound, lethal dose of chemicals in the body to annihilate tumors. Such release mechanisms using X-rays convert benign chemicals into prodrugs or on-call drugs, a process that largely eliminates radiotherapy. Using X-rays to trigger the release of drugs from nanoparticles was never attempted prior to Guo et al. [8].

The work of Guo et al. [8] was inspired by O'Brien et al. [231] and [232] in which liposome-enclosed doxorubicin (DOX) was released in water under X-ray irradiation. O'Brien's work was part of a larger body of research on photopolymerization of phospholipids, traced back to the early work in the 1980s by O'Brien et al. [233]. Two reviews on this field of research were published by Puri et al. [234] and Blumenthal et al. [235]. In some of these works, release was possible in pure water after exposure to 2 Gy of X-rays. However, the extreme scavenging environment in the cell would make this mechanism ineffective because the dose needed to create enough reactive oxygen species to break down the bilipid layer would be much higher, of the order of tens of Gy, therefore defeating the purpose of using this method to lower the side effect of radiotherapy.

Other groups have worked in this area as well. For example, Siepmann et al. [236] showed drug release from microparticles under γ-ray irradiation. However, the dose range was far above those used in radiotherapy. The authors employed between 4 and 33 kGy to release 5-fluorouracil from polylactide-glycolide microparticles. They found the initial release of drugs was accelerated by γ-ray irradiation. Benoit et al. [237] employed the triggered release system described above to treat tumor-bearing rats. Triggered release resulted in an almost 10 DEU enhancement over radiation alone. Although not exactly nanomaterials were used, this work demonstrated the potential and the results would be improved.

Xu and Zhang et al. [9] employed di-Se block copolymer constructed aggregates to trap chemo drugs and then used ionizing radiation to generate reactive oxygen species to cleave the Se-Se bond and cracked open the aggregates to release drugs. A schematic is shown in Fig. 9.42 (left panel). The authors used ^{60}Co radiation and up to 500 Gy of radiation. The authors found that nearly 70% of the drug doxorubicin trapped in the aggregates was released after a 50 Gy irradiation, beyond which the release percentage saturated. They also found that release continued after irradiation. For 50 Gy dose, release continued for nearly 5 h after irradiation. At 5 Gy, approximately 40% of the drug was released within 3 h after irradiation. HepG2 cells were used for in vitro work, and the results are shown in Fig. 9.42 (right panel). The reduction in viability was 20%, which was less than many nanoparticle-assisted radiation damage of cancer cells shown in Sect. 9.5. It is unclear whether Se-Se bond cleavage was caused by radicals generated from X-rays interacting with water around the selenide nanoparticles or produced locally through interactions between X-rays and the nanoparticles.

If reactive oxygen species such as singlet oxygen or hydroxyl radicals are considered as drugs, then nanomaterial-enhanced radiotherapy may be considered for X-ray trigger release of drugs. However, in reality these species are not treated as
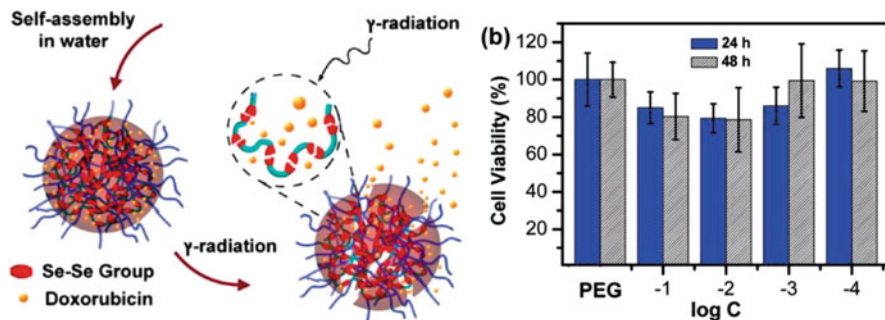
Fig. 9.42 Release of doxorubicin from diselenide block copolymer nanoparticles under ionizing irradiation for cell destruction. The left panel shows the proposed mechanism, and the right panel shows the results. (Reprinted with permission from Xu and Zhang et al. [9]. Copyright (2011) American Chemical Society.)

drugs. So here only the methods of releasing traditional forms of drugs are discussed. Photodynamic therapy does not belong to this part of discussion for the same reason.

In two patent disclosures, Fologea et al. [238] reported a method of using 6 MV X-rays to trigger the release of drugs stored in liposomes. The priority date of the issued patent was Mar 31, 2009, although no formal publication in the literature was available. The inventors used a dose of 4 Gy radiation at a 2 Gy/min dose rate. Dye molecules were trapped in liposomes to simulate drug release upon X-ray irradiation. Their work was similar to those described by O'Brien et al., which is mentioned above. The result in cells would be different because of the high scavenging nature of the cellular environment as in the case of O'Brian et al. On the other hand, this problem could be solved using the internally activatable release mechanism proposed by the inventors, although that part was not experimentally tested. The major difference, also a major advantage, was that reagents used to induce opening of liposomes were unlocked from within the liposomes. Figure 9.43 shows the proposed mechanism, which would avoid the dependency on the radicals generated by X-rays outside the liposomes. However, the experimental results cited in the patent did not fully support the proposed elegant but complex mechanism.

Yan et al. [74] developed a drug with DOX encapsulated in gold nanoparticles which also contained cancer cell targeting ligands. The average size of gold nanoparticles was 17 nm. The authors examined DNA DSBs using γ-H2AX assay in HeLa cells. DOX release was triggered by being in solution for ~10 h. A 1.7 DEU total enhancement was achieved with 3 Gy of 160 kVp X-ray irradiation of HeLa cells incubated with DOX-loaded gold nanoparticles. No data was available on X-ray alone.

Guo et al. [8] reported an X-ray-triggered release nanosystem in which they conjugated DOX-bound DNA strands to the surface of 15 nm diameter gold nanoparticles. The left panel of Fig. 9.44 illustrates the structure of the nanosystem and a schematic of the working mechanism. Upon X-ray irradiation of 100 kVp from a microfocus X-ray source, the results of clonogenic assay of MCF-7 breast cancer tumor cells showed a 40% reduction in cell viability after a 10 Gy dose of radiation.

Fig. 9.43 A hypothetic drug release system that could be triggered with X-rays and would not rely on species from outside. Whether this can be realized is still need to be tested experimentally [239]
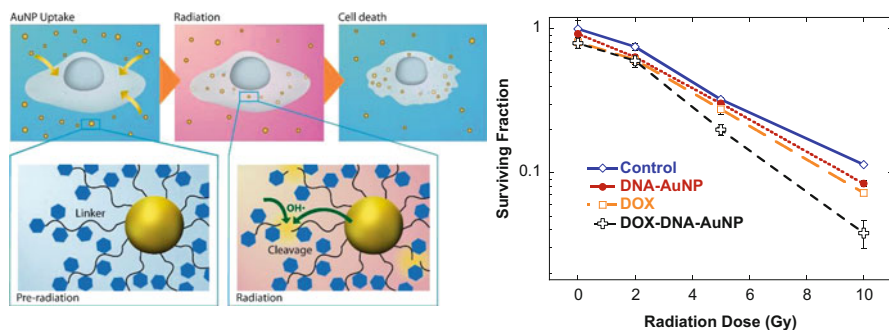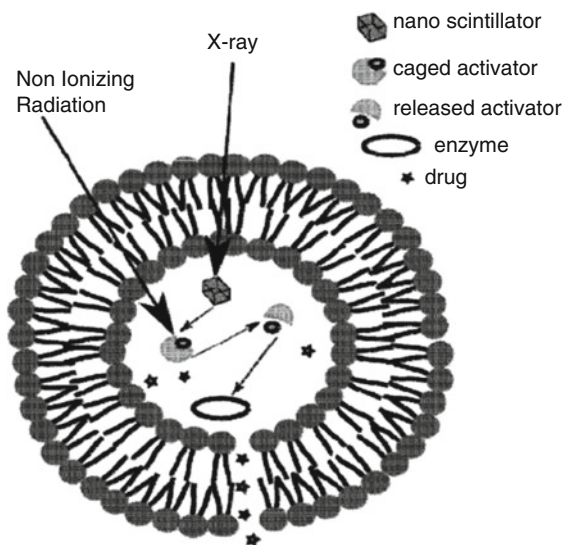
Fig. 9.44 Release of doxorubicin from gold nanoparticles under X-ray irradiation. The left panel illustrates how DOX destructs cells when the molecules are released from the gold nanoparticles. The right panel shows the surviving fraction curve as a function of X-ray dose. (Adapted with permission from Guo et al. [8]. Copyright (2013) of the Royal Society of Chemistry.)

The addition of large amounts of DNA-covered gold nanoparticles did not seem to create any enhancement, which was intriguing and might be caused by scavenging of these nanoparticles similar to that found in the gold nanotube case described in Chaps. 2 and 5. If indeed these gold nanoparticles scavenged hydroxyl radicals, then the amount of enhancement would be significantly higher when scavenging was contained or eliminated.

The triggered release can be combined with the continuous scanning focusing technique described in Sect. 9.7. Triggered release would occur at the focus when triggered release is combined scanning focusing of X-rays.

9.9   Other Reviews

Medical applications are one of the most popular topics within the discipline of X-ray nanochemistry. It is fair to state that currently medical applications of X-ray nanochemistry are a more popular topic than X-ray nanochemistry itself, which is still an obscure topic until this book is written or even after this book is published. Nonetheless, many breakthroughs in X-ray nanochemistry in the near future may change this situation, and we expect X-ray nanochemistry to become a better known topic in the near future. There are many reviews on medical applications of X-ray nanochemistry. In the following, several reviews are discussed. Readers can also refer to these reviews for special discussions that are not covered in this book.

Hainfeld et al. [189] reviewed the works of using gold nanoparticles for radiotherapy. The authors discussed many aspects related to gold nanoparticles for X-ray radiotherapy, including the choice of elements, X-ray energy, theoretically predicted dose enhancement, and requirements for nanoparticles. The authors compared enhancement by gold with iodine, a practical standard for enhancement and contrast, and found an approximately 3 DEU improvement in several energy ranges. However, the authors also noted drastic differences between mice models and human pathology. Many improvements are needed if gold nanoparticles are to be used to clinically treat cancer patients in the framework of using gold nanoparticles as radiosensitizers. For example, LD_{50} of 1.9 nm gold nanoparticles needed for adequate dose enhancement factors is too high, near the toxic level. Many other factors such as targeting that can significantly influence the effectiveness of treatment are still under development.

Juzenas et al. [240] reviewed the field of using quantum dots and nanoparticles for radiation therapy of cancer. The review pointed out that quantum dots generally interacted with UV-Vis light to produce electron-hole pairs, which produced more singlet oxygen. X-rays also interacted with quantum dots to produce singlet oxygen, so the quantum dots functioned as a photodynamic reagent. The review summarized many of the works published in the field of X-ray nanochemistry before 2008. The article also mentioned many materials that could potentially be used for X-ray enabled photodynamic therapy as well as radiosensitizing nanomaterials. The authors mentioned the work performed on polyphenol extract as an antioxidant and radiosensitizing agent. They also showed the structure of nanoparticle scintillators covered with porphyrins. The latter produced singlet oxygen to destruct cells when the nanomaterial-porphyrin composite was irradiated with X-rays.

Kobayashi et al. [241] reviewed radiotherapy of using heavy elements for enhancement of radiation effects. The authors focused on compounds that contain high-Z elements and discussed limitations of delivering molecular chemo drugs into tumors. They noted the non-selectiveness nature of these drugs. Nanoparticles as the source of dose enhancement were discussed, but no specific limitations were mentioned by the authors. The focus was to use nanoparticles to directly sensitize radiotherapy.
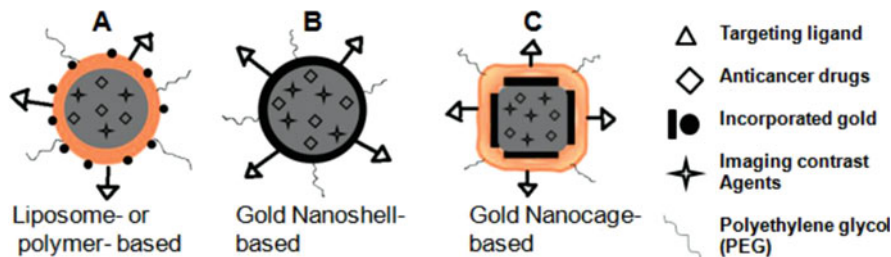
Fig. 9.45 Multiple component nanomaterials that can be used to treat tumor under X-ray irradiation. (Adapted with permission from Chithrani and Jelveh [245] under CC BY 3.0 license.)

   Shortly after Chithrani et al. [35] published the results of testing gold nanoparticles as radiation sensitizers, the authors [242] reviewed the use of gold nanoparticles for combinational therapy, which included enhancement by gold nanoparticles for radiotherapy. In additional to nanomaterials for radiotherapy, the authors also reviewed the work in the areas of photodynamic therapy and photothermal therapy. The authors suggested a multifunctional nanoparticle platform for future therapeutics and imaging. Figure 9.45 shows their proposed nanostructures for therapy. The nanostructures included several components such as targeting, anticancer drugs, imaging agents, and gold nanoparticles, which were relatively small compared with the whole assembly.

   Murphy and El-Sayed et al. [243] provided an extensive review on the use of gold nanoparticles in biomedicine, but did not mention applications of gold nanoparticles as radiosensitizers, suggesting that gold nanoparticle-assisted radiotherapy was not well recognized yet in 2011. Kuncic et al. [116] reviewed imaging and therapy works using nanoparticles under irradiation of light and ionizing radiation. The authors pointed out that titanium oxide nanoparticles could be a suitable image contrast agent. The unit WP contrast increase by the material is approximately 125 HU per 0.1 g/mL or 1250 HU WP^{-1}, which was higher than almost all the contrast agents shown in Fig. 9.15.

   Jain et al. [214] reviewed the work of using gold nanoparticles to treat cancer. They discussed gold nanoparticles as drug carriers, contrast agents, thermal drugs, and radiosensitizers. The authors cited many papers published in the area of gold nanoparticles from 1992 to 2009 and showed an exponential growth of publications as a function of time. The review covered theory, in vitro and in vivo work. The authors also discussed clinical trials using gold nanoparticles, but did not discuss the project being conducted by Nanobiotix Inc. Jain et al. [244] published another review on prostate cancer diagnostics and treatment using metal nanoparticles and ionizing radiation. Two nanoparticles were discussed in detail: one was 15 nm gold nanoparticles and the other was sub-5 nm AGuIX@ nanoparticles that had a high loading of Gd.

   Dorsey and Sun et al. [245] summarized results of using high-Z elements in the form of nanoparticles to image and treat cancer or tumor in animals. The authors discussed properties of gold nanoparticles for imaging and therapy. Both in vitro and

in vivo works were reviewed. The authors also included some of their own results in the article. They demonstrated enhancement of approximately 1.0 DEU using gold nanoparticles under 6 MV X-rays, which were much higher than the values obtained by others as shown here. The results suggested possible chemical or biological enhancement discussed in Chaps. 3 and 4. The incubation concentrations were 1 and 10 mg/mL of PEGylated gold nanoparticles.

Anant et al. [246] reviewed the work in the area of using nanoparticles to radiosensitize therapy. The authors identified three areas of (1) sensitizing, (2) reversing radiation resistance, and (3) radioprotection. Several nanomaterials, including gold nanoparticles, quantum dots, and iron oxide nanoparticles, were discussed. The focus was sensitizing while the other two factors were cursorily mentioned. Gu et al. [247] reviewed the literature of using metal nanoparticles as radiosenisitizers. The review included publications in theoretical modeling of physical enhancement as well as in vitro and in vivo studies. Attention was given to silver nanoparticles.

Barberi-Heyob et al. [248] reviewed the parameters the authors considered important to radiotherapy enhanced by nanoparticles. Their intention was to critically analyze the factors that affect the transformation from preclinical to clinical applications for the nanomaterial-assisted radiation therapy. The focus was still on radiosensitization, meaning the main modality to be employed was still radiation itself. The use of nanomaterials was primarily to increase the effectiveness of damaging targets with radiation. The authors identified the main problems facing radiosensitization technology and attributed the lack of translational work to a lack of standardization. The authors provided a detailed analysis of the dose enhancement factor obtained by 64 groups using different ionizing radiation of different energies. A similar graph to what are shown in Fig. 9.28 and Fig. 9.37 is presented. Although the data showed large standard deviations, the spread of dose enhancement factors was relatively narrow, ranging from 0.1 to 1.3 for different X-ray energies and not as a function of weight percentage of gold in water. The authors indicated the desire to standardize the protocols for performing in vitro and in vivo work.

Sicard-Roselli et al. [249] reviewed the literature on studying radiosensitization by nanoparticles and discussed a few parameters such as energy dependency and biological effect that was close to what is referred to as biological enhancement in Chap. 4 of this book. The review also discussed the current deficiencies in the research area of radiosensitization using nanoparticles. A number of questions were raised in the review. The review also grouped the effects into physical, chemical, and biological, similar to the arrangement of this book in Chaps. 2, 3, and 4.

Magné et al. [216] reviewed the publications in radiotherapy with the emphasis of their impact on future clinical practice. Haume et al. [250] reviewed the literature on using gold nanoparticles for cancer treatment. The authors discussed a number of issues and parameters of gold nanoparticles that may affect the outcome of using gold nanoparticles for radiosensitization.

Rosa et al. [251] summarized the results on the literature dealing with radiosensitizing of cell damage using gold nanoparticles. The results presented by the authors pointed to a similar conclusion as shown in Chap. 4 and a few other reviews. The main point was that many publications measured similar enhancement values even though the experimental conditions were quite different. The authors

discussed several cellular activities such as cell cycles, DNA damage and repair, and the bystander effect, and discussed how these processes could be connected to enhanced damage to cells by gold nanoparticles under X-ray irradiation.

Allen et al. [252] reviewed the literature of using gold nanoparticles for cancer radiotherapy. The authors selected at least four application areas of gold nanoparticles, including imaging, diagnostics, delivery, and therapy. The authors also chose three mechanisms of radiosensitization, which were physical, chemical, and biological. Instead of sensitization, the authors called the processes effect enhancement, similar to what is given in this book. Specifically, the authors pointed to three cases of biological enhancement, which were reactive oxygen species production and oxidative stress, cell cycle effects, and inhibition of DNA repair. The authors also discussed the ideal gold nanoparticles for radiosensitization in the future, which were still largely based on using the radiotherapeutic properties of gold nanoparticles to directly damage cellular components.

Another document that is closely related to this chapter was a book published recently by Cho et al. [253]. The focus of the book was to evaluate the current status of research in several fields, including clinical radiation oncology, nanotechnology, and biomedical engineering, with the goal of providing a comprehensive survey of the current literature that facilitates clinical translation. As a result, more clinical related topics such as targeting and imaging were discussed. Also discussed in the book were regulatory issues.

9.10   Conclusions and Future Work

Medical applications of X-ray nanochemistry, including imaging, in vitro and in vivo work, have been the center of attention of X-ray nanochemistry research from the beginning. It is probably more appropriate to call this chapter X-ray nanotechnology or even X-ray nanomedicine. As this chapter has shown, the magnitude of enhancement using nanoparticles to enhance the effect of ionizing radiation to destroy cells is on the order of 1.0 DEU, regardless of the amount of nanoparticles used, and the benefits and limitations of using this concept are clear.

The main benefit of using nanoparticles is that if nanomaterials can be safely delivered to tumor sites in large enough quantities and at a reasonably low cost, then they can help increase the effectiveness of radiotherapy by nearly one DEU. This may be enough for physicians to convince patients or FDA to approve this treatment method. The use of nanomaterials, together with various X-ray focusing methods such as continuous scanning focusing method, may provide the needed modality to destroy tumors or at least temporarily stop their growth. The scanning focusing itself is worth trying, although the delivery of the focused dose needs to be guided prior to irradiation.

The most obvious limitation, however, also derives from the one DEU enhancement per one WP of gold in tissue. This means a significant enhancement can only be achieved with a large amount of gold in the targeted volume of tissue, if there is no

anti-enhancement. If approximately one DEU enhancement is acceptable, then smaller than one WP gold nanoparticles may be used.

Recognizing these benefits and limitations, the next logical step is to figure out the mechanisms of the observed enhancement so that it is possible to further improve enhancement or create new knowledge bases for various applications in the medical field. This requires a quantum leap or revolutionary paradigm shift. For example, the size of nanomaterials including nanomachines needs to be optimized for maximum uptake by tumors. If biological enhancement favors sub-10 nm diameter nanoparticles and if uptake favors 50 nm nanoparticles, then a compromise must be made. On the other hand, if triggered release can be made, then one can use 50 nm or even 500 nm diameter nanomachines to release nuclear DNA targeting drugs within or even outside the cell, therefore winning both uptake and entering the nuclei battles. These will happen only after a thorough understanding of X-ray nanochemistry.

These potentially new powerful methods of treating cancers may inspire researchers to conduct fundamental research in the discipline of X-ray nanochemistry so that one can continuously improve the sensitivity by creating newer triggering mechanisms. There are at least 10,000 organic chemical reactions and with the inclusion of transition metal complexes and catalysis, as discussed in Chap. 10, it seems extremely possible that one can discover many sensitive and efficient reactions that can help develop effective chemical systems to respond to X-ray irradiation and release drugs in cells to treat cancer anywhere in the body.

X-ray nanochemistry will advance in all fronts. The most important discoveries will happen at the fundamental chemical and nanochemical levels. Many clinical works may happen with fruitful collaborations between chemists and doctors. This iteration between advancing basic and applied sciences is like developing semiconductor materials and modern electronics. One needs to improve the materials and the devices in a concerted effort to make breakthroughs. Therefore, it is critical to have close collaborations between medical doctors and physical scientists. Such collaborations will help accelerate the advancement of the field and improve the overall productivity so that patients can enjoy the best care at the earliest times.

References

1. Kassis, A. I. (2003). Cancer therapy with Auger electrons: Are we almost there? *Journal of Nuclear Medicine, 44*, 1479–1481.
2. Sung, W., Jung, S., & Ye, S. J. (2016). Evaluation of the microscopic dose enhancement for nanoparticle-enhanced Auger therapy. *Physics in Medicine and Biology, 61*, 7522–7535.
3. Guo, T. (2004, August). Nanoparticle enhanced X-ray therapy. ACS Annual Meeting, Philadelphia.
4. Guo, T. (2006). Nanoparticle radiosensitizers. US patent application number: US 11/728,943; publication number: US20080003183 A1 and WO2006037081A2.
5. Hainfeld, J. F., Slatkin, D. N., & Smilowitz, H. M. (2004). The use of gold nanoparticles to enhance radiotherapy in mice. *Physics in Medicine and Biology, 49*, N309–N315.
6. Foley, E., Carter, J., Shan, F., & Guo, T. (2005). Enhanced relaxation of nanoparticle-bound supercoiled DNA in X-ray radiation. *Chemical Communications*, 3192–3194.

7. Roco, M. C., & Tech, N. S. E. (2004). Nanoscale science and engineering: Unifying and transforming tools. *AICHE Journal, 50*, 890–897.

8. Starkewolf, Z. B., Miyachi, L., Wong, J., & Guo, T. (2013). X-ray triggered release of doxorubicin from nanoparticle drug carriers for cancer therapy. *Chemical Communications, 49*, 2545–2547.

9. Ma, N., Xu, H. P., An, L. P., Li, J., Sun, Z. W., & Zhang, X. (2011). Radiation-sensitive diselenide block co-polymer micellar aggregates: Toward the combination of radiotherapy and chemotherapy. *Langmuir, 27*, 5874–5878.

10. Maggiorella, L., Barouch, G., Devaux, C., Pottier, A., Deutsch, E., Bourhis, J., Borghi, E., & Levy, L. (2012). Nanoscale radiotherapy with hafnium oxide nanoparticles. *Future Oncology, 8*, 1167–1181.

11. Chen, J., Li, M. F., Yi, X., Zhao, Q., Chen, L., Yang, C., Wu, J. C., & Yang, K. (2017). Synergistic effect of thermo-radiotherapy using au@FeS Core-Shell nanoparticles as multifunctional therapeutic nanoagents. *Particle and Particle Systems Characterization, 34*.

12. Stewart, C., Konstantinov, K., McKinnon, S., Guatelli, S., Lerch, M., Rosenfeld, A., Tehei, M., & Corde, S. (2016). First proof of bismuth oxide nanoparticles as efficient radiosensitisers on highly radioresistant cancer cells. *Physica Medica, 32*, 1444–1452.

13. Chang, Y. Z., He, L. Z., Li, Z. B., Zeng, L. L., Song, Z. H., Li, P. H., Chan, L., You, Y. Y., Yu, X. F., Chu, P. K., et al. (2017). Designing core-shell gold and selenium nanocomposites for cancer radiochemotherapy. *ACS Nano, 11*, 4848–4858.

14. Leach, J. K., Van Tuyle, G., Lin, P. S., Schmidt-Ullrich, R., & Mikkelsen, R. B. (2001). Ionizing radiation-induced, mitochondria-dependent generation of reactive oxygen/nitrogen. *Cancer Research, 61*, 3894–3901.

15. Zhang, X. M., Yang, H. J., Gu, K., Chen, J. A., Rui, M. J., & Jiang, G. L. (2011). In vitro and in vivo study of a nanoliposomal cisplatin as a radiosensitizer. *International Journal of Nanomedicine, 6*, 437–444.

16. Li, X., Zhou, H. Y., Yang, L., Du, G. Q., Pai-Panandiker, A. S., Huang, X. F., & Yan, B. (2011). Enhancement of cell recognition in vitro by dual-ligand cancer targeting gold nanoparticles. *Biomaterials, 32*, 2540–2545.

17. Rahman, W. N., Corde, S., Yagi, N., Aziz, S. A. A., Annabell, N., & Geso, M. (2014). Optimal energy for cell radiosensitivity enhancement by gold nanoparticles using synchrotron-based monoenergetic photon beams. *International Journal of Nanomedicine, 9*, 2459–2467.

18. Regulla, D. F., Hieber, L. B., & Seidenbusch, M. (1998). Physical and biological interface dose effects in tissue due to X-ray-induced release of secondary radiation from metallic gold surfaces. *Radiation Research, 150*, 92–100.

19. Gara, P. M. D., Garabano, N. I., Portoles, M. J. L., Moreno, M. S., Dodat, D., Casas, O. R., Gonzalez, M. C., & Kotler, M. L. (2012). ROS enhancement by silicon nanoparticles in X-ray irradiated aqueous suspensions and in glioma C6 cells. *Journal of Nanoparticle Research, 14*, 741.

20. Herold, D. M., Das, I. J., Stobbe, C. C., Iyer, R. V., & Chapman, J. D. (2000). Gold microspheres: A selective technique for producing biologically effective dose enhancement. *International Journal of Radiation Biology, 76*, 1357–1364.

21. Choi, G. H., Seo, S. J., Kim, K. H., Kim, H. T., Park, S. H., Lim, J. H., & Kim, J. K. (2012). Photon activated therapy (PAT) using monochromatic synchrotron x-rays and iron oxide nanoparticles in a mouse tumor model: Feasibility study of PAT for the treatment of superficial malignancy. *Radiation Oncology, 7*, 184.

22. Liu, C. J., Wang, C. H., Chien, C. C., Yang, T. Y., Chen, S. T., Leng, W. H., Lee, C. F., Lee, K. H., Hwu, Y., Lee, Y. C., et al. (2008). Enhanced x-ray irradiation-induced cancer cell damage by gold nanoparticles treated by a new synthesis method of polyethylene glycol modification. *Nanotechnology, 19*(295104), 1–5.

23. Xu, L. F., Qiu, X. F., Zhang, Y. T., Cao, K., Zhao, X. Z., Wu, J. H., Hu, Y. Q., & Guo, H. Q. (2016). Liposome encapsulated perfluorohexane enhances radiotherapy in mice without additional oxygen supply. *Journal of Translational Medicine, 14*, 268.

24. Kleinauskas, A., Rocha, S., Sahu, S., Sun, Y. P., & Juzenas, P. (2013). Carbon-core silver-shell nanodots as sensitizers for phototherapy and radiotherapy. *Nanotechnology, 24*, 325103.

25. Youkhana, E., Feltis, B., Blencowe, A., & Geso, M. (2017). Titanium dioxide nanoparticles as radiosensitisers: An in vitro and phantom-based study. *International Journal of Medical Sciences, 14*, 602–614.

26. Taggart, L. E., McMahon, S. J., Butterworth, K. T., Currell, F. J., Schettino, G., & Prise, K. M. (2016). Protein disulphide isomerase as a target for nanoparticle-mediated sensitisation of cancer cells to radiation. *Nanotechnology, 27*, 215101.

27. Pan, C. L., Chen, M. H., Tung, F. I., & Liu, T. Y. (2017). A nanovehicle developed for treating deep-seated bacteria using low-dose X-ray. *Acta Biomaterialia, 47*, 159–169.

28. Liu, C. J., Wang, C. H., Chen, S. T., Chen, H. H., Leng, W. H., Chien, C. C., Wang, C. L., Kempson, I. M., Hwu, Y., Lai, T. C., et al. (2010). Enhancement of cell radiation sensitivity by pegylated gold nanoparticles. *Physics in Medicine and Biology, 55*, 931–945.

29. Lim, S. N., Pradhan, A. K., Barth, R. F., Nahar, S. N., Nakkula, R. J., Yang, W. L., Palmer, A. M., Turro, C., Weldon, M., Bell, E. H., et al. (2015). Tumoricidal activity of low-energy 160-KV versus 6-MV X-rays against platinum-sensitized F98 glioma cells. *Journal of Radiation Research, 56*, 77–89.

30. Bhattarai, S. R., Derry, P. J., Aziz, K., Singh, P. K., Khoo, A. M., Chadha, A. S., Liopo, A., Zubarev, E. R., & Krishnan, S. (2017). Gold nanotriangles: Scale up and X-ray radiosensitization effects in mice. *Nanoscale, 9*, 5085–5093.

31. Diaz, R., Hariri, G., Passarella, R. J., Wu, H., Fu, A., & Hallahan, D. E. (2008). Radiation-guided platinum drug delivery using recombinant peptides. *International Journal of Radiation Oncology, Biology, Physics, 72*, S1–S1.

32. Wang, G. D., Nguyen, H. T., Chen, H. M., Cox, P. B., Wang, L. C., Nagata, K., Hao, Z. L., Wang, A., Li, Z. B., & Xie, J. (2016). X-ray induced photodynamic therapy: A combination of radiotherapy and photodynamic therapy. *Theranostics, 6*, 2295–2305.

33. Yang, W. S., Read, P. W., Mi, J., Baisden, J. M., Reardon, K. A., Larner, J. M., Helmke, B. P., & Sheng, K. (2008). Semiconductor nanoparticles as energy mediators for photosensitizer-enhanced radiotherapy. *International Journal of Radiation Oncology, Biology, Physics, 72*, 633–635.

34. Shi, M. H., Paquette, B., Thippayamontri, T., Gendron, L., Guerin, B., & Sanche, L. (2016). Increased radiosensivity of colorectal tumors with intra-tumoral injection of low dose of gold nanoparticles. *International Journal of Nanomedicine, 11*, 5323–5333.

35. Chithrani, D. B., Jelveh, S., Jalali, F., van Prooijen, M., Allen, C., Bristow, R. G., Hill, R. P., & Jaffray, D. A. (2010). Gold nanoparticles as radiation sensitizers in cancer therapy. *Radiation Research, 173*, 719–728.

36. Yong, Y., Zhang, C. F., Gu, Z. J., Du, J. F., Guo, Z., Dong, X. H., Xie, J. N., Zhang, G. J., Liu, X. F., & Zhao, Y. L. (2017). Polyoxometalate-based radiosensitization platform for treating hypoxic tumors by attenuating radioresistance and enhancing radiation response. *ACS Nano, 11*, 7164–7176.

37. Liu, X., Liu, Y., Zhang, P. C., Jin, X. D., Zheng, X. G., Ye, F., Chen, W. Q., & Li, Q. (2016). The synergistic radiosensitizing effect of tirapazamine-conjugated gold nanoparticles on human hepatoma HepG2 cells under X-ray irradiation. *International Journal of Nanomedicine, 11*, 3517–3530.

38. Al Zaki, A., Joh, D., Cheng, Z. L., De Barros, A. L. B., Kao, G., Dorsey, J., & Tsourkas, A. (2014). Gold-loaded polymeric micelles for computed tomography-guided radiation therapy treatment and radiosensitization. *ACS Nano, 8*, 104–112.

39. Saberi, A., Shahbazi-Gahrouei, D., Abbasian, M., Fesharaki, M., Baharlouei, A., & Arab-Bafrani, Z. (2017). Gold nanoparticles in combination with megavoltage radiation energy increased radiosensitization and apoptosis in colon cancer HT-29 cells. *International Journal of Radiation Biology, 93*, 315–323.

40. Kim, S. R., & Kim, E. H. (2017). Gold nanoparticles as dose-enhancement agent for kilovoltage X-ray therapy of melanoma. *International Journal of Radiation Biology, 93*, 517–526.

41. Zhang, P. P., Qiao, Y., Xia, J. F., Guan, J. J., Ma, L. Y., & Su, M. (2015). Enhanced radiation therapy with multilayer microdisks containing radiosensitizing gold nanoparticles. *ACS Applied Materials & Interfaces, 7*, 4518–4524.

42. Ma, N. N., Jiang, Y. W., Zhang, X. D., Wu, H., Myers, J. N., Liu, P. D., Jin, H. Z., Gu, N., He, N. Y., Wu, F. G., et al. (2016). Enhanced radiosensitization of gold Nanospikes via hyperthermia in combined cancer radiation and photothermal therapy. *ACS Applied Materials & Interfaces, 8*, 28480–28494.

43. Fang, X., Wang, Y. L., Ma, X. C., Li, Y. Y., Zhang, Z. L., Xiao, Z. S., Liu, L. J., Gao, X. Y., & Liu, J. (2017). Mitochondria-targeting Au nanoclusters enhance radiosensivity of cancer cells. *Journal of Materials Chemistry B, 5*, 4190–4197.

44. Li, Y. J., Perkins, A. L., Su, Y., Ma, Y. L., Colson, L., Horne, D. A., & Chen, Y. (2012). Gold nanoparticles as a platform for creating a multivalent poly-SUMO chain inhibitor that also augments ionizing radiation. *Proceedings of the National Academy of Sciences of the United States of America, 109*, 4092–4097.

45. Butterworth, K. T., Coulter, J. A., Jain, S., Forker, J., McMahon, S. J., Schettino, G., Prise, K. M., Currell, F. J., & Hirst, D. G. (2010). Evaluation of cytotoxicity and radiation enhancement using 1.9 nm gold particles: Potential application for cancer therapy. *Nanotechnology, 21* (295101), 1–9.

46. Klein, S., Sommer, A., Distel, L. V. R., Hazemann, J. L., Kroner, W., Neuhuber, W., Muller, P., Proux, O., & Kryschi, C. (2014). Superparamagnetic iron oxide nanoparticles as novel X-ray enhancer for low-dose radiation therapy. *The Journal of Physical Chemistry. B, 118*, 6159–6166.

47. Ito, S., Miyoshi, N., Degraff, W. G., Nagashima, K., Kirschenbaum, L. J., & Riesz, P. (2009). Enhancement of 5-Aminolevulinic acid-induced oxidative stress on two cancer cell lines by gold nanoparticles. *Free Radical Research, 43*, 1214–1224.

48. Lee, S. M., Tsai, D. H., Hackley, V. A., Brechbiel, M. W., & Cook, R. F. (2013). Surface-engineered nanomaterials as X-ray absorbing adjuvant agents for Auger-mediated chemo-radiation. *Nanoscale, 5*, 5252–5256.

49. Huang, P., Bao, L., Zhang, C. L., Lin, J., Luo, T., Yang, D. P., He, M., Li, Z. M., Gao, G., Gao, B., et al. (2011). Folic acid-conjugated silica-modified gold nanorods for X-ray/CT imaging-guided dual-mode radiation and photo-thermal therapy. *Biomaterials, 32*, 9796–9809.

50. Jain, S., Coulter, J. A., Hounsell, A. R., Butterworth, K. T., McMahon, S. J., Hyland, W. B., Muir, M. F., Dickson, G. R., Prise, K. M., Currell, F. J., et al. (2011). Cell-specific radiosensitization by gold nanoparticles at megavoltage radiation energies. *International Journal of Radiation Oncology, Biology, Physics, 79*, 531–539.

51. McMahon, S. J., Hyland, W. B., Muir, M. F., Coulter, J. A., Jain, S., Butterworth, K. T., Schettino, G., Dickson, G. R., Hounsell, A. R., O'Sullivan, J. M., et al. (2011). Biological consequences of nanoscale energy deposition near irradiated heavy atom nanoparticles. *Scientific Reports, 1*. https://doi.org/10.1038/srep00018.

52. Latimer, C. L. (2013). Octaarginine labelled 30 nm gold nanoparticles as agents for enhanced radiotherapy. Department of Medical Biophysics, University of Toronto, Toronto, Vol. Master of Science, p. 81.

53. Seo, S. J., Han, S. M., Cho, J. H., Hyodo, K., Zaboronok, A., You, H., Peach, K., Hill, M. A., & Kim, J. K. (2015). Enhanced production of reactive oxygen species by gadolinium oxide nanoparticles under core-inner-shell excitation by proton or monochromatic X-ray irradiation: Implication of the contribution from the interatomic de-excitation-mediated nanoradiator effect to dose enhancement. *Radiation and Environmental Biophysics, 54*, 423–431.

54. Hwu, J. R., Lin, Y. S., Josephrajan, T., Hsu, M. H., Cheng, F. Y., Yeh, C. S., Su, W. C., & Shieh, D. B. (2009). Targeted paclitaxel by conjugation to iron oxide and gold nanoparticles. *Journal of the American Chemical Society, 131*, 66–68.

55. Liu, Y. F., Zhang, Y. B., Wang, S. P., Pope, C., & Chen, W. (2008). Optical behaviors of ZnO-porphyrin conjugates and their potential applications for cancer treatment. *Applied Physics Letters, 92*, 143901.

56. Clement, S., Deng, W., Camilleri, E., Wilson, B. C., & Goldys, E. M. (2016). X-ray induced singlet oxygen generation by nanoparticle-photosensitizer conjugates for photodynamic therapy: Determination of singlet oxygen quantum yield. *Scientific Reports, 6*, 19954.

57. Scaffidi, J. P., Gregas, M. K., Lauly, B., Zhang, Y., & Vo-Dinh, T. (2011). Activity of psoralen-functionalized nanoscintillators against cancer cells upon X-ray excitation. *ACS Nano, 5*, 4679–4687.

58. Rahman, W. N., Davidson, R., Yagi, N., Bansal, V., Geso, M., & Darby, I. (2011). Influence of gold nanoparticles on radiation dose enhancement and cellular migration in microbeam-irradiated cells. *BioNanoScience, 1*, 4–13 4.

59. Setua, S., Ouberai, M., Piccirillo, S. G., Watts, C., & Welland, M. (2014). Cisplatin-tethered gold nanospheres for multimodal chemo-radiotherapy of glioblastoma. *Nanoscale, 6*, 10865–10873.

60. Wu, H., Lin, J., Liu, P. D., Huang, Z. H., Zhao, P., Jin, H. Z., Ma, J., Wen, L. P., & Gu, N. (2016). Reactive oxygen species acts as executor in radiation enhancement and autophagy inducing by AgNPs. *Biomaterials, 101*, 1–9.

61. Retif, P., Reinhard, A., Paquot, H., Jouan-Hureaux, V., Chateau, A., Sancey, L., Barberi-Heyob, M., Pinel, S., & Bastogne, T. (2016). Monte Carlo simulations guided by imaging to predict the in vitro ranking of radiosensitizing nanoparticles. *International Journal of Nanomedicine, 11*, 6169–6179.

62. Wang, G. N., Gao, W., Zhang, X. J., & Mei, X. F. (2016). Au nanocage functionalized with ultra-small Fe3O4 nanoparticles for targeting T-1-T-2 dual MRI and CT imaging of tumor. *Scientific Reports, 6*, 28258.

63. Chithrani, B. D., Ghazani, A. A., & Chan, W. C. W. (2006). Determining the size and shape dependence of gold nanoparticle uptake into mammalian cells. *Nano Letters, 6*, 662–668.

64. Zhang, X. J., Xing, J. Z., Chen, J., Ko, L., Amanie, J., Gulavita, S., Pervez, N., Yee, D., Moore, R., & Roa, W. (2008). Enhanced radiation sensitivity in prostate cancer by gold-nanoparticles. *Clinical and Investigative Medicine, 31*, E160–E167.

65. Kong, T., Zeng, J., Wang, X. P., Yang, X. Y., Yang, J., McQuarrie, S., McEwan, A., Roa, W., Chen, J., & Xing, J. Z. (2008). Enhancement of radiation cytotoxicity in breast-cancer cells by localized attachment of gold nanoparticles. *Small, 4*, 1537–1543.

66. Roa, W., Zhang, X. J., Guo, L. H., Shaw, A., Hu, X. Y., Xiong, Y. P., Gulavita, S., Patel, S., Sun, X. J., Chen, J., et al. (2009). Gold nanoparticle sensitize radiotherapy of prostate cancer cells by regulation of the cell cycle. *Nanotechnology, 20*(375101), 1–9.

67. Antosh, M. P., Wijesinghe, D. D., Shrestha, S., Lanou, R., Huang, Y. H., Hasselbacher, T., Fox, D., Neretti, N., Sun, S., Katenka, N., et al. (2015). Enhancement of radiation effect on cancer cells by gold-pHLIP. *Proceedings of the National Academy of Sciences of the United States of America, 112*, 5372–5376.

68. Her, S., Cui, L., Bristow, R. G., & Allen, C. (2016). Dual action enhancement of gold nanoparticle radiosensitization by pentamidine in triple negative breast cancer. *Radiation Research, 185*, 549–562.

69. Yu, B., Liu, T., Du, Y., Luo, Z., Zheng, W., & Chen, T. (2016). X-ray-responsive selenium nanoparticles for enhanced cancer chemo-radiotherapy. *Colloid Surface B, 139*, 180–189.

70. McMahon, S. J., Hyland, W. B., Muir, M. F., Coulter, J. A., Jain, S., Butterworth, K. T., Schettino, G., Dickson, G. R., Hounsell, A. R., O'Sullivan, J. M., et al. (2011). Nanodosimetric effects of gold nanoparticles in megavoltage radiation therapy. *Radiotherapy and Oncology, 100*, 412–416.

71. Yu, X. J., Li, A., Zhao, C. Z., Yang, K., Chen, X. Y., & Li, W. W. (2017). Ultrasmall semimetal nanoparticles of bismuth for dual-modal computed tomography/photoacoustic imaging and synergistic thermoradiotherapy. *ACS Nano, 11*, 3990–4001.

72. Liu, J. X., Du, Y. H., Liu, J., Zhao, Z., Cheng, K., Chen, Y. S., Wei, Y. C., Song, W. Y., & Zhang, X. (2017). Design of MoFe/Beta@CeO2 catalysts with a core-shell structure and their catalytic performances for the selective catalytic reduction of NO with NH3. *Applied Catalysis B: Environmental, 203*, 704–714.

73. Khoshgard, K., Hashemi, B., Arbabi, A., Rasaee, M. J., & Soleimani, M. (2014). Radiosensitization effect of folate-conjugated gold nanoparticles on HeLa cancer cells under orthovoltage superficial radiotherapy techniques. *Physics in Medicine and Biology, 59*, 2249–2263.

74. Zhou, H. Y., Zhang, Y., Su, G. X., Zhai, S. M., & Yan, B. (2013). Enhanced cancer cell killing by a targeting gold nanoconstruct with doxorubicin payload under X-ray irradiation. *RSC Advances, 3*, 21596–21603.

75. Chithrani, B. D., & Chan, W. C. W. (2007). Elucidating the mechanism of cellular uptake and removal of protein-coated gold nanoparticles of different sizes and shapes. *Nano Letters, 7*, 1542–1550.

76. Dou, Y., Guo, Y. Y., Li, X. D., Li, X., Wang, S., Wang, L., Lv, G. X., Zhang, X. N., Wang, H. J., Gong, X. Q., et al. (2016). Size-tuning ionization to optimize gold nanoparticles for simultaneous enhanced CT imaging and radiotherapy. *ACS Nano, 10*, 2536–2548.

77. Roa, W., Yang, A., Li, P., Kong, T., Yang, J., Pervez, N., McQuarrie, S., McEwan, A., Chen, J., & Xing, J. (2007). Functional gold nanoparticles enhance radiation cytotoxicity in breast and prostate cancer cells. *Radiotherapy and Oncology, 84*, S83–S83.

78. Kudgus, R. A., Szabolcs, A., Khan, J. A., Walden, C. A., Reid, J. M., Robertson, J. D., Bhattacharya, R., & Mukherjee, P. (2013). Inhibiting the growth of pancreatic adenocarcinoma in vitro and in vivo through targeted treatment with designer gold nanotherapeutics. *PLoS One, 8*, e57522.

79. Zhang, P. P., Qiao, Y., Wang, C. M., Ma, L. Y., & Su, M. (2014). Enhanced radiation therapy with internalized polyelectrolyte modified nanoparticles. *Nanoscale, 6*, 10095–10099.

80. Zhu, Z. J., Tang, R., Yeh, Y. C., Miranda, O. R., Rotello, V. M., & Vachet, R. W. (2012). Determination of the intracellular stability of gold nanoparticle monolayers using mass spectrometry. *Analytical Chemistry, 84*, 4321–4326.

81. Subiel, A., Ashmore, R., & Schettino, G. (2016). Standards and methodologies for characterizing radiobiological impact of high-Z nanoparticles. *Theranostics, 6*, 1651–1671.

82. Hariri, G., Yan, H. P., Wang, H. L., Han, Z. Z., & Hallahan, D. E. (2010). Radiation-guided drug delivery to mouse models of lung cancer. *Clinical Cancer Research, 16*, 4968–4977.

83. Kang, B., Mackey, M. A., & El-Sayed, M. A. (2010). Nuclear targeting of gold nanoparticles in cancer cells induces DNA damage, causing cytokinesis arrest and apoptosis. *Journal of the American Chemical Society, 132*, 1517–1519.

84. Nativo, P., Prior, I. A., & Brust, M. (2008). Uptake and intracellular fate of surface-modified gold nanoparticles. *ACS Nano, 2*, 1639–1644.

85. Yu, M. K., Park, J., & Jon, S. (2012). Targeting strategies for multifunctional nanoparticles in cancer imaging and therapy. *Theranostics, 2*, 3–44.

86. Ng, S. K., Ma, L., Qiu, Y., Xun, X., Webster, T. J., & Su, M. (2016). Enhancing cancer radiation therapy with cell penetrating peptide modified gold nanoparticles. *Austin Journal of Biomedical Engineering, 3*(id1033), 1031–1038.

87. Hainfeld, J. F., & Smilowitz, H. M. (2015). Nuclear targeted gold nanoparticles for radiation enhancement. *Cancer Research, 75*, Abstract 1807.

88. Cormode, D. P., Naha, P. C., & Fayad, Z. A. (2014). Nanoparticle contrast agents for computed tomography: A focus on micelles. *Contrast Media & Molecular Imaging, 9*, 37–52.

89. Xu, C. J., Tung, G. A., & Sun, S. H. (2008). Size and concentration effect of gold nanoparticles on X-ray attenuation as measured on computed tomography. *Chemistry of Materials, 20*, 4167–4169.

90. Cheong, S. K., Jones, B. L., Siddiqi, A. K., Liu, F., Manohar, N., & Cho, S. H. (2010). X-ray fluorescence computed tomography (XFCT) imaging of gold nanoparticle-loaded objects using 110 kVp x-rays. *Physics in Medicine and Biology, 55*, 647–662.

91. Jones, B. L., & Cho, S. H. (2011). The feasibility of polychromatic cone-beam x-ray fluorescence computed tomography (XFCT) imaging of gold nanoparticle-loaded objects: A Monte Carlo study. *Physics in Medicine and Biology, 56*, 3719–3730.

92. Jones, B., Manohar, N., Karellas, A., & Cho, S. (2012). Polychromatic cone-beam X-ray fluorescence computed tomography of gold nanoparticle-loaded objects. *Medical Physics, 39*, 3986–3987.

93. Manohar, N., Reynoso, F. J., & Cho, S. H. (2013). Experimental demonstration of direct L-shell x-ray fluorescence imaging of gold nanoparticles using a benchtop x-ray source. *Medical Physics, 40*, 080702.

94. Manohar, N., Jones, B. L., & Cho, S. H. (2014). Improving x-ray fluorescence signal for benchtop polychromatic cone-beam x-ray fluorescence computed tomography by incident x-ray spectrum optimization: A Monte Carlo study. *Medical Physics, 41*, 101906.

95. Meng, L., Fu, G., Li, N., Newville, M., Eng, P., & La Riviere, P. (2010). X-ray fluorescence tomography using imaging detectors. *Proceedings of SPIE, 7804*, B1–B9.

96. Wen, H., Bennett, E. E., Hegedus, M. A., & Carroll, S. C. (2008). Spatial harmonic imaging of X-ray scattering initial results. *IEEE Transactions on Medical Imaging, 27*, 997–1002.

97. Bazalova, M., Kuang, Y., Pratx, G., & Xing, L. (2012). Investigation of X-ray fluorescence computed tomography (XFCT) and K-edge imaging. *IEEE Transactions on Medical Imaging, 31*, 1620–1627.

98. Bazalova, M., Weil, M. D., Wilfley, B., & Graves, E. E. (2012). Monte Carlo model of the scanning beam digital x-ray (SBDX) source. *Physics in Medicine and Biology, 57*, 7381–7394.

99. Kuang, Y., Pratx, G., Bazalova, M., Meng, B. W., Qian, J. G., & Xing, L. (2013). First demonstration of multiplexed X-ray fluorescence computed tomography (XFCT) imaging. *IEEE Transactions on Medical Imaging, 32*, 262–267.

100. Guo, R., Wang, H., Peng, C., Shen, M. W., Pan, M. J., Cao, X. Y., Zhang, G. X., & Shi, X. Y. (2010). X-ray attenuation property of dendrimer-entrapped gold nanoparticles. *Journal of Physical Chemistry C, 114*, 50–56.

101. Hariri, G., Wellons, M. S., Morris, W. H., Lukehart, C. M., & Hallahan, D. E. (2011). Multifunctional FePt nanoparticles for radiation-guided targeting and imaging of cancer. *Annals of Biomedical Engineering, 39*, 946–952.

102. Luo, T., Huang, P., Gao, G., Shen, G. X., Fu, S., Cui, D. X., Zhou, C. Q., & Ren, Q. S. (2011). Mesoporous silica-coated gold nanorods with embedded indocyanine green for dual mode X-ray CT and NIR fluorescence imaging. *Optics Express, 19*, 17030–17039.

103. Rand, D., Ortiz, V., Liu, Y. A., Derdak, Z., Wands, J. R., Taticek, M., & Rose-Petruck, C. (2011). Nanomaterials for X-ray imaging: Gold nanoparticle enhancement of X-ray scatter imaging of hepatocellular carcinoma. *Nano Letters, 11*, 2678–2683.

104. Guo, T., & Davidson, R. A. (2016). Nanoparticle assisted scanning focusing X-ray fluorescence imaging and enhanced treatment. *Radiat Res. 185*, 87-95.

105. Guo, T., & Davidson, R. A. (2015). Nanoparticle assisted scanning focusing X-ray fluorescence imaging and enhanced treatment. Patent publication number: WO/2015/031675; international application number: PCT/US2014/053259. Publication date: May 03, 2015.

106. Boote, E., Fent, G., Kattumuri, V., Casteel, S., Katti, K., Chanda, N., Kannan, R., Katti, K., & Churchill, R. (2010). Gold nanoparticle contrast in a phantom and juvenile swine: Models for molecular imaging of human organs using X-ray computed tomography. *Academic Radiology, 17*, 410–417.

107. Hainfeld, J. F., Slatkin, D. N., Focella, T. M., & Smilowitz, H. M. (2006). Gold nanoparticles: A new X-ray contrast agent. *The British Journal of Radiology, 79*, 248–253.

108. Hainfeld, J. F., Smilowitz, H. M., O'Connor, M. J., Dilmanian, F. A., & Slatkin, D. N. (2013). Gold nanoparticle imaging and radiotherapy of brain tumors in mice. *Nanomedicine, 8*, 1601–1609.

109. Alric, C., Taleb, J., Le Duc, G., Mandon, C., Billotey, C., Le Meur-Herland, A., Brochard, T., Vocanson, F., Janier, M., Perriat, P., et al. (2008). Gadolinium chelate coated gold

nanoparticles as contrast agents for both X-ray computed tomography and magnetic resonance imaging. *Journal of the American Chemical Society, 130*, 5908–5915.

110. Yusa, N., Jiang, M., Mizuno, K., & Uesaka, M. (2009). Numerical evaluation of the effectiveness of colloidal gold as a contrast agent. *Radiological Physics and Technology, 2*, 33–39.

111. Jones, B. L., Manohar, N., Reynoso, F., Karellas, A., & Cho, S. H. (2012). Experimental demonstration of benchtop x-ray fluorescence computed tomography (XFCT) of gold nanoparticle-loaded objects using lead- and tin-filtered polychromatic cone-beams. *Physics in Medicine and Biology, 57*, N457–N467.

112. Kim, D., Jeong, Y. Y., & Jon, S. (2010). A drug-loaded aptamer-gold nanoparticle bioconjugate for combined CT imaging and therapy of prostate cancer. *ACS Nano, 4*, 3689–3696.

113. van Schooneveld, M. M., Cormode, D. P., Koole, R., van Wijngaarden, J. T., Calcagno, C., Skajaa, T., Hilhorst, J., 't Hart, D. C., Fayad, Z. A., Mulder, W. J. M., et al. (2010). A fluorescent, paramagnetic and PEGylated gold/silica nanoparticle for MRI, CT and fluorescence imaging. *Contrast Media & Molecular Imaging, 5*, 231–236.

114. Manohar, N. (2011). Effect of source X-ray energy spectra on the detection of fluorescence photons from gold nanoparticles. *Medical Physics,* Georgia Institute of Technology, Atlanta, Vol. M.S., p. 38.

115. Le Duc, G., Miladi, I., Alric, C., Mowat, P., Brauer-Krisch, E., Bouchet, A., Khalil, E., Billotey, C., Janier, M., Lux, F., et al. (2011). Toward an image-guided microbeam radiation therapy using gadolinium-based nanoparticles. *ACS Nano, 5*, 9566–9574.

116. Smith, L., Kuncic, Z., Ostrikov, K., & Kumar, S. (2012). Nanoparticles in cancer imaging and therapy. *Journal of Nanomaterials,* 891318, 1–7.

117. Kunzel, R., Okuno, E., Levenhagen, R. S., & Umisedo, N. K. (2013). Evaluation of the X-ray absorption by gold nanoparticles solutions. *Nanotechnology, 5*(865283), 203.

118. Tu, S. J., Yang, P. Y., Hong, J. H., & Lo, C. J. (2013). Quantitative dosimetric assessment for effect of gold nanoparticles as contrast media on radiotherapy planning. *Radiation Physics and Chemistry, 88*, 14–20.

119. Rivera, E. J., Tran, L. A., Hernandez-Rivera, M., Yoon, D., Mikos, A. G., Rusakova, I. A., Cheong, B. Y., Cabreira-Hansen, M. D., Willerson, J. T., Perin, E. C., et al. (2013). Bismuth@US-tubes as a potential contrast agent for X-ray imaging applications. *Journal of Materials Chemistry B, 1*, 4792–4800.

120. Cole, L. E., Vargo-Gogola, T., & Roeder, R. K. (2014). Contrast-enhanced X-ray detection of breast microcalcifications in a murine model using targeted gold nanoparticles. *ACS Nano, 8*, 7486–7496.

121. Deyhimihaghighi, N., Mohd Noor, N., Soltani, N., Jorfi, R., Erfani Haghir, M., Adenan, M. Z., Saion, E., & Khandaker, M. U. (2014). Contrast enhancement of magnetic resonance imaging (MRI) of polymer gel dosimeter by adding Platinum nano-particles. *Journal of Physics: Conference Series, 546*, 012013.

122. Xia, H. X., Yang, X. Q., Song, J. T., Chen, J., Zhang, M. Z., Yan, D. M., Zhang, L., Qin, M. Y., Bai, L. Y., Zhao, Y. D., et al. (2014). Folic acid-conjugated silica-coated gold nanorods and quantum dots for dual-modality CT and fluorescence imaging and photothermal therapy. *Journal of Materials Chemistry B, 2*, 1945–1953.

123. Wathen, C. A., Caldwell, C., Chanda, N., Upendran, A., Zambre, A., Afrasiabi, Z., Chapaman, S. E., Foje, N., Leevy, W. M., & Kannan, R. (2015). Selective X-ray contrast enhancement of the spleen of living mice mediated by gold nanorods. *Contrast Media & Molecular Imaging, 10*, 188–193.

124. Rand, D., Derdak, Z., Carlson, R., Wands, J. R., & Rose-Petruck, C. (2015). X-ray scatter imaging of hepatocellular carcinoma in a mouse model using nanoparticle contrast agents. *Scientific Reports, 5*, 15673.

125. McQuade, C., Al Zaki, A., Desai, Y., Vido, M., Sakhuja, T., Cheng, Z. L., Hickey, R. J., Joh, D., Park, S. J., Kao, G., et al. (2015). A multifunctional nanoplatform for imaging, radiotherapy, and the prediction of therapeutic response. *Small, 11*, 834–843.

126. Elmenoufy, A. H., Tang, Y. A., Hu, J., Xu, H. B., & Yang, X. L. (2015). A novel deep photodynamic therapy modality combined with CT imaging established via X-ray stimulated silica-modified lanthanide scintillating nanoparticles. *Chemical Communications, 51*, 12247–12250.

127. Lv, R. C., Yang, P. P., He, F., Gai, S. L., Li, C. X., Dai, Y. L., Yang, G. X., & Lin, J. (2015). A yolk-like multifunctional platform for multimodal imaging and synergistic therapy triggered by a single near-infrared light. *ACS Nano, 9*, 1630–1647.

128. Kim, T., Lee, N., Arifin, D. R., Shats, I., Janowski, M., Walczak, P., Hyeon, T., & Bulte, J. W. M. (2017). In vivo micro-CT imaging of human mesenchymal stem cells labeled with gold-poly-l-lysine nanocomplexes. *Advanced Functional Materials, 27*, 1604213.

129. Duan, S., Yang, Y. J., Zhang, C. L., Zhao, N. N., & Xu, F. J. (2017). NIR-responsive polycationic gatekeeper-cloaked hetero-nanoparticles for multimodal imaging-guided triple-combination therapy of cancer. *Small, 13*, 1603133.

130. Wathen, C. A., Foje, N., van Avermaete, T., Miramontes, B., Chapaman, S. E., Sasser, T. A., Kannan, R., Gerstler, S., & Leevy, W. M. (2013). In vivo X-ray computed tomographic imaging of soft tissue with native, intravenous, or oral contrast. *Sensors, 13*, 6957–6980.

131. Liu, X., Zhang, X., Zhu, M., Lin, G. H., Liu, J., Zhou, Z. F., Tian, X., & Pan, Y. (2017). PEGylated au@Pt nanodendrites as novel theranostic agents for computed tomography imaging and photothermal/radiation synergistic therapy. *ACS Applied Materials & Interfaces, 9*, 279–285.

132. Mieszawska, A. J., Mulder, W. J. M., Fayad, Z. A., & Cormode, D. P. (2013). Multifunctional gold nanoparticles for diagnosis and therapy of disease. *Molecular Pharmaceutics, 10*, 831–847.

133. Jakhmola, A., Anton, N., & Vandamme, T. F. (2012). Inorganic nanoparticles based contrast agents for X-ray computed tomography. *Advanced Healthcare Materials, 1*, 413–431.

134. Cole, L. E., Ross, R. D., Tilley, J. M. R., Vargo-Gogola, T., & Roeder, R. K. (2015). Gold nanoparticles as contrast agents in x-ray imaging and computed tomography. *Nanomedicine, 10*, 321–341.

135. Liu, Y. L., Liu, J. H., Ai, K. L., Yuan, Q. H., & Lu, L. H. (2014). Recent advances in ytterbium-based contrast agents for in vivo X-ray computed tomography imaging: Promises and prospects. *Contrast Media & Molecular Imaging, 9*, 26–36.

136. Gao, Y. P., & Li, Y. S. (2016). Gold nanostructures for cancer imaging and therapy. In Z. Dai (Ed.), *Advances in nanotheranostics I, Springer Series in Biomaterials Science and Engineering* (Vol. 6, pp. 53–101). Berlin/Heidelberg: Springer.

137. Patel, L. N., Zaro, J. L., & Shen, W. C. (2007). Cell penetrating peptides: Intracellular pathways and pharmaceutical perspectives. *Pharmaceutical Research, 24*, 1977–1992.

138. Cesbron, Y., See, V., Free, P., Nativo, P., Shaheen, U., Rigden, D. J., Spiller, D. G., Fernig, D. G., White, M. R. H., Prior, I. A., et al. (2010). Intracellular delivery and fate of peptide-capped gold nanoparticles. *Biophysical Journal, 98*, 203a.

139. Popovtzer, R., Agrawal, A., Kotov, N. A., Popovtzer, A., Balter, J., Carey, T. E., & Kopelman, R. (2008). Targeted gold nanoparticles enable molecular CT imaging of cancer. *Nano Letters, 8*, 4593–4596.

140. Cole, L. E., Vargo-Gogola, T., & Roeder, R. K. (2014). Bisphosphonate-functionalized gold nanoparticles for contrast-enhanced X-ray detection of breast microcalcifications. *Biomaterials, 35*, 2312–2321.

141. Zhang, X. D., Wu, D., Shen, X., Chen, J., Sun, Y. M., Liu, P. X., & Liang, X. J. (2012). Size-dependent radiosensitization of PEG-coated gold nanoparticles for cancer radiation therapy. *Biomaterials, 33*, 6408–6419.

142. Cho, S. H. (2005). Estimation of tumor dose enhancement due to gold nanoparticles during typical radiation treatments: A preliminary Monte Carlo study. *Medical Physics, 32*, 2162–2162.

143. McMahon, S. J., Mendenhall, M. H., Jain, S., & Currell, F. (2008). Radiotherapy in the presence of contrast agents: A general figure of merit and its application to gold nanoparticles. *Physics in Medicine and Biology, 53*, 5635–5651.

144. Gokeri, G., Kocar, C., & Tombakoglu, M. (2010). Monte Carlo simulation of microbeam radiation therapy with an interlaced irradiation geometry and an Au contrast agent in a realistic head phantom. *Physics in Medicine and Biology, 55*, 7469–7487.

145. Lechtman, E., Chattopadhyay, N., Cai, Z., Mashouf, S., Reilly, R., & Pignol, J. P. (2011). Implications on clinical scenario of gold nanoparticle radiosensitization in regards to photon energy, nanoparticle size, concentration and location. *Physics in Medicine and Biology, 56*, 4631–4647.

146. Martinez-Rovira, I., & Prezado, Y. (2011). Monte Carlo dose enhancement studies in microbeam radiation therapy. *Medical Physics, 38*, 4430–4439.

147. Ngwa, W., Makrigiorgos, G. M., & Berbeco, R. I. (2012). Gold nanoparticle enhancement of stereotactic radiosurgery for neovascular age-related macular degeneration. *Physics in Medicine and Biology, 57*, 6371–6380.

148. Lechtman, E., Mashouf, S., Chattopadhyay, N., Keller, B. M., Lai, P., Cai, Z., Reilly, R. M., & Pignol, J. P. (2013). A Monte Carlo-based model of gold nanoparticle radiosensitization accounting for increased radiobiological effectiveness. *Physics in Medicine and Biology, 58*, 3075–3087.

149. Amato, E., Italiano, A., Leotta, S., Pergolizzi, S., & Torrisi, L. (2013). Monte Carlo study of the dose enhancement effect of gold nanoparticles during X-ray therapies and evaluation of the anti-angiogenic effect on tumour capillary vessels. *Journal of X-Ray Science and Technology, 21*, 237–247.

150. Mesbahi, A., Jamali, F., & Gharehaghaji, N. (2013). Effect of photon beam energy, gold nanoparticle size and concentration on the dose enhancement in radiation therapy. *BioImpacts: BI, 29-35(29)*, 3.

151. Jeynes, J. C. G., Merchant, M. J., Spindler, A., Wera, A. C., & Kirkby, K. J. (2014). Investigation of gold nanoparticle radiosensitization mechanisms using a free radical scavenger and protons of different energies. *Physics in Medicine and Biology, 59*, 6431–6443.

152. Li, W. B., Müllner, M., Greiter, M. B., Bissardon, C., Xie, W. Z., Schlattl, H., Oeh, U., Li, J. L., & Hoeschen, C.. (2014). Monte Carlo simulations of dose enhancement around gold nanoparticles used as X-ray imaging contrast agents and radiosensitizers. Medical Imaging 2014: Physics of Medical Imaging. *Proceedings of SPIE, 9033*, 90331K.

153. Wardlow, N., Polin, C., Villagomez-Bernabe, B., & Currell, F. (2015). A simple model to quantify radiolytic production following electron emission from heavy-atom nanoparticles irradiated in liquid suspensions. *Radiation Research, 184*, 518–532.

154. Xie, W. Z., Friedland, W., Li, W. B., Li, C. Y., Oeh, U., Qiu, R., Li, J. L., & Hoeschen, C. (2015). Simulation on the molecular radiosensitization effect of gold nanoparticles in cells irradiated by x-rays. *Physics in Medicine and Biology, 60*, 6195–6212.

155. Ferrero, V., Visona, G., Dalmasso, F., Gobbato, A., Cerello, P., Strigari, L., Visentin, S., & Attili, A. (2017). Targeted dose enhancement in radiotherapy for breast cancer using gold nanoparticles, part 1: A radiobiological model study. *Medical Physics, 44*, 1983–1992.

156. Sung, W. M., Ye, S. J., McNamara, A. L., McMahon, S. J., Hainfeld, J., Shin, J., Smilowitz, H. M., Paganetti, H., & Schuemann, J. (2017). Dependence of gold nanoparticle radiosensitization on cell geometry. *Nanoscale, 9*, 5843–5853.

157. Zabihzadeh, M., Moshirian, T., Ghorbani, M., Knaup, C., & Behrooz, M. A. (2016). A Monte Carlo study on dose enhancement by homogenous and inhomogeneous distributions of gold nanoparticles in radiotherapy with low energy X-rays. *Journal of Biomedical Physics and Engineering*, I–XVI.

158. Zygmanski, P., & Sajo, E. (2016). Nanoscale radiation transport and clinical beam modeling for gold nanoparticle dose enhanced radiotherapy (GNPT) using X-rays. *The British Journal of Radiology, 89*, 20150200.

159. Oliver, P. A. K., & Thomson, R. M. (2017). A Monte Carlo study of macroscopic and microscopic dose descriptors for kilovoltage cellular dosimetry. *Physics in Medicine and Biology, 62*, 1417–1437.

160. Lee, C., Cheng, N. N., Davidson, R. A., & Guo, T. (2012). Geometry enhancement of nanoscale energy deposition by X-rays. *Journal of Physical Chemistry C, 116*, 11292–11297.

161. Ma, L., Zou, X. J., Bui, B., Chen, W., Song, K. H., & Solberg, T. (2014). X-ray excited ZnS: Cu,Co afterglow nanoparticles for photodynamic activation. *Applied Physics Letters, 105*, 013702.

162. Huang, F. K., Chen, W. C., Lai, S. F., Liu, C. J., Wang, C. L., Wang, C. H., Chen, H. H., Hua, T. E., Cheng, Y. Y., Wu, M. K., et al. (2010). Enhancement of irradiation effects on cancer cells by cross-linked dextran-coated iron oxide (CLIO) nanoparticles. *Physics in Medicine and Biology, 55*, 469–482.

163. Zou, X. J., Yao, M. Z., Ma, L., Hossu, M., Han, X. M., Juzenas, P., & Chen, W. (2014). X-ray-induced nanoparticle-based photodynamic therapy of cancer. *Nanomedicine, 9*, 2339–2351.

164. McQuaid, H. N., Muir, M. F., Taggart, L. E., McMahon, S. J., Coulter, J. A., Hyland, W. B., Jain, S., Butterworth, K. T., Schettino, G., Prise, K. M., et al. (2016). Imaging and radiation effects of gold nanoparticles in tumour cells. *Scientific Reports*, 6, 19442.

165. Detappe, A., Thomas, E., Tibbitt, M. W., Kunjachan, S., Zavidij, O., Parnandi, N., Reznichenko, E., Lux, F., Tillement, O., & Berbeco, R. (2017). Ultrasmall silica-based bismuth gadolinium nanoparticles for dual magnetic resonance-computed tomography image guided radiation therapy. *Nano Letters, 17*, 1733–1740.

166. Stefancikova, L., Lacombe, S., Salado, D., Porcel, E., Pagacova, E., Tillement, O., Lux, F., Depes, D., Kozubek, S., & Falk, M. (2016). Effect of gadolinium-based nanoparticles on nuclear DNA damage and repair in glioblastoma tumor cells. *Journal of Nanbiotechnology, 14*, 63.

167. Clement, S., Chen, W. J., Anwer, A. G., & Goldys, E. M. (2017). Verteprofin conjugated to gold nanoparticles for fluorescent cellular bioimaging and X-ray mediated photodynamic therapy. *Microchimica Acta, 184*, 1765–1771.

168. Ghaemi, B., Mashinchian, O., Mousavi, T., Karimi, R., Kharrazi, S., & Amani, A. (2016). Harnessing the cancer radiation therapy by lanthanide-doped zinc oxide based theranostic nanoparticles. *ACS Applied Materials & Interfaces, 8*, 3123–3134.

169. Khoei, S., Mahdavi, S. R., Fakhimikabir, H., Shakeri-Zadeh, A., & Hashemian, A. (2014). The role of iron oxide nanoparticles in the radiosensitization of human prostate carcinoma cell line DU145 at megavoltage radiation energies. *International Journal of Radiation Biology, 90*, 351–356.

170. Brown, R., Tehei, M., Oktaria, S., Briggs, A., Stewart, C., Konstantinov, K., Rosenfeld, A., Corde, S., & Lerch, M. (2014). High-Z nanostructured ceramics in radiotherapy: First evidence of Ta_2O_5-induced dose enhancement on radioresistant cancer cells in an MV photon field. *Particle and Particle Systems Characterization, 31*, 500–505.

171. Kumar, R., Korideck, H., Ngwa, W., Berbeco, R. I., Makrigiorgos, G. M., & Sridhar, S. (2013). Third generation gold nanoplatform optimized for radiation therapy. *Translational Cancer Research, 2*, 228–239.

172. Yousef, I., Seksek, O., Gil, S., Prezado, Y., Sule-Susoe, J., & Martinez-Rovira, I. (2016). Study of the biochemical effects induced by X-ray irradiations in combination with gadolinium nanoparticles in F98 glioma cells: First FTIR studies at the Emira laboratory of the SESAME synchrotron. *Analyst, 141*, 2238–2249.

173. Takahashi, J., & Misawa, M. (2007). Analysis of potential radiosensitizing materials for X-ray-induced photodyanmic therapy. *NanoBiotechnology, 3*, 116–126 116.

174. Ngwa, W., Korideck, H., Kassis, A. I., Kumar, R., Sridhar, S., Makrigiorgos, G. M., & Cormack, R. A. (2013). In vitro radiosensitization by gold nanoparticles during continuous low-dose-rate gamma irradiation with I-125 brachytherapy seeds. *Nanomedicine-Nanotechnology, 9*, 25–27.

175. Bao, Z. R., He, M. Y., Quan, H., Jiang, D. Z., Zheng, Y. H., Qin, W. J., Zhou, Y. F., Ren, F., Guo, M. X., & Jiang, C. Z. (2016). FePt nanoparticles: A novel nanoprobe for enhanced HeLa cells sensitivity to chemoradiotherapy. *RSC Advances, 6*, 35124–35134.

176. Kraščḗkovā, S., Giuliani, A., Lacerda, S., Pallier, A., Mercere, P., Toth, E., & Refregiers, M. (2015). X-ray-induced radiophotodynamic therapy (RPDT) using lanthanide micelles: Beyond depth limitations. *Nano Research, 8*, 2373–2379.

177. Rossi, F., Bedogni, E., Bigi, F., Rimoldi, T., Cristofolini, L., Pinelli, S., Alinovi, R., Negri, M., Dhanabalan, S. C., Attolini, G., et al. (2015). Porphyrin conjugated SiC/SiOx nanowires for X-ray-excited photodynamic therapy. *Scientific Reports*, 5, 7606.

178. Nakayama, M., Sasaki, R., Ogino, C., Tanaka, T., Morita, K., Umetsu, M., Ohara, S., Tan, Z. Q., Nishimura, Y., Akasaka, H., et al. (2016). Titanium peroxide nanoparticles enhanced cytotoxic effects of X-ray irradiation against pancreatic cancer model through reactive oxygen species generation in vitro and in vivo. *Radiation Oncology, 11*, 91.

179. Huang, C. W., Kearney, V., Moeendarbari, S., Jiang, R. Q., Christensen, P., Tekade, R., Sun, X. K., Mao, W. H., & Hao, Y. W. (2015). Hollow gold nanoparticles as biocompatible radiosensitizer: An in vitro proof of concept study. *Journal of Nano Research, 32*, 106–U140.

180. Jiang, X. Y., Du, B. J., Yu, M. X., Jia, X., & Zheng, J. (2016). Surface-ligand effect on radiosensitization of ultrasmall luminescent gold nanoparticles. *Journal of Innovative Optical Health Sciences, 9*, 1642003.

181. Zhang, X. D., Guo, M. L., Wu, H. Y., Sun, Y. M., Ding, Y. Q., Feng, X., & Zhang, L. A. (2009). Irradiation stability and cytotoxicity of gold nanoparticles for radiotherapy. *International Journal of Nanomedicine, 4*, 165–173.

182. Levy, L., Pottier, A., Rouet, A., Marill, J., Devaux, C., & Germain, M. (2009). Inorganic nanoparticles of high density to destroy cells in-vivo, WO2009 147214 A1.

183. Geng, F., Song, K., Xing, J. Z., Yuan, C. Z., Yan, S., Yang, Q. F., Chen, J., & Kong, B. H. (2011). Thio-glucose bound gold nanoparticles enhance radio-cytotoxic targeting of ovarian cancer. *Nanotechnology, 22*(285101), 1–8.

184. Yang, C., Neshatian, M., van Prooijen, M., & Chithrani, D. B. (2014). Cancer nanotechnology: Enhanced therapeutic response using peptide-modified gold nanoparticles. *Journal of Nanoscience and Nanotechnology, 14*, 4813–4819.

185. Carter, J. D., Cheng, N. N., Qu, Y. Q., Suarez, G. D., & Guo, T. (2007). Nanoscale energy deposition by x-ray absorbing nanostructures. *The Journal of Physical Chemistry. B, 111*, 11622–11625.

186. Hossain, M., Luo, Y., Sun, Z. Y., Wang, C. M., Zhang, M. H., Fu, H. Y., Qiao, Y., & Su, M. (2012). X-ray enabled detection and eradication of circulating tumor cells with nanoparticles. *Biosensors & Bioelectronics, 38*, 348–354.

187. Detappe, A., Rottmann, J., Kunjachan, S., Tillement, O., & Berbeco, R. (2015). Theranostic gadolinium-based AGuIX nanoparticles for MRI-guided radiation therapy. *Medical Physics, 42*, 3566–3566.

188. Wang, J. P., Pang, X. J., Tan, X. X., Song, Y. L., Liu, L., You, Q., Sun, Q., Tan, F. P., & Li, N. (2017). A triple-synergistic strategy for combinational photo/radiotherapy and multi-modality imaging based on hyaluronic acid-hybridized polyaniline-coated WS2 nanodots. *Nanoscale, 9*, 5551–5564.

189. Hainfeld, J. F., Dilmanian, F. A., Slatkin, D. N., & Smilowitz, H. M. (2008). Radiotherapy enhancement with gold nanoparticles. *The Journal of Pharmacy and Pharmacology, 60*, 977–985.

190. Jaboin, J. I., Fu, A., Hariri, G., Han, Z., & Hallahan, D. (2007). Novel radiation-guided nanoparticle drug delivery system for prostate cancer. *International Journal of Radiation Oncology, Biology, Physics, 69*, S111–S111.

191. Chang, M. Y., Shiau, A. L., Chen, Y. H., Chang, C. J., Chen, H. H. W., & Wu, C. L. (2008). Increased apoptotic potential and dose-enhancing effect of gold nanoparticles in combination with single-dose clinical electron beams on tumor-bearing mice. *Cancer Science, 99*, 1479–1484.

192. Popovtzer, A., Mizrachi, A., Motiei, M., Bragilovski, D., Lubimov, L., Levi, M., Hilly, O., Ben-Aharon, I., & Popovtzer, R. (2016). Actively targeted gold nanoparticles as novel radiosensitizer agents: An in vivo head and neck cancer model. *Nanoscale, 8*, 2678–2685.

193. Tseng, S. J., Chien, C. C., Liao, Z. X., Chen, H. H., Kang, Y. D., Wang, C. L., Hwu, Y., & Margaritondo, G. (2012). Controlled hydrogel photopolymerization inside live systems by X-ray irradiation. *Soft Matter, 8*, 1420–1427.

194. Anijdan, S. H. M., Mahdavi, S. R., Shirazi, A., Zarrinfard, M. A., & Hajati, J. (2013). Megavoltage X-ray dose enhancement with gold nanoparticles in tumor bearing mice. *International Journal of Molecular and Cellular Medicine (IJMCM), 3*, 118–124.

195. Krishnan, S., Diagaradjane, P., Goudrich, G. P., & Payne, J. D. (2013). Enhancement of radiation therapy by targeted high-Z nanoparticles. US 2013/0225901 A1.

196. Kunjachan, S., Detappe, A., Kumar, R., Ireland, T., Cameron, L., Biancur, D. E., Motto-Ros, V., Sancey, L., Sridhar, S., Makrigiorgos, G. M., et al. (2015). Nanoparticle mediated tumor vascular disruption: A novel strategy in radiation therapy. *Nano Letters, 15*, 7488–7496.

197. Fan, W. P., Bu, W. B., Zhang, Z., Shen, B., Zhang, H., He, Q. J., Ni, D. L., Cui, Z. W., Zhao, K. L., Bu, J. W., et al. (2015). X-ray radiation-controlled NO-release for on-demand depth-independent hypoxic radiosensitization. *Angewandte Chemie, International Edition, 54*, 14026–14030.

198. Chen, N., Yang, W. T., Bao, Y., Xu, H. L., Qin, S. B., & Tu, Y. (2015). BSA capped Au nanoparticle as an efficient sensitizer for glioblastoma tumor radiation therapy. *RSC Advances, 5*, 40514–40520.

199. Chen, H. M., Wang, G. D., Chuang, Y. J., Zhen, Z. P., Chen, X. Y., Biddinger, P., Hao, Z. L., Liu, F., Shen, B. Z., Pan, Z. W., et al. (2015). Nanoscintillator-mediated X-ray inducible photodynamic therapy for in vivo cancer treatment. *Nano Letters, 15*, 2249–2256.

200. Zhang, X. D., Luo, Z. T., Chen, J., Song, S. S., Yuan, X., Shen, X., Wang, H., Sun, Y. M., Gao, K., Zhang, L. F., et al. (2015). Ultrasmall glutathione-protected gold nanoclusters as next generation radiotherapy sensitizers with high tumor uptake and high renal clearance. *Scientific Reports*, 5.

201. Yi, X., Chen, L., Zhong, X. Y., Gao, R. L., Qian, Y. T., Wu, F., Song, G. S., Chai, Z. F., Liu, Z., & Yang, K. (2016). Core-shell Au@MnO2 nanoparticles for enhanced radiotherapy via improving the tumor oxygenation. *Nano Research, 9*, 3267–3278.

202. Zhao, N., Yang, Z. R., Li, B. X., Meng, J., Shi, Z. L., Li, P., & Fu, S. (2016). RGD-conjugated mesoporous silica-encapsulated gold nanorods enhance the sensitization of triple-negative breast cancer to megavoltage radiation therapy. *International Journal of Nanomedicine, 11*, 5595–5610.

203. Li, M. F., Zhao, Q., Yi, X., Zhong, X. Y., Song, G. S., Chai, Z. F., Liu, Z. A., & Yang, K. (2016). Au@MnS@ZnS core/shell/shell nanoparticles for magnetic resonance imaging and enhanced cancer radiation therapy. *ACS Applied Materials & Interfaces, 8*, 9557–9564.

204. Liu, J. J., Chen, Q., Zhu, W. W., Yi, X., Yang, Y., Dong, Z. L., & Liu, Z. (2017). Nanoscale-coordination-polymer-shelled manganese dioxide composite nanoparticles: A multistage redox/pH/H$_2$O$_2$-responsive cancer theranostic nanoplatform. *Advanced Functional Materials, 27*, 1605926.

205. Smilowitz, H. M., Hainfeld, J. F., Dilmanian, F. A., Zhong, Z., Slatkin, D. N., & Kalef-Ezra, J. A. (2010). Gold nanoparticles enhance the radiation therapy of a murine squamous cell carcinoma. *Physics in Medicine and Biology, 55*, 3045–3059.

206. Chen, W., & Zhang, J. (2006). Using nanoparticles to enable simultaneous radiation and photodynamic therapies for cancer treatment. *Journal of Nanoscience and Nanotechnology, 6*, 1159–1166.

207. Davidson, R. A., Sugiyama, C., & Guo, T. (2014). Determination of absolute quantum efficiency of X-ray nano phosphors by thin film photovoltaic cells. *Analytical Chemistry, 86*, 10492–10496.

208. Alric, C., Serduc, R., Mandon, C., Taleb, J., Le Duc, G., Le Meur-Herland, A., Billotey, C., Perriat, P., Roux, S., & Tillement, O. (2008). Gold nanoparticles designed for combining dual modality imaging and radiotherapy. *Gold Bulletin, 41*, 90–97.

209. Hebert, E. M., Debouttiere, P. J., Lepage, M., Sanche, L., & Hunting, D. J. (2010). Preferential tumour accumulation of gold nanoparticles, visualised by magnetic resonance imaging:

Radiosensitisation studies in vivo and in vitro. *International Journal of Radiation Biology, 86*, 692–700.

210. Townley, H. E., Rapa, E., Wakefield, G., & Dobson, P. J. (2012). Nanoparticle augmented radiation treatment decreases cancer cell proliferation. *Nanomedicine-Nanotechnology, 8*, 526–536.

211. Townley, H. E., Kim, J., & Dobson, P. J. (2012). In vivo demonstration of enhanced radiotherapy using rare earth doped titania nanoparticles. *Nanoscale, 4*, 5043–5050.

212. Liu, P. D., Jin, H. Z., Guo, Z. R., Ma, J., Zhao, J., Li, D. D., Wu, H., & Gu, N. (2016). Silver nanoparticles outperform gold nanoparticles in radiosensitizing U251 cells in vitro and in an intracranial mouse model of glioma. *International Journal of Nanomedicine, 11*, 5003–5013.

213. Lien, J., Peck, K. A., Su, M. Q., & Guo, T. (2016). Sub-monolayer silver loss from large gold nanospheres detected by surface plasmon resonance in the sigmoidal region. *Journal of Colloid and Interface Science, 479*, 173–181.

214. Jain, S., Hirst, D. G., & O'Sullivan, J. M. (2012). Gold nanoparticles as novel agents for cancer therapy. *The British Journal of Radiology, 85*, 101–113.

215. Kotb, S., Detappe, A., Lux, F., Appaix, F., Barbier, E. L., Tran, V. L., Plissonneau, M., Gehan, H., Lefranc, F., Rodriguez-Lafrasse, C., et al. (2016). Gadolinium-based nanoparticles and radiation therapy for multiple brain melanoma metastases: Proof of concept before phase I trial. *Theranostics, 6*, 418–427.

216. Rancoule, C., Magne, N., Vallard, A., Guy, J. B., Rodriguez-Lafrasse, C., Deutsch, E., & Chargari, C. (2016). Nanoparticles in radiation oncology: From bench-side to bedside. *Cancer Letters, 375*, 256–262.

217. Norman, A., & Iwamoto, K. S. (1991). Therapy X-ray scanner, 5,008,907.

218. Uesaka, M., Mizumo, K., Sakumi, A., Meiling, J., Yusa, N., Nishiyama, N., & Nakagawa, K. (2007). Pinpoint KEV/MEV X-ray sources for X-ray drug delivery system. PAC, IEEE, Albuquerque, Vol. THPMN035, p. 2793.

219. Montenegro, M., Nahar, S. N., Pradhan, A. K., Huang, K., & Yu, Y. (2009). Monte Carlo simulations and atomic calculations for auger processes in biomedical nanotheranostics. *The Journal of Physical Chemistry. A, 113*, 12364–12369.

220. Zhang, E., Ntumba, K., & Nadeau, J. (2010). Enhanced cytotoxicity of doxorubicin conjugated to ultrasmall au nanoparticles. *Nanotechnology, 3*, 316–319.

221. Davidson, R. A., & Guo, T. (2016). Nanoparticle-assisted scanning focusing X-ray therapy with needle beam X rays. *Radiation Research, 185*, 87–95.

222. Lukianova-Hleb, E. Y., Ren, X. Y., Sawant, R. R., Wu, X. W., Torchilin, V. P., & Lapotko, D. O. (2014). On-demand intracellular amplification of chemoradiation with cancer-specific plasmonic nanobubbles. *Nature Medicine, 20*, 778–784.

223. Fan, W. P., Shen, B., Bu, W. B., Zheng, X. P., He, Q. J., Cui, Z. W., Zhao, K. L., Zhang, S. J., & Shi, J. L. (2015). Design of an intelligent sub-50 nm nuclear-targeting nanotheranostic system for imaging guided intranuclear radiosensitization. *Chemical Science, 6*, 1747–1753.

224. Fan, W. P., Shen, B., Bu, W. B., Zheng, X. P., He, Q. J., Cui, Z. W., Ni, D. L., Zhao, K. L., Zhang, S. J., & Shi, J. L. (2015). Intranuclear biophotonics by smart design of nuclear-targeting photo−/radio-sensitizers co-loaded upconversion nanoparticles. *Biomaterials, 69*, 89–98.

225. Koger, B., & Kirkby, C. (2016). Optimization of photon beam energies in gold nanoparticle enhanced arc radiation therapy using Monte Carlo methods. *Physics in Medicine and Biology, 61*, 8839–8853.

226. Morita, K., Miyazaki, S., Numako, C., Ikeno, S., Sasaki, R., Nishimura, Y., Ogino, C., & Kondo, A. (2016). Characterization of titanium dioxide nanoparticles modified with polyacrylic acid and H2O2 for use as a novel radiosensitizer. *Free Radical Research, 50*, 1319–1328.

227. Moeendarbari, S., Tekade, R., Mulgaonkar, A., Christensen, P., Ramezani, S., Hassan, G., Jiang, R., Oz, O. K., Hao, Y. W., & Sun, X. K. (2016). Theranostic nanoseeds for efficacious internal radiation therapy of unresectable solid tumors. *Scientific Reports, 6*, 20614.

228. Chen, Y. Y., Song, G. S., Dong, Z. L., Yi, X., Chao, Y., Liang, C., Yang, K., Cheng, L., & Liu, Z. (2017). Drug-loaded mesoporous tantalum oxide nanoparticles for enhanced synergetic chemoradiotherapy with reduced systemic toxicity. *Small, 13*, 1602869.

229. Chevillard, S., Vielh, P., Campana, F., Bastian, G., & Coppey, J. (1992). Cytotoxic effects and pharmacokinetic analysis of combined Adriamycin and X-ray treatments in human organotypic cell-cultures. *Anti-Cancer Drugs, 3*, 133–137.

230. Shibamoto, Y., Zhou, L., Hatta, H., Mori, M., & Nishimoto, S. (2000). A novel class of antitumor prodrug, 1-(2'-oxopropyl)-5-fluorouracil (OFU001), that releases 5-fluorouracil upon hypoxic irradiation. *Japanese Journal of Cancer Research, 91*, 433–438.

231. Mueller, A., Bondurant, B., & O'Brien, D. F. (2000). Visible-light-stimulated destabilization of PEG-liposomes. *Macromolecules, 33*, 4799–4804.

232. Spratt, T., Bondurant, B., & O'Brien, D. F. (2003). Rapid release of liposomal contents upon photoinitiated destabilization with UV exposure. *Biochimica et Biophysica Acta-Biomembranes, 1611*, 35–43.

233. Lopez, E., Obrien, D. F., & Whitesides, T. H. (1982). Structural effects on the photo-polymerization of bilayer-membranes. *Journal of the American Chemical Society, 104*, 305–307.

234. Yavlovich, A., Smith, B., Gupta, K., Blumenthal, R., & Puri, A. (2010). Light-sensitive lipid-based nanoparticles for drug delivery: Design principles and future considerations for biological applications. *Molecular Membrane Biology, 27*, 364–381.

235. Puri, A., & Blumenthal, R. (2011). Polymeric lipid assemblies as novel theranostic tools. *Accounts of Chemical Research, 44*, 1071–1079.

236. Faisant, N., Siepmann, J., Oury, P., Laffineur, V., Bruna, E., Haffner, J., & Benoit, J. P. (2002). The effect of gamma-irradiation on drug release from bioerodible microparticles: A quantitative treatment. *International Journal of Pharmaceutics, 242*, 281–284.

237. Roullin, V. G., Mege, M., Lemaire, L., Cueyssac, J. P., Venier-Julienne, M. C., Menei, P., Gamelin, E., & Benoit, J. P. (2004). Influence of 5-fluorouracil-loaded microsphere formulation on efficient rat glioma radiosensitization. *Pharmaceutical Research, 21*, 1558–1563.

238. Fologea, E., Salamo, G., Henry, R., Borrelli, M. J., & Corry, P. M. (2010). Method of controlling drug release from a liposome carrier. US patent application number: US20120041357A1; priority date: Mar. 31, 2009.

239. Fologea, D., Salamo, G., Henry, R., Borrelli, M. J., & Corry, P. M. (2010). Method of controlled drug release from a liposome carrier, United State Patent: US 8808733 B2. Issued date: Aug. 19, 2014.

240. Juzenas, P., Chen, W., Sun, Y. P., Coelho, M. A. N., Generalov, R., Generalova, N., & Christensen, I. L. (2008). Quantum dots and nanoparticles for photodynamic and radiation therapies of cancer. *Advanced Drug Delivery Reviews, 60*, 1600–1614.

241. Kobayashi, K., Usami, N., Porcel, E., Lacombe, S., & Le Sech, C. (2010). Enhancement of radiation effect by heavy elements. *Mutation Research, Reviews in Mutation Research, 704*, 123–131.

242. Jelveh, S., & Chithrani, D. B. (2011). Gold nanostructures as a platform for combinational therapy in future cancer therapeutics. *Cancer, 3*, 1081–1110.

243. Dreaden, E. C., Alkilany, A. M., Huang, X. H., Murphy, C. J., & El-Sayed, M. A. (2012). The golden age: Gold nanoparticles for biomedicine. *Chemical Society Reviews, 41*, 2740–2779.

244. Coulter, J. A., Butterworth, K. T., & Jain, S. (2015). Prostate cancer radiotherapy: Potential applications of metal nanoparticles for imaging and therapy. *The British Journal of Radiology, 88*, 20150256.

245. Dorsey, J. F., Sun, L., Joh, D. Y., Witztum, A., Al Zaki, A., Kao, G. D., Alonso-Basanta, M., Avery, S., Tsourkas, A., & Hahn, S. M. (2013). Gold nanoparticles in radiation research: Potential applications for imaging and radiosensitization. *Translational Cancer Research, 2*, 280–291.

246. Kwatra, D., Venugopal, A., & Anant, S. (2013). Nanoparticles in radiation therapy: A summary of various approaches to enhance radiosensitization in cancer. *Translational Cancer Research, 2*, 330–342.

247. Su, X. Y., Liu, P. D., Wu, H., & Gu, N. (2014). Enhancement of radiosensitization by metal-based nanoparticles in cancer radiation therapy. *Cancer Biology & Medicine, 11*, 86–91.

248. Retif, P., Pinel, S., Toussaint, M., Frochot, C., Chouikrat, R., Bastogne, T., & Barberi-Heyob, M. (2015). Nanoparticles for radiation therapy enhancement: The key parameters. *Theranostics, 5*, 1030–1045.

249. Brun, E., & Sicard-Roselli, C. (2016). Actual questions raised by nanoparticle radiosensitization. *Radiation Physics and Chemistry, 128*, 134–142.

250. Haume, K., Rosa, S., Grellet, S., Smialek, M. A., Butterworth, K. T., Solov'yov, A. V., Prise, K. M., Golding, J., & Mason, N. J. (2016). Gold nanoparticles for cancer radiotherapy: A review. *Cancer Nanotechnology, 7*, 8.

251. Rosa, S., Connolly, C., Schettino, G., Butterworth, K. T., & Prise, K. (2017). Biological mechanisms of gold nanoparticle radiosensitization. *Cancer Nanotechnology, 8*(1).

252. Her, S., Jaffray, D. A., & Allen, C. (2017). Gold nanoparticles for applications in cancer radiotherapy: Mechanisms and recent advancements. *Advanced Drug Delivery Reviews, 109*, 84–101.

253. Cho, S. H., & Krishnan, S. (2013). Cancer nanotechnology: Principles and applications of radiation oncology, W. R. Hendee (p. 284). Boca Raton: CRC Press.

Chapter 10
Applications of X-Ray Nanochemistry in Catalysis

Running a business or any project is like taking a downhill mogul run - it is all about managing the transition. You can have a great run even though it does not look like you are going directly home most of the time.

10.1 Introduction

Catalytic reactions can benefit from X-ray nanochemistry. The impact of X-ray nanochemistry on catalysis may be understood from three perspectives. First, classical catalytic reactions involving X-ray irradiation may be improved through X-ray nanochemical research. Exploration of catalysis involving ionizing radiation and nanomaterials began in the 1920s. The goal at that time was to understand what reactions could be driven by ionizing radiation and what would happen when the mixture of nanomaterial catalysts and regular samples were irradiated with X-rays or γ-rays. Since then, many chemical systems have been studied; one example was hydrogen production with the assistance of nanomaterials under ionizing irradiation. This topic has been particularly interesting to the nuclear industry. Mesiel [1] reviewed publications in this area. Although much of the work focuses on using more energetic γ-rays, one can imagine that the same working principles applicable to γ-rays can be extended to X-rays. X-ray nanochemistry should have a broader range of applications because of higher absorption cross-sections of X-rays by nanomaterials than γ-rays.

The first section of the chapter is devoted to traditional catalysis assisted by X-ray nanochemistry. For example, type 1 physical enhancement can increase production of hydroxyl radicals, which can increase the yield of H_2 if hydroxyl radicals are used to drive the production of H_2. Nanomaterials including metal and metal oxide nanoparticles are suitable for catalysis under X-ray irradiation due to their high absorption of X-rays. It is important to point out that catalysis is different from radiolysis, a topic discussed in Chap. 11.

The second area of application in the catalytic research field that can be impacted by X-ray nanochemistry is photocatalysis. Specific nanomaterials are needed to support X-ray-driven photocatalysis. A specific demand on nanomaterials to support

photocatalysis is that they need to possess the ability to generate electron-hole pairs. Type 1 or 2 physical enhancement can help increase the yield of electron-hole pair production. Type 3 physical enhancement can also assist the generation of electron-hole pairs through the emission of UV-Vis light from nanomaterials. An example in this area is CO_2 reduction. There have been many cases of studying CO_2 reduction under ionizing radiation such as X-rays. In such a reaction, X-rays and catalysis were used to convert CO_2 to methanol or other chemicals. One particularly interesting potential application is to use background ionizing radiation with the assistance of photocatalysts in the X-ray region to convert CO_2 to other chemicals, if CO_2 can be pumped underground and stored as described by Benson et al. [2]. One may even speculate that this is how some fossil fuels, such as petroleum, are made. Another possibility is to utilize nuclear waste and nanomaterial catalysts to efficiently convert CO_2 into useful chemicals. It is possible that these reactions could happen in nature in high radiation background regions or around nuclear waste.

The third area of application of X-ray nanochemistry in catalysis is outlined and discussed in Chap. 3, in which chemical enhancement is defined within X-ray nanochemistry as reactions enabled by catalytic processes occurring on the surface of catalytic nanoparticles. Types 1 and type 2 chemical enhancement are proposed. As shown in Chap. 3, increased production of 7-OHCCA from 3-CCA is detected, and the magnitude of increase exceeds what can be explained by typical physical enhancement. Many other reactions follow similar pathways and are supported through chemical enhancement. Applications of X-ray nanochemistry in this area of catalysis can help elucidate how chemical enhancement works, addressing, for instance, whether enhancement is caused by X-ray-driven nanomaterials or enabled by X-ray-produced species such as superoxide or hydroxyl radicals. Both concepts rely on catalytic properties of nanomaterials.

Although in this chapter catalysis is treated as an application of X-ray nanochemistry, it must be recognized that catalysis is also an intrinsic part of X-ray nanochemistry. For example, photocatalysis can be used to generate electron-hole pairs that produce radicals such as hydroxyl radicals and solvated electrons, whose increased production can cause type 2 chemical enhancement. Moreover, it is foreseeable that type 3 physical enhancement can be combined with traditional photocatalysts to enable X-ray photochemistry. All these processes suggest that catalysis is part of X-ray nanochemistry. Conversely, catalysis can be stated as the fundamental part of X-ray nanochemistry, and chemical enhancement would be the application of catalysis. However, catalysis is traditionally an applied topic of physics, chemistry, and materials science. Following this convention, we consider catalysis as an application that X-ray nanochemistry can help improve.

Given that ionizing radiation is ubiquitous in nature, and nanomaterials or similar materials are abundant in nature as well, it is possible that catalytic reactions involving nanomaterials and X-rays occur more often than we think and can help us in more ways than we have realized. Historically, the usefulness of X-ray-nanomaterial interactions in nature has been minimal or nonexistent, possibly because of small reaction cross-sections and limited methods to detect interactions. Furthermore, nanomaterials have not been properly prepared for X-ray

nanochemistry until just a few years ago. One example was the case of uranium nanoparticles in the body under background radiation discussed in Chap. 2, where it was speculated that uranium particles in the body might enhance radiation effects by a few thousand times. It was later found that the magnitude of enhancement was only a factor of 10, which agreed with theoretical predictions described in Chap. 2. However, only physical enhancement or its equivalent was considered in predicting the enhancement. If catalysis is involved, such as that described in Chap. 3 and in this chapter, and if a multiplication algorithm or other algorithms of enhancements as discussed in Chap. 5 exist, then it is possible to reach enhancement of the order of 1000 DEU or higher. Such high enhancements may be combined with other mechanisms to convert the absorbed X-ray photons into many other chemical, biological, mechanical, optical, physical, and magnetic events. This means that the original speculation made by Busby in 2005 of uranium particles causing a 5000 DEU enhancement was not far-fetched. A more detailed analysis is given in Sect. 10.5.

10.2   Fundamental Principles for Catalysis

As explained above, there are at least three possible areas of applications for X-ray nanochemistry in catalysis. These three areas and pathways are illustrated in Fig. 10.1. Their existence is caused by the fundamental chemical pathways through which catalysis is accomplished as the result of X-ray irradiation of nanomaterials in media.
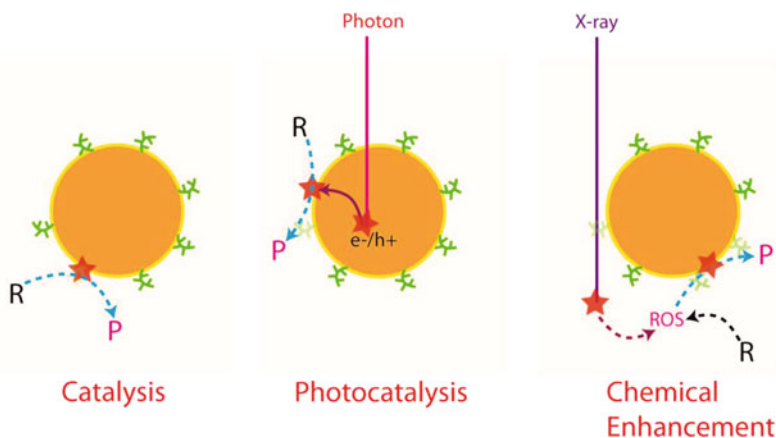
Fig. 10.1 Three pathways for X-ray nanochemistry enabled catalysis, illustrating similarities and differences among these three processes. The left panel shows traditional catalysis at the surface of the nanoparticle. The middle panel illustrates how an X-ray photon drives photocatalysis, which is mediated by an electron-hole pair created inside the nanoparticle. The right panel shows chemical enhancement discussed in Chap. 3. In this case, a ROS reacts with a reactant R to form an intermediate, which is eventually converted to the product P

The first is conventional heterogeneous catalysis, as shown in the left panel of Fig. 10.1. In this case, a reactant R comes in contact with the surface of a catalytically active nanoparticle and is converted to product P. Photocatalysis is the second case, shown in the middle panel of Fig. 10.1. Here, electron-hole pairs are produced, which either directly react with reactants absorbed on the surface of catalytic nanoparticles to form product(s) (middle panel) or oxidize or reduce to form other species that then react with R to form P. The third pathway is via chemical enhancement, as shown in Fig. 10.1 (right panel). Each of these three areas is explained further in the following.

10.2.1   Heterogeneous Catalysis Without Activation

Heterogeneous catalysis is a well-established discipline and catalysts play many roles. One of the most crucial roles is to lower reaction energy barriers. Gold nanoparticle oxidation of CO to CO_2 is a typical example of a catalytic reaction. With catalysts, the energy barrier going from reactants CO and O_2 to the product CO_2 is lowered, as described by Bond et al. [3]. Once products are formed, they can leave the catalysts relatively easily, and catalysts return to their state prior to the reaction. When X-rays are involved, this branch of research can be called X-ray-driven catalysis or simply X-ray catalysis.

Another example is the catalytic reduction of CO_2 to methanol, proposed to be a multiple-electron and multiple-H atom exchange reaction with at least six catalytic reaction steps. The proposed steps as suggested by Wu et al. [4] are shown in Fig. 10.2. Another pathway leads to the product of CH_4, which is not shown in Fig. 10.2.

Decomposition of hydrogen peroxide is another example of heterogeneous catalysis, which can be catalyzed on the surface of Pt or similar nanoparticles, a process studied by Laverne et al. [5]. The proposed reaction steps are shown in Eqs. 10.1, 10.2 and 10.3, although the actual reactions may be more complex than the proposed
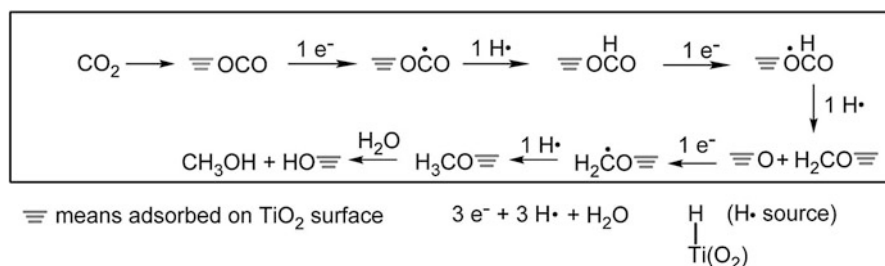
Fig. 10.2 A typical example of CO_2 reduction reaction pathways involving catalysts, CO_2, electrons, and H atoms. As many as three electrons and three H atoms may be needed to produce methanol from CO_2. The mechanisms are adapted based on those proposed by Wu et al. [4]

ones due to the existence of multiple intermediates. Once catalysts are involved (not shown here), reactions are more complex.

$$H_2O_2 \rightarrow 2 \bullet OH \tag{10.1}$$

$$\bullet OH + H_2O_2 \rightarrow HO_2 + H_2O \tag{10.2}$$

$$2HO_2 \rightarrow H_2O_2 + O_2 \tag{10.3}$$
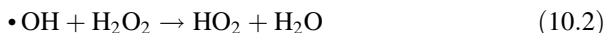
For metallic surfaces, reactions may be initiated by electron donation and finish with eventual production of oxygen gas and water. In X-ray nanochemistry, reactive oxygen species are generally involved. A number of catalytic reactions can produce hydroxyl radicals, similar to Fenton reactions. Smimov et al. [6] showed that it was possible to use nanomaterials to assist hydroxyl radical production. The authors used γ-Fe_2O_3 nanoparticles to replace Fe^{3+} in Fenton reactions and observed increased production of hydroxyl radicals. This result has at least two implications. First, iron oxide nanoparticles were shown to function similarly to iron ions. Second, since Fe^{3+} (ions) and gold nanoparticles cannot be used together in Fenton reactions, Fe_2O_3 nanoparticles offer an alternative so that chemically produce hydroxyl radicals can be used with gold nanoparticles to benchmark chemical enhancement without using X-rays.

10.2.2   *Heterogeneous Photocatalysis*

Photochemistry investigates chemical reactions driven by light of wavelengths from 100 to 2500 nm. Photocatalysis, defined similarly, uses these photons to drive catalysis on the surface of nanomaterials. X-ray photons can drive the same processes as UV-Vis light while expanding the scope of photocatalysis by accessing additional processes enabled by high-energy X-ray photons. It is hence possible to call this branch of research X-ray-driven photocatalysis, X-ray photochemistry, or simply X-ray photocatalysis.

X-ray photocatalysis, if it is the name to be used here, can be homogeneous or heterogeneous, depending on whether the catalysts are metal complexes or nanomaterials. A third scenario involves metal complexes conjugated to the surface of nanomaterials, and the hybrid product may possess unique advantages associated with both homogeneous and heterogeneous catalysts. However, homogeneous photocatalysis is not discussed here even though it may be relevant.

Photocatalysis is a popular subject in the current literature because of the potential to utilize solar power to produce chemicals. The common step of photocatalysis is absorption of light to produce electron-hole pairs, which function as redox reagents. One such catalytic reaction is the split of water into hydrogen and oxygen by sunlight. If this reaction is more economic than electrolysis of water using solar-based photovoltaic cells, and if hydrogen can be developed into a safe and convenient energy source, then photocatalysis of splitting water may be one of the most

Fig. 10.3 Typical photocatalysis mechanism. Sunlight is used to generate electron-hole pairs. Electrons are used to reduce chemicals and holes are used to oxidize chemicals. H_2 and O_2 are the products in this example. VB means valence band, CB indicates conduction band
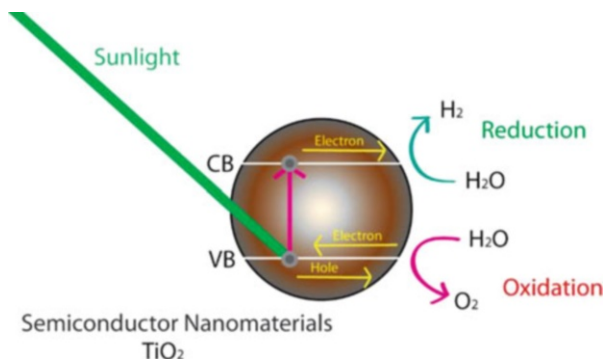
important reactions in photocatalysis or even in chemistry. Figure 10.3 shows a typical process. Many nanomaterials have been used as catalysts for water splitting using sunlight. For example, TiO_2 nanotubes were used by Grime et al. [7] to split water. Electron-hole pairs were produced and then migrated to the surface where they reacted with water to generate oxygen and hydrogen.

One of the main differences between X-ray photocatalysis and regular photochemistry is that each X-ray photon can produce a cluster of high-density electron-hole pairs in semiconductor nanomaterials. Therefore, the catalysts used in X-ray photochemistry have to be more efficient to allow these electron-hole pairs to be more effectively utilized before recombination. A similar problem exists in narrow bandgap semiconductor nanomaterials when they are exposed to visible light. In this case, multiple electron-hole pairs or excitons are produced by a single visible photon. This problem facing X-ray photocatalysis and X-ray nanochemistry has not been properly addressed. If this problem can be addressed in X-ray nanochemistry, the solution may lend help to solving problems associated with the multiple exciton generation in regular photocatalysis.

There are differences between X-ray photocatalysis and X-ray catalysis. One such difference is that catalysts in X-ray photocatalysis always absorb X-rays or electrons, which may not happen in X-ray catalysis. In X-ray catalysis, it could be the solution or medium that absorbs X-rays to produce reactive oxygen species that then activate the catalyst or react at the surface of nanoparticle catalysts.

10.2.3   Chemical Enhancement

Chemical enhancement is described in Chap. 3. Two types of chemical enhancement are presented. The principles are briefly described in this section. The emphasis here is placed on how chemical enhancement may assist catalysis, even though chemical enhancement itself is based on catalysis. Type 1 chemical enhancement relies on catalytic conversion of reactant intermediates to products by nanomaterials, which
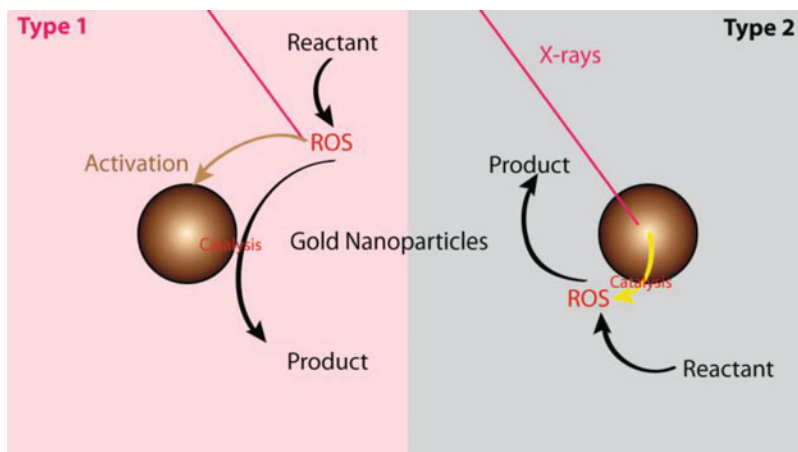
Fig. 10.4 Two types of chemical enhancements. As explained in Chap. 3, the first type (left panel) relies on catalytic properties of nanomaterials to convert intermediates to products. Type 2 chemical enhancement (right panel) uses nanoparticles as catalysts to produce more reactive oxygen species, and these species react with reactants to increase the yield of products

are either catalytically active, or activated by X-rays, or X-ray generated species such as hydroxyl or superoxide radicals. Figure 3.15 shows one such process. Notice that type 1 chemical enhancement does not invoke increased production of reactive oxygen species by nanomaterials. Many reactions have been shown to be catalyzed by this type of enhancement, and it can be understood as the reactions being driven by type 1 chemical enhancement. Figure 10.4 (left panel) summarizes type 1 chemical enhancement.

Type 2 chemical enhancement is different in the sense that it is caused by reactive oxygen species catalytically produced by X-rays interacting with nanomaterials. This means the yield of hydroxyl or superoxide radicals is higher due to the presence of nanomaterials. Again, we consider catalysis driven by this type of enhancement to be type 2 chemical enhancement-driven catalysis. Figure 10.4 (right panel) shows types 2 chemical enhancement and the sequence of catalytic steps. It is speculated by Misawa et al. [8] that type 2 chemical enhancement is caused by X-ray fluorescence from nanomaterials.

Based on the discussion given above, many catalytic reactions can be categorized into these two types of enhancement. Such a categorization helps guide the understanding of reaction mechanisms as well as discovery of new reactions that belong to these enhancements. More work is needed to fully unite all these concepts and processes.

In the following three sections, results of the study of these three types of catalytic reactions in X-ray nanochemistry applications are discussed.

10.3   X-Ray Heterogeneous Catalysis

X-ray heterogeneous catalysis is defined as regular heterogeneous catalysis involving X-ray generated species such as electrons or radicals. This means the surface or surfactants on the surface of the nanomaterials are intrinsically catalytically active. Any reactions involving both X-rays and nanomaterial catalysts would be considered to be in this category. However, photocatalysis and chemical-driven catalysis do not belong to this category. Figure 10.5 shows a typical reaction mechanism described by Zaera et al. [9], which showed several possible reaction steps covered by X-ray heterogeneous catalysis. In their work, Zaera et al. found a unique chemical system in which transition metal complexes on the surface of metal interacted with electrons released from the metal under X-ray irradiation to drive the formation of thin organic films on the metal surface. The transition metal complex was pentakis (dimethylamido)tantalum (PDMAT). Upon irradiation of the tantalum foil underneath the complexes with Al K_α radiation at 1.487 keV, methyl radicals were formed, and polymerization reactions occurred between the radical and adjacent complex. The polymerization reaction resulted in the formation of a thin uniform film on tantalum foils. As it is shown in Fig. 10.5, tantalum surface and complexes played active catalytic roles during the polymer formation process.

Another feature associated with certain nanoparticles is surface plasmon resonance (SPR). Gold, silver, and platinum metal nanoparticles possess intense SPR peaks. When combined with radicals produced by ionizing radiation, including X-rays, these metal nanoparticles behave as catalysts to enhance redox reactions at their surfaces. Kwon et al. [10] reported such a process in a specially made electrolytic cell consisting of thin Pt film-coated TiO_2 nanostructures in water irradiated by beta emitters. Energetic electrons interacted with water and TiO_2 to produce radicals and electron-hole pairs, respectively. The electrons and holes, as well as radicals, then moved to the surface of the thin Pt film, and the reactions at the
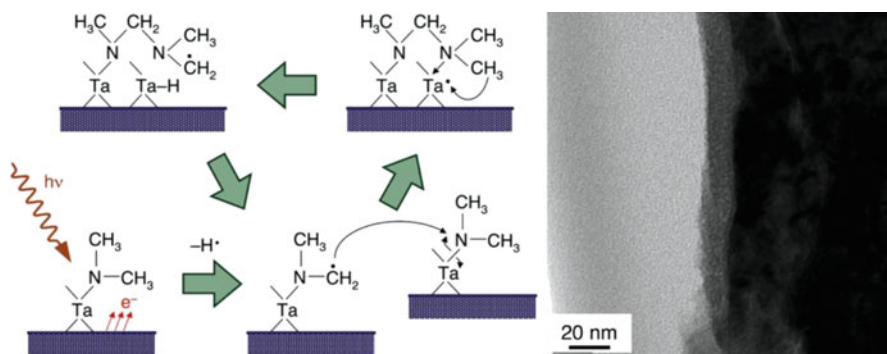
Fig. 10.5 Catalytic reactions involving photon-generated electrons on the surface of a metal foil. A thin organic film was formed on the surface of a transition metal substrate. The 1.4 keV X-ray photons used in this work can be replaced by hard X-rays. (Reprinted with permission from Zaera et al. [9]. Copyright (2012) American Chemical Society.)
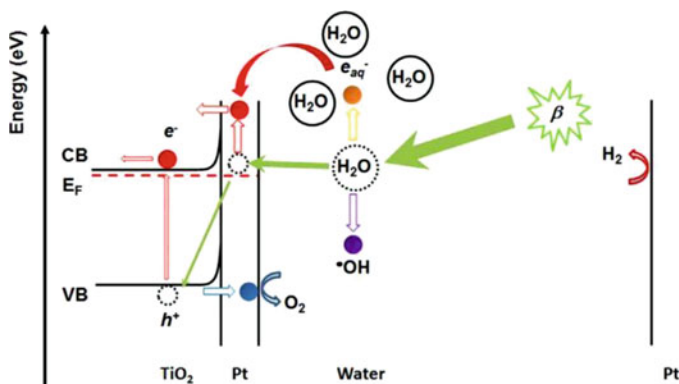
Fig. 10.6 Catalysis involving X-ray generated electron-hole pairs and radicals. Various catalytic reactions occurred on the surface of thin Pt films. Only heterogeneous catalysis was involved and no photocatalysis occurred here. (Adapted with permission from Kwon et al. [10] under CC BY NC ND 4.0 license.)

Pt film surface completed the cycle of water-splitting reactions and generated electrical currents. The proposed mechanism is shown in Fig. 10.6. According to this work, Pt films were the catalysts, and TiO_2 nanostructures did not directly involve catalysis. This reaction, therefore, did not belong to X-ray photocatalysis.

A specific type of catalytic reaction is catalytic radiolysis of CO_2 or water. Without catalysis, the work involving nanomaterials and ionizing radiation belongs to radiolysis, which is described in Chap. 11. The results discussed in this section relate to reactions that are catalyzed by nanomaterials. In one example, zeolite-assisted CO_2 reduction under γ-ray irradiation was reported by Garibov et al. [11]. The authors speculated that CO_2 adsorbed on zeolite was ionized, most likely by electrons generated as a result of absorption of X-rays. CO_2 cations then received one electron to form CO and O on the surface of zeolite. The yield of CO in units of G values was different for different zeolites. Table 10.1 shows the results and lithium-exchanged NaY zeolites (LiNaY zeolite) generated the highest CO yield. In their yield calculations, the authors assumed that a fixed amount of CO_2 adsorbed on zeolites underwent transformation.

There have been many studies using X-rays to prepare nanomaterials by irradiating ionic metal precursors in aqueous solutions. They are not reviewed here for the reason that catalysis was not mentioned in these studies. However, none of these studies ruled out catalysis when discussing the formation mechanisms. Future work may be needed to study and understand the formation processes.

Neta et al. [12] discussed how Cu catalyzed reduction of CO_2 under irradiation. The catalysts were produced in situ, through reduction of Cu(II) to Cu(0) and then to colloidal particles or Cu(I), which was done chemically with the addition of ascorbic acid or other reducing agents. The authors used γ-rays from a Varian linear accelerator emitting 1 μs 6 MeV electron pulses. This in situ preparation of catalysts is not discussed in the book for the reason stated above. The authors showed CO_2 was

Table 10.1 Decomposition of CO_2 on zeolites under γ-ray irradiation. LiNaY zeolite supported the highest G value of CO production

Zeolite	Pore size (Å)	G (CO/100 eV)
NaX	7–8	0.036
CaA	4–5	0.044
NaY	13	0.540
CaM	–	0.320
BaM	–	0.230
LiNaY	13	1.250

Adapted from Garibov et al. [11]

Fig. 10.7 CO (solid circle) and H_2 (empty circle) from irradiation of CO_2 in $CuSO_4$ solution (0.5 mmol L^{-1}). There is a clear saturation dose for CO production, which is not the same for H_2 production. This suggests the two reaction pathways were different. (Reprinted with permission from Neta et al. [12]. Copyright (2001) American Chemical Society.)
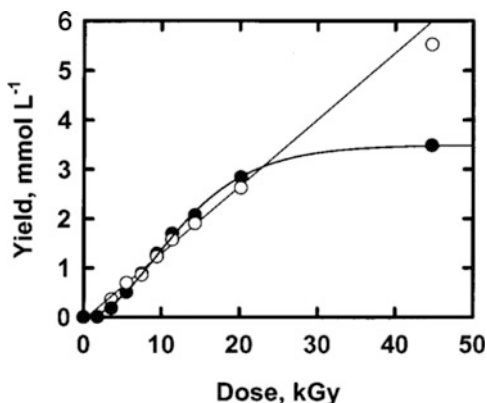
first reduced to radical $\bullet CO_2^-$ because no radicals were produced in the presence of acetone, a scavenger of solvated electrons. From this result, the authors suggested that the formation of CO_2^- radicals was necessary for the production of CO. The authors added formic acid into the mixture and observed formation of CO. They reasoned that acetone abstracted hydrogen from formic acid to form CO_2^-. Figure 10.7 shows the results of CO production from CO_2. Saturation was clearly seen above 20 kGy of radiation. However, this saturation could be caused by the exhaust of Cu^{2+} in the solution. As this work employed copper nanomaterial catalysts made in situ, it is possible to use nanoparticle catalysts prior to irradiation to fulfill the same requirement.

Catalysis requires large surface areas of catalysts and hence small nanoparticles are preferred over bulk metals. Watanabe et al. [13] demonstrated a system that was similar to the originally defined X-ray photocatalysis system, except for the use of bulk metal instead of semiconductor nanoparticles. In their work, ^{60}Co γ-rays were used. The authors used 25 stainless steel plates. If metallic nanoparticles instead of plates were used, then surface areas would be significantly increased. The authors speculated that metal plates absorbed γ-rays and emitted low-energy electrons, which then interacted with CO_2 to produce CO. Numerical simulations were performed to interpret the results. CO yield was measured as a function of the element used in the sandwiching plates, and the authors found that adding Pb plates increased the production of CO by twofold. Figure 10.8 displays their results, which
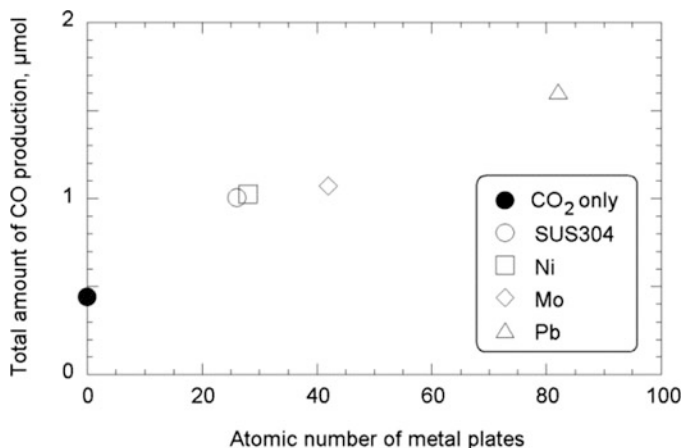
Fig. 10.8 CO_2 decomposition to form CO. The results show that Pb generated the most decomposition, which agreed with their theoretical simulations that pointed to the role of Auger electrons emitted from these metal plates. The results using molecular sieves also supported this explanation. (Adapted from Watanabe et al. [13]. With Permission of Springer.)

show the yield of CO production as a function of the amount of the metal material used in the measurement. The results showed that when molecular sieves were used, there was no CO production. The authors, based on the molecular sieve results, attributed the production of CO to Auger electrons because the molecular sieve material was considered to attenuate low-energy Auger electrons. Even though the authors stated that there was no catalysis occurring here, this work is discussed here to show the potential of replacing the metal bulk plates with metal nanoparticles so that both Auger electrons and catalysis can be used to promote CO_2 decomposition.

10.4 X-Ray Photocatalysis Using Nanomaterials

As mentioned above, photochemistry limits the range of wavelengths of the excitation light to 100 to 2500 nm. Discussion in this section is confined to X-ray initiated photochemistry with the assistance of nanomaterials. X-ray photocatalysis assisted by nanomaterials uses X-rays to produce electron-hole pairs in nanomaterials that drive catalytic reactions, or uses X-rays to generate photons in the 100–2500 nm range in nanoscintillators to drive these reactions. Due to the complexity of photocatalysis, X-ray photocatalysis is more complicated and more difficult to study than photocatalysis itself. X-ray generated electron-hole pairs for catalytic work can be called one-step X-ray photocatalytic processes. If X-ray scintillators are used together with regular photocatalysts, then the combined process is called two-step X-ray photocatalytic reactions. Both processes use semiconductor nanomaterials to catalyze reactions at their surface.

Many published works use γ-rays. Hence, works using γ-rays are discussed here as well because X-rays should be more effective than γ-rays in terms of the strength of interactions between radiation and nanomaterials based on their absorption cross-sections. X-ray nanochemistry can lean on these works performed with γ-rays for support and inspiration. As stated in Chap. 1, γ-rays and X-rays were considered similar by those who worked in the field in early times. It is reasonable to say that at those early stages, studying catalysis with γ-rays were more important than X-rays because of the connections to nuclear reactions and nuclear technologies. X-rays are now more widely used because of the safety concerns of γ-rays, the convenience of using X-ray sources, and the usefulness of the X-rays for chemical analysis. On the other hand, principles of X-ray nanochemistry should be applicable to γ-ray nanochemistry as well. This means that the knowledge learned from studying X-ray nanochemistry is useful and transferable to the work involving γ-rays.

Meisel et al. [14] discussed the reduction of methyl viologen (MV^{2+}) on the surface of silica nanoparticles by electrons. The authors found that electrons generated in the form of electron-hole pairs were captured by the surface-bound MV^{2+}. This was similar to the reaction between solvated electrons e_{aq}^- and MV^{2+} in solution. This work is mentioned here even though catalysis was not explicitly mentioned by the authors. If catalysis were present, then the reaction would be an X-ray photocatalytic reaction.

The breakdown of other molecules can happen catalytically. In a chapter dedicated to the discussion of hydrogen production from water using radiolysis, Cecal et al. [15] discussed catalytic radiolysis. Some of the catalytic results were also described in the report by Cecal et al. [16]. The radiation source was ^{60}Co and the catalysts were oxides, such as BeO, SiO_2, TiO_2, and ZrO_2. Although the results were obtained with γ-rays due to the original goal of using nuclear power, X-rays can also be used with these chemical systems to produce hydrogen catalytically. The authors found that ZrO_2 was the best catalyst among the materials tested. However, because ZrO_2 was also the catalyst with the highest electron density in this study, the results needed to be deconvoluted to understand the true role of catalysis.

Other larger molecules can also be decomposed catalytically under X-rays, albeit at lower efficiencies than UV or Vis light. In a short communication, Jimenez-Becerril et al. [17] reported their observation of photocatalysis in the case of decomposition of 4-cholorphenol in solution under γ-ray irradiation. The authors used several oxide materials as photocatalysts, although no electron microscopy such as TEM images was available. ^{60}Co was used as the γ-ray source. There was some similarity between this work and radiolysis described in Chap. 11. The difference is that radiolysis described in Chap. 11 does not need to involve catalysis or photocatalysis. Up to 10 kGy of dose was used; the decay of 4-cholorphenol was linear within the first kGy and saturated beyond 2.0 kGy. All three oxides, SiO_2, TiO_2, and Al_2O_3, generated a similar trend for the remnant 4-cholorphenol as a function of the dose.

Cates et al. [18] discussed the decomposition of phenol on nanoparticles irradiated with 205 kVp X-rays. The nanomaterials were bismuth oxides including Bi_2O_6 nanoplates and $BiPO_4$ microparticles. The loss of phenol through the use of the
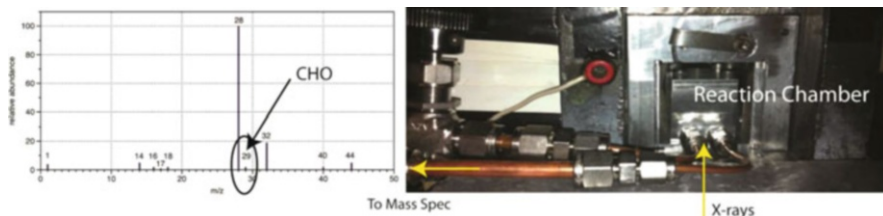
Fig. 10.9 CO_2 reduction in water by copper nanoparticles on the surface of WO_x nanoparticles. The reaction chamber is shown in the right panel and the X-ray source is underneath the reactor. Total pressure was 760 torr and the reaction time was 3 h. The X-ray source was operated at 100 kVp and 250 μA. The 29 amu peak shown in the left panel represents CHO^+ cation (Lien, Ph.D. Thesis, 2017)

nanomaterials was the same as radiation alone. However, the amount of total organic carbon (TOC) produced by radiation alone was different from that by nanomaterials with radiation, and the best result was obtained with $BiWO_4$ nanoparticles under X-ray irradiation. Nearly 25% of TOC was lost after 500 Gy irradiation. In contrast, no TOC loss was observed with X-ray radiation alone. The authors argued that the loss of TOC was caused by the production of volatile carbon compounds such as CO_2.

X-ray photocatalysis was studied by Guo et al. (Lien et al., Ph.D. Thesis, 2017) in which copper oxide nanoparticles were made and decorated on WO_x nanoparticles to reduce CO_2 in water vapor. The apparatus of the experiment is shown in Fig. 10.9 (right panel). A microfocus X-ray source was used and an aluminum reactor was built to house the reaction. 18 to 35 torr of water vapor was filled into the chamber and CO_2 was then filled so that the chamber was maintained at 760 torr total pressure. A compact mass spectrometer was used to measure the reactants and products. For a 3-hour reaction under 100 kVp irradiation at a dose rate of 20 Gy/min, CHO^+ cation was measured at mtorr level, as shown in the left panel of Fig. 10.9. The conversion efficiency was at the ppm level.

10.5   Chemical Enhancement

Chemical enhancement is described in Chap. 3. In this section, the emphasis is to use chemical enhancement to improve catalysis.

There are several ways to improve catalyzing chemical reactions using chemical enhancement. The general mechanism involving type 1 chemical enhancement is to activate normally non-catalytic nanoparticles with reactive oxygen species produced by X-ray irradiation of water or other media. This approach has the advantage of not requiring nanomaterials to absorb X-rays. Two examples of type 1 chemical enhancement reported in the literature are hydroxylation and polymerization, as shown in Chap. 3. Polymerization can be enhanced with the highest enhancement
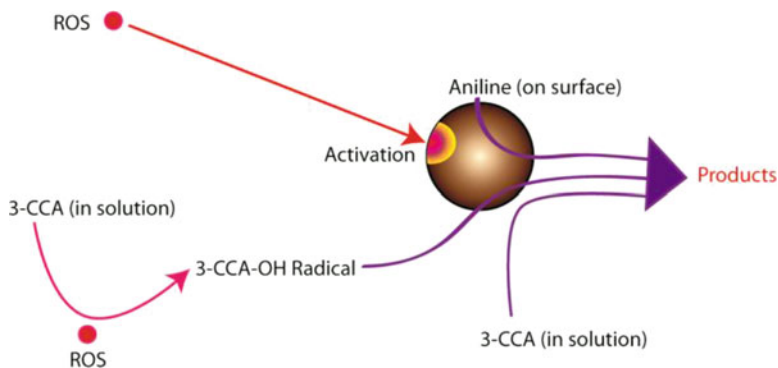
Fig. 10.10 Chemical enhancement of oxidation and polymerization of aniline reported by Guo et al. [19] and 3-CCA by Guo et al. [20]. The catalytic oxidation of aniline and hydroxylation of 3-CCA are both shown, together with a simpler, more direct pathway of 3-CCA to 7-OHCCA reaction

factor observed for this reaction to date, which was nearly 30 DEU. Figure 10.10 shows the proposed mechanism and reactions. In this case, according to Guo et al. [19], the aniline monomer was polymerized on the surface of gold shell silver core nanostructures. A similar and yet different catalytic process was reported by Guo et al. [20]. In the latter case, the gold surface was claimed to be activated by superoxide radicals to catalyze the conversion of 3-CCA hydroxylation. As it was demonstrated experimentally, the enhancement diminished when superoxide radicals were removed by superoxide dismutase (SOD) scavengers.

Several groups have investigated DNA strand breaks in solutions and catalytic properties of nanomaterials may be critical. For example, Guo et al. in Foley et al. [21] and Carter et al. [22] as well as McMahon et al. [23] reported DNA strand breaks whose yield could not be explained by physical enhancement alone. Instead, chemical enhancement was proposed. However, to date, the exact mechanisms are still unknown. It may be caused by stabilization of radicals after hydrogen abstraction, or hydroxylation of the bases of DNA, or other mechanisms. These results are shown in Chap. 3. Table 10.2 shows the estimated physical enhancement values and the measured enhancement values.

Similar to the 3-CCA dosimetric reaction enhanced by chemical enhancement and described in Chap. 3, oxidation of 4-methylthiophenylmethanol (MTPM) and 2-phenylthioethanol (PTE) on the surface of TiO_2 nanoparticles may be improved with chemical enhancement. Majima et al. [25] showed that hydroxyl radicals adsorbed on TiO_2 particles after radiolysis was responsible for oxidation of MTPM and PTE molecules in aqueous solutions. The average size of TiO_2 nanoparticles was 22 nm. The ionizing radiation was 28 MeV electrons. Nitrous oxide N_2O was added into the solution to help convert solvated electrons to hydroxyl radicals. The authors stated that they observed TiO_2 surface-bound hydroxyl radicals, and MTPM or PTE molecules, also known as the substrate, were oxidized at the surface. If hydroxyl radicals reacted with the substrates and the oxidation reaction

Table 10.2 Results showing possible contribution of chemical enhancement through hydroxylation reactions

Authors	Guo et al. [22]	McMahon et al. [24]
Experimental conditions	3 nm gold nanoparticle, 100 kVp X-rays	1.9 nm gold nanoparticles
Reaction	Plasmid DNA SSBs	Plasmid DNA SSBs
Predicted physical enhancement	0.2	0.01
Observed total enhancement	2.0	0.3
Difference (ratio)	4	300
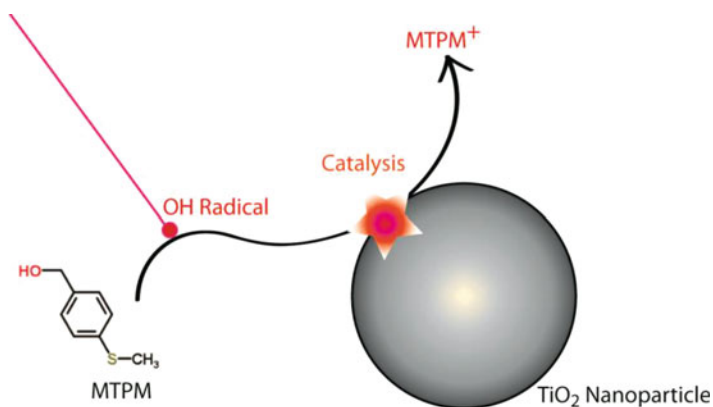
Fig. 10.11 Proposed pathway of oxidation of 4-methylthiophenylmathanol (MTPM) by surface-bound hydroxyl radicals or hydroxyl radicals in solution. The TiO_2 nanoparticles may catalyze the reaction and help form MTPM cations, or they can absorb hydroxyl radicals and oxidize MTPM. This proposed pathway is based on that proposed by Fujitsuka and Majima et al. [26]

was completed catalytically at the TiO_2 nanoparticle surface, then this case is similar to type 1 chemical enhancement. Figure 10.11 shows a proposed reaction pathway derived from chemical enhancement. The authors later used the same concept to cleave DNA conjugated to the surface of TiO_2 particles, whose results were reviewed by Fujitsuka and Majima [26].

Meisel et al. [27] investigated submicron-sized gold particles (0.4–0.75 μm) catalyzing the production of H_2 from $(CH_3)_2C•OH$ radicals under irradiation of ionization radiation. They employed large quantities of gold, up to 50% by weight or 50 WP, and observed G values increasing by 100%, which was equivalent to a 1.0 DEU enhancement. Figure 10.12 shows the results. 50 WP was the second highest gold percentage weight in solution reported in the literature. The highest was 100 WP achieved with gold nanotubes by Guo et al. [28]. If the gold was in the form of nanoparticles and if they did not scavenge reactive oxygen species, then the enhancement should be up to 50 DEU. The result of 1 DEU measured enhancement indicated that these gold particles were similarly scavenging as the gold nanotubes shown in Chaps. 3 and 5. Hydrogen formation was not enhanced in gold particle

Fig. 10.12 H_2 production from tert-butyl alcohol catalyzed by gold particles under ^{60}Co irradiation. (Adapted with permission from Meisel et al. [27]. Copyright (2006) American Chemical Society.)
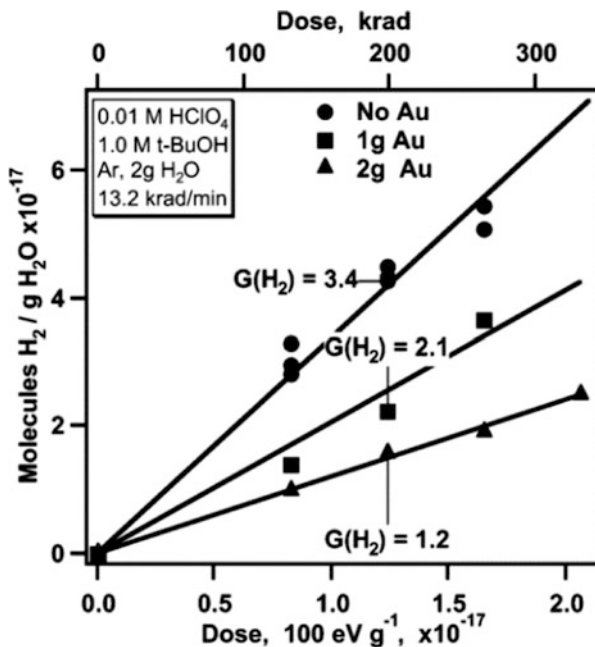
aqueous solutions. The authors suggested a similar catalytic reaction pathway as the 3-CCA radical intermediates catalyzed by superoxide radical-activated gold surfaces, only in this case hydrogen atoms were involved. Hydrogen atoms were suggested to be produced from protons reacting with solvated electrons, which was reasonable because the reaction occurred at a pH of 2.

The results shown in Chap. 3 by Misawa et al. [8] could be expanded to produce other chemicals under X-ray irradiation, and the driving force is type 2 chemical enhancement. The reaction the authors observed was catalytic production of superoxide radicals at the surface of gold nanoparticles. However, no direct detection of catalytically produced superoxide radicals was made. Instead, dihydroethidium (DHE) was used to react with superoxide radicals, and fluorescent assays were used to probe the product of that reaction. No detailed catalytic mechanism was proposed for the catalytic production of superoxide radicals at the gold surface, although secondary X-ray fluorescence was suggested to play a role. If this was true, then adding X-ray fluorescent nanomaterials such as light elements near gold nanoparticles could be useful to increase production of superoxide radicals. Figure 3.17 shows the process proposed by Misawa et al.

Potential areas of application of chemical enhancement include the study of the environmental and health impacts of nanoparticles of heavy elements, like uranium in depleted uranium. Not only can these nanoparticles enhance the absorption of ionizing radiation, they can also be catalytically active. In the past, the chemical nature of these particles was not considered. Nonetheless, extremely high enhancement factors were suggested. For example, uranium particles were speculated to

generate large dose enhancements by Busby [29] who predicted the enhancement of up to 5000 DEU. This estimation was cited by Tickell [30]. However, it was later revised to be less than 20 DEU by Pattison et al. [31], who employed a theoretical model built on a Monte Carlo simulation package EGS4 to predict the enhancement factor for 1 to 10 μm uranium particles. Their calculation results showed that for 1 μm particles, the enhancement was between 1 and 1.5 DEU and increased to 1.3–3.3 DEU when the size of the particle was increased to 10 μm. The enhancement on the inside of 10 μm particles with a cavity was 8.7 DEU to 16.7 DEU. As it was a single particle in the calculation, the simulated enhancement was caused largely by type 2 physical enhancement, which should be over 40 DEU at the surface of the particle when under 33 keV X-ray irradiation. The enhancement would be no greater than 50 DEU at the surface, which was still far below 5000 DEU as predicted by Busby [29]. However, if clusters of particles were present, then the enhancement could double or be even higher. Furthermore, if catalysis is involved, the enhancement could be a few hundred DEU or higher if the algorithms described in Chap. 5 hold. Under these extreme cases, the particles may impact health or the environment.

10.6 Conclusions and Future Work

This chapter discusses catalysis and associated concepts closely related to X-ray nanochemistry. Three types of catalytic reactions within the scope of X-ray nanochemistry are discussed in this chapter. Such division makes it easier to isolate many factors that contribute to the total enhancement. In the area of X-ray heterogeneous catalysis, a large number of reactions are studied. X-ray nanochemistry resembles but is much more complicated than photocatalysis. These similarities and differences make it interesting to study X-ray nanochemistry.

Another important notation is that catalysis favors small nanomaterials with high surface areas per unit mass. And yet for absorption of X-rays, as shown in Chap. 2, large nanoparticles are preferred if their solubility is high. If catalysis requires direct X-ray absorption by catalysts, then only large nanoparticles are acceptable. Demands for these two opposite aspects need to be reconciled if both enhancements are required. One possibility is that the medium acts as the X-ray absorber and the small nanoparticles are used as catalysts. This is the basis for type 1 chemical enhancement. In this case, the reactive oxygen species, electrons, or other particles generated in water interact with small nanoparticles to enable catalysis under X-ray irradiation.

Many aspects of catalysis may be used to improve X-ray nanochemical reactions. For example, metalloenzymes may prove to be helpful in terms of enhancing X-ray effects. The published results are limited to simple nanochemical processes to date. No elaborate nanomaterials or catalysts have yet been developed.

There are reactions that may only be excited or accessible by X-rays. The energy transfer pathways need to be carefully investigated in order to efficiently drive these reactions. Currently, UV-Vis photons or even infrared photons are able to drive

many catalytic reactions. Nonetheless, there are catalytic chemical systems where those low-energy photons cannot access. In those systems, it is useful to use X-ray photocatalysis.

Time-resolved measurements using optical and X-ray pulses may see growth in the area of X-ray nanochemical research. To date, most of the catalysis is studied with kinetic tools, leaving room for speculation. Ultimately, dynamic measurements will have to be performed to validate the hypotheses derived from kinetic data.

References

1. Meisel, D. (2004). Radiation effects in nanoparticle suspensions. In L. M. Liz-Marzán & P. V. Kamat (Eds.), *Nanoscale materials* (pp. 119–134). New York: Kluwer Academic Publishers.
2. Benson, S., & Cook, P. (2005). Underground geolofical storage. In B. Metz, O. Davisdson, H. de Coninck, M. Loos, & L. Meyer (Eds.), *Carbon dioxide capture and storage* (pp. 195–276). New York: Cambridge University Press.
3. Bond, G. C., Louis, C., & Thompson, D. T. (2006). Catalysis by gold, G. J. Hutchings (p. 366). London: Imperial College Press.
4. Wu, J. C. S., & Huang, C. (2010). In situ DRIFTS study of photocatalytic CO_2 reduction under UV irradiation. *Chemical Engineering in China, 4*, 120–126.
5. Hiroki, A., & LaVerne, J. A. (2005). Decomposition of hydrogen peroxide at water-ceramic oxide interfaces. *The Journal of Physical Chemistry. B, 109*, 3364–3370.
6. Voinov, M. A., Pagan, J. O. S., Morrison, E., Smirnova, T. I., & Smirnov, A. I. (2011). Surface-mediated production of hydroxyl radicals as a mechanism of iron oxide nanoparticle biotoxicity. *Journal of the American Chemical Society, 133*, 35–41.
7. Varghese, O. K., Paulose, M., LaTempa, T. J., & Grimes, C. A. (2009). High-rate solar photocatalytic conversion of CO2 and water vapor to hydrocarbon fuels. *Nano Letters, 9*, 731–737.
8. Misawa, M., & Takahashi, J. (2011). Generation of reactive oxygen species induced by gold nanoparticles under x-ray and UV irradiations. *Nanomedicine & Nanotechnology, 7*, 604–614.
9. Kim, T., & Zaera, F. (2012). X-ray-initiated metal-promoted thin film growth. *Journal of Physical Chemistry C, 116*, 8594–8600.
10. Kim, B. H., & Kwon, J. W. (2014). Plasmon-assisted radiolytic energy conversion in aqueous solutions. *Scientific Reports, 4*, 5249.
11. Garibov, A. A., Velibekova, G. Z., & Agayev, T. N. (1987). Heterogeneous radiolysis of CO_2 in the presence of zeolites. *Radiation Physics and Chemistry, 29*, 71–73.
12. Grodkowski, J., & Neta, P. (2001). Copper-catalyzed radiolytic reduction of CO_2 to CO in aqueous solutions. *The Journal of Physical Chemistry. B, 105*, 4967–4972.
13. Watanabe, D., Yoshida, T., Allen, C., & Tanabe, T. (2007). Enhancement of gamma-ray radiolysis of carbon dioxide with the assistance of solid materials. *Journal of Radioanalytical and Nuclear Chemistry, 272*, 461–465.
14. Schatz, T., Cook, A. R., & Meisel, D. (1999). Capture of charge carriers at the silica nanoparticle-water interface. *The Journal of Physical Chemistry. B, 103*, 10209–10213.
15. Cecal, A., & Humelnicu, D. (2011). Hydrogen output from catalyzed radiolysis of water. In P. Tsvetkov (Ed.), *Nuclear power – Development, operation and sustainability* (pp. 489–510). Rijeka: InTech.
16. Cecal, A., Goanta, M., Palamaru, M., Stoicescu, T., Popa, K., Paraschivescua, A., & Anita, V. (2001). Use of some oxides in radiolytical decomposition of water. *Radiation Physics and Chemistry, 62*, 333–336.

17. Gonzalez-Juarez, J. C., Jimenez-Becerril, J., & Cejudo-Alvarez, J. (2010). Degradation of 4-chlorophenol by gamma radiation of Cs-137 and X-rays. *Journal of the Mexican Chemical Society, 54*, 157–159.

18. Sahu, S. P., & Cates, E. L. (2017). X-ray Radiocatalytic activity and mechanisms of bismuth complex oxides. *Journal of Physical Chemistry C, 121*, 10538–10545.

19. Davidson, R. A., & Guo, T. (2012). An example of X-ray nanochemistry: SERS investigation of polymerization enhanced by nanostructures under X-ray irradiation. *Journal of Physical Chemistry Letters, 3*, 3271–3275.

20. Cheng, N. N., Starkewolf, Z., Davidson, A. R., Sharmah, A., Lee, C., Lien, J., & Guo, T. (1950). Chemical enhancement by nanomaterials under X-ray irradiation. *Journal of the American Chemical Society Communication, 2012*(134), 1950–1953.

21. Foley, E., Carter, J., Shan, F., & Guo, T. (2005). Enhanced relaxation of nanoparticle-bound supercoiled DNA in X-ray radiation. *Chemical Communications*, 3192–3194.

22. Carter, J. D., Cheng, N. N., Qu, Y. Q., Suarez, G. D., & Guo, T. (2007). Nanoscale energy deposition by x-ray absorbing nanostructures. *The Journal of Physical Chemistry. B, 111*, 11622–11625.

23. Butterworth, K. T., McMahon, S. J., Currell, F. J., & Prise, K. M. (2012). Physical basis and biological mechanisms of gold nanoparticle radiosensitization. *Nanoscale, 4*, 4830–4838.

24. McMahon, S. J., Hyland, W. B., Muir, M. F., Coulter, J. A., Jain, S., Butterworth, K. T., Schettino, G., Dickson, G. R., Hounsell, A. R., O'Sullivan, J. M., et al. (2011). Biological consequences of nanoscale energy deposition near irradiated heavy atom nanoparticles. *Scientific Reports, 1*. https://doi.org/10.1038/srep00018.

25. Tojo, S., Tachikawa, T., Fujitsuka, M., & Majima, T. (2004). Oxidation processes of aromatic sulfides by hydroxyl radicals in colloidal solution of TiO_2 during pulse radiolysis. *Chemical Physics Letters, 384*, 312–316.

26. Fujitsuka, M., & Majima, T. (2011). Recent approach in radiation chemistry toward material and biological science. *Journal of Physical Chemistry Letters, 2*, 2965–2971.

27. Merga, G., Milosavljevic, B. H., & Meisel, D. (2006). Radiolytic hydrogen yields in aqueous suspensions of gold particles. *The Journal of Physical Chemistry. B, 110*, 5403–5408.

28. Carter, J. D., Cheng, N. N., Qu, Y. Q., Suarez, G. D., & Guo, T. (2012). Enhanced single strand breaks of supercoiled DNA in a matrix of gold nanotubes under X-ray irradiation. *Journal of Colloid and Interface Science, 378*, 70–76.

29. Busby, C. (2005). Depleted uranium weapons, metal particles, and radiation dose. *European Journal of Biology and Bioelectromagnetics, 1*, 82–93.

30. Tickell, O. (2008). How war debris could cause cancer. *New Scientist (1971), 199*, 8–9.

31. Pattison, J. E., Hugtenburg, R. P., & Green, S. (2010). Enhancement of natural background gamma-radiation dose around uranium microparticles in the human body. *Journal of The Royal Society Interface, 7*, 603–611.

Chapter 11
Applications of X-Ray Nanochemistry in Sensing, Radiolysis, and Environmental Research

Good wine makes good conversation; Good people make good countries.

11.1 Introduction

X-ray nanochemistry may influence our life and surroundings in ways more than medical imaging and cancer treatment. Many of the basic and applicable principles are interconnected. For example, in the previous three chapters in Part IV of this book, DNA strand breaks, tumor destruction, and catalysis are closely connected to physical or chemical enhancement discussed in Part II, which are directly dependent on the nanomaterials and methods of detection described in Chaps. 6 and 7. The reverse is also true. The applications may provide useful feedback to and can even expand fundamental aspects of X-ray nanochemistry. For instance, damage to biomolecules and cells as discussed in Chaps. 8 and 9 may provide valuable feedback to biological enhancement described in Chap. 4; the photocatalysis described in Chap. 10 can help improve the understanding of chemical enhancement or type 3 physical enhancements described in Chaps. 2 and 3. In this chapter, three potential application areas are discussed, which are radiolysis, sensing, and environmental remediation. Each of these three areas is a stand-alone topic and is part of X-ray nanochemistry.

Radiolysis has dominated the landscape of radiation chemistry prior to using nanomaterials in an elaborate and comprehensive fashion to enhance the effectiveness of X-ray irradiation. In the past, nanoparticles were used either unknowingly, or knowingly but with relatively simple surface chemistry and without the enhancement described in Chaps. 2, 3, 4, and 5. With the assistance of X-ray nanochemistry, radiolysis may be greatly expanded in the future. As it is shown in this book, adding nanomaterials to samples under X-ray irradiation not only increases X-ray absorption and creates physical enhancement including additional UV emission, but also promotes catalysis that significantly increases the yield of radiolysis. Studies of radiolysis involving nanomaterials and molecules of various sizes have been reported in the literature. Some of the molecules have been discussed in the other chapters. Here, the emphasis is placed on the decomposition of large organic molecules.

Many of the results reported to date employ γ-rays. The results obtained with γ-rays are often improved when X-rays are used due to increased absorption cross-sections of X-rays interacting with the chemicals involved, although the purpose of research may be completely changed. For example, hydrogen production by zirconia nanoparticles was studied by LaVerne et al. [1] for nuclear energy application purposes. However, there is no apparent immediate and practical value of using X-rays to produce hydrogen gas. The literature on studying radiolysis with γ-rays is reviewed in this section because the same principles are applicable to X-ray radiolysis; often the same study performed with γ-rays in the past can be done with X-rays to achieve better results without using expensive and often cost-prohibitive γ-ray sources.

Besides radiolysis, detection of ionizing radiation such as X-rays with nanomaterials can be important in protecting professionals as well as consumers, such as those who are sensitive to effects of ionizing radiation. Currently, there are many types of commercially available radiation sensors, but none of them uses X-ray nanochemistry technologies. The existing enhancement technologies using nanomaterials are still too immature to support sensitive and inexpensive detection of ionizing radiation, including X-rays. Besides recording radiation dosage, sensing can also be performed in the form of imaging by detecting certain materials at certain locations, including those at hidden or difficult to see or reach places. X-ray nanochemistry can be used in remote sensing, and its spatial resolution can be high, of the order of a few nanometers, as demonstrated by Guo et al. [2]. The publication showed that it was possible to probe the distance between two nanoparticles with nanometer spatial resolutions in hidden places. All these materials are covered in Sect. 11.4.

In a third application area to be discussed in this chapter, environmental remediation is described as a benefit from radiolysis of environmentally detrimental chemicals. Environmental research can also take advantage of chemical or physical enhancement as defined in X-ray nanochemistry so that X-ray or γ-ray energy can be converted to local chemical energies to breakdown the most persistent and toxic chemicals in the environment. In Sect. 11.5, published results are discussed to highlight this potential. In the future, these results can be further improved so that decomposition of these environmentally unfriendly chemicals can happen at much higher efficiencies and lower costs.

In this chapter, the published works in these three areas are reviewed and discussed. In addition, basic principles related to these three areas are also briefly discussed in Sect. 11.2 to give readers a more complete survey of the literature in these areas.

11.2   Basic Principles

This section deals with principles that govern the three areas of applications of X-ray nanochemistry discussed in the rest of the chapter. These principles are not the enhancement principles described in Part II. Radiolysis without nanomaterials and

nanomaterial-assisted radiolysis are discussed first. For sensing, both nanomaterial-assisted sensing and new methodologies involving nanomaterials and X-rays are given. No formal theory has been developed in the area of environmental remediation using X-ray nanochemistry.

11.2.1 Radiolysis

Radiolysis studies reactions that decompose chemicals under irradiation of ionizing radiation. A typical radiolytic reaction is decomposition of water, which has been extensively researched. Several review articles as well as book chapters, e.g., those in Farhataziz et al. [3], are written on this topic. As a result, radiolysis of water, a critical process to understanding many other important concepts such as chemical enhancement, is only briefly reviewed here. This is not the only place in this book where radiolysis of water is mentioned. Chapter 3 also briefly discusses irradiation of water with X-rays. The emphasis in Chap. 3 is placed on the generation of reactive oxygen species. The emphasis of this section is placed on the decomposition of solute molecules dissolved in water, especially in the presence of nanomaterials. Synthesis of nanomaterials under X-ray irradiation is not covered here.

11.2.1.1 Radiolysis of Water (by X-Rays)

X-rays interact with water to produce many reactive species. As stated in Chaps. 2 and 3, X-rays with energies between 10 and 1000 keV interact with water mainly through Compton scattering, which produces lower-energy X-ray photons and electrons, with most of the electrons having kinetic energy at approximately 2 keV and a small amount at 25 keV. The electrons and lower-energy X-ray photons then interact with water molecules to produce radicals including solvated electrons, hydrogen atoms, hydroxyl and superoxide radicals, perhydroxyl radicals, as well as the closed-shell molecule hydrogen peroxide.

The yield of these species changes as a function of time after their generation. For pulsed radiolysis using X-rays or electrons as the radiation source, yields are measured in G values, which are the number of a species produced per 100 eV of absorbed energy. Table 11.1 lists the G values of several of the most popular reactive oxygen species, as well as solvated electrons. These are the G values at 1 ps after

Table 11.1 Pulsed and steady state G values of radiolysis of water for low linear energy transfer (LET) radiation such as X-rays

	e^- (aq)	•H	H_2	•OH	•HO_2	H_2O_2
Pulsed (at 1 ps)	4.8	0.62	0.15	5.7		
Steady state	2.7	0.55	0.45	2.8	0.026	0.7

The values are adapted from Farhataziz et al. [3]

irradiation of water with a pulsed radiation source. For steady state, which means the products reach a steady state, the G values are also given in Table 11.1.

These are the yield of the species without any additives. Adding nanomaterials into the samples may significantly influence the generation mechanisms of these species. Currently there are many, albeit inconsistent, reports with respect to the dependency of generation of reactive oxygen species on nanomaterials. Further, the measurements may be affected by chemical enhancement, including anti-enhancement. The results reported in this area in recent years are briefly summarized in Sect. 11.3.

11.2.1.2 Radiolysis of Molecules Other than Water

X-ray or ionizing radiation radiolysis of molecules other than water without the use of nanomaterials has also been studied for a long time. Some of the processes involve the reactive species discussed in the previous subsection. There are many examples using reactive oxygen species to oxidize or reduce chemicals that lead to decomposition of chemicals. These reactions can be complex. For example, DNA strand breaks are complex reactions, usually starting with hydrogen abstraction or hydroxylation. CO_2 decomposition in water has also been widely reported. For example, the mechanism provided by Harteck et al. [4] is shown in reaction Eqs. 11.1, 11.2, 11.3, 11.4, 11.5, 11.6 and 11.7. The number of reactions was later expanded to include many more species in the theoretical modeling presented by Kummler et al. [5]. When catalytic reactions are possible, reaction mechanisms are much more complicated, as shown in Sect. 10.2.1. Again, most of the reported works to date are done with γ-rays, although it is reasonable to assume that when X-rays are employed, the yield of decomposition measured in G values will be higher. The dominant choice of using γ-rays in the past was mainly because of the connections to nuclear industry and partially due to interstellar research. With X-rays, the goal of research can be expanded to exploration of reaction pathways of converting CO_2 to other more useful chemicals.

$$CO_2 \rightarrow CO + O \tag{11.1}$$

$$CO \rightarrow C + O \tag{11.2}$$

$$C + CO \rightarrow C_2O \tag{11.3}$$

$$C_2O + CO \rightarrow C_3O_2 \tag{11.4}$$

$$C_3O_2 + O \rightarrow C_2O + CO_2 \tag{11.5}$$

$$C \rightarrow graphite \tag{11.6}$$

$$C_2O, C_3O_2 \rightarrow polymers \tag{11.7}$$
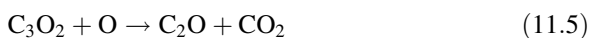
Wu et al. [6] studied reduction of CO_2 in aqueous solutions under γ-ray irradiation with the addition of many chemicals, including cuprous sulfite (Cu (II) and SO_3

$^{2-}$). Their original goal was to fixate CO_2 in the atmosphere. The authors investigated the effect of 22 compounds on the reduction of CO_2 dissolved in water. CO, CH_4, and C_2H_6 were measured after γ-ray exposure, and CO production yield on the order of 1% was the highest for a mixture of Na_2SO_3 and $CuSO_4$. On the other hand, Fe powder was most effective in terms of producing CH_4 and C_2H_6. The authors speculated that sulfite ions reacted with oxygen atoms to form sulfate ions as shown in Eqs. 11.8 and 11.9.

$$CO_2 + \gamma\text{-ray} \rightarrow CO + O \qquad (11.8)$$

$$SO_3{}^{2-} + O \rightarrow SO_4{}^{2-} \qquad (11.9)$$
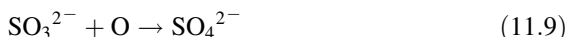
No explanations were given as to how Cu(II) increased the yield of reaction 11.8. One possibility was that small Cu nanoparticles formed in solution catalyzed reaction 11.8 as speculated by Wu et al. in Tseng et al. [7] and Liu et al. [8].

Pilling et al. [9] studied the irradiation of ices of H_2O/CO_2 mixtures without any metal catalysts. They used 52 MeV Ni^{13+} ions and found that after an exposure to $2 - 3 \times 10^{12}$ ions/cm^2 irradiation, CO_2/CO and H_2O_2/H_2O were at fixed ratios of 0.1 and 0.01, respectively. Because of the high linear energy transfer (LET) associated with the ions, the yield of the products would be 1000 times lower if X-rays were used, putting CO_2/CO ratios around 100. Other products were also found, which included CO, O_3, CO_3, H_2CO_3, H_2O_2, formic acid, formaldehyde, and methanol.

These works are mentioned here because they studied mechanisms without nanomaterials. Other results of the study of decomposition of CO_2 and other molecules involving nanomaterials will be presented later in Sect. 11.3.

11.2.1.3 Radiolysis with Additives Including Nanomaterials

With the addition of nanomaterials, radiolysis can be enhanced. This is similar to catalysis described in Chap. 10, and the principles governing these processes are the same. The simplest explanation for the observed enhancement by nanomaterials is the increase of emission of elections that can directly decompose chemicals, either adsorbed on the surface of nanomaterials or in the surrounding. Notice that solvated electrons, although capable of reducing chemicals, cannot ionize or directly decompose chemicals. The increased production of energetic electrons can come from increased absorption of X-rays by nanomaterials, which belongs to types 1 and 2 physical enhancement described in Chap. 2. The enhancement can also come from the emission of UV-Vis light, which is type 3 physical enhancement described in Sect. 2.4.4.

The enhancement can also come from products catalyzed by nanomaterials under X-ray irradiation, which is chemical enhancement. If reactive oxygen species are increased through chemical processes such as catalysis, it is type 2 chemical enhancement. If there is no net increase of reactive oxygen species and there is still a measurable enhancement, then it is possible that type 1 chemical enhancement is in place. These pathways are discussed in Chap. 3.

11.2.2   Sensing

Research of nanomaterials to improve sensing of ionizing radiation has just begun. Both materials and methods are being explored. Transducers and readout devices are being developed as well. However, there are few reports to date, and the principles are largely underdeveloped. Here, the principles are only briefly speculated based on the existing literature. One example is to produce more stable radicals so that electron spin resonance (EPR) spectroscopy can be used to more directly determine the enhancement and the actual dose based on the amount of radicals produced. X-ray nanochemistry can be employed to enhance the effectiveness of X-ray irradiation and therefore the signal-to-noise ratio in the detection of ionizing radiation. However, currently the enhancement factor ranges from a fraction of one DEU to a few DEU. If the enhancement can be as large as two to three orders of magnitude higher when using systematically created nanomaterials and nanosystems, then it is possible to develop unique radiation sensors for personal usages and other purposes. In addition, new devices may be developed based on recent results of detection of radicals created in mixtures of nanoparticles and spin traps. Although these materials and devices have not yet developed into actual products that can be used in the field, it is foreseeable to develop them to meet special sensing needs in the future.

11.2.3   Environmental Remediation

X-ray nanochemistry can find applications in environmental work in several ways. The most straightforward way is to use X-ray nanochemistry to help decompose organic matter for environmental cleanup or remediation. Radiolysis enhanced by nanomaterials is the most straightforward way to accomplish this goal. The principles described in Sect. 11.2.1 are applicable here. However, currently there is still a large gap between what has been done and what can be done, and only a limited number of published reports are available in the literature. Nonetheless, many environmentally hazardous chemicals that are difficult to remove or destroy may be decomposed using methods developed in the future based on X-ray nanochemical principles. A list of these molecules is given here in Table 11.2.

Table 11.2 Environmentally unfriendly chemicals that can be decomposed using X-ray nanochemistry

Molecules	Toxicity
Perfluoroalkyl acid (PFAA)	Liver cancer
Perfluorooctanoic acid (PFOA)	Cancer
Polychlorinated dibenzo-p-dioxins (PCDD)	Cancer, disrupt hormone systems
Polychlorinated biphenyls (PCBs)	Cancer, attach immune systems
Dichlorodiphenyltrichloroethane (DDT)	May harm reproduction systems

11.3   Radiolysis with X-Rays and Nanomaterials as Catalysts

In Chap. 10 several aspects related to X-ray heterogeneous catalysis are covered. Here, the emphasis is placed on radiolytic decomposition of chemicals in the presence of nanomaterials under X-ray irradiation. In the past, much work was done with γ-rays, and these works are presented here because using X-rays in place of γ-rays can generally improve the efficiency of the γ-ray-driven chemical reactions if penetration depth is not restricted. When thick samples have to be used, then γ-rays should be more suitable. Reviews of this topic are available. For example, Meisel [10] reviewed radiolysis assisted with particles under ionizing radiation. Cecal and Humelnicu [11] reviewed the work in the area of hydrogen production in water with the assistance of nanomaterials under irradiation of ionizing radiation. These reviews provide helpful guidance to future work in this field.

11.3.1   Radiolysis of Water and Hydrogen Production Assisted by Nanomaterials

The most common experiment involving radiolysis is decomposition of water to produce hydrogen. This reaction has two merits. The first derives from production of hydrogen for fuels, and studying its production with ionizing radiation has a few advantages, including all-day operation of chemical production powered by background radiation or possible use of nuclear wastes. The second merit is the avoidance of the production of hydrogen, so that hydrogen production can be prevented in nuclear plants or waste containers to avoid dangerous situations such as explosion. The discussion here centers on these two themes.

One of the earliest studies using X-rays to produce hydrogen was done by Allen et al. [12]. The authors studied water hydrolysis under X-ray irradiation with additives other than nanomaterials. They employed hard X-rays emitted from bombarding a solid gold target with 2 MeV electrons. They measured hydrogen production from different solutions of ferrous sulfate and salt ($FeSO_4$, KBr, KI), peroxide, and oxygen. The authors considered that these ionic species must interact with hydrogen radicals to prevent the formation of hydrogen molecules. This pathway, if existed, would not forbid the use of catalysts.

Zeolite structures could also help radiolytic hydrogen gas formation. Masaki et al. [13] used two types of zeolites, NaY and HY, and found that HY was three times better than NaY. ^{60}Co was used as the radiation source and EPR spectroscopy was used to measure radicals. The measured G value was near 1.0, which was equivalent to 0.1 μmol J^{-1}. Apparently, these zeolites were not as effective as some of the oxides reported by Le Caer [14] (vide infra).

Okitsu et al. [15] employed both TiO_2 and Al_2O_3 particles and studied hydrogen production. The authors used γ-rays, and the results showed that Al_2O_3 enhanced the
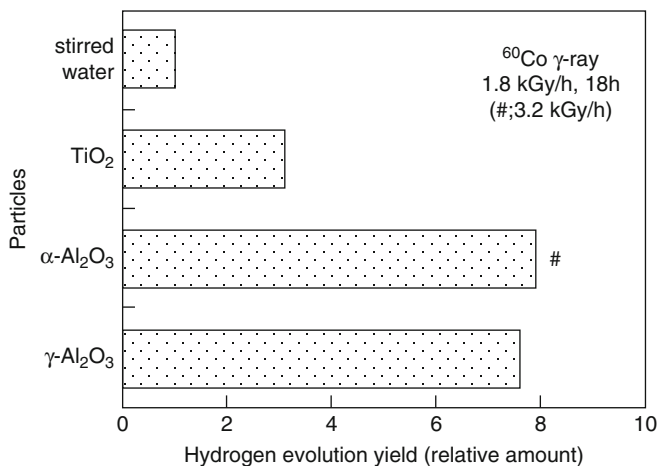
Fig. 11.1 Hydrogen production yield from four different samples, demonstrating the catalytic properties of oxide nanoparticles. (Reprinted from Okitsu et al. [15]. Copyright (1999) with permission from Elsevier.)

yield by 7–8 times. The surface morphology of Al_2O_3 and TiO_2 was different. The results are shown in Fig. 11.1. The authors also placed gold and other noble metals on the surface of these particles and found that Pt on TiO_2 was 2.2 times better than TiO_2. Metals on alumina apparently reduced the yield, and metals on TiO_2 were not as good as γ-Al_2O_3 alone.

Seino et al. [16] also found that adding TiO_2 or Al_2O_3 nanoparticles into water increased the yield of hydrogen production. They observed the dose dependency as well as the nanoparticle size dependency. 7–33 nm nanoparticles were used. The G values were low, on the order of 0.005–0.025. In another publication by Seino et al. [17], effect of pH on hydrogen generation by 30 nm titania nanoparticles was studied. The results suggested that there was little hydrogen production at a pH below 6 without nanoparticles. With nanoparticles, the yield of hydrogen gas production effectively occurred even at pH = 3.0.

In the early 2000s, Cecal et al. used several oxide nanosystems and different radiation sources to investigate hydrogen production. In a chapter in the book titled *Nuclear Power, Deployment, Operation and Sustainability*, Cecal et al. [11] discussed the production of hydrogen gas using several methods, including those methods that involved the assistance of zeolites and particles. The results are similar to the results discussed in Chap. 10.

LaVerne et al. [18] investigated radiolysis of water in the presence of CeO_2 and ZrO_2 microparticles. The authors used γ-rays and found a substantial increase in hydrogen production when the particles were added. They claimed that with one or two layers of water molecules on different particles, the yield of hydrogen production increased by a few fold over pure water. However, not all the particles performed the same way. They attributed the increase production of hydrogen to the increased production of excitons. They observed "drastic" difference between

these two particles. The authors revisited the same topic later [19]. In this latter work, they used dried particles and then treated the particles in different degrees of humidity and assumed that there were different layers of water on the surface of the particles prepared under these humidity settings. For one to two layers, the yield was very high, with the G value for H_2 production almost reaching 20 for CeO_2. For ZrO_2, the G value improved from 6 to 150. Energy transfer from the oxide to the water layer was discussed, although the transfer did not differ too much between CeO_2 and ZrO_2.

LaVerne et al. [20] observed that silica nanoparticles increased H_2 production when small silica nanoparticles (8–30 nm diameter) were used. Large silica particles in the slurry form did not generate any enhancement. The authors suggested that low-energy electrons emitted from small silica nanoparticles interacted with water and produced H_2. LaVerne [1] found that tetragonal nanoparticle ZrO_2 had greater activity than CeO_2 and was much better than the monoclinic ZrO_2 nanoparticles. The author suggested that annealing the nanoparticles from tetragonal to monoclinic resulted in loss of activity. G values were between 0.6 and 1.6. In comparison, water alone produced hydrogen at G value of 0.45 under γ-ray irradiation.

Renault et al. [21] studied radiolysis of water stored in pores of silica nanostructures. The yield was 0.3 in units of G value for hydrogen. The results did not change when hydroxyl radical scavengers were added. The authors claimed that nanowater was mainly responsible for the improved results of hydrogen production. The results are shown in Fig. 11.2.

Renault et al. [22] presented the results of their study of radiolysis of water in nanoporous gold. They prepared the gold samples by etching away Ag from a Ag-Au alloy. They reported a sevenfold increase in hydroxyl radical production
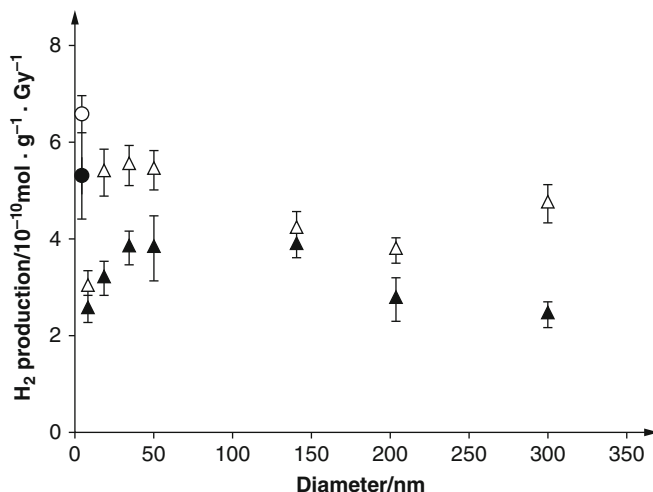
Fig. 11.2 Porous silica-assisted production of H_2. The pore size influenced the yield. Solid symbols are for dry glass samples, and empty symbols are for hydrated samples. A factor of two increase is visible for small pore silica. (Reprinted with permission from Renault et al. [21]. Copyright (2005) by John Wiley and Sons.)

near gold on short time scales. However, the production (or the increase) was suppressed by reactions with metal on long time scales. The results suggested that time-resolved measurements will be important. The authors used benzoic acid (BA) to react with hydroxyl radicals to form fluorescent products (similar to 3-CCA) to detect hydroxyl radicals. They considered the lifetime of the radical to be short, of the order of a few microseconds. The authors stated that BA was not as sensitive as coumarin but was used in a larger range of concentration. As the concentration of BA increased, the G value increased, suggesting that the lifetime was short or the distance between the gold surface and the radicals was small.

Maeda et al. [23] produced hydrogen by irradiating silica gel and metal oxide in water with ^{60}Co γ-rays. The silica gel apparently attracted water into their pores (1–2 nm size). The conditions of silica gel preparation, such as drying, were found to be important. Water absorbed on the surface of metal oxides was found to be easily hydrolyzed, which agreed with what Laverne et al. stated above. Two nm pore size was found to be optimal for maximum hydrogen production. This was slightly different from Gervais et al. [24] who found 10 nm pore size to produce the most solvated electrons. G values (H_2) were between 0.5 and 3. No enhanced absorption of γ-rays by nanomaterials was mentioned.

Meisel et al. [25] presented their results of using gold nanoparticles for hydrogen production in water. They studied size and surface effects of redox catalytic reactions. They stated that some reactions were affected by the presence of gold nanoparticles and some were not. In their discussion, they also clearly endorsed the idea of hydrogen radicals producing molecular hydrogen. The authors used 50 WP of gold, a significant amount, and attributed catalytic reduction of radicals to the observed results. The gold particles they used were microspheres of 1280 nm in diameter. The authors assumed the surface was important to the production of hydrogen. Figure 11.3 shows their results.

Meisel et al. [26] studied hydrogen production using silica-supported Ag nanoparticles. They used alcohol in the solution to scavenge radicals and obtained a G value of 0.45 for H_2 production. The H_2 G value increased from 1.1 without Ag to 1.9 with 0.12 mM Ag, although more Ag led to decrease of the G value.

The yield of organic reactions can also be increased by adding nanoparticles. Jung et al. [27] researched the effect of decomposition of ethylene diamine tetra acetic acid (EDTA) and found that addition of TiO_2 nanoparticles led to increased production of molecular hydrogen and destruction of EDTA molecules. This was possible because EDTA on TiO_2 stabilized reaction intermediates. The authors suggested that this method can be used to decompose harmful organic molecules while producing fuels such as hydrogen. Similar to nanomaterials, supramolecules may also help. A patent filed by Brewer et al. [28] described how to use supramolecules of Ru and Rh compounds under visible light to produce hydrogen. These molecules were known as photocatalysts. It is possible that these molecules can also produce hydrogen under X-rays or other ionizing radiation.

Yoshida et al. [29] used 3 μm or larger $A_{12}O_3$ particles to study hydrogen production under γ-ray irradiation and found that compared to water alone, adding these particles led to the increase in the yield of hydrogen production by two orders
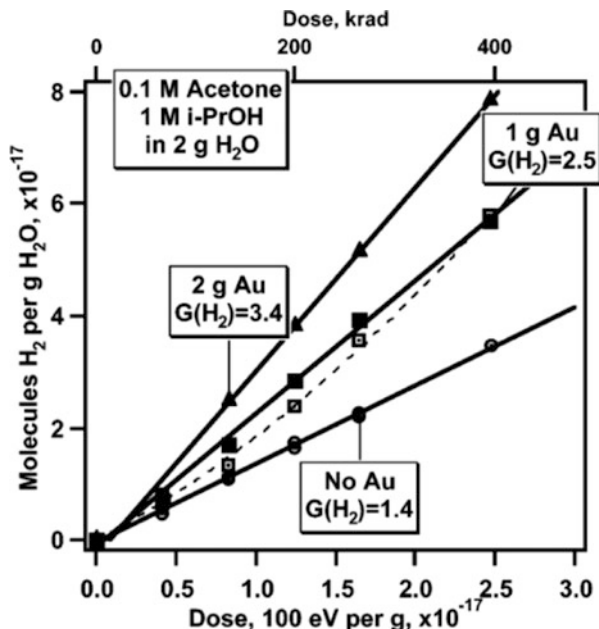
Fig. 11.3 Gold nanoparticle-assisted production of H_2. Enhancement is visible when gold was added, and the enhancement was approximately 1.0 DEU per 100 WP of gold in water, suggesting that the gold was highly scavenging even though it provided physical enhancement. (Adapted with permission from Meisel et al. [25]. Copyright (2006) American Chemical Society.)

of magnitude. The largest particles they used were 6 mm in diameter. ^{60}Co at a dose rate of 4.57 kGy/h was used for irradiation. Hydrogen produced was between 0.3 and 3.48 μmol/mL, which were much higher than the 0.0134 μmol/mL obtained from pure water. The enhancement could come from several factors including physical enhancement discussed in Chap. 2 and possibly chemical enhancement discussed in Chap. 3.

In a similar study, Kumagai et al. [30] investigated radiolysis of mordenite in sea water under γ-ray irradiation. Hydrogen production was monitored. The authors attributed the additional production of hydrogen to the energy absorbed by mordenite at the yield of 2.3×10^{-8} mol/J. Addition of seawater increased hydrogen production, which was attributed to the salt present in seawater.

Gervais et al. [24] theoretically examined the production of electrons and hydroxyl radicals by irradiation of silica nanoparticles in water with 50 keV electrons. The authors studied the role of the energy levels or band structure of water and silica and recognized that the bandgap of silica was slightly greater than that of water. The results showed that the production of electrons and hydroxyl radicals was heavily influenced by the pore size of silica, with electron production more sensitively dependent on the pore size. Although as stated in Chap. 2 that the difference between cross-sections of ionization of gold and water for electrons is much smaller

Fig. 11.4 Yield of solvated electron and hydroxyl radical production as a function of the pore size of porous silica under irradiation. (Adapted with permission from Gervais et al. [24]. Copyright (2010) American Chemical Society.)
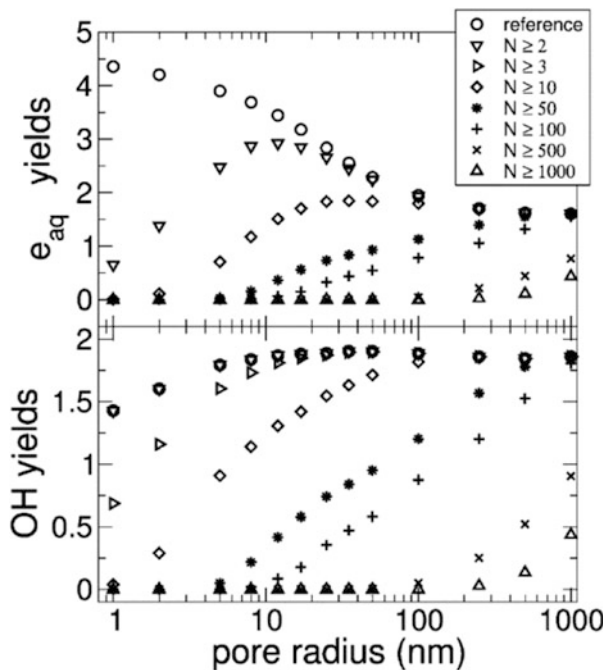
than X-rays, electron attachment and vibrational excitation of water were more efficient than X-rays for water and silica. The results showed that species such as solvated electrons and hydroxyl radicals in each pore changed as a function of pore size, as shown in Fig. 11.4. Particularly, the results showed the production of solvated electrons was optimal for 10 nm pore size silica.

Mostafavi et al. [31] studied the effect of TiO_2 nanoparticles on hydrogen production by ^{60}Co γ-ray irradiation as well as by 28 MeV $^4He_2^+$ ions. Mass spectrometry was used to measure hydrogen production, and G values were between 0.135 and 0.19 for ion irradiation. Ion irradiation caused the G value (H_2) to increase from 1.04 to 1.35. For γ-rays, the G value increased to 0.53, which was higher than the ions.

Le Caer [14] reviewed water radiolysis and discussed the influence of oxide surfaces on hydrogen production under ionizing radiation. The time frame in which radiolysis occurred was described. The yields of radiolytic reaction products for different irradiation particles were given. The results are listed in Table 11.3. The conclusion of the review indicated that hydrogen production strongly depends on the surface of oxides. The author also mentioned that very efficient energy transfer could take place at the interface.

Solvated electrons were studied by Crowell et al. [32]. They used 1–57 nm pore size silica to study solvated electrons using absorption spectroscopy. The authors considered the water in the pores as nanowater and found such water behaves differently from regular water, similar to the findings made by Renault et al. and

Table 11.3 Radiolytic yields (μmol J^{-1}) for γ-rays and high-energy electrons as given by Le Caer in [14]. γ-rays and electrons both have a linear energy transfer (LET) rate of 0.2–0.3 keV μm^{-1}

Radiation	e_{aq}^-	•OH	•H	H_2	H_2O_2	•O_2H
γ and electrons (0.1–10 MeV) (pH = 3–11)	0.28	0.28	0.06	0.047	0.073	0.0027
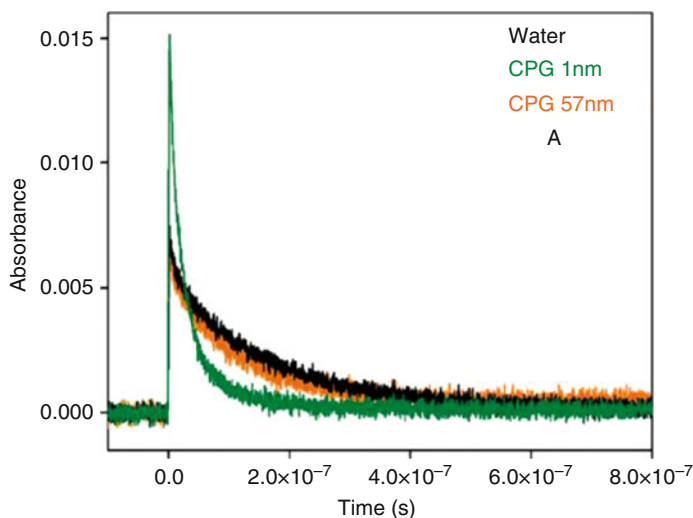
Fig. 11.5 Nanowater in porous silica for assisted production of H_2. Solvated electron signals are shown here. There is a sharp difference between small pores (1 nm) and the bulk water or water in large pores (57 nm). (Adapted with permission from Crowell et al. [32]. Copyright (2012) American Chemical Society.)

Laverne et al. mentioned earlier. It was found that initial yields of solvated electrons doubled as the pore size decreased from 57 nm (whose results are close to bulk water) to 1 nm. Clearly, silica of different pores behaved differently. Since the pore size was not continuously adjusted, the result shown in Fig. 11.5 could not be directly compared with Gervais et al. [24].

Frances et al. [33] investigated hydrogen production following radiolytic reactions under γ-ray irradiation of water in zeolites. ^{137}Cs was used for irradiation, and zeolite 4A was used for the experiment. The results of hydrogen production are shown in Fig. 11.6. Adding zeolites increased hydrogen production by nearly threefold. Their work was the basis of a more recent study done by Frances et al. [34], who studied self-radiolysis of tritiated water stored in zeolite 4A. The zeolite was noted to play two roles. First, it increased decomposition of water by providing energy to the trapped water. Secondly, it enhanced recombination of major stable radiolytic products. These explanations could also apply to the γ irradiation study whose results are shown in Fig. 11.6.
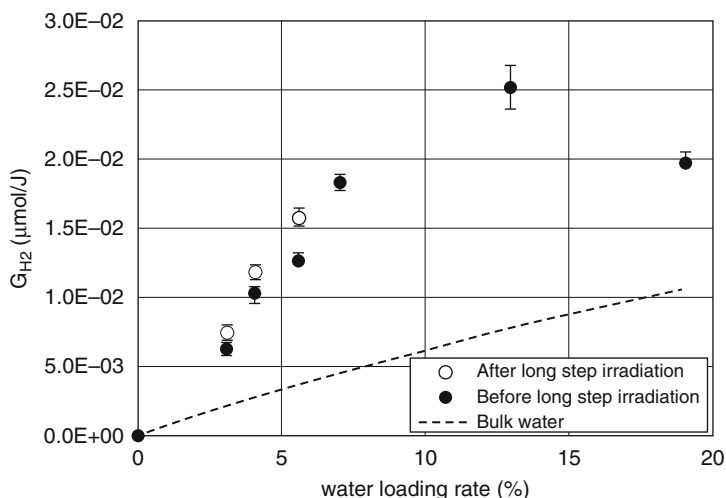
Fig. 11.6 Zeolite-assisted production of H_2. Under γ-ray irradiation. Optimal loading of water was 13%. (Reprinted from Frances et al. [33]. Copyright (2015) with permission from Elsevier.)

These experiments can be further optimized for future nanomaterials under X-ray irradiation. The photocatalysts for hydrogen production to date have not been optimized, and the overall yield (quantum efficiency) is still low, below 5% in most cases. X-ray photolysis of water may benefit from general photolysis work and provides useful supporting information for unique catalytic systems for photolysis of water.

11.3.2 Radiolysis of CO_2 with X-Rays Assisted by Nanomaterials

Works discussed in this subsection are part of X-ray nanochemistry. Although some of them may not employ catalysts, nanomaterials are involved. In one example, Fujita et al. [35] reported the results of pH-dependency measurements of γ-ray (from ^{60}Co) irradiated iron-containing water solutions saturated with CO_2. Fe powder with 29 m^2/g unit mass surface area was used in the work. The authors found that pH decreased quickly after irradiation. The authors stated that H^+ generation was significantly increased by adding CO_2 to water. pH decreased to about 2.2 after a few minutes of 100–200 Gy irradiation, and pH gradually recovered to 3.5 after irradiation. Adding Ar instead of CO_2 increased the final pH from 3.5 to 4.5. Initial H^+ change was the highest when ~0.1 g Fe powder was added. Several factors were considered to contribute to the increased production of protons.

Another example was shown by Yoshida et al. [36] who investigated decomposition of CO_2 by metals under γ-ray irradiation. They used metals to increase the

Table 11.4 Theoretical and experimental yields of CO production from γ-ray irradiated metals according to Yoshida et al. [36]

Materials	Surface area (cm^2)	Yield ($\times 10^{-3}$)	Electron yield (theoretical)
Pure water		0.21	0.13
Stainless steel	2780	0.73	0.18
Stainless steel	30,100	1.43	0.18
Lead	2780	1.30	0.33

absorption of γ-rays to emit low-energy electrons. CO yield was measured. The authors also theoretically studied electron emission from different metals under ^{60}Co 1.3 MeV γ-ray irradiation. Since γ-ray absorption cross-sections for different elements are similar, which are within a factor of two among the metals studied, the increase was mainly caused by the difference in density between the nanomaterials and water. This was different from gold in water under X-ray irradiation in which the absorption cross-section of gold was two orders of magnitude higher than oxygen. The experimental results showed that CO production quadrupled as the metal volume increased for the metals used in the experiments. The measured yield of decomposition was the highest for stainless steel mesh, possibly due to the tenfold higher surface area compared to lead plates, even though the latter had a higher Z value as well as higher density. When similar stainless steel plates were used, lead plates produced twice as much CO, which agreed with the theoretical results. Table 11.4 lists the relevant results. The volume of the metals was held constant.

11.3.3 Decomposition of Hydrogen Peroxide

H_2O_2 is another molecule that can be decomposed with ionizing radiation. Only the results obtained with nanomaterials and were not spontaneously catalyzed are discussed here because many metal nanoparticles spontaneously catalyze the decomposition of H_2O_2. For example, gold or silver surfaces could decompose H_2O_2 even without X-ray irradiation. Dependency on pH and other variables were explored by several groups as well. These works established that gold and silver surfaces were intrinsically catalytically active toward the decomposition of H_2O_2. It was therefore interesting to investigate how ionizing radiation worked with nanomaterials that normally would not catalyze the decomposition of H_2O_2. It is worth noting that ionizing radiation itself can also produce a small amount of H_2O_2 in water, which further complicates the decomposition process.

LaVerne et al. [37] discussed the decomposition of H_2O_2 at high temperatures assisted with ceramic oxides under irradiation of ^{60}Co γ-rays. The sizes of the ceramic particles were large, on the order of 117–641 nm. The results indicated that some oxides, such as CeO_2 and ZrO_2, dramatically increased H_2O_2 decomposition. Figure 11.7 shows the results. The Arrhenius constants for CeO_2 and ZO_2 were 1.7×10^3 and 3.8×10^4 $s^{-1}m^{-2}$, which were one to two orders of magnitude
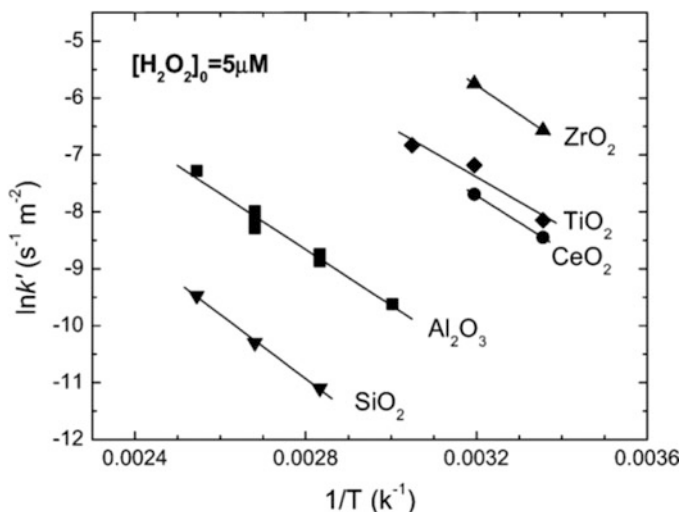
Fig. 11.7 Hydrogen peroxide decomposition in the presence of ceramic oxides under γ-rays. (Adapted with permission from LaVerne et al. [37]. Copyright (2005) American Chemical Society.)

higher than those for SiO_2 or Al_2O_3. The activation energies, on the other hand, were 5 kJ mol^{-1} and 41 kJ mol^{-1}. Catalysis can be studied without ionizing radiation for comparison purposes because Pt nanoparticles are also catalytically active in the presence of H_2O_2. Nonetheless, when irradiated with ionizing radiation, the mechanisms are different due to participation by other active species.

Guo et al. [38] studied a new nanomaterial they called Agu that had less than a 2 nm layer of silver coated on approximately 100 nm gold nanospheres. The surface plasmon resonance (SPR) response of this material (see Chap. 6 for details) followed a sigmoidal function with respect to silver thickness, with the most sensitive region (measured by growth) being between 0.9 and 1.6 nm of silver thickness. Either H_2O_2 or X-rays could remove the silver layer, creating the sensitive sigmoidal response. In the process, H_2O_2 was decomposed, although it followed a complex pathway.

11.3.4 Decomposition of Large Molecules

Yoshida et al. [39] discovered that adding metals increased the degradation of chemicals in solutions such as dibutyl phthalate (DBP) in water. They used γ-rays and observed an increase in the yield of degradation in the presence of metal (Al, Ni, Mo, W, and Pb) plates. The energy of γ-rays was 1.3 MeV, and the dose was 50 Gy; the DBP peak was almost gone after 44 kGy of irradiation, determined by UV absorption spectroscopy. The authors also theoretically studied energy dependency and found that 200–400 keV were optimal. W and Mo metals were found to be the most efficient elements for degradation. Pb was only 25% as effective.

The largest molecules decomposed by ionizing radiation, such as X-rays, with the assistance of nanomaterials were plasmid DNA strands of a few thousand base pairs. Several works were reported in the literature, and increased yields were reported in the presence of gold nanoparticles of different sizes. For example, Guo et al. [40], Guo et al. [41] and [42], and McMahon et al. [43] all reported enhanced damage to plasmid DNA molecules, and their results are shown in Chap. 3 in the form of chemical enhancement. It is important to point out that regardless of the true enhancement mechanisms, the degree of damage to these large molecules was increased significantly with the addition of gold nanoparticles. The increases were much higher than those predicted based on physical enhancement.

11.4 Sensing Applications Using X-Ray Nanochemistry

Miller et al. [44] from IBM reported on using polysilanes as radiation sensitizing materials. The original work did not include nanomaterials or X-rays. The results showed chain scission and molecular reduction upon irradiation with 248 nm light. The authors speculated the involvement of silyl radicals. It was possible that X-rays or other types of ionizing radiation could produce similar results.

Mulvaney et al. [45] discussed a new nanomaterial with which the authors used to detect electrons trapped in gold nanoparticle cores coated with a layer of porous SnO_2. The gold nanoparticles were 15 nm in diameter and were covered with a 10 nm thick layer of SnO_2. Upon irradiation with γ-rays, the authors stated that approximately 2000 electrons or negative charges were trapped in each gold nanoparticle core.

Quantum dots may be used as radiation sensors. Gao et al. [46] examined the possibility of using ZnO and CdTe quantum dots to detect superficial X-rays from 36.9 to 64.9 keV, at which energy physica enhancement from gold nanoparticles in water is the highest. The size of these two quantum dots was between 1 and 8 nm based on SEM measurements. Their results showed more uniform response in this energy range for CdTe than ZnO quantum dots. The authors compared the performance of the quantum dot sensors with other contemporary sensors.

A number of chemicals were used together with EPR spectroscopy to enhance the effectiveness of X-ray irradiation and function as sensors. Formates and dithionates were good candidates, as demonstrated by Lund et al. [47]. Guidelli et al. [48] discussed the use of silver nanoparticles to increase the sensitivity of alanine for EPR detection of carbon radicals derived from alanine. The results are shown in Fig. 11.8. These were promising results for medical applications but far below the requirements for making sensors to detect background radiation. In principle, it is possible to use X-ray nanochemistry to further improve the sensitivity of these existing sensors of ionizing radiation.

Marques et al. [49] reported a dosimetric study of MAGIC-f gel mixed with gold nanoparticles. They irradiated the samples with 250 kVp X-rays and a 5 Gy exposure. With 0.02–0.1 mM gold concentrations, the authors observed an up to 106%
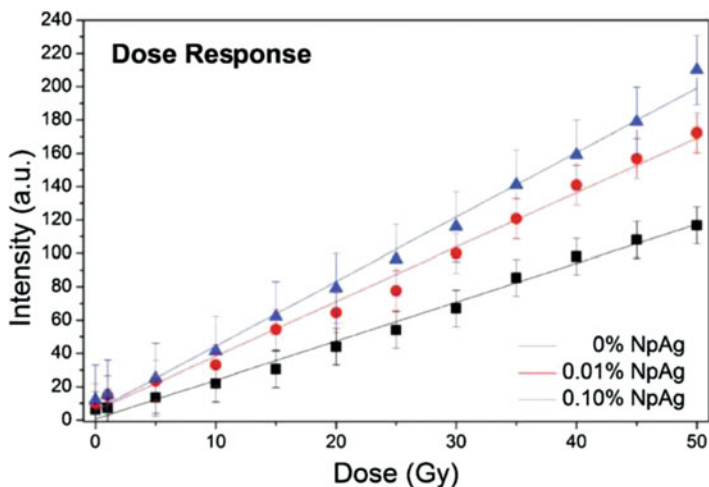
Fig. 11.8 EPR measurement of silver nanoparticle enhanced radical production. Responses to dose are shown for three silver concentrations. (Adapted with permission from Guidelli et al. [48]. Copyright (2012) American Chemical Society.)

increase in response or a 1.06 DEU enhancement, which began to plateau above 0.02 mM. The enhancement was determined by the nuclear magnetic transversal relaxation rate (R2). The results are shown in Fig. 11.9. The measured enhancement values were compared with the theoretically predicted values, and the authors claimed that there was a close matching between the two sets of data. The approach demonstrated the potential of using nanomaterials to advance methods of radiation sensing.

Alqathami and Geso et al. [50] explored dose enhancement in gold nanoparticle-embedded tissue-equivalent mixtures irradiated with 100 kV and 6 MV X-rays. The authors mixed polyurethane resin precursors with initiators and LMG dye molecules to make the tissue-equivalent material. Gold nanoparticles were mixed with these chemicals to enhance absorption of X-rays. The average size of the gold nanoparticles was 50 nm. The enhancement was determined based on the ratio of slopes of optical density change as a function of X-ray dosage with gold nanoparticles to without gold nanoparticles. The loading of gold was only 0.5 mM or 0.01 WP (0.098 g/1000 g). The enhancement for 100 kVp and 6 MV was 1.77 and 1.1 DEU, respectively. Figure 11.10 shows their results, which show an enhancement of approximately 1.0 DEU.

Rakowski et al. [51] developed a composite material consisting of a nanofilm of gold deposited on top of a radiochromic film to detect the enhancement from the gold film, which was 23 nm thick. Under irradiation of 50 kVp X-rays, the dose enhancement ratio (DER) was 0.29 DEU integrated within 13.6 μm of water. The authors also theoretically simulated the enhancement and found that maximum DER reached 18 DEU within 250 nm of the gold film.
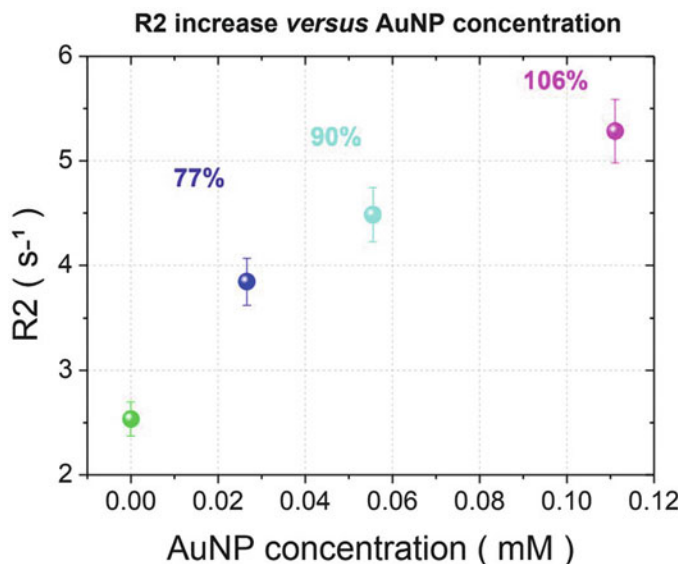
Fig. 11.9 R2 measurement of enhancement using gold nanoparticles. (Adapted from Marques et al. [49]. Used with permission, CC BY 2.0. © Institute of Physics and Engineering in Medicine. Reproduced by permission of IOP Publishing. All rights reserved.)
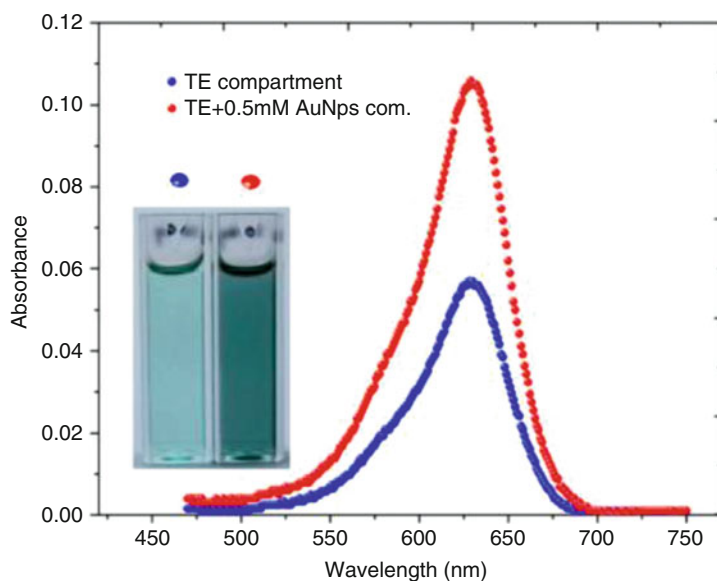
Fig. 11.10 Enhancement of dosimeter performance by gold nanoparticles. LMG dye immersed in polyurethane resin was used as the matrix to respond to X-ray irradiation. Color change was detected with UV-Vis spectroscopy. (Reprinted from Alqathami and Geso et al. [50]. Copyright (2013) with permission from Elsevier.)

Rege et al. [52] reported a method of using ionizing radiation to produce gold nanoparticles from specially prepared gold ions in the sensing solution. Colorimetry was used to determine the dosage. The lowest dose detected was 0.5 Gy of ionizing radiation. The key was to prepare ions before irradiation so that they were easily reduced by a small amount of reducing agents produced by ionizing radiation. In this work, Au(III) was reduced to Au(I) chemically prior to radiation, similar to aged Au ions used in the synthesis of gold nanotubes employed by Guo et al. [42]. In addition to aging, cetyl trimethylammonium bromide (CTAB) ligands were used to increase the probability of aggregation of gold atoms to form small gold nanoparticles. Rege et al. [53] developed a new dosimetric tool that uses colorimetric plasmonic response from gold nanoparticles formed in situ under X-ray irradiation. Gold salt was poured into a gel that also had cetyl or dodecyl trimethylammonium bromide (C_xTAB, x = 16 or 12) and ascorbic acid. Under X-ray irradiation, the gel changed color as gold ions were reduced to form nanorods or nanoparticles. They called the nanoparticle forming solution under X-ray irradiation a nanosensor. As little as 0.5 Gy of X-ray, irradiation was detected. Such a method allowed convenient determination of the X-ray dose used in tumor treatment.

The Agu work performed recently by Guo et al. [38] could also aid sensing. A thin silver coating on spherical gold nanospheres could be used as an indicator to detect X-rays or other chemical etching reagents. A segment of a sigmoid response observed as a function of thickness of silver is shown in Fig. 11.11. The thickness change to the silver layer could be caused by either chemical etching or irradiation of X-rays. This new nanomaterial exhibited a sensitive surface plasmon resonance (SPR) response when the thickness of silver was changed from 0.9 to 1.6 nm on approximately 100 nm diameter gold nanospheres. To remove the surface silver, the authors employed X-ray radiation from a 100 kVp microfocus source and irradiated aqueous solutions. Figure 11.11 also shows the results of SPR peak shifts as a function of X-ray dose. Although a large dose of X-rays (i.e., ~100 Gy) was needed to cause significant SPR peak shift, it was possible to detect <40 Gy of X-ray irradiation based on the SPR shift.

Fig. 11.11 Etching of silver from Agu under X-ray irradiation detected by surface plasmon resonance (SPR) absorption spectroscopy. SPR shift was 2 nm per 400 Gy of X-ray irradiation. The centroid of SPR profiles could be determined with a 0.25 nm resolution. (Reprinted from Guo et al. [38]. Copyright (2016) with permission from Elsevier.)
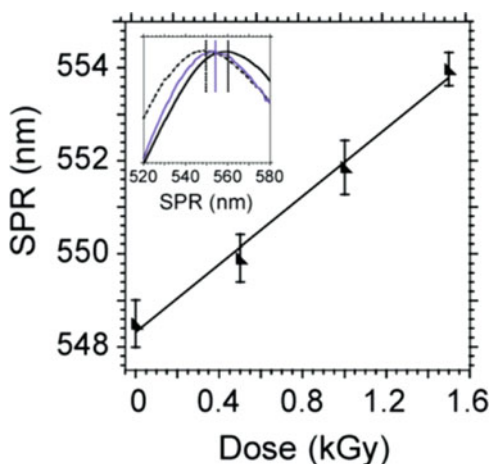
Another recent work related to sensing was the study of a new concept of X-ray-induced energy transfer (XIET) reported by Guo et al. [2] in which relative energy transfer efficiencies in the form of dose enhancement were measured. The experimental illustration is given in Sect. 2.4.3.4. In this study, the authors demonstrated that energy transfer from nanomaterial donors made of heavy elements to the nearby nanomaterial acceptors made of light elements could be used to sense ionizing radiation. The chemical content in the acceptors was modified by the energy transfer upon irradiation, and the degree of modification can be quantified with enhancement defined in Chaps. 2, 3, 4, and 5. For example, the enhancement could be measured by sending nanoparticle probes in the acceptors into a sensing region buried deep in an optically opaque object that is relatively transparent to X-rays. The opaque object with the acceptors is then irradiated with X-rays, and the probes are retrieved and measured. The enhancement or XIET efficiency is higher for those nanoscale probes positioned within nanometers of the target of materials made of heavy elements.

11.5   Environmental Research Applications Using X-Ray Nanochemistry

Mitomo et al. [54] studied degradation of poly(L-lactic acid) under irradiation of γ-rays. As the damage was believed to be caused by radicals, using X-rays should give rise to better results than γ-rays. However, the dose they used was up to 200 kGy, which was on the high end of the dose employed in the research described in this book. This dose may be reduced when X-rays are used, due to stronger interactions between the molecules and X-rays. The work also did not use nanoparticles. If nanoparticles were used, then the amount of damage should be increased, which can further reduce the dose. The results showed that as the dose increased, the melting temperature and average molecular weight decreased. There seemed to be saturation beyond initial 200 kGy of irradiation based on the average molecular data (right panel in Fig. 11.12). On the other hand, the melting temperature results (left panel in Fig. 11.12) did not follow the same trend. The authors attributed the saturation observed in the average molecular weight results to the recombination reaction of free radicals.

Hoertz et al. [55] investigated radiocatalytic degradation of organic species with the assistance of nanomaterials. They employed γ-rays and semiconductor nanoparticles Al_2O_3, TiO_2, and ZrO_2. The work focused on several types of TiO_2 nanomaterials, including annealed and unannealed homemade nanopowder, as well as commercially available nanoparticles. The authors found that the most promising material was TiO_2 under ^{60}Co irradiation to decompose sulforhodamine molecules. The targets were mixed with nanomaterials in aqueous solutions. They attributed the damage to hydroxyl radicals produced in the solution based on the existing literature on the subject.
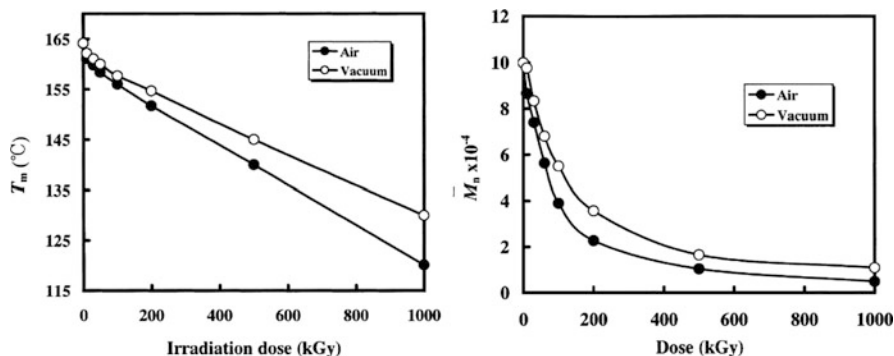
Fig. 11.12 Degradation of poly(L-lactic acid) under irradiation. Melting temperature and average molecular weight were measured and shown in the left and right panel, respectively. No nanoparticles were used. (Reprinted from Mitomo et al. [54]. Copyright (2001) with permission from Elsevier.)

11.5.1 Nanomaterials under X-Ray Irradiation for Remediation

Adding nanomaterials should increase decomposition of chemicals in the environment by X-rays. As shown in Chaps. 2, 3, 4, and 5, nanomaterials help increase the effectiveness of X-ray irradiation. As long as the nanomaterials are not toxic to the environment, they can be used as environmental remediation reagents. Although X-rays have not been used as the energy source to treat contaminated water or soil, it is foreseeable that inexpensive nanomaterial catalysts in combination with X-rays may be developed in the future to selectively treat the toughest contamination in the environment.

11.5.2 Nanomaterials as Protection Reagents

As shown in Chap. 3, not all nanomaterials can enhance the effectiveness of X-ray irradiation. Most nanomaterials actually do the opposite, which is to reduce the effectiveness of X-ray irradiation unless special care is taken with respect to the preparation of the nanomaterials. In these cases, nanomaterials can protect certain parts of the environment. To date, only a few systematic works have been done in the area of creating the best X-ray or ionizing radiation antidotes. Ironically, iodide is one of the recommended ionizing radiation antidotes but was also one of the best candidates for Auger therapy before the discovery of nanomaterials as radiation sensitizers. Many ionizing radiation antidotes are chemical compounds and may be conjugated to nanomaterials to improve their effectiveness. Liu et al. [56] reported

conjugation of Trolox, a vitamin E analogue and a reactive oxygen scavenger, to gold nanoparticles. The product, AuNP@Trolox, was found nine times more scavenging than Trolox.

11.6 Conclusions and Future Work

Radiolysis, sensing, and environmental remediation work are the three areas of application of X-ray nanochemistry described in this chapter. Basic principles are briefly reviewed. Publications in these three areas are reviewed, and though they are encouraging, not all of them involve both nanomaterials and X-rays. Many of the works reviewed here use γ-rays, whose results should be predictably improved if X-rays are instead utilized. For those publications using bulk metals, the results should also see improvements when nanomaterials are used.

The existing literature in these three areas only reveals a glimpse of what X-ray nanochemistry may accomplish. There are many possibilities of using X-ray nanochemistry to improve radiolysis, sensing, and environmental work. Future sensing devices may be developed using new principles similar to those shown in Chaps. 2, 3, 4, and 5. As X-rays are convenient to use and highly penetrating, X-ray nanochemistry may have more profound impacts in all three areas.

It is also possible that these applications will provide valuable feedback on how to improve X-ray nanochemistry. For example, sensing may be used to report enhancement; if X-ray to signal conversion efficiency is high enough or can be amplified, then sensing may become a sensitive method to determine enhancement. Similarly, radiolytic methods can help improve the enhancement or enhancement measurements. Future work will bridge these gaps between applications and fundamental aspects of X-ray nanochemistry.

References

1. LaVerne, J. A. (2005). H_2 formation from the radiolysis of liquid water with zirconia. *The Journal of Physical Chemistry. B, 109*, 5395–5397.
2. Sharmah, A., Yao, Z., Lu, L., & Guo, T. (2016). X-ray-induced energy transfer between nanomaterials under X-ray irradiation. *Journal of Physical Chemistry C, 120*, 3054–3060.
3. Farhataziz, & Rodgers, M. A. J. (1987). *Radiation chemistry: Principles and applications* (p. 527). New York: VCH Publishers, Inc..
4. Harteck, P., & Dondes, S. (1955). Decomposition of carbon dioxide by ionizing radiation. 1. *The Journal of Chemical Physics, 23*, 902–908.
5. Kummler, R., Leffert, C., Im, K., Piccirelli, R., Kevan, L., & Willis, C. (1977). Numerical-model of carbon-dioxide radiolysis. *The Journal of Physical Chemistry, 81*, 2451–2463.
6. Wu, X. Z., Hatashita, M., Enokido, Y., & Kakihana, H. (2000). Reduction of carbon dioxide in gamma ray irradiated carbon dioxide: Water system containing Cu^{2+} and SO_3^{2}. *Chemistry Letters, 29*, 572–573.

7. Tseng, I. H., Chang, W. C., & Wu, J. C. S. (2002). Photoreduction of CO_2 using sol-gel derived titania and titania-supported copper catalysts. *Applied Catalysis B: Environmental, 37*, 37–48.

8. Liu, D., Fernandez, Y., Ola, O., Mackintosh, S., Maroto-Valer, M., Parlett, C. M. A., Lee, A. F., & Wu, J. C. S. (2012). On the impact of Cu dispersion on CO_2 photoreduction over Cu/TiO_2. *Catalysis Communications, 25*, 78–82.

9. Pilling, S., Duarte, E. S., Domaracka, A., Rothard, H., Boduch, P., & da Silveira, E. F. (2010). Radiolysis of H2O:CO2 ices by heavy energetic cosmic ray analogs. *Astronomy and Astro-physics, 523*, A77.

10. Meisel, D. (2004). Radiation effects in nanoparticle suspensions. In L. M. Liz-Marzán & P. V. Kamat (Eds.), *Nanoscale materials* (pp. 119–134). New York: Kluwer Academic Publishers.

11. Cecal, A., & Humelnicu, D. (2011). Hydrogen output from catalyzed radiolysis of water. In P. Tsvetkov (Ed.), *Nuclear power – Development, operation and sustainability* (pp. 489–510). Rijeka: InTech.

12. Johnson, E. R., & Allen, A. O. (1952). The molecular yield in the decomposition of water by hard X-rays. *Journal of the American Chemical Society, 74*, 4147–4150.

13. Nakashima, M., & Masaki, N. M. (1996). Radiolytic hydrogen gas formation from water adsorbed on type Y zeolites. *Radiation Physics and Chemistry, 47*, 241–245.

14. Le Caer, S. (2011). Water radiolysis: Influence of oxide surfaces on H_2 production under ionizing radiation. *Water, 3*, 235–253.

15. Yamamoto, T. A., Seino, S., Katsura, M., Okitsu, K., Oshima, R., & Nagata, Y. (1999). Hydrogen gas evolution from alumina nanoparticles dispersed in water irradiated with gamma-ray. *Nanostructured Materials, 12*, 1045–1048.

16. Seino, S., Yamamoto, T. A., Fujimoto, R., Hashimoto, K., Katsura, M., Okuda, S., & Okitsu, K. (2001). Enhancement of hydrogen evolution yield from water dispersing nanoparticles irradiated with gamma-ray. *Journal of Nuclear Science and Technology, 38*, 633–636.

17. Seino, S., Yamamoto, T. A., Fujimoto, R., Hashimoto, K., Katsura, M., Okuda, S., & Okitsu, K. (2001). Effect of pH on hydrogen evolution yield from water dispersing tirania nanoparticles enhanced by gamma ray. *Materials Research Society Symposia Proceedings, 676*, Y3.43.41–45.Y3.43.1.

18. LaVerne, J. A., & Tandon, L. (2002). H_2 production in the radiolysis of water on CeO_2 and ZrO_2. *The Journal of Physical Chemistry. B, 106*, 380–386.

19. Roth, O., Dahlgren, B., & LaVerne, J. A. (2012). Radiolysis of water on ZrO2 nanoparticles. *Journal of Physical Chemistry C, 116*, 17619–17624.

20. LaVerne, J. A., & Tonnies, S. E. (2003). H_2 production in the radiolysis of aqueous SiO_2 suspensions and slurries. *The Journal of Physical Chemistry. B, 107*, 7277–7280.

21. Rotureau, P., Renault, J. P., Lebeau, B., Patarin, J., & Mialocq, J. C. (2005). Radiolysis of confined water: Molecular hydrogen formation. *ChemPhysChem, 6*, 1316–1323.

22. Musat, R., Moreau, S., Poidevin, F., Mathon, M. H., Pommeret, S., & Renault, J. P. (2010). Radiolysis of water in nanoporous gold. *Physical Chemistry Chemical Physics, 12*, 12868–12874.

23. Maeda, Y., Kawana, Y., Kawamura, K., Hayami, S., Sugihara, S., & Okaib, T. (2005). Hydrogen gas evolution from water included in a silica gel cavity and on metal oxides with γ-ray irradiation. *Journal of Nuclear and Radiochemical Sciences, 6*, 131–134 131.

24. Ouerdane, H., Gervais, B., Zhou, H., Beuve, M., & Renault, J. P. (2010). Radiolysis of water confined in porous silica: A simulation study of the physicochemical yields. *Journal of Physical Chemistry C, 114*, 12667–12674.

25. Merga, G., Milosavljevic, B. H., & Meisel, D. (2006). Radiolytic hydrogen yields in aqueous suspensions of gold particles. *The Journal of Physical Chemistry. B, 110*, 5403–5408.

26. Zidki, T., Cohen, H., Meyerstein, D., & Meisel, D. (2007). Effect of silica-supported silver nanoparticles on the dihydrogen yields from irradiated aqueous solutions. *Journal of Physical Chemistry C, 111*, 10461–10466.

27. Jung, J., Jeong, H. S., Chung, H. H., Lee, M. J., Jin, J. H., & Park, K. B. (2003). Radiocatalytic H_2 production with gamma-irradiation and TiO_2 catalysts. *Journal of Radioanalytical and Nuclear Chemistry, 258*, 543–546.

28. Brewer, K. J., & Elvington, M.. (2006). Supramolecular complexes as photocatylysts for the production of hydrogen from water. US 7122171 B2.

29. Yoshida, T., Tanabe, T., Sugie, N., & Chen, A. (2007). Utilization of gamma-ray irradiation for hydrogen production from water. *Journal of Radioanalytical and Nuclear Chemistry, 272*, 471–476.

30. Kumagai, Y., Kimura, A., Taguchi, M., Nagaishi, R., Yamagishi, I., & Kimura, T. (2013). Hydrogen production in gamma radiolysis of the mixture of mordenite and seawater. *Journal of Nuclear Science and Technology, 50*, 130–138.

31. Essehli, R., Crumiere, F., Blain, G., Vandenborre, J., Pottier, F., Grambow, B., Fattahi, M., & Mostafavi, M. (2011). H-2 production by gamma and He ions water radiolysis, effect of presence TiO2 nanoparticles. *International Journal of Hydrogen Energy, 36*, 14342–14348.

32. Musat, R. M., Cook, A. R., Renault, J. P., & Crowell, R. A. (2012). Nanosecond pulse radiolysis of Nanoconfined water. *Journal of Physical Chemistry C, 116*, 13104–13110.

33. Frances, L., Grivet, M., Renault, J. P., Groetz, J. E., & Ducret, D. (2015). Hydrogen radiolytic release from zeolite 4A/water systems under gamma irradiations. *Radiation Physics and Chemistry, 110*, 6–11.

34. Frances, L., Douilly, M., Grivet, M., Ducret, D., & Theobald, M. (2015). Self-radiolysis of tritiated water stored in zeolites 4A: Production and behavior of H_2 and O_2. *Journal of Physical Chemistry C, 119*, 28462–28469.

35. Fujita, N., Fukuda, Y., Matsuura, C., & Saigo, K. (1996). Radiation-enhanced H^+ generation in iron-containing solution saturated with CO_2. *Radiation Physics and Chemistry, 48*, 297–304.

36. Yoshida, T., Tanabe, T., Okabe, Y., Sawasaki, T., & Chen, A. (2005). Decomposition of carbon dioxide by metals during gamma irradiation. *Radiation Research, 164*, 332–335.

37. Hiroki, A., & LaVerne, J. A. (2005). Decomposition of hydrogen peroxide at water-ceramic oxide interfaces. *The Journal of Physical Chemistry. B, 109*, 3364–3370.

38. Lien, J., Peck, K. A., Su, M. Q., & Guo, T. (2016). Sub-monolayer silver loss from large gold nanospheres detected by surface plasmon resonance in the sigmoidal region. *Journal of Colloid and Interface Science, 479*, 173–181.

39. Yoshida, T., Tanabe, T., Chen, A., Miyashita, Y., Yoshida, H., Hattori, T., & Sawasaki, T. (2003). Method for the degradation of dibutyl phthalate in water by gamma-ray irradiation. *Journal of Radioanalytical and Nuclear Chemistry, 255*, 265–269.

40. Foley, E., Carter, J., Shan, F., & Guo, T. (2005). Enhanced relaxation of nanoparticle-bound supercoiled DNA in X-ray radiation. *Chemical Communications*, 3192–3194.

41. Carter, J. D., Cheng, N. N., Qu, Y. Q., Suarez, G. D., & Guo, T. (2007). Nanoscale energy deposition by x-ray absorbing nanostructures. *The Journal of Physical Chemistry. B, 111*, 11622–11625.

42. Carter, J. D., Cheng, N. N., Qu, Y. Q., Suarez, G. D., & Guo, T. (2012). Enhanced single strand breaks of supercoiled DNA in a matrix of gold nanotubes under X-ray irradiation. *Journal of Colloid and Interface Science, 378*, 70–76.

43. McMahon, S. J., Hyland, W. B., Brun, E., Butterworth, K. T., Coulter, J. A., Douki, T., Hirst, D. G., Jain, S., Kavanagh, A. P., Krpetic, Z., et al. (2011). Energy dependence of gold nanoparticle radiosensitization in plasmid DNA. *Journal of Physical Chemistry C, 115*, 20160–20167.

44. Miller, R. D., Hofer, D., Fickes, G. N., Willson, C. G., Marinero, E., Trefonas, P., & West, R. (1986). Soluble polysilanes – An interesting new class of radiation sensitive materials. *Polymer Engineering and Science, 26*, 1129–1134.

45. Oldfield, G., Ung, T., & Mulvaney, P. (2000). Au@SnO2 core-shell nanocapacitors. *Advanced Materials, 12*, 1519–1522.

46. Gao, X., Kang, Q. S., Yeow, J. T. W., & Barnett, R. (2010). Design and evaluation of quantum dot sensors for making superficial x-ray energy radiation measurements. *Nanotechnology, 21*, 285502.

47. Lund, E., Gustafsson, H., Danilczuk, M., Sastry, M. D., Lund, A., Vestad, T. A., Malinen, E., Hole, E. O., & Sagstuen, E. (2005). Formates and dithionates: Sensitive EPR-dosimeter materials for radiation therapy. *Applied Radiation and Isotopes, 62*, 317–324.

48. Guidelli, E. J., Ramos, A. P., Zaniquelli, M. E. D., Nicolucci, P., & Baffa, O. (2012). Synthesis and characterization of gold/alanine nanocomposites with potential properties for medical application as radiation sensors. *ACS Applied Materials & Interfaces, 4*, 5844–5851.
49. Marques, T., Schwarcke, M., Garrido, C., Zucolotto, O. B., & Nicolucci, P. (2010). Gel dosimetry analysis of gold nanoparticle application in kilovoltage radiation therapy. *Journal of Physics: Conference Series, 250*, 012084.
50. Alqathami, M., Blencowe, A., Yeo, U. J., Doran, S. J., Qiao, G., & Geso, M. (2012). Novel multicompartment 3-dimensional radiochromic radiation dosimeters for nanoparticle-enhanced radiation therapy dosimetry. *International Journal of Radiation Oncology, Biology, Physics, 84*, E549–E555.
51. Rakowski, J. T., Laha, S. S., Snyder, M. G., Buczek, M. G., Tucker, M. A., Liu, F. C., Mao, G. Z., Hillman, Y., & Lawes, G. (2015). Measurement of gold nanofilm dose enhancement using unlaminated radiochromic film. *Medical Physics, 42*, 5937–5944.
52. Pushpavanam, K., Narayanan, E., Chang, J., Sapareto, S., & Rege, K. (2015). A colorimetric plasmonic nanosensor for dosimetry of therapeutic levels of ionizing radiation. *ACS Nano, 9*, 11540–11550.
53. Pushpavanam, K., Inamdar, S., Chang, J., Bista, T., Sapareto, S., & Rege, K. (2017). Detection of therapeutic levels of ionizing radiation using plasmonic nanosensor gels. *Advanced Functional Materials, 27*.
54. Nugroho, P., Mitomo, H., Yoshii, F., & Kume, T. (2001). Degradation of poly(L-lactic acid) by gamma-irradiation. *Polymer Degradation and Stability, 72*, 337–343.
55. Hoertz, P. G., Magnus-Aryitey, D., Gupta, V., Norton, C., Doorn, S., & Ennis, T. (2013). Photocatalytic and radiocatalytic nanomaterials for the degradation of organic species. *Radiation Physics and Chemistry, 84*, 51–58.
56. Nie, Z., Liu, K. J., Zhong, C. J., Wang, L. F., Yang, Y., Tian, Q., & Liu, Y. (2007). Enhanced radical scavenging activity by antioxidant-functionalized gold nanoparticles: A novel inspiration for development of new artificial antioxidants. *Free Radical Biology & Medicine, 43*, 1243–1254.

Part V
Conclusions and Future Work

Chapter 12
Conclusions and Future Work

You only need to take your science seriously, not yourself

12.1 Conclusions

The data shown in this book clearly demonstrates the existence of enhanced effectiveness of X-ray irradiation assisted by nanomaterials. The effects shown to date include increased chemical reaction yields, destruction of cells, reduced tumor growth, increased imaging contrast, and increased light emission. These results have created the foundation for future experiments. Moreover, theories have been developed to understand the origin of the enhancement. In this book, three categories, physical, chemical, and biological enhancement, are defined and analyzed in Chaps. 2, 3, 4, and 5. Each category has several types, which are also identified in the book. The categorization and discussion intend to interpret the experimentally observed enhancements. Furthermore, this categorization and theoretical developments have led to creating higher total enhancements such as those demonstrated in Chap. 5. Nanomaterials, methods, and instrumentation are reviewed in Chaps. 6 and 7. Many existing nanomaterials are simple, synthesized to absorb X-rays while performing other functions such as high solubility and tumor targeting. The fast growing part of X-ray nanochemistry is clearly in the area of cancer treatment, which is discussed in Chaps. 8 and 9. Other applications in the areas of catalysis, sensing, and environmental work are discussed in Chaps. 10 and 11.

In practice, high enhancement values, without considering biological effects, have been achieved using either special nanomaterials or the combination of small and large nanoparticles. The magnitudes of several measured enhancements are greater than 30 DEU using nanochemical and bacterial systems. Measured enhancements in most studies, however, are less than 1.0 DEU, which is both encouraging and alarming at the same time. Intense efforts on fundamental studies are required to understand and improve the situation.

12.2   Future Work in X-Ray Nanochemistry

The development of X-ray nanochemistry is like a typical growth process of many events that can be best described by a sigmoid curve. It takes many years to incubate an idea. Then the idea expands quickly for a few years or decades to become mature. What we are seeing now is probably the end of the incubation time in terms of the development of X-ray nanochemistry. The rapid or exponential growth period of X-ray nanotechnology may not be too far from now.

   The amount of work done to date in this new area of research is significant. However, there is much more to learn and create within X-ray nanochemistry. As the nanomaterials become progressively more complex and advanced, it is possible that many new phenomena will be generated or discovered. These new processes, together with new instruments, may help redefine how X-ray nanochemistry may impact many practical applications such as imaging, detection, medical treatment, and energy and environmental applications. In the following, new research activities in four areas are discussed.

12.2.1   Nanomaterial Syntheses

Nanomaterials are the foundation of X-ray nanochemistry as well as its applications. Nanomaterials bearing simple first generation nanomaterial characteristics as defined by Roco et al. [1] in his original vision of nanomaterials may be enough to drive physical enhancement. However, a much more effective way to enhance the effectiveness of X-ray irradiation is to combine many categories and types of enhancement to generate a much higher total enhancement. This requires the development of more advanced nanomaterials, including complex and hybrid nanomaterials, possible hybrid nanomaterials with biological molecules and processes. One can then use these materials to develop novel functions to effectively respond to low doses of X-ray radiation at the dental or chest X-ray level. New X-ray nanochemistry principles based on these new nanomaterials will have to be developed.

   Based on the discussion in this book, it seems difficult to use nanomaterials to create significant direct and additional damage to cells and tumors in the body under X-ray irradiation. This is because external environments such as cells or tumors may severely and adversely alter or suppress how nanomaterials respond to X-ray irradiation. On the other hand, X-ray triggered methods demonstrated by Guo et al. [2] seem to be more efficient because all the components critical to X-ray triggering mechanisms can be stored within a nanomachine. Biological systems can further improve the efficiency of these nanomachines, as speculated by Fologea et al. [3]. Inorganic or organometallic chemistry can help improve the efficiency of response to X-ray irradiation by nanomaterials. These new nanomaterials may not only revolutionize cancer treatment but also create new applications such as new security nanomaterials or X-ray charged batteries.

12.2.2   Instrument Development

As nanomaterials are being developed, characterization of enhancement mechanisms becomes more urgently needed. Currently almost all mechanistic studies are performed ex situ using kinetic methods. As a result, many explanations are speculative. This may be improved using a number of state-of-the-art methods such as X-ray spectroscopy using pulsed X-ray sources. These dynamic studies will help understand whether gold atoms in nanoparticles are activated by reactive oxygen species generated in water or caused by X-ray ionization. If in situ EPR methods are available, then it is possible to investigate the true causes for chemical enhancement. Other methods such as X-ray photoelectron spectroscopic (XPS) measurements performed on solution samples may help understand energy transfer mechanisms between donors and acceptors within the X-ray-induced energy transfer framework. These physical methods are needed to characterize the nanomaterials as complex nanomachines are assembled.

New instruments have been developed within X-ray nanochemistry to characterize enhancement. The in situ fluorescence spectrometer and photovoltaic thin film detector to determine the absolute quantum yield of scintillators developed by Guo et al. [4] as well as the instrument to study DNA strand breaks by low-energy electrons in vacuum by Sanche [5] are two examples, even though the latter is only remotely related to X-ray nanochemistry. A potential instrument may be built on the basis of the XIET principle discussed in Chap. 2, which shows the possibility of using the enhancement such as type 2 physical enhancement to determine the distance between nanoparticle energy donors and acceptors as demonstrated in a work reported by Guo et al. [6]. This implies that it is possible to use X-rays to image nanoparticle interactions in opaque samples. Other possibilities include the combination of computed tomography (CT) and nanoparticles with improved sensitivity.

Other instruments that utilize compact X-ray sources may be developed. Currently microfocus X-ray sources are commonly used. In the future, it is foreseeable that nanofocus X-ray sources may be developed and interfaced with optical and other instruments. This is especially promising after X-ray nanochemistry is more fully developed.

It is anticipated that a large number of instruments will be developed to meet the demand for X-ray nanochemistry research. Characterization of the enhancement in situ, whether it is in vitro or in vivo, will be developed because currently the methods are mostly ex situ.

12.2.3   Basic Research Areas Linked to X-Ray Nanochemistry

Another future area of work involves the energy industry. X-rays are highly penetrating. It is possible to transfer X-ray energy to other forms of energy such as chemicals, photons, and electrons. Several examples are given in this book. X-ray

nanochemistry will help improve these transfers. For example, it is possible to transfer X-ray energy to photon energy and use it to perform various tasks. The photon energy can be utilized locally, depending on the surrounding. If it is combined with other types of applications that normally involve photons, then novel technologies may be derived. X-ray-induced photovoltaics is one example. It means that X-rays may be used to charge batteries. The efficiency obtained from simple calculations suggests that the current mode of operation will not produce enough voltage for charging. However, future work may make it possible.

X-ray nanochemistry can also lend help to developing applications for nuclear and other ionizing radiation. Currently there are many efforts around the world in this area of research. Nanochemistry plays a minimal role so far due to the lack of trained students and lack of overlapping between traditional radiation chemistry and X-ray nanochemistry. Meisel et al. in the Radiation Laboratory at Notre Dame University had pioneered some early work in this area, and their colleagues have continued to work in this direction. A synergistic effort is needed to include all the experts in these fields to create novel nanomaterials and discover new mechanisms to help advance the field.

One of the important and yet almost untapped areas of research is time-resolved studies of important processes in X-ray nanochemistry. This is strongly tied to the development nanomaterials as well. The availability of many ultrafast X-ray facilities in the world makes it attractive to develop experiments to validate and discover dynamic processes either hypothesized or speculated in the literature, some of which are described in this book. The ability to visualize relaxation processes may create new many opportunities.

Many areas of biology may be studied with tools, methods, and processes offered within X-ray nanochemistry. For instance, the bystander effect may be better and more precisely studied if a large amount of energy can be precisely delivered to a specific location in the cell with nanometer spatial resolution. When nanomaterials can be better interfaced with biological samples such as demonstrated in nanobiology, and because X-rays can deliver large amounts of energy to anywhere within the body with high location precision, X-ray nanochemistry may help develop more powerful tools to investigate biology. If biological enhancement can be proven, improved, and combined with other enhancements, then many new biological processes may be studied.

Another area that can use much more scrutiny is nanomaterial interactions with soft X-rays. These studies, if designed properly, can isolate some of the important processes so that primary absorption events and the secondary events can be separated.

12.2.4   Applications

Important applications of X-ray nanochemistry can happen in the medical field. Currently most works are done to demonstrate that it is possible to create an

enhancement to the damage of various biological targets including tumors in the human body. Proteins, cells, and tumors in animals have been studied. These methods are primitive, however, and future development of X-ray nanochemistry should significantly improve the designs of the experiments, possibly revolutionizing the landscape of cancer treatment.

For example, currently almost all studies employ simple gold nanoparticles to generate electrons or radicals to damage biological targets near the nanoparticles. This has two implications. First, a large quantity of nanoparticles is needed to cause effective damage because of the fixed relationship between physical enhancement and the amount of gold nanoparticles shown in Chap. 2. Although it is possible to deliver up to 30 WP of gold into cells as shown by Starkewolf et al. [2], it is unknown whether this feat can be accomplished to tumors in the body. Secondly, targeting, and pharmacokinetics have to be understood and properly executed before effective destruction can take place because the nanoparticles need to be in tumors. Future work will tackle these "peripheral" techniques by improving the nanomaterials used for enhancement.

Other possible future works are in the field of environmental science. X-ray nanochemistry can assist focusing X-ray energy to a target; a process can be used either to probe a target or to damage it. If this target is environmentally interesting, then it is possible to use X-ray nanochemistry in environmental remediation or sensing. One example is to use X-ray to decompose molecules, as it has been shown that it is possible to use γ-rays to assist catalytic breakdown of organic molecules. These works are shown in Chaps. 3 and 11. Future work should focus on developing efficient chemistry to convert X-ray energy to these chemical energies.

Another field that may benefit from X-ray nanochemistry is imaging. X-rays are penetrating and easy to use. Chapter 2 shows that it is possible to use enhancement such as type 2 physical enhancement to determine the distance between nanoparticle energy donors and acceptors by Guo et al. [7]. This implies that it is possible to use X-rays to image nanoparticle interactions. Other possibilities include the combination of computed tomography (CT) and nanoparticles with improved sensitivity so that less nanomaterials are needed. Currently large quantities of nanoparticles are needed, as shown in Fig. 9.15.

It is difficult to predict what will happen to X-ray nanochemistry eventually. As shown in this book, many fundamental aspects of X-ray nanochemistry can be studied and improved, and many potential areas within X-ray nanochemistry can be developed. For example, X-ray photocatalysis may be expanded to driving efficient catalytic reactions in buried or hidden places. In the end, it is the impact of these fundamental studies that will determine the fate of X-ray nanochemistry.

References

1. Roco, M. C., & Tech, N. S. E. (2004). Nanoscale science and engineering: Unifying and transforming tools. *AICHE Journal, 50*, 890–897.
2. Starkewolf, Z. B., Miyachi, L., Wong, J., & Guo, T. (2013). X-ray triggered release of doxorubicin from nanoparticle drug carriers for cancer therapy. *Chemical Communications, 49*, 2545–2547.
3. Fologea, E., Salamo, G., Henry, R., Borrelli, M. J., & Corry, P. M. (2010). Method of controlling drug release from a liposome carrier. United State Patent: US 8808733 B2. Issued date: Aug. 19, 2014.
4. Davidson, R. A., Sugiyama, C., & Guo, T. (2014). Determination of absolute quantum efficiency of X-ray Nano phosphors by thin film photovoltaic cells. *Analytical Chemistry, 86*, 10492–10496.
5. Sanche, L. (2002). Nanoscopic aspects of radiobiological damage: Fragmentation induced by secondary low-energy electrons. *Mass Spectrometry Reviews, 21*, 349–369.
6. Sharmah, A., Yao, Z., Lu, L., & Guo, T. (2016). X-ray-induced energy transfer between nanomaterials under X-ray irradiation. *Journal of Physical Chemistry C, 120*, 3054–3060.
7. Sharmah, A., Mukherjee, S., Yao, Z., Lu, L., & Guo, T. (2016). Concentration-dependent association between weakly attractive nanoparticles in aqueous solutions. *Journal of Physical Chemistry C, 120*, 19830–19836.

Appendix A
A Monte Carlo Program Package for Predicting Physical Enhancement from Nanomaterials Under X-Ray Irradiation

Introduction

This appendix describes a theoretical modeling package developed by the Guo group at UC Davis. The package uses a Monte Carlo method to calculate physical enhancement by nanomaterials under X-ray irradiation. A Matlab version was created and published in 2007 by Guo et al. [1], and the Mathematica package was first published in 2012 by Guo et al. [2]. The current package uses the Geant4 code to calculate electron emission from atoms in nanomaterials upon X-ray absorption and the NOREC code to calculate energy deposition in water by electrons. Shapes of nanomaterials are created in a number of C++ programs, and visualization and implementation are done in homemade Mathematica programs. The whole package is called LLSG, using the initial letters of the last names of the authors who helped develop the package (Lee-Lu-Sharmah-Guo).

As shown in Chap. 2, there are several ways to model physical enhancement. The fundamental physical principles to model physical enhancement by nanomaterials under X-ray irradiation are similar to those of atoms and the bulk, which have been successfully developed over the last century. The main difference between modeling nanomaterials and other materials is that the shape of nanostructures needs to be considered. These shapes modify the energy spectrum of electrons released from the nanomaterials under X-ray irradiation. Many packages are now available to calculate physical enhancement, although some are more user-friendly than others. A brief summary of these packages is given in Sect. 2.3.3.

As stated above, Guo et al. [1–3] developed the Monte Carlo-based simulation package to calculate enhancement generated from different nanostructures when irradiated by ionizing radiation such as X-rays. Prior to the work published in 2012, calculations performed in the Guo group, with all the physical processes considered, were done with homemade programs similar to that of PENELOPE [4]. In the 2012 publication, the atomic processes were replaced with Geant4 v. 9.6, and energy deposition in water was performed using NOREC. The remaining homemade part

was transformed from the Matlab code to the C++ code that created the shapes of nanomaterials from which electrons were emitted as a result of interactions between X-rays and nanomaterials. Mathematica was chosen for its features of visualization and implementation. The combined program is the LLSG package.

The main contribution of LLSG is the use of nanomaterials of various shapes and compositions. Geant4 and other similar packages have basic shape features to predict physical enhancement of nanostructures. However, they are often not adequate to model complicated nanostructures demanded by X-ray nanochemistry research.

It is important to point out that many of the existing modeling calculations predict only energy deposition enhancement. They, including the LLSG package shown here, do not calculate the amounts of reactive oxygen species or other properties such as DNA damage or hydroxylation or polymerization reactions using the quantum chemistry methods. There are several packages such as Geant4-DNA or PARTRAC that have incorporated some chemical or biochemical features are briefly reviewed in Chap. 2, although neither package includes actual molecular (quantum) simulations to model actual biochemical reactions.

Description of the Simulation Method

The package developed by Guo et al. [2] calculates physical enhancement by nanostructures of different shapes, compositions, and assemblies. The central parts of the simulation are X-ray absorption by nanomaterials, electron emission from nanomaterials, electron transport, and energy deposition in both water and nanomaterials. Monte Carlo approach is used to follow each X-ray photon and then electron. The enhancement is defined as the ratio of energy deposition in water with nanomaterials to without nanomaterials, which gives relative enhancement. Relative enhancement is then subtracted by 1 to obtain absolute enhancement. In this simulation package, enhancement factor is the numerical value of the dose incurred in water with nanomaterials when irradiated with the flux of X-rays that deposit 1 Gy of X-rays in pure water. The units of enhancement are dose enhancement units (DEU).

Energy loss of electrons in nanomaterials is modeled after the Bethe formula [5], which does not produce more electrons as electrons traverse in materials but simply reduces the energy of the electrons of interest as they traverse the nanomaterials. If transport does not occur in the volume of interest such as in type 1 or 2 physical enhancement regions, then the deposition is not recorded. This means energy deposition events in nanomaterials are not recorded. If the deposition occurs in water, then the amount of energy deposition is recorded for enhancement determination.

Figure A.1 shows the overall flowchart. The Monte Carlo method, which has built-in Geant4 and NOREC, is interfaced with the homemade C++ program along with the nanomaterial shape features as a code in Mathematica and is linked to the C
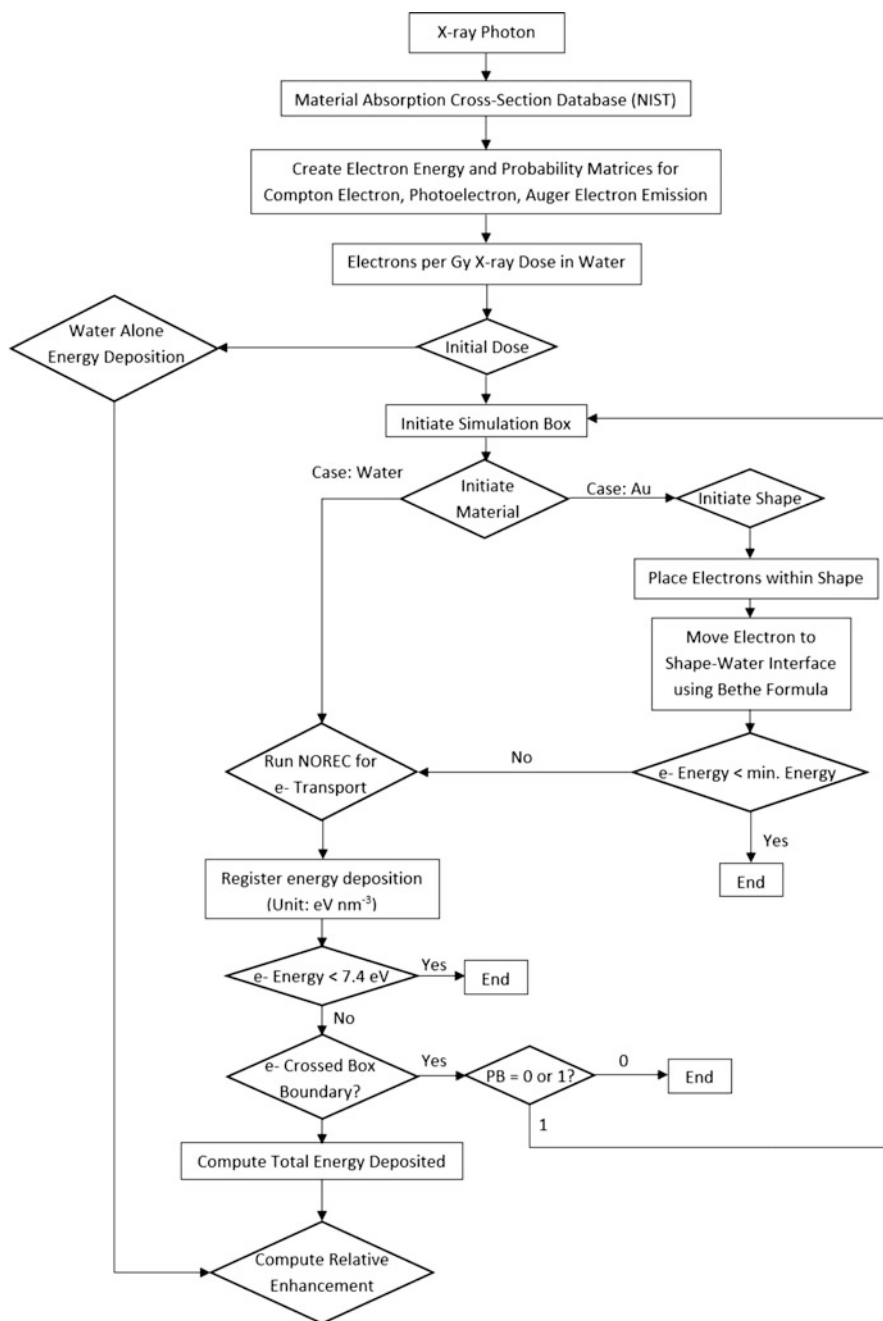
Fig. A.1 Overall flowchart. The simulation begins at X-ray absorption and creation of electrons. These electrons are then traverse nanomaterials and water. Energy deposited in water is recorded. Shapes of nanomaterials are embedded in the program. The number of electrons used in the simulation is specified at the beginning. Each electron is followed until its energy is below 7.4 eV. Enhancement value is then computed using the normalized energy deposited in water volume of interest

++ program. An executable file is then built. All implementation and visualization is carried out in Mathematica by calling the C++ generated executable.

Figure A.2 shows the production of electrons from nanomaterials upon X-ray absorption. Two processes are investigated. The first is photoelectron emission. This is handled by the code G4CrossSectionHandler/EPDL97. Once a vacancy is created, the filling of the vacancy is simulated using the Geant4 G4AtomicDeexcitation/ EADL code, which examines all the vacancies until they are pushed to the continuum.

Figure A.3 shows the flowchart for electron transport in the medium such as water. The flowchart shows the routine that is used to perform the electron transport
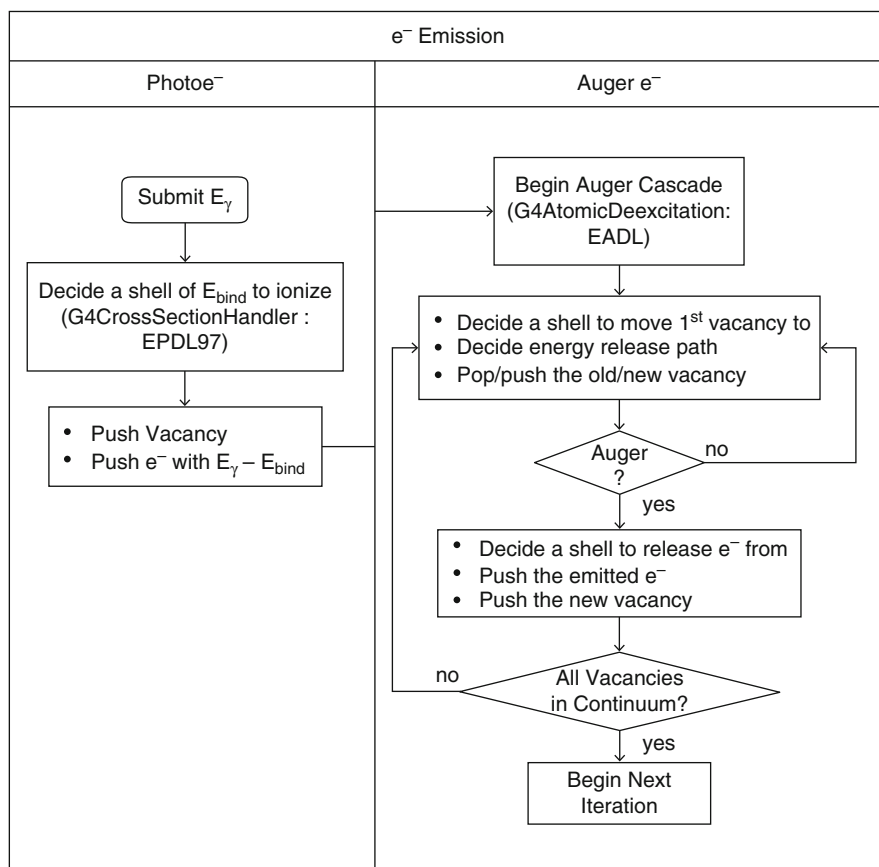
Fig. A.2 Flowchart of the algorithm that tracks the relaxation history of electrons emitted from X-ray absorbing atoms with a distribution of photoelectrons carrying different energies resulting from absorption of an X-ray photon (of energy E_γ) by an atom. Low-energy electromagnetic package from Geant4 Collaboration (G4CrossSectionHandler and G4AtomicDeexciation) available online from CERN is employed in the simulation. (Adopted from Guo et al. [2]. Copyright (2012) American Chemical Society)
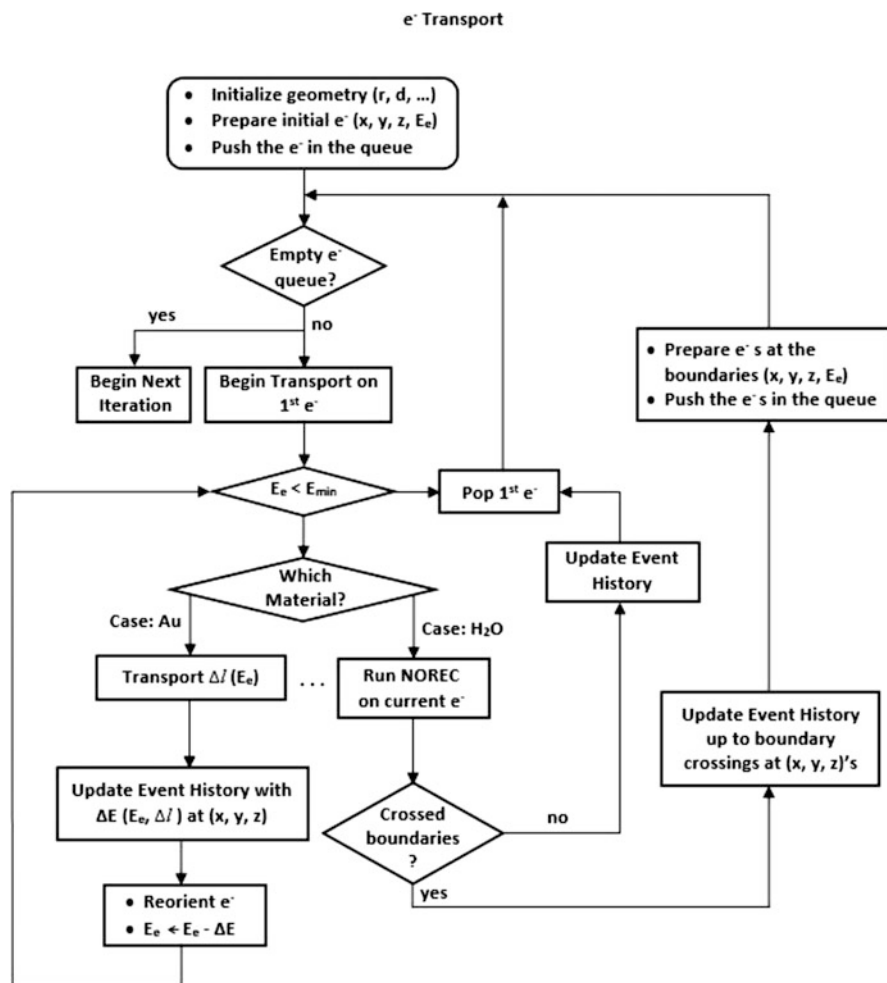
e⁻ Transport

Fig. A.3 Flowchart of the algorithm that tracks the transport of electrons in Au or other nanomaterials and in water. A geometry is defined first, which is given in the Mathematica program. Then a number of electrons are emitted from a randomly selected gold atom in the gold nanostructure. These electrons then traverse through the nanostructure and then water until their energy is lower than 7.4 eV. Bethe formula is used to calculate energy loss in the gold nanostructure or nanostructures of other compositions, and NOREC is used to calculate energy loss in water. (Adopted from Guo et al. [2]. Copyright (2012) American Chemical Society)

simulation. This routine is repeated with a fixed geometry and at different initial electron energies E_e to obtain the average energy deposition. The initial electron is placed in a chosen starting material (e.g., Au) at a random position and direction. The electron then enters the electron queue, and the transport begins. The NIST Electron Inelastic-Mean-Free-Path Database and Electron Elastic-Scattering Cross-Section Database are used in the simulation of transport in Au, and the energy

lost in each step Δl is computed using a continuous energy loss formula. Once the electron moves out of Au and reaches water, NOREC is used to simulate the transport of both primary and secondary electrons in water. These electrons are tested for boundary crossing, and the electrons that enter a material (e.g., Au) are again placed in the electron queue with the positions (x_i, y_i, z_i) and the energy E_i (i represents the ith electron) at the time of crossing. The electrons are transported individually until the electron queue is empty. Each electron is removed from the queue when the energy goes below E_{min} (7.4 eV) either in water or in other materials.

Algorithm

The program integrates Geant4 modules, NIST database, and NOREC with home-made codes in C++ and Mathematica to calculate X-ray absorption, electron generation, electron transport, and electron energy loss in nanomaterials and water with different types and shapes of material. The compiled C++ programs and header files are placed in folders together with the required codes from Geant4 and NOREC as well as the homemade Monte Carlo code that includes geometrical shapes. In the following subsections, steps taken to build the executable are described. The procedure is shown as follows.

Building the Modules

Assembling the Program Components

The first part is to add Geant4 modules into the homemade Monte Carlo program written in C++. Geant4 source file and the related data files can be downloaded from the official Geant4 website (http://geant4.cern.ch/). The Geant4 modules G4CrossSectionHandler (EPDL97) and G4AtomicDeexcitation (EADL) are incorporated into the homemade Monte Carlo program to account for ionization of the photoelectron electron and the subsequent auger cascade, respectively. The second part is to incorporate NOREC module into the homemade Monte Carlo program to simulate event-by-event history of a primary electron along with all its secondary particles in liquid water as they traverse through liquid water until a threshold energy of 7.4 eV is reached. The third part is to write a C++ program for generating different geometric shapes of nanomaterials. The program is then compiled to generate an executable file, which is called "nano." The simulation can be run and visualized using Mathematica program after installing the C++ program generated executable. A separate Mathematica routine, named varShapes, is written to call the geometric shapes written in C++. The entire program with all the source files, data files, C++ program, and the Mathematica routine for calling C++ written geometric shapes are saved in one directory called NANO.

Initialization

When running the simulation in Mathematica, first set the directory to where the program and related files are stored:

```
SetDirectory["C:\\Users\\usrn\Desktop\NANO"]
```

Then call the Mathematica routine for geometric shapes:

```
Get["varShapes.m"]
```

The command `?varShapes`*` lists the geometric shapes (and related command) that can be used for simulation. The list of shapes included in calculation is listed below.

DrawBall	DrawSixSame	GetErgPlate	GetPlateB	GetVerticesSixSame	GetVInPlate	PlotTrj
DrawCage	DrawThree	GetErgPlateB	GetTrjSolution	GetVerticesThree	GetVInPlateB	SumoutROI
DrawCylinder	DrawThreeSame	GetErgPlateT	GetTrjx	GetVerticesThreeSame	GetVInPlateT	SumROI
DrawDodeca	DrawTorus	GetErgSatellite	GetSix	GetVerticesTwo	GetVInSatellite	SumT1
DrawDodecaSame	DrawTwo	GetErgShell	GetSixSame	GetVerticesTwoSame	GetVInShell	SumT2
DrawEgg	DrawTwoSame	GetErgSix	GetThree	GetVFive	GetVInSix	toIntegerFromType
DrawFive	GetCoordPlateB	GetErgSixSame	GetThreeSame	GetVFiveSame	GetVInSixSame	TransformParamCage
DrawFiveSame	GetDensity	GetErgThree	GetTwo	GetVFlower	GetVInThree	TransformParamCylinder
DrawFlower	GetEDDx	GetErgThreeSame	GetTwoSame	GetVFour	GetVInThreeSame	TransformParamDodeca
DrawFour	GetElec	GetErgTorus	GetVCage	GetVFourSame	GetVInTorus	TransformParamEgg
DrawFourSame	GetEnh	GetErgTwo	GetVCylinder	GetVIcosa	GetVInTwo	TransformParamFive
DrawIcosa	GetEnhSameVShell	GetErgTwoSame	GetVDodeca	GetVIcosaSame	GetVInTwoSame	TransformParamFour
DrawIcosaSame	GetErgCage	GetFluxPerOy	GetVDodecaSame	GetVInCage	GetVOne	TransformParamIcosa
DrawLattice	GetErgCylinder	GetRelax	GetVEgg	GetVInCylinder	GetVOneSame	TransformParamOne
DrawOne	GetErgDodeca	GetSatErg	GetVerticesDodeca	GetVInDodeca	GetVPentakis	TransformParamPentakis
DrawOneSame	GetErgDodecaSame	GetSatShellErg	GetVerticesDodecaSame	GetVInDodecaSame	GetVPentakisSame	TransformParamPlate
DrawoutFlower	GetErgEgg	GetDodeca	GetVerticesFive	GetVInEgg	GetVPlate	TransformParamPlateB
DrawoutROI	GetErgFive	GetDodecaSame	GetVerticesFiveSame	GetVInFive	GetVPlateB	TransformParamPlateT
DrawPentakis	GetErgFiveSame	GetFive	GetVerticesFlowerFour	GetVInFiveSame	GetVPlateT	TransformParamShell
DrawPentakisSame	GetErgFlower	GetFiveSame	GetVerticesFour	GetVInFlower	GetVSatellite	TransformParamSix
DrawPlate	GetErgFour	GetFour	GetVerticesFourSame	GetVInFour	GetVShell	TransformParamThree
DrawPlateB	GetErgFourSame	GetFourSame	GetVerticesIcosa	GetVInFourSame	GetVSix	TransformParamTorus
DrawPlateT	GetErgIcosa	GetIcosa	GetVerticesIcosaSame	GetVInIcosa	GetVSixSame	TransformParamTwo
DrawSameVShell	GetErgIcosaSame	GetIcosaSame	GetVerticesOne	GetVInIcosaSame	GetVThree	
DrawSatellite	GetErgOne	GetOne	GetVerticesOneSame	GetVInOne	GetVThreeSame	
DrawShell	GetErgOneSame	GetOneSame	GetVerticesPentakis	GetVInOneSame	GetVTorus	
DrawShellHedron	GetErgPentakis	GetPentakis	GetVerticesPentakisSame	GetVInPentakis	GetVTwo	
DrawSix	GetErgPentakisSame	GetPentakisSame	GetVerticesSix	GetVInPentakisSame	GetVTwoSame	

To run the simulation for enhancement calculation, install the Monte Carlo code executable generated in C++:

```
Install["nano.exe"]
```

Generic Variables

Three variables are important to the calculation. The first is "`ntrj`" which is the number of electrons emitted from atoms in the added nanomaterials. The convergence of calculations depends on this number—the greater the number, the more convergence the calculation. However, the calculating time is also proportional to the number. If time allows, it is recommended to have the maximum number of electrons emitted from the atoms so that the calculation satisfactorily converges. The second variable is "`xray`," which is the energy of X-rays. It is monochromatic.

If a spectrum of X-rays is desired, then the enhancement at each X-ray energy has to be computed, and the results are combined to produce the result. The X-ray flux of any desired X-ray energy is automatically chosen to deposit a uniform dose of 1 Gy in water. The flux is then normalized using the number of absorptions (trajectories). The term trajectory is used here, although it means the number of electrons emitted after X-ray absorption. In many calculations, 1000 electrons are used to obtain converging results.

Two routines are critical. The first is the routine "GetEDDx," which is used to calculate the energy deposition density (unit: eV cm^{-3} Gy^{-1}) in water at different distances from the origin.

The second routine "GetEnh" is used to calculate the enhancement. Theoretically, the enhancement should be calculated as a ratio of energy deposition density using GetEDDx at locations due to a nanoparticle in water to the energy deposited in water due to water alone obtained. In practice, energy deposition in water in the presence of nanomaterials in Gy is the enhancement because the flux of X-rays is normalized to 1 Gy of X-ray-induced energy deposition in pure water.

Description of Enhancement Calculation

Below is the representative description of how an enhancement calculation is performed for a gold nanoparticle in water inside a given box.

$$\text{Relative Enhancement} = \frac{\text{Energy Deposition in presence of Nanomaterial (EDD)}}{\text{Energy Deposition by Water Alone}}$$

(A.1)

Whereas,

$$\text{Absolute Enhancement} = \frac{\text{Energy Deposition in presence of Nanomaterial (EDD)}}{\text{Energy Deposition by Water Alone}} - 1$$

(A.2)

Stepwise breakdown of general enhancement calculation for unit dose is described below:

- Compute X-ray flux per Gy of dose and energy deposited per unit dose in water.
- Obtain energy deposition due to nanomaterial (EDDx) in the unit of eV/nm^3:

  - Set material type (Au, Ag, SiO$_2$, etc.), shape, size in nm, geometry, X-ray energy in keV, box size, periodic boundary condition, number of electrons for simulation.
  - Compute volume of box in nm^3, volume of material in nm^3, and delete water volume equal to material volume.

- – Obtain tables for electron absorption cross-section (g/ cm^2) table, electron emission spectrum, and electron emission probability for "x" keV photon for the material.
- – Compute and tabulate EDDe (energy deposition for each electron).
- – Count and sum absorption and emission probability-weighted energy deposition due to all electrons (EDDX).

• Compute relative enhancement = EDDx/energy deposited per unit dose in water.

For X-ray doses other than the unit dose, energy deposition is linearly scaled for both water and the material prior to computing relative enhancement.

Examples of Calculations Calculating Physical Enhancement in Mathematica

Some of the calculation details are shown below, which can further explain how LLSG works.

Type 2 Physical Enhancement (T2PE) from Nanomaterials

For a nanomaterial that produces enhancement under X-ray irradiation, it is possible to predict either the type 1 or 2 physical enhancement. The calculation is set in a box, filled with water and desired nanostructures as shown in Fig. A.4. This box is like a unit cell in a crystal. A periodic boundary condition flag (PB) is used to specify whether the unit is a stand-alone box or if there are other boxes around it. When PB = 1, as shown in Fig. A.4, the calculation results include contribution from neighboring boxes, which means electrons leaving the box will return and reenter the

PB=0   PB=1
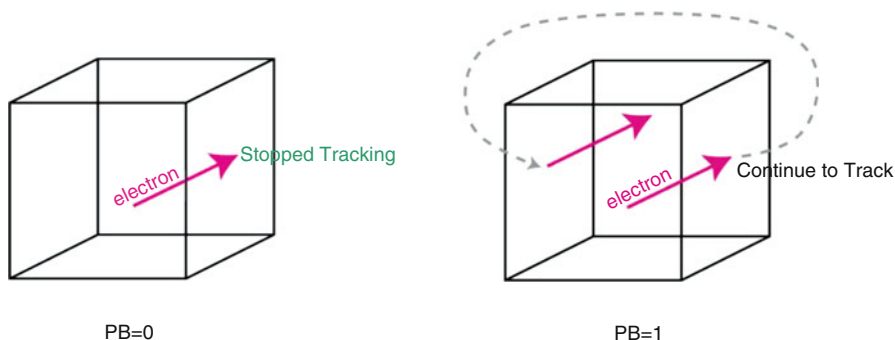
Fig. A.4 Explanation of the periodic boundary condition in enhancement calculations. When PB = 0, electrons leaving the box will not be tracked and therefore are considered to be terminated in the calculation. When PB = 1, the electron left in the box will be sent to the opposite, as if the electron never left the box, until the energy of the electron is lower than 7.4 eV

box as specified by the periodic condition until the electron energy falls below 7.4 eV. When PB = 0, the calculation is on a single nanostructure in a water cube/box, and electrons leaving the box do not return. As a result, when PB = 0, there should be no type 1 physical enhancement.

For a single spherical solid gold nanoparticle, the command to perform the calculation is:

```
Calculation Name = GetEnh[GetEDDx[{"Material Symbol"}, {Material
radius.}, X-ray Energy in keV, ntrj, Box Size., PB]]
```

The output generated can be plotted using Mathematica commands. For simplicity the output for each calculation here is shown after a specified calculation code is given.

If type 2 physical enhancement (T2PE) (i.e., PB = 0) due to a 100 nm diameter gold nanoparticle under irradiation by 40 keV X-rays is to be calculated, the command for enhancement calculation for a box size of 1000 nm (box size can be used to control or specify the nanoparticle concentration) and using 1000 trajectories is:

```
Au50T2 = GetEnh[GetEDDx[{"Au"}, {50.}, 40, 1000, 1000., 0]]
```

The results can be plotted in Mathematica using command:

```
ListPlot[Au50T2, PlotRange -> {{x1,x2}, {y1, y2}}, Frame -> True,
Joined -> True, FrameLabel -> {"x-label", "y-label"}
```
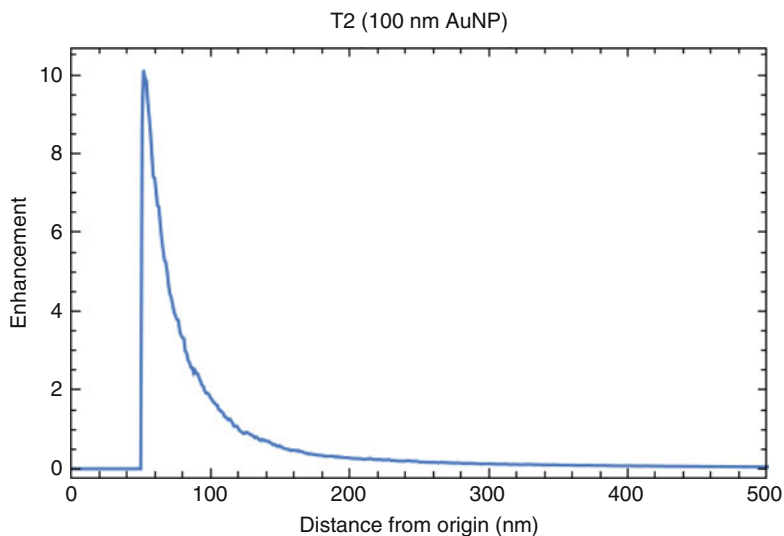

The data can also be exported as a text file using command shown below and will save the data file in "desktop" as a text file with a file name Au50T2.dat.

```
Export["C:\\Users\\PC-Name\\Desktop\\Au50T2.dat", Au50T2]
```

If one wants to calculate T2PE due to silver nanoparticle, then one has to use the "Ag" as the material symbol. For example:

```
Ag50T2 = GetEnh[GetEDDx[{"Ag"}, {50.}, 40, 1000, 1000., 0]]
```

T2 (100 nm AgNP)
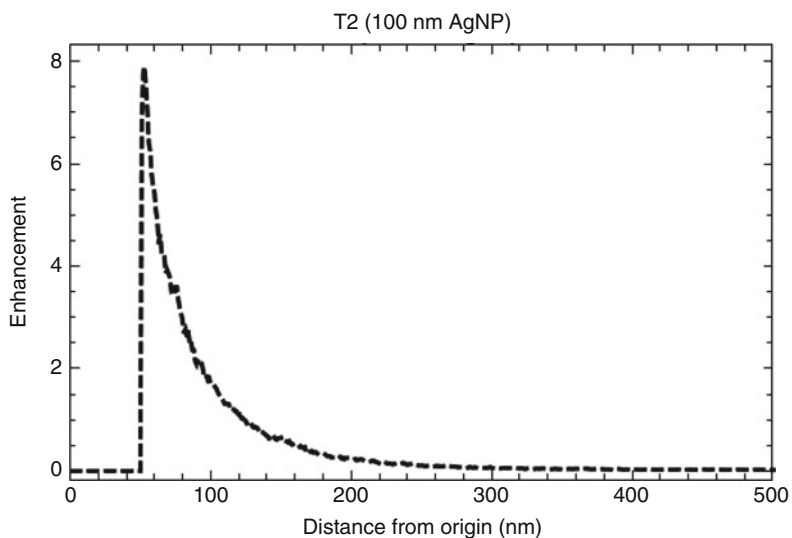
For a spherical shell of gold and with water inside and outside the shell, the command line looks like this:

```
AuShell50T2=GetEnh[GetEDDx[{"H2O", "Au"}, {50., 10.}, 40, 1000,
1000., 0]]
```

T2 (120 nm Au Nanoshell of 10 nm thick shell)
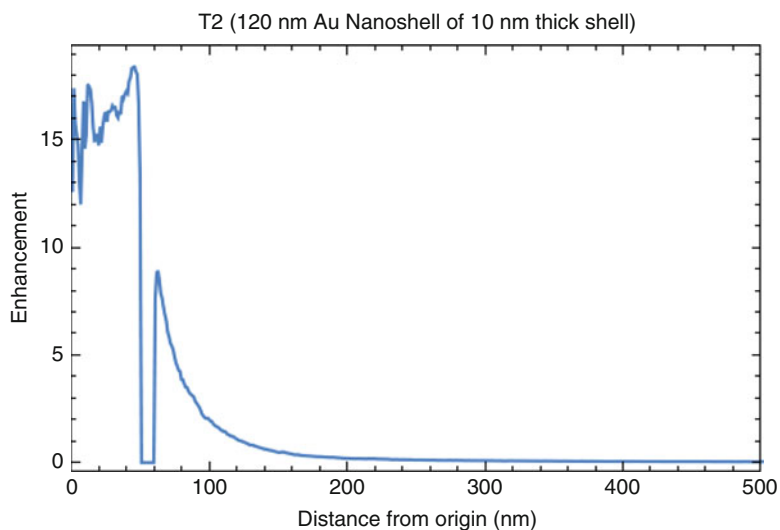
To calculate T2PE for silver nanoshell, it is sufficient to use "Ag" as material symbol, as shown below:

```
Agshell50T2 = GetEnh[GetEDDx[{"H2O", "Ag"}, {50., 10.}, 40, 1000,
1000., 0]]
```

T2 (120 nm Ag Nanoshell of 10 nm thick shell)
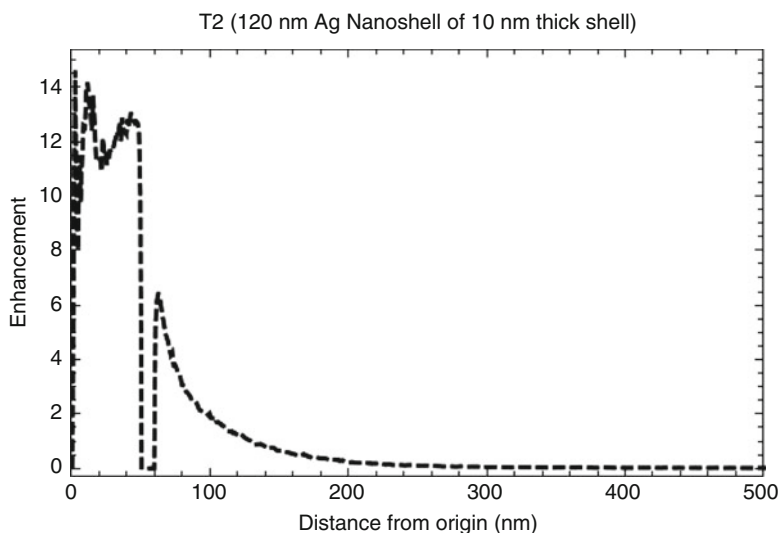
The data can either be plotted or exported as text file using similar command as shown for a gold particle above. The specified command indicates that the shell thickness is 10 nm, whereas the inner radius is 50 nm, thus representing a gold spherical shell of 120 nm in diameter. The inner radius is represented by water indicating that the nanostructure is a hollow gold shell with water interior of 100 nm diameter and outer gold layer of 10 nm thickness.

Type 1 Physical Enhancement from Nanomaterials

The type 1 physical enhancement (T1PE) is calculated by setting the periodic boundary condition flag PB to 1. For example, to determine T1PE (i.e., PB = 1) due to a 100 nm diameter gold nanoparticle under irradiation by 40 keV X-rays, the command for enhancement calculation for a box size of 1000 nm and using 1000 trajectories is:

```
Au50T1 = GetEnh[GetEDDx[{"Au"}, {50.}, 40, 1000, 1000., 1]]
```

T1 (100 nm AuNP)
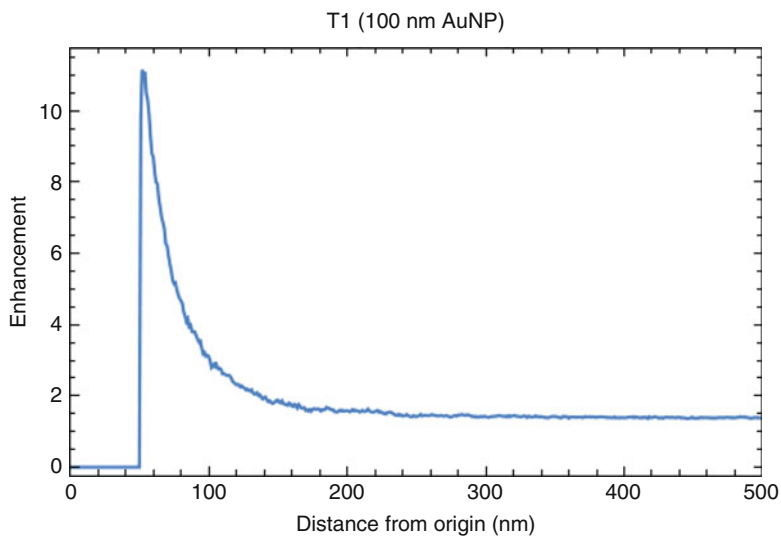
It is worth pointing out that enhancement far away from the gold nanoparticle is no longer zero. Similarly, T1PE for 120 nm Au nanoshell with 10 nm thick shell can be calculated as:

```
Aushell50T1 = GetEnh[GetEDDx[{"H2O", "Au"}, {50., 10.}, 40, 1000,
1000., 1]]
```


T1 (120 nm Au Nanoshell of 10 nm thick shell)
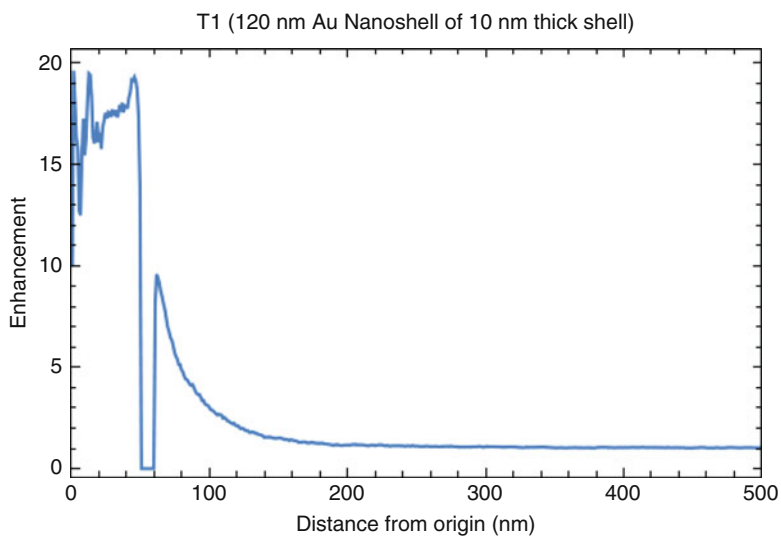
A brief list of representative calculations as implemented in Mathematica is listed in Appendix B.

Contacts

Those who are interested in getting a copy of LLSG package can send an email request to tguo@ucdavis.edu. A downloading website may be created if the demand is strong. The package is free of charge with proper attribution.

References

1. Carter, J. D., Cheng, N. N., Qu, Y. Q., Suarez, G. D., & Guo, T. (2007). Nanoscale energy deposition by x-ray absorbing nanostructures. *The Journal of Physical Chemistry. B, 111*, 11622–11625.
2. Lee, C., Cheng, N. N., Davidson, R. A., & Guo, T. (2012). Geometry enhancement of nanoscale energy deposition by X-rays. *Journal of Physical Chemistry C, 116*, 11292–11297.
3. Sharmah, A., Yao, Z., Lu, L., & Guo, T. (2016). X-ray-induced energy transfer between nanomaterials under X-ray irradiation. *Journal of Physical Chemistry C, 120*, 3054–3060.
4. Salvat, F., Fernandez-Varea, J. M., & Sempau, J. (2011). *PENELOPE-2011: A code system for Monte Carlo simulation of electron and photon transport*. Spain: Nuclear Energy Agency.
5. Joy, D., & Luo, S. (1989). An empirical stopping power relationship for low-energy electrons. *Scanning, 11*, 176–180.

Appendix B
Sample Calculations of LLSG

These are the actual examples obtained by running the Mathematica program. Therefore, no figure captions are given. Comments are given within the Mathematica program. Plots are generated after the commands are executed.

```
SetDirectory["C:\\Users\\Guo Lab\\Desktop\\NANO"]
C:\Users\Guo Lab\Desktop\NANO
Get["varShapes.m"]
Install["nano.exe"]
```
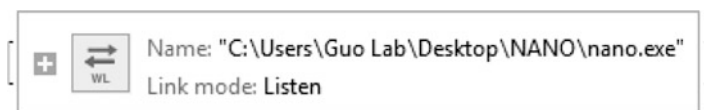


```
(*T2 Enhancement for 100 nm Au particle*)

Au50T2=GetEnh[GetEDDx[{"Au"},{50.},40,1000,1000.,0]];
ListPlot[Au50T2,PlotRange->{{0,500},Full},Frame->True,
PlotLabel->"T2 (100 nm AuNP)",Joined->True,FrameLabel->{"Distance
from origin (nm)","Enhancement"}]
```
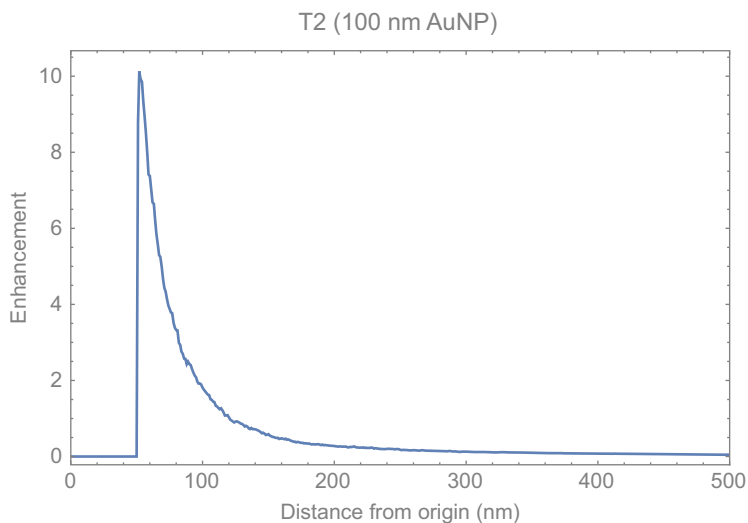
T2 (100 nm AuNP)

(*T1 Enhancement for 100 nm Au particle*)

```
Au50T1=GetEnh[GetEDDx[{"Au"},{50.},40,1000,1000.,1]];
ListPlot[Au50T1,PlotRange->{{0,500},Full},Frame->True,
PlotLabel->"T1 (100 nm AuNP)",Joined->True,FrameLabel->{"Distance
from origin (nm)","Enhancement"}]
```
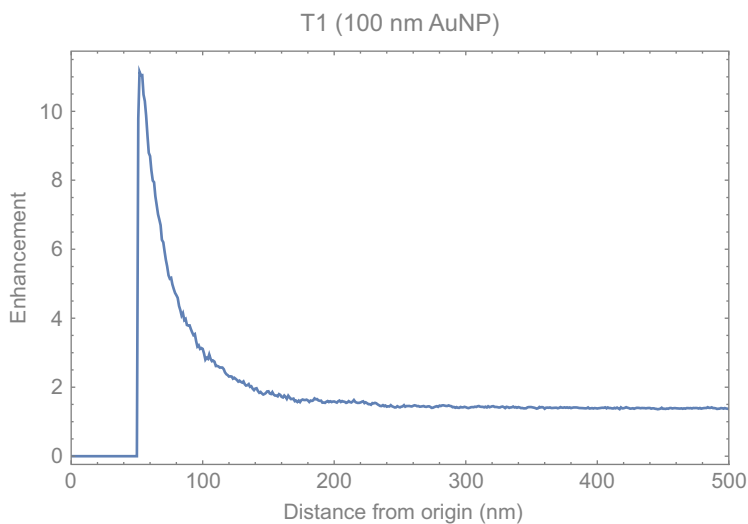
T1 (100 nm AuNP)

```
(*T2 Enhancement for 120 nm spherical Au shell with 10 nm thick shell
and 100 nm inner diameter*)

Aushell50T2=GetEnh[GetEDDx[{"H2O","Au"},{50.,
10.},40,1000,1000.,0]];
ListPlot[Aushell50T2,PlotRange->{{0,500},Full},Frame->True,
PlotLabel-> "T2 (120 nm Au Nanoshell of 10 nm thick shell)",Joined-
>True,FrameLabel->{"Distance from origin (nm)","Enhancement"}]
```


T2 (120 nm Au Nanoshell of 10 nm thick shell)
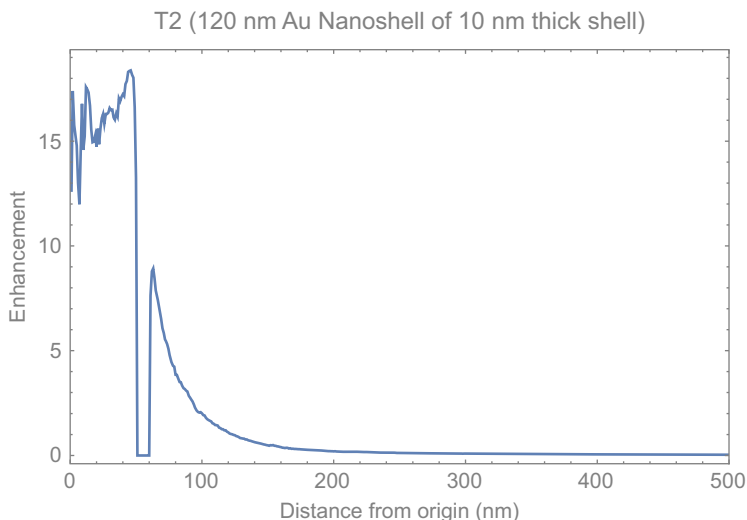
```
(* T1 Enhancement for 120 nm spherical Au shell with 10 nm thick shell
and 100 nm inner diameter*)

Aushell50T1=GetEnh[GetEDDx[{"H2O","Au"},{50.,
10.},40,1000,1000.,1]];
ListPlot[Aushell50T1,PlotRange->{{0,500},Full},Frame->True,
PlotLabel-> "T1 (120 nm Au Nanoshell of 10 nm thick shell)",Joined-
>True,FrameLabel->{"Distance from origin (nm)","Enhancement"}]
```

T1 (120 nm Au Nanoshell of 10 nm thick shell)
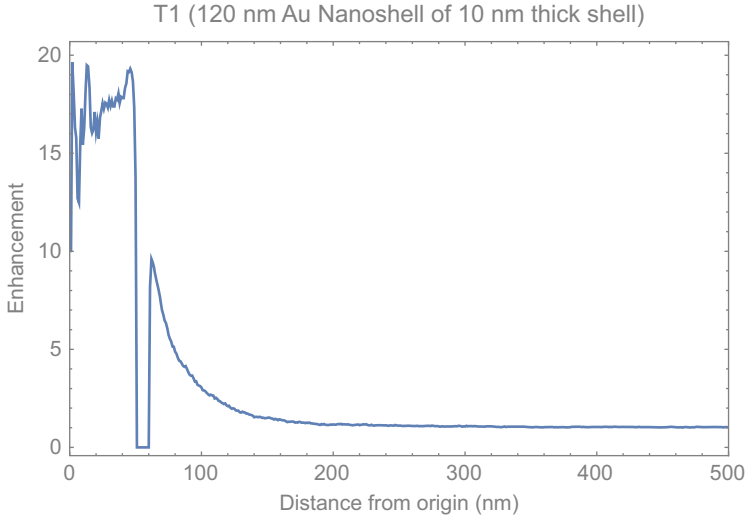
(*T2 Enhancement for 100 nm Ag particle*)

```
Ag50T2=GetEnh[GetEDDx[{"Ag"},{50.},40,1000,1000.,0]];
ListPlot[Ag50T2,PlotRange->{{0,500},Full},Frame->True,
PlotStyle-> {Black, Dashed, Thick},PlotLabel-> "T2 (100 nm AgNP)",
Joined->True,FrameLabel->{"Distance from origin
(nm)","Enhancement"}]
```
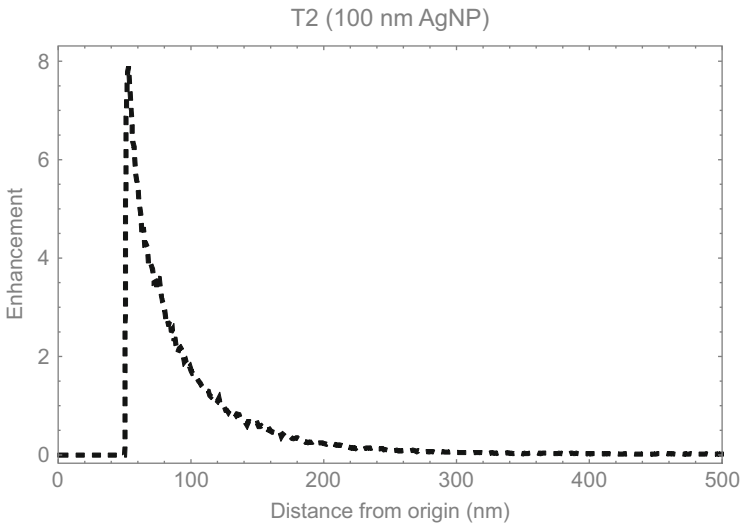
T2 (100 nm AgNP)

```
(* T1 Enhancement for 120 nm spherical Au shell with 10 nm thick shell
and 100 nm inner diameter*)
```

```
Agshell50T2=GetEnh[GetEDDx[{"H2O","Ag"},{50.,
10.},40,1000,1000.,0]];
ListPlot[Agshell50T2,PlotRange->{{0,500},Full},Frame->True,
PlotStyle-> {Black, Dashed, Thick},PlotLabel-> "T2 (120 nm Ag
Nanoshell of 10 nm thick shell)",Joined->True,FrameLabel->
{"Distance from origin (nm)","Enhancement"}]
```


T2 (120 nm Ag Nanoshell of 10 nm thick shell)
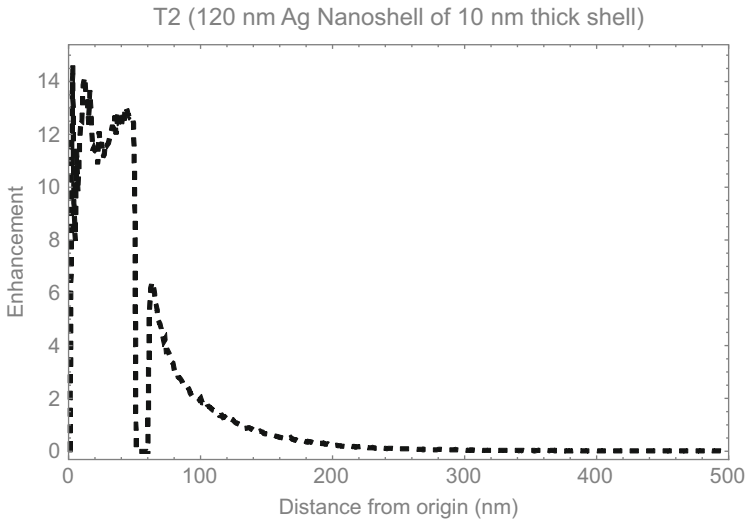
```
(*A calcium phosphate shell (CaP) satellite and a AuNP*)
r=50.0;d=10.0;R=50.0;xray=40;ntrj=1000;distRange=Range
[0.0,100.0,10.0];GraphicsRow[Table[DrawSatellite[r,d,R,L],{L,
distRange}]]
```



```
ergDepFromShell=GetErgSatellite["CaP","Shell",R,0.,r,d,xray,3.
*2*(r+d+2*R),ntrj]
0.540282
ergDepFromBall=Table[GetErgSatellite["Au","Ball",R,dist,r,d,
xray,3.*2*(r+d+dist+2*R),ntrj],{dist,distRange}]
{4.06113,3.6051,2.26051,1.98854,2.127,1.50759,1.30803,
1.12849,0.922778,0.792548,0.834466}
EnhFromShell=(ergDepFromShell/(4π/3 (r^3)))//GetEnh
0.165363
AllShellEnh={EnhFromShell,EnhFromShell,EnhFromShell,
EnhFromShell,EnhFromShell,EnhFromShell,EnhFromShell,
EnhFromShell,EnhFromShell,EnhFromShell,EnhFromShell}
```

```
{0.165363,0.165363,0.165363,0.165363,0.165363,0.165363,
0.165363,0.165363,0.165363,0.165363,0.165363}
EnhFromBall=(ergDepFromBall/(4π/3 (r^3)))//GetEnh
{1.24298,1.1034,0.691867,0.608628,0.651006,0.461423,0.400344,
0.345392,0.282432,0.242573,0.255403}
EnhFromTotal=((ergDepFromBall+ergDepFromShell)/(4π/3 (r^3)))//
GetEnh
{1.40834,1.26877,0.85723,0.773991,0.816368,0.626786,0.565707,
0.510755,0.447795,0.407936,0.420765}
ticks=Table[i,{i,0,100,10}];ListPlot[{Transpose[{ticks,
AllShellEnh}],Transpose[{ticks,EnhFromBall}],Transpose[{ticks,
EnhFromTotal}]},PlotRange->All,Joined->True,Frame->True,
FrameLabel->{"Distance from origin (nm)","Enhancement"},
PlotLegends->{"Shell","Ball (AuNP)","Total"}]
```
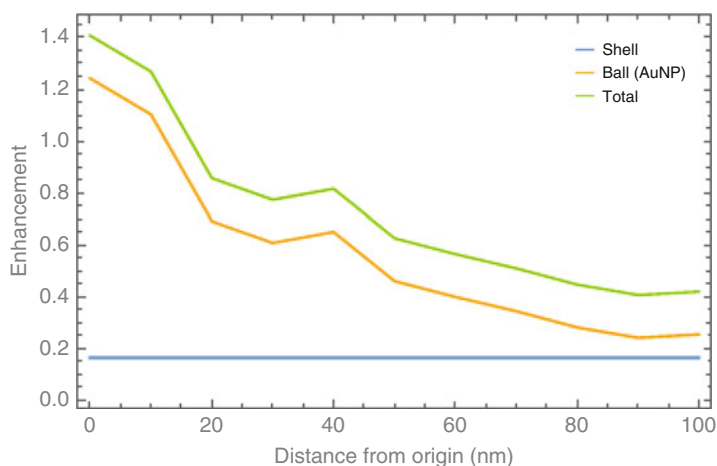


```
(*A calcium phosphate shell (CaP) satellite and multiple AuNPs*)
r=50.0;d=10.0;R=50.0;xray=40;range={1,3,6};GraphicsRow[Table
[DrawFlower[r,d,R,n],{n,range}]]
```



```
L=1.0;ergDepFromBall=GetErgFlower["Au","Ball",R,L,r,d,xray,3.
*2*(r+d+2*R),ntrj]
4.06113
ergDepFromShell=GetErgFlower["CaP","Shell",R,L,r,d,xray,3.*2*(r
+d+2*R),ntrj]
```

```
0.540282
Enh33Shell=(ergDepFromShell/(4π/3 (r^3)))//GetEnh
0.165363
Enh33Shell=((ergDepFromBall+ergDepFromShell)/(4π/3 (r^3)))//
GetEnh
1.40834
Enh33Shelln3=((3*ergDepFromBall+ergDepFromShell)/(4π/3 (r^3)))//
GetEnh
3.8943
Enh33Shelln6=((6*ergDepFromBall+ergDepFromShell)/(4π/3 (r^3)))//
GetEnh
7.62323


(*For multiple gold nanoparticles on silica shells such that total
mass of gold remains same*)

gparamHedron={50.,10.};xray=40;simbox=1000.;ntrj=1000;
OneHedronEnh=(GetErgOne["Au",gparamHedron,xray,simbox,ntrj]/
GetVinOne[gparamHedron])//GetEnh
1.52038

TwoHedronEnh=(GetErgTwo["Au",gparamHedron,xray,simbox,ntrj]/
GetVinTwo[gparamHedron])//GetEnh
2.56535

ThreeHedronEnh=(GetErgThree["Au",gparamHedron,xray,simbox,
ntrj]/GetVinThree[gparamHedron])//GetEnh
2.93275

FourHedronEnh=(GetErgFour["Au",gparamHedron,xray,simbox,ntrj]/
GetVinFour[gparamHedron])//GetEnh
3.35691

FiveHedronEnh=(GetErgFive["Au",gparamHedron,xray,simbox,ntrj]/
GetVinFive[gparamHedron])//GetEnh
3.74449

SixHedronEnh=(GetErgSix["Au",gparamHedron,xray,simbox,ntrj]/
GetVinSix[gparamHedron])//GetEnh
3.89291

IcosaHedronEnh=(GetErgIcosa["Au",gparamHedron,xray,simbox,
ntrj]/GetVinIcosa[gparamHedron])//GetEnh
5.27155

DodecaHedronEnh=(GetErgDodeca["Au",gparamHedron,xray,simbox,
ntrj]/GetVinDodeca[gparamHedron])//GetEnh
6.79264

PentakisHedronEnh=(GetErgPentakis["Au",gparamHedron,xray,
simbox,ntrj]/GetVinPentakis[gparamHedron])//GetEnh
8.46715
```
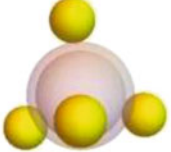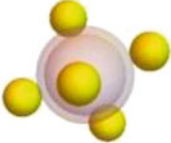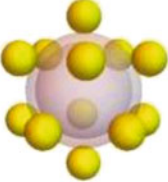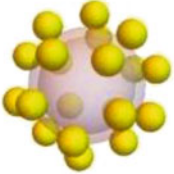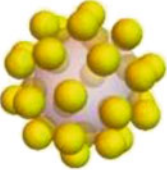
```
shellHedronEnh=(GetErgShell["Au",gparamHedron,xray,simbox,
ntrj]/GetVinShell[gparamHedron])//GetEnh
16.7901

test1=Grid[{
 {"Shape","Enhancement","Parameters"},
 {DrawOne[gparamHedron],OneHedronEnh,  Grid[{{"radius VOI =",50},
{"radius ball =",GettOne[50,10]},{"x-ray =",xray}}]},{DrawTwo
[gparamHedron],TwoHedronEnh,   Grid[{{"radius VOI =",50},{"radius
ball =",GettTwo[50,10]},{"x-ray =",xray}}]},{DrawThree
[gparamHedron],ThreeHedronEnh,   Grid[{{"radius VOI =",50},
{"radius ball =",GettThree[50,10]},{"x-ray =",xray}}]},{DrawFour
[gparamHedron],FourHedronEnh,   Grid[{{"radius VOI =",50},{"radius
ball =",GettFour[50,10]},{"x-ray =",xray}}]},{DrawFive
[gparamHedron],FiveHedronEnh,   Grid[{{"radius VOI =",50},{"radius
ball =",GettFive[50,10]},{"x-ray =",xray}}]},{DrawSix
[gparamHedron],SixHedronEnh,   Grid[{{"radius VOI =",50},{"radius
ball =",GettSix[50,10]},{"x-ray =",xray}}]},{DrawIcosa
[gparamHedron],IcosaHedronEnh,   Grid[{{"radius VOI =",50},
{"radius ball =",GettIcosa[50,10]},{"x-ray =",xray}}]},
 {DrawDodeca[gparamHedron],DodecaHedronEnh,Grid[{{"radius
VOI=",50},{"radius ball =",GettDodeca[50,10]},{"x-ray =",
xray}}]},
 {DrawPentakis[gparamHedron],PentakisHedronEnh,Grid[{{"radius
VOI=",50},{"radius ball =",GettPentakis[50,10]},{"x-ray =",
xray}}]},
 {DrawShellHedron[gparamHedron],shellHedronEnh,Grid[{{"radius
shell=",50},{"thickness =",10},{"x-ray =",xray}}]}},Frame->All]
```

Shape	Enhancement	Parameters
	1.52038	radius VOI = 50 radius ball = 44.9794 x-ray = 40
	2.56535	radius VOI = 50 radius ball = 35.7002 x-ray = 40
	2.93275	radius VOI = 50 radius ball = 31.187 x-ray = 40
	3.35691	radius VOI = 50 radius ball = 28.3353 x-ray = 40
	3.74449	radius VOI = 50 radius ball = 26.3041 x-ray = 40

Shape	Enhancement	Parameters
	3.89291	radius VOI = 50 radius ball = 24.7531 x-ray = 40
	5.27155	radius VOI = 50 radius ball = 19.6466 x-ray = 40
	6.79264	radius VOI = 50 radius ball = 16.5706 x-ray = 40
	8.46715	radius VOI = 50 radius ball = 14.1676 x-ray = 40
	16.7901	radius shell = 50 thickness = 10 x-ray = 40

```
(*For enhancement within region bound by two sheet-like arrays of
gold nanoparticles*)

Lplate=200.;hplate=5.;ndivide=5.;DrawPlateT[{Lplate,hplate,
ndivide}]
```
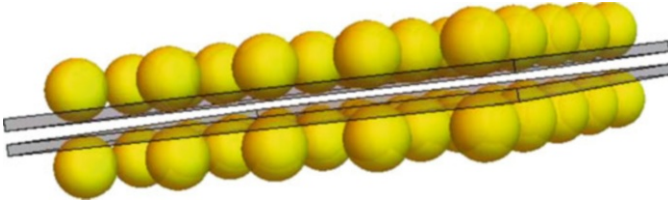


```
GetErgPlateT["Au",{Lplate,hplate,ndivide},40.,1.5*Max
[Lplate,12.+hplate],100]/GetVinPlateT[{Lplate,hplate,
ndivide}]//GetEnh
9.07521

(*Calculation and visualition of electron tracks for gold
nanoshell*)

   (*for Xray = 15 keV*)

rsh=50.0;dsh=10.0;xray=15;dose=50.;BSize=500.;shellTrj=GetTrjx
[{"H2O","Au"},{rsh,dsh},xray,dose,"TRJ","",10*2*(rsh+dsh),0];
AuShellTrj=PlotTrj[shellTrj,rsh,dsh,1/1 BSize]
```
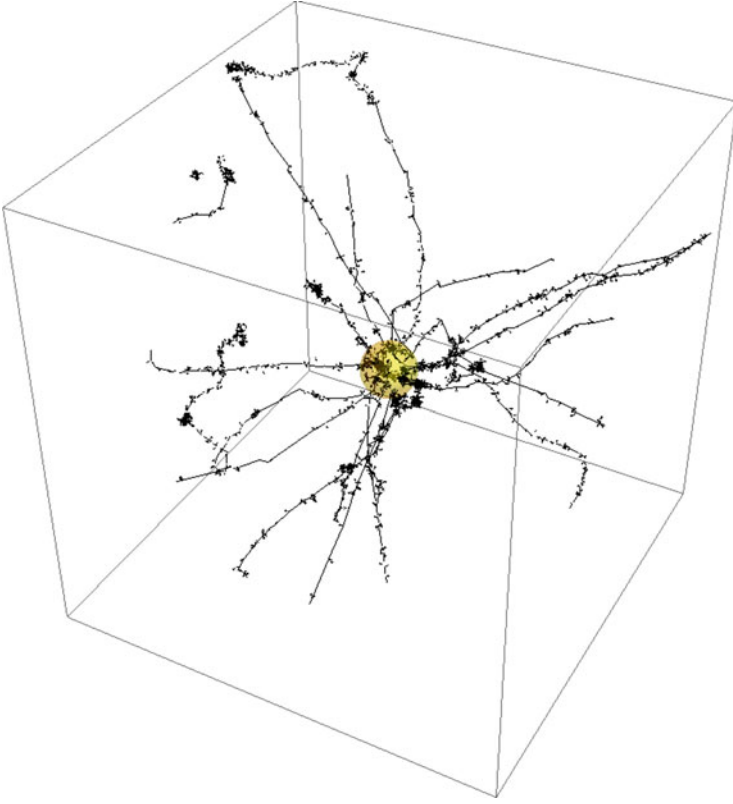
```
Show[%121,Axes->True]
```
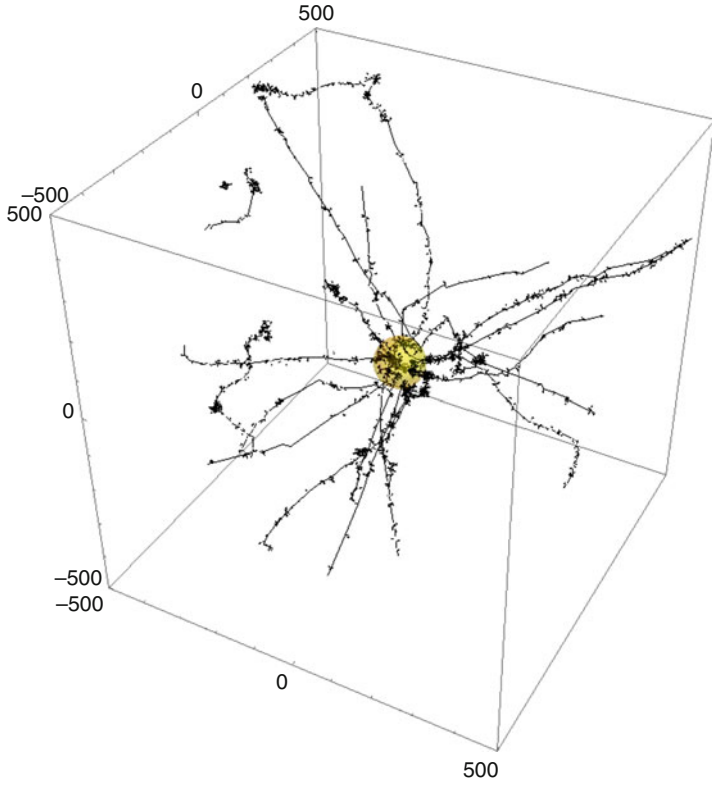
(*for Xray = 40 keV*)

```
    (*for Xray = 40 keV*)

rsh=50.0;dsh=10.0;xray=40;dose=50.;BSize=500.;shellTrj=GetTrjx
[{"H2O","Au"},{rsh,dsh},xray,dose,"TRJ","",10*2*(rsh+dsh),0];
AuShellTrj=PlotTrj[shellTrj,rsh,dsh,1/1 BSize]
```
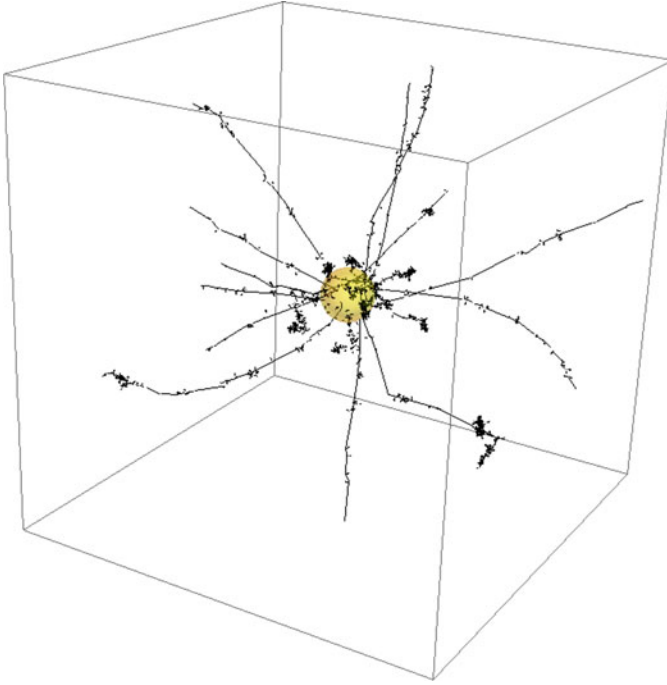
```
Show[%97,Axes->True]
```
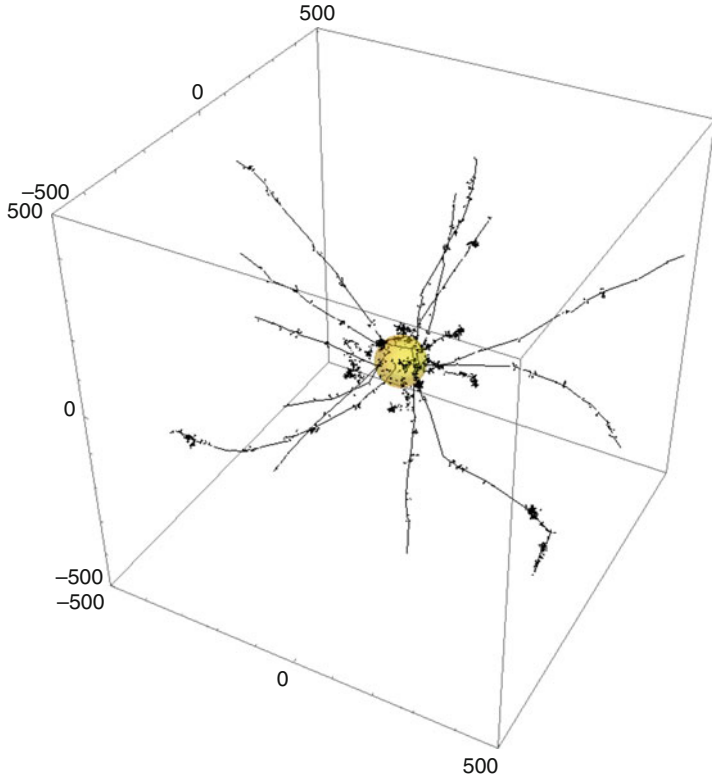
(*for Xray = 81 keV*)

```
(*for Xray = 81 keV*)

rsh=50.0;dsh=10.0;xray=81;dose=50.;BSize=500.;shellTrj=GetTrjx
[{"H2O","Au"},{rsh,dsh},xray,dose,"TRJ","",10*2*(rsh+dsh),0];
AuShellTrj=PlotTrj[shellTrj,rsh,dsh,1/1 BSize]
```

```
Show[%124,Axes->True]
```

End

Index